Outer Continental Shelf Environmental Assessment Program

Final Reports of Principal Investigators

Volume 70 **October 1990**

U.S. DEPARTMENT OF COMMERCE
National Oceanic and Atmospheric Administration
National Ocean Service
Office of Oceanography and Marine Assessment
Ocean Assessments Division
Alaska Office

U.S. DEPARTMENT OF THE INTERIOR
Minerals Management Service
Alaska OCS Region
OCS Study, MMS 90-0084

"Outer Continental Shelf Environmental Assessment Program Final Reports of Principal Investigators" ("OCSEAP Final Reports") continues the series entitled "Environmental Assessment of the Alaskan Continental Shelf Final Reports of Principal Investigators."

It is suggested that reports in this volume be cited as follows:

Greisman, P. 1985. Western Gulf of Alaska tides and circulation. U.S. Dep. Commer., NOAA, OCSEAP Final Rep. 70: 1–121.

Liu, S.-K., and J. J. Leendertse. 1987. Modeling the Alaskan continental shelf waters. U.S. Dep. Commer., NOAA, OCSEAP Final Rep. 70: 123–275.

Mofjeld, H. O., and J. D. Schumacher. 1983. Final report on residual tidal currents and processing of pressure and current records from the eastern Bering Sea Shelf. U.S. Dep. Commer., NOAA, OCSEAP Final Rep. 70: 277–349.

Muench, R. D., J. D. Schumacher, S. P. Hayes, and R. L. Charnell. 1978. Northeast Gulf of Alaska program. U.S. Dep. Commer., NOAA, OCSEAP Final Rep. 70: 351–439.

Schumacher, R. D. 1982. Transport processes in the North Aleutian Shelf. U.S. Dep. Commer., NOAA, OCSEAP Final Rep. 70: 441–588.

Coon, M. D., and G. S. Knoke. 1990. Performance and compatibility analysis of oil weathering and transport-related models for use in the environmental assessment process. U.S. Dep. Commer., NOAA, OCSEAP Final Rep. 70: 589–652.

OCSEAP Final Reports are published by the U.S. Department of Commerce, National Oceanic and Atmospheric Administration, National Ocean Service, Ocean Assessments Division, Alaska Office, Anchorage, and primarily funded by the Minerals Management Service, U.S. Department of the Interior, through interagency agreement.

Requests for receipt of OCSEAP Final Reports on a continuing basis should be addressed to:

NOAA–OMA–OAD
Alaska Office
Federal Bldg., U.S. Courthouse Room A13
222 West Eighth Ave., #56
Anchorage, AK 99513–7543

Outer Continental Shelf Environmental Assessment Program

Final Reports of Principal Investigators

Volume 70

October 1990

U.S. DEPARTMENT OF COMMERCE
National Oceanic and Atmospheric Administration
National Ocean Service
Office of Oceanography and Marine Assessment
Ocean Assessments Division
Alaska Office

U.S. DEPARTMENT OF THE INTERIOR
Minerals Management Service
Alaska OCS Region
OCS Study, MMS 90-0084

Anchorage, Alaska

The facts, conclusions, and issues appearing in these reports are based on research results of the Outer Continental Shelf Environmental Assessment Program (OCSEAP), which is managed by the National Oceanic and Atmospheric Administration, U.S. Department of Commerce, and funded (wholly or in part) by the Minerals Management Service, U.S. Department of the Interior, through an Interagency Agreement.

Mention of a commercial company or product does not constitute endorsement by the National Oceanic and Atmospheric Administration. Use for publicity or advertising purposes of information from this publication concerning proprietary products or the tests of such products is not authorized.

The content of these reports has not been altered from that submitted by the Principal Investigators. In some instances, grammatical, spelling, and punctuation errors have been corrected to improve readability; some figures and tables have been enhanced to improve clarity in reproduction.

Outer Continental Shelf Environmental Assessment Program

Final Reports of Principal Investigators

VOLUME 70 OCTOBER 1990

CONTENTS

WESTERN GULF OF ALASKA TIDES AND CIRCULATION

by

Paul Greisman

Dobrocky Seatech Ltd.
9865 West Saanich Road
P.O. Box 6500
Sidney, B.C. V8L 4M7

Final Report
Outer Continental Shelf Environmental Assessment Program
Research Unit 657

July 1985

ACKNOWLEDGMENTS

I would like to express my gratitude to the many NOAA staff who participated in this study. The tide gauges and current meters were flawlessly prepared by T. Jackson, while the CTD system was set up by S. Macri. The officers and crew of the NOAA ship FAIRWEATHER provided enthusiastic support, Bosun Herb Padilla deserves special credit for his organization of the deck. Dr. M. Jawed Hameedi was the technical authority and provided useful advice to us despite his move (concurrent with the project) from Juneau to Anchorage.

Professor Tom Royer of the Institute of Marine Science at the University of Alaska lent his experience in the region to the project. He provided all the runoff and freshwater discharge data as well as numerous references which were used in this study.

The field work was performed by Randy Kashino and Dale McCullough of Dobrocky Seatech. The data recovery rate (100%) speaks for their expertise. The data processing and tidal analyses were performed by Allan Blaskovich of Dobrocky Seatech.

This study was funded by the Minerals Management Service, U.S. Department of the Interior, through interagency agreement with the National Oceanic and Atmospheric Administration, U.S. Department of Commerce, as part of the Outer Continental Shelf Environment Assessment Program.

TABLE OF CONTENTS

LIST OF FIGURES

LIST OF FIGURES (continued)

LIST OF TABLES

1. INTRODUCTION

During June and August 1984, tidal height, current and CTD data were collected in the Western Gulf of Alaska principally as input to a numerical model of the continental shelf circulation. The model will be used to help assess the risks associated with a potential oilspill and will aid in the sale of leases by the Minerals Management Service.

The field program was carried out by Dobrocky Seatech technicians R. Kashino and D. McCullough from the NOAA vessel FAIRWEATHER. Current meters, tide gauges, acoustic releases and CTD were furnished and prepared by NOAA, while Seatech designed and fabricated the moorings. Seven tide gauges and four current meter moorings of two current meters each were deployed in June and all instruments were recovered in August. The data recovery was 100% attesting to the care taken in instrument set-up by NOAA's Pacific Marine Environmental Laboratory and the thoroughness of the field technicians. Details of the field program may be found in the field report (September 1984).

Current meters and tide gauge deployment sites are shown in Figure 1.1 along with the locations of the cross-shelf CTD transects. CTD measurements were also made at the current meter sites in order to permit computation of the internal tide modal structure. Specifics of the deployments of the tide gauges and current meters are given in Tables 1.1 and 1.2.

Aanderaa model RCM-4 current meters were used at all locations. The current meters recorded temperature, conductivity and pressure as well as speed and direction. A 15 minute sampling interval was used. Modified Savonius rotors were used on all instruments with the exception of the shallow meter at Sanak Island where an Alekseyev rotor was employed to reduce aliasing due to surface waves.

All tide gauges were Aanderaa model TG3A; a 7.5 minute sampling interval was used.

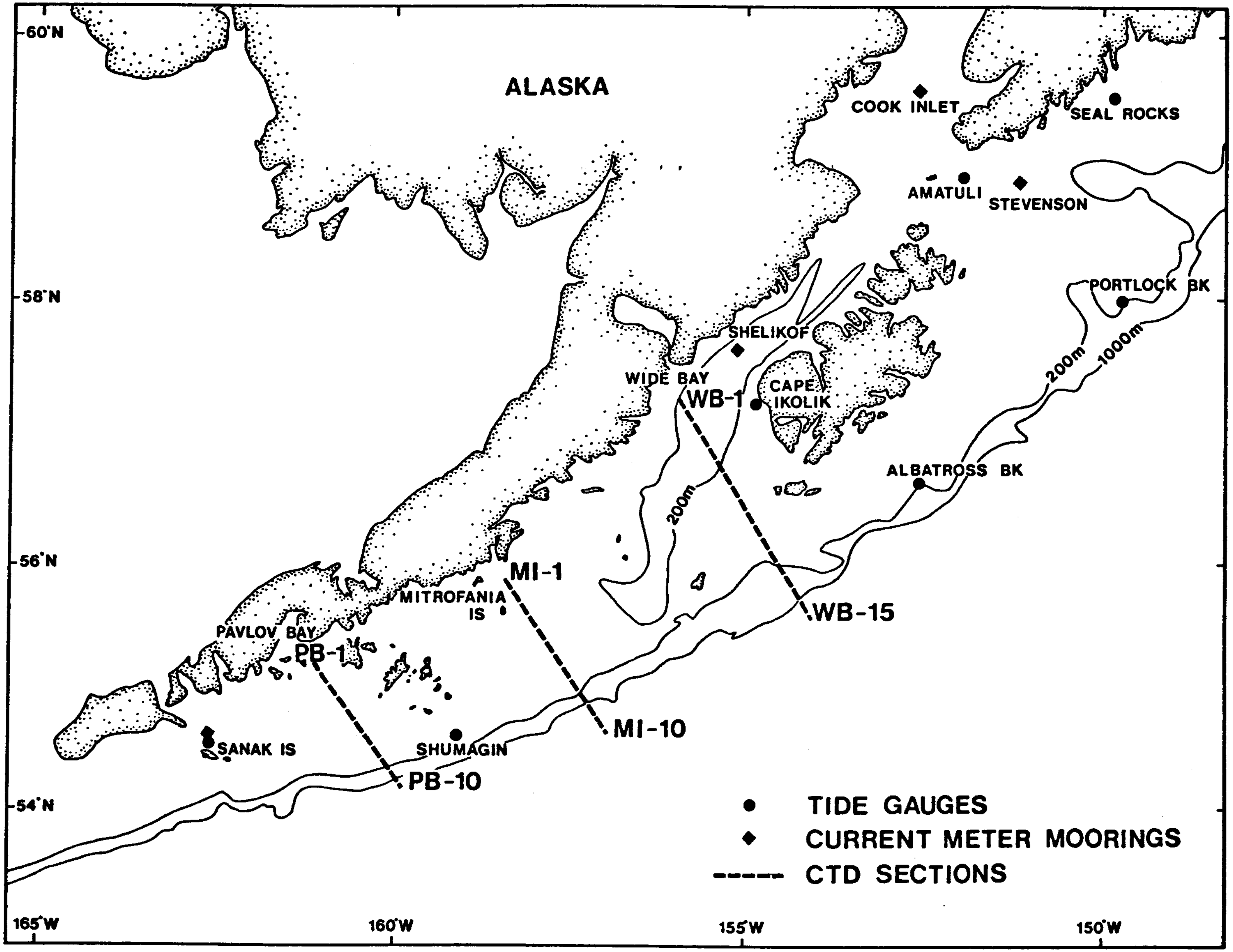

Figure 1.1 - Location of current meters, tide gauges, and CTD sections.

TABLE 1.1
CURRENT METER DEPLOYMENT SPECIFICS

Location		Water Depth (m)	C.M. No.	C.M. Depth (m)	First Good Record (GMT)		Last Good Record (GMT)	
Stevenson Entrance	58°53'73N	113	2493	45	1800	13 June 84	0945	9 Aug 84
North of								
Portlock Bk	150°57'23W		1807	75	1800	13 June 84	0945	9 Aug 84
Cook Inlet	59°35'02N	62	3710	36	0430	14 June 84	2015	9 Aug 84
	152°29'00W		3614	52	0430	14 June 84	2015	9 Aug 84
Shelikof Strait	57°39'00N	250	3127	40	2130	14 June 84	1400	10 Aug 84
	155°03'33W		1812	150	2130	14 June 84	1400	10 Aug 84
Sanak								
(Deer Island)	54°35'25N	49	3185*	18.5	1000	16 June 84	0445	13 Aug 84
	162°43'77W		1987	38.5	1000	16 June 84	0445	13 Aug 84

All current meters were equipped with temperature, conductivity and pressure sensors.

Sampling interval was 15 minutes on all current meters.

*This current meter was modified to utilize the Alekseyev rotor now available from Aanderaa.

TABLE 1.2
TIDE GAUGE DEPLOYMENT SPECIFICS

Location			Depth (m)	T.G. No.	First Good Record (GMT)		Last Good Record (GMT)	
Albatross Bank	56°33'48N	152°26'95W	163	107	1200	12 June 84	0407.5	8 Aug 84
Portlock Bank	58°01'03N	149°29'58W	174	205	0100	13 June 84	1615	8 Aug 84
Seal Rocks	59°29'93N	149°29'57W	112	188	1000	13 June 83	0430	9 Aug 84
Amatuli Island	59°00'13N	151°50'03W	168	87	2230	13 June 84	1400	9 Aug 84
Cape Ikolik	57°15'00N	154°45'30W	62	120	0100	15 June 84	2315	10 Aug 84
Shumagin (Simeonof Is)	54°31'93N	158°58'08W	192	119	2000	15 June 84	1907.5	11 Aug 84
Sanak (Deer Is)	54°35'25N	162°43'77W	48	209	1000	16 June 84	0452.5	13 Aug 84

Sampling interval was 7.5 minutes for all tide gauges.

The current meters were deployed on taut line moorings of 1/4" 7 x 19 wire rope. Buoyancy was provided at the top of the mooring, above the lower current meter and above the acoustic release. Train wheels were used for anchors. Tide gauge moorings consisted of concrete blocks with recesses for the tide gauge. Sketches of each mooring type are presented in Figures 1.2 through 1.6. All moorings were suspended in the water column then gently lowered to the bottom with a device which releases upon loss of tension.

1.1 DATA REDUCTION

The Aanderaa data tapes were translated and converted to physical units using calibrations supplied by NOAA. Salinities were computed from temperature, conductivity and pressure with the UNESCO (1980) formula.

Time series plots were produced for each instrument and are available in our Data Report (Greisman 1984). Also produced were progressive vector diagrams, stick plots and histograms. These products aided in quality control as well as in forming a general impression of the data set.

Harmonic analyses of the tide gauge data and tidal stream analyses of the current meter data were performed using the methods of Foreman (1977 and 1978). The complete analyses are presented in Appendix 1.

Tables 1.3 and 1.4 show the tidal analyses for the largest constituents for the heights and currents respectively. Greenwich phase is used throughout. In the tidal stream analyses MAJ represents the amplitude of the semi-major axis of the tidal ellipse; MIN represents the semi-minor axis of the ellipse. The sign of MIN indicates the sense of rotation; positive implies anti-clockwise and negative clockwise. INC is the orientation of the northern semi-major axis of the ellipse anti-clockwise from east (mathematical rather than geographic convention). G is the Greenwich phase and represents the time at which the rotating velocity vector coincides with the northern semi-major axis of the ellipse.

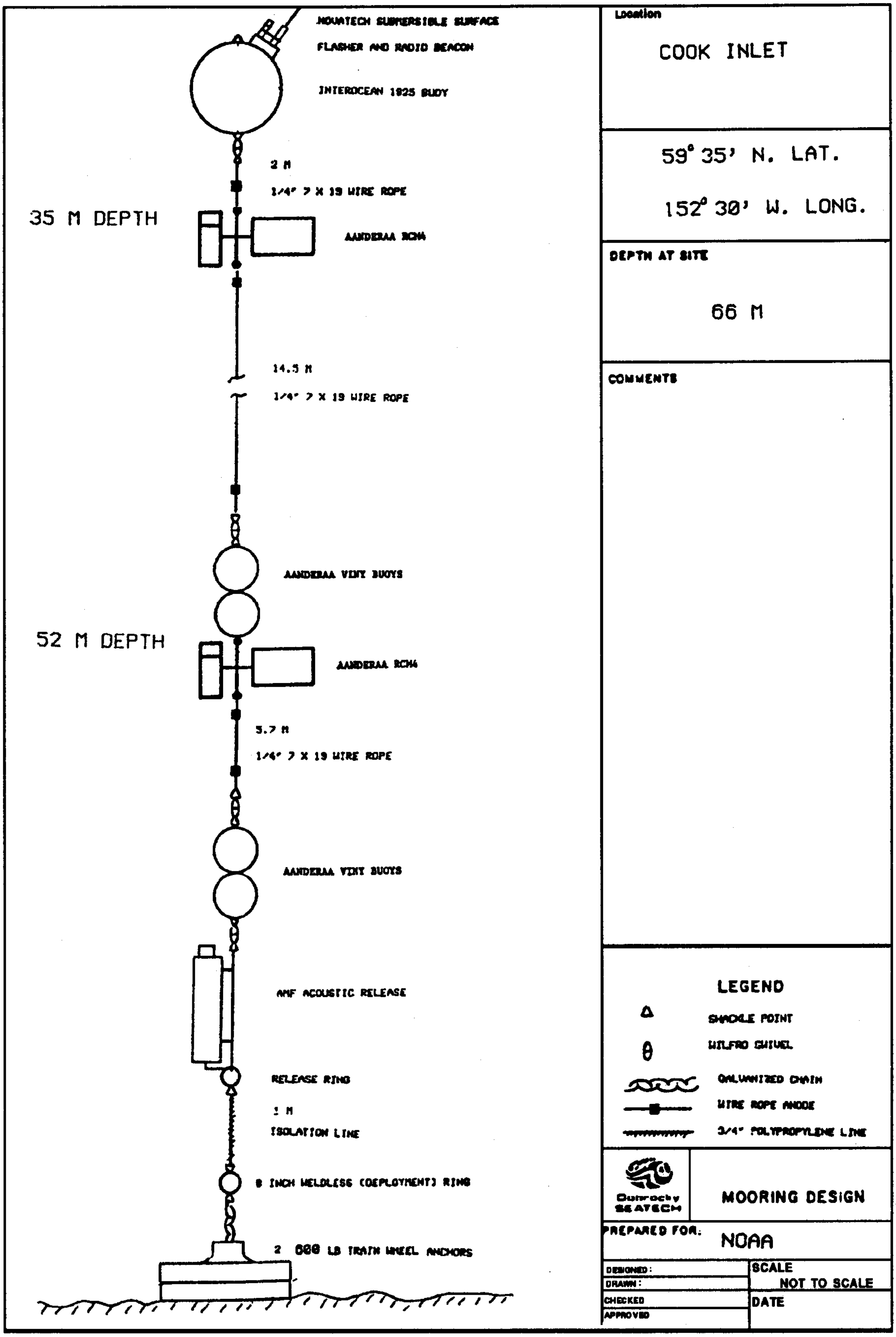

Figure 1.2 - Mooring configuration at Cook Inlet.

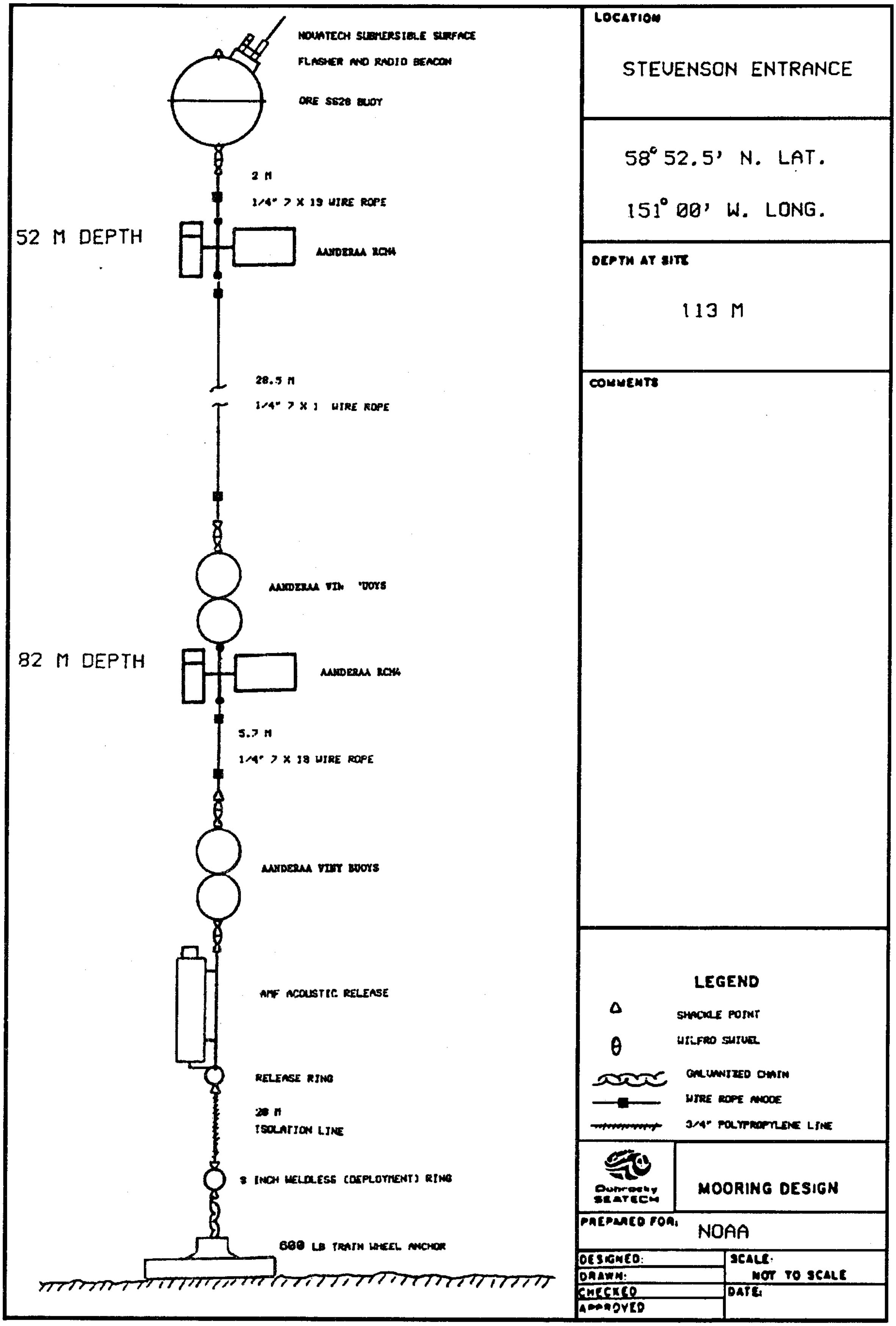

Figure 1.3 - Mooring configuration at Stevenson Entrance.

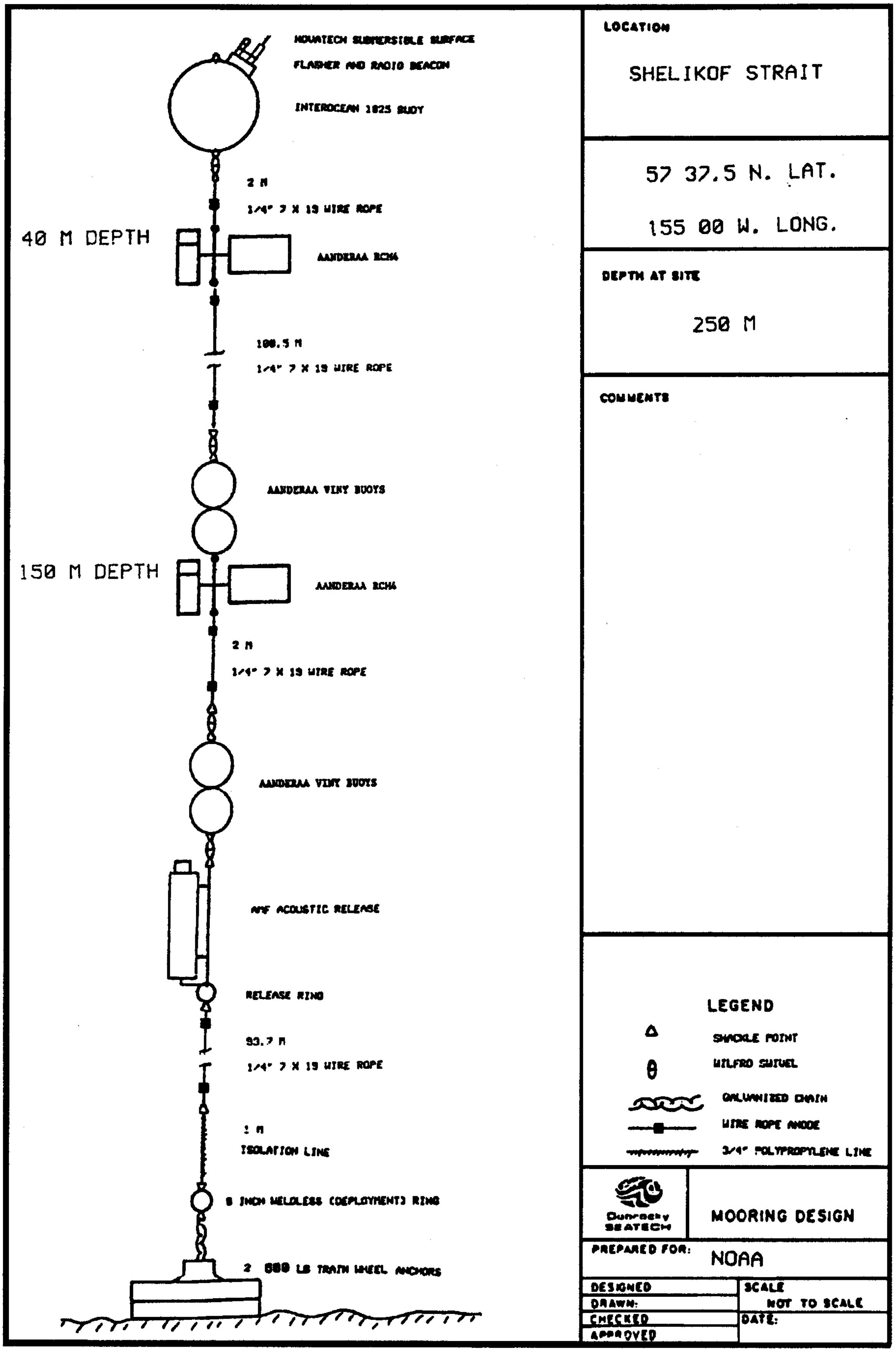

Figure 1.4 - Mooring configuration at Shelikof Strait.

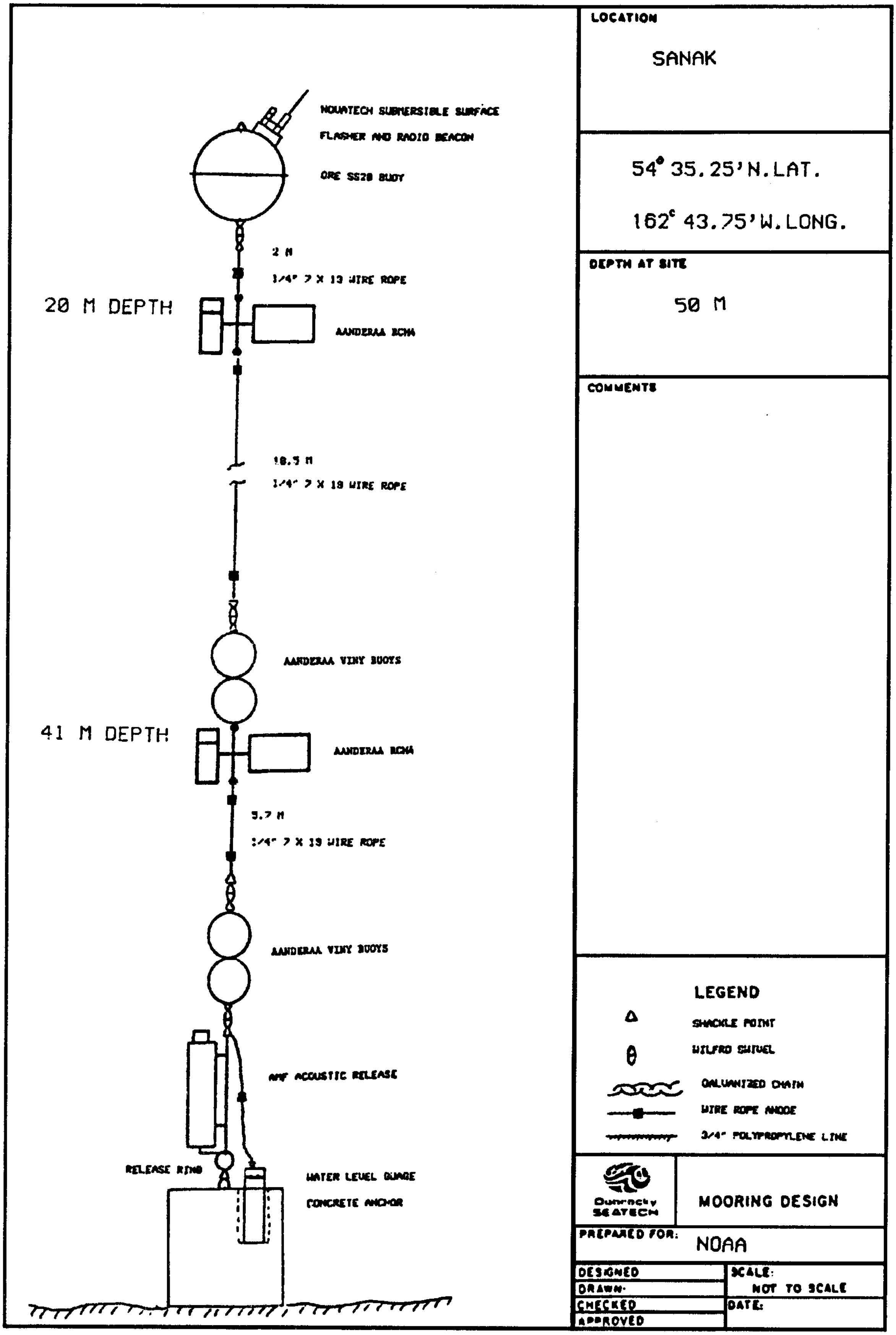

Figure 1.5 - Mooring configuration at Sanak.

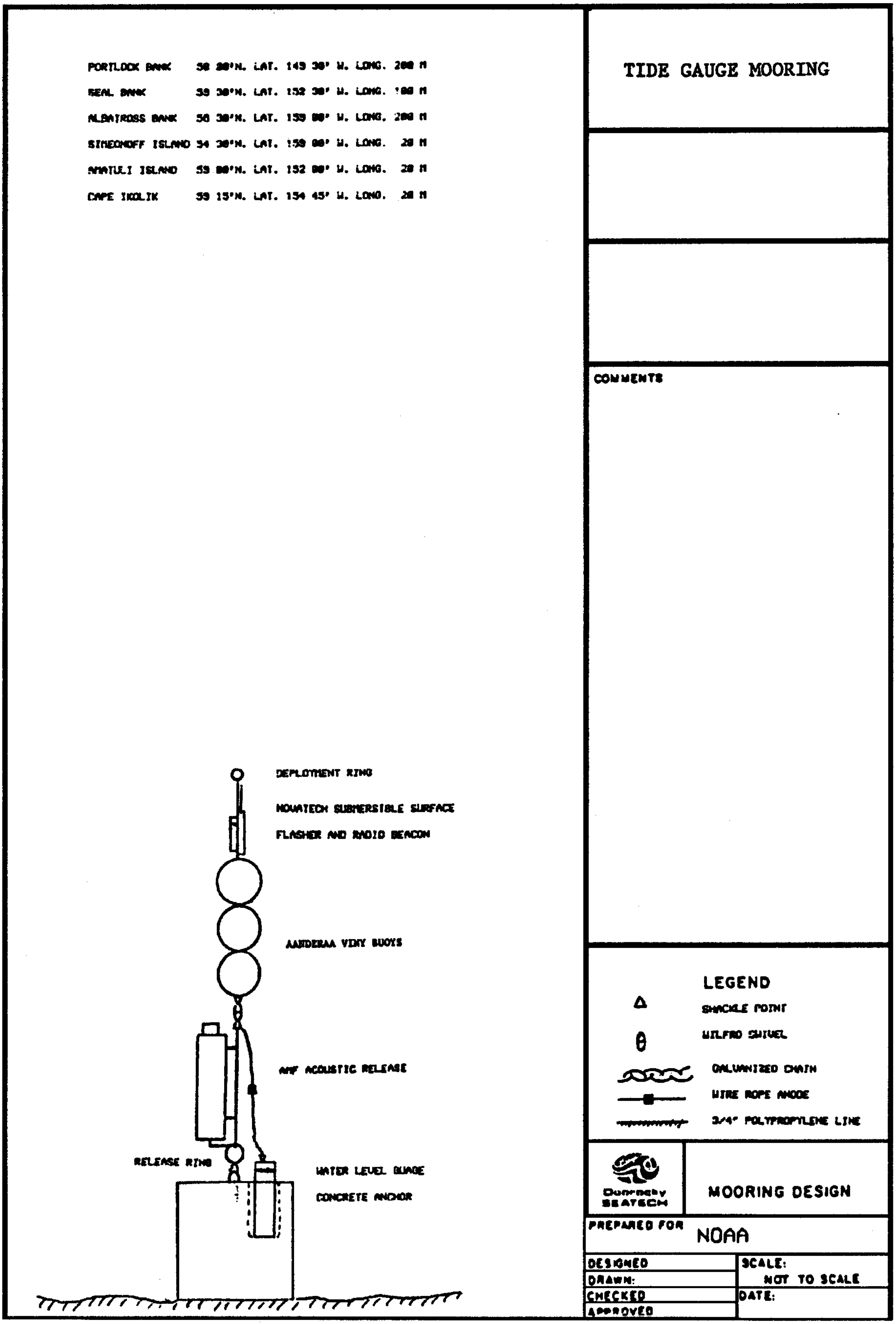

Figure 1.6 - Mooring configuration for the tide gauges.

TABLE 1.3
MAJOR TIDAL CONSTITUENTS
AMPLITUDES (METRES) AND GREENWICH PHASES

	Principal Lunar Diurnal		Soli-Lunar Declinational (Divisional)		Larger Lunar Elliptic (Semi-Diurnal)		Principal Lunar (Semi-Diurnal)		Principal Solar (Semi-Diurnal)		
STATION	O_1		K_1		N_2		M_2		S_2		$F = \frac{K_1 + O_1}{M_2 + S_2}$
	A	G	A	G	A	G	A	G	A	G	
Sanak	.2691	269.93	.5041	293.03	.1331	314.13	.6306	330.12	.1579	003.55	0.981
Portlock Bk.	.2916	252.72	.5572	276.60	.1902	278.57	1.0140	293.48	.2499	334.36	0.672
Seal Rk.	.2846	256.09	.5431	279.69	.2216	274.53	1.1975	289.94	.3016	331.25	0.552
Cape Ikolik	.3070	265.70	.5928	289.37	.2770	303.52	1.3889	317.00	.3757	001.87	0.510
Shumagin	.2769	266.50	.5175	289.08	.1371	302.39	.6713	317.25	.1690	353.99	0.945
Albatross Bk.	.2905	255.04	.5528	278.29	.1698	279.03	.8940	294.57	.2171	334.37	0.759
Amatuli Is.	.3082	262.95	.5834	287.24	.3011	297.41	1.5548	312.60	.4184	357.54	0.452

TABLE 1.4
TIDAL STREAM ANALYSES
INCLUDING TIDAL HEIGHT ANALYSES FROM NEARBY TIDE GAUGES

		O_1						K_1					
STATION	DEPTH	MAJ	MIN	INC	G	A	G	MAJ	MIN	INC	G	A	G
Stevenson	54	3.7	-0.78	98	14			6.6	-2.2	101	41		
Stevenson	82	3.5	-1.7	91	22			6.4	-3.5	108	36		
Amatuli I						.308	263					.583	287
Shelikof Str.	46	1.8	-0.13	39	227			3.4	0.08	41	244		
Shelikof Str.	157	1.5	-0.06	49	205			3.0	-0.15	48	226		
C. Ikolik						.307	266					.593	289
Sanak	20	2.3	-1.1	177	105			4.0	-2.0	167	145		
Sanak	41	3.5	-0.90	1	274			7.1	-3.1	166	136		
Sanak						.269	270					.504	293
Cook In.	35	9.5	-0.70	79	224			19.0	-3.5	77	244		
Cook In.	52	8.0	-0.07	69	220			17.6	-3.4	78	239		

		N_2						M_2						S_2					
STATION	DEPTH	MAJ	MIN	INC	G	A	G	MAJ	MIN	INC	G	A	G	MAJ	MIN	INC	G	A	G
Stevenson	54	5.9	1.5	94	51			30.2	0.62	102	66			10.1	0.59	97	112		
Stevenson	82	6.0	-0.3	94	55			36.3	1.65	91	76			11.6	1.10	84	126		
Amatuli I						.301	297					1.555	313					.418	358
Shelikof Str.	46	2.5	0.7	39	230			13.8	-.02	40	251			4.5	-.03	41	297		
Shelikof Str.	157	3.1	1.0	46	233			14.9	.60	43	248			4.3	.14	47	296		
C. Ikolik						.277	304					1.389	317					.376	002
Sanak	20	0.7	-0.3	90	269			3.1	.47	113	285			1.1	-.11	77	336		
Sanak	41	0.8	-0.5	64	239			4.1	1.08	90	253			1.5	-.61	30	267		
Sanak						.133	314					.631	330					.158	004
Cook In.	35	14.4	-2.4	81	285			73.5	-8.9	78	308			19.8	-2.5	84	352		
Cook In.	52	13.2	-3.6	83	279			59.8	-2.0	74	305			14.8	-1.8	84	346		

NOTE: Semi-major and semi-minor ellipse axes in CMS^{-1}; INC is inclination of the northern semi-major axis anti-clockwise from east; G is the Greenwich phase A tidal height amplitude in metres.

The CTD data were translated, calibrated versus bottle casts, and vertical profiles plotted for each cast. The profiles are presented in the data report. Listings of roughly 1 m depth averaged values were produced for use in preparing cross sections.

More details on the data reduction are available in the data report.

1.2 OVERVIEW OF THE DATA

98.6% of the variance in the tide gauge records is due to tidal oscillations while 67% of the variance in the current meter records is tidal. In addition, the mean flows recorded at the current meters were about 4 cm s^{-1}, i.e. roughly an order of magnitude smaller than the tidal currents. Clearly the flow kinetic energy in the region is dominated by tides during the summer. However, from our data set we cannot address the winter period when easterly gales may have a great influence upon circulation on the shelf.

1.3 ANALYSES UNDERTAKEN

In Section 2 of this report conclusions based upon the distribution of properties (the CTD data) are presented and discussed. These include computations of dynamic height topographies and geostrophic current speeds and directions.

Section 3 comprises analyses of the tidal oscillations. Cotidal charts, tidal energy propagation and internal tides are discussed.

Section 4 deals with the non-tidal, specifically the subtidal, oscillations. We found ourselves somewhat limited in these analyses because of the relatively short period of measurement. The two month period between June and August 1984 is, of course, too short to address seasonal signals such as gross changes in the wind field and seasonal runoff variations. Nevertheless, aspects of the forcing of long period oscillations in the Western Gulf of Alaska, particularly Shelikof Strait are discussed.

2. PROPERTY FIELDS

(Salinity, Temperature, Density, Dynamic Topography)

The results of the June and August 1984 CTD surveys are discussed in this section. Field methods, calibration and quality control of the data were presented in the data report. It should be borne in mind that these data are of fair quality only probably due to the poor condition of the CTD winch slip rings.

2.1 CROSS SECTIONS

Cross sections of temperature, salinity and sigma-t were prepared for the Pavlov Bay, Mitrofania Island and Wide Bay sections for both June and August. The locations of these sections are shown in Figure 2.1. Salinity, temperature and sigma-t sections are presented in pairs for June, then August to enhance the reader's appreciation of temporal changes. It should be remembered that the data are non-synoptic, the occupation of stations along each section having consumed about one day.

2.1.1 Temperature

The most striking feature of the temperature sections (Figures 2.2, 2.3, 2.8, 2.9, 2.14, 2.15) is the pronounced warming of the surface layers to about 50 m depth between June and August. Surface temperature increased about 5° C during this period both over the continental shelf and slope. Since the measured mean flows are on the order of 5 cm s^{-1}, the temperature field would have been advected only about 200 km between June and August. The warming of the surface layers is, therefore, almost certainly due to local insolation. The water column is everywhere temperature stratified below a few meters depth with the exception of the Trinity Islands Bank shown in the Wide Bay Section. Here the temperature is nearly constant with depth in both June and August likely due to strong

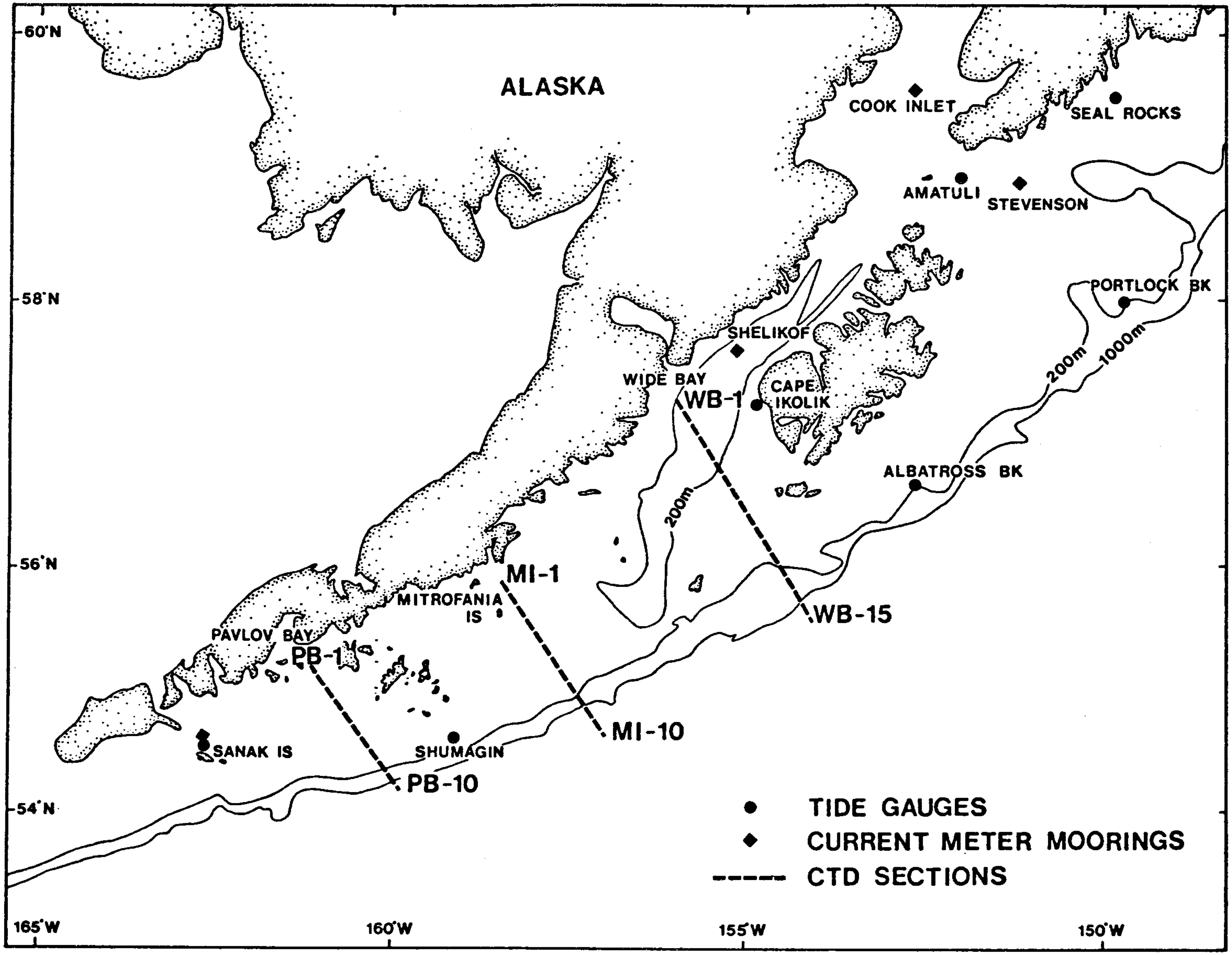

Figure 2.1 - Location chart for salinity, temperature, and sigma-t cross sections.

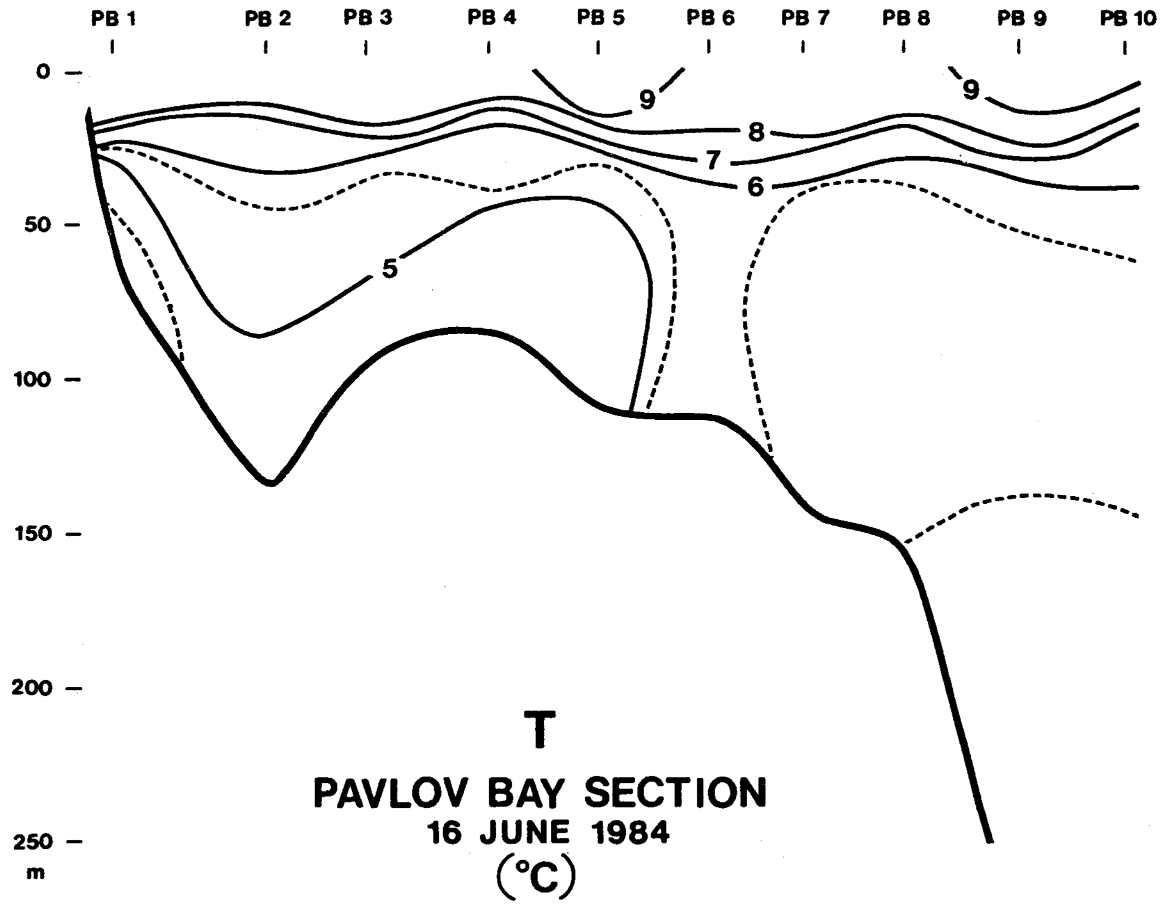

Figure 2.2 - Temperature, Pavlov Bay, June.

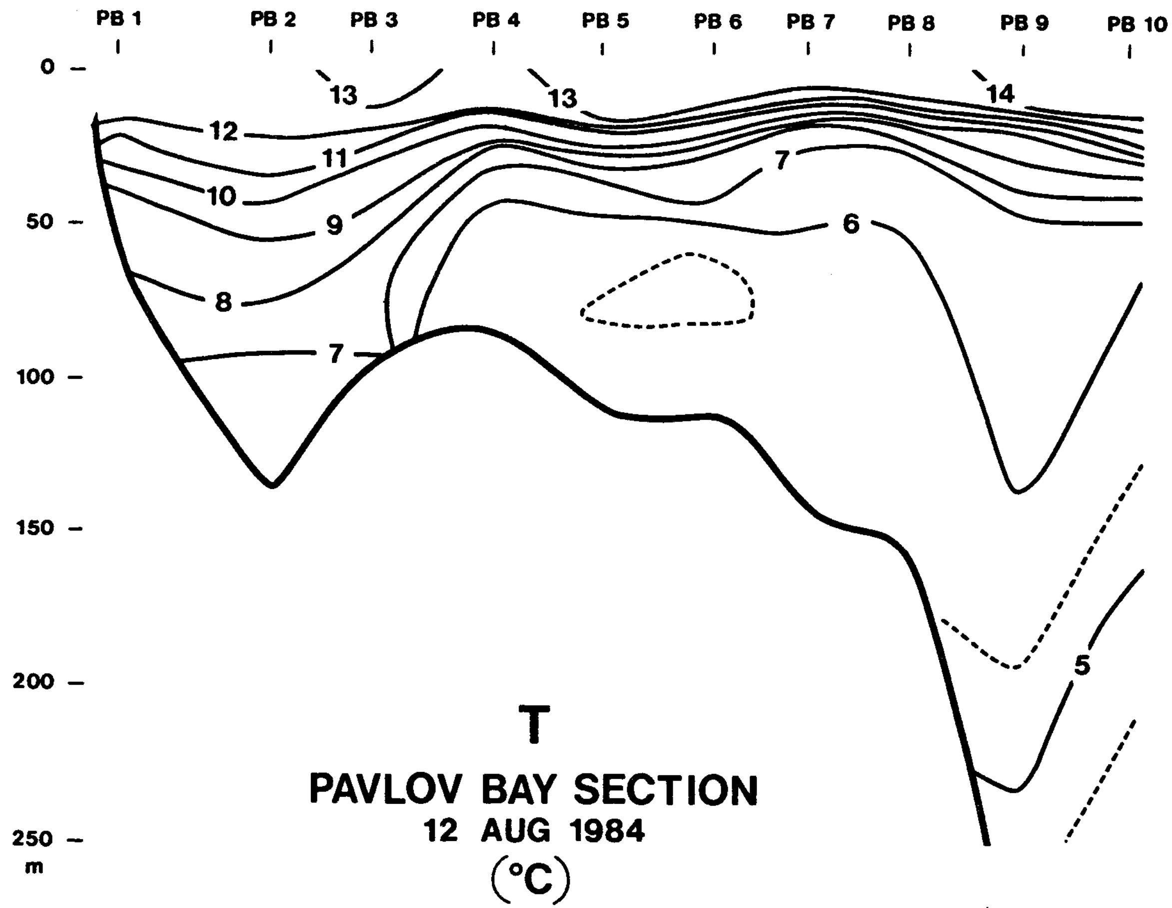

Figure 2.3 - Temperature, Pavlov Bay, August.

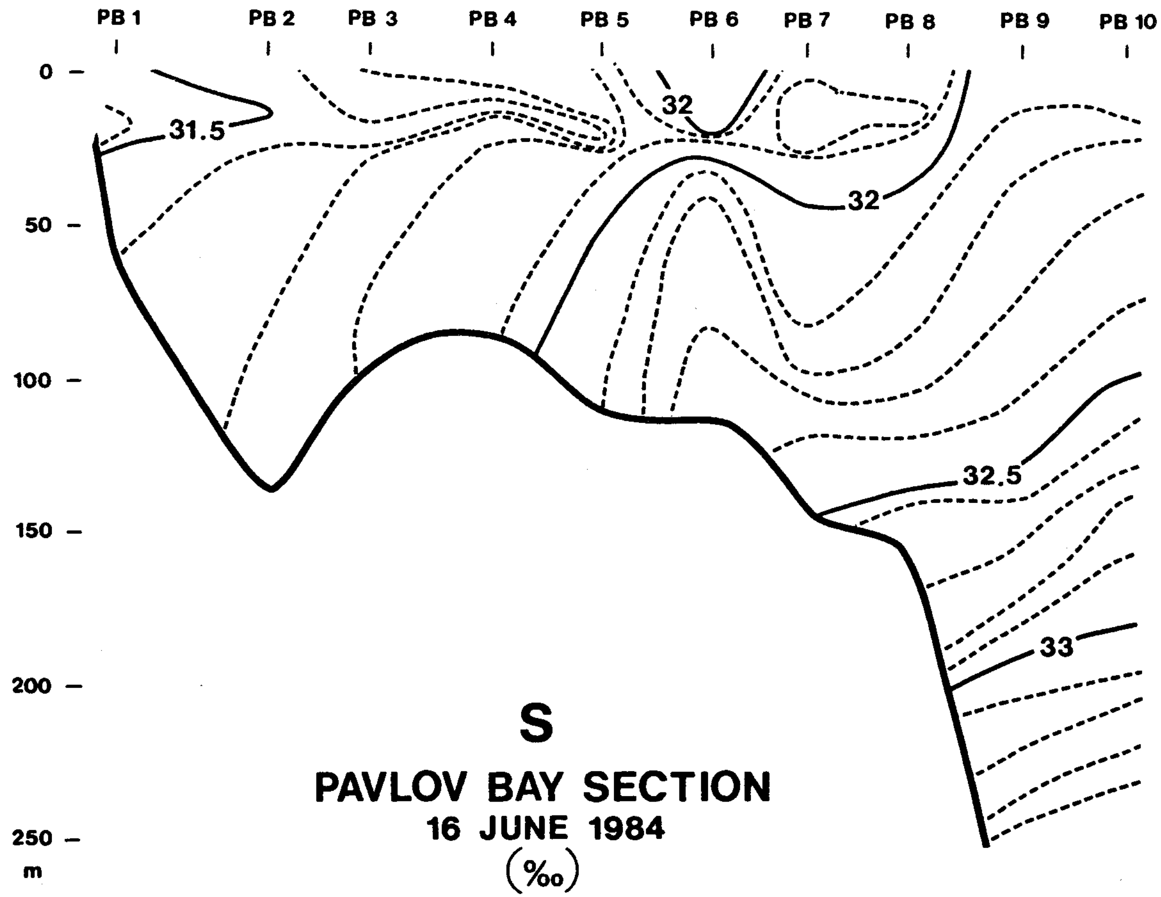

Figure 2.4 - Salinity, Pavlov Bay, June.

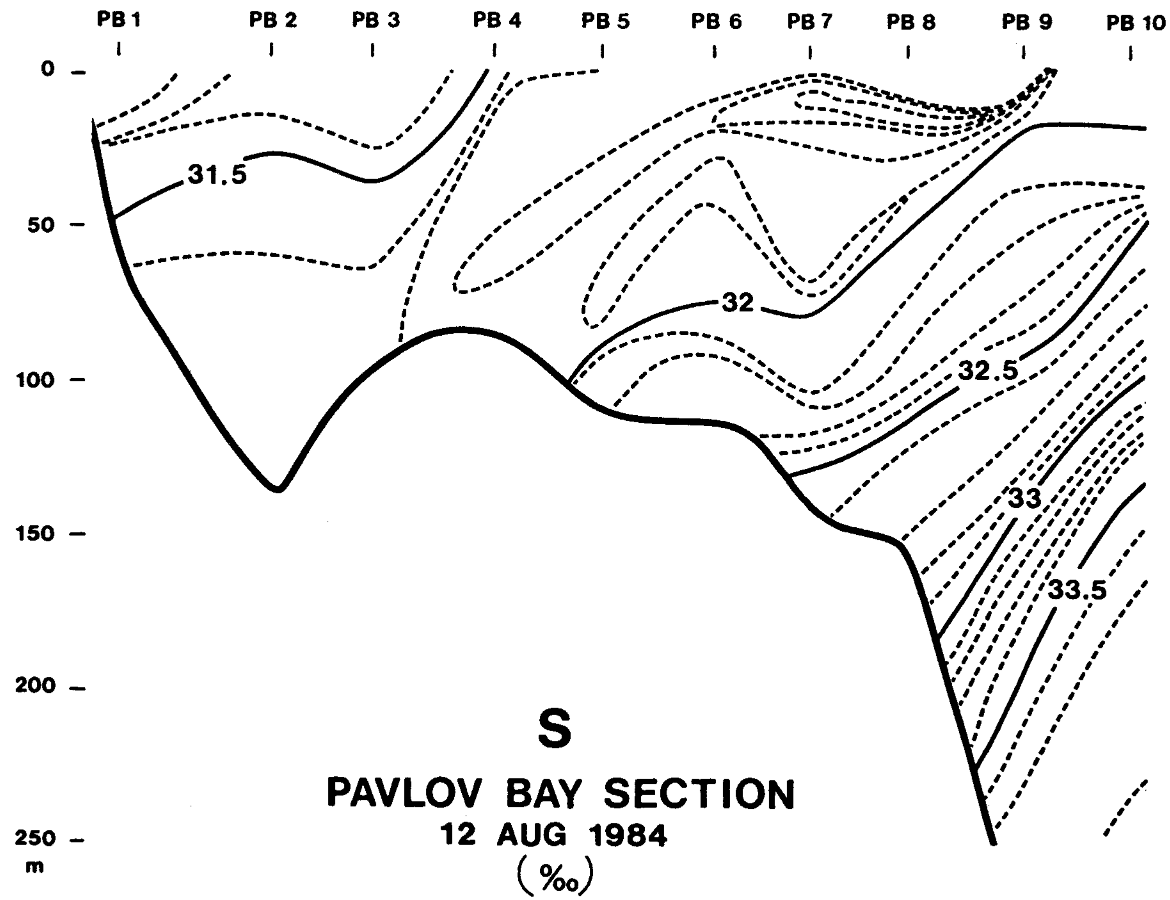

Figure 2.5 - Salinity, Pavlov Bay, August.

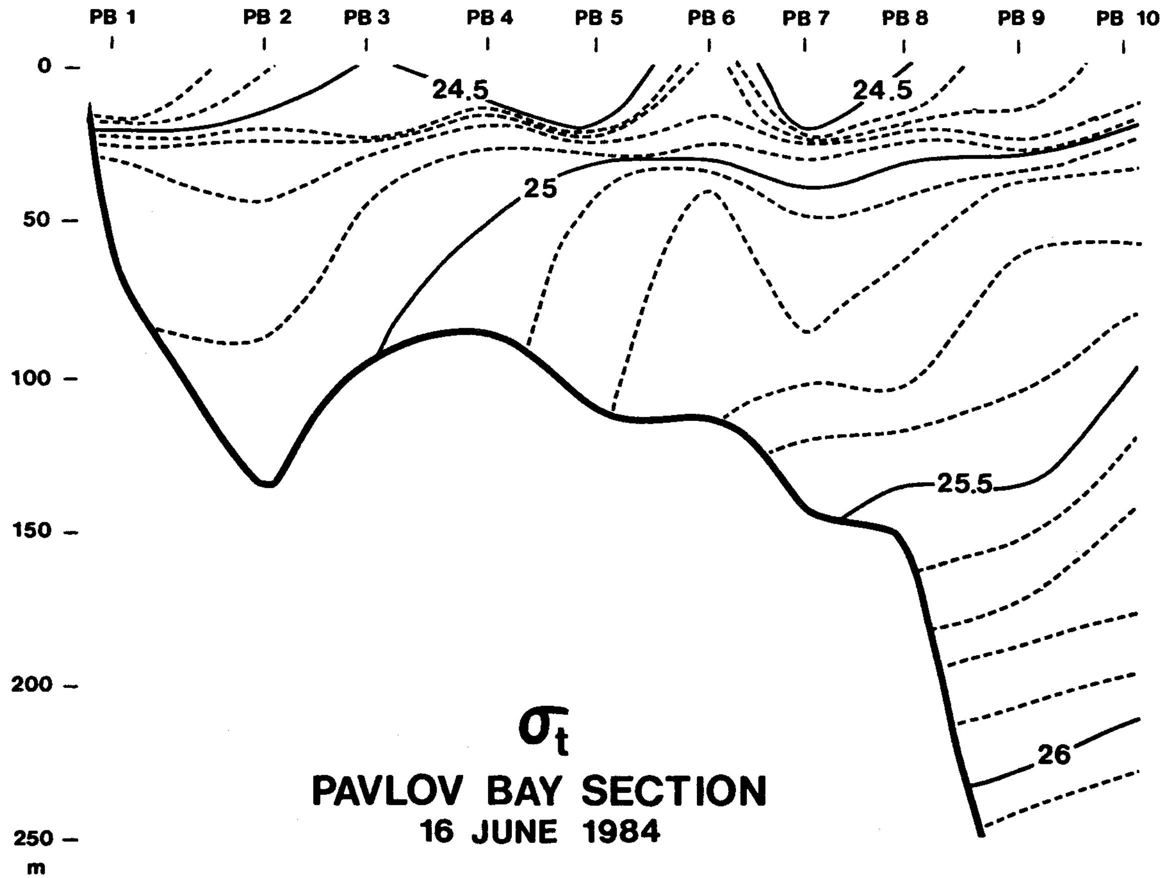

Figure 2.6 - Sigma-t, Pavlov Bay, June.

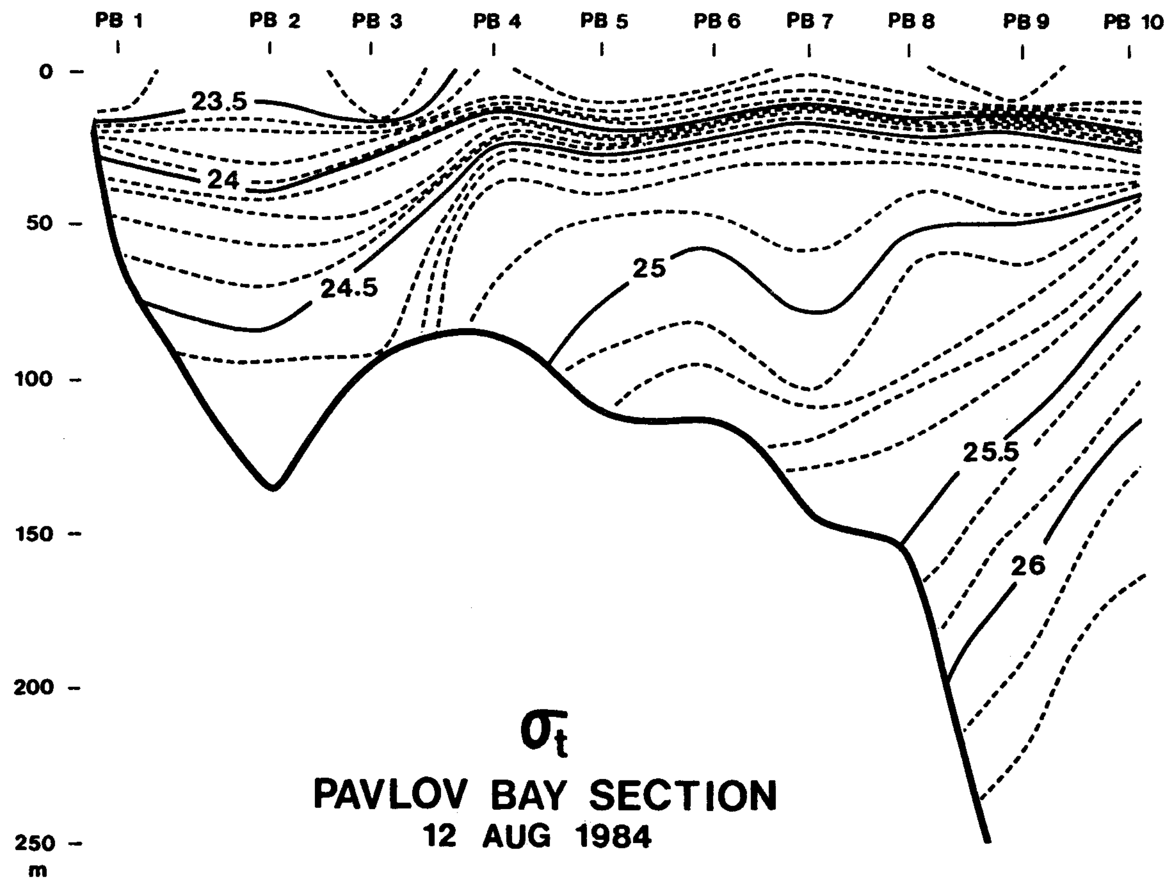

Figure 2.7 - Sigma-t, Pavlov Bay, August.

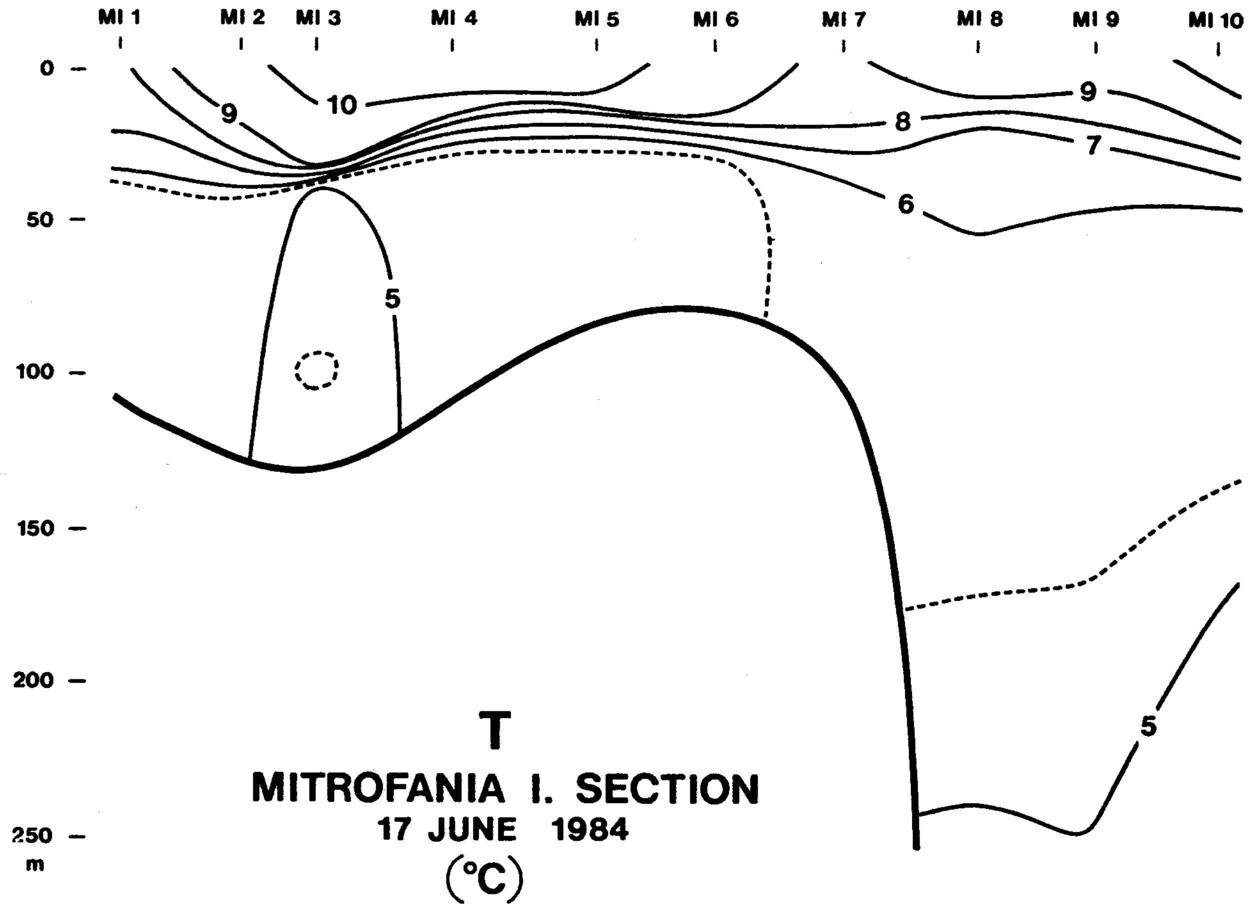

Figure 2.8 - Temperature, Mitrofania Island, June.

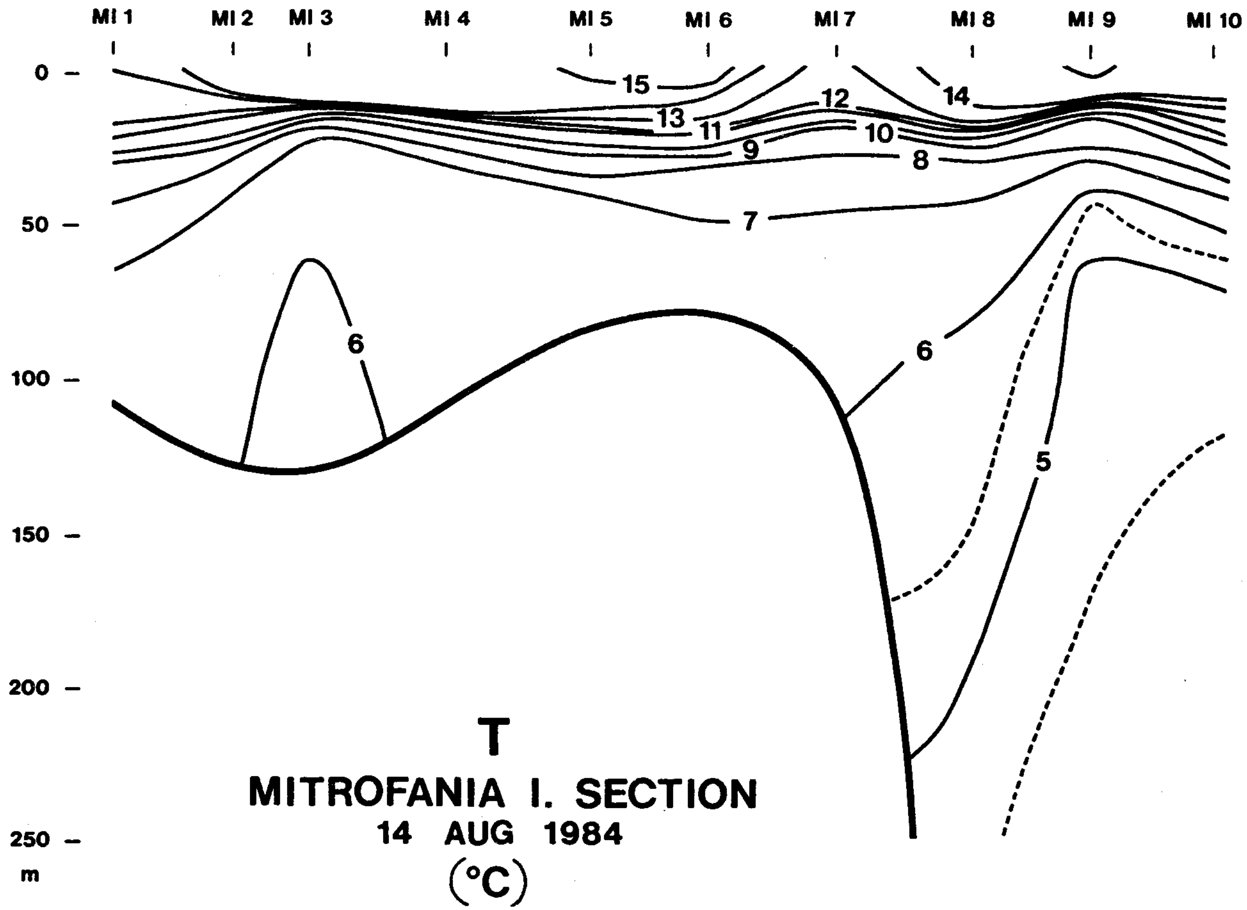

Figure 2.9 - Temperature, Mitrofania Island, August.

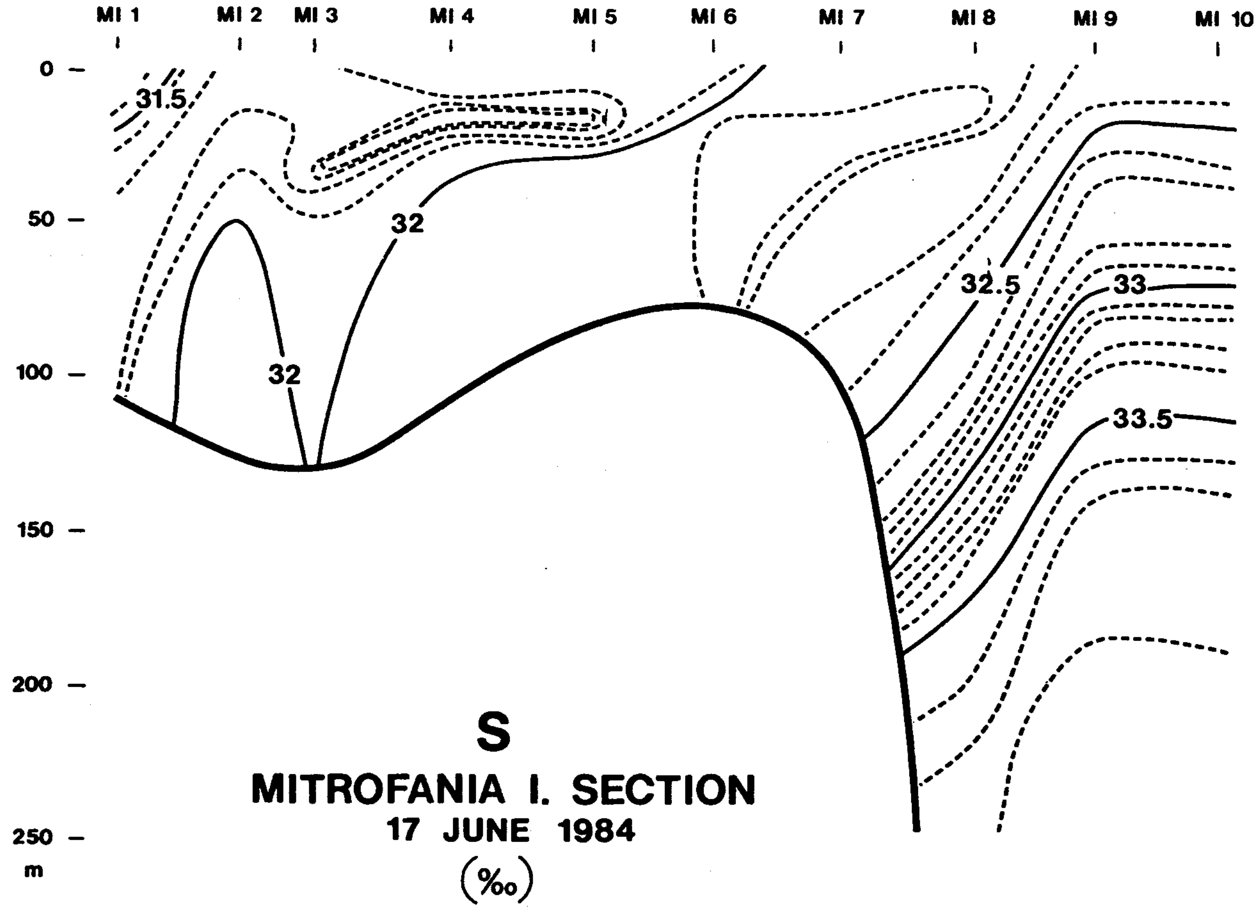

Figure 2.10 - Salinity, Mitrofania Island, June.

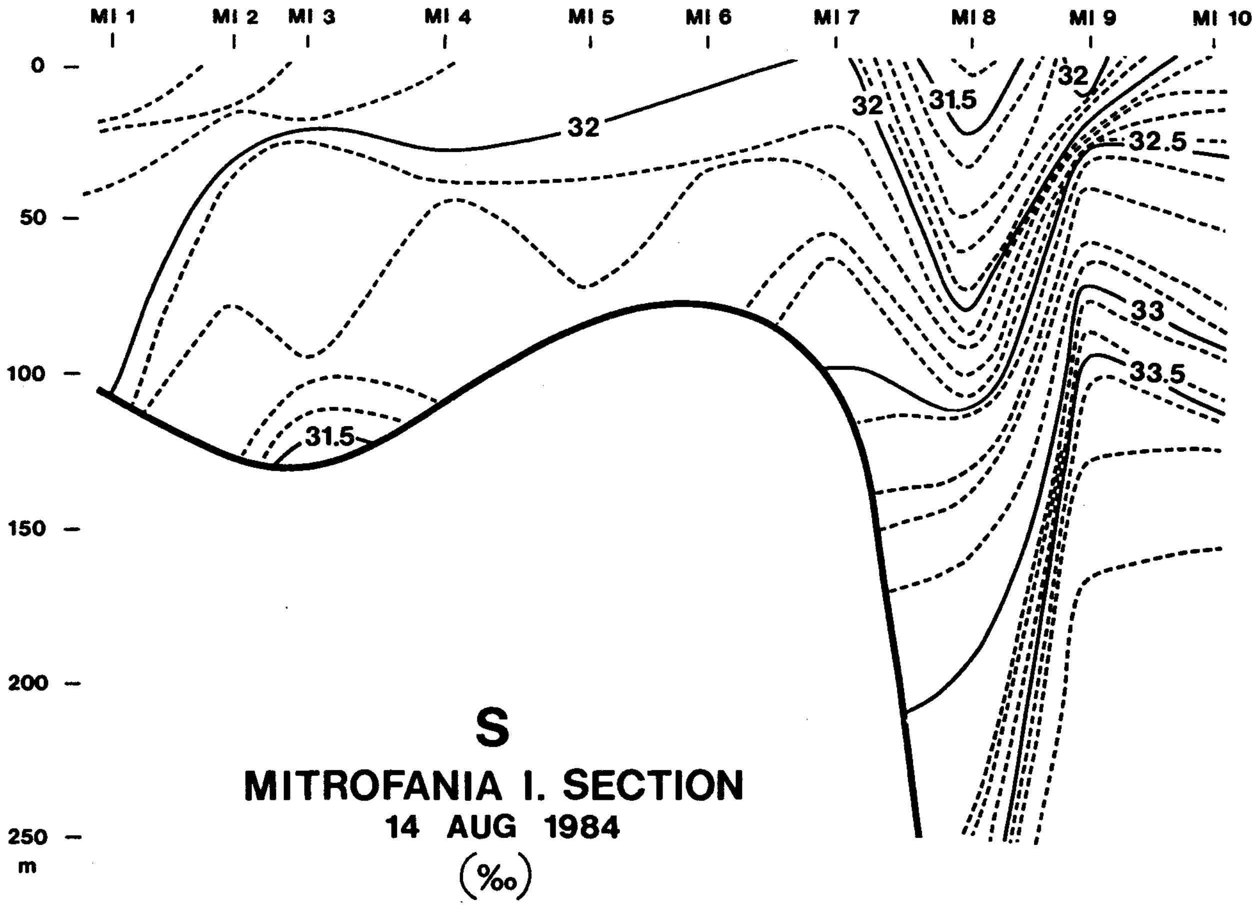

Figure 2.11 - Salinity, Mitrofania Island, August.

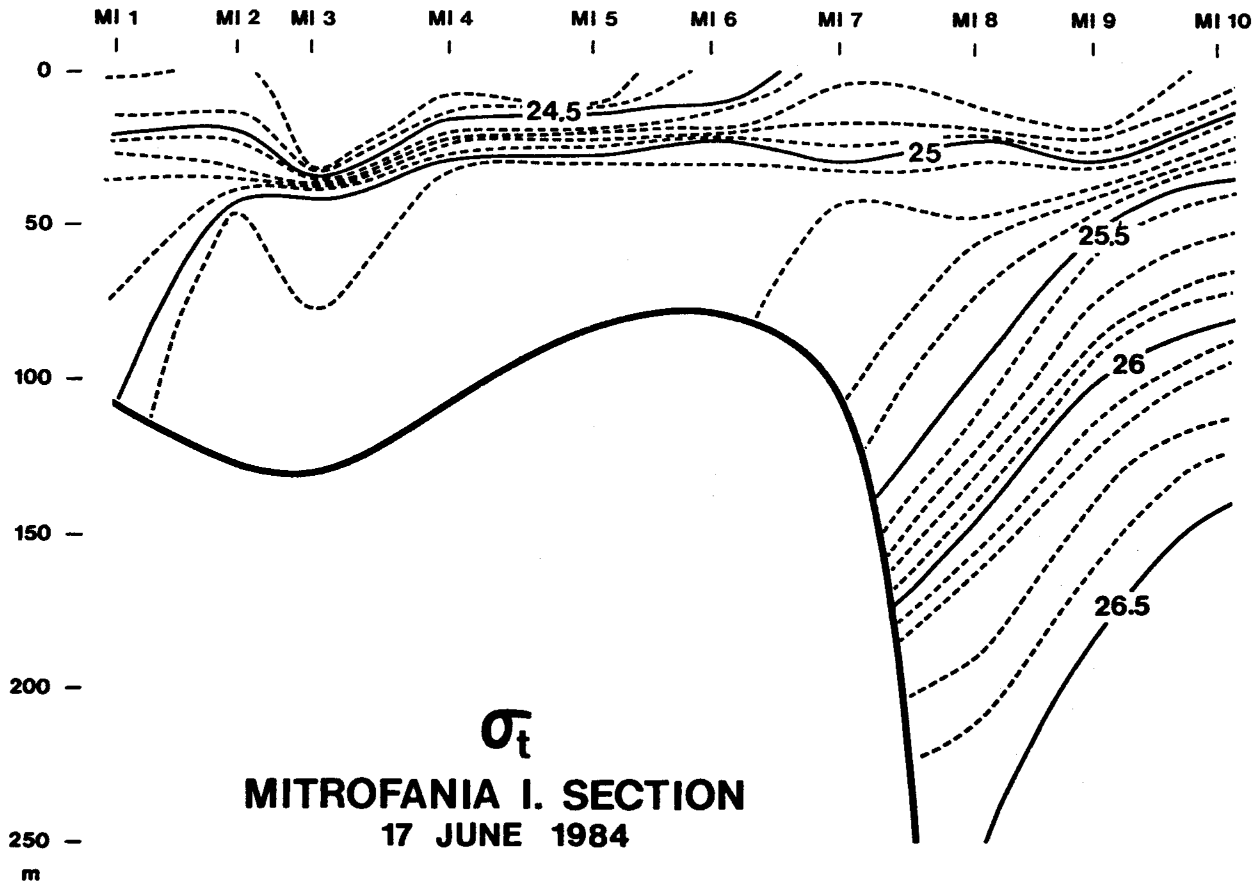

Figure 2.12 - Sigma-t, Mitrofania Island, June.

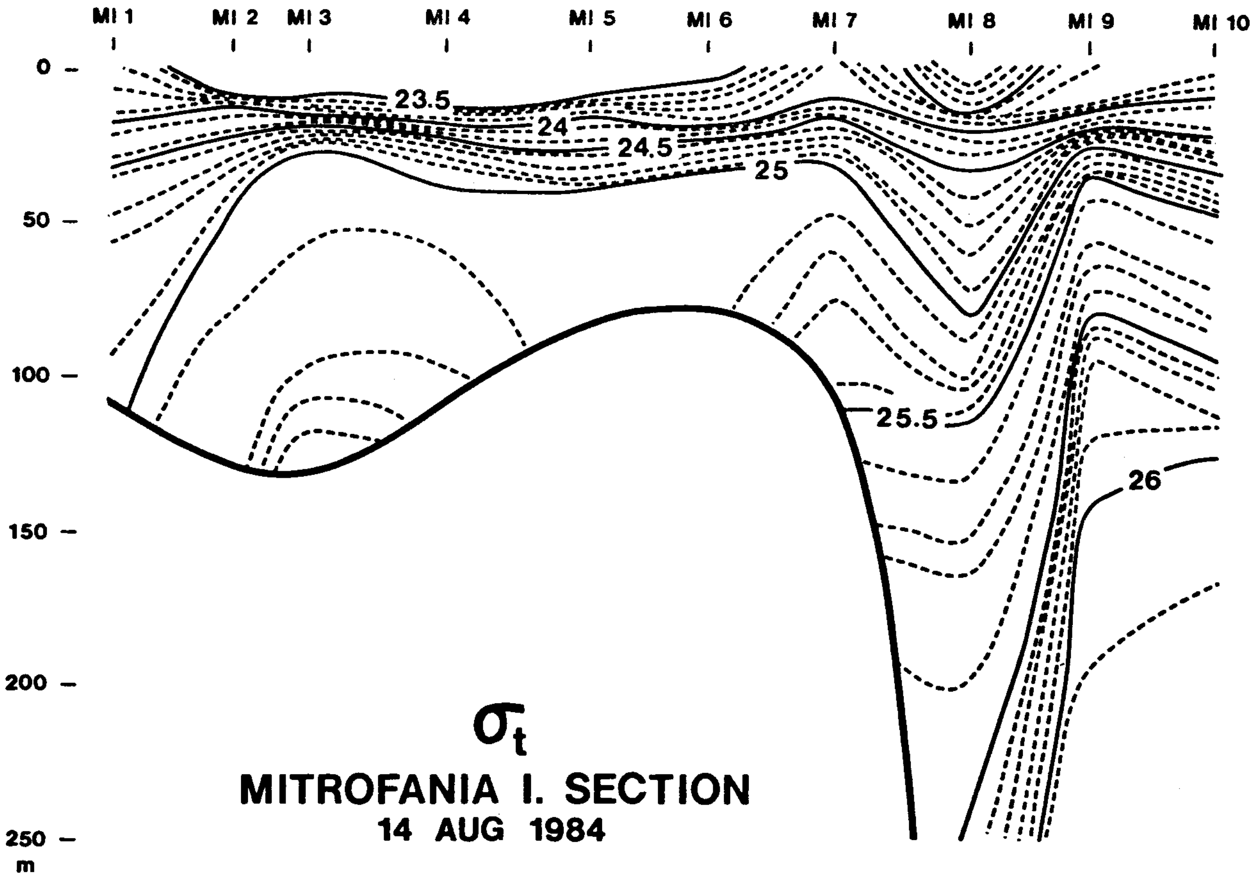

Figure 2.13 - Sigma-t, Mitrofania Island, August.

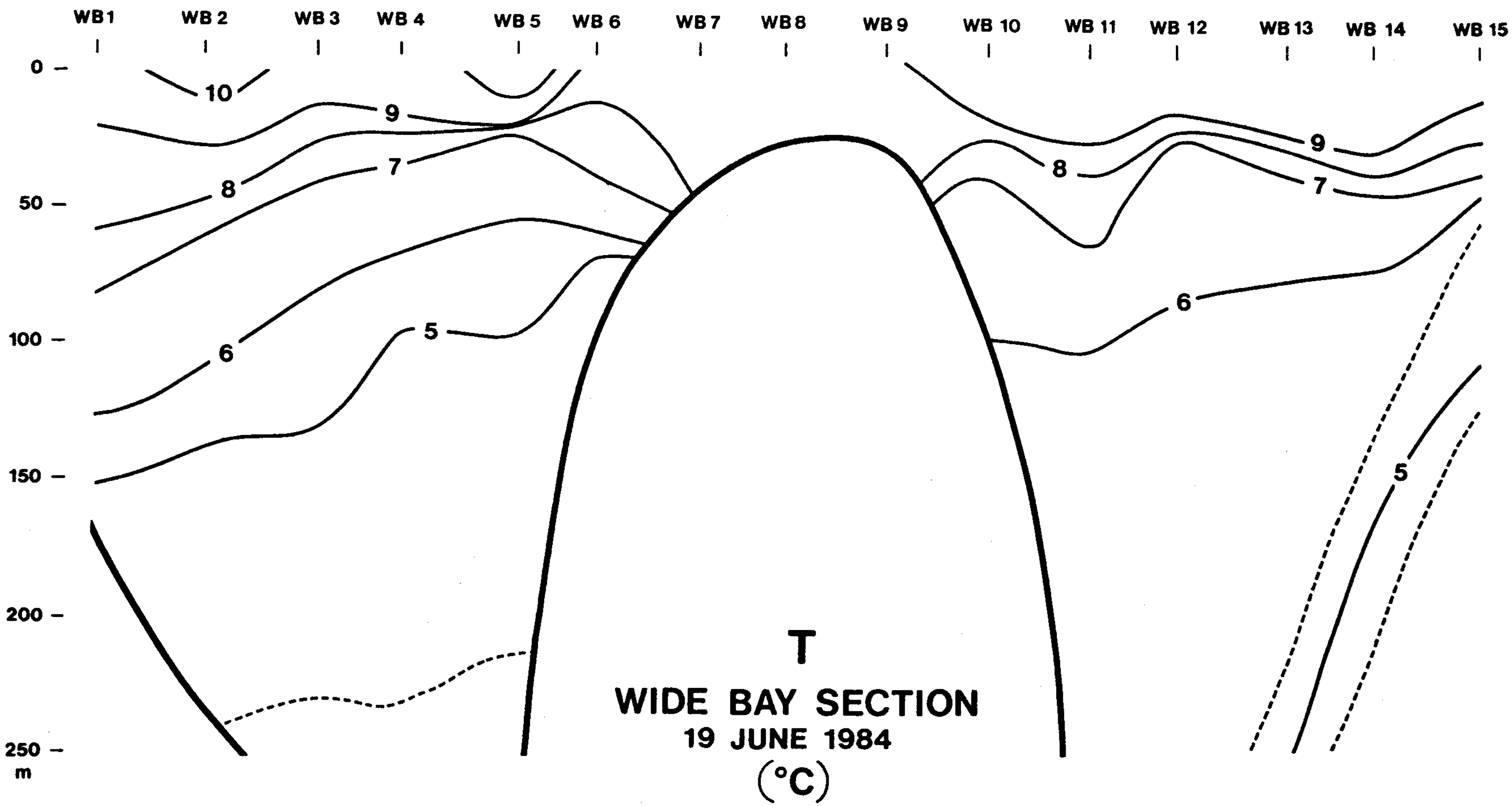

Figure 2.14 - Temperature, Wide Bay, June.

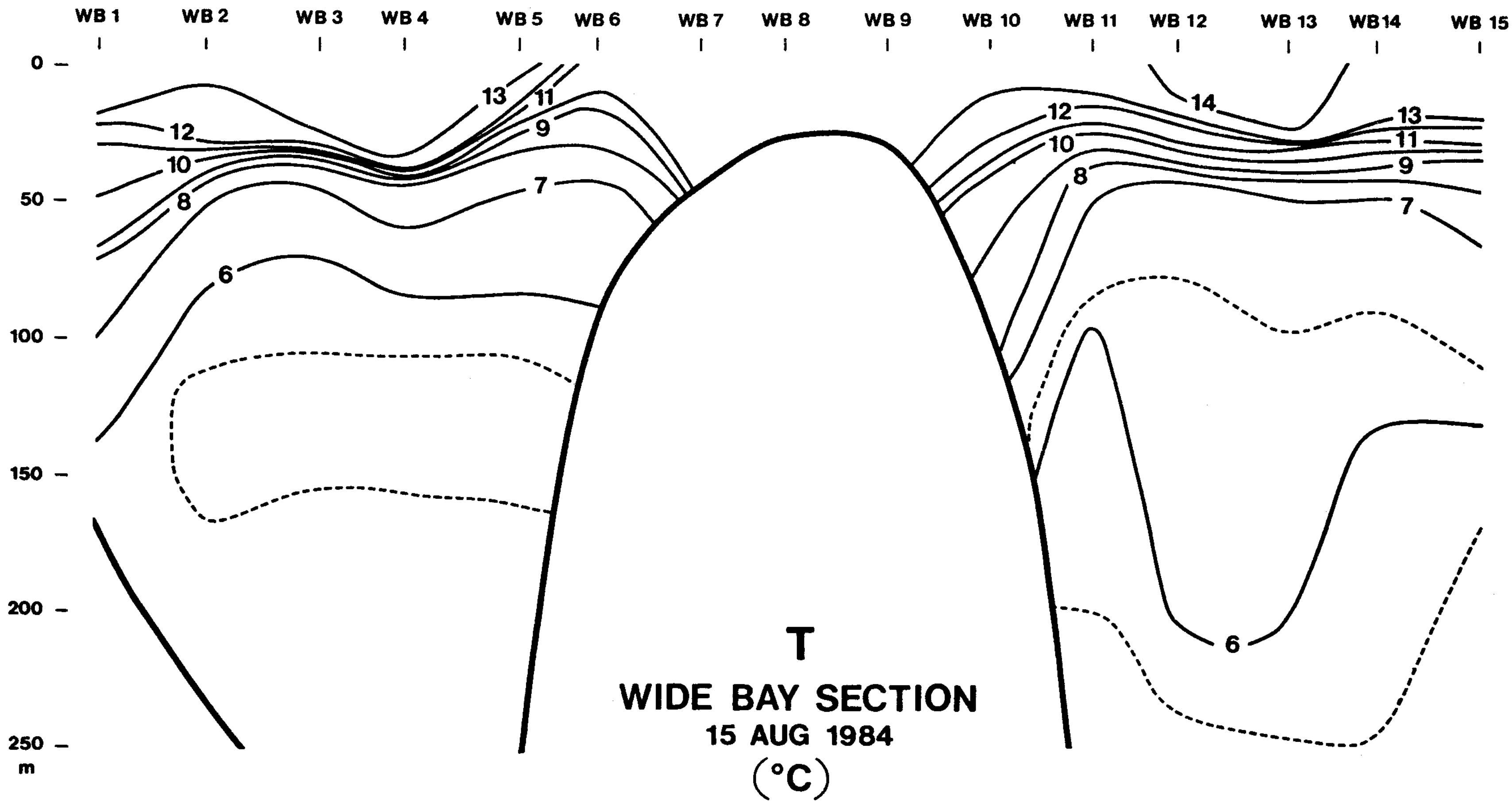

Figure 2.15 - Temperature, Wide Bay, August.

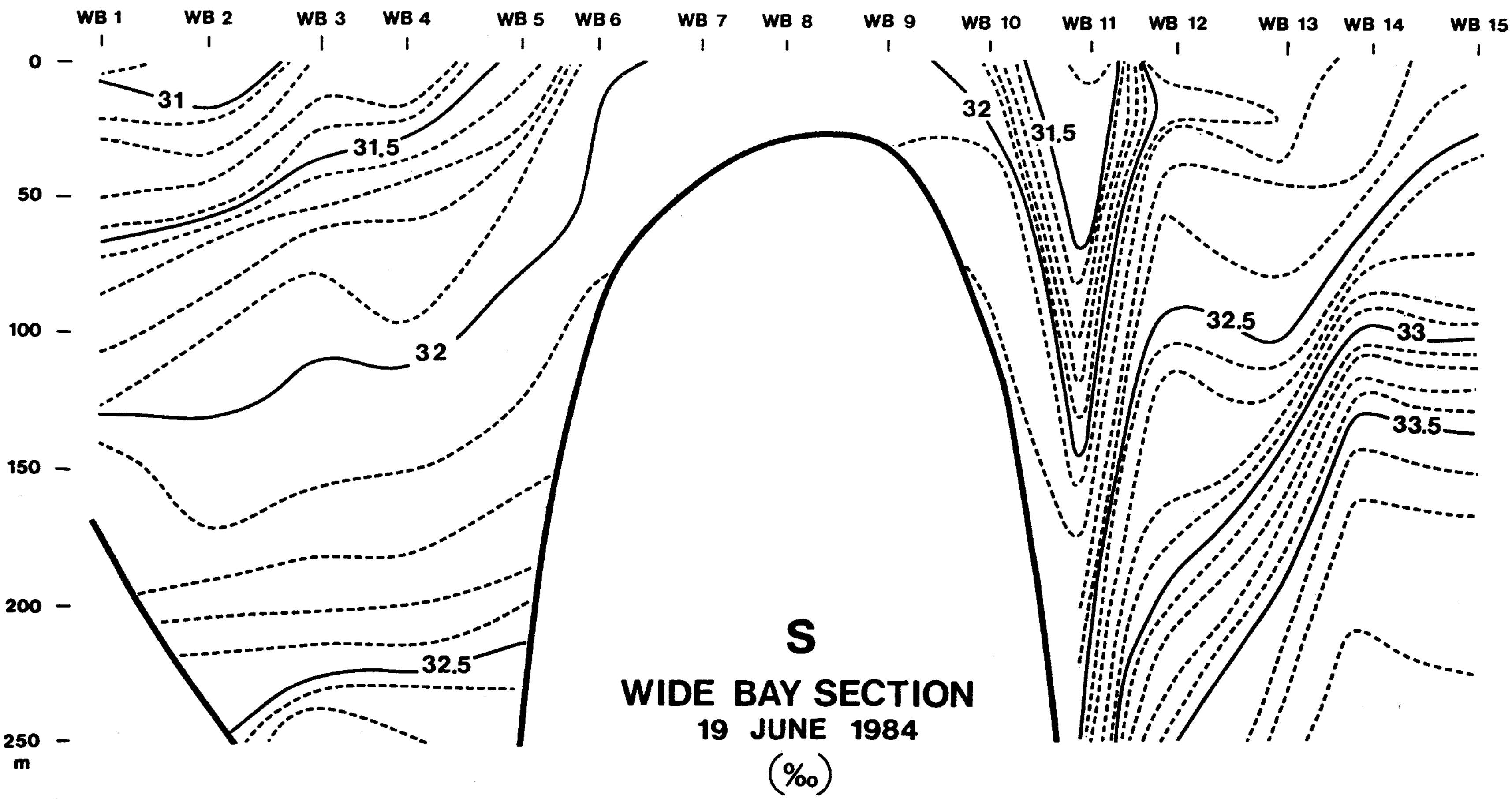

Figure 2.16 - Salinity, Wide Bay, June.

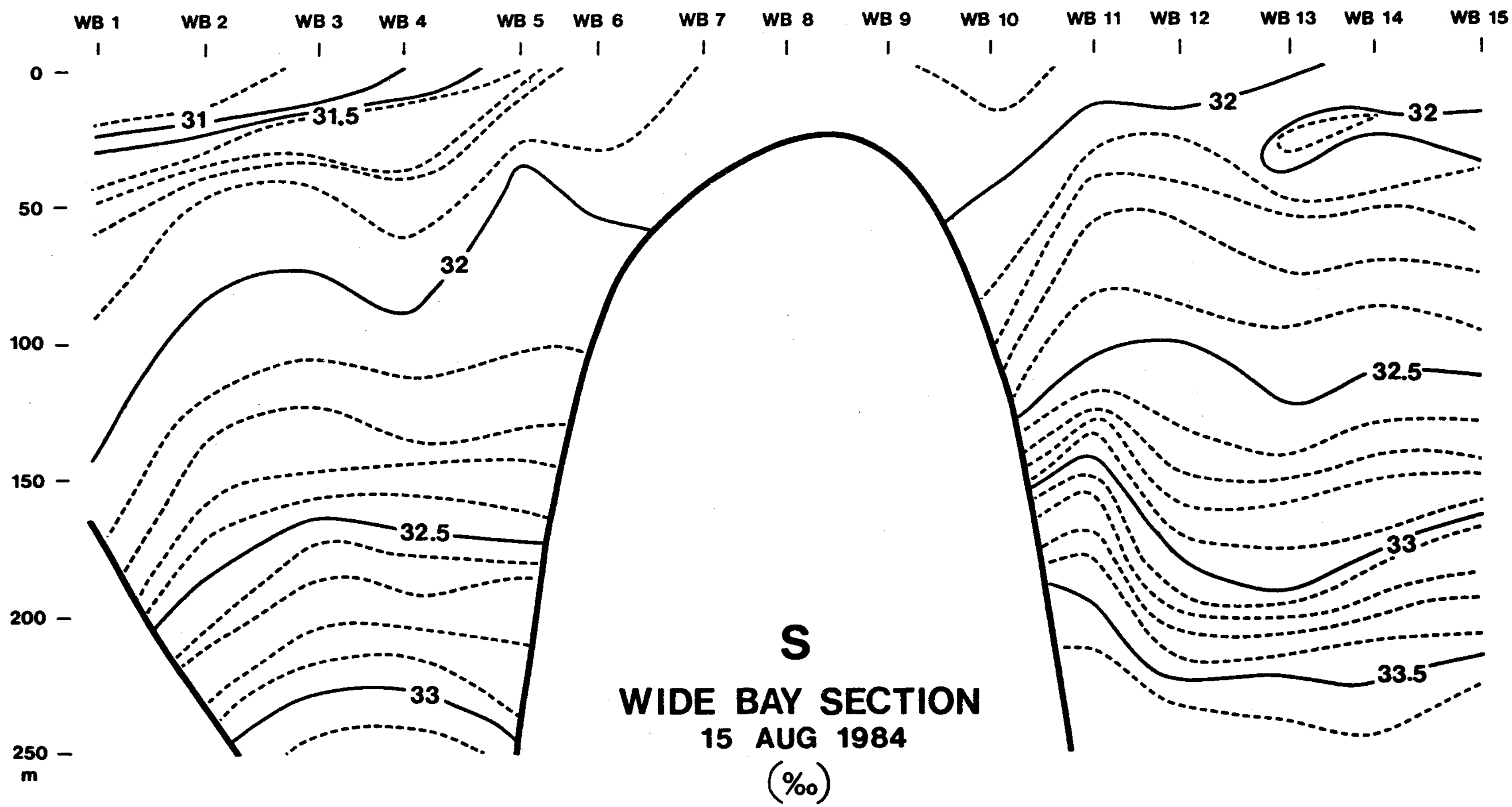

Figure 2.17 - Salinity, Wide Bay, August.

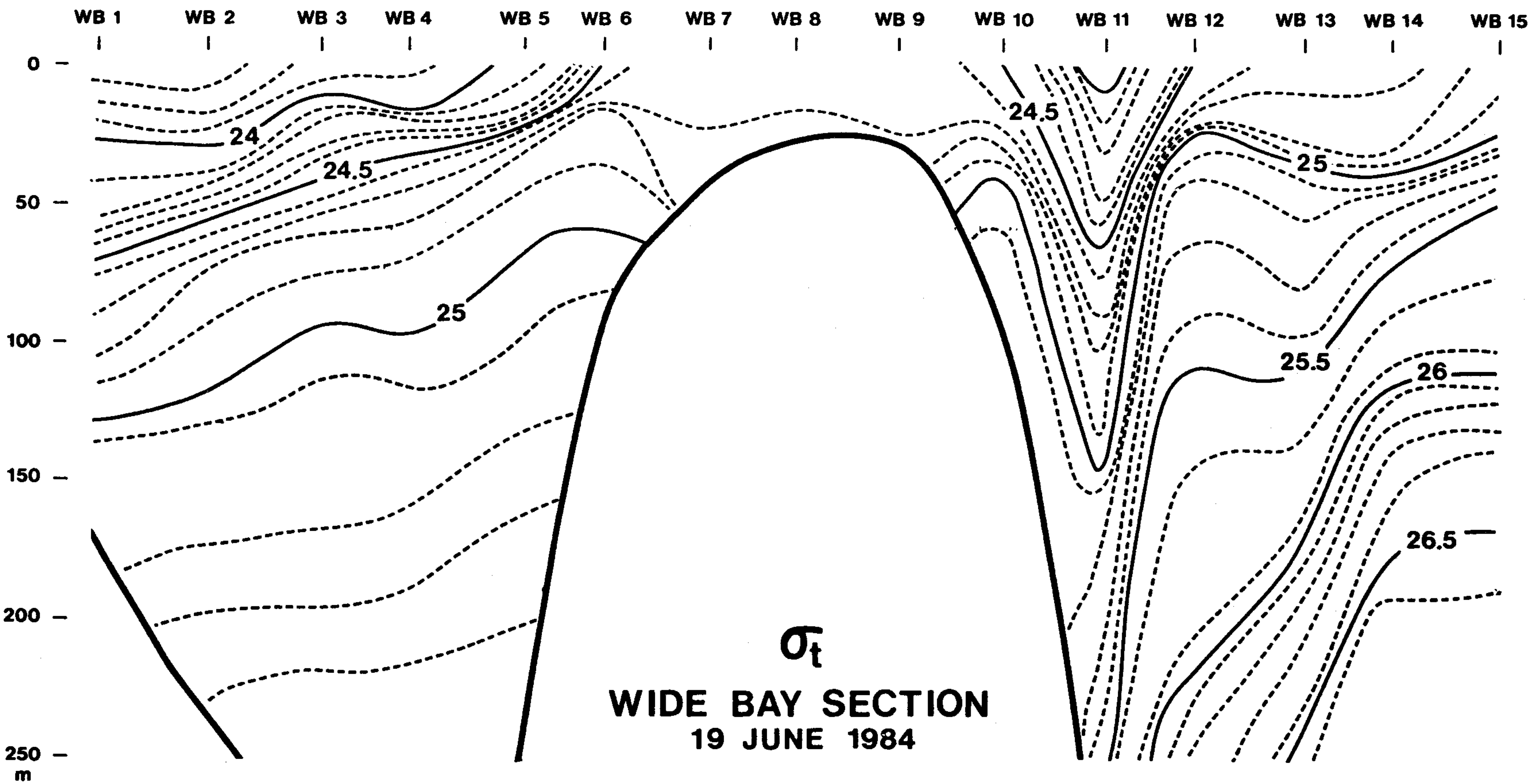

Figure 2.18 - Sigma-t, Wide Bay, June.

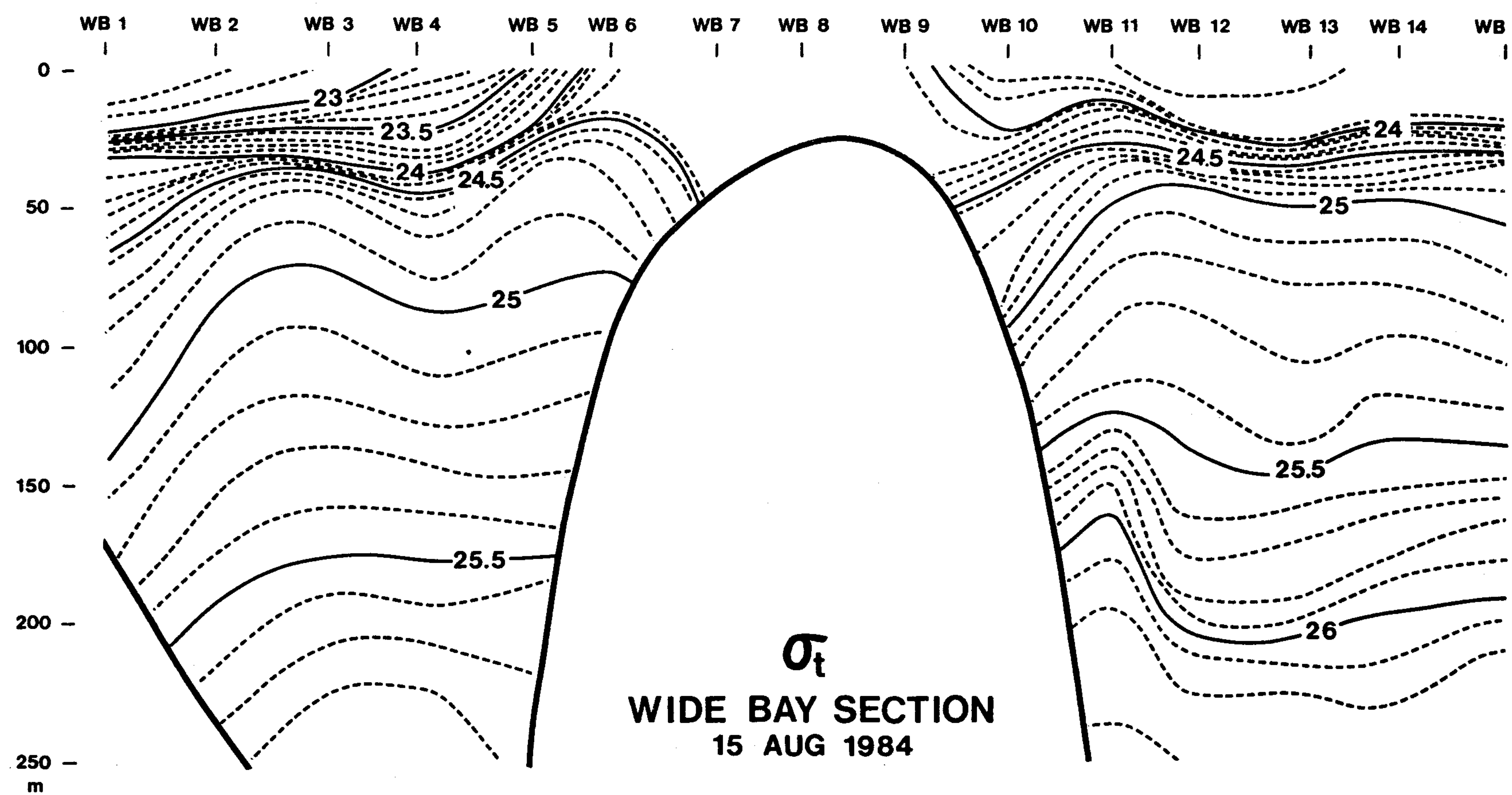

Figure 2.19 - Sigma-t, Wide Bay, August.

tidal mixing in this shallow region. Vertical homogeneity of the water column over Portlock Bank reported by Schumacher et al (1978) and Schumacher and Reed (1980) was also attributed to tidal mixing. It is likely that restratification occurs, at least in the upper layers, during periods of maximum river discharge.

Although the contours have been substantially smoothed, wave-like features still appear on the isotherms particularly at the shallower depths. Such waves are not surprising in light of the strong internal tides (discussed in Section 3.2.2).

2.1.2 Salinity

Unlike the temperature sections, the salinity sections (Figures 2.4, 2.5, 2.10, 2.11, 2.16, 2.17) do not show a pronounced temporal change. There is some indication of freshening over the shelf in the Pavlov Bay section but this process is not apparent in the other two sections. Extremely strong horizontal salinity gradients were measured over the continental slope on the Mitrofania Island section in August (Figure 2.11) and the Wide Bay section in June (Figure 2.14). These gradients are well mirrored in the sigma-t sections, the latter variable being dominated by salinity at low tempertures.

2.1.3 Sigma-t

As a non-linear function of temperature and salinity, sigma-t is more strongly dependent upon salinity at low temperatures and, conversely, more dependent upon temperature at high temperatures. The result in the Western Gulf of Alaska is that sigma-t temporal changes parallel those of temperature in the near surface layers and of salinity in the deeper layers. At all three sections (Figures 2.6, 2.7, 2.12, 2.13, 2.18, 2.19) the density stratification in the upper 50 m approximately doubled between June and August while the deeper stratification remained almost constant. In June very strong horizontal gradients of density were observed over the continental slope in the Wide Bay Section (Figure 2.18). Similarly strong horizontal gradients were observed over the continental slope in the Mitrofania Island section in August (Figure 2.13). This feature may have been advected, or propagated, along the slope between June and August; the mean advection speed would be about 4 cm s^{-1}. The gradients are suggestive of an anticyclonic (clockwise) eddy of about 13 km in radius. Similar features were described by Favorite and Ingraham (1977) and Schumacher et al, (1979). An eddy whose signature is visible in the mass field should have a radius roughly comparable to the internal Rossby radius which is defined as

$$r = \sqrt{g\frac{\Delta\rho}{\rho}\,h}\Big/f \qquad (2\text{-}1)$$

where g is gravity, ρ density, h is the thickness of the surface layer and f is the Coriolis parameter over the continental slope. r has a value of between 6 and 12 km so that this eddy-like feature is of appropriate size to satisfy dynamic balances. In particular if the eddy were generated by baroclinic instability it would correspond closely in size to the most unstable (and therefore predominant) wavelength (if wave length = 2r) according to Mysak, et al (1981). The agreement between the apparent eddy radius and the internal Rossby radius supports the observations but does not necessarily imply formation by baroclinic instability.

The presence of anticyclonic (clockwise) eddies over the continental slope raises the possibility of cross-slope exchange of water and nutrients due to instabilities. For example, baroclinic instabilities are characterized by turbulent property exchanges across the mean flow and thus along the mean pressure gradient (Smith, 1976). These cross depth gradient fluxes can be visualized as the breaking of waves on the isopycnal surfaces when the slopes of the surfaces exceed critical values. The "breaking waves" propagate along the initial isopycnal slope, i.e. across the mean flow.

It will be seen in the next sections that the station spacing is not quite small enough to properly resolve spatial variability of the size of the internal Rossby radius. While this drawback has little effect upon qualitative representation of the distribution of properties, it limits the utility of the dynamic method by which geostrophic currents are computed from horizontal density gradients.

2.2 DYNAMIC HEIGHTS, GEOSTROPHIC CURRENTS

Geostrophic shears can be integrated from an assumed level of no motion to yield estimates of the baroclinic geostrophic current profile. This long-standing method has both its strong adherents and detractors. The latter are critical of some of the assumptions of the "Dynamic Method" and have shown that they do not apply in many regions. For the present data set the most important limitations are lack of synopticity and, to a lesser extent, insufficiently dense station spacing.

The thermal wind equations, from which the dynamic method arises, assume a steady flow. Implicit is that vertical motion of the isopycnals is negligible. In the presence of a strong internal wave field, however, this is simply not the case. Several investigators have surmounted the obstacle of time-varying flows in computations of geostrophic currents by averaging density measurements over a tidal cycle. Such a procedure is extremely consumptive of ship time and was not attempted in our field work. The computed dynamic heights and geostrophic currents therefore neither represent a tidal average nor an instantaneous realization of the flow. We would suggest that where the mean flow energy is small compared to the tidal energy, geostrophic current computations do little more than yield a qualitative view of the flow field.

In order to produce stream lines of the geostrophic flow, the dynamic height anomaly between selected pressure surfaces was plotted and contoured. The charts for June and August are presented on the same page for ease of comparison in Figure 2.20 through 2.23. Figure 2.20 shows the dynamic height topography of the surface relative to 10 decibars. The plots are an indication of the density of the mixed layer; the larger anomalies representing less dense water. The influence of warmer and fresher waters nearshore is shown. The anomalies increased between June

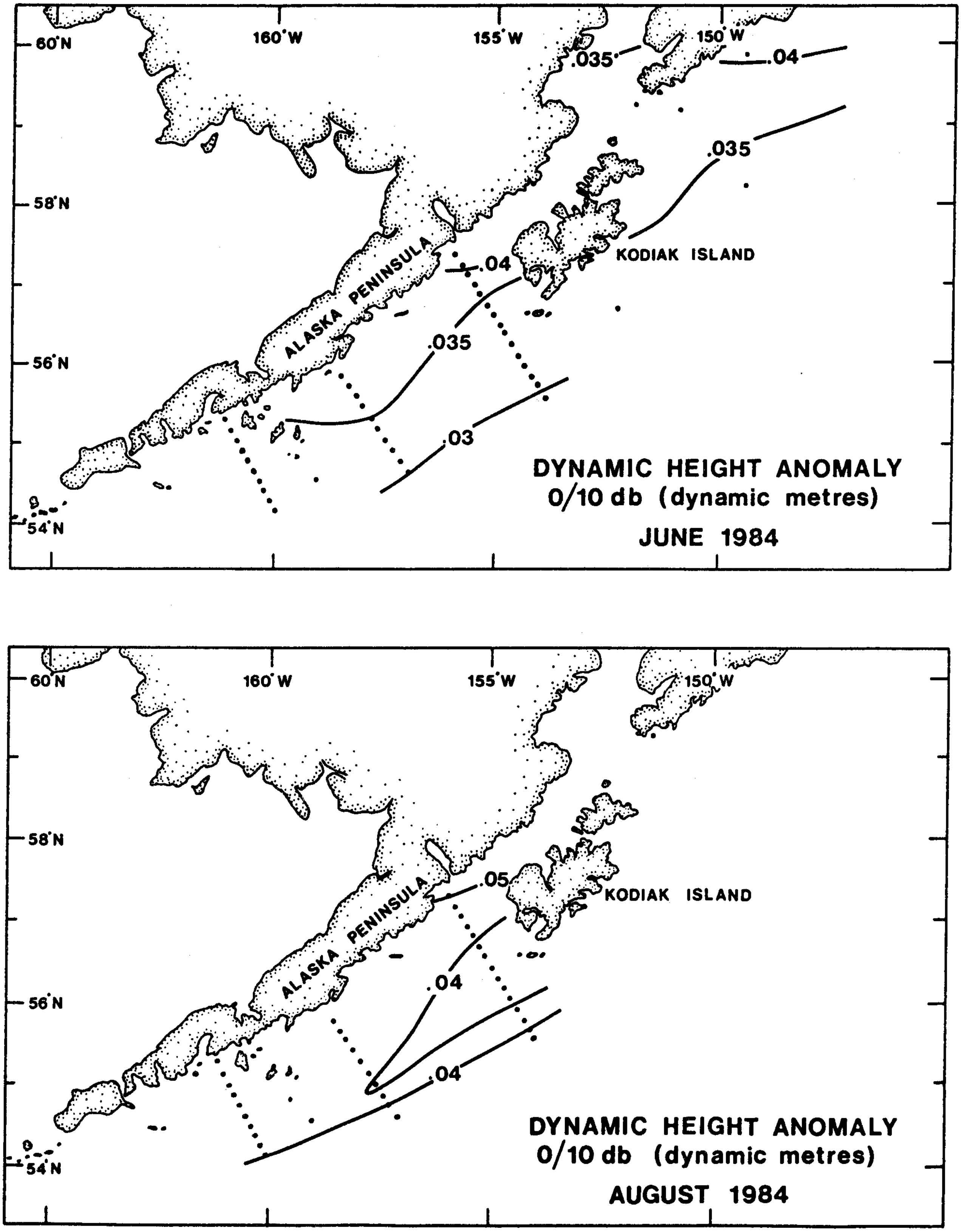

Figure 2.20 - Dynamic height topography, 0/10 db, June and August 1984.

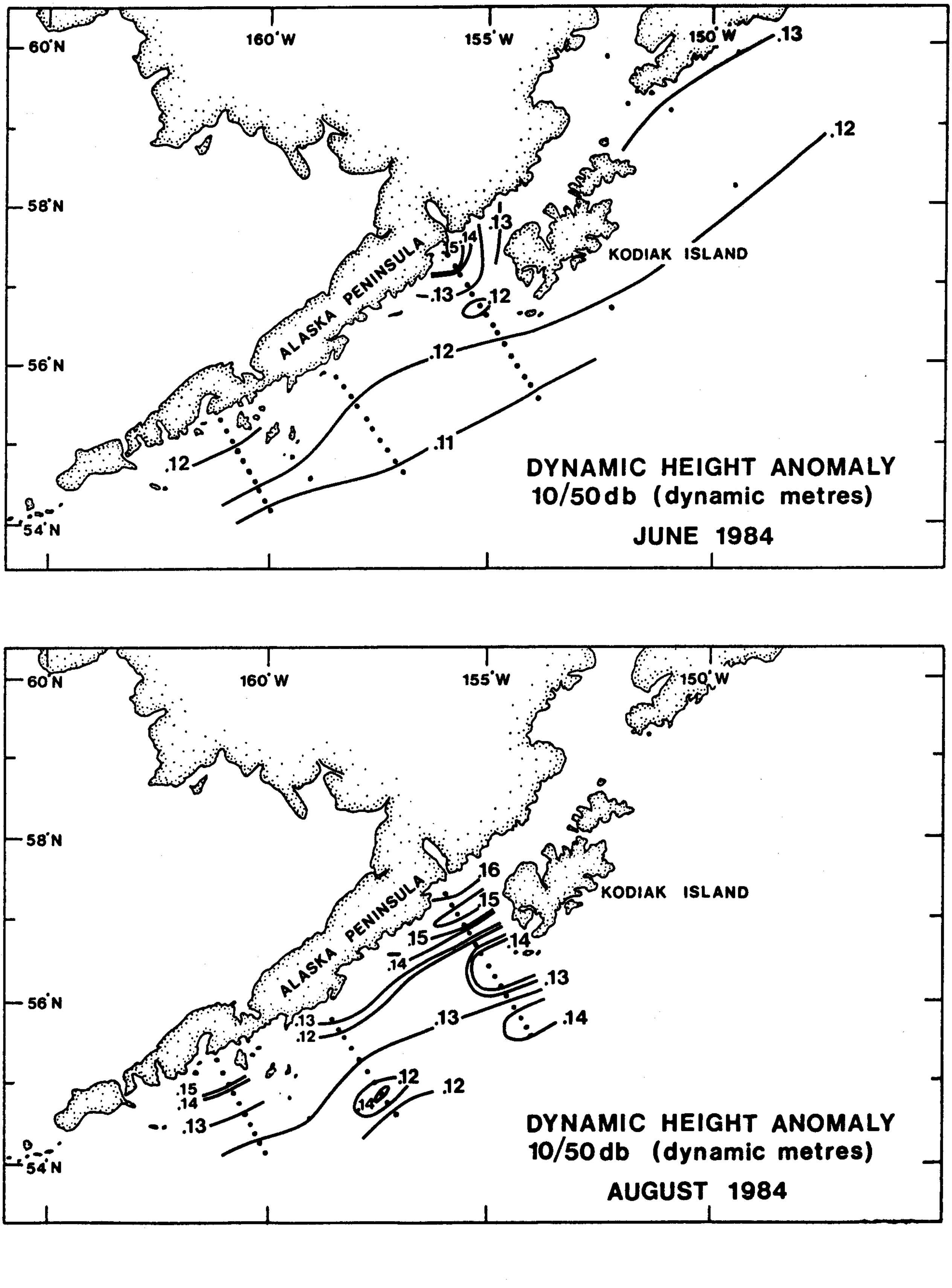

Figure 2.21 - Dynamic height topography, 10/50 db, June and August 1984.

and August due to continued insolation. Figures 2.21 and 2.22 represent the topography of the 10 and 0 db surfaces relative to 50 db. The geostrophic flow field in the upper 50 m is thus portrayed.

The velocity differences between surfaces can be computed by

$$\Delta u = \frac{10 \, \Delta D}{fL} \qquad (2\text{-}2)$$

where Δu is the velocity difference, ΔD is the difference in dynamic height anomaly between two stations, f is the Coriolis parameter and L is the distance between stations. The 10/50 db and 0/50 db charts show that the geostrophic velocity shear in the upper layers was generally less than 10 cm s^{-1} and on average across the shelf about 3 cm s^{-1}. The 10/50 and 0/50 db charts are virtually identical demonstrating the density gradients in the upper 10 m contributed little to the geostrophic flow field. Considerably more horizontal structure was present in August than in June above the 50 decibar surface probably due to increased river discharge toward the end of summer which introduced fresher water. Both the freshening itself and the enhanced stratification promoting heating of the surface layers would have contributed to the contrast between June and August. However, the mean flow (for example through the Wide Bay or eastern most section) changed little between June and August. The mean velocity in the upper 50 m was southwestward at a speed of about 2 or 3 cm s^{-1} relative to 50 db.

Figure 2.23 shows the dynamic topography of the 10 db surface relative to 100 db. Vertical velocity shear is most apparent along and near the shelf break where vertical velocity differences in June are on the order of 8 cm s^{-1} and the direction of flow is to the southwest. In August the flow along the shelf break is about 4 cm s^{-1} and generally directed toward the northeast. An outflow on the order of 5 cm s^{-1} is directed southwestward from Shelikof Strait in both June and August. This figure is in fairly good agreement with the mean flow measured over the two month period at the current meter at 46 m depth in Shelikof Strait.

In all the dynamic height topography charts the mean flow from the shore to the shelf break is directed toward the southwest in agreement with the contemporary view of the Alaska Coastal Current regime, e.g. Royer (1981).

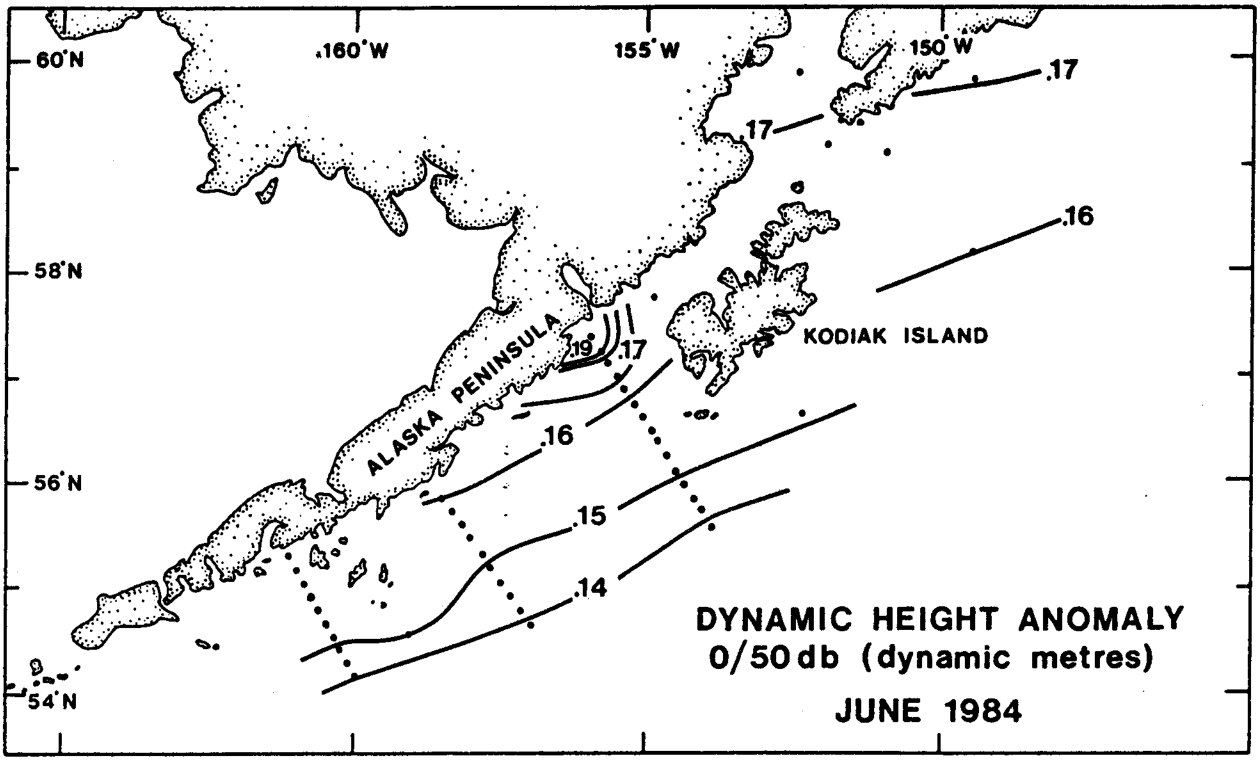

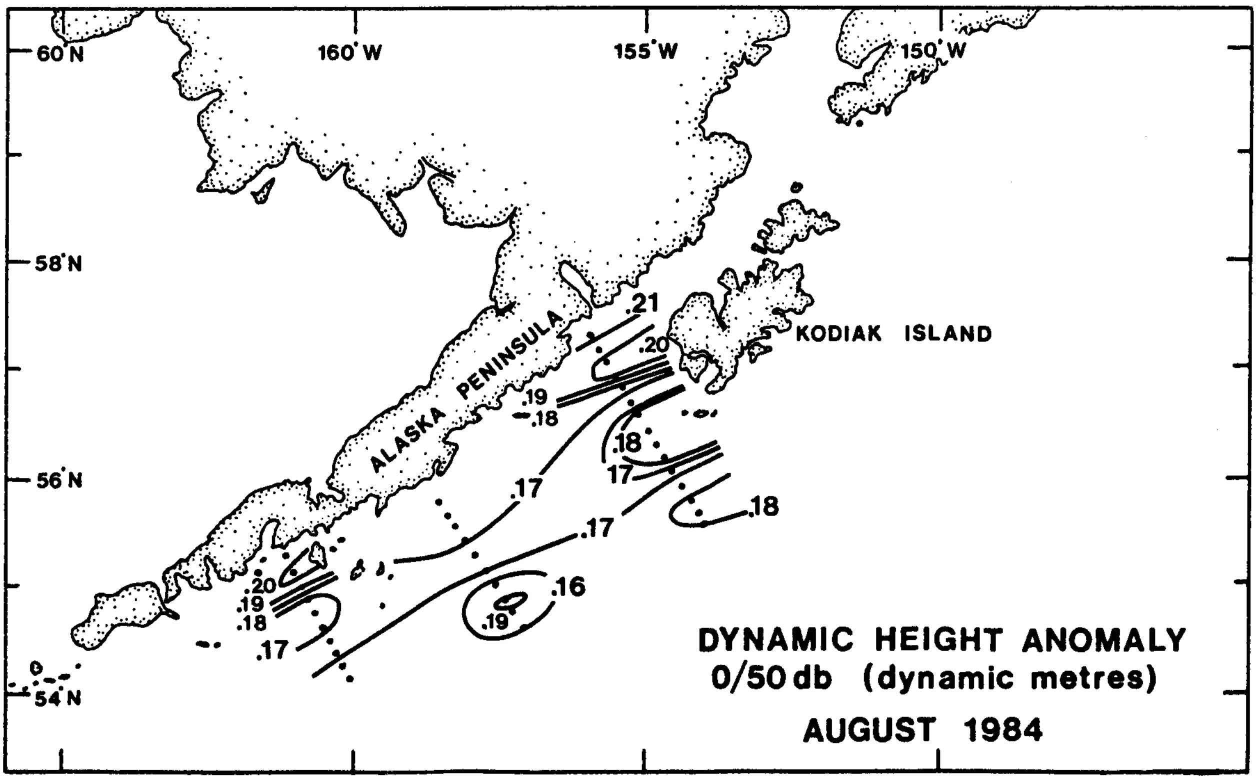

Figure 2.22 - Dynamic height topography, 0/50 db, June and August 1984.

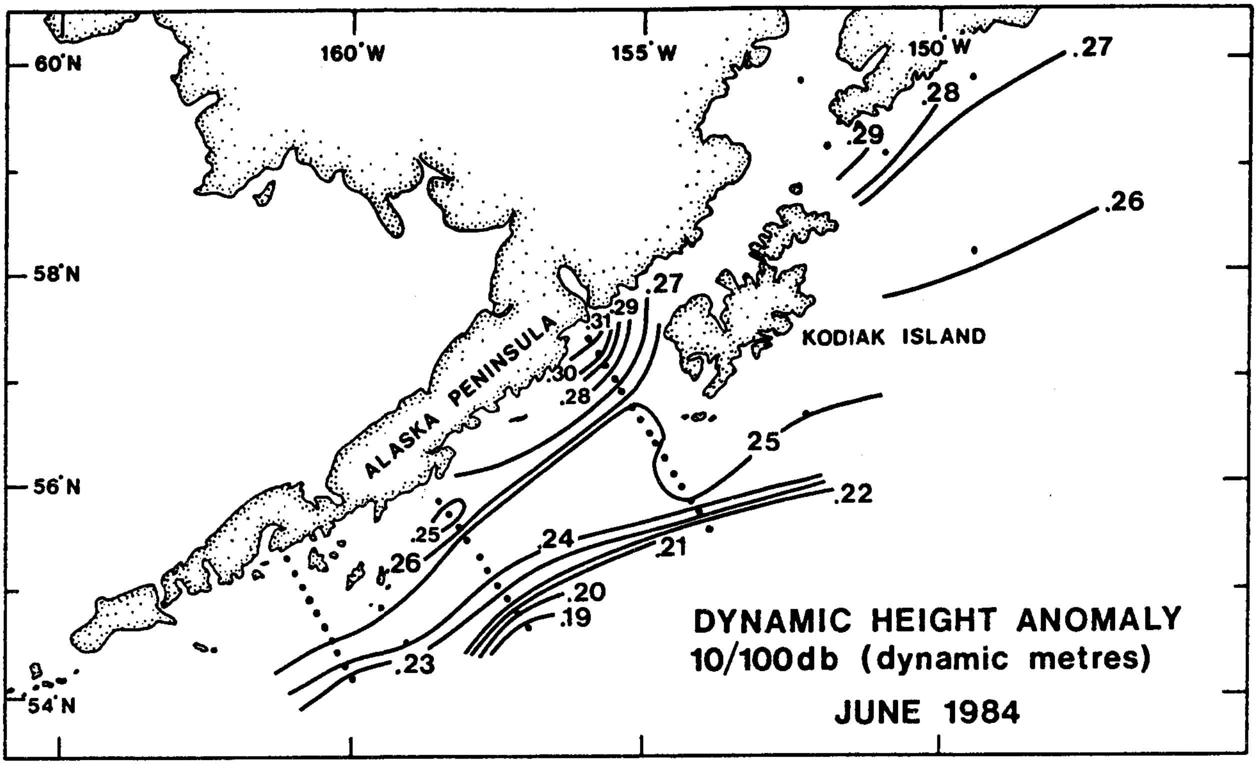

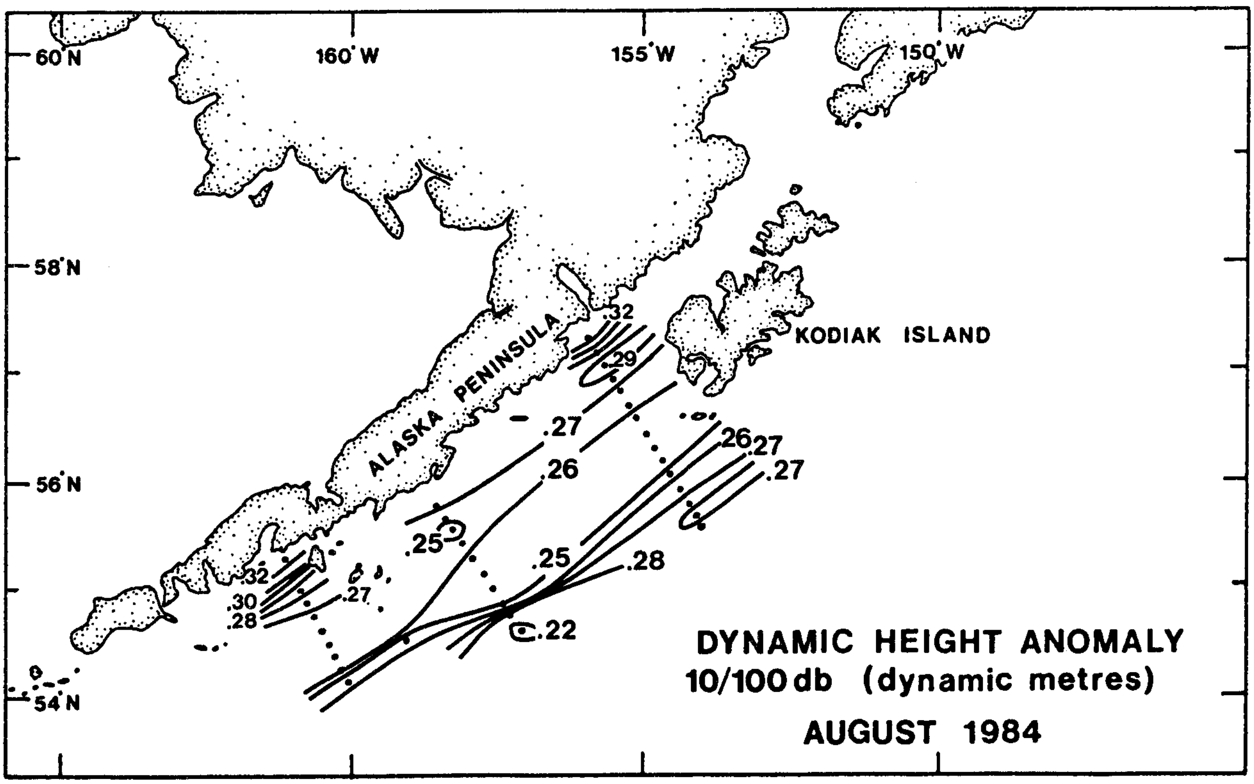

Figure 2.23 - Dynamic height topography, 10/100 db, June and August 1984.

An attempt was made to establish a level of no motion across the shelf and to unify the geostrophic shears into cross section of velocity. In author's view the procedure is more artistic than quantitative. Such cross sections of velocity do, however, give a sense of structure of the velocity field. Isotachs for June and August are presented for each of the sections in Figure 2.24 through 2.29. The details of the structure are clearly limited by the station spacing which was somewhat larger than the internal Rossby radius of deformation. In addition, the quality of the CTD data is rather poor and spurious structures may have been introduced to these cross sections.

2.3 SURFACE SALINITIES AND TEMPERATURES

Charts of the surface salinity and temperature distributions during June and August are shown in Figures 2.30 through 2.33.

The 32.0 ppt surface isohaline appears to follow the shelf break during both June and August. Values are similar to those reported by Reed et al, (1979). There is an indication of the freshening of the surface waters in Shelikof Strait during the summer, but the sampling stations were very sparse in that region. The salinity increased monotonically offshore in agreement with the concept of a runoff driven southwesterly flow along the shelf. No salinity minimum was found over the shelf break as has been reported by Favorite and Ingraham (1977) or Royer and Muench (1977) for Spring conditions. It appears, rather, that summer conditions prevailed during the period June through August 1984.

The surface temperature charts show mainly a general increase in temperature due to insolation over the summer. There is an indication of the presence of cooler surface waters near-shore than offshore in both months probably due to relatively cold river discharge. The cross-shelf horizontal temperature gradients remain almost constant between June and August.

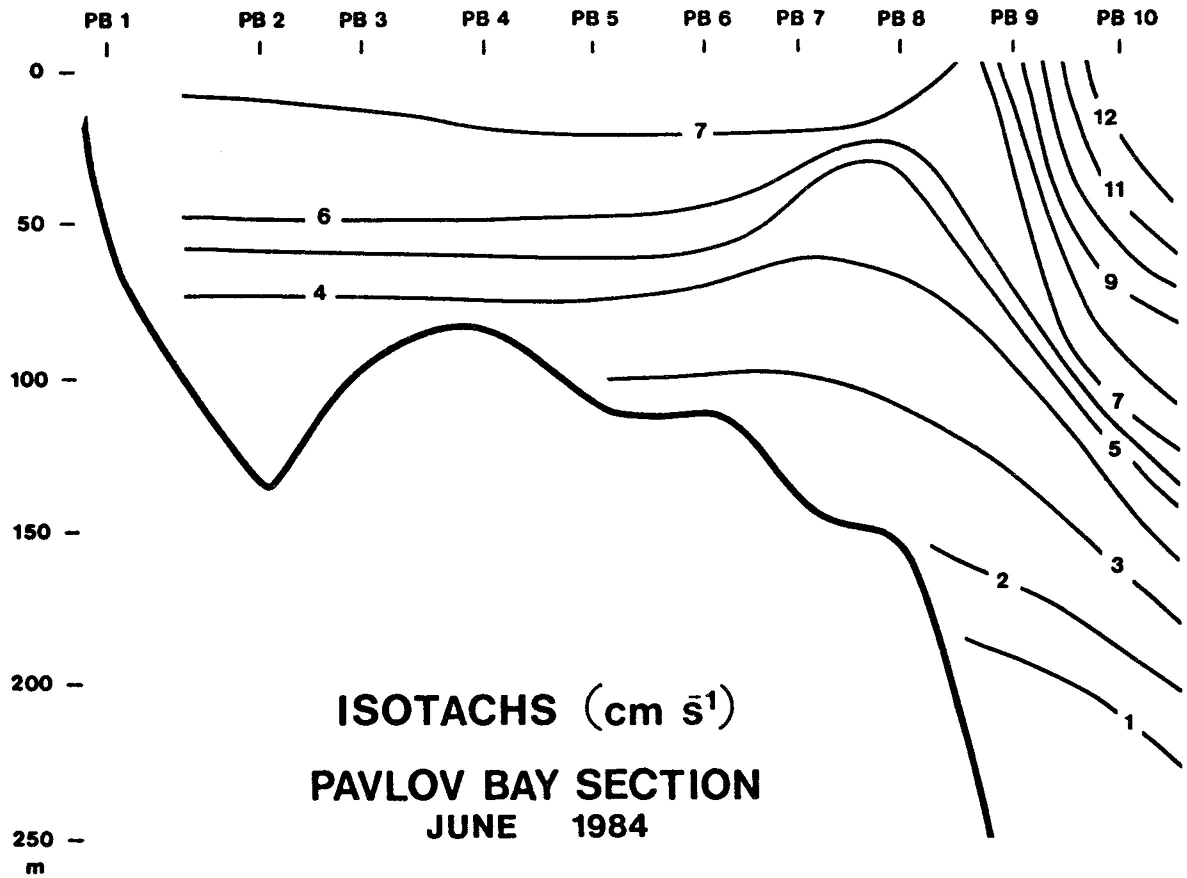

Figure 2.24 - Isotachs, Pavlov Bay, June. Positive flows are out of the page; i.e., to the southwest.

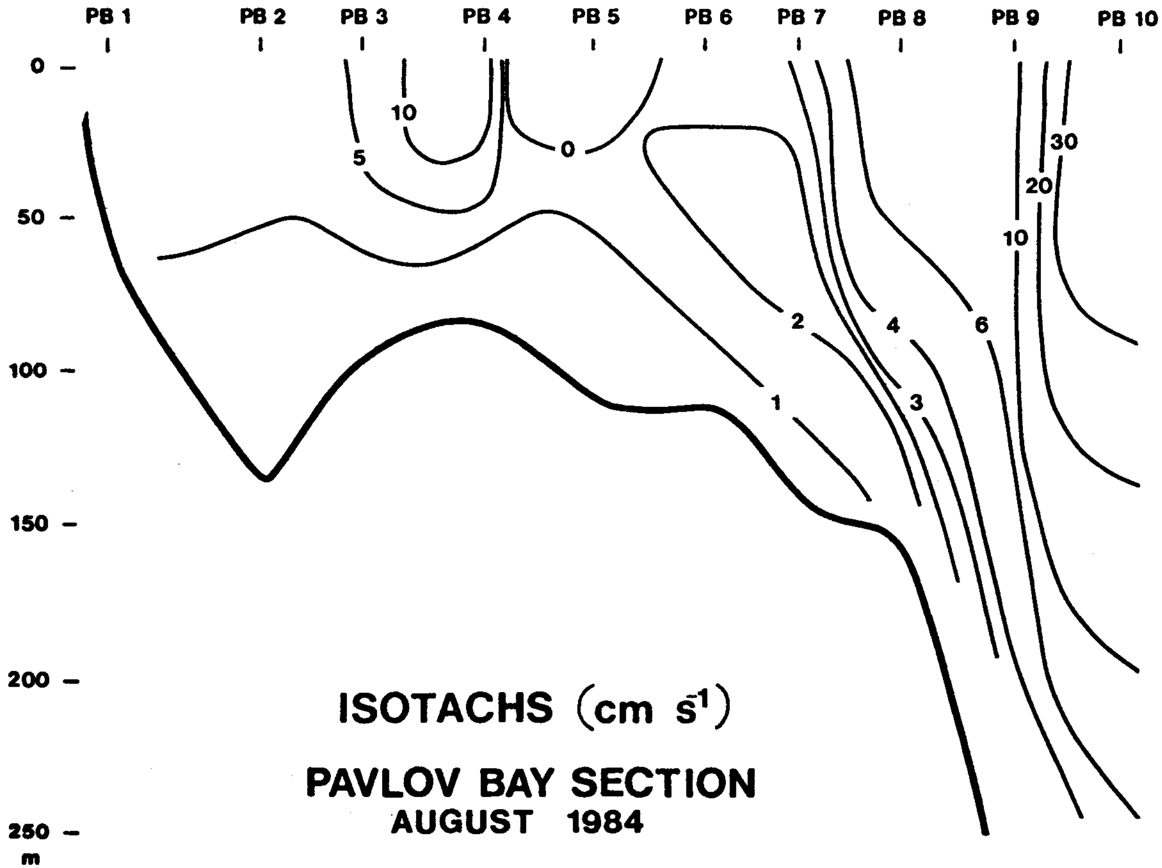

Figure 2.25 - Isotachs, Pavlov Bay, August. Positive flows are out of the page; i.e., to the southwest.

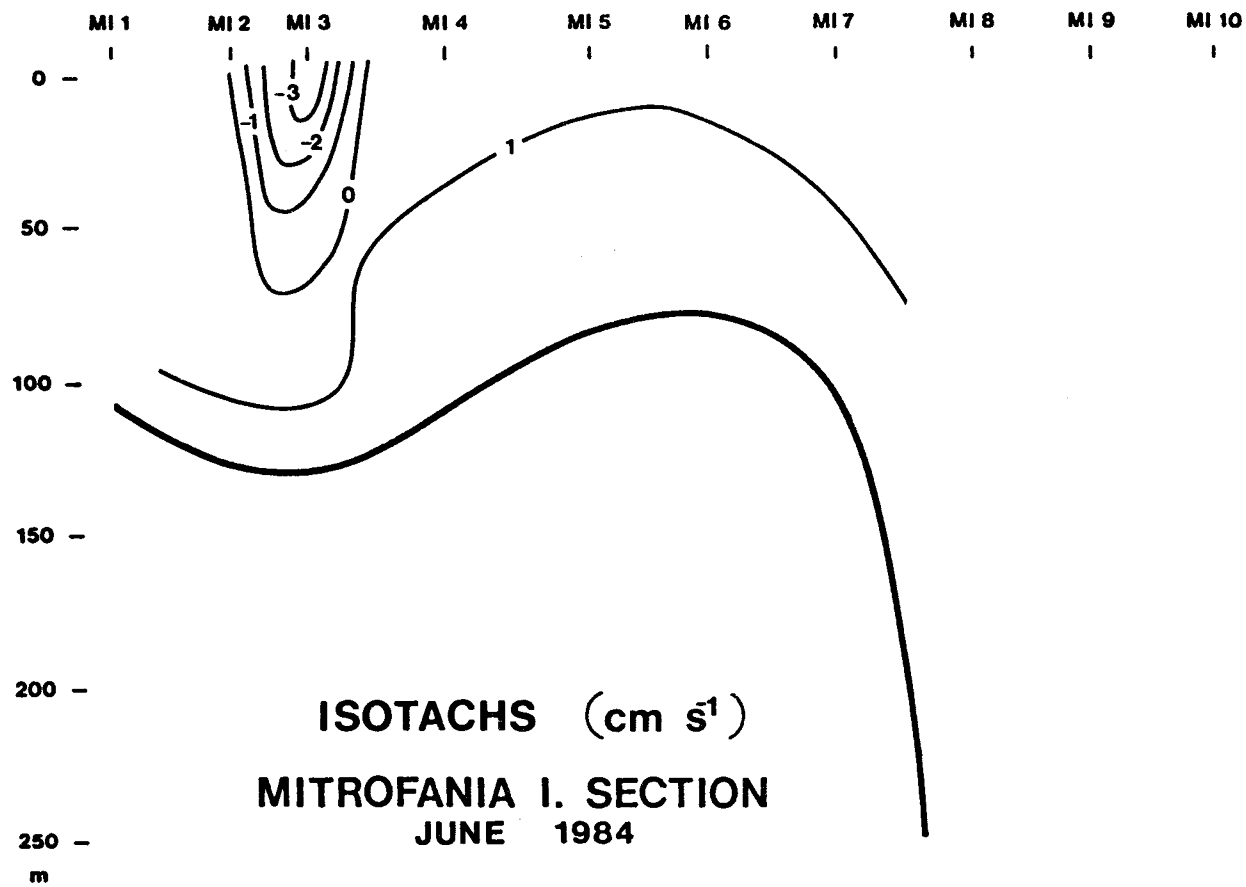

Figure 2.26 - Isotachs, Mitrofania Island, June. Positive flows are out of the page; i.e., to the southwest.

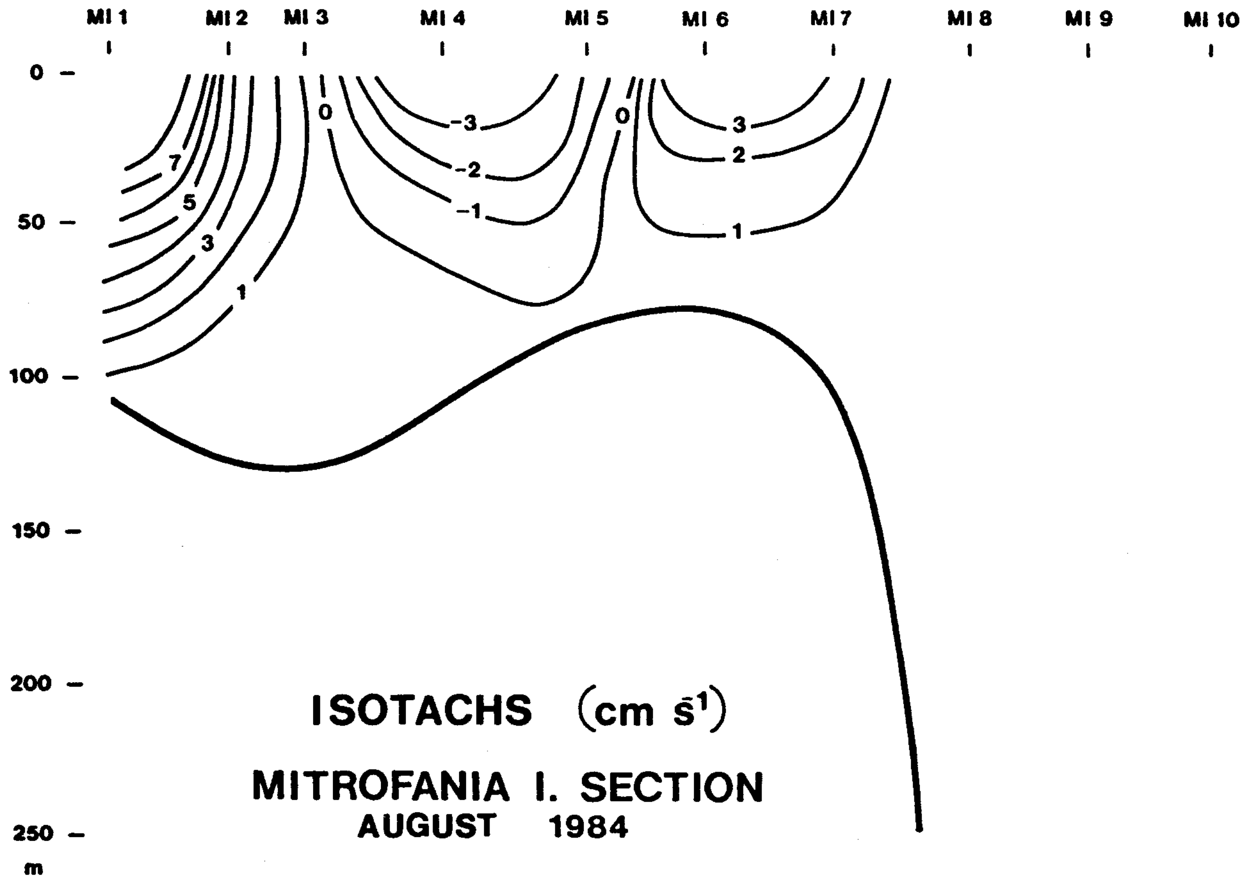

Figure 2.27 -- Isotachs, Mitrofania Island, August. Positive flows are out of the page; i.e., to the southwest.

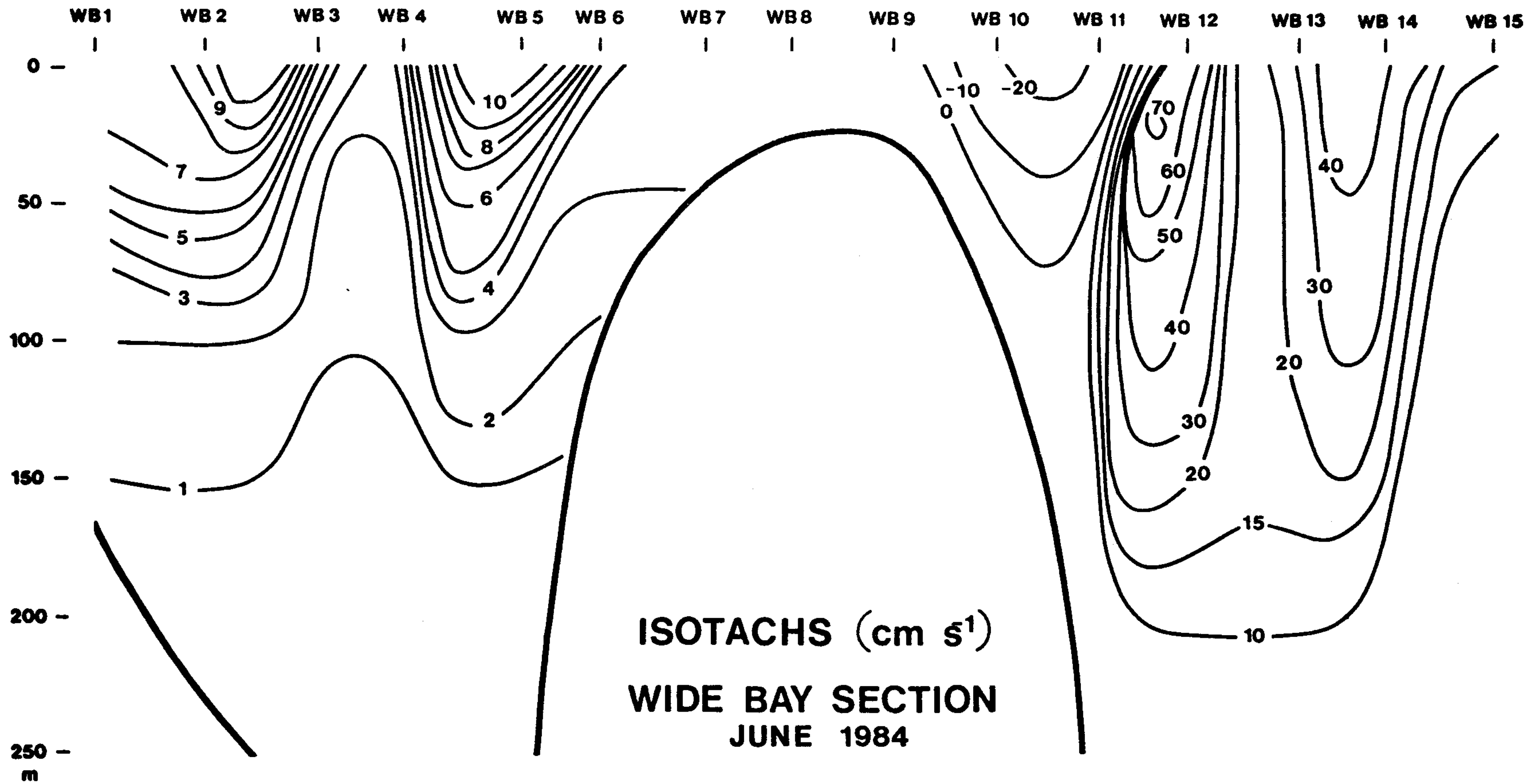

Figure 2.28 - Isotachs, Wide Bay, June. Positive flows are out of the page; i.e., to the southwest.

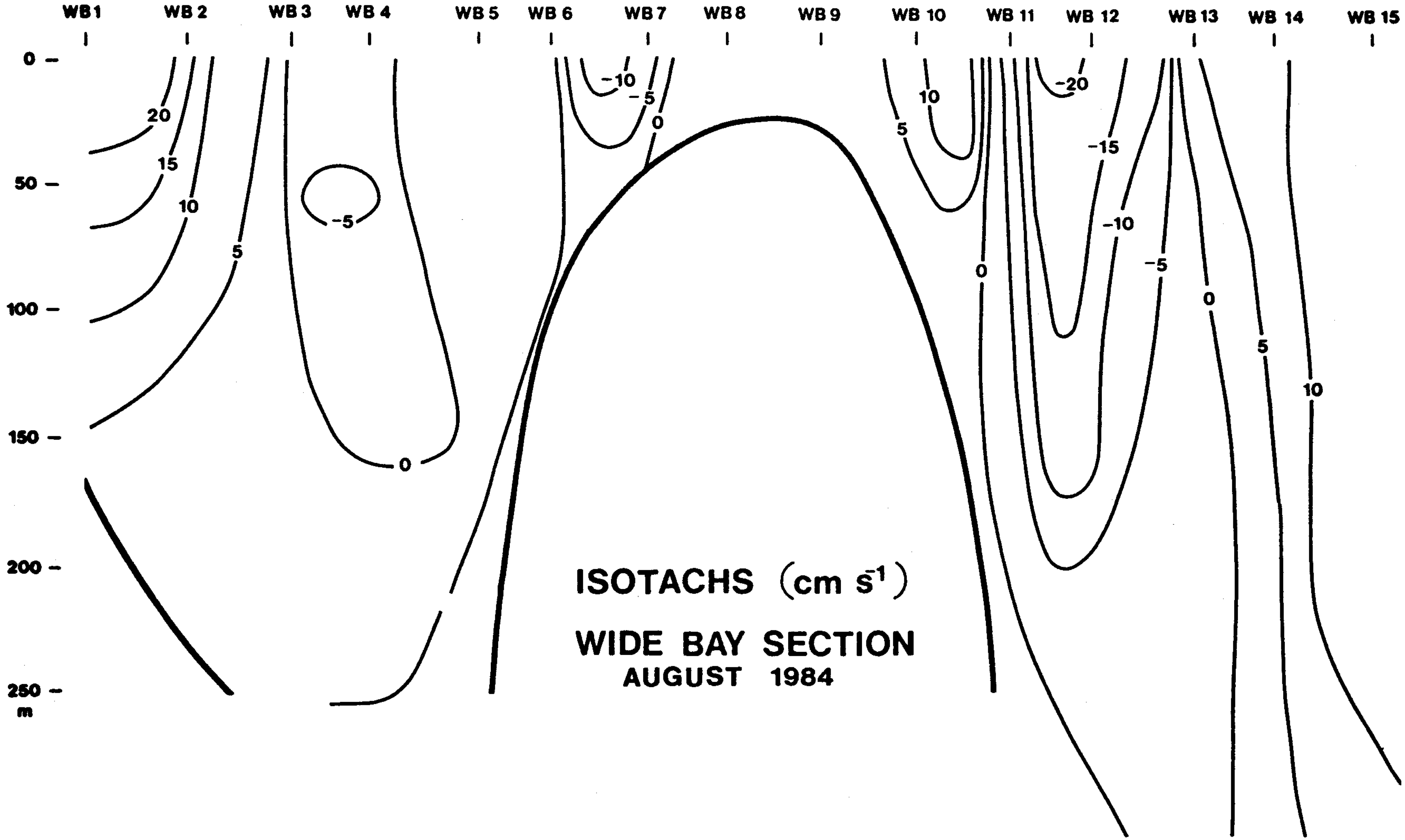

Figure 2.29 - Isotachs, Wide Bay, August. Positive flows are out of the page; i.e., to the southwest.

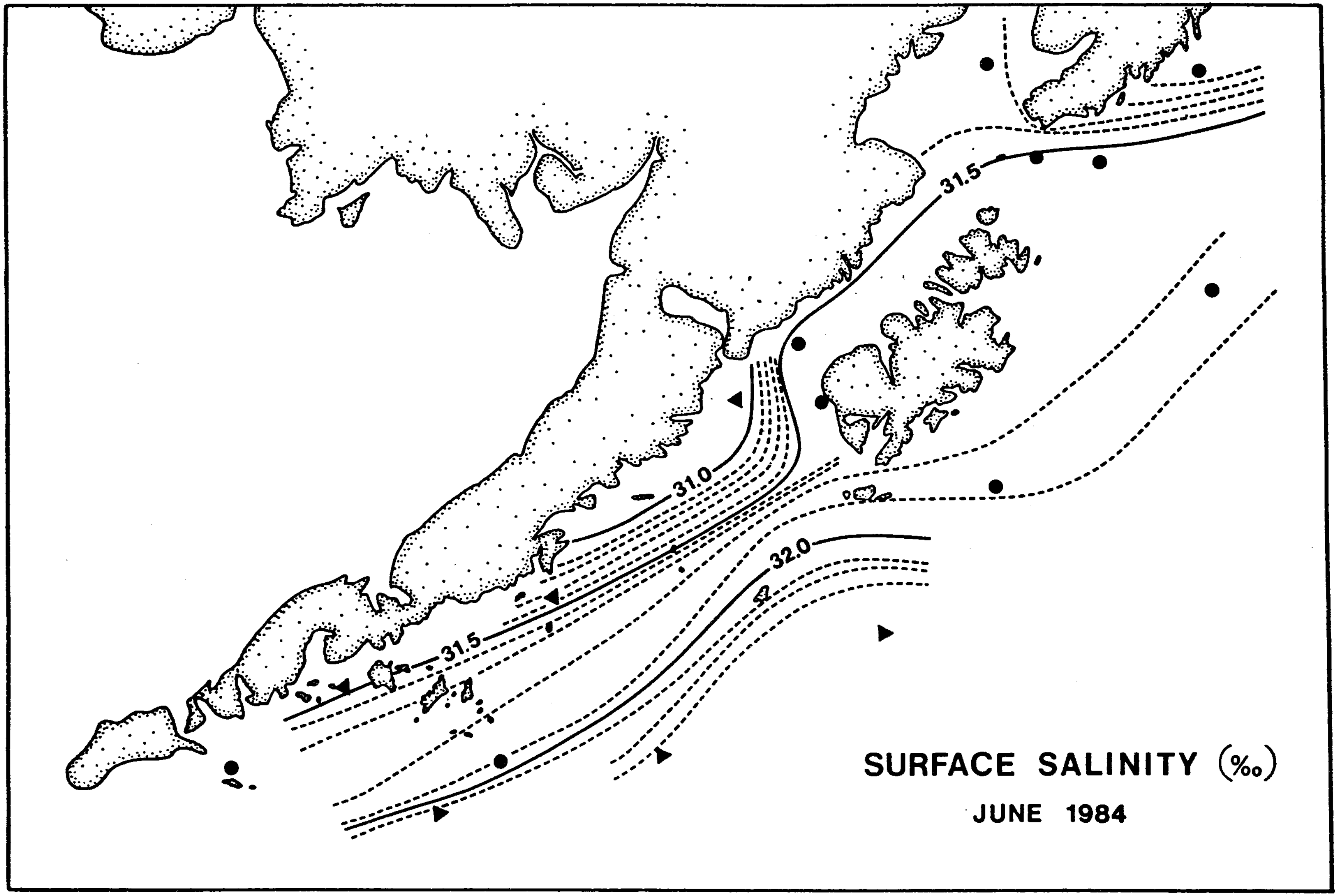

Figure 2.30 - Surface salinity, June.

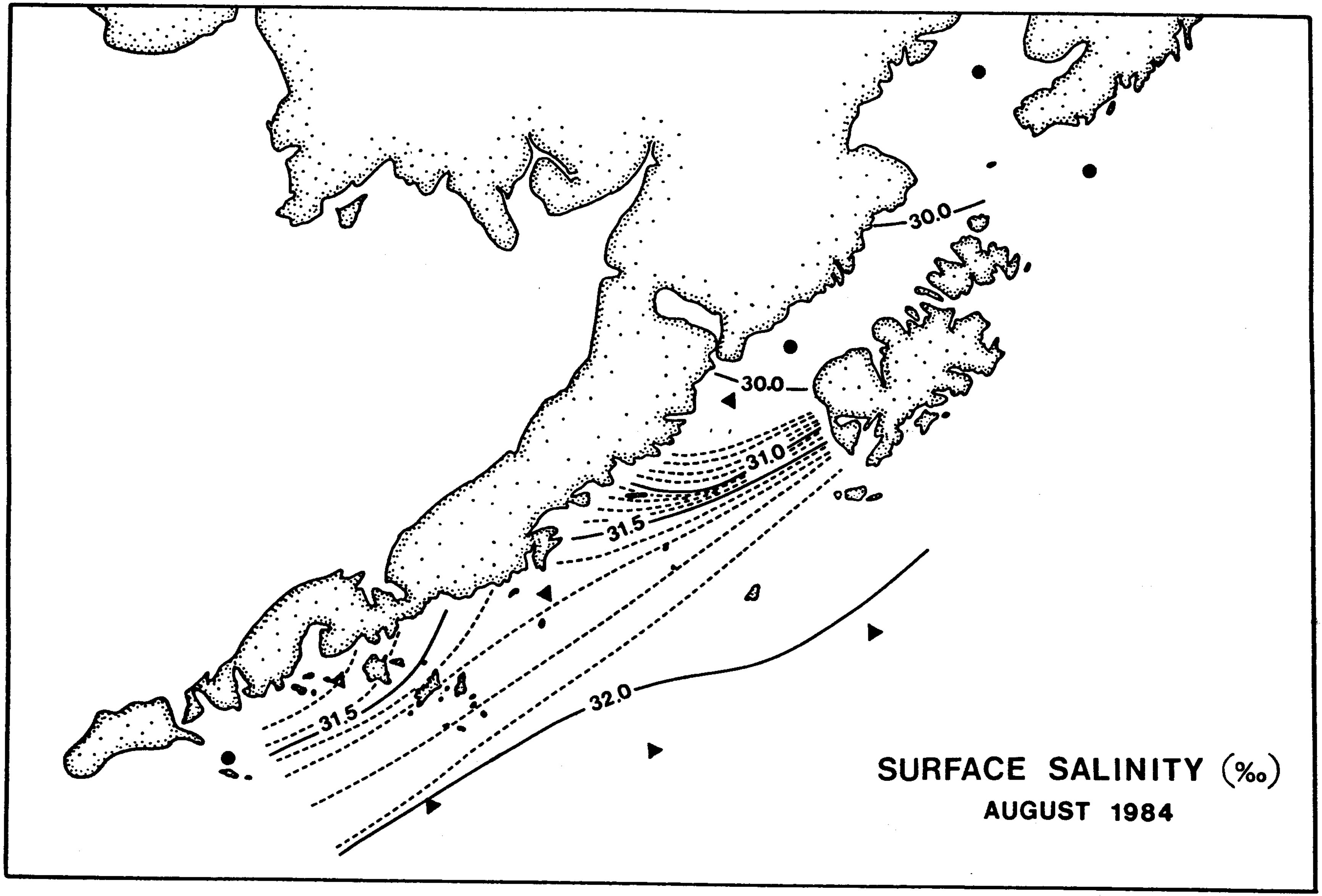

Figure 2.31 - Surface salinity, August.

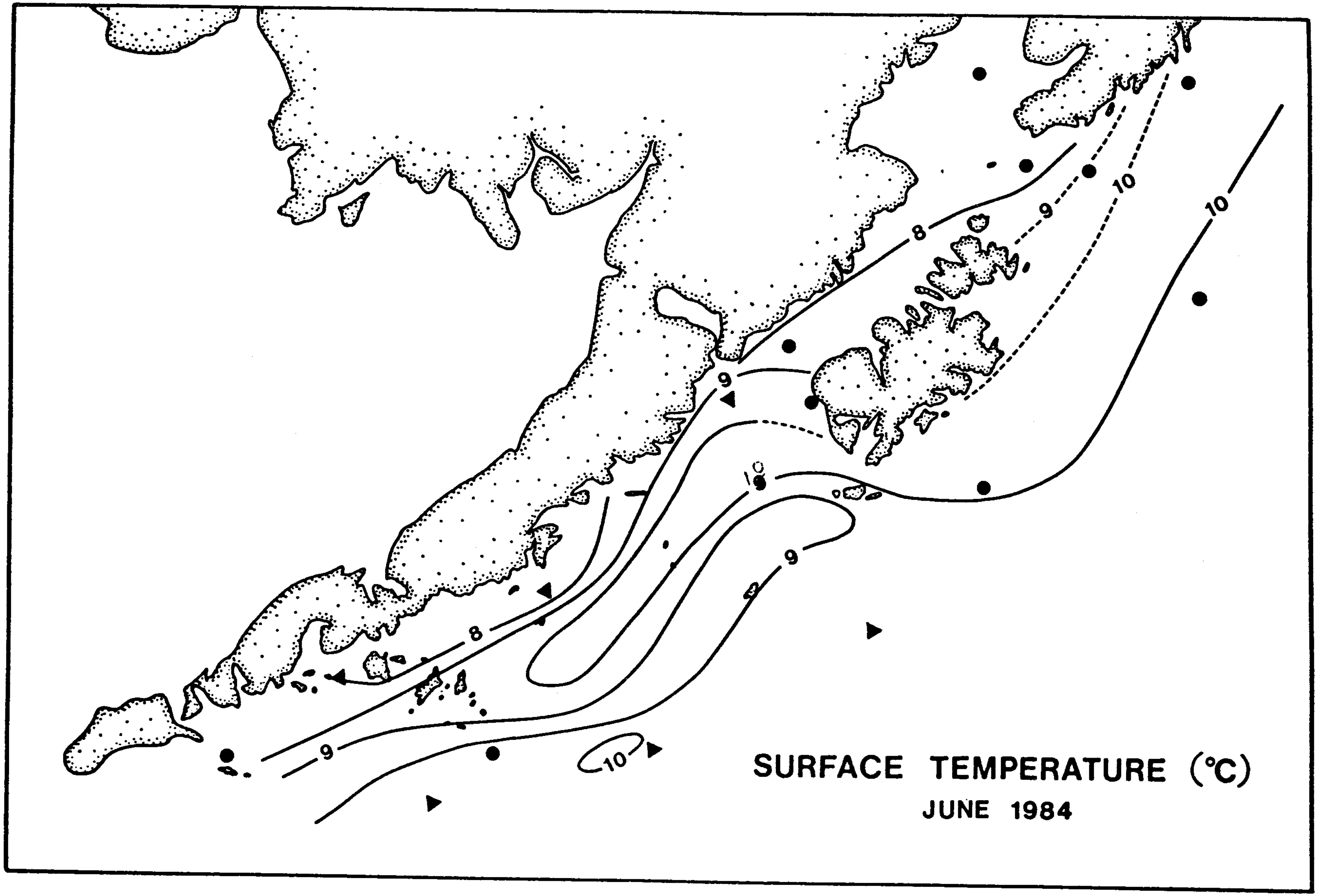

Figure 2.32 - Surface temperature, June.

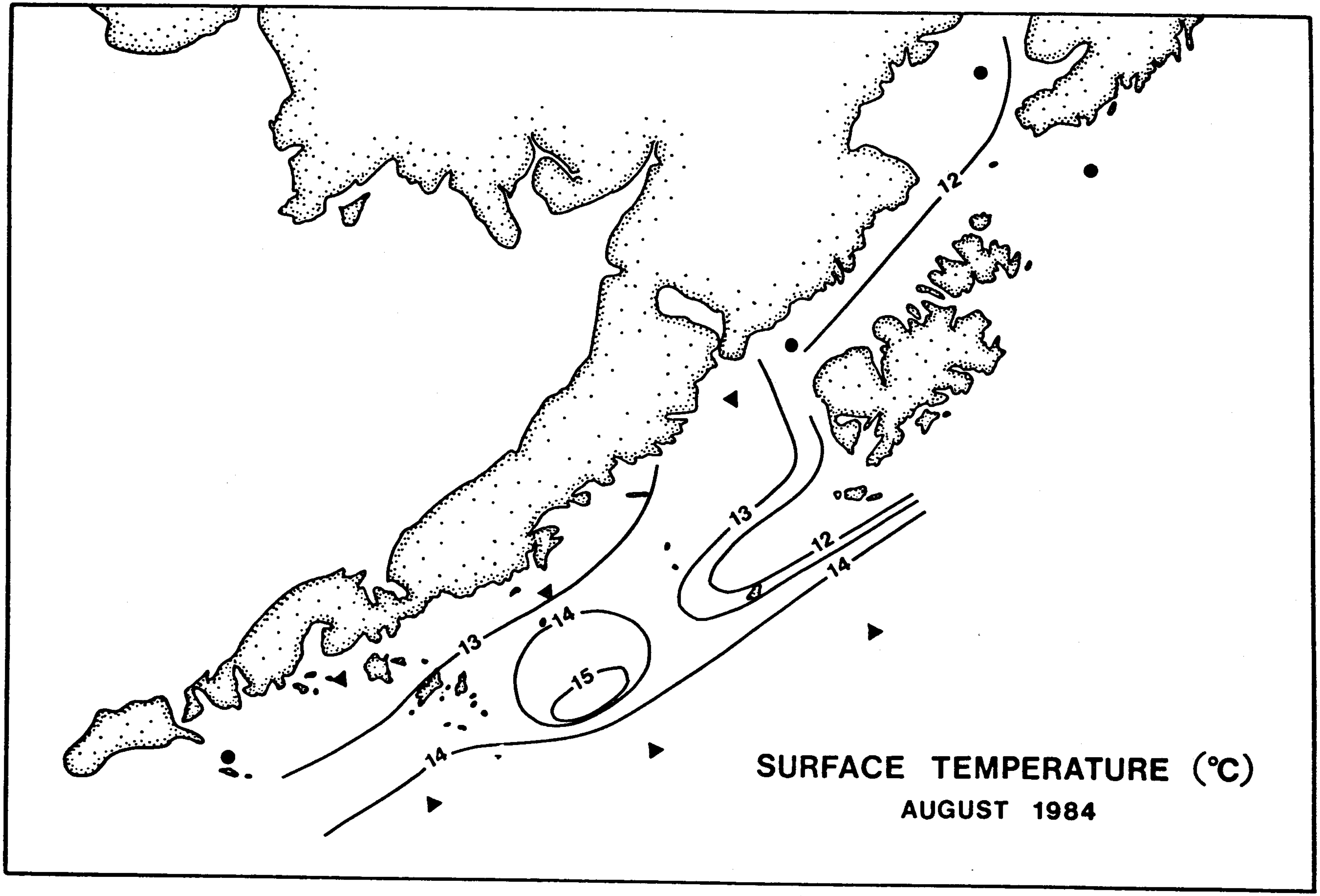

Figure 2.33 - Surface temperature, August.

3. TIDAL OSCILLATIONS

In this report we examine the tidal and subtidal components of the spectra of sea surface and current oscillations separately. The forcing function for the tides is deterministic and well understood so the tidal section of the report can be quantitative in nature. On the other hand, sub-tidal oscillations, including the mean flow may be forced or maintained through a variety of mechanisms so that several statistical procedures have been employed. These are discussed in Section 4.

3.1 TIDAL HEIGHT

The tidal analyses show that the tides in the region are mixed, mainly semi-diurnal. Form numbers (the ratio of the two largest diurnal to the two largest semi-diurnal components) vary between 0.51 and 0.98. Since the relative magnitudes of the tidal constituents vary substantially among the seven tide gauge locations, it is useful to examine the total tidal oscillation as represented by the spring tidal range.

The largest tides of the year occur when the K_1 component is in phase with the M_2 and S_2 components (usually around the solstices). A good approximation of the maximum tidal range can be computed from

$$R_{max} = 2(M_2+S_2+N_2+K_1+O_1). \qquad (3\text{-}1)$$

These ranges are listed below in Table 3.1 along with the estimated maximum ranges at Anchorage and Kodiak.

The highest tides in the region of study occur at Seal Rock, Cape Ikolik and Amatuli Island. The causes for these high ranges are likely shoaling and the reflection of substantial tidal energy from the coast with the attendant formation of partially standing tide waves. Tidal energy propagation is addressed in Section 3.2.

Table 3.1 Maximum Tidal Ranges

Location	Range (m)
Sanak	3.39
Portlock Bank	4.61
Seal Rock	5.10
Cape Ikolik	5.88
Shumagin	3.54
Albatross Bk.	4.25
Amatuli Is.	6.33
Anchorage (estimate)	11.3
Kodiak (estimate)	4.0

Cotidal charts for the four largest constituents have been plotted and are presented in Figures 3.1 through 3.4. These charts show lines of equal Greenwich phase (cophase lines) and equal amplitude (corange lines). In all cases the tide appears to propagate from northeast to southwest, but there is a suggestion (from the sparse data points) that the tidal propagation is onto the shelf west of Kodiak Island. In non-dissipative (frictionless) systems the corange lines should be normal to the cophase lines. This is roughly the case for the M_2 constituent on the outer shelf. The amplitude of the M_2 constituent increases toward Cook Inlet indicating either pronounced shoaling or that some of the tidal energy is reflected in that area. However the Tide Tables show a six hour phase lag between Seldovia and Anchorage indicative of a progressive wave and little reflection. The increase in amplitude in Cook Inlet is, therefore, probably due solely to the decrease in depth.

The S_2, K_1 and O_1 cotidal charts display cophase and corange lines which are parallel - suggestive of a progressive wave in which energy is transported, eventually being dissipated by bottom friction.

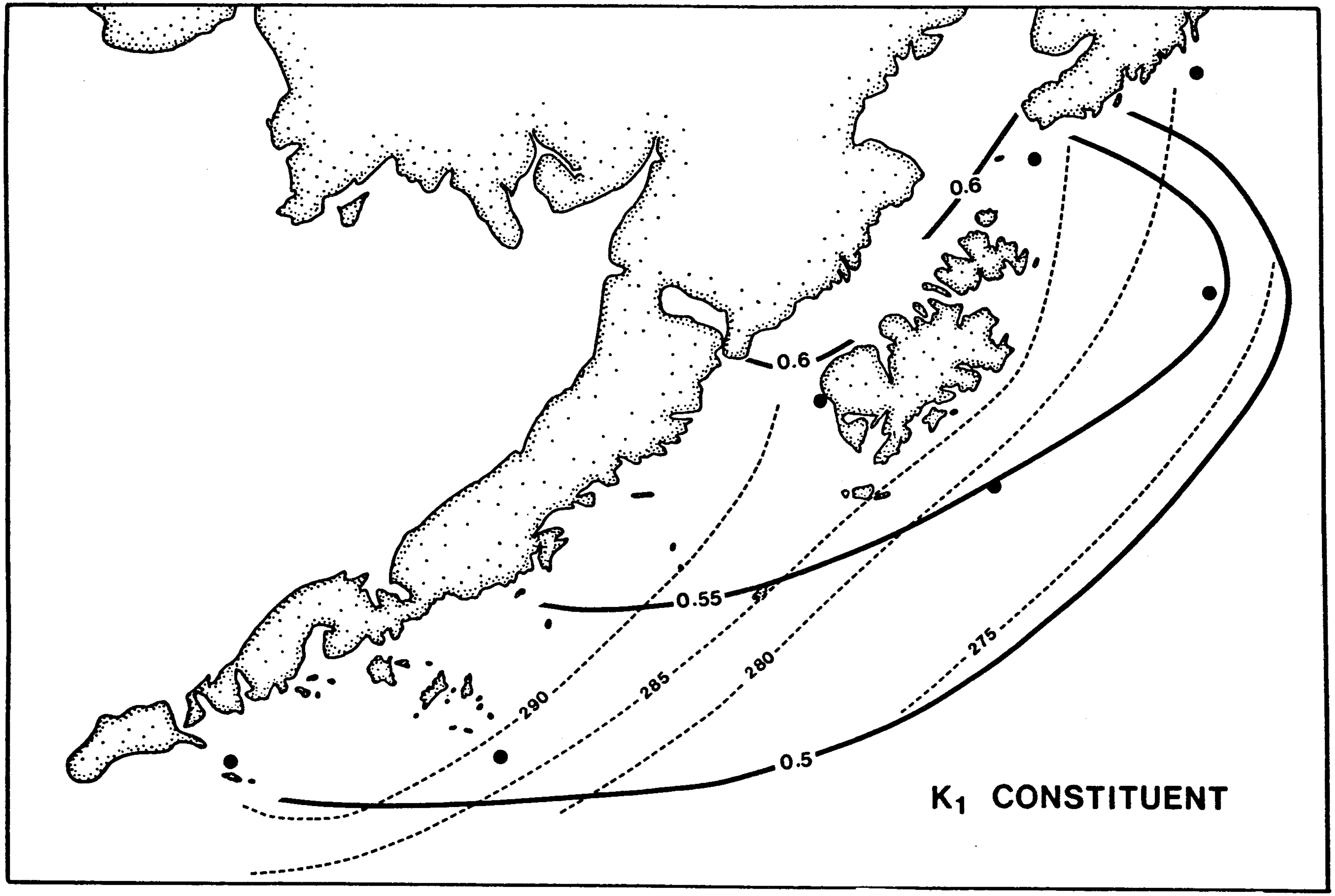

Figure 3.1 - Cotidal chart for the K_1 constituent. Corange line (solid) in meters, cophase lines (dashed) in degrees relative to Greenwich.

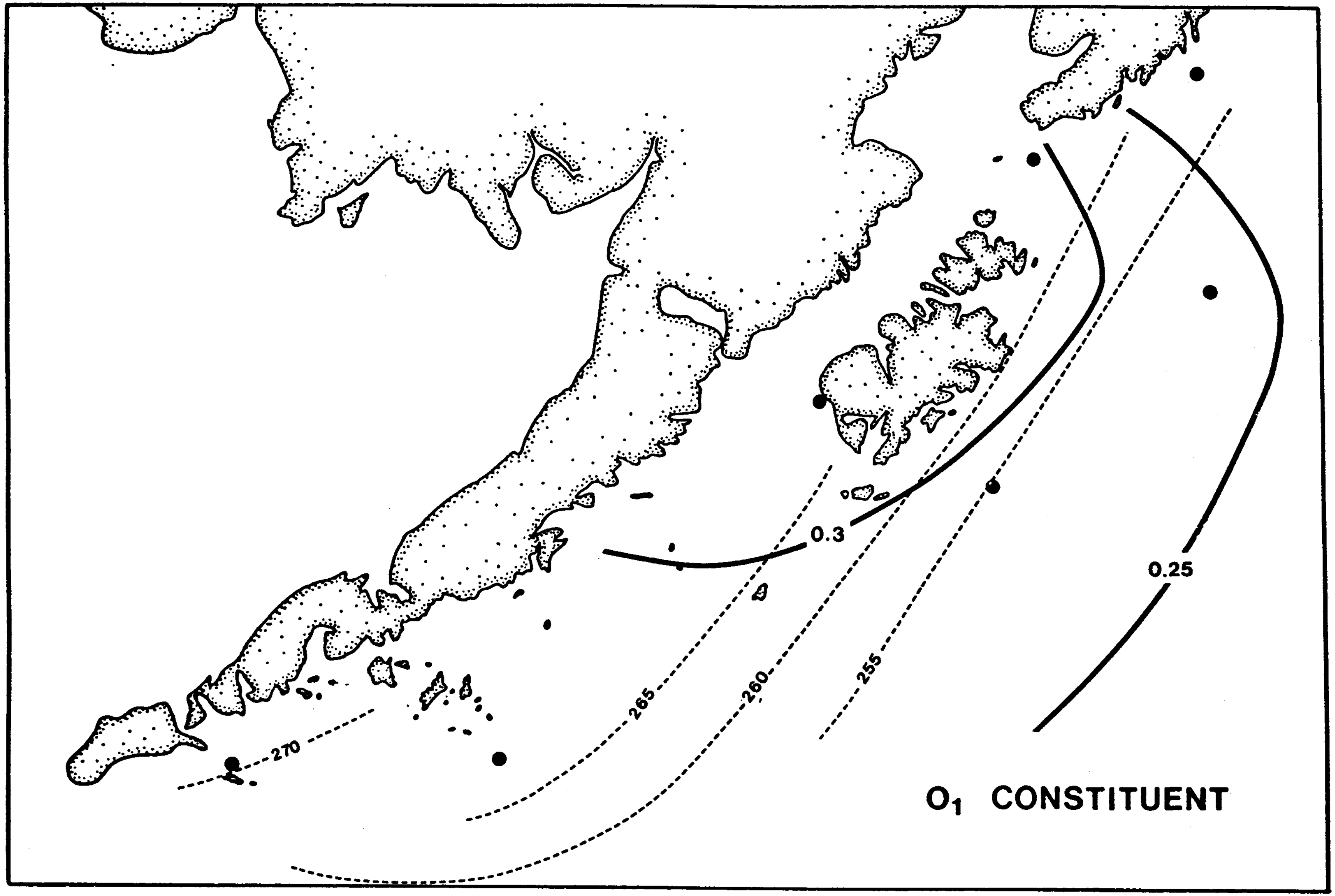

Figure 3.2 - Cotidal chart for the O_1 constituent. Corange line (solid) in meters, cophase lines (dashed) in degrees relative to Greenwich.

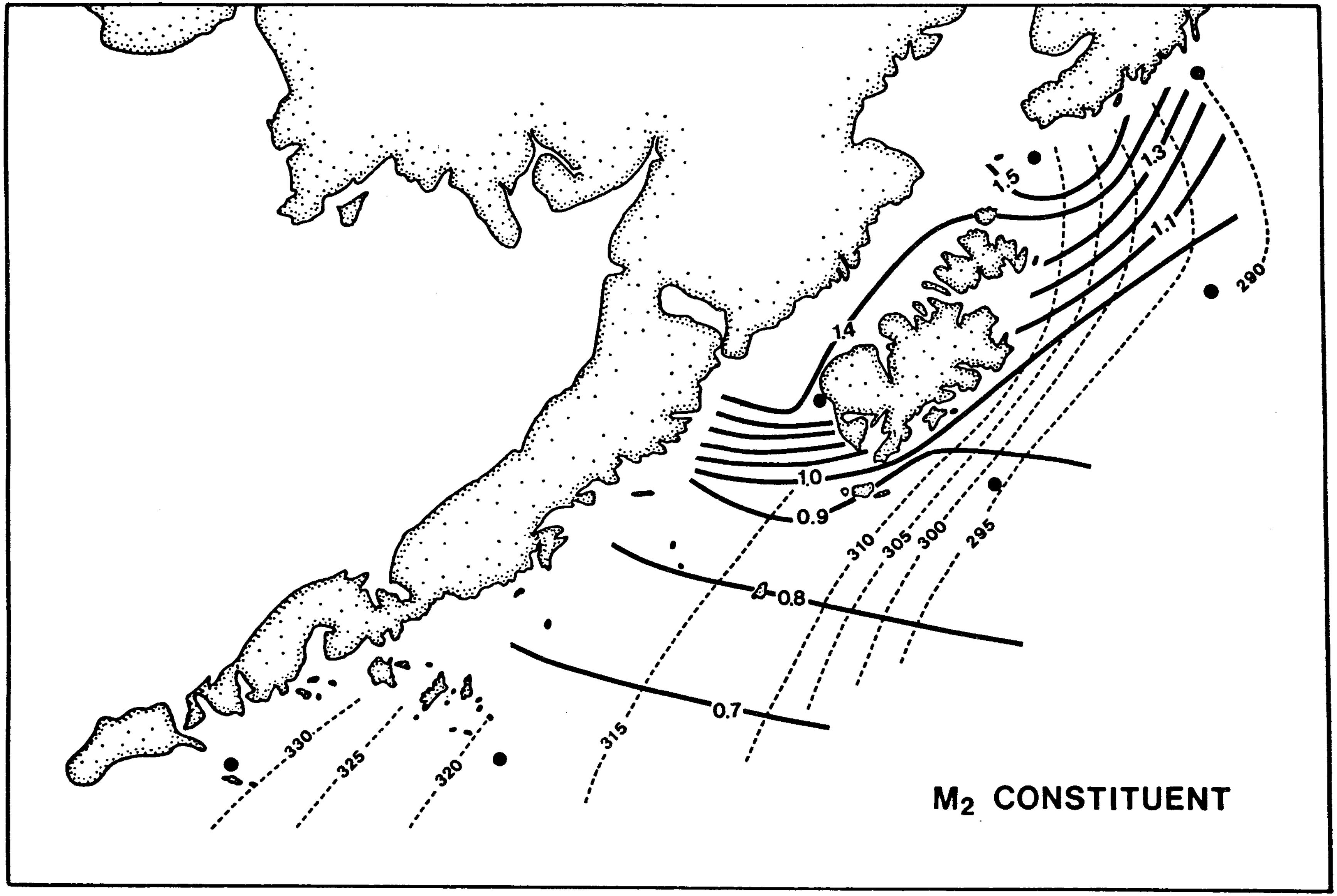

Figure 3.3 - Cotidal chart for the M_2 constituent. Corange line (solid) in meters, cophase lines (dashed) in degrees relative to Greenwich.

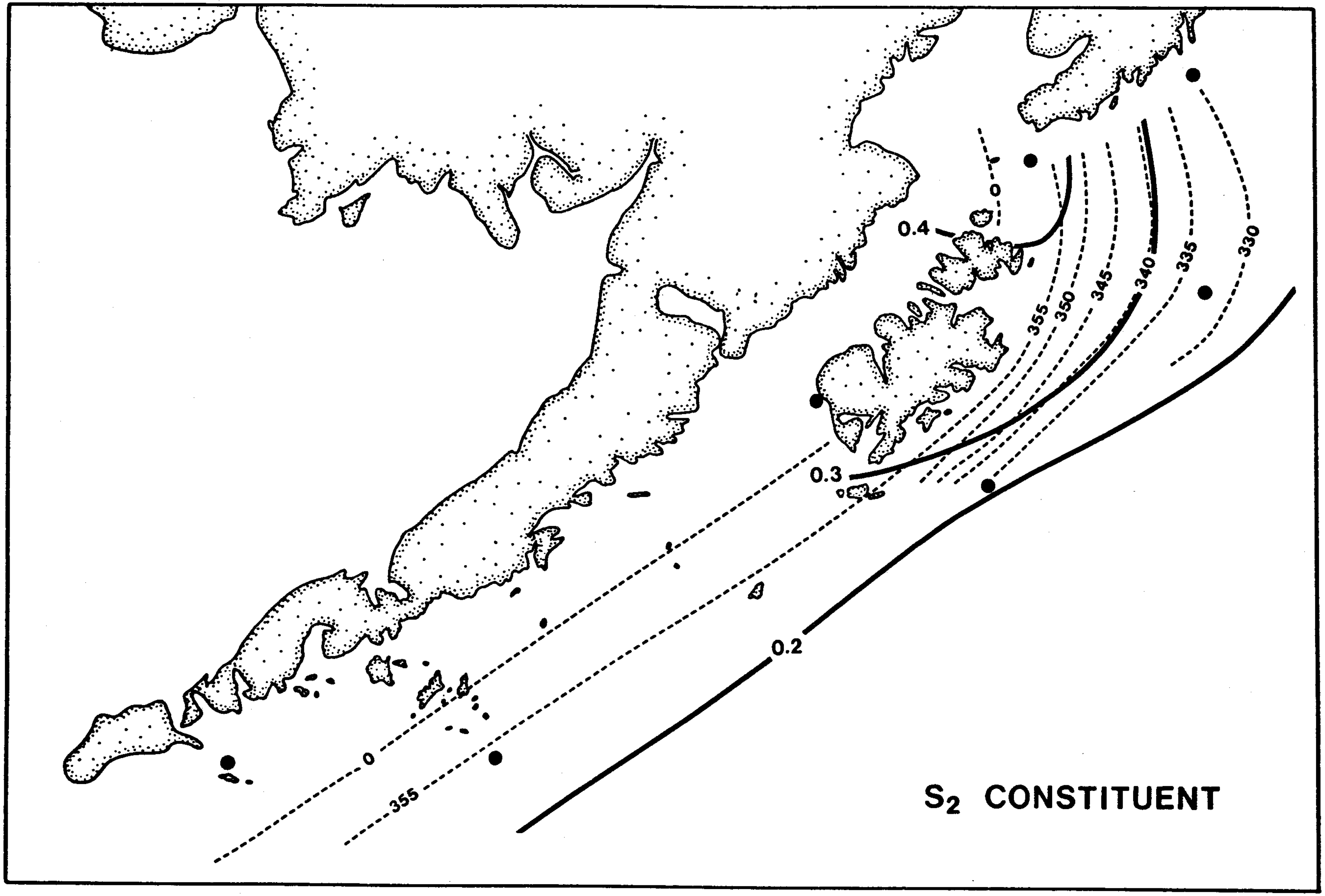

Figure 3.4 - Cotidal chart for the S_2 constituent. Corange line (solid) in meters, cophase lines (dashed) in degrees relative to Greenwich.

Although the cotidal charts are very rough, one can gain some confidence in them by noting that for the M_2, S_2 and K_1 constituents the bottom topography is quite well reflected in the speed of the waves as determined by the distance between cophase lines: the propagation speed is lower over Portlock Bank than in other areas.

3.2 TIDAL CURRENTS

3.2.1 Tidal Energy Propagation

The power propagated per unit width of a tide wave or energy flux can be computed using the results of the tidal stream and tidal height analyses. The energy flux per unit width integrated over depth and over the tidal period for any constituent is

$$E = \rho\, gh \frac{1}{2\pi} \int_0^{2\pi} A \cos(nt) V \cos(nt + \theta) dt \qquad (3\text{-}2)$$

(e.g. Platzman, 1971) where E is the energy flux, ρ is the density of sea water, g is gravity, h is the depth, A is the amplitude of the tidal height oscillation, V is the amplitude of the tidal current, n is the frequency of the constituent and θ is the phase difference between the tidal height and tidal current. Integration of equation 3-2 yields

$$E = 1/2\ \rho\, ghAV \cos\theta. \qquad (3\text{-}3)$$

Thus when the tidal current is in phase with the tidal height (maximum current at high water) a purely progressive wave is present, there is no reflection, and all tidal energy is propagated in the direction of the major axis of the tidal ellipse. When the current is 90° out of phase with the tidal height, then the tide wave is purely standing in character, there exists complete reflection and no net energy flux.

Visual comparison of the current and pressure time series from the Cook Inlet mooring (harmonic analysis of the pressure record from the current meters is inadvisable due to limited resolution) yields a near zero phase difference implying progressive tide waves which dissipate much of their energy on the extensive flats in Cook Inlet. On the other hand, the tidal height and current are about 66° out of phase at the Shelikof Strait mooring; characteristic of little energy propagation and a tide wave nearly standing in character.

The practical significance of these observations is that maximum currents occur roughly mid-way between low and high tide in Shelikof Strait but closer to low and high tide in southern Cook Inlet.

Quantitative evaulation of the energy flux by equation 3-3 is possible where tide gauges and current meters are in close proximity. The pressure sensors on the current meters were not of great enough precision to permit reliable tidal analyses. We have computed the tidal energy flux per meter of channel width for the four largest constituents. It should be noted that the direction of energy propagation is along the major axis of the tidal ellipse. This direction is given in the tidal stream analysis with a $\pm$ 180° ambiguity, but the current phase is computed according to the direction of the semi-major axis specified. If a negative energy flux resulted from the calculation for Table 3.2, then a 180° correction was applied to the direction of the semi-major ellipse axis given in the tidal analyses. The DIR column of Table 3.2 therefore shows the actual direction of tidal energy flux.

The tidal current constituents used in the computations were approximately the barotropic components of the tidal current constituents (exactly for M_2). The barotropic component was computed from knowledge of the modal structure and the tidal currents at two depths (see section 3.2.2). The most confidence can be placed on the results from Sanak where the current meters and tide gauges were on the same mooring. The Cape Ikolok tide gauge and Shelikof Strait current meter appear to yield logical results while the Amatuli Island gauge and Stevenson Entrance meters display a peculiar phase lag.

Table 3.2 Tidal Energy Flux

Location	A (m)	V (m/s)	θ (°)	h (m) (Approx)	DIR (°True)	Power (kw/m)
O_1						
Sanak	0.27	0.029	- 10	45	091	1.8
Ikolik-Shelikof	0.31	0.016	50	200	046	3.2
Amatuli-Stevenson	0.31	0.036	245	100	176	2.4
K_1						
Sanak	0.50	0.056	153	45	104	5.8
Ikolik-Shelikof	0.59	0.032	54	200	045	11.4
Amatuli-Stevenson	0.58	0.065	249	100	166	7.0
M_2						
Sanak	0.63	.034	36	45	349	4.0
Ikolik-Shelikof	1.39	.145	68	200	048	77.3
Amatuli-Stevenson	1.55	.287	241	100	173	111.6
S_2						
Sanak	0.16	.011	64	45	37	0.2
Ikolik-Shelikof	1.39	.044	65	200	46	7.2
Amatuli-Stevenson	0.42	.101	239	100	179	11.3

Tidal energy propagation for all the constituents appears to be northeastward into Shelikof Strait. The mean phase lag between the tidal heights and currents at the southwestern end of Shelikof Strait is about 60 degrees which implies that about half the tidal energy is reflected.

At Sanak, tidal energy is propagated to the north and east (between 349° and 104° true). The diurnal constituents propagate nearly eastward while the semi-duirnal constituents nearly northward. There appears to be no consistency among constituents regarding the standing/progressive nature of the tide waves.

At Stevenson Entrance all four tidal constituents appear to propagate energy to the south. The current meters at this site exhibit comparable Greenwich phases and the phase difference between heights and currents is nearly constant. An error in timing is therefore very unlikely. Also unlikely is the presence of an amphidrome on Portlock Bank for all the tidal constituents. The phase differences between the Amatuli gauge and the Cook Inlet current meters are less than 10° for the semi-duirnal constituents thus consistent will the notion of a progressive wave in southern Cook Inlet and substantial tidal energy dissipation over the shallows there (independent confirmation of our current measurements in Cook Inlet exist in the report of Patchen et al, (1981)). At this writing we are unable to explain the apparent anomalous southward propagation of tidal energy in Stevenson Entrance.

The magnitude of the tidal energy flux in the vicinity of Kodiak Island is about 90 kilowatts per meter of channel width. Using 25 km as an appropriate width for Shelikof Strait, this amounts to about 2.25×10^9 watts, about 0.1% of the tidal energy in the world ocean (LeBlond and Mysak, 1978). The data appear to indicate that the tidal energy flux is northeastward into Shelikof Strait. Presumably much of this energy is dissipated in Cook Inlet but the apparent southward energy flux at Stevenson Entrance is still puzzling.

3.2.2 Internal Tides

Internal tides may be generated on the continental slope and can account for substantial phase differences between near surface and deep flows. In addition to the velocity signature of such oscillations, there exist concomitant vertical oscillations of the density surfaces. Unlike the surface or barotropic tides, the internal tides are characterized by velocity and displacement fields which are functions of depth.

The vertical velocity can be represented as:

$$w = W(z) \exp\,[i\,(kx - nt)] \tag{3-4}$$

where w is the vertical velocity, W(z) is the depth varying amplitude of the velocity fluctuation, k is a horizontal wave number vector and n is the angular frequency of the wave. The vertical mode structure can be found from the linearized internal wave equation:

$$\frac{\partial^2}{\partial t^2}(\nabla^2 w) + N^2(z)\,\nabla_h^2 w + f^2\,\frac{\partial^2 w}{\partial z^2} = 0 \tag{3-5}$$

where N (z) is the Vaisala frequency $= \sqrt{-\frac{g}{\rho}\,\frac{\partial \rho}{\partial z}}$, and f is the Coriolis parameter. Substitution of eq 3-4 into eq 3-5 yields

$$\frac{d^2 W}{dz^2} + \left[\frac{N(z) - n^2}{n^2 - f^2}\right] k^2\, W = 0 \tag{3-6}$$

(Further details of internal wave dynamics can be found in Phillips, 1966.) Solution of eq. 3-6 can be performed numerically if the distribution of density with depth is known. Such solutions yield a vertical structure of vertical velocities. The Z derivative of the vertical velocity is proportional to the horizontal velocity so that a normalized distribution of horizontal velocity amplitude as a function of depth can be computed.

Mode structures were computed from the June and August CTD data taken at the current meter moorings.

The structures of the first modes for vertical displacements and horizontal velocities for the M_2 constituent are shown in Figure 3.5 along with the density structure in Cook Inlet in August. Note that the maximum horizontal velocity associated with internal tides occurs at the surface and that zero horizontal velocity occurs at a depth of 25 meters where the vertical excursion of the isopycnals and the vertical velocity are the greatest.

The modal structures for the horizontal velocities yield relative magnitudes of the internal oscillation at various depths. For example, at the Cook Inlet mooring in August the amplitudes of the internal velocity oscillations at the two current meters are in the ratio of -0.27/-0.36. The amplitudes of the first internal (baroclinic) and surface (barotropic) tidal oscillations can be computed from this mode structures and the tidal stream analyses of two current time series.

For a given tidal frequency, n, the combined amplitude and phase of the oscillations at the current meters is obtained from the tidal stream analyses. If only the oscillations along the major axes of the tidal ellipses are considered then the oscillations may be represented by

$$V_i = A_i \cos (nt - G_i) \qquad (3\text{-}7)$$

where i = 1,2 for shallow, deep, V_i are the total tidal velocities, A_i are the amplitudes of these velocities and G_i are the Greenwich phases. If m_i are the normalized amplitudes of the velocity fluctuations then the amplitudes and phases of the baroclinic and barotropic oscillations can be computed. These are:

$$BT = \frac{m_1 A_2 \sin \varphi}{(m_1 - m_2) \sin \alpha} \qquad \text{(barotropic amplitude)} \qquad (3\text{-}8)$$

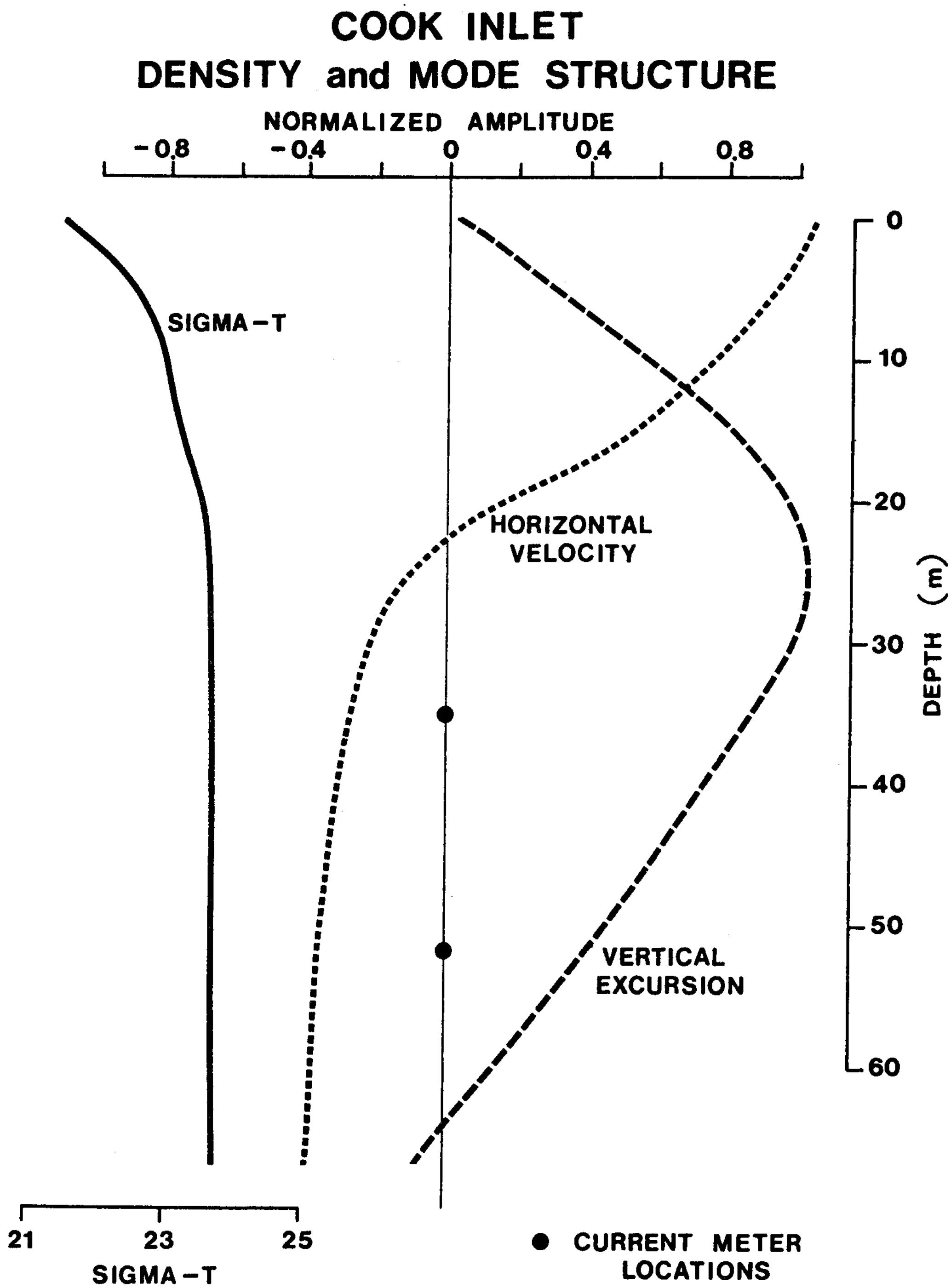

Figure 3.5 - Lowest internal mode structure for the M_2 constituent in Cook Inlet.

$$\tan\alpha = \frac{m_1 A_2 \sin\varphi}{m_1 A_2 \cos\varphi - m_2 A_1} \qquad \text{(barotropic phase)} \qquad (3\text{-}9)$$

$$BC = \frac{A_2 \sin\varphi}{(m_2 - m_1)\sin\beta} \qquad \text{(baroclinic amplitude)} \qquad (3\text{-}10)$$

$$\tan\beta = \frac{A_2 \sin\varphi}{A_2 \cos\varphi - A_1} \qquad \text{(baroclinic phase)} \qquad (3\text{-}11)$$

where $\varphi = G_1 - G_2$ and α and β are phases relative to G_1.

Where possible we used the average stratification (June and August) at the mooring sites to compute the mode structures. These often varied considerably due to the vertical oscillation of the isopycnals. Ideally the density data from which the modes were computed would have been measured over a tidal cycle and averaged. Recognizing the limitations of our density profile data we computed the baroclinic and barotropic modes for the largest (M_2) tidal constituent to obtain an estimate of the internal oscillations, these are listed in Table 3.3.

By far the largest internal tides appear to occur at the Cook Inlet mooring. Indeed examination of the temperaure and salinity time series from the meter at 35 m depth in Cook Inlet shows temperature and salinity oscillations of about 0.4° and 0.4°/oo, respectively. Using the temperature and salinity gradients measured in June and August we can estimate the height of the internal tide

$$H \simeq \frac{\Delta T}{\partial T/\partial z} \simeq \frac{\Delta S}{\partial S/\partial z} \qquad (3\text{-}12)$$

where H is the height of the internal tide and ΔT and ΔS are the tidal excursions of the temperature and salinity values (assuming negligible horizontal gradients). Equation 3-12 yields values of about 30 meters for the vertical excursion of a water parcel at a mean depth of 35 m in Cook Inlet. Such a vertical excursion would produce a horizontal velocity which can be approximated by:

Table 3.3 Barotropic and Baroclinic Velocities For The M_2 Tidal Constitutent (Amplitudes in cm/s)

Cook Inlet

$BT = 96.2 \cos(nt - 2.8° - G_1)$

$BC = -58.6 \cos(nt - 12.8° - G_1)$

Shelikof Strait

$BT = 14.5 \cos(nt + 1.7° - G_1)$

$BC = -1.3 \cos(nt + 30.9° - G_1)$

Stevenson

$BT = 28.7 \cos(nt - 3.5° - G_1)$

$BC = 17.4 \cos(nt - 47.6° - G_1)$

Sanak

$BT = 3.4 \cos(nt - 3.5° - G_1)$

$BC = -1.6 \cos(nt - 67.2° - G_1)$

$$V_{(internal)} = \left(\frac{g}{h}\right)^{1/2} \left(\frac{\Delta\rho}{\rho}\right)^{1/2} \eta \qquad (3\text{-}13)$$

where ρ is the density, g gravity, η the amplitude of the internal wave and h the depth over which $\Delta\rho$ is computed. Eq. 3-13 yields a value of about 35 cm s^{-1} for the fluid velocity associated with internal waves of tidal period in Cook Inlet. This is in qualitative agreement with the amplitude presented in Table 3.3; surprisingly so. Clearly an internal wave of 30 m height in 65 m water depth is no longer a small amplitude wave and many of the assumptions of the theory are inadequate.

Our conclusion here is that substantial internal wave energy of tidal period is present in Cook Inlet. Without tidally averaged CTD data, we cannot confidently ascribe precise amplitudes to these oscillations; however, our observations as well as our computations show that internal tides are present in Cook Inlet. It is therefore unlikely that a purely barotropic tidal model will adequately represent this region.

4. SUBTIDAL OSCILLATIONS

In this section the energy associated with subtidal oscillations is discussed and an attempt made to relate it to atmospheric driving forces. The region is, of course, dominated by tidal oscillations, the tidal kinetic energy accounting for between 50% and 95% of the total kinetic energy. The spectral distribution of energy is shown for the longshore velocity component in Shelikof Strait in Figure 4.1. In Cook Inlet, for example, the mean flows are about 5 cm s^{-1} while the tidal flows exceed 80 cm s^{-1}. For the purposes of this section the tidal oscillations can be considered "noise" and thus for the subtidal oscillations the signal to noise ratio is generally poor. For example any effect due to sea breezes of diurnal period would be completely masked by the tidal flows.

4.1 MEAN FLOWS

The mean velocities recorded over the two month deployment period are shown in Table 4.1. At Stevenson Entrance a weak mean flow to the southeast at depth and south southwest at mid-depth may be due to outflow from the Cook Inlet area. The vertical shear of the alongshore velocity is in the same sense as that measured in Shelikof Strait however, so that the Stevenson Entrance regime could be considered to be linked to Shelikof Strait. It should be noted that mean westerly flow in Stevenson Entrance is suggested in the dynamic topographies of Favorite and Ingraham (1977). In Cook Inlet the mean flow is east northeast at both depths, differing in direction by about 45° from the orientation of the Inlet. It is probable that the recorded mean flows in Cook Inlet are due largely to rectification of strong tidal flows. Such rectification is indicated in the presence of "shallow water" tidal constituents of substantial size. The MK3 and M4 components (terdiurnal and quarter-diurnal respectively) are both of comparable magnitude to the mean flow. The presence of these "difference frequencies" indicates that non-linear effects also produce "sum frequencies". For example the M4 constituent (lunar quarter-diurnal) is a

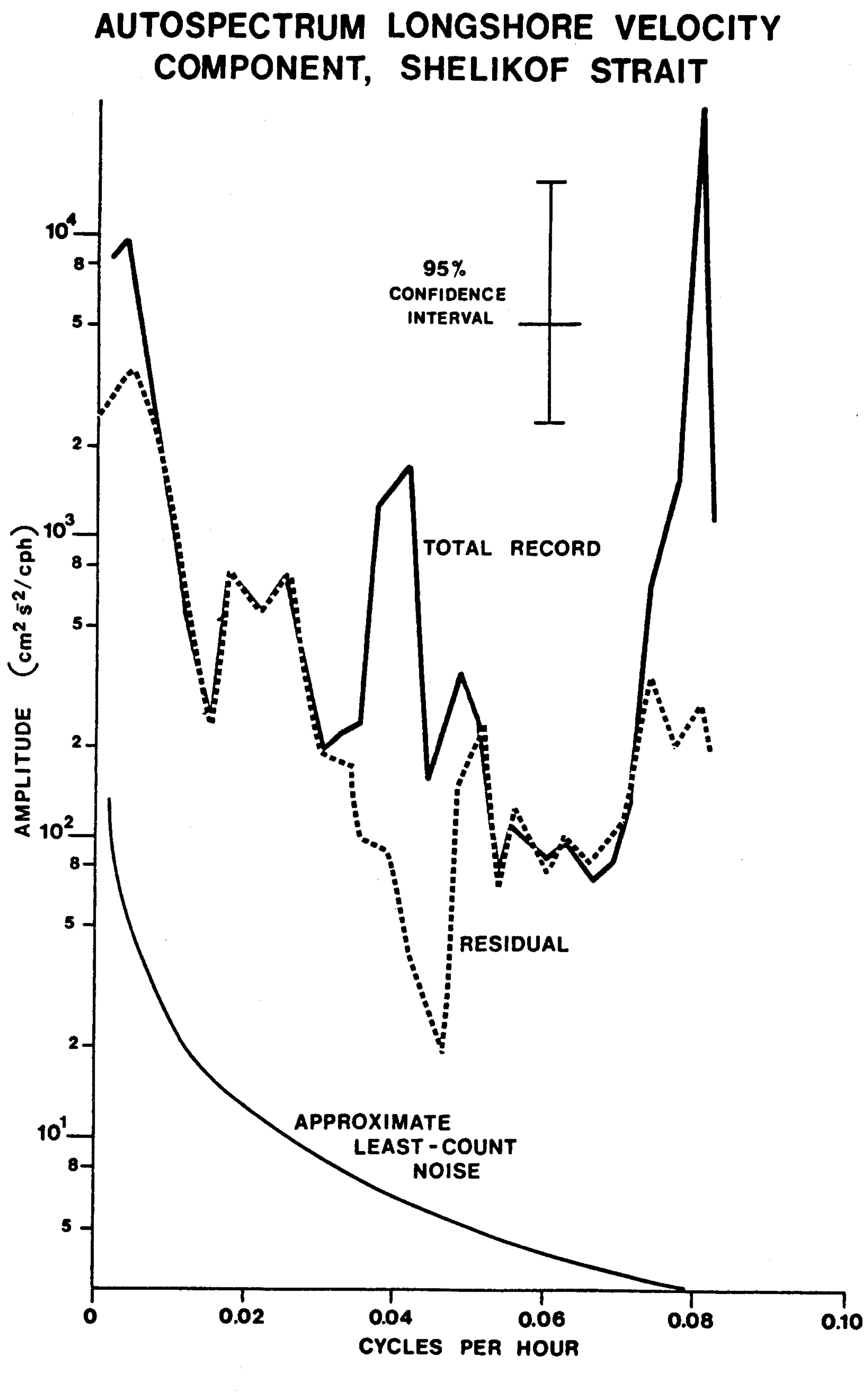

Figure 4.1 - Autospectrum alongshore (225° T) component, 46 m depth in Shelikof Strait.

Table 4.1 Mean Velocities at the Eight Current Meters

Location	Instrument Depth (m)	Water Depth (m)	Speed (cm s-1)	Direction °True
Stevenson	54	113	2.1	212
Entrance	82		2.6	135
Cook	35	66	4.3	078
Inlet	52		5.6	064
Sanak	20	50	2.3	254
Island	41		3.1	299
Shelikof	46	250	3.8	210
Strait	157		1.3	037

manifestation of the shoaling of the M_2 constituent. Also associated with the generation of the M_4 constituent is the generation of a DC (mean flow component). The process is perhaps best envisaged as the beating of two tidal constituents. The beat frequencies are the sum and difference of the two frequencies. In the limit as the two constituents approach an identical frequency, oscillations of twice the fundamental frequency and zero frequency are produced.

At Sanak, where the tidal amplitudes are much smaller, the shallow water tidal constituents are of negligible size and the mean flows at both 20 and 41 meters depth are directed roughly toward the west. This mean flow is generally reflective of the flow of the coastal current.

In Shelikof Strait moderate tidal currents and deep water combine to minimize non-linear tidal effects. The shallow water constituents are small and the mean flows are representative of quasi-steady processes. At the shallow meter the flow is toward the southwest, while at the lower meter it is toward the northeast. Such a velocity distribution is characteristic of an estuarine flow in which the fresher lighter waters move seaward compensated by a slower, but vertically more extensive return flow. Schumacher et al, (1978) suggested that the inflow of deep water into Shelikof Strait occurs to balance the loss of deep water entrained by the outflowing surface waters. Further observations will be necessary to fully describe the estuarine-like flow in Shelikof Strait.

4.2 LOW FREQUENCY FLOWS

The region within about 20 km of the southern Alaska Coast is dominated by the Alaska Coastal Current according to Royer (1981). Maximum speeds can be over 60 cm s^{-1} and transports can exceed 1 x 10^6 m^3 s^{-1}. Royer attributed the variations in the current to variations in freshwater discharge and found wind stress to be a very minor influence. The annual cycle of increasing stratification in early fall and decreasing stratification in late winter changes the magnitude of the internal Rossby radius. Royer mentioned this variation but did not seem to link it with the width of the current itself. In fact, as the stratification increases, the coastal current will become wider.

The Shelikof Strait current meter mooring of the present study was located approximately 14 km offshore of the Alaska Peninsula. The internal Rossby radius in Shelikof Strait during the deployment was between 3.5 km in June and 6.5 km in August. Data from Xiong and Royer (1984) indicate that the maximum internal Rossby radius that might be encountered in Shelikof Strait is about 16 km and would occur in fall at the peak of the freshwater discharge. If the intensity of the flow is proportional to

$$\exp(-y/r_i) \tag{4-1}$$

where y is the offshore distance then the strength of the current from its centerline to the mooring would be reduced by a factor between 10 and 50. It is, therefore, unlikely that flow or flow variations associated with the Alaska Coastal Current would have been measured at the Shelikof Strait mooring or at any of the others deployed during this study.

In order to test the above hypothesis, we employed data for the daily discharges of the Knik and Susitna Rivers (kindly supplied by Professor Royer) to represent the freshwater discharge along this section of the coast. The combined discharge of these rivers peaks in July-August at about 1000 $m^3\ s^{-1}$. The daily mean discharges of these rivers and the alongshore velocity component at 46 m depth in Shelikof Strait are plotted in Figure 4.2. There is no apparent correlation between the discharge and the current; certainly the reversals of the current are not reflected in discharge. The possibility, of course, exists that the currents are driven by freshwater discharge far "upstream", for example, along the coast of southeast Alaska. However, the lengths of the present current records do do not permit comparison over the monthly time scales which would be required to investigate such a driving mechanism.

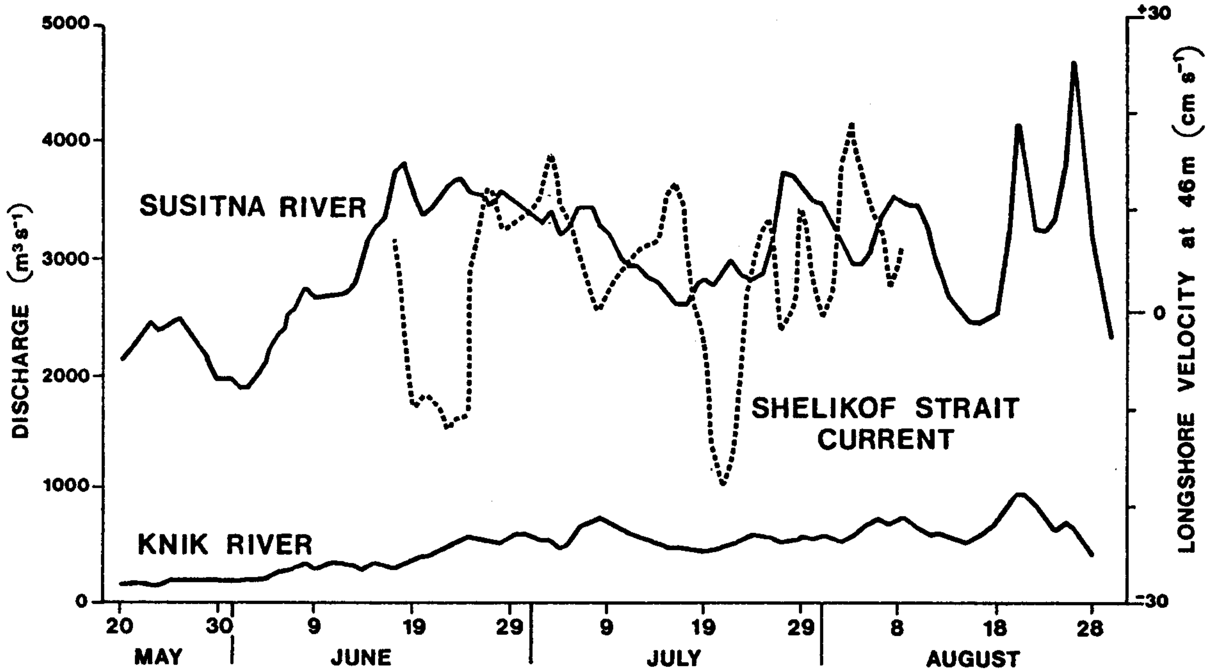

Figure 4.2 - Daily discharge of the Knik and Susitna Rivers (solid lines) and the mean daily alongshore component of flow at 46 m depth in Shelikof Strait (broken line).

The well defined variations in the flow through Shelikof Strait are apparent in either the time series data (Appendix 2) or the tidal analyses (Appendix 1). Energy at the MM (lunar monthly) and MSF (luni-solar fortnightly) is relatively high and not reflective of the ratios of the astronomical forcing functions at these frequencies to that at the M2 frequency (9% and less than 1% of M2 respectively). Presence of energy at these frequencies more properly indicates long period oscillations.

In that there appeared to be no correlation between the Shelikof Strait currents and freshwater discharge, we investigated possible atmospheric driving of the currents.

Figure 4.1 shows the autospectra of the alongshore (225° T) velocity component for the raw time series and for the time series with the tidal oscillations removed (residual). The principal tidal frequencies are in the region of 0.04 and 0.08 cycles per hour. The curve at the bottom of the figure represents the noise level due to the resolution limitations of the current meter. The 95% confidence interval is shown. For the spectrum of the residual currents there is significant energy near 0.02 cph (50 hours) as well as at the very low end of the spectrum (periods of about 15 to 20 days).

For the lowest frequencies we cannot procede with a meaningful cross-spectral analyses since only three or four realizations of oscillations of these periods occur in our two month records. We have, however visually compared the velocity time series with time series based upon the sea surface atmospheric pressure data obtained from the Naval Fleet Numerical Oceanography Center at Monterey.

Using the six hourly pressure grid (grid spacing approximately 300 km) we computed geostrophic winds. These winds were then decomposed into alongshore and offshore components. In addition, we computed surface wind stress by 1) rotating the geostrophic velocity vector 20° counter-clockwise to account for Ekman turning; 2) taking 70% of the geostrophic velocity to simulate the frictional dissipation in the boundary layer; 3) squaring the wind speed and 4) applying a drag coefficient of 1.2×10^{-3}. These procedures can be expressed as:

$$\vec{\tau} = |\vec{\tau}| \exp(i\gamma) = \rho_a C_D (0.7W)^2 \exp[i(\delta + 20°)] \tag{4-2}$$

where $\vec{\tau}$ is the surface wind stress vector, ρ_a is the density of air, C_D the drag coefficient, W the geostrophic wind speed δ the direction of the geostrophic wind vector anti clockwise from east γ and the direction of the surface stress vector. It should be borne in mind that the precise magnitudes of the drag coefficients, air density and the ratio of 10 m wind speed to geostrophic wind speed are unimportant in coherence computations.

The longshore and offshore components of the surface stress vector were then plotted versus time. Comparison of current, wind and wind stress component time series yielded no striking correlation. Time series plots of the current velocity components in Shelikof Strait and the atmospheric pressure gradient, windspeed and wind stress are shown in Appendix 2. Although long period variations spanning about 10 days are clearly present in the current records these are not mirrored in the meteorological records. Either these variations are not locally driven, are driven by a non-meteorological process, the surface pressure grid is too coarse to resolve the Shelikof Strait winds, or an agency other than wind stress is responsible for the current oscillations. The oscillation are probably not attributable to baroclinic instabilities since these are thought to have periods in Shelikof Strait of about four days (Mysak et al, 1981).

4.3 SUBTIDAL OSCILLATIONS OF PERIOD LESS THAN SEVEN DAYS

In this range of the spectrum we have enough realizations to apply cross-spectral techniques. Since we are dealing with synoptic scale atmospheric pressure maps, however, wavelengths greater than 600 km only can be rigorously addressed. Table 4.2 lists the periods at which coherences above the 95% confidence level were found between variables.

The fluctuations in the cross-shelf sea surface slope (between Ikolik and Albatross Bank) were coherent with the longshore wind stress at periods of about 35 hours. The alongshelf (Ikolik-Amatuli) sea surface slope was coherent in this range of periods with both the longshore and offshore wind stress.

Table 4.2 Periods for Which Significant Coherences Were Found

	Alongshore Wind Stress	Onshore Wind Stress
Shelikof Strait		
47 m Current Components		
alongshore	5 days	-
offshore	-	-
Shelikof Strait		
157 m Current Components		
alongshore	7 days, 3 days	5 days
offshore	35 hours	-
Cross-shelf Pressure Gradient		
(Ikolik-Albatross)	35 hours	-
Along-shelf Pressure Gradient		
(Ikolik-Amatuli)	35 hours	35 hours

Clearly, the cross-shelf sea surface slope (Ikolik-Albatross) responds to alongshore shore wind-stresses of periods of just over one day (the time lag is about 12 hours). The alongshore sea surface slope however (Ikolik-Amatuli) responds significantly to both alongshore and onshore wind stress.

The shallow alongshore currents appear to respond primarily to alongshore stress oscillations of about five day period while the deeper alongshore currents appear to respond to both alongshore and offshore stresses.

If we assume that both current meters are located within the geostrophic interior of the fluid, that is outside the surface and bottom Ekman layers, then the behavior of the cross-shelf pressure gradient should mirror that of the alongshore current component. Inspection of Table 4.2 reveals that this is not the case. Additionally, it is difficult to explain the high coherence between the onshore wind stress and the along-shelf pressure gradient.

Unfortunately, we cannot draw conclusions from the observed coherences. We can only speculate that the geostrophic winds are not a good indication of the atmospheric forcing over Shelikof Strait. It is likely that the local topography greatly alters the wind field, e.g., as described by Kozo (1980).

The oscillations in Shelikof Strait, therefore, are still unexplained. It is extremely unlikely that they are driven by coastal freshwater discharge so that the remaining mechanisms are the atmospheric pressure field, wind stress or wave-like instabilities.

5. SUMMARY

5.1 PROPERTY FIELDS

Between June and August 1984, the surface temperature increased by about 5°C in the Western Gulf of Alaska due to insolation. Cross sections of density revealed an eddy-like feature of dimensions comparable with the internal Rossby radius which propagated (or was advected) westward at a speed of about 4 cm s^{-1}. If the feature was associated with baroclinic instability, then a mechanism for cross slope exchange of water and nutrients was present.

The station spacing and the lack of synopticity of the CTD limit the the utility of the computed geostrophic currents. In general, however, westerly flows as high as 60 cm s^{-1} were computed over the continental slope while westerly flows up to 10 cm s^{-1} were computed over the continental shelf.

The property distributions were similar to those reported by previous investigators.

5.2 TIDAL OSCILLATIONS

The tides in the region are mixed, mainly semi-diurnal with spring tide ranges of between 3.5 and 6.5 m. Cotidal charts show the major tidal constituents propagating from northeast to southwest with some suggestion of shoreward propagation west of Kokiak Island. Computations of tidal energy flux are generally consistent with the cotidal charts with the exception of the Stevenson Entrance location. At this site, southward propagation of energy is computed.

Substantial tidal period internal wave energy was computed for the M_2 constituent in Cook Inlet. Internal tide waves have associated velocity, amplitudes and heights of about 50 cm s^{-1} and 30 m respectively. The implication is that a 60 m height internal tide wave is present at spring tide. In 65 m water depth such an oscillation is extremely unlikely without strong non-linearities in the flow field. A purely linear-barotropic tidal model will, therefore, likely be inadequate to predict the flow field in Cook Inlet.

5.3 SUBTIDAL OSCILLATIONS

The current data collected during this study were inadequate to address variations in the Alaska Coastal Current for two reasons: first, the records are only two months long and, second, the moorings were located no closer than 15 km to the coast. The offshore length scale of the current during June-August is expected to be between 3 and 7 km so that the current meters would not have sensed the coastal current.

Mean flows ranged between 1.3 and 5.6 cm s^{-1}, and were directed generally southwestward along the shelf with two important exceptions. In Shelikof Strait, the mean flow at depth was northeastward implying an estuarine type of flow regime there. In Cook Inlet the mean flows was east by northeast nearly across the inlet. The Cook Inlet mean flows are probably a manifestation of a secondary circulation the most likely driving force for which is tidal rectification.

No success was achieved in relating the variations in the geostrophic winds with the variations in the flow on the continental shelf. We speculate that this is due to ageostrophic atmospheric flow caused by the presence of coastal mountains.

6. REFERENCES CITED

Favorite, F and W.J. Ingraham, Jr., 1977. On flow in northwestern Gulf of Alaska, May 1971. Journ. Oceanogr. Soc. Japan, 33:67-81.

Foreman, M.G.G., 1977. Manual for Tidal Heights Analysis and Prediction. Pacific Marine Science Report 77-10. Institute of Ocean Sciences, Patricia Bay, Victoria, B.C.

Forman, M.G.G., 1978. Manual for Tidal Currents Analysis and Prediction. Pacific Marine Science Report 78-6. Institute of Ocean Sciences, Patricia Bay, Victoria, B.C.

Greisman, P., 1984. Data Report. Oceanographic Data and Circulation, Western Gulf of Alaska prepared for NOAA, Ocean Assessment Division, Anchorage. Dobrocky Seatech Ltd., 382 pp.

Kozo, T.L., 1980. Mountain Barrier Baroclinicity Effects on Surface Winds Along the Alaskan Arctic Coast. Geophys. Res. Letrs. 7(5):377-380.

Le Blond, P.H. and L.A. Mysak, 1978. Waves in the Ocean. Elsevier, Amsterdam. 602 pp.

Mysak, L.A., R.D. Muench and J.D. Schumacher, 1981. Baroclinic Instability in a Downstream Varying Channel: Shelikof Strait, Alaska. Journal of Physical Oceanography, 11 (7):950-969.

Patchen, R.C., J.T. Bruce and M.J. Connolly, 1981. Cook Inlet Circulatory Survey: 1973-75. NOS Oceanographic Circulatory Survey Report No. 4. U.S. Department of Commerce, NOAA. 89 pp.

Phillips, O.M., 1966. The Dynamics of the Upper Ocean. Cambridge University Press. 261 pp.

Platzman, G.W., 1971. Ocean Tides and Related Waves. In Mathematical Problems in the Geophysical Sciences, pt. 2. (W.H. Reill ed.), Lectures in Applied Math. V. 14, Am. Math. Soc. Providence, R.I. 239-291.

Reed, R.K., R.D. Muench and J.D. Schumacher, 1979. On the baroclinic transport of the Alaska Stream near Kodiak Island.

Royer, T.C. and R.D. Muench, 1977. On the ocean temperature distribution in the Gulf of Alaska 1974-1975. Journ. Phys. Oceanogr. 7:92-99.

Royer, T.C., 1979. On the effect of precipitation and runoff on coastal circulations in the Gulf of Alaska, Journ. Phys. Oceanogr. 9:555-563.

Royer, T.C., 1981. Baroclinic Transport in the Gulf of Alaska, Part II. A freshwater driven coastal current. Journ. Mar. Res. 39(2):251-266.

Schumacher, J.D., R. Silcox, D. Dreeves and R.D. Muench, 1978. Winter Circulation and Hydrography Over the Continental Shelf of the Northwest Gulf of Alaska. NOAA Tech. Rep. ERL 404-PMEL 31.

Schumacher, J.D., R.K. Reed, M. Grigsby and D. Dreeves, 1979. Circulation and Hydrography Near Kodiak Island September to November 1977. NOAA Tech. Mem. ERL PMEC-13.

Schumacher, J.D. and R.K. Reed, 1980. Coastal Flow in the Northwest Gulf of Alaska: The Kenai Current. Journal of Geophysical Research 85: 6680-6688.

Smith, P.C., 1976. Baroclinic Instability in the Denmark Strait Overflow. Journ. Phys. Oceanogr. 6:355-371.

Xiong, Q and T.C. Royer, 1984. Coastal Temperature and Salinity in the Northern Gulf of Alaska, 1970-1983. Journal of Geophysical Research, 89(5):8061-8068.

Appendix 1

Tidal Analyses

GULF OF ALASKA

ANALYSIS OF HOURLY TIDAL HEIGHTS

STN: AMATULI ISLAND LAT: 59 0 7.8 N
DEPTH: 167 M LONG: 151 50 1.8 W
START: 2300Z 13/ 6/84 END: 1400Z 9/ 8/84
NO.OBS.= 1360 NO.PTS.ANAL.= 1360 MIDPT: 600Z 12/ 7/84

	NAME	FREQUENCY (CY/HR)	A (M)	G
	----	---------	---	---
1	Z0	0.00000000	166.2659	0.00
2	MM	0.00151215	0.0257	145.38
3	MSF	0.00282193	0.0323	328.20
4	ALP1	0.03439657	0.0068	62.74
5	2Q1	0.03570635	0.0137	303.66
6	Q1	0.03721850	0.0468	271.60
7	O1	0.03873065	0.3082	262.95
8	NO1	0.04026860	0.0214	331.62
9	K1	0.04178075	0.5834	287.24
10	J1	0.04329290	0.0200	324.87
11	OO1	0.04483084	0.0092	293.79
12	UPS1	0.04634299	0.0033	270.03
13	EPS2	0.07617730	0.0068	169.58
14	MU2	0.07768947	0.0470	213.74
15	N2	0.07899922	0.3011	297.41
16	M2	0.08051139	1.5548	312.60
17	L2	0.08202356	0.0125	294.06
18	S2	0.08333331	0.4184	357.54
19	ETA2	0.08507365	0.0199	302.03
20	MO3	0.11924207	0.0127	194.15
21	M3	0.12076712	0.0022	46.03
22	MK3	0.12229216	0.0171	218.41
23	SK3	0.12511408	0.0059	219.66
24	MN4	0.15951067	0.0070	322.32
25	M4	0.16102278	0.0163	359.70
26	SN4	0.16233259	0.0010	356.16
27	MS4	0.16384470	0.0084	58.07
28	S4	0.16666669	0.0037	37.73
29	2MK5	0.20280355	0.0058	211.90
30	2SK5	0.20844740	0.0013	50.83
31	2MN6	0.24002206	0.0016	359.03
32	M6	0.24153417	0.0045	53.37
33	2MS6	0.24435616	0.0021	146.80
34	2SM6	0.24717808	0.0012	88.31
35	3MK7	0.28331494	0.0010	265.07
36	M8	0.32204562	0.0014	272.69

GULF OF ALASKA

ANALYSIS OF HOURLY TIDAL HEIGHTS

STN: ALBATROSS BANK LAT: 56 33 28.8 N
DEPTH: 165 M LONG: 152 26 57.0 W
START: 1200Z 12/ 6/84 END: 400Z 8/ 8/84
NO.OBS.= 1361 NO.PTS.ANAL.= 1361 MIDPT: 2000Z 10/ 7/84

	NAME	FREQUENCY (CY/HR)	A (M)	G
1	ZO	0.00000000	164.4422	0.00
2	MM	0.00151215	0.0206	165.74
3	MSF	0.00282193	0.0155	333.31
4	ALP1	0.03439657	0.0045	170.37
5	2Q1	0.03570635	0.0096	320.29
6	Q1	0.03721850	0.0432	256.19
7	O1	0.03873065	0.2905	255.04
8	NO1	0.04026860	0.0154	318.87
9	K1	0.04178075	0.5528	278.29
10	J1	0.04329290	0.0243	312.61
11	OO1	0.04483084	0.0089	315.17
12	UPS1	0.04634299	0.0011	211.94
13	EPS2	0.07617730	0.0077	203.52
14	MU2	0.07768947	0.0177	178.66
15	N2	0.07899922	0.1698	279.03
16	M2	0.08051139	0.8940	294.57
17	L2	0.08202356	0.0142	313.45
18	S2	0.08333331	0.2171	334.37
19	ETA2	0.08507365	0.0094	275.77
20	MO3	0.11924207	0.0021	232.38
21	M3	0.12076712	0.0017	230.21
22	MK3	0.12229216	0.0025	226.88
23	SK3	0.12511408	0.0009	152.34
24	MN4	0.15951067	0.0004	55.15
25	M4	0.16102278	0.0007	216.40
26	SN4	0.16233259	0.0006	344.03
27	MS4	0.16384470	0.0009	99.80
28	S4	0.16666669	0.0011	191.48
29	2MK5	0.20280355	0.0009	163.82
30	2SK5	0.20844740	0.0008	282.14
31	2MN6	0.24002206	0.0001	163.15
32	M6	0.24153417	0.0013	150.91
33	2MS6	0.24435616	0.0011	255.48
34	2SM6	0.24717808	0.0003	271.15
35	3MK7	0.28331494	0.0006	252.30
36	M8	0.32204562	0.0003	316.73

GULF OF ALASKA

ANALYSIS OF HOURLY TIDAL HEIGHTS

STN: SHUMAGIN LAT: 54 31 55.8 N
DEPTH: 193 M LONG: 158 58' 4.8 W
START: 2000Z 15/ 6/84 END: 1900Z 11/ 8/84
NO.OBS.= 1368 NO.PTS.ANAL.= 1368 MIDPT: 700Z 14/ 7/84

	NAME	FREQUENCY (CY/HR)	A (M)	G
1	Z0	0.00000000	192.0029	0.00
2	MM	0.00151215	0.0148	176.47
3	MSF	0.00282193	0.0232	0.27
4	ALP1	0.03439657	0.0052	293.93
5	2Q1	0.03570635	0.0066	292.27
6	Q1	0.03721850	0.0510	271.57
7	O1	0.03873065	0.2769	266.50
8	NO1	0.04026860	0.0244	322.55
9	K1	0.04178075	0.5175	289.08
10	J1	0.04329290	0.0129	310.28
11	OO1	0.04483084	0.0106	279.33
12	UPS1	0.04634299	0.0042	316.70
13	EPS2	0.07617730	0.0037	239.89
14	MU2	0.07768947	0.0173	188.56
15	N2	0.07899922	0.1371	302.39
16	M2	0.08051139	0.6713	317.25
17	L2	0.08202356	0.0147	351.66
18	S2	0.08333331	0.1690	353.99
19	ETA2	0.08507365	0.0083	322.62
20	MO3	0.11924207	0.0014	352.73
21	M3	0.12076712	0.0017	222.90
22	MK3	0.12229216	0.0006	250.66
23	SK3	0.12511408	0.0007	215.00
24	MN4	0.15951067	0.0003	199.91
25	M4	0.16102278	0.0011	232.74
26	SN4	0.16233259	0.0002	58.20
27	MS4	0.16384470	0.0003	112.42
28	S4	0.16666669	0.0017	199.84
29	2MK5	0.20280355	0.0020	197.44
30	2SK5	0.20844740	0.0002	195.38
31	2MN6	0.24002206	0.0009	266.61
32	M6	0.24153417	0.0014	318.15
33	2MS6	0.24435616	0.0014	346.82
34	2SM6	0.24717808	0.0005	43.08
35	3MK7	0.28331494	0.0010	268.95
36	M8	0.32204562	0.0009	301.68

GULF OF ALASKA

ANALYSIS OF HOURLY TIDAL HEIGHTS

STN: CAPE IKOLIK LAT: 57 15 0.0 N
DEPTH: 62 M LONG: 154 45 18.0 W
START: 100Z 15/ 6/84 END: 2300Z 10/ 8/84
NO.OBS.= 1367 NO.PTS.ANAL.= 1367 MIDPT: 1200Z 13/ 7/84

	NAME	FREQUENCY (CY/HR)	A (M)	G
1	Z0	0.00000000	61.2714	0.00
2	MM	0.00151215	0.0183	154.76
3	MSF	0.00282193	0.0260	1.68
4	ALP1	0.03439657	0.0032	352.93
5	2Q1	0.03570635	0.0113	306.23
6	Q1	0.03721850	0.0515	271.30
7	O1	0.03873065	0.3070	265.70
8	NO1	0.04026860	0.0245	327.00
9	K1	0.04178075	0.5928	289.37
10	J1	0.04329290	0.0192	329.15
11	OO1	0.04483084	0.0116	274.81
12	UPS1	0.04634299	0.0047	307.11
13	EPS2	0.07617730	0.0062	269.65
14	MU2	0.07768947	0.0261	212.33
15	N2	0.07899922	0.2770	303.52
16	M2	0.08051139	1.3889	317.00
17	L2	0.08202356	0.0202	319.81
18	S2	0.08333331	0.3757	1.87
19	ETA2	0.08507365	0.0201	315.96
20	MO3	0.11924207	0.0054	99.62
21	M3	0.12076712	0.0054	11.05
22	MK3	0.12229216	0.0167	155.14
23	SK3	0.12511408	0.0096	202.21
24	MN4	0.15951067	0.0086	199.64
25	M4	0.16102278	0.0299	220.50
26	SN4	0.16233259	0.0036	241.71
27	MS4	0.16384470	0.0127	287.22
28	S4	0.16666669	0.0054	317.39
29	2MK5	0.20280355	0.0040	169.34
30	2SK5	0.20844740	0.0011	266.61
31	2MN6	0.24002206	0.0024	141.08
32	M6	0.24153417	0.0043	152.29
33	2MS6	0.24435616	0.0031	212.66
34	2SM6	0.24717808	0.0008	153.50
35	3MK7	0.28331494	0.0008	336.89
36	M8	0.32204562	0.0014	9.47

GULF OF ALASKA

ANALYSIS OF HOURLY TIDAL HEIGHTS

STN: SEAL ROCKS LAT: 59 29 55.8 N
DEPTH: 114 M LONG: 149 29 34.2 W
START: 1000Z 13/ 6/84 END: 400Z 9/ 8/84
NO.OBS.= 1363 NO.PTS.ANAL.= 1363 MIDPT: 1900Z 11/ 7/84

	NAME	FREQUENCY (CY/HR)	A (M)	G
1	Z0	0.00000000	113.3633	0.00
2	MM	0.00151215	0.0234	133.86
3	MSF	0.00282193	0.0403	356.06
4	ALP1	0.03439657	0.0061	90.30
5	2Q1	0.03570635	0.0117	308.39
6	Q1	0.03721850	0.0410	263.84
7	O1	0.03873065	0.2846	256.09
8	NO1	0.04026860	0.0172	325.07
9	K1	0.04178075	0.5431	279.69
10	J1	0.04329290	0.0209	316.09
11	OO1	0.04483084	0.0088	302.19
12	UPS1	0.04634299	0.0021	252.49
13	EPS2	0.07617730	0.0053	148.33
14	MU2	0.07768947	0.0340	176.16
15	N2	0.07899922	0.2216	274.53
16	M2	0.08051139	1.1975	289.94
17	L2	0.08202356	0.0109	305.84
18	S2	0.08333331	0.3016	331.25
19	ETA2	0.08507365	0.0121	273.02
20	MO3	0.11924207	0.0036	179.17
21	M3	0.12076712	0.0012	298.42
22	MK3	0.12229216	0.0043	191.79
23	SK3	0.12511408	0.0031	162.93
24	MN4	0.15951067	0.0013	334.68
25	M4	0.16102278	0.0085	13.66
26	SN4	0.16233259	0.0015	3.70
27	MS4	0.16384470	0.0042	114.67
28	S4	0.16666669	0.0007	290.37
29	2MK5	0.20280355	0.0018	245.35
30	2SK5	0.20844740	0.0015	268.12
31	2MN6	0.24002206	0.0022	320.85
32	M6	0.24153417	0.0062	41.30
33	2MS6	0.24435616	0.0024	117.96
34	2SM6	0.24717808	0.0014	38.02
35	3MK7	0.28331494	0.0007	328.63
36	M8	0.32204562	0.0013	336.99

GULF OF ALASKA

ANALYSIS OF HOURLY TIDAL HEIGHTS

STN: PORTLOCK BANK LAT: 58 0 1.8 N
DEPTH: 178 M LONG: 149 29 34.8 W
START: 100Z 13/ 6/84 END: 1600Z 8/ 8/84
NO.OBS.= 1360 NO.PTS.ANAL.= 1360 MIDPT: 800Z 11/ 7/84

	NAME	FREQUENCY (CY/HR)	A (M)	G
1	ZO	0.00000000	177.0711	0.00
2	MM	0.00151215	0.0272	156.61
3	MSF	0.00282193	0.0218	341.60
4	ALP1	0.03439657	0.0041	112.08
5	2Q1	0.03570635	0.0104	312.84
6	Q1	0.03721850	0.0424	258.27
7	O1	0.03873065	0.2916	252.72
8	NO1	0.04026860	0.0171	318.75
9	K1	0.04178075	0.5572	276.60
10	J1	0.04329290	0.0227	313.52
11	OO1	0.04483084	0.0094	301.53
12	UPS1	0.04634299	0.0014	232.87
13	EPS2	0.07617730	0.0027	153.79
14	MU2	0.07768947	0.0273	184.22
15	N2	0.07899922	0.1902	278.57
16	M2	0.08051139	1.0140	293.48
17	L2	0.08202356	0.0094	299.76
18	S2	0.08333331	0.2499	334.36
19	ETA2	0.08507365	0.0093	278.84
20	MO3	0.11924207	0.0029	263.94
21	M3	0.12076712	0.0027	249.16
22	MK3	0.12229216	0.0014	287.67
23	SK3	0.12511408	0.0009	112.25
24	MN4	0.15951067	0.0003	293.32
25	M4	0.16102278	0.0015	297.13
26	SN4	0.16233259	0.0015	324.41
27	MS4	0.16384470	0.0010	49.75
28	S4	0.16666669	0.0002	17.43
29	2MK5	0.20280355	0.0016	158.97
30	2SK5	0.20844740	0.0009	288.21
31	2MN6	0.24002206	0.0006	336.75
32	M6	0.24153417	0.0023	61.48
33	2MS6	0.24435616	0.0007	129.92
34	2SM6	0.24717808	0.0008	55.71
35	3MK7	0.28331494	0.0008	81.17
36	M8	0.32204562	0.0011	169.50

GULF OF ALASKA

ANALYSIS OF HOURLY TIDAL HEIGHTS

STN: SANAK LAT: 54 35 15.0 N
DEPTH: 51 M LONG: 162 43 46.2 W
START: 1100Z 16/ 6/84 END: 400Z 13/ 8/84
NO.OBS.= 1386 NO.PTS.ANAL.= 1386 MIDPT: 700Z 15/ 7/84

	NAME	FREQUENCY (CY/HR)	A (M)	G
	----	---------	---	---
1	Z0	0.00000000	51.0813	180.00
2	MM	0.00151215	0.0097	210.41
3	MSF	0.00282193	0.0220	8.72
4	ALP1	0.03439657	0.0043	256.34
5	2Q1	0.03570635	0.0040	312.70
6	Q1	0.03721850	0.0476	274.08
7	O1	0.03873065	0.2691	269.93
8	NO1	0.04026860	0.0244	324.25
9	K1	0.04178075	0.5041	293.03
10	J1	0.04329290	0.0096	299.74
11	OO1	0.04483084	0.0113	291.54
12	UPS1	0.04634299	0.0024	341.03
13	EPS2	0.07617730	0.0038	228.10
14	MU2	0.07768947	0.0173	196.83
15	N2	0.07899922	0.1331	314.13
16	M2	0.08051139	0.6306	330.12
17	L2	0.08202356	0.0173	347.43
18	S2	0.08333331	0.1579	3.55
19	ETA2	0.08507365	0.0074	337.79
20	MO3	0.11924207	0.0025	13.46
21	M3	0.12076712	0.0023	248.32
22	MK3	0.12229216	0.0027	53.03
23	SK3	0.12511408	0.0017	319.22
24	MN4	0.15951067	0.0014	73.10
25	M4	0.16102278	0.0006	89.53
26	SN4	0.16233259	0.0012	119.45
27	MS4	0.16384470	0.0009	222.07
28	S4	0.16666669	0.0027	219.48
29	2MK5	0.20280355	0.0022	181.33
30	2SK5	0.20844740	0.0027	184.51
31	2MN6	0.24002206	0.0038	128.19
32	M6	0.24153417	0.0095	139.34
33	2MS6	0.24435616	0.0069	202.12
34	2SM6	0.24717808	0.0021	254.16
35	3MK7	0.28331494	0.0022	303.21
36	M8	0.32204562	0.0016	341.89

GULF OF ALASKA

ANALYSIS RESULTS IN CURRENT ELLIPSE FORM
AMPLITUDES HAVE BEEN SCALED ACCORDING TO APPLIED FILTERS

STN: STEVENSON ENTRANCE LAT: 58 53 43.8 N
DEPTH: 54 M LONG: 150 57 13.8 W
START: 2000Z 13/ 6/84 END: 800Z 9/ 8/84

	NAME	FREQUENCY (CY/HR)	MAJOR (CM/S)	MINOR (CM/S)	INC	G	G+	G-
1	Z0	0.00000000	2.111	0.000	57.8	180.0	122.2	237.8
2	MM	0.00151215	3.924	-2.361	45.0	55.4	10.5	100.4
3	MSF	0.00282193	2.861	-2.021	84.7	68.2	343.6	152.9
4	ALP1	0.03439657	0.476	-0.391	179.0	156.0	337.0	334.9
5	2Q1	0.03570635	0.728	0.126	109.4	93.1	343.7	202.5
6	Q1	0.03721850	1.000	0.344	97.5	17.0	279.5	114.5
7	O1	0.03873065	3.742	-0.774	98.1	13.7	275.6	111.8
8	NO1	0.04026860	0.258	0.040	106.4	156.6	50.2	263.1
9	K1	0.04178075	6.571	-2.157	100.6	40.5	300.0	141.1
10	J1	0.04329290	0.558	0.438	126.2	75.9	309.8	202.1
11	OO1	0.04483084	0.450	-0.140	75.4	349.8	274.5	65.2
12	UPS1	0.04634299	0.395	0.087	7.3	12.6	5.3	19.9
13	EPS2	0.07617730	1.338	0.774	74.1	304.2	230.2	13.3
14	MU2	0.07768947	2.474	0.503	67.2	31.8	324.6	98.9
15	N2	0.07899922	5.889	1.478	93.5	50.5	317.0	143.9
16	M2	0.08051139	30.198	0.621	102.1	66.3	324.1	168.4
17	L2	0.08202356	1.484	-0.098	116.5	37.0	280.5	153.5
18	S2	0.08333331	10.086	0.591	97.2	112.3	15.1	209.5
19	ETA2	0.08507365	1.137	0.717	80.1	100.2	20.1	180.3
20	MO3	0.11924207	0.645	0.246	74.4	182.6	108.2	257.1
21	M3	0.12076712	0.545	-0.231	17.1	228.3	211.2	245.4
22	MK3	0.12229216	1.015	0.195	50.4	280.5	230.1	331.0
23	SK3	0.12511408	0.417	0.173	25.5	329.1	303.6	354.6
24	MN4	0.15951067	0.141	-0.060	98.3	6.9	268.6	105.2
25	M4	0.16102278	0.691	0.538	5.7	259.3	253.6	265.0
26	SN4	0.16233259	0.415	-0.185	126.4	262.2	135.8	28.5
27	MS4	0.16384470	0.526	-0.342	2.0	357.1	355.0	359.1
28	S4	0.16666669	0.651	0.354	43.5	319.7	276.3	3.2
29	2MK5	0.20280355	0.922	0.247	55.3	283.3	228.0	338.6
30	2SK5	0.20844740	0.187	0.105	149.7	214.2	64.4	3.9
31	2MN6	0.24002206	0.535	-0.153	15.8	303.1	287.3	318.8
32	M6	0.24153417	0.923	-0.041	36.3	310.8	274.5	347.2
33	2MS6	0.24435616	0.720	-0.050	58.9	328.8	269.9	27.7
34	2SM6	0.24717808	0.525	0.128	134.8	98.0	323.2	232.7
35	3MK7	0.28331494	0.492	0.110	101.4	233.6	132.2	335.0
36	M8	0.32204562	0.338	0.135	151.1	45.9	254.7	197.0

GULF OF ALASKA

ANALYSIS RESULTS IN CURRENT ELLIPSE FORM

AMPLITUDES HAVE BEEN SCALED ACCORDING TO APPLIED FILTERS

STN: STEVENSON ENTRANCE — LAT: 58 53 43.8 N
DEPTH: 82 M — LONG: 150 57 13.8 W
START: 2000Z 13/ 6/84 — END: 800Z 9/ 8/84

	NAME	FREQUENCY (CY/HR)	MAJOR (CM/S)	MINOR (CM/S)	INC	G	G+	G-
1	Z0	0.00000000	2.576	0.000	134.9	180.0	45.1	314.9
2	MM	0.00151215	3.302	-0.808	30.9	50.5	19.7	81.4
3	MSF	0.00282193	2.993	-1.034	17.5	149.0	131.5	166.5
4	ALP1	0.03439657	0.221	-0.191	70.4	202.2	131.8	272.6
5	2Q1	0.03570635	0.424	-0.006	69.0	63.5	354.5	132.5
6	Q1	0.03721850	0.826	0.220	59.6	54.5	354.9	114.1
7	O1	0.03873065	3.456	-1.668	91.3	21.5	290.2	112.8
8	NO1	0.04026860	0.268	0.138	10.0	109.7	99.7	119.7
9	K1	0.04178075	6.411	-3.464	108.3	35.9	287.6	144.3
10	J1	0.04329290	0.931	0.647	66.9	69.2	2.3	136.2
11	OO1	0.04483084	0.343	0.130	82.8	55.6	332.8	138.4
12	UPS1	0.04634299	0.248	0.085	166.1	324.1	158.1	130.2
13	EPS2	0.07617730	1.490	0.759	60.7	357.5	296.8	58.2
14	MU2	0.07768947	2.926	0.764	26.1	57.8	31.7	83.9
15	N2	0.07899922	5.988	-0.342	94.1	55.1	321.0	149.3
16	M2	0.08051139	36.348	1.649	91.2	76.0	344.7	167.2
17	L2	0.08202356	3.619	2.749	1.0	20.6	19.6	21.6
18	S2	0.08333331	11.584	1.104	83.6	126.3	42.7	210.0
19	ETA2	0.08507365	0.820	0.024	95.6	67.9	332.3	163.5
20	MO3	0.11924207	0.323	-0.026	60.0	352.2	292.3	52.2
21	M3	0.12076712	0.252	0.121	136.3	16.3	240.0	152.6
22	MK3	0.12229216	0.809	-0.112	33.4	40.8	7.4	74.3
23	SK3	0.12511408	0.271	0.036	32.5	85.7	53.2	118.2
24	MN4	0.15951067	0.983	0.046	79.4	92.0	12.6	171.4
25	M4	0.16102278	1.492	0.128	24.7	127.5	102.8	152.2
26	SN4	0.16233259	1.139	0.294	150.7	238.2	87.6	28.9
27	MS4	0.16384470	0.461	-0.179	57.3	151.4	94.2	208.7
28	S4	0.16666669	0.672	0.618	107.4	215.4	108.0	322.8
29	2MK5	0.20280355	0.679	0.233	40.2	7.4	327.2	47.7
30	2SK5	0.20844740	0.125	0.079	96.0	171.2	75.2	267.1
31	2MN6	0.24002206	0.310	-0.054	96.4	85.4	349.0	181.8
32	M6	0.24153417	0.283	0.167	58.8	320.1	261.3	19.0
33	2MS6	0.24435616	0.474	0.131	41.4	45.7	4.3	87.1
34	2SM6	0.24717808	0.220	-0.003	105.0	188.3	83.3	293.3
35	3MK7	0.28331494	0.558	0.182	140.2	307.0	166.8	87.2
36	M8	0.32204562	0.299	-0.172	15.4	88.4	73.1	103.8

GULF OF ALASKA

ANALYSIS RESULTS IN CURRENT ELLIPSE FORM
AMPLITUDES HAVE BEEN SCALED ACCORDING TO APPLIED FILTERS

STN: COOK INLET LAT: 59 35 1.2 N
DEPTH: 35 M LONG: 152 29 0.0 W
START: 500Z 14/ 6/84 END: 1800Z 9/ 8/84

	NAME	FREQUENCY (CY/HR)	MAJOR (CM/S)	MINOR (CM/S)	INC	G	G+	G-
1	Z0	0.00000000	4.304	0.000	12.1	360.0	347.9	12.1
2	MM	0.00151215	1.922	1.178	117.8	165.3	47.4	283.1
3	MSF	0.00282193	4.297	-1.351	99.1	264.3	165.2	3.4
4	ALP1	0.03439657	0.591	-0.411	95.0	26.4	291.4	121.5
5	2Q1	0.03570635	0.757	-0.323	108.6	256.8	148.3	5.4
6	Q1	0.03721850	1.892	0.098	91.8	241.0	149.1	332.8
7	O1	0.03873065	9.482	-0.695	78.5	223.7	145.2	302.3
8	NO1	0.04026860	0.897	-0.069	105.1	290.7	185.6	35.8
9	K1	0.04178075	19.006	-3.527	77.4	243.9	166.5	321.2
10	J1	0.04329290	0.602	0.184	54.4	292.2	237.8	346.6
11	OO1	0.04483084	0.837	-0.097	104.2	264.7	160.5	9.0
12	UPS1	0.04634299	0.428	0.020	124.4	237.3	112.9	1.6
13	EPS2	0.07617730	1.706	-1.474	51.9	193.8	141.9	245.6
14	MU2	0.07768947	6.366	-0.209	96.6	199.5	102.9	296.2
15	N2	0.07899922	14.444	-2.391	81.2	285.2	204.0	6.4
16	M2	0.08051139	73.533	-8.936	78.1	308.4	230.3	26.5
17	L2	0.08202356	1.290	1.098	6.6	357.0	350.4	3.6
18	S2	0.08333331	19.821	-2.525	84.1	352.1	268.1	76.2
19	ETA2	0.08507365	1.028	-0.461	95.4	278.3	183.0	13.7
20	MO3	0.11924207	1.905	-0.115	70.3	112.1	41.7	182.4
21	M3	0.12076712	1.271	-0.679	74.7	29.7	315.1	104.4
22	MK3	0.12229216	2.642	-0.081	84.6	145.0	60.4	229.6
23	SK3	0.12511408	1.306	-0.512	57.0	207.1	150.1	264.2
24	MN4	0.15951067	0.941	-0.658	92.7	161.7	69.0	254.4
25	M4	0.16102278	2.622	-1.012	65.7	179.0	113.3	244.6
26	SN4	0.16233259	0.362	-0.100	75.8	239.5	163.8	315.3
27	MS4	0.16384470	0.922	-0.193	77.2	215.0	137.8	292.3
28	S4	0.16666669	0.867	-0.480	9.6	23.6	13.9	33.2
29	2MK5	0.20280355	0.973	-0.022	108.1	304.2	196.1	52.2
30	2SK5	0.20844740	0.273	-0.148	44.3	175.9	131.6	220.2
31	2MN6	0.24002206	0.517	-0.007	158.6	194.8	36.2	353.4
32	M6	0.24153417	0.833	-0.077	49.8	101.3	51.6	151.1
33	2MS6	0.24435616	0.593	-0.218	154.4	334.4	180.0	128.7
34	2SM6	0.24717808	0.384	-0.044	171.3	352.0	180.6	163.3
35	3MK7	0.28331494	0.531	-0.118	149.4	109.0	319.5	258.4
36	M8	0.32204562	0.424	-0.178	4.3	328.9	324.7	333.2

GULF OF ALASKA

ANALYSIS RESULTS IN CURRENT ELLIPSE FORM
AMPLITUDES HAVE BEEN SCALED ACCORDING TO APPLIED FILTERS

STN: COOK INLET — LAT: 59 35 1.2 N
DEPTH: 52 M — LONG: 152 29 0.0 W
START: 500Z 14/ 6/84 — END: 2200Z 13/ 7/84

	NAME	FREQUENCY (CY/HR)	MAJOR (CM/S)	MINOR (CM/S)	INC	G	G+	G-
1	Z0	0.00000000	5.464	0.000	25.9	360.0	334.1	25.9
2	MSF	0.00282193	3.256	-1.136	110.4	248.8	138.4	359.2
3	2Q1	0.03570635	1.045	-0.480	55.8	343.4	287.6	39.2
4	Q1	0.03721850	1.980	-0.183	70.6	236.5	165.8	307.1
5	O1	0.03873065	7.990	-0.067	69.0	220.4	151.4	289.4
6	NO1	0.04026860	0.679	0.122	120.4	323.8	203.4	84.2
7	K1	0.04178075	16.570	-3.415	78.0	238.6	160.7	316.6
8	J1	0.04329290	1.078	0.115	7.4	286.4	279.0	293.7
9	OO1	0.04483084	1.061	0.298	114.7	272.9	158.2	27.7
10	UPS1	0.04634299	0.429	-0.256	36.0	220.9	184.9	257.0
11	N2	0.07899922	13.229	-3.590	83.2	278.7	195.6	1.9
12	M2	0.08051139	59.845	-1.996	74.2	304.8	230.6	19.0
13	S2	0.08333331	14.814	-1.754	83.6	346.3	262.7	69.9
14	ETA2	0.08507365	1.108	-0.948	10.2	260.2	250.0	270.4
15	MO3	0.11924207	2.104	-0.622	62.2	112.4	50.2	174.7
16	M3	0.12076712	1.449	-0.530	59.0	53.7	354.7	112.7
17	MK3	0.12229216	2.352	-0.228	62.8	150.4	87.6	213.3
18	SK3	0.12511408	1.771	-0.904	67.8	213.9	146.1	281.8
19	MN4	0.15951067	1.277	-0.474	65.1	250.3	185.2	315.4
20	M4	0.16102278	1.528	-0.846	115.3	105.2	349.9	220.6
21	MS4	0.16384470	0.699	0.146	158.7	206.1	47.3	4.8
22	S4	0.16666669	0.888	-0.686	2.8	348.5	345.7	351.3
23	2MK5	0.20280355	1.314	0.168	83.1	296.9	213.8	20.0
24	2SK5	0.20844740	0.517	-0.108	21.9	200.9	179.1	222.8
25	2MN6	0.24002206	0.768	-0.380	97.5	310.0	212.5	47.5
26	M6	0.24153417	0.880	-0.106	14.8	40.9	26.1	55.7
27	2MS6	0.24435616	0.468	-0.389	133.8	314.6	180.7	88.4
28	2SM6	0.24717808	0.532	-0.065	45.2	239.6	194.4	284.9
29	3MK7	0.28331494	0.692	-0.296	167.5	116.8	309.3	284.4
30	M8	0.32204562	0.439	-0.298	55.8	287.3	231.5	343.1

GULF OF ALASKA

ANALYSIS RESULTS IN CURRENT ELLIPSE FORM
AMPLITUDES HAVE BEEN SCALED ACCORDING TO APPLIED FILTERS

STN: SANAK　　LAT: 54 35 15.0 N
DEPTH: 20 M　　LONG: 162 43 46.2 W
START: 1200Z 16/ 6/84　　END: 300Z 13/ 8/84

	NAME	FREQUENCY (CY/HR)	MAJOR (CM/S)	MINOR (CM/S)	INC	G	G+	G-
	----	---------	-----	-----	---	---	---	---
1	Z0	0.00000000	2.261	0.000	15.7	180.0	164.3	195.7
2	MM	0.00151215	0.426	0.084	94.4	173.3	78.9	267.8
3	MSF	0.00282193	2.939	-0.146	0.9	146.9	146.0	147.8
4	ALP1	0.03439657	0.527	0.048	18.6	84.1	65.5	102.7
5	2Q1	0.03570635	0.469	0.091	64.3	117.5	53.3	181.8
6	Q1	0.03721850	0.251	-0.019	54.8	227.3	172.5	282.0
7	O1	0.03873065	2.285	-1.082	176.8	104.7	287.9	281.5
8	NO1	0.04026860	0.488	-0.077	94.7	35.3	300.6	130.0
9	K1	0.04178075	3.981	-1.997	166.9	145.2	338.3	312.1
10	J1	0.04329290	0.726	-0.440	10.2	349.9	339.6	0.1
11	OO1	0.04483084	0.232	0.197	41.6	38.9	357.3	80.5
12	UPS1	0.04634299	0.345	0.004	32.5	344.0	311.4	16.5
13	EPS2	0.07617730	1.098	-0.810	4.2	112.7	108.5	116.9
14	MU2	0.07768947	0.420	-0.150	12.1	82.9	70.8	95.0
15	N2	0.07899922	0.684	-0.261	89.9	269.0	179.1	359.0
16	M2	0.08051139	3.121	0.469	112.8	285.1	172.3	37.9
17	L2	0.08202356	0.984	0.133	65.3	341.8	276.5	47.1
18	S2	0.08333331	1.091	-0.110	76.6	335.5	258.9	52.1
19	ETA2	0.08507365	0.403	-0.033	56.0	213.8	157.8	269.8
20	MO3	0.11924207	0.231	0.035	91.2	186.5	95.3	277.7
21	M3	0.12076712	0.153	-0.032	3.8	355.3	351.5	359.2
22	MK3	0.12229216	0.324	-0.227	138.6	237.0	98.4	15.5
23	SK3	0.12511408	0.237	0.001	125.9	195.3	69.5	321.2
24	MN4	0.15951067	0.247	0.013	77.5	295.1	217.6	12.6
25	M4	0.16102278	0.255	-0.045	20.2	117.8	97.6	138.0
26	SN4	0.16233259	0.068	-0.048	23.1	184.3	161.2	207.4
27	MS4	0.16384470	0.218	-0.133	149.1	30.3	241.1	179.4
28	S4	0.16666669	0.239	-0.025	94.1	231.3	137.2	325.4
29	2MK5	0.20280355	0.092	0.064	75.1	344.7	269.7	59.8
30	2SK5	0.20844740	0.131	0.060	168.8	255.3	86.5	64.0
31	2MN6	0.24002206	0.204	0.050	70.3	46.2	335.9	116.5
32	M6	0.24153417	0.349	0.086	108.5	104.4	355.9	212.9
33	2MS6	0.24435616	0.323	-0.023	39.2	100.6	61.3	139.8
34	2SM6	0.24717808	0.127	0.007	179.6	246.0	66.5	65.6
35	3MK7	0.28331494	0.168	-0.042	57.0	208.8	151.7	265.8
36	M8	0.32204562	0.058	-0.004	76.4	141.7	65.3	218.1

GULF OF ALASKA

ANALYSIS RESULTS IN CURRENT ELLIPSE FORM
AMPLITUDES HAVE BEEN SCALED ACCORDING TO APPLIED FILTERS

STN: SANAK — LAT: 54 35 15.0 N
DEPTH: 41 M — LONG: 162 43 46.2 W
START: 1200Z 16/ 6/84 — END: 200Z 13/ 8/84

	NAME	FREQUENCY (CY/HR)	MAJOR (CM/S)	MINOR (CM/S)	INC	G	G+	G-
1	Z0	0.00000000	3.086	0.000	150.8	360.0	209.2	150.8
2	MM	0.00151215	1.195	-0.687	145.6	307.9	162.3	93.5
3	MSF	0.00282193	1.414	0.176	170.3	329.5	159.2	139.9
4	ALP1	0.03439657	0.421	-0.306	86.3	296.9	210.6	23.3
5	2Q1	0.03570635	0.322	-0.016	9.1	154.6	145.5	163.7
6	Q1	0.03721850	0.659	-0.023	33.7	284.4	250.7	318.1
7	O1	0.03873065	3.465	-0.904	1.0	274.4	273.4	275.4
8	NO1	0.04026860	0.544	0.063	12.6	325.2	312.6	337.8
9	K1	0.04178075	7.146	-3.135	165.6	135.7	330.2	301.3
10	J1	0.04329290	1.040	-0.267	160.3	168.7	8.4	328.9
11	OO1	0.04483084	0.754	-0.216	163.7	152.4	348.7	316.0
12	UPS1	0.04634299	0.271	-0.057	125.2	213.9	88.7	339.0
13	EPS2	0.07617730	0.624	0.063	5.9	285.7	279.8	291.6
14	MU2	0.07768947	0.470	-0.125	16.9	[illegible]	78.8	112.5
15	N2	0.07899922	0.786	-0.486	64.3	238.5	174.3	302.8
16	M2	0.08051139	4.121	1.077	89.6	252.6	163.0	342.3
17	L2	0.08202356	0.731	-0.162	98.1	91.0	352.9	189.1
18	S2	0.08333331	1.476	-0.607	30.1	267.4	237.4	297.5
19	ETA2	0.08507365	0.056	0.023	164.1	14.6	210.5	178.8
20	MO3	0.11924207	0.402	-0.135	153.0	256.5	103.5	49.5
21	M3	0.12076712	0.117	-0.065	76.5	9.2	292.8	85.7
22	MK3	0.12229216	0.394	-0.063	89.0	293.6	204.6	22.5
23	SK3	0.12511408	0.314	-0.108	9.0	99.0	89.9	108.0
24	MN4	0.15951067	0.322	-0.089	35.9	158.8	122.9	194.7
25	M4	0.16102278	0.110	-0.011	65.1	52.3	347.2	117.4
26	SN4	0.16233259	0.180	0.068	55.7	162.1	106.5	217.8
27	MS4	0.16384470	0.123	0.004	112.0	140.9	28.9	252.9
28	S4	0.16666669	0.190	0.145	11.7	125.4	113.7	137.1
29	2MK5	0.20280355	0.244	-0.030	16.2	50.6	34.4	66.8
30	2SK5	0.20844740	0.082	-0.037	94.3	95.7	1.4	189.9
31	2MN6	0.24002206	0.333	-0.027	118.6	133.4	14.8	252.0
32	M6	0.24153417	0.271	0.195	85.0	107.0	22.0	192.0
33	2MS6	0.24435616	0.296	-0.037	72.0	163.2	91.2	235.2
34	2SM6	0.24717808	0.058	0.033	96.8	292.4	195.5	29.2
35	3MK7	0.28331494	0.110	0.031	85.2	197.0	111.8	282.2
36	M8	0.32204562	0.118	-0.031	110.3	272.9	162.6	23.2

GULF OF ALASKA

ANALYSIS RESULTS IN CURRENT ELLIPSE FORM
AMPLITUDES HAVE BEEN SCALED ACCORDING TO APPLIED FILTERS

STN: SHELIKOF STRAIT LAT: 57 39 0.0 N
DEPTH: 46 M LONG: 155 3 19.8 W
START: 2300Z 14/ 6/84 END: 1200Z 10/ 8/84

	NAME	FREQUENCY (CY/HR)	MAJOR (CM/S)	MINOR (CM/S)	INC	G	G+	G-
	----	---------	-----	-----	---	---	---	---
1	Z0	0.00000000	3.839	0.000	59.8	180.0	120.2	239.8
2	MM	0.00151215	12.868	5.271	116.3	261.9	145.7	18.2
3	MSF	0.00282193	5.479	-0.565	28.5	223.2	194.7	251.6
4	ALP1	0.03439657	0.531	0.356	45.6	161.5	115.9	207.1
5	2Q1	0.03570635	0.741	0.473	5.2	39.0	33.8	44.1
6	Q1	0.03721850	0.978	0.273	104.6	299.5	195.0	44.1
7	O1	0.03873065	1.754	-0.126	38.9	227.1	188.2	266.0
8	NO1	0.04026860	0.429	-0.014	119.5	25.3	265.8	144.7
9	K1	0.04178075	3.449	0.076	41.3	243.6	202.4	284.9
10	J1	0.04329290	0.616	-0.240	99.4	330.9	231.5	70.3
11	OO1	0.04483084	0.252	0.044	44.6	135.1	90.4	179.7
12	UPS1	0.04634299	0.199	0.106	145.8	174.8	29.0	320.6
13	EPS2	0.07617730	0.873	0.833	5.7	331.7	326.1	337.4
14	MU2	0.07768947	0.979	-0.165	31.1	228.7	197.6	[illegible]
15	N2	0.07899922	2.529	0.692	38.5	230.2	191.7	268.7
16	M2	0.08051139	13.766	-0.023	39.9	250.7	210.9	290.6
17	L2	0.08202356	2.234	0.772	119.5	156.9	37.4	276.5
18	S2	0.08333331	4.516	-0.032	41.2	297.1	255.9	338.3
19	ETA2	0.08507365	1.105	0.417	85.5	221.8	136.3	307.2
20	MO3	0.11924207	0.292	0.249	125.3	137.4	12.1	262.7
21	M3	0.12076712	0.478	0.048	143.8	269.2	125.4	53.1
22	MK3	0.12229216	0.306	-0.031	11.5	126.0	114.6	137.5
23	SK3	0.12511408	0.191	0.064	25.4	155.0	129.6	180.5
24	MN4	0.15951067	0.289	0.019	171.3	253.5	82.2	64.9
25	M4	0.16102278	0.527	0.118	13.3	348.0	334.7	1.3
26	SN4	0.16233259	0.374	-0.117	110.8	289.1	178.3	40.0
27	MS4	0.16384470	0.351	0.032	7.5	0.5	353.0	8.0
28	S4	0.16666669	0.347	0.257	157.4	171.8	14.4	329.2
29	2MK5	0.20280355	0.386	0.136	170.2	315.9	145.6	126.1
30	2SK5	0.20844740	0.206	0.035	95.1	223.7	128.6	318.8
31	2MN6	0.24002206	0.141	0.073	123.6	196.4	72.8	320.0
32	M6	0.24153417	0.132	-0.060	104.5	293.9	189.4	38.5
33	2MS6	0.24435616	0.212	0.115	177.4	157.8	340.4	335.1
34	2SM6	0.24717808	0.239	0.158	57.7	252.9	195.2	310.5
35	3MK7	0.28331494	0.307	-0.007	73.6	337.1	263.5	50.7
36	M8	0.32204562	0.170	0.087	109.3	33.1	283.9	142.4

GULF OF ALASKA

ANALYSIS RESULTS IN CURRENT ELLIPSE FORM
AMPLITUDES HAVE BEEN SCALED ACCORDING TO APPLIED FILTERS

STN: SHELIKOF STRAIT — LAT: 57 39 0.0 N
DEPTH: 157 M — LONG: 155 3 19.8 W
START: 2300Z 14/ 6/84 — END: 1200Z 10/ 8/84

	NAME	FREQUENCY (CY/HR)	MAJOR (CM/S)	MINOR (CM/S)	INC	G	G+	G-
	----	---------	-----	-----	---	---	---	---
1	ZO	0.00000000	1.343	0.000	52.6	360.0	307.4	52.6
2	MM	0.00151215	5.314	2.274	123.6	263.7	140.1	27.3
3	MSF	0.00282193	4.241	-1.419	48.3	205.2	157.0	253.5
4	ALP1	0.03439657	0.245	0.011	151.7	104.5	312.8	256.2
5	2Q1	0.03570635	0.241	0.080	80.6	18.9	298.2	99.5
6	Q1	0.03721850	0.514	0.277	103.9	299.9	196.1	43.8
7	O1	0.03873065	1.496	-0.061	49.4	205.1	155.7	254.5
8	NO1	0.04026860	0.241	0.121	161.5	80.5	279.0	242.0
9	K1	0.04178075	2.956	-0.148	47.9	226.4	178.5	274.3
10	J1	0.04329290	0.396	-0.006	132.1	342.2	210.1	114.3
11	OO1	0.04483084	0.285	-0.013	94.8	239.6	144.8	334.4
12	UPS1	0.04634299	0.301	0.090	155.2	209.8	54.5	5.0
13	EPS2	0.07617730	0.591	0.268	141.3	317.0	175.7	98.3
14	MU2	0.07768947	0.482	0.349	53.2	147.0	93.9	200.2
15	N2	0.07899922	3.111	1.006	45.8	233.4	187.6	279.2
16	M2	0.08051139	14.870	0.598	43.0	248.2	205.2	291.3
17	L2	0.08202356	1.725	0.210	119.2	138.4	19.2	257.6
18	S2	0.08333331	4.333	0.141	46.8	296.0	249.2	342.8
19	ETA2	0.08507365	0.602	-0.114	49.3	269.9	220.5	319.2
20	MO3	0.11924207	0.308	0.068	45.0	136.3	91.3	181.3
21	M3	0.12076712	0.251	0.008	87.5	259.9	172.4	347.4
22	MK3	0.12229216	0.496	-0.073	30.1	164.3	134.2	194.4
23	SK3	0.12511408	0.246	-0.144	170.0	66.2	256.2	236.1
24	MN4	0.15951067	0.208	0.150	33.1	204.0	170.9	237.2
25	M4	0.16102278	0.307	0.014	114.4	299.6	185.2	54.0
26	SN4	0.16233259	0.169	-0.019	175.4	7.5	192.1	183.0
27	MS4	0.16384470	0.239	0.043	108.3	6.3	258.0	114.6
28	S4	0.16666669	0.205	0.100	46.1	220.3	174.2	266.3
29	2MK5	0.20280355	0.187	0.038	42.5	114.6	72.1	157.1
30	2SK5	0.20844740	0.125	0.057	90.7	96.5	5.8	187.1
31	2MN6	0.24002206	0.141	0.054	12.0	10.4	358.5	22.4
32	M6	0.24153417	0.103	-0.060	53.4	313.5	260.2	6.9
33	2MS6	0.24435616	0.111	-0.010	163.9	246.3	82.4	50.3
34	2SM6	0.24717808	0.111	0.071	18.5	306.2	287.7	324.7
35	3MK7	0.28331494	0.156	0.050	27.5	359.7	332.2	27.3
36	M8	0.32204562	0.098	-0.009	68.3	31.0	322.7	99.3

Appendix 2

Time Series of Filtered Velocity, Geostrophic Wind, Surface Wind Stress

TIME SERIES OF U, V AND LONGSHORE, OFFSHORE CONPONENTS

SHELIKOF STRAIT METER 3127 DEPTH(m) 46 TYPE FILTERED

57 39' 00"N 155 03' 19.8"W AANDERAA RCM DT(min) 360

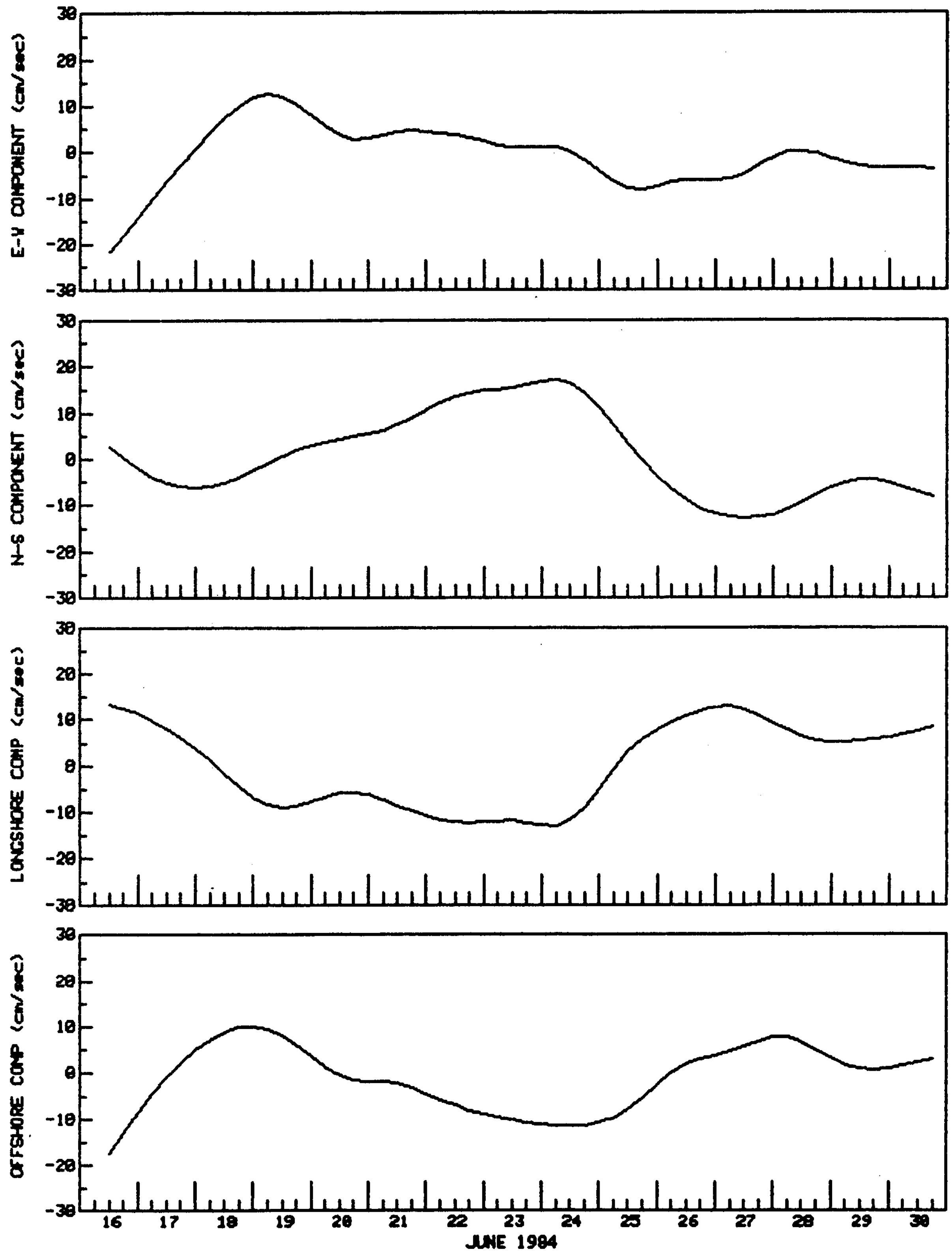

TIME SERIES OF U, V AND LONGSHORE, OFFSHORE CONPONENTS
SHELIKOF STRAIT METER 3127 DEPTH(m) 46 TYPE FILTERED
57 39' 00"N 155 03' 19.8"W AANDERAA RCM DT(min) 360

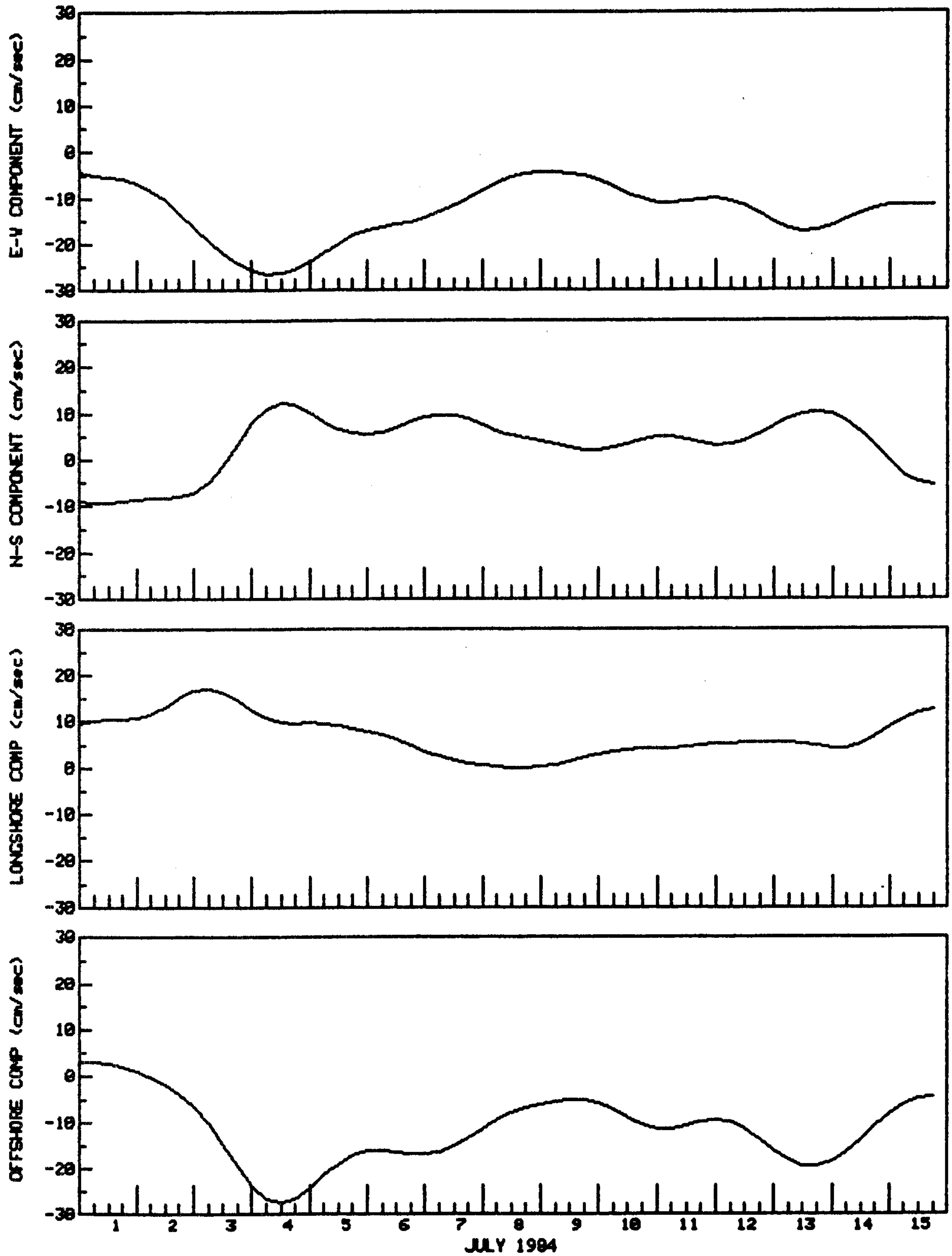

TIME SERIES OF U, V AND LONGSHORE, OFFSHORE CONPONENTS
SHELIKOF STRAIT METER 3127 DEPTH(m) 46 TYPE FILTERED
57 39' 00"N 155 03' 19.8"W AANDERAA RCM DT(min) 360

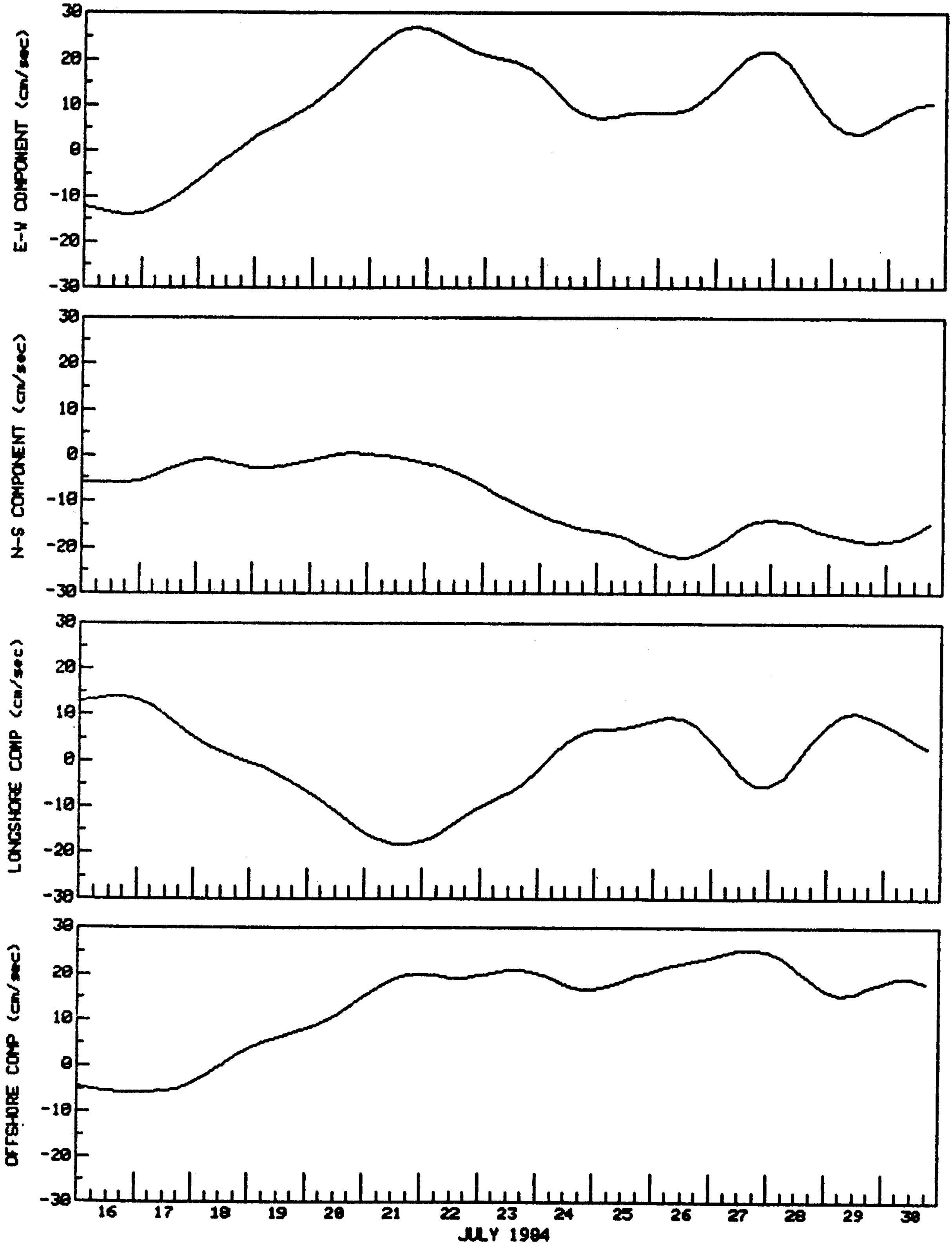

TIME SERIES OF U, V AND LONGSHORE, OFFSHORE CONPONENTS
SHELIKOF STRAIT   METER 3127   DEPTH(m) 46   TYPE FILTERED
57 39' 00"N   155 03' 19.8"W   AANDERAA RCM   DT(min) 360

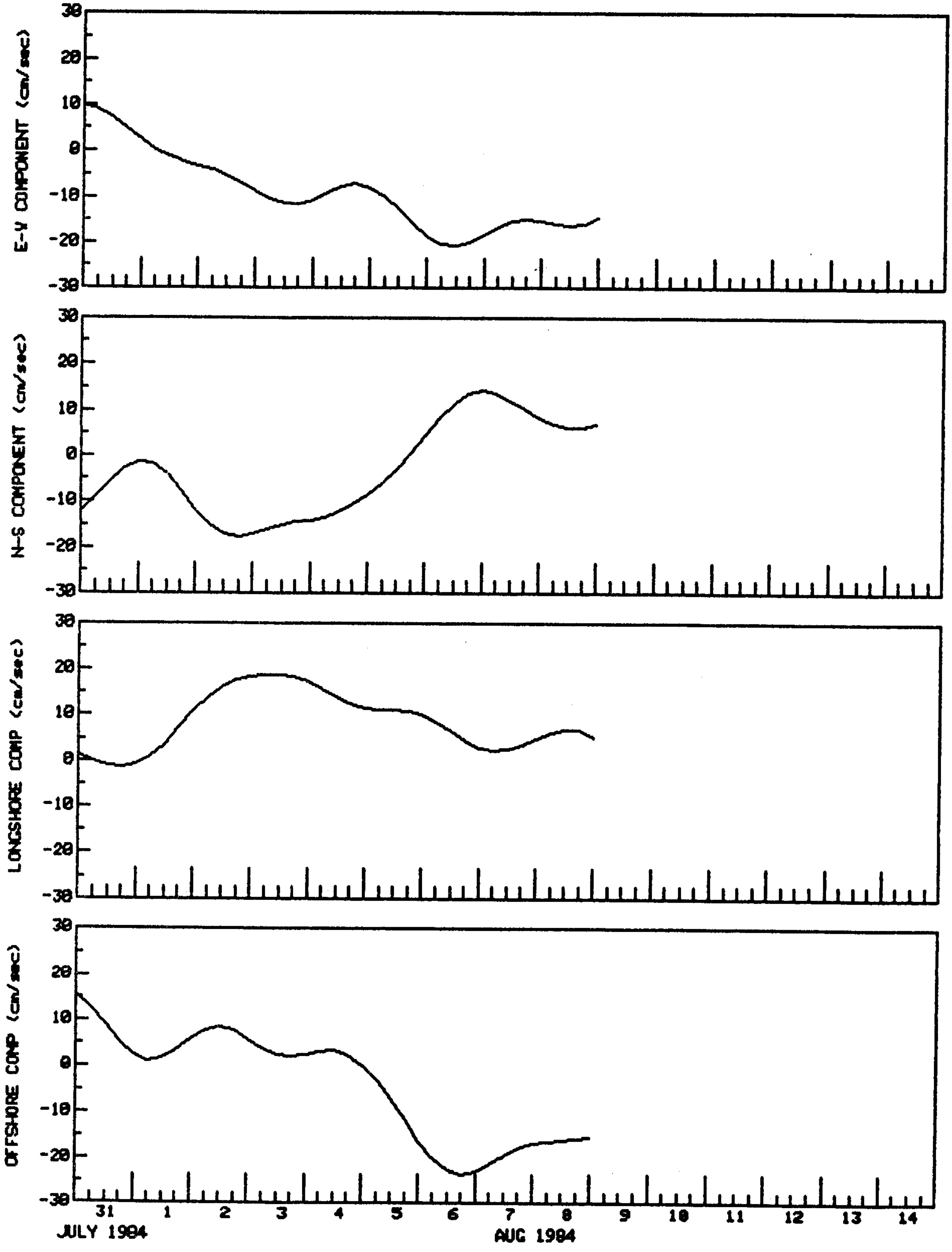

TIME SERIES OF OFFSHORE COMPONENT OF
PRESSURE GRADIENT, GEOSTROPHIC WIND AND SURFACE WIND STRESS

SHELIKOF STRAIT DT(min) 360

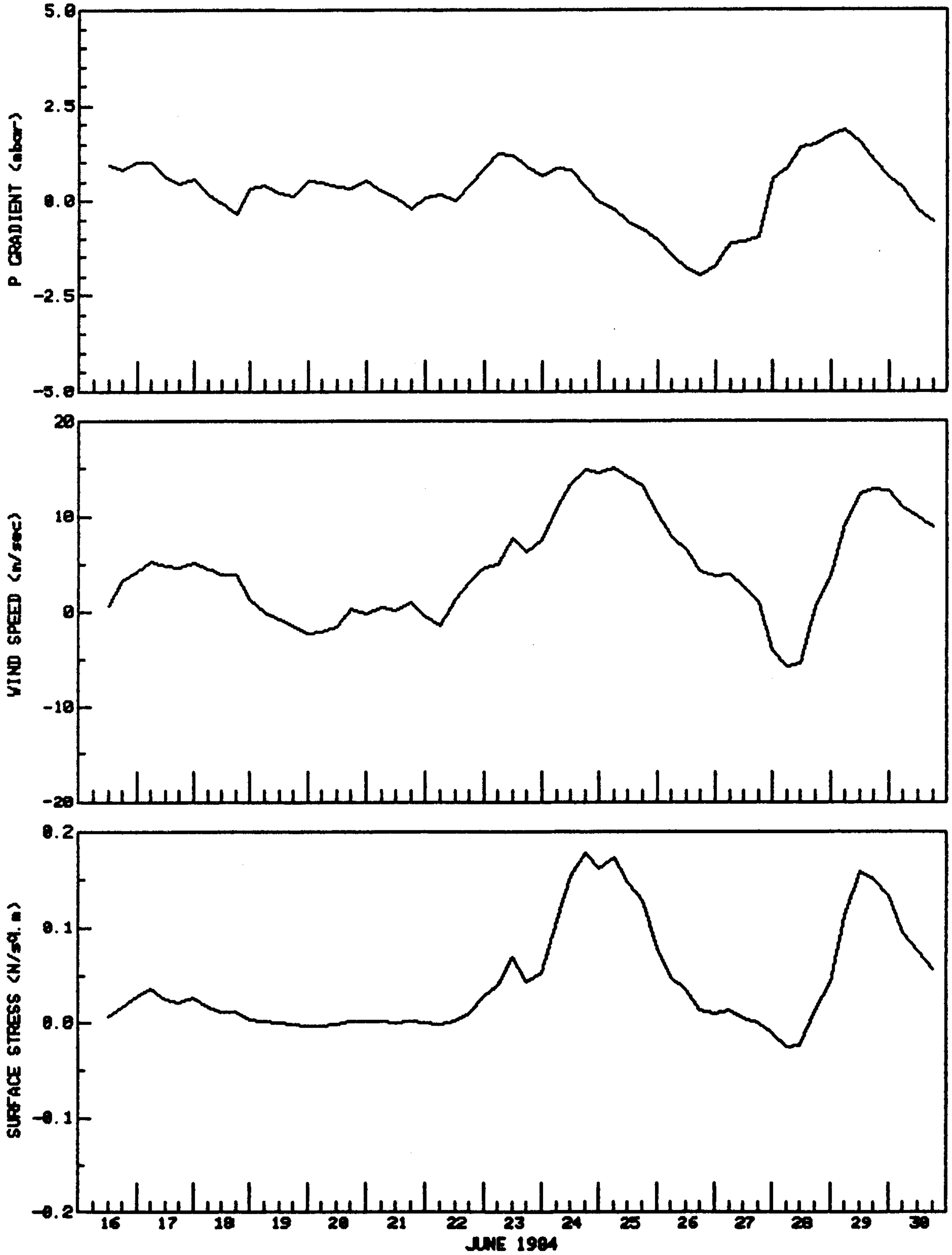

TIME SERIES OF OFFSHORE COMPONENT OF
PRESSURE GRADIENT, GEOSTROPHIC WIND AND SURFACE WIND STRESS
SHELIKOF STRAIT DT(min) 360

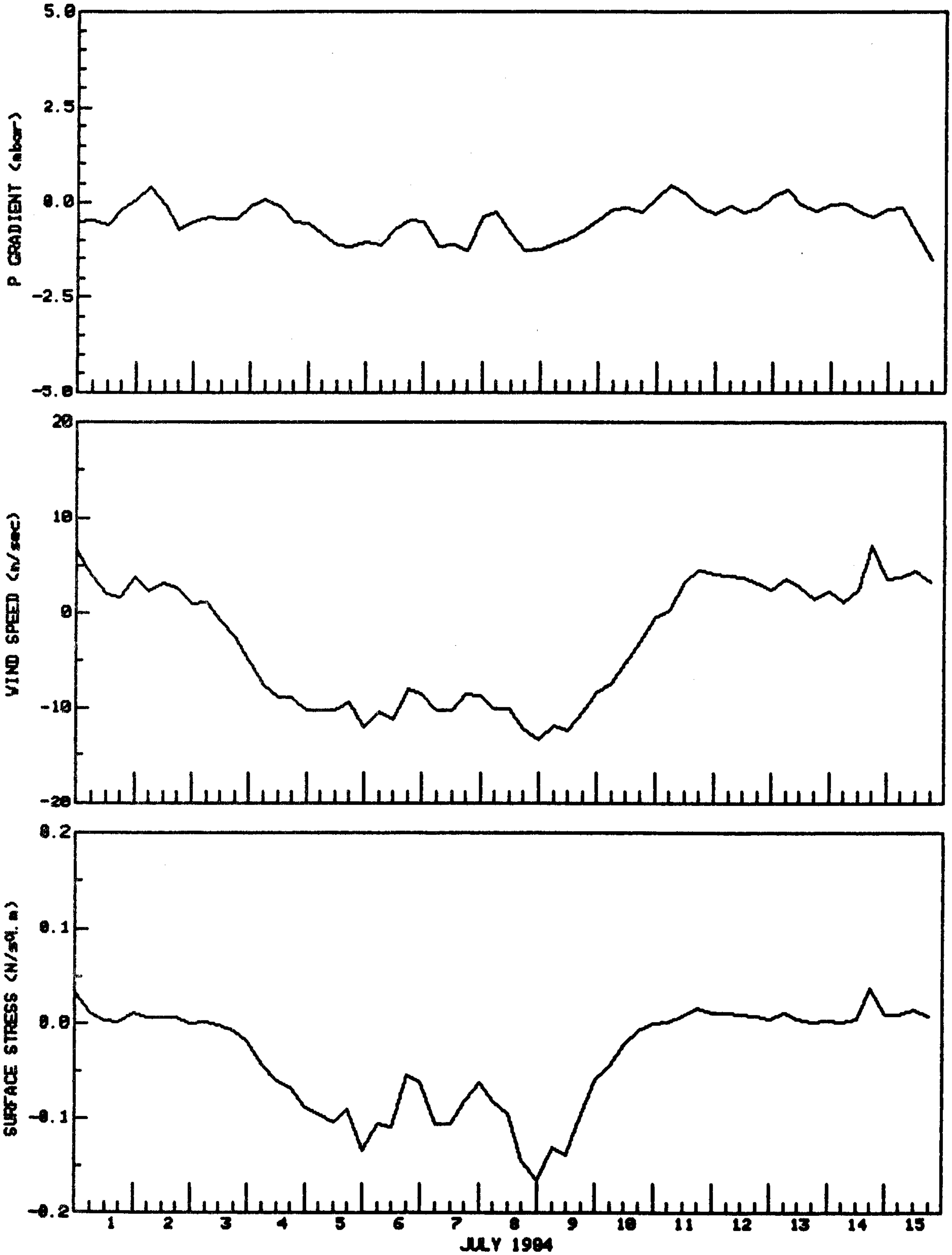

TIME SERIES OF OFFSHORE COMPONENT OF
PRESSURE GRADIENT, GEOSTROPHIC WIND AND SURFACE WIND STRESS
SHELIKOF STRAIT DT(min) 360

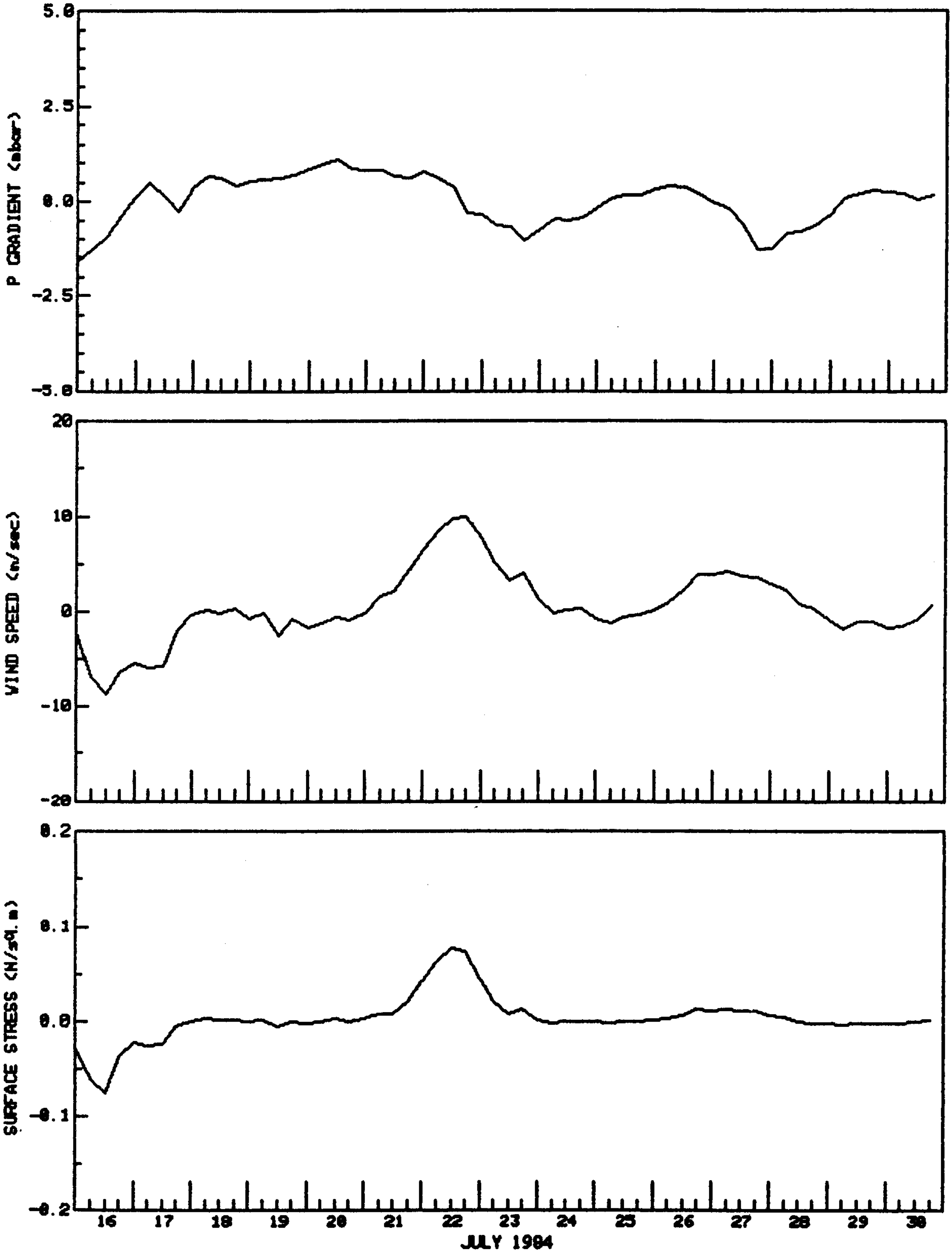

TIME SERIES OF OFFSHORE COMPONENT OF
PRESSURE GRADIENT, GEOSTROPHIC WIND AND SURFACE WIND STRESS
SHELIKOF STRAIT DT(min) 360

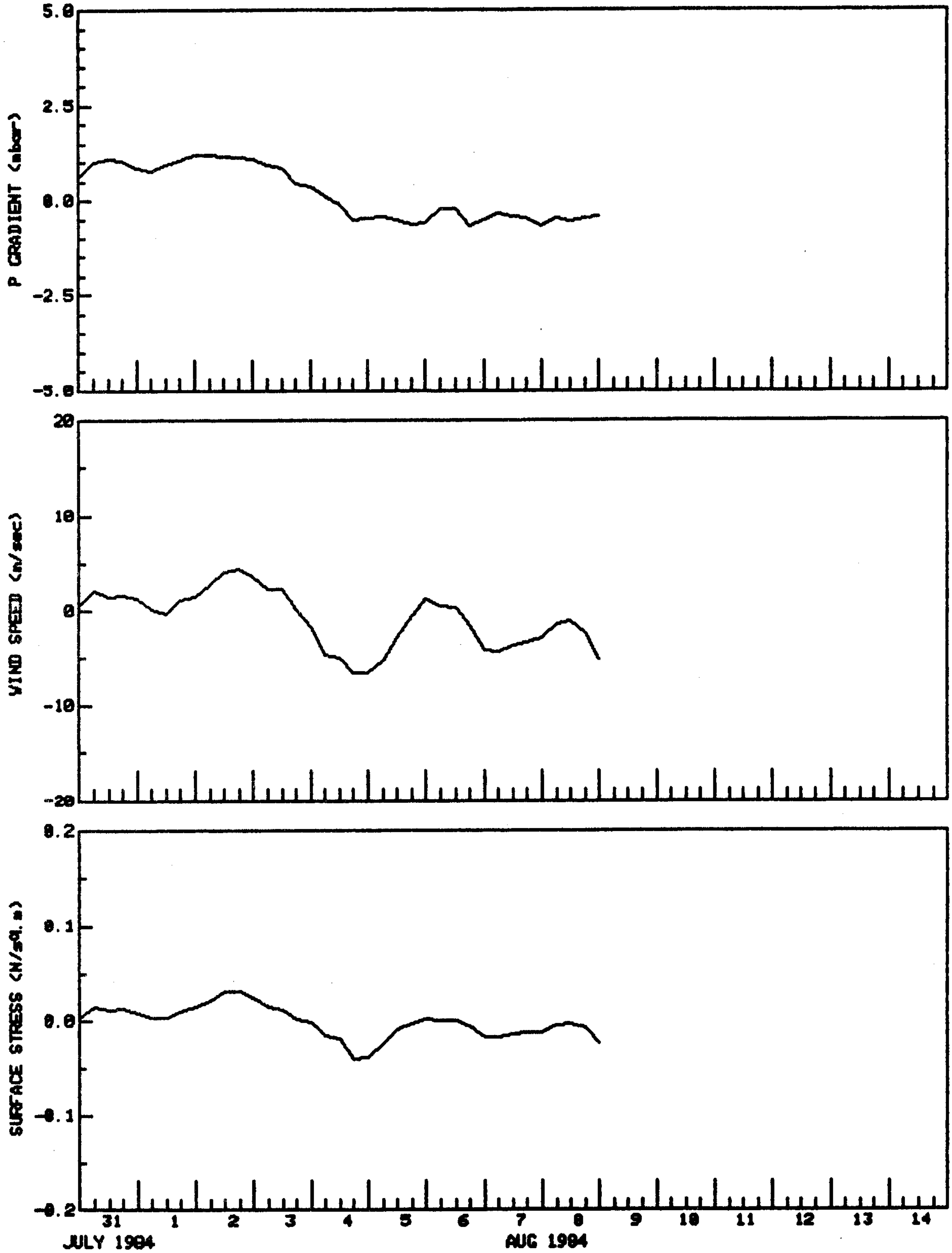

TIME SERIES OF LONGSHORE COMPONENT OF
PRESSURE GRADIENT, GEOSTROPHIC WIND AND SURFACE WIND STRESS

SHELIKOF STRAIT DT(min) 360

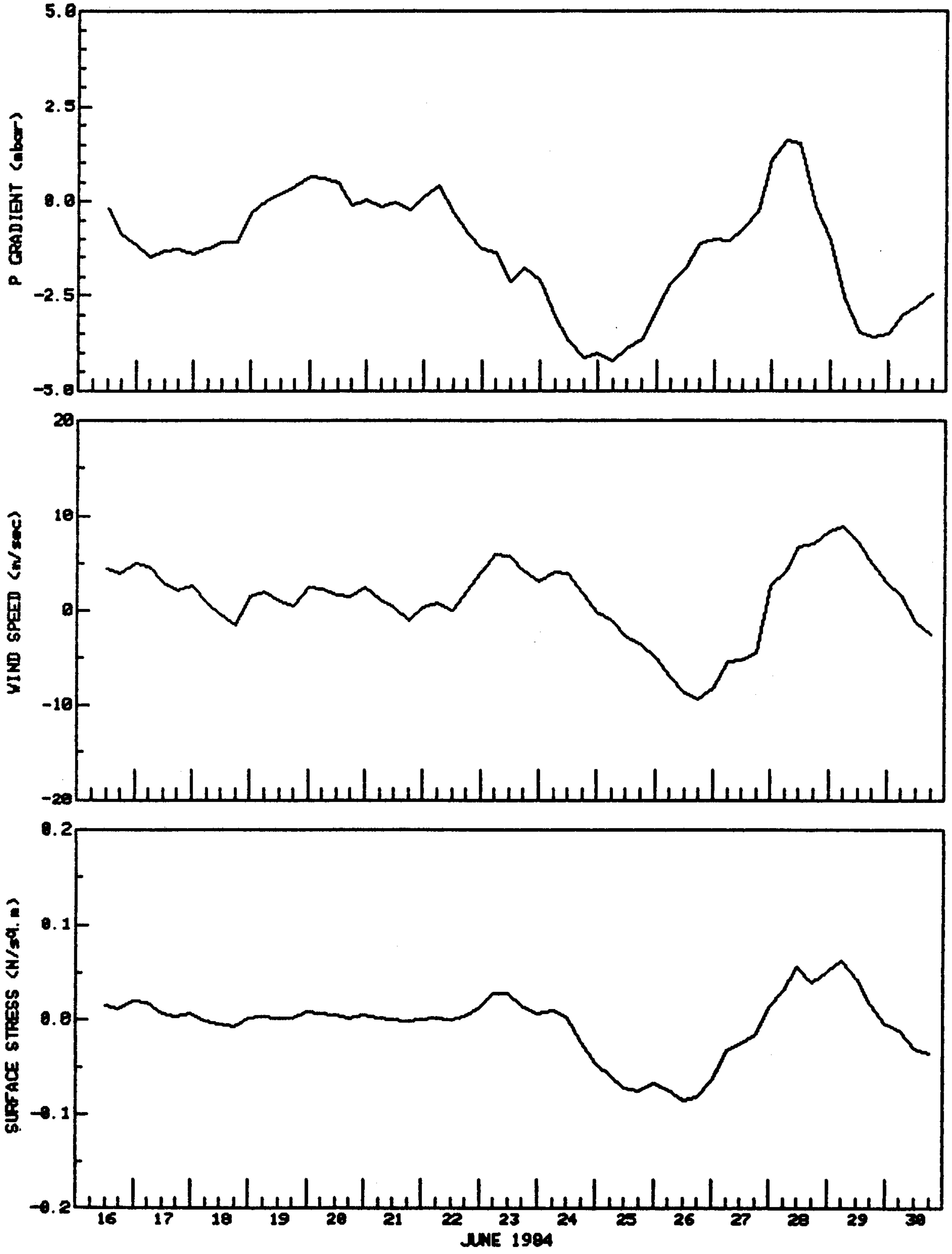

TIME SERIES OF LONGSHORE COMPONENT OF
PRESSURE GRADIENT, GEOSTROPHIC WIND AND SURFACE WIND STRESS

SHELIKOF STRAIT DT(min) 360

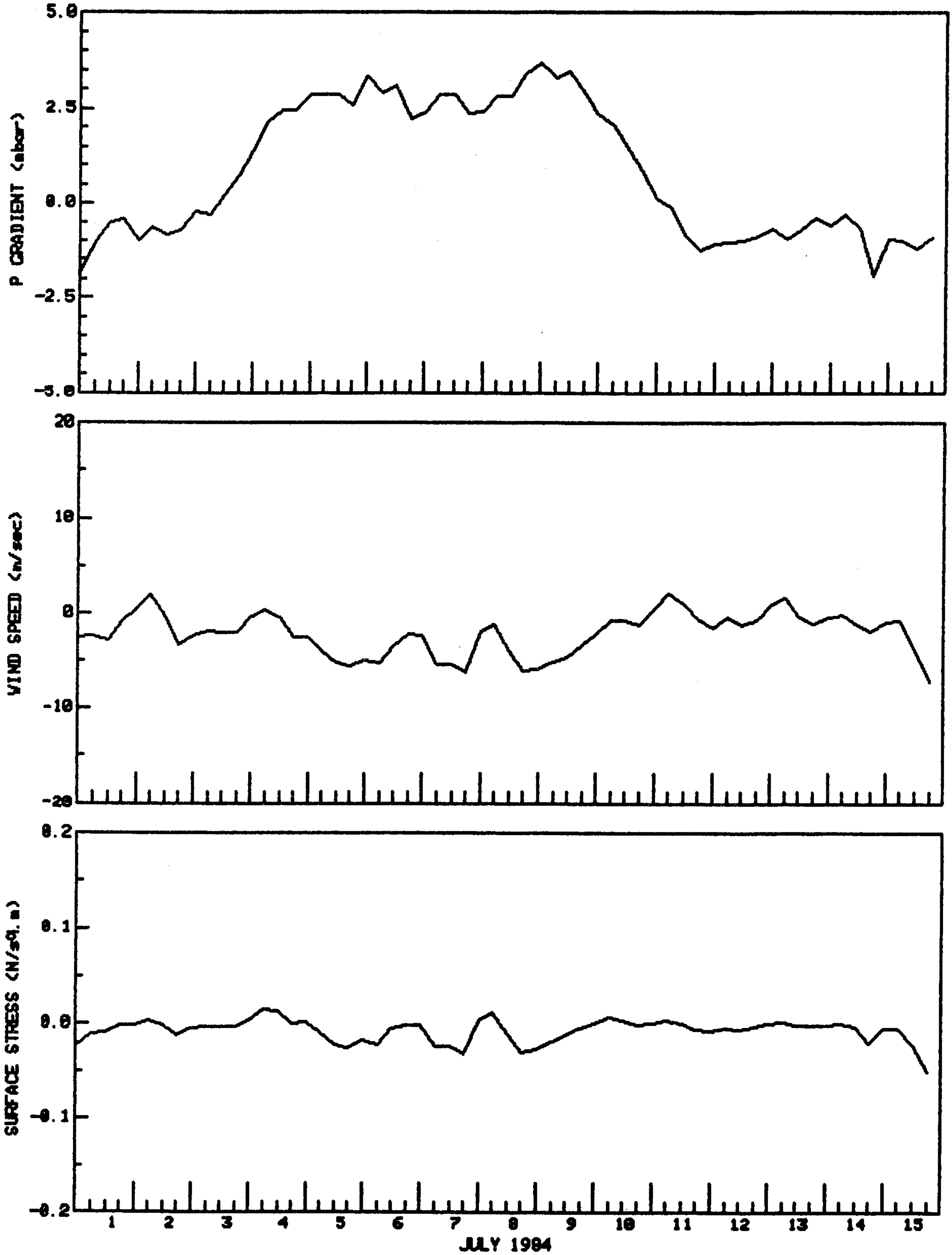

TIME SERIES OF LONGSHORE COMPONENT OF
PRESSURE GRADIENT, GEOSTROPHIC WIND AND SURFACE WIND STRESS
SHELIKOF STRAIT DT(min) 360

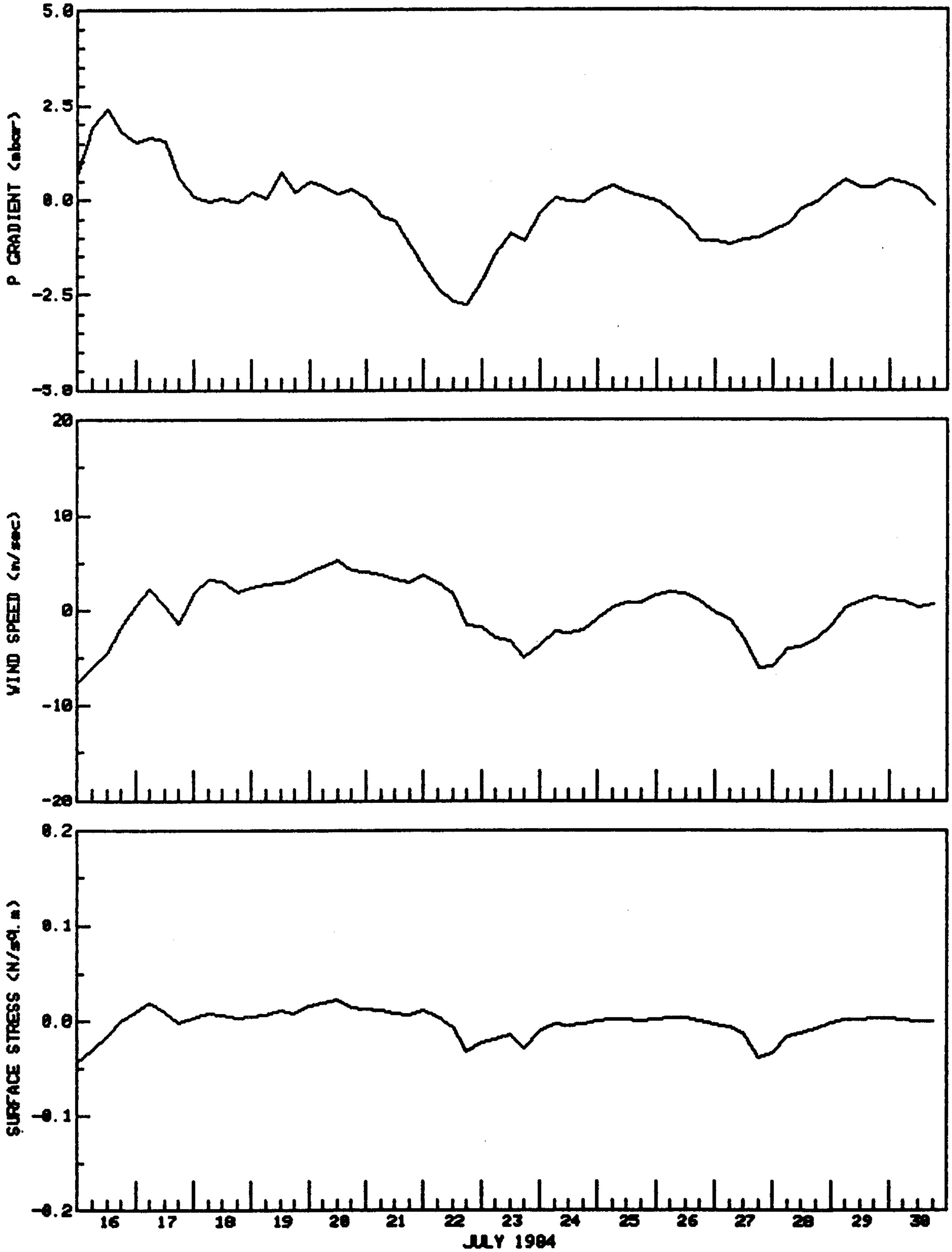

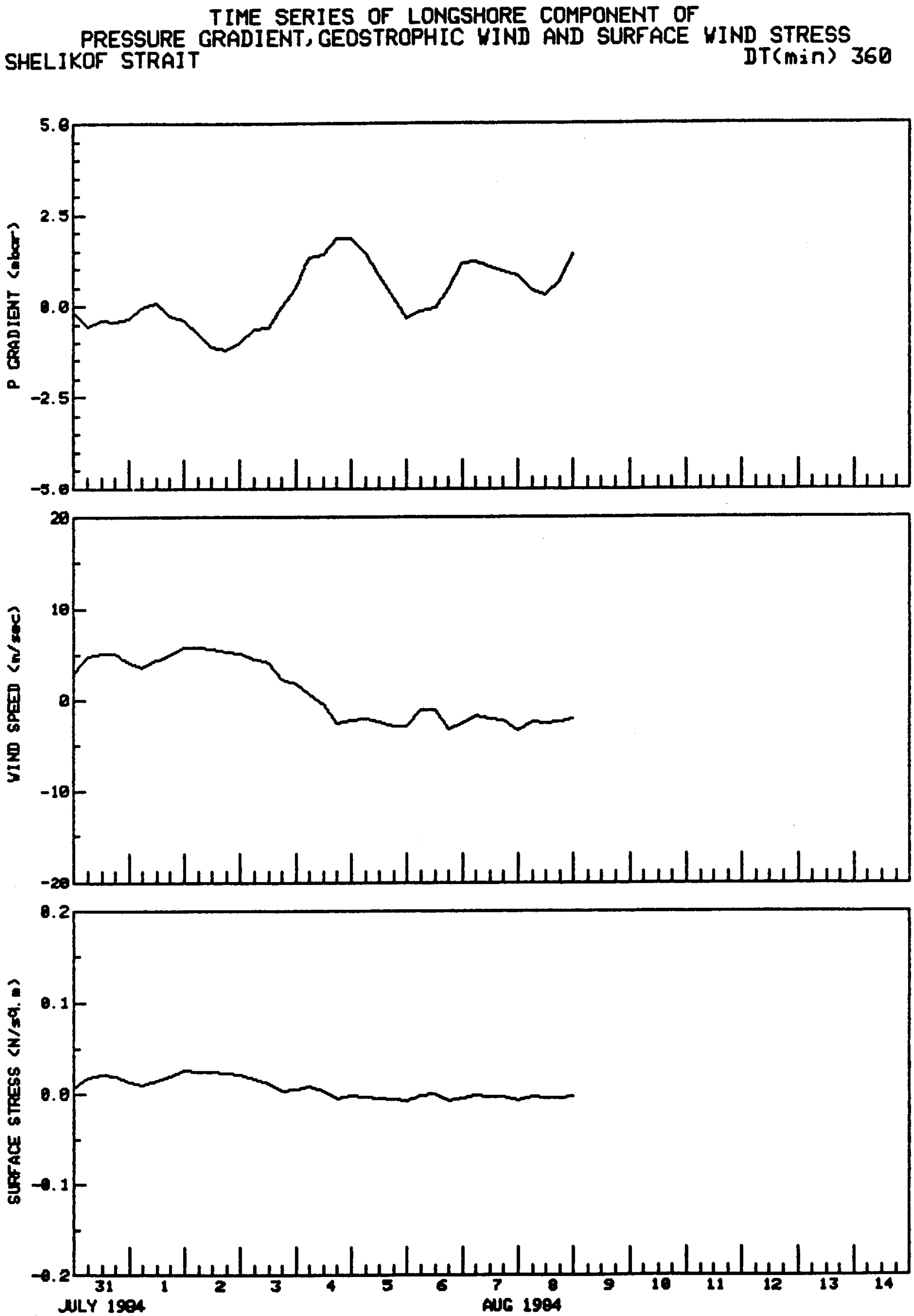
TIME SERIES OF LONGSHORE COMPONENT OF
PRESSURE GRADIENT, GEOSTROPHIC WIND AND SURFACE WIND STRESS
SHELIKOF STRAIT
DT(min) 360
P GRADIENT (mbar)
5.0
2.5
0.0
-2.5
-5.0
WIND SPEED (m/sec)
20
10
0
-10
-20
SURFACE STRESS (N/sq.m)
0.2
0.1
0.0
-0.1
-0.2
31
1
2
3
4
5
6
7
8
9
10
11
12
13
14
JULY 1984
AUG 1984

MODELING THE ALASKAN CONTINENTAL SHELF WATERS

by

Shiao-Kung Liu and J. J. Leendertse

The RAND Corporation
1700 Main Street
P.O. Box 2138
Santa Monica, California 90406

Final Report
Outer Continental Shelf Environmental Assessment Program
Research Unit 435

October 1987

ACKNOWLEDGMENTS

The study was supported by the Minerals Management Service, Department of the Interior, through an interagency agreement with the National Oceanic and Atmospheric Administration, under which a multiyear program responding to the needs of petroleum development of the Alaskan continental shelf is managed by the Outer Continental Shelf Environmental Assessment Program (OCSEAP) office.

The execution of this study would not have been possible without our RAND colleague A. B. Nelson. With much skill he prepared the programs and the numerous program modifications that were used in the analyses. We thank him for his effort and for the time he spent at RAND outside normal office hours to accomplish his tasks and to meet the close deadlines imposed by the project.

The report was reviewed by five anonymous reviewers outside RAND and also by RAND colleagues F. Murray and M. Juncosa. We would like to thank them for their efforts.

We also want to thank Geni R. Coughlan who expertly and professionally prepared the drafts and final report with great patience.

PREFACE

This report gives an account of studies made over a period of six years under a contract between the National Oceanic and Atmospheric Administration (NOAA) and The RAND Corporation. Preparation of this report was funded by The RAND Corporation.

RAND's initial modeling studies supported investigations made by other scientists of NOAA and universities concerning the physical processes in and on the waters of the Alaskan outer continental shelf. Gradually it became clear that probabilistic oil spill trajectory simulations directly usable in impact analysis were needed in addition to the field investigations of physical oceanographic processes. Efforts were then redirected from a scientific modeling study (aiming to obtain a better understanding of the complicated hydrodynamic processes of the Alaskan continental shelf) to analysis and simulations directly usable for impact assessments. Most of the study results were submitted in digital form to the Minerals Management Service.

In modeling studies made to better understand the physical processes, generally only a limited part of the system is modeled. This type of modeling is well understood and accepted by most, since the physical processes can be quite clearly formulated in mathematical expressions. Modeling for impact assessments and policy analysis is different. Here, scenarios have to be selected and processes have to be screened as to their relevance in the final results, and the modeling requires the execution of a large number of modeling steps in sequence.

Few modeling studies of this type have been made for the environmental impact assessment of Arctic waters. For this reason, in this report the authors particularly emphasize descriptions of the processes that were included and how these processes are incorporated in the overall analysis. Thus with this study the authors intend to support the environmental impact assessments made by others by stating what was considered here and how all of the results have been combined.

In making the analyses reported here, the authors made extensive use of computer simulations, but most of the critical analyses were made by conventional means. The analyses of the Alaskan coastal system have been more difficult and tedious than other analyses made of other coastal areas. The primary reason for this difficulty has been the lack of field data. For example, parts of the Beaufort Sea beneath the permanent polar ice cap are not charted. Carrying out a monitoring program in the large remote offshore areas of Alaska is difficult and expensive, particularly as the presence of sea ice poses unique problems. Many instrument packages were lost during the data collection efforts.

Even with these difficulties, the modeling studies have been very rewarding to the authors. Many times the analyses were confirmed by field data collected after a certain area had been modeled.

The authors found the hydrodynamic and weather systems in the study areas very complicated, but valued the opportunity to study the major dynamic processes involved. Obviously, there is still much to be learned about the hydrodynamics of one of the widest continental shelves in the world.

SUMMARY

This report presents the development of three-dimensional numerical models of the Bering Sea, the Chukchi Sea, the Beaufort Sea, and the Gulf of Alaska. These models are formulated on ellipsoidal horizontal grids and variable vertical grids covering a total area of more than three million square kilometers and slightly more than half of the entire U.S. coastline.

The hydrodynamic model is coupled to a two-dimensional stochastic weather model and an oil spill trajectory/weathering model. The former also simulates stochastically the cyclogenetic/cyclolytic processes within the modeled area.

The report also compares the computed results with available field data. These include tides, baroclinic circulation, ice distribution/movement, and the partition of kinetic energetics in the frequency domain.

TABLE OF CONTENTS

LIST OF FIGURES

LIST OF TABLES

1. INTRODUCTION

This report presents modeling studies of the hydrodynamic and related physical processes of the Alaskan coastal waters for impact assessments of the exploration and exploitation of oil reserves on the Alaskan outer continental shelf.

At present, the Prudhoe Bay field in northern Alaska contributes a substantial amount of the current domestic oil production of the United States. Oil is also expected to be present on the continental shelf of Alaska, and it is estimated that approximately 28 percent of the total U.S. oil reserve is located beneath the shallow ice-covered seas of the Alaskan continental shelf (Weeks and Weller, 1984). To explore and to exploit these rich oil resources, engineers must confront hostile oceanographic conditions such as high tides, waves, strong currents, and dangerous working conditions associated with the sea ice. Results from the modeling work reported here will provide useful information on the environmental factors affecting the design of engineering works for the exploration and exploitation of these oil reserves.

The Alaskan continental shelf is rich in fishery resources. Being one of the most productive fishing grounds in the northern Pacific, the potential ecological impact of an oil spill is also of major concern. Another major concern is the impact of oil spills on wildlife, particularly in those areas where wildlife congregate during certain periods of the year. As a result, the major application of the models we developed during our studies has been for the assessment of risk associated with petroleum development within the region. For this reason, a major part of this report describes the methodology used for the computation of oil dispersion, weathering, and movements, and the results of these computations.

Initially our studies were limited to the determination of water movements resulting from tides and the distribution of densities in the considered water bodies. Soon after we began our modeling work, we realized that results of a hydrodynamic model cannot provide much data for environmental assessment without regional weather information and models for the computation of the movement, dispersion, and weathering of oil spills.

The studies reported here were made in conjunction with environmental research studies performed by others. The work includes all the waters of the Alaskan continental shelf, but some areas were covered with more geographic detail than others.

In each chapter of this report, studies for each particular process are presented. Thus in each chapter the formulation of the model is described and results are presented for the different application areas.

Chapter 2 outlines the mathematical formulation and the solution scheme of the hydrodynamic modeling system. Because of the strong buoyancy effects caused by ice melting in the water column, and because of the intense momentum transfer process associated with frequent storm activity, a new turbulence closure scheme is used. The scheme is somewhat different from the traditional approach and is described in Chapter 2. Also represented are the behavior and performance of the numerical model. Particularly important is the model's verification on the partition of energy in the frequency domain for both homogeneous and nonhomogeneous tubulent flows. This is an essential step in model development.

Chapter 3 describes the modeling of hydrodynamic processes including tides, wind-driven currents, and the residual circulation induced by the baroclinic field. The Alaskan coastal waters are part of three major oceanic systems—the Arctic Ocean, the Bering Sea, and the Gulf of Alaska. Each system has its own distinct characteristics, but they interact in a complex, yet interesting way. These important features are also presented in this chapter.

One special feature of the Alaskan coastal waters is the frequent presence of storms. These large moving storms produce strong winds that alter the areawide hydrodynamic processes through long-period oscillation within the system. The intense storms not only pose a threat to the offshore, oil related activities but also play a significant role in environmental risk analyses such as the reversal of ice transport between the Bering Sea and the Arctic Ocean. The cyclogenetic/cyclolytic processes associated with these extratropical storms are complex and stochastic in nature. The probabilities associated with the storm-related parameters have to be considered together with the environmental risk factors. Because of this, stochastic models are developed to estimate the weather elements associated with the modeling systems such as the variability of wind fields. These analyses are presented in Chapter 4.

Another special feature of the Alaskan coastal waters we included in our studies is the presence of ice. Chapter 5 gives a description of the ice modeling work. Nearly half of our modeled area lies within the Arctic Circle. In this region the waters can be completely free of ice at some time of year and completely covered with ice at other times. The presence of ice complicates the modeling work considerably, particularly when the knowledge of polar ice is incomplete.

In Chapter 6 we describe the transport, dispersion, and weathering of spilled oil. To provide information for oil spill risk analyses, the movements of spilled oil were computed for at least one month under summer conditions. If simulated spills occurred during winter, the simulation period had to be extended, sometimes for several months. In the computational methods we developed for this purpose, we accounted for the movements of oil under ice.

Wind is a major input to the oil trajectory computations. The wind model described in Chapter 4 is used for this purpose. In some instances, information had to be provided on the distribution of oil in the water after a spill. With excellent cooperation from other research institutions, we were able to develop a model for the dispersion of oil that included the oil weathering process. The procedures for these oil dispersion computations are also presented in Chapter 6.

2. THE THREE-DIMENSIONAL MODELING SYSTEM

In the modeling system, the three-dimensional hydrodynamic model is one of the most important models. This model is formulated according to the equations of motion for water and ice, continuity, state, the balance of heat, salt, pollutant, and turbulent energy densities, on a three-dimensional finite grid. The vertical momentum, mass, heat, and turbulent energy exchange coefficients are computed from the turbulent energy, thus the model contains a turbulence closure computation. Turbulent energy dissipation resulting from the mixing of heavier water with lighter water is accounted for in the turbulence closure.

For the derivation of basic equations, the reader is referred to Liu and Leendertse (1978), in which aspects such as open boundary conditions, numerical stability, solution discontinuity, and conservation properties are also described.

In the present model, the horizontal grid conforms to the earth's ellipsoidal coordinates and the arbitrary vertical grid spacing approximates the bottom topography of the modeled area. The results are subsequently transformed into the Universal Mercator projection for graphical representation. For simplicity, the system of modeling equations is presented here using the standard finite difference notation on a regular spatial grid network in the horizontal direction, and on an irregular grid in the vertical (Fig. 2.1). The coordinates i, j, k, and n are used to denote discrete points in the x, y, z, and t domain. The finite difference formulation adapted for the computation takes the following form:

$$\overline{\delta_t \zeta} = -\sum_k \left[\delta_x\left(\overline{h}^x u\right) + \delta_y\left(\overline{h}^y v\right)\right] \quad \text{at } i, j, n \tag{2.1}$$

where the variation of the water level ζ is derived from the continuity equation by vertical integration, and h is the layer thickness. The momentum equation in the x-direction:

$$\overline{\delta_t(\overline{h}^x u)}^t = -\delta_x\left(\overline{\overline{h}^x u}^x \, \overline{u}^x\right) - \delta_y\left(\overline{\overline{h}^y v}^x \, \overline{u}^y\right) - \overline{h}^x \delta_z\left(\overline{u}^z \, \overline{w}^x\right) + f\overline{h}^x \overline{v}^{xy} - \frac{1}{\overline{\rho}^x} \overline{h}^x \delta_x p$$

$$+ \frac{1}{\overline{\rho}^x}\left[h\delta_z\left(E_x \delta_z \overline{u}^{2t}\right) + \delta_x\left(hA_x \delta_x u\right)_- + \delta_y\left(\overline{\overline{h}^x \, \overline{A_y}^x}^y \delta_y u\right)_-\right]$$

$$\text{at } i + 1/2, j, k, n \tag{2.2}$$

where E_x is the vertical momentum exchange coefficient, and A_x, A_y are the horizontal exchange coefficients in x-direction and y-direction, respectively.

The momentum equation in the y-direction:

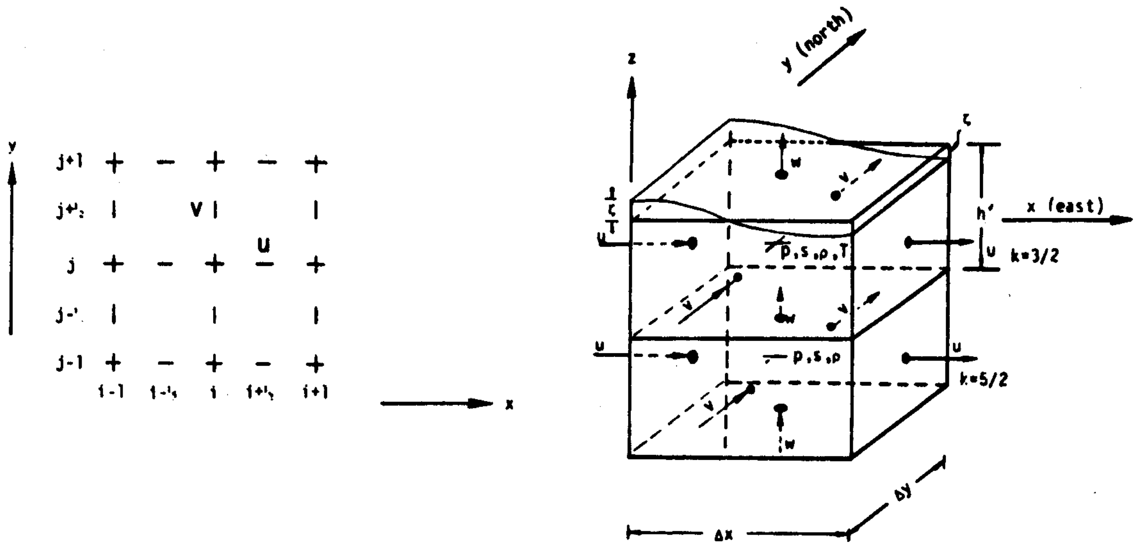

Space-staggered computation grid and relative position of variables

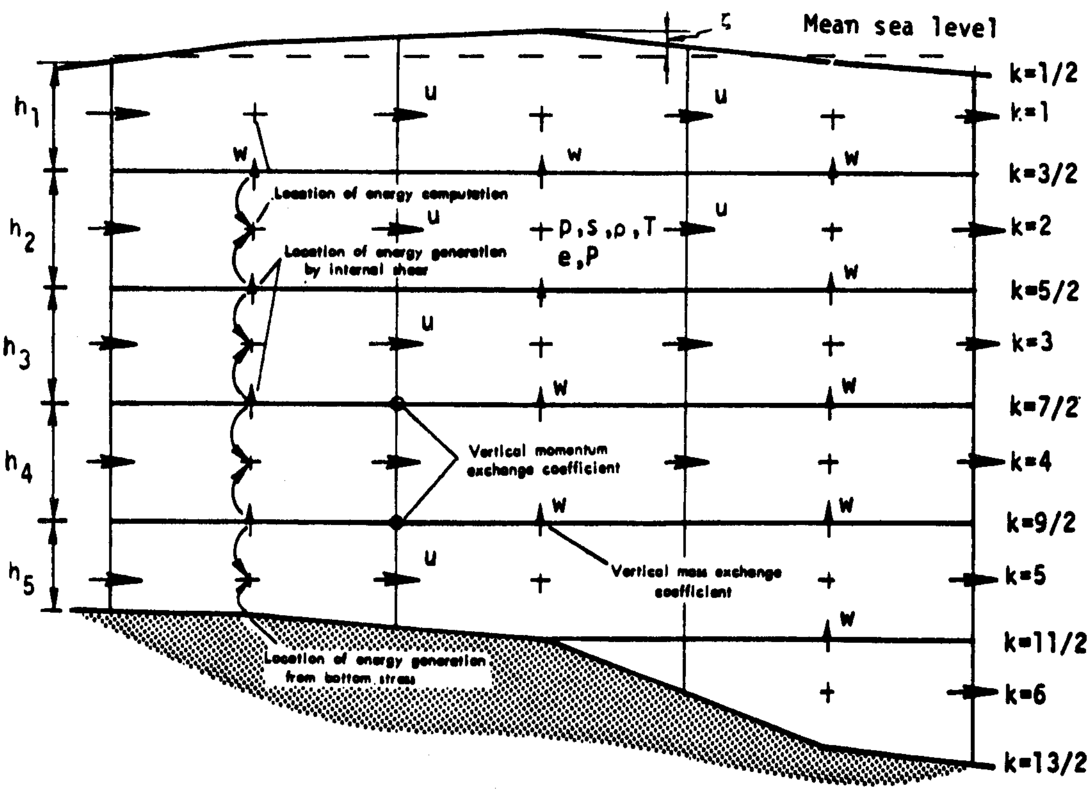

Location of variables on the X-Z plane

Fig. 2.1—Location of variables.

$$\overline{\delta_t\left(\bar{h}^y v\right)}^t = -\delta_x\left(\overline{\bar{h}^x u}^y\, \bar{v}^x\right) - \delta_y\left(\overline{\bar{h}^y v}^y\, \bar{v}^y\right) - \bar{h}^y \delta_z\left(\bar{v}^z \bar{w}^y\right) - f\bar{h}^y \bar{u}^{xy} - \frac{1}{\bar{\rho}^y}\, \bar{h}^y \delta_y p$$

$$+ \frac{1}{\bar{\rho}^y}\left[h\delta_z\left(E_y \delta_z \bar{v}^{2t}\right) + \delta_x\left(\overline{\bar{h}^y \bar{A}_x^y}^x\, \delta_x v\right)_- + \delta_y\left(hA_y \delta_y v\right)_-\right]$$

$$\text{at } i, j + ½, k, n \tag{2.3}$$

The mass-balance equation for salt,

$$\overline{\delta_t\left(hs\right)}^t = -\delta_x\left(\bar{h}^x u\bar{s}^x\right) - \delta_y\left(\bar{h}^y v\bar{s}^y\right) - h\delta_z\left(w\bar{s}^z\right)$$

$$+ \delta_x\left(\bar{h}^x D_x \delta_x s\right)_- + \delta_y\left(\bar{h}^y D_y \delta_y s\right)_- - hs_z\left(\kappa\delta_z \bar{s}^{2t}\right)$$

$$\text{at } i, j, k, n \tag{2.4}$$

where D_x and D_y are the horizontal diffusion coefficients, s is the salinity (salt concentration), and κ is the vertical mass exchange coefficient. For temperature:

$$\overline{\delta_t\left(hT\right)}^t = -\delta_x\left(\bar{h}^x u\bar{T}^x\right) - \delta_y\left(\bar{h}^y v\bar{T}^y\right) - h\delta_z\left(w\bar{T}^z\right)$$

$$+ \delta_x\left(\bar{h}^x D_x \delta_x T\right)_- + \delta_y\left(\bar{h}^y D_y \delta_y T\right)_- + h\delta_z\left(\kappa'\delta_z \bar{T}^{2t}\right)$$

$$\text{at } i, j, k, n \tag{2.5}$$

where κ' is the vertical thermodiffusion coefficient.

For the SGS energy density in the system,

$$\overline{\delta_t\left(he\right)}^t = -\delta_x\left(\bar{h}^x u\bar{e}^x\right) - \delta_y\left(\bar{h}^y v\bar{e}^y\right) - h\delta_z\left(w\bar{e}^z\right)$$

$$+ \delta_x\left(\bar{h}^x D_x \delta_x e\right)_- + \delta_y\left(\bar{h}^y D_y \delta_y e\right)_- + h\delta_z\left(E_e \delta_z \bar{e}^{2t}\right) + h\overline{S_e}^z - D_e h$$

$$\text{at } i, j, k, n \tag{2.6}$$

where E_e is the vertical momentum exchange coefficient. For the pollutant constituent concentration:

$$\overline{\delta_t\left(hP\right)}^{t} = -\delta_x\left(\bar{h}^{x} u \bar{P}^{x}\right) - \delta_y\left(\bar{h}^{y} v \bar{P}^{y}\right) - h\delta_z\left(w\bar{P}^{z}\right)$$

$$+ \delta_x\left(\bar{h}^{x} D_x \delta_x P\right)_- + \delta_y\left(\bar{h}^{y} D_y \delta_y P\right)_- + h\delta_z\left(\kappa\delta_z \bar{P}^{2t}\right) + hS_P - D_P h$$

$$\text{at } i, j, k, n \qquad (2.7)$$

The equation of state is approximated by:

$$\rho = \frac{\left[5890 + 38T - 0.375T^2 + 3s\right]}{\left[(1779.5 + 11.25T - 0.0745T^2) - (3.8 + 0.01T)s + 0.698(5890 + 38T - 0.375T^2 + 3s)\right]}$$

$$\text{at } i, j, k, n + l \qquad (2.8)$$

The continuity equation is used to compute the vertical velocity:

$$\delta_z w = -\delta_x\left(\bar{h}^{x} u\right) - \delta_y\left(\bar{h}^{y} v\right) \qquad \text{at } i, j, k, n + l \qquad (2.9)$$

Similar equations for velocity components u and v can be written for the top and bottom layers, but now the effects of wind and bottom friction must be considered. We have at the surface:

$$\overline{\delta_t\left(\bar{h}^{x} u\right)}^{t} = -\delta_x\left(\overline{\bar{h}^{x} u}^{x}\, \bar{u}^{x}\right) - \delta_y\left(\overline{\bar{h}^{y} v}^{x}\, \bar{u}^{y}\right) - \bar{h}^{x}\delta_z\left(\bar{u}^{z}\bar{w}^{x}\right) + f\bar{h}^{x}\bar{v}^{xy} - \frac{1}{\bar{\rho}^{x}}\bar{h}^{x}\delta_x P$$

$$+ \frac{1}{\bar{\rho}^{x}}\left[\Theta\rho_a w_a^2 \sin\psi - \left(E_x\delta_z\bar{u}^{2t}\right)_{k=3/2} + \delta_x\left(hA_x\delta_x u\right)_- + \delta_y\left(\overline{\bar{h}^{x}\,\bar{A}_y^{x}}^{y}\,\delta_y u\right)_-\right]$$

$$\text{at } i + ½, j, l, n \qquad (2.10)$$

where ψ is the clockwise angle between the model's y-axis and the direction toward which the wind is blowing and where Θ represents the wind-stress coefficient. In the y-direction, the momentum equation becomes:

$$\overline{\delta_t(\bar{h}^{y} v)}^{t} = -\delta_x\left(\overline{\bar{h}^{x} u}^{y}\, \bar{v}^{x}\right) - \delta_y\left(\overline{\bar{h}^{y} v}^{y}\, \bar{v}^{y}\right) - \bar{h}^{y}\delta_z\left(\bar{u}^{z}\bar{w}^{y}\right) - f\bar{h}^{y}\bar{v}^{xy} - \frac{1}{\bar{\rho}^{y}}\bar{h}^{y}\delta_y p$$

$$+ \frac{1}{\bar{\rho}^{y}}\left[\Theta\rho_a w_a^2 \cos\psi - \left(E_y\delta_z\bar{v}^{2t}\right)_{k=3/2} + \delta_x\left(\overline{\bar{h}^{y}\,\bar{A}_x^{y}}^{x}\,\delta_x v\right)_- + \delta_y\left(hA_y\delta_y v\right)_-\right]$$

$$\text{at } i, j, + ½, l, n \qquad (2.11)$$

where w_a is wind speed, and ρ_a represents the density of air. At the bottom layer the momentum equations become:

$$\overline{\delta_t(\bar{h}^x u)}^t = -\delta_x\left(\overline{\bar{h}^x u}^x \bar{u}^x\right) - \delta_y\left(\overline{\bar{h}^y v}^x \bar{u}^y\right) - \bar{h}^x \delta_z\left(\bar{u}^z \bar{w}^x\right) + f\bar{h}^x \bar{v}^{xy} - \frac{1}{\bar{\rho}^x} \bar{h}^x \delta_x p$$

$$+ \frac{1}{\bar{\rho}^x}\left\{ \left(E_x \delta_z \bar{u}^{2t}\right)_{k=K-1/2} - \bar{\rho}^x g u_-\left[u_-^2 + \left(\bar{v}_-^{xy}\right)^2\right]^{1/2} \Big/ \left(\bar{C}^x\right)^2 \right.$$

$$\left. + \delta_x\left(hA_x\delta_x u\right)_- + \delta_y\left(\overline{\bar{h}^x \bar{A}_y^x}^y \delta_y u\right)_- \right\} \quad \text{at } i + ½, j, K, n$$

$$\overline{\delta_t(\bar{h}^y v)}^t = -\delta_x\left(\overline{\bar{h}^x u}^y \bar{v}^x\right) - \delta_y\left(\overline{\bar{h}^y v}^y \bar{v}^y\right) - \bar{h}^y \delta_z\left(\bar{v}^z \bar{w}^y\right) - f\bar{h}^y \bar{u}^{xy} - \frac{1}{\bar{\rho}^y} \bar{h}^y \delta_y p \tag{2.12}$$

$$+ \frac{1}{\bar{\rho}^x}\left\{ \left(E_y \delta_z \bar{v}^{2t}\right)_{k=K-1/2} - \bar{\rho}^y g v_-\left[\left(\bar{u}_-^{xy}\right)^2 + v_-^2\right]^{1/2} \Big/ \left(\bar{C}^y\right)^2 \right.$$

$$\left. + \delta_x\left(\overline{\bar{h}^y \bar{A}_x^y}^x \delta_x v\right)_- + \delta_y\left(hA_y\delta_y v\right)_- \right\} \quad \text{at } i, j, + ½, K, n \tag{2.13}$$

where C is the Chezy coefficient:

In the modeled area, each vertical motion of water mass has to work against buoyancy forces induced by the density gradient. If the available kinetic energy of the turbulent motion is insufficient to overcome this stabilizing effect, turbulence is inhibited and suppressed. As a consequence, the process of momentum and mass-heat exchange will be lower than the neutral stability condition. The criteria for the onset of this turbulence-suppressing process in the system can be obtained from the local density gradient and turbulent energy level. Therefore, the variability of the vertical exchange coefficients in the model is computed by a turbulence closure technique using local turbulence intensity, e:

$$E_y = \bar{\rho}^{yz}\, \overline{L\sqrt{e_-}}^{xz} \tag{2.14}$$

$$E_x = \bar{\rho}^{xz}\, \overline{L\sqrt{e_-}}^{xz} \tag{2.15}$$

$$E_e = a_1\, \overline{L\sqrt{e_-}}^{z} \tag{2.16}$$

$$\kappa = a_4 \overline{L \sqrt{e_-}}^z \qquad (2.17)$$

where a_1 , a_4 are turbulence closure constants and L denotes the length scale, which can be approximated by an additional transport equation (Rodi, 1980), or by a parametric expression based on work by Kranenberg (1984, 1985) and Joppe (1985).

$$\frac{1}{L} = \frac{1}{\ell_m} + \frac{1}{\ell_s} \qquad (2.18)$$

where

$$\ell_m = \kappa' z (1 - z/d)^{1/2}$$

$$\ell_s = C_s(\kappa \rho_o / (g \partial\rho/\partial z) \qquad (2.19)$$

κ' is the von Karman constant, z represents the vertical distance from the bottom to the point considered, and d is the vertical distance from the surface to the bottom.

In the horizontal direction, the exchange coefficient is computed in two parts as a function of the local vorticity gradient and the local grid dimension. The first part is:

$$A = \gamma \left| \left(\delta_x \overline{\omega}^y + \delta_y \overline{\omega}^x \right) \right| \left(\Delta \ell \right)^3 \qquad (2.20)$$

where ω is the vorticity, γ is a coefficient, and $\Delta\ell$ is the local grid size. This part represents the exchange for a wave number lower than the spatial Nyquist frequency. The second part represents the contribution from the homogeneous subgrid scale turbulence above the spatial Nyquist frequency, which can be computed according to Kolmogorov's turbulence spectrum theory. The gross horizontal exchange coefficient is therefore:

$$D_x = \overline{A}^x + a_5 \Delta \ell^{4/3} \qquad (2.21)$$

$$D_y = \overline{A}^y + a_5 \Delta \ell^{4/3} \qquad (2.22)$$

where a_5 is a function of the energy dissipation rate. In a strict sense, molecular diffusion, which is quite small (and a property of the fluid), could be added as the third part. These three parts thus cover the turbulent dispersion/diffusion process over the entire spectral partition without overlapping.

In the model the amount of reduction in the vertical exchange resulting from stratification is based on the direct computation of the local gain in potential energy induced by vertical mixing. The exact amount is then taken out of the local turbulent (kinetic) energy budget. In the equation of energy (Eq. (2.6)), the generation and dissipation terms become:

$$\overline{S}_e^z - D_e = \underbrace{a_3 \overline{L\sqrt{e}}^z \left[\left(\delta_z \overline{u}^x\right)^2 + \left(\delta_z \overline{v}^y\right)^2 \right]}_{(1)} + \underbrace{a_3 \overline{L\sqrt{e}}^z \frac{g}{\overline{h}^z \rho} \left(\delta_z \overline{\rho}^z\right)}_{(2)} \tag{2.23}$$

$$\underbrace{- a_2 e^{3/2}/L}_{(3)}$$

where the first term denotes production, the second term represents the portion supplied that is used in potential energy increase, and the third term is dissipation.

The model algorithm allows a variable layer thickness to be used. In all models the thickness of the upper two layers is roughly half the mixed layer depth. Near the pycnocline the layer thickness is reduced to obtain the vertical resolution that is needed to model the mass and momentum exchanges and the dynamics with the appropriate accuracy.[1] These processes are of primary importance in our modeling work and are one of the major reasons why three-dimensional models were used in our analyses.

For oil spill trajectory computations and for computations of the dispersion of oil on the surface of the sea, surface currents are needed. These currents can be obtained by an extrapolation starting in the middle of the top layer. An analytical solution similar to the solution by Ekman (see Neumann and Pierson, 1966) is used. Ekman uses a fixed vertical eddy coefficient in his computations, whereas in our work this coefficient is variable. These time- and spatially varying coefficients are derived from simulations with the three-dimensional model by means of the turbulence closure procedure described above.

During the development stage of the modeling system, subsurface currents have been computed by means of vertical turbulent closure of both first- and second-order schemes, similar to that described by Launder and Spalding (1972). During tests, in the absence of a wind-induced free-surface energy source, both one- and two-equation models have worked well. However, under variable wind (or storm) conditions, and sometimes with floating ice, there is little experimental information on the surface effects of wind-induced turbulence that could be used as the basis for providing parameters for specifying length scale (Rodi, 1980).

As illustrated in Figs. 2.2 and 2.3, the model produces logarithmic vertical velocity profiles in homogeneous oscillating flow (straight line on a semilog plot). It can also reproduce nonviscous analytical solutions when all diffusion coefficients are set to zero.

Consider the turbulent closure computation when the model is driven at the open boundary by a monochromatic wave, in this case, a semidiurnal M2 tidal component into the Chesapeake Bay (see Fig. 2.4). In the model's interior, the scheme can produce the cascade of

[1]We did not introduce vertical coordinate transformations in which the layers are a fixed fraction of the full ocean depth even though such an approach reduces the programming effort considerably, as boundary conditions are very much simplified. When such transformations are used, the model loses its effectiveness, as this procedure introduces artificial mixing. This can be visualized by considering a deep point and an adjacent shallow point of the grid with water of low salinity. When the currents have a direction from the shallow area to the deeper area, then the water at the bottom layer of the shallow area is moved directly into the bottom layer in the deeper area and we obtain strong artificial mixing.

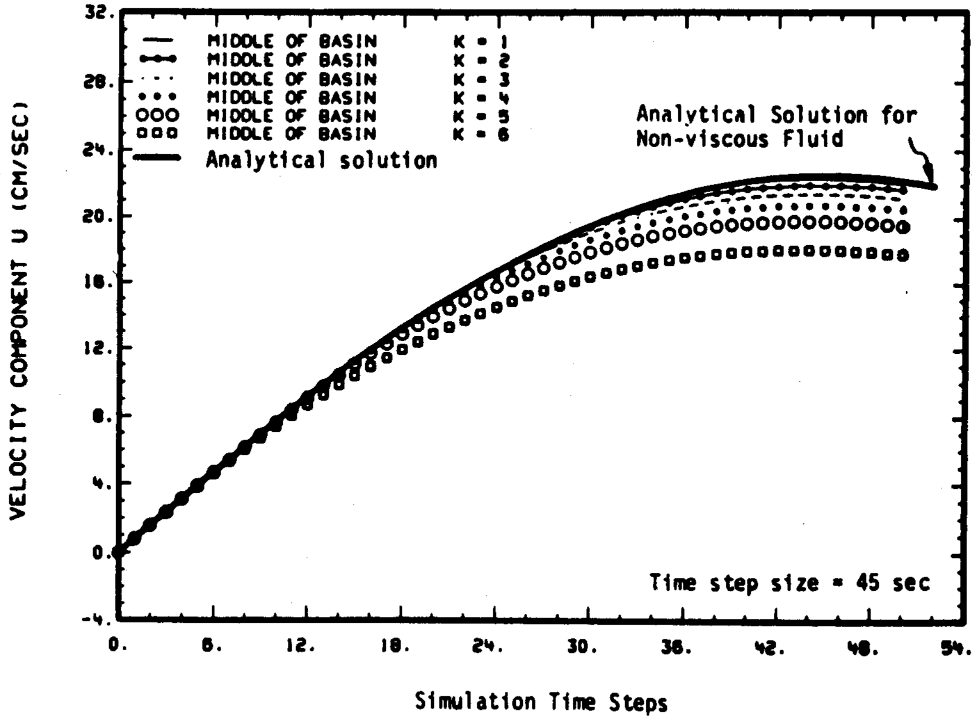

Fig. 2.2—Comparison of mean flow velocity component u, computed by numerical method, to nonviscous fluid, computed by analytical solution.

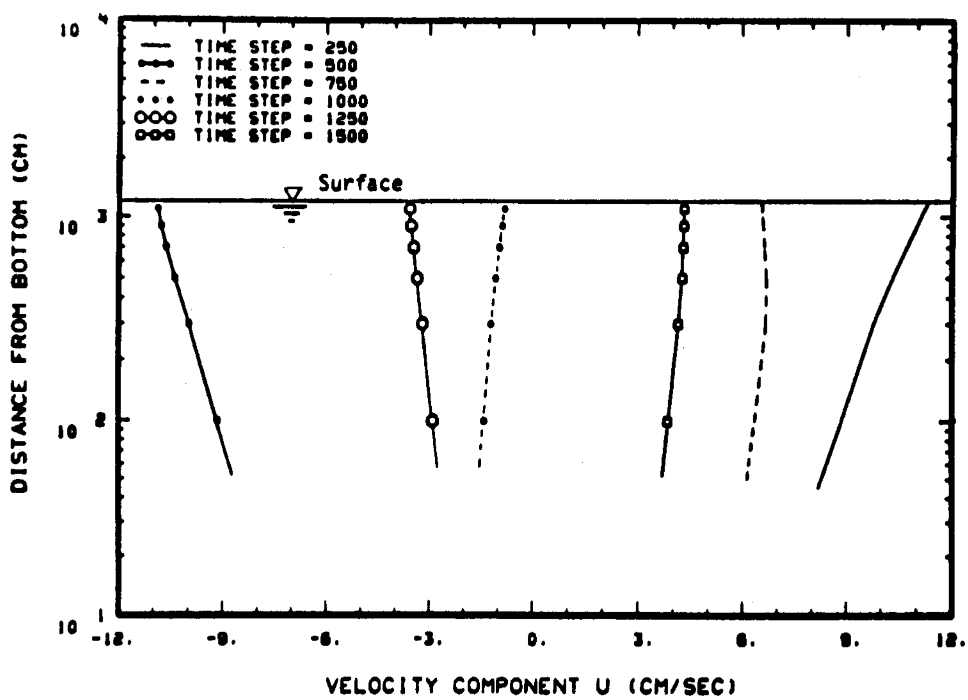

Fig. 2.3—Vertical distribution of velocity component u in the middle of the homogeneous oscillating basin (logarithmic vertical scale).

energy distribution according to the universal "minus five-third power law" (Hinze, 1959) through the model's nonlinear advective process. (Also, see the recent measurements by Heathershaw, 1979, and Elliott, 1984.)

In stratified geophysical flow, the density-induced vertical exchange often has a time scale much shorter than its horizontal baroclinic counterpart. It also plays an important role in the coastal ecological balance via the euphotic/energetic processes. It, therefore, creates stringent demands on the accuracy of modeling. On one hand, advances made in other disciplines, such as aerodynamic modeling, can often be applied to the geophysical flows, but, on the other hand, the differences in the free-surface and other boundary treatments make the closure technique not necessarily identical for stratified flows because coastal flows are primarily two-dimensional. Recent findings on the nonequilibrium statistical characteristics of turbulence have shown that the universal Kolmogorov-constant of the turbulence spectrum has to be modified for two-dimensional turbulence. Peaks of the spectra for two-dimensional turbulence are not uniquely located; however, they depend on the energy input and the relative location from the boundary (the so-called localization factor). Models relying on the Richardson-number-related parameters are especially susceptible to field measurement inaccuracies.

Consequently, over the past several years we have modified our earlier models that required Richardson-number-related parameters to an energy balance approach (Eq. (2.23)).

For the stratified fluid, when the computed spectra of the vertical displacements (in the surface layer, within pycnocline and near bottom, Liu and Leendertse, 1979) are plotted on a log-log scale (Fig. 2.5), the distribution of significant energy within this spectra agrees with the observed spectra of the first-mode internal wave (Gordon, 1978).

When the Bering Sea model reported herein is driven with the predicted tide (not measured), the computed subsurface current in the model's interior point agrees fairly well with the observed subsurface current both in magnitude and in direction (Fig. 2.6). When the computed velocities and the relative turbulence intensities at 15 layers are normalized with respect to the bottom, the vertical distribution of relative turbulence intensities (circles in Fig. 2.7) is nearly the same when compared with the standard NACA (later NASA) calibration curve of air flow measured in a brass pipe. In that graph, the insulation of momentum transfer across the pycnocline is evident.

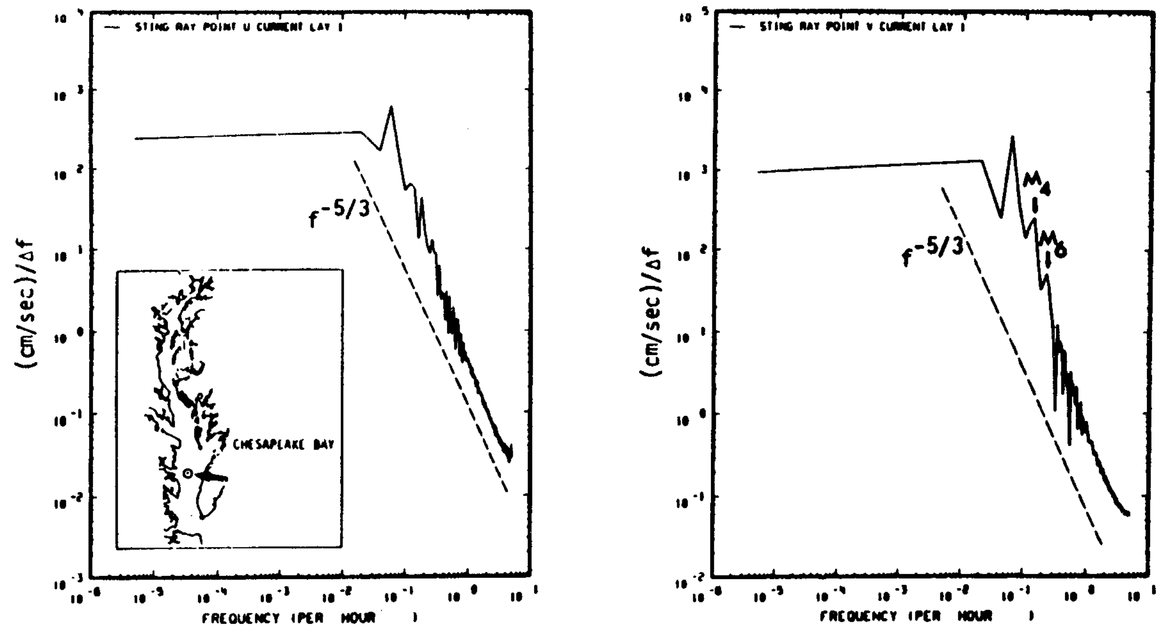

Fig. 2.4—Driven only with M2 tide (monochromatic wave) at the open boundary, the proposed numerical scheme can produce the cascade of energy distribution according to the universal "minus five-third" through the model's nonlinear advective process (Hinze, 1959).

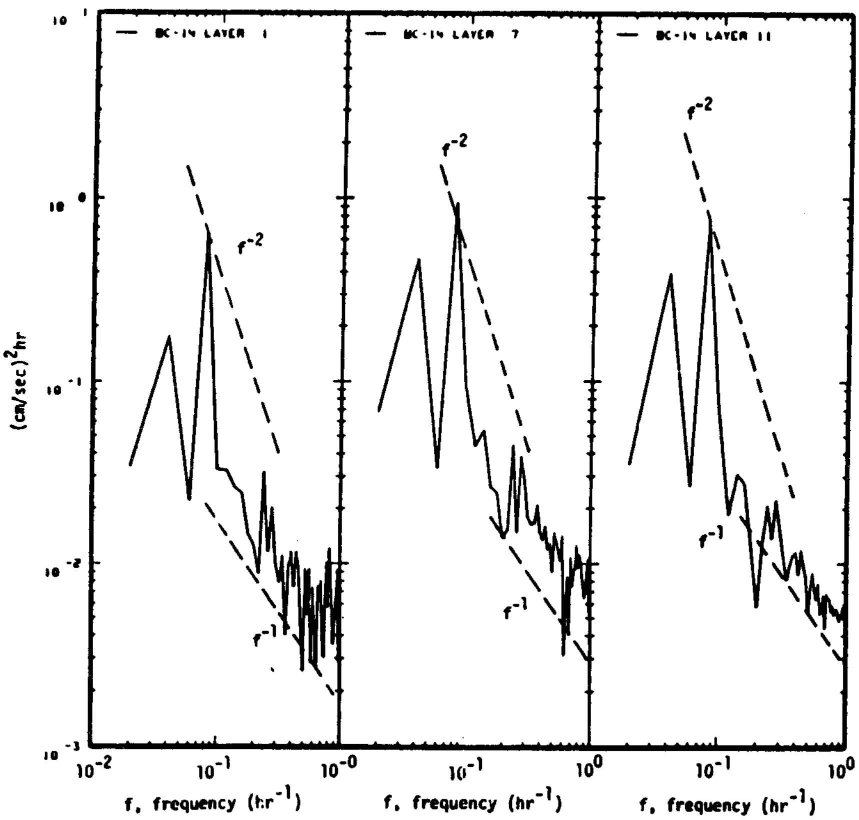

Fig. 2.5—For the stratified fluid, the computed spectra of the vertical displacements (in the surface layer, within pycnocline and near bottom) and significant energy distribution agree with the observed spectra of the first mode of internal waves (Gordon, 1978).

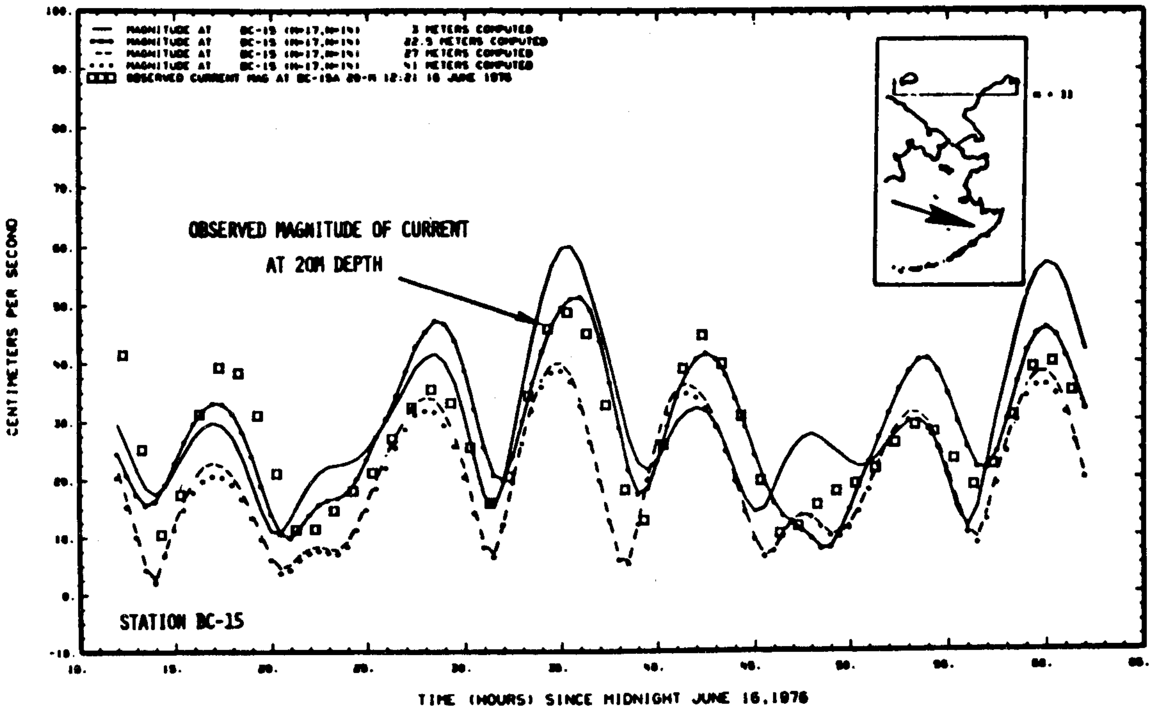

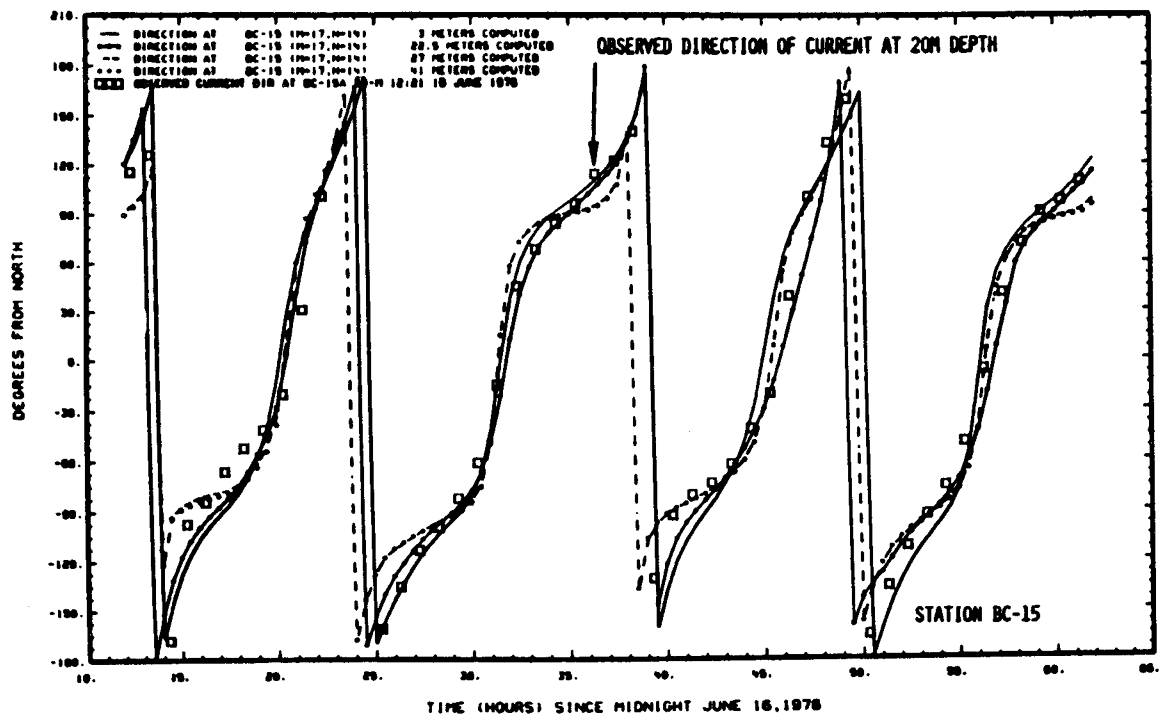

Fig. 2.6—When driven with the predicted tide, the computed subsurface currents in the Bering Sea agree fairly well with the observed subsurface currents, both in magnitude and in direction (Liu and Leendertse, 1979).

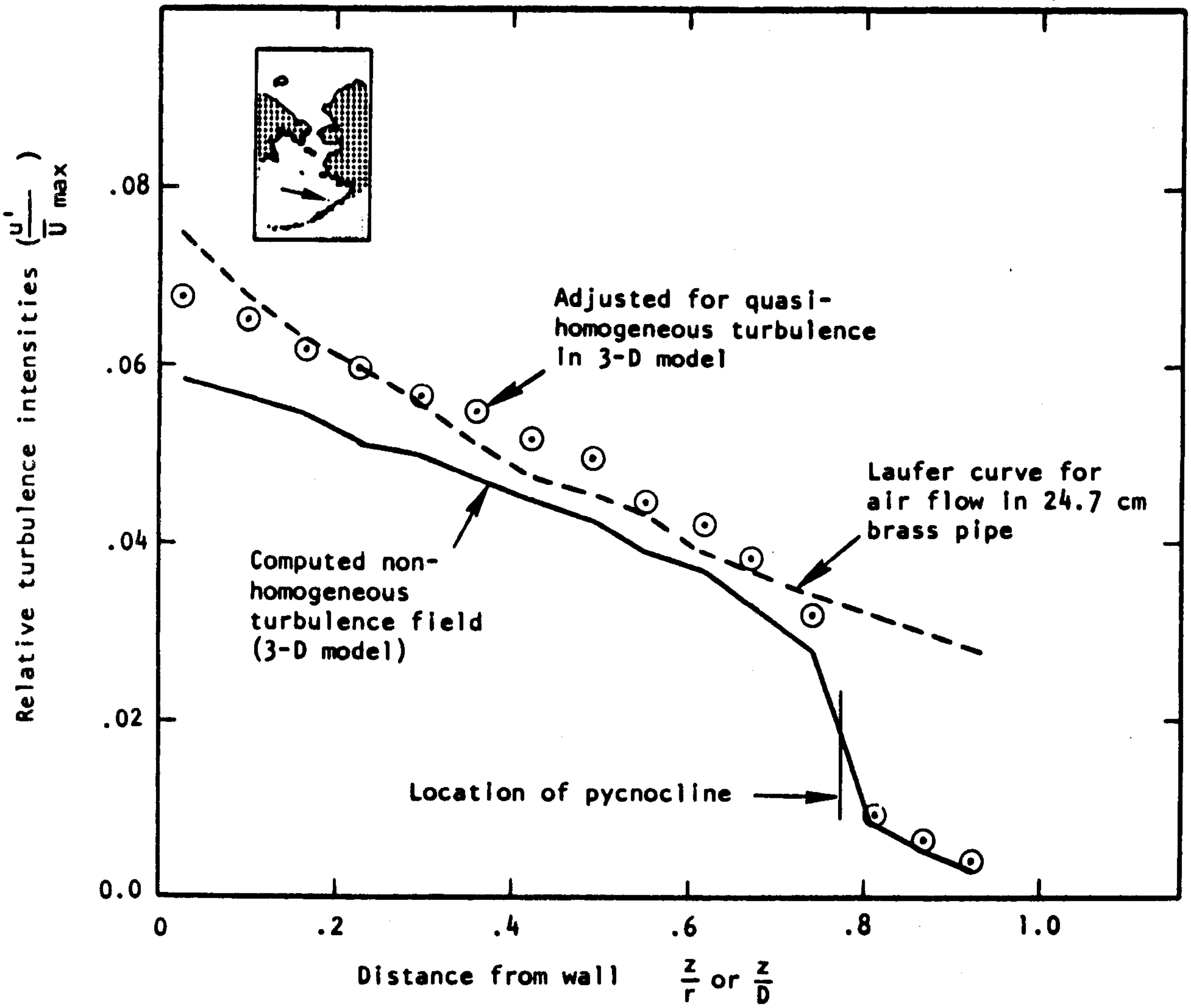

Fig. 2.7—Comparison of relative turbulence intensities between the three-dimensional model for stratified flow field and the standard verification curve of air flow measured in a pipe (Laufer, 1954).

3. MODELING COASTAL HYDRODYNAMIC PROCESSES

MODELING TIDES, RESIDUALS, AND BAROCLINIC CIRCULATION IN THE ALASKAN OUTER CONTINENTAL SHELF

Tides are probably the most important and consistent driving force in the Alaskan shelf waters. For example, about 90 percent of current energies over the Bering shelf are of tidal origin. Tides over these shelves are driven primarily by astronomical tides of the Pacific Ocean and of the Arctic Ocean. Amplitudes of the Pacific tides are substantially larger than the Arctic tides and they penetrate through the Aleutian Islands, entering the Bering Sea. The two tidal systems encounter each other near the Bering Strait where exchange of water masses takes place. Tides are believed to be one of three major factors that cause the exchange of water. Other than atmospheric forcing and density-induced circulation, the difference in tidal characteristics between the Bering Sea and the Chukchi Sea is that they also induce residual currents through the Bering Strait.

When in deep water, tides do not generate significant tidal currents. Consequently, bottom dissipation and the shore's effects are minimal. Tides, as a long wave, tend to maintain their characteristics without much deformation until they reach the continental shelf. When tides propagate through the shallow shelf area, the nonlinear advection terms in the equation of motion generate higher harmonics of the fundamental frequency. When bottom dissipation is not considered, the second harmonic increases in amplitude with the distance of propagation into the coastal zone. On the other hand, bottom friction generates odd harmonics. A sloping bottom and configuration of the shoreline induce the dispersion of tidal energy across frequencies by the mechanism of nonlinear advective transport. These higher-order mechanisms not only modify tidal levels along the coastline, but more important, they create residual transport responsible for carrying floating and soluble substances for longer time periods, which was of particular importance to the impact studies.

Thus models were built to simulate the tides in the Alaskan coastal waters. The models used in our studies are shown in Fig. 3.1. As this figure indicates, we developed submodels in some of the model areas. The areas covered by these submodels were of particular interest in the impact studies and required more geographical detail or were intended to provide estimates of tides and currents to plan field surveys in subsequent years.

The model for the Gulf of Alaska extends westerly to 165°W with its southern boundaries at 52°. Water-level boundary conditions from Muench and Schumacher (1980) and Schwiderski (1978) were used at all seaward extremities of the modeled area. The grid size in latitudinal direction was 0.25°, and in longitudinal direction 0.5°. The model has ten layers in the vertical direction.

The submodel of the western Gulf extended to the edge of the continental shelf and had more resolution. The grid size on latitudinal direction was 0.125°, and in longitudinal direction 0.25°. The water-level boundary conditions were obtained from the Gulf of Alaska model.

For the investigation of the hydrodynamic processes in the eastern Bering Sea, the primary model was of the continental shelf of the Bering Sea together with the Chukchi Sea (Fig. 3.1). The Chukchi Sea was included in the model as the tides of the Pacific Ocean interact with the tides of the Arctic Ocean near the Bering Strait, and it was expected that

Fig. 3.1—Coverage of the Alaskan coastal area by various models and submodels.

this interaction would generate nonlinear residual currents. The model extends from 54°N to 74°N, and from 178°E to 156°W. The grid size in a northerly direction was 0.5° and in the longitudinal direction 1° was chosen. The model has a boundary running very close to the continental shelf break (Fig. 3.1). The tidal boundary conditions were based upon published data and water-level boundaries were used at all open boundaries. This three-dimensional model has ten layers in the vertical in the deeper sections. The seaward boundaries were obtained from tide gauge measurements obtained by the Pacific Marine Environmental Laboratory (Pearson et al., 1981a, 1981b) in the vicinity of the model boundary.

The model of the Beaufort Sea covers the waters north of Alaska to 73°N. The western boundary is at 162°W and overlaps part of the Chukchi Sea model. The eastern boundary extends to the Mackenzie River delta at 133°W. The grid size in latitudinal direction is 0.16666° and in longitudinal direction 0.5°.

Even though our final interest is the residual circulation, the basic tidal mechanisms over these shelf areas are the first to be determined. We will proceed with the analyses from the southern coast, thence to the west coast, and finally to the northern Beaufort Sea.

MODELING TIDES IN THE GULF OF ALASKA SHELF

The model of the Gulf of Alaska is the largest model covering the Alaskan coastal waters developed by the authors. Because of the complex coastal features, a series of nested submodels is needed to resolve the circulation dynamics of the near-shore lagoons and the ecologically sensitive passage (Figs. 3.2 and 3.3). The embayment in the northeast corner of Fig. 3.2 is Cook Inlet, where the largest astronomical tides in the Pacific are found—sometimes reaching 13 meters. Also present are strong currents and residual circulation induced by nonlinear interaction between the advective mechanism and the bathymetry of the coast. The three-dimensional perspective diagram in the upper part of Fig. 3.4 illustrates the along-shore view of higher modes in the water-level variation with the highest point at the head of Cook Inlet, whereas the lower diagram shows cross-shore variations. Figure 3.5 shows the computed co-tidal chart for the semidiurnal component and the comparison between the computed amplitudes and phases at four locations where observed data are available (Schumacher and Muench, 1980). Figures 3.6 through 3.9 present the computed horizontal/vertical velocity components and the turbulent energy densities at levels 1, 3, 5, 7, 8, and 9 at a location near the opening of Cook Inlet (Portlock Bank). At that location the computed hodograph in Fig. 3.10 nearly matches the observed current ellipse. The vertical distribution of the magnitude of the computed current (Fig. 3.11) indicates that the vertical variability departs substantially from the logarithmic distribution commonly present in a shallow tidal embayment.

The computed tidal ellipses for the entire Gulf of Alaska (from Vancouver Island to the Aleutian Islands) are presented in Fig. 3.12. To show the strong tidal currents within Cook Inlet and over shelf areas, the plotting scale is set at 200 cm/sec per grid spacing. The maximum tidal currents can reach 140 cm/sec in either direction. Computed tidal residual current distribution within the Gulf of Alaska is presented in Fig. 3.13. In Fig. 3.13 the maximum residual current in Cook Inlet is approximately 7.5 cm/sec, which is 5.5 percent of the local maximum tidal current. Over the shelf and in Shalikof Strait the direction of the residual current is primarily to the southwest. Results from the model of the Gulf of Alaska have been reported in Liu and Leendertse (1987) in which aspects of the partitioning of tidally induced energetics are discussed.

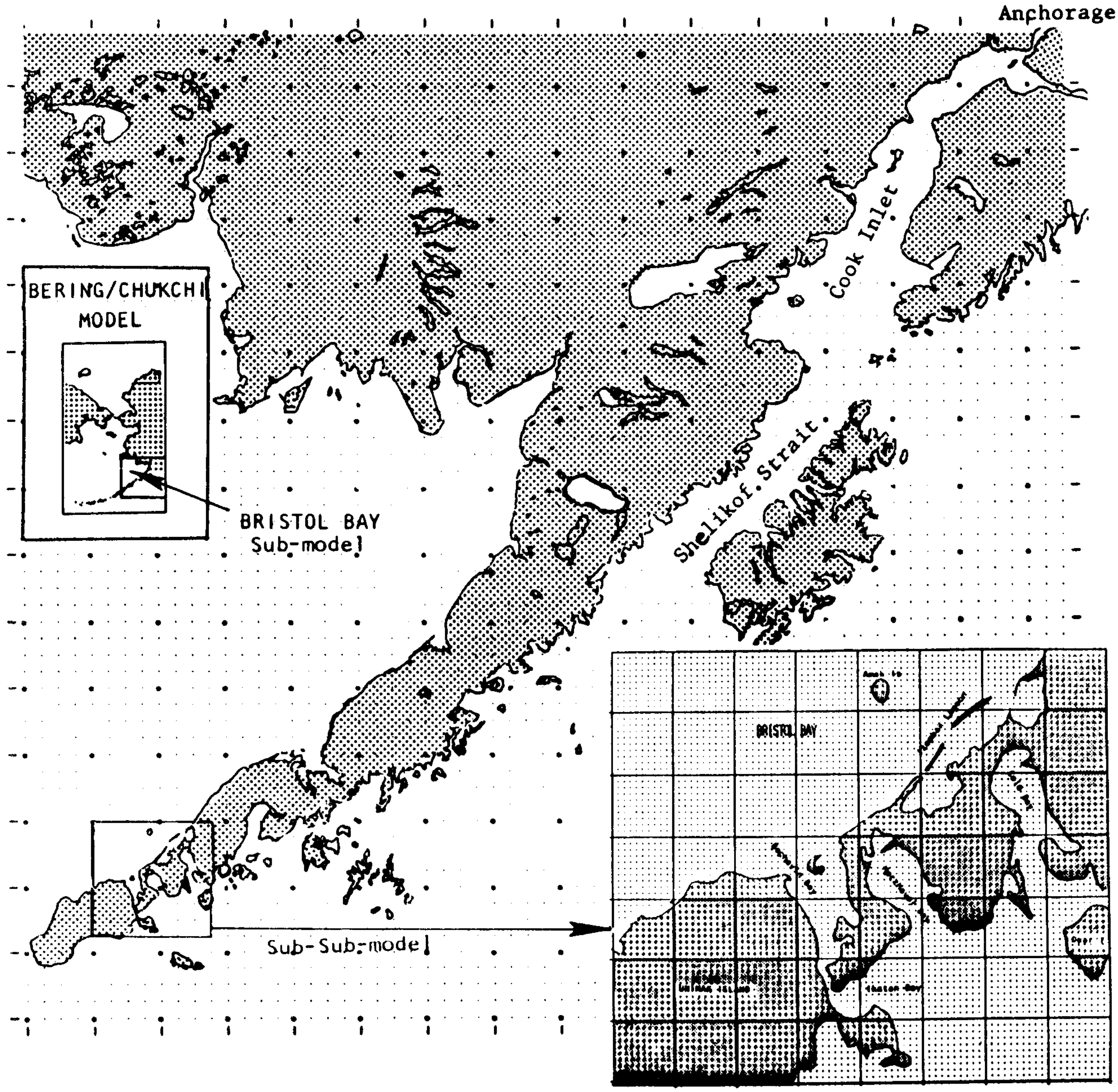

Fig. 3.2—A submodel of the Bering Sea covering the area of Bristol Bay and a portion of the Gulf of Alaska. Insert map at the lower right corner is another submodel of this one, covering the area of Izembak Lagoon.

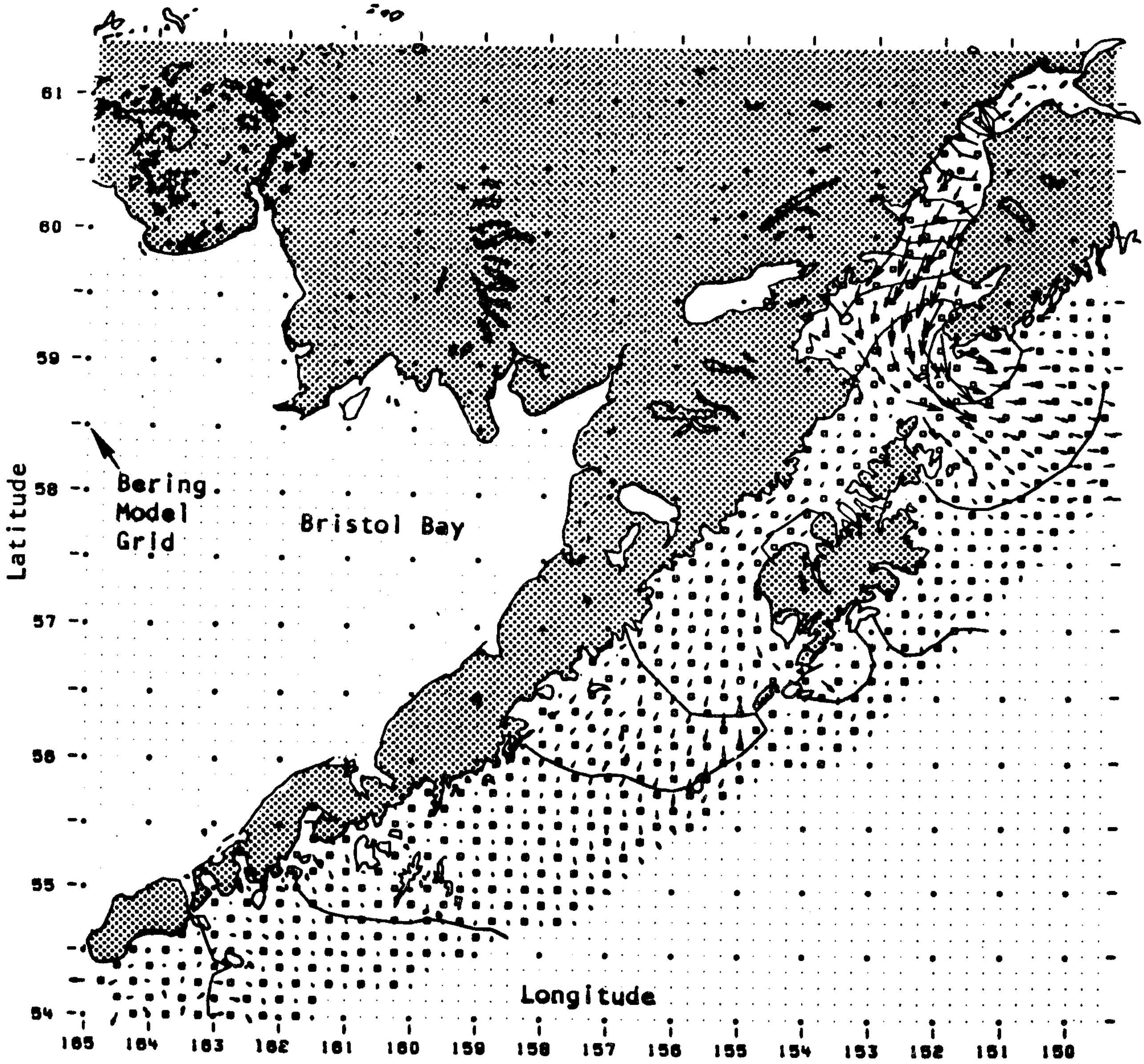

Fig. 3.3—The rise and fall of water levels and the computed tidal currents in the model of the western Gulf of Alaska. The figure illustrates the falling of water level (□) over the shelf and within part of the Cook Inlet. In the meantime, the water level near Anchorage is still rising (+).

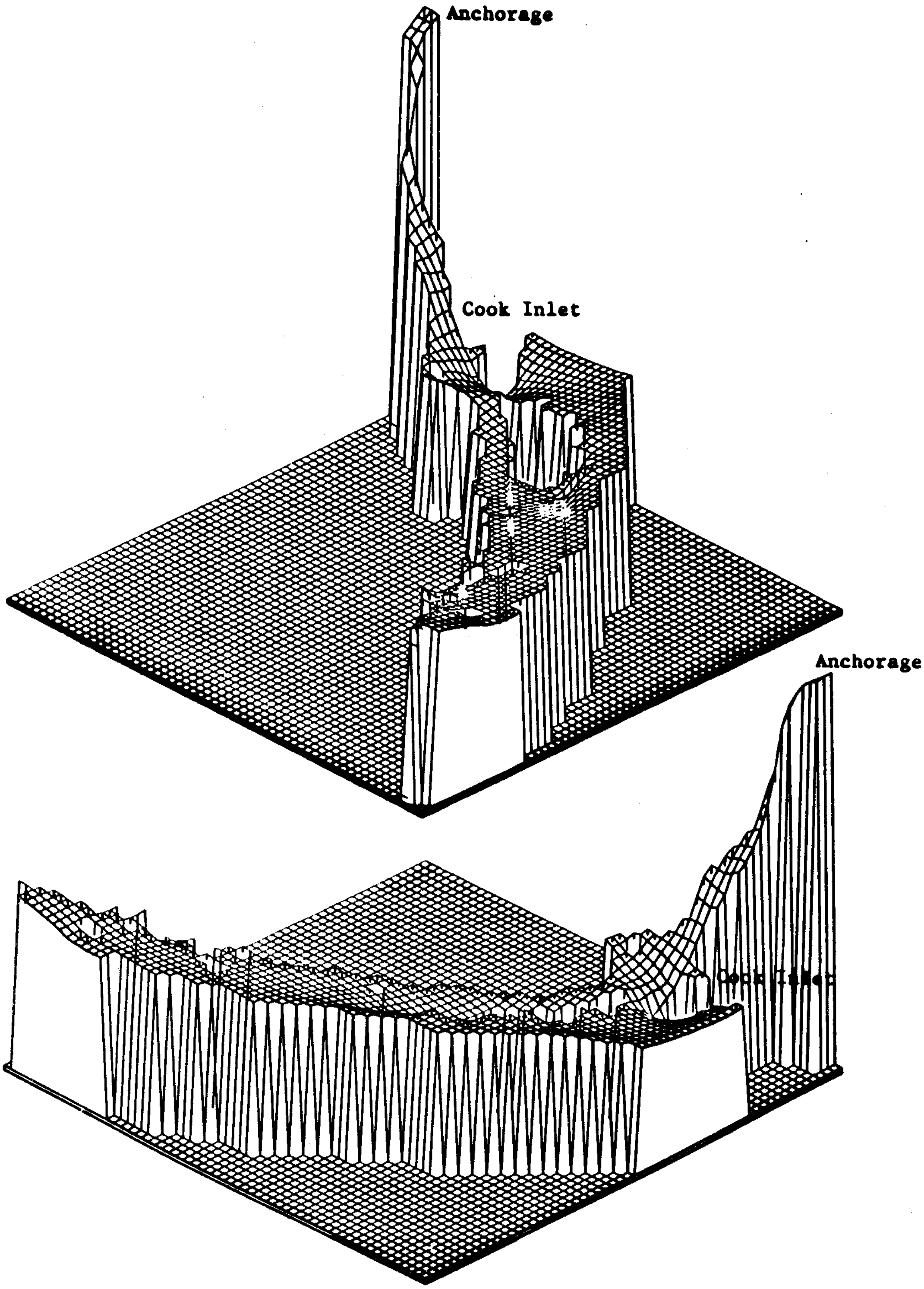

Fig. 3.4—Three-dimensional perspective diagrams illustrate the along-shore view of higher modes in the water-level variation with the highest point at the head of Cook Inlet near Anchorage (upper diagram). The lower diagram shows the cross-shore variation.

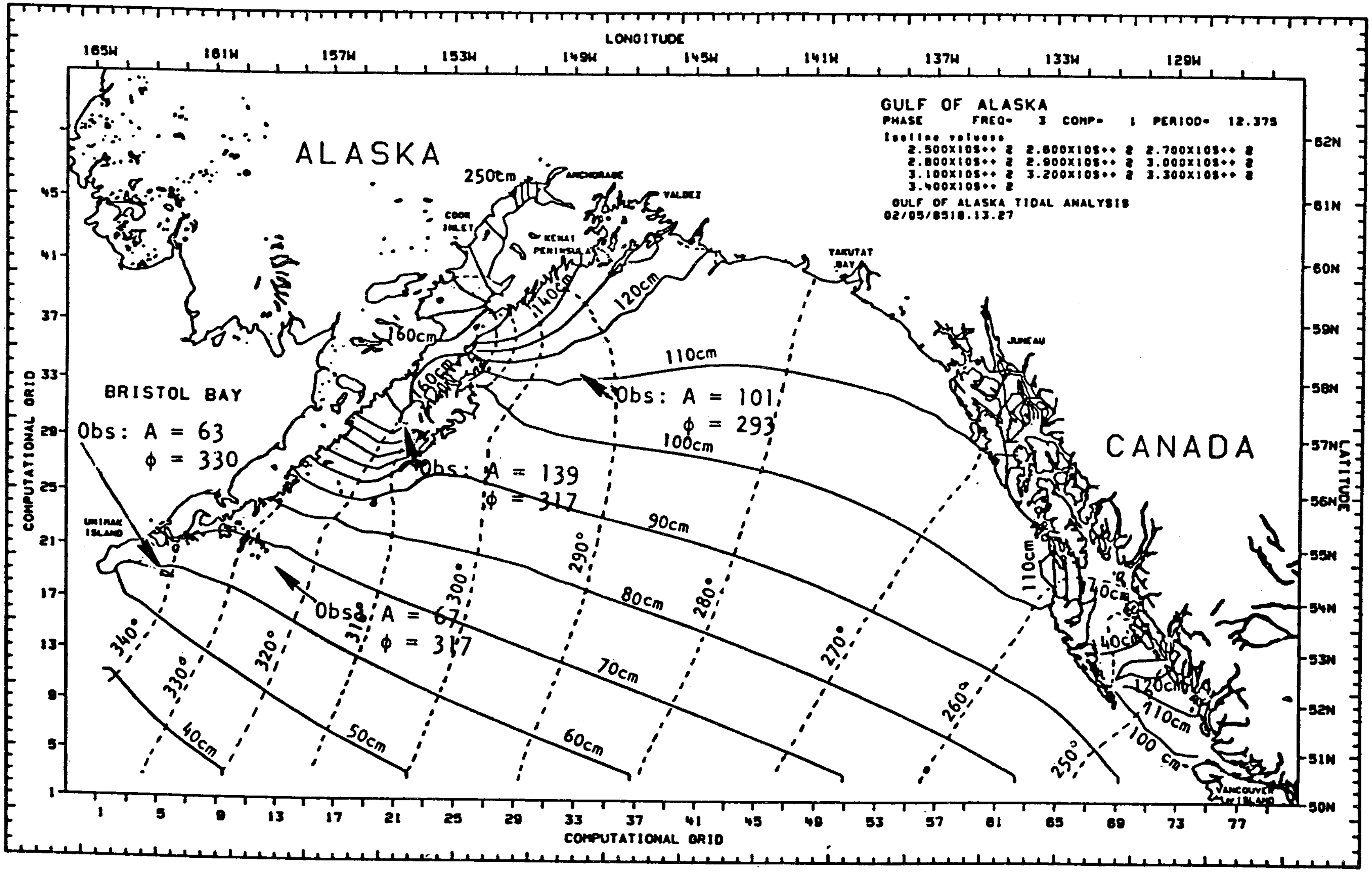

Fig. 3.5—Computed co-tidal chart for the semidiurnal component (primarily M2). Each 10° in phase represents approximately 20 minutes lag relative to the Greenwich mean phase. The maximum tidal amplitudes, reaching 250 cm, are found in the Cook Inlet.

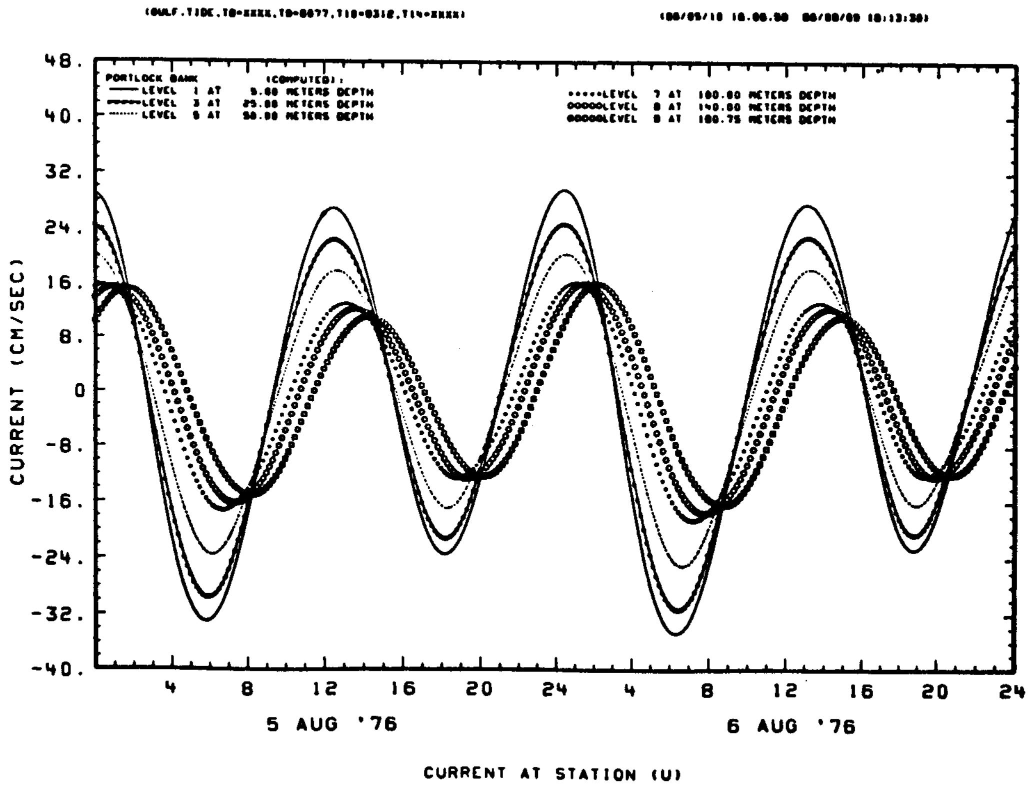

Fig. 3.6—The computed east-west velocity components at six representative layers near the mouth of Cook Inlet (Portlock Bank).

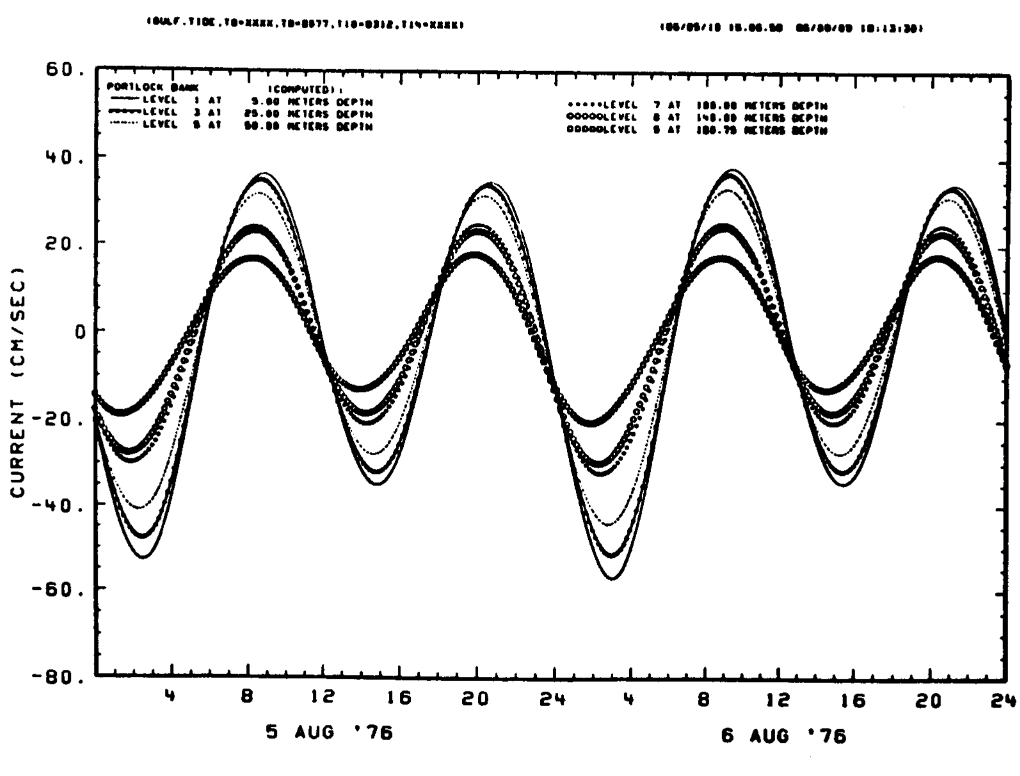

Fig. 3.7—The computed north-south velocity components at six representative layers near the mouth of Cook Inlet (Portlock Bank).

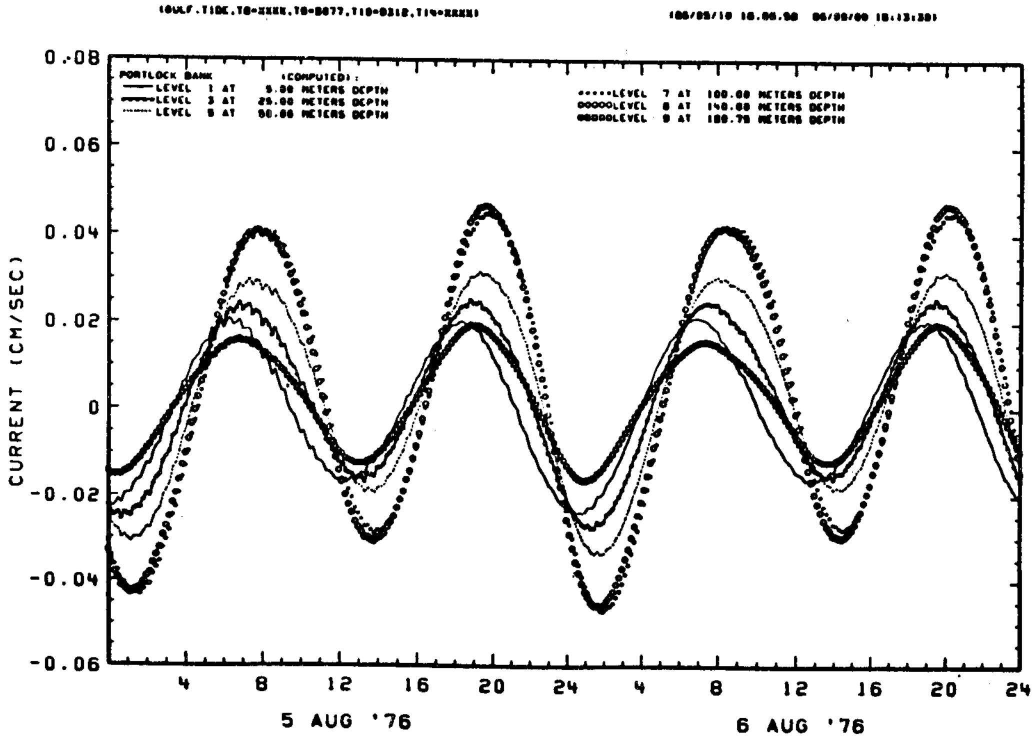

Fig. 3.8–The computed vertical velocity components at six representative layers near the mouth of Cook Inlet (Portlock Bank).

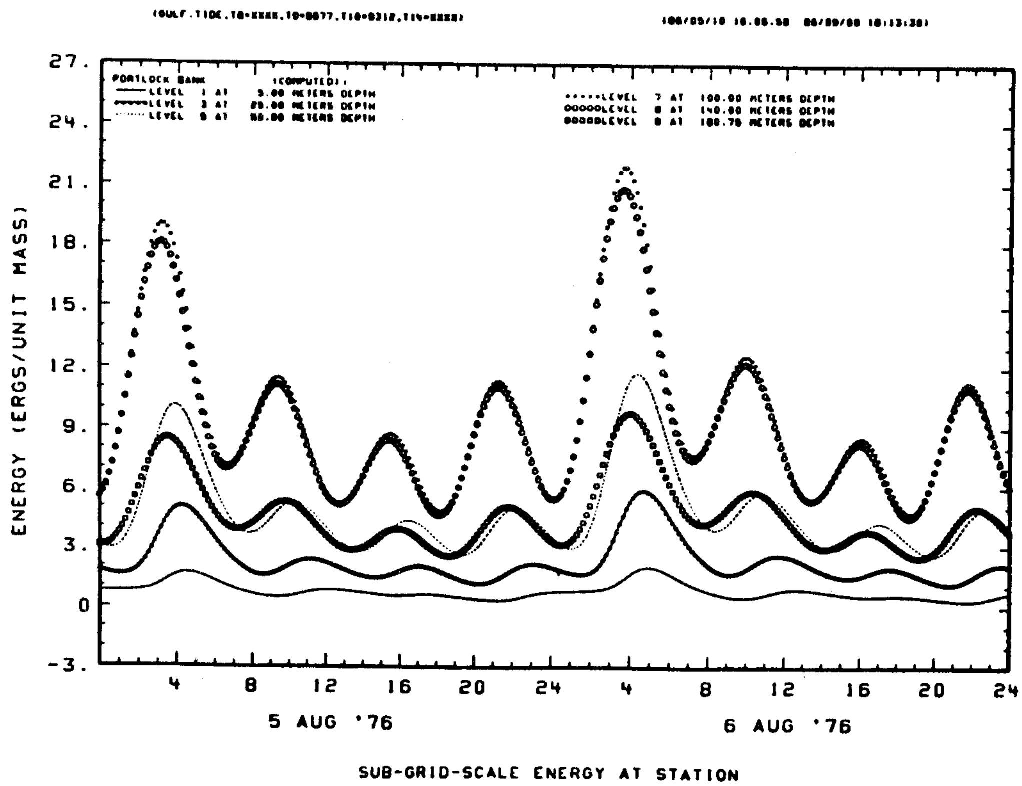

Fig. 3.9–The computed turbulent energy densities at six representative layers near the mouth of Cook Inlet (Portlock Bank).

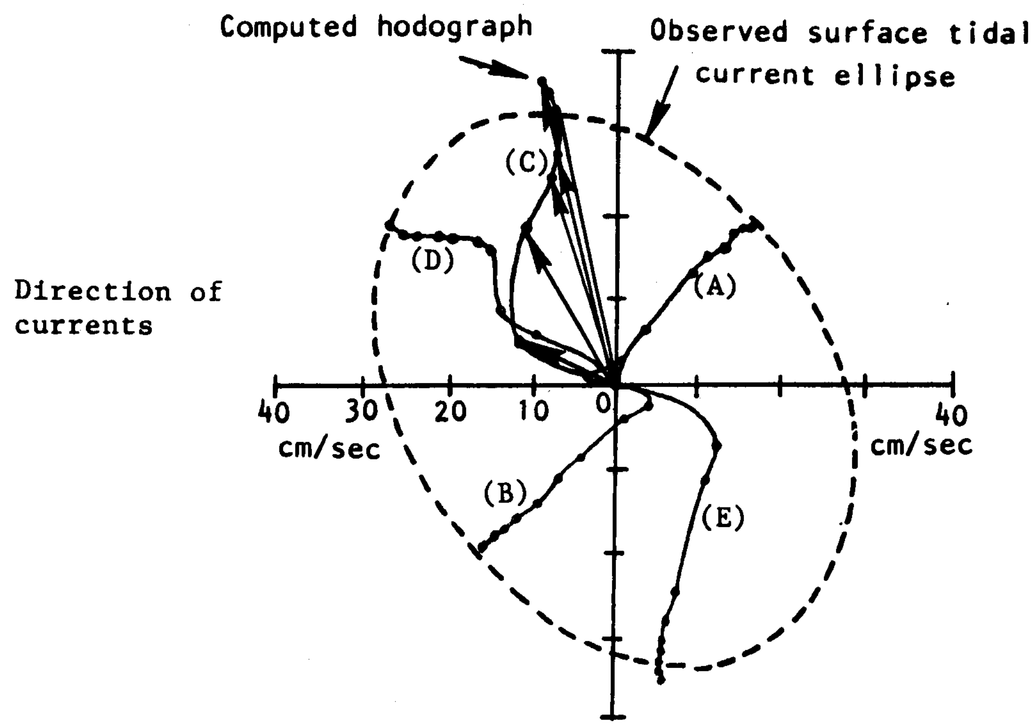

Fig. 3.10—Comparison between the computed hodograph and the measured surface tidal current ellipse.

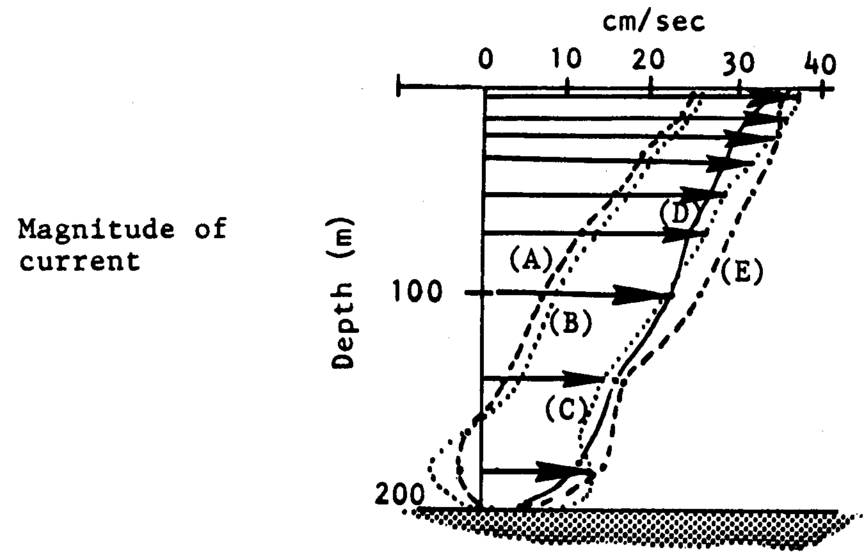

Fig. 3.11—Vertical distribution of magnitude of the computed currents illustrated in the hodograph (near Cook Inlet).

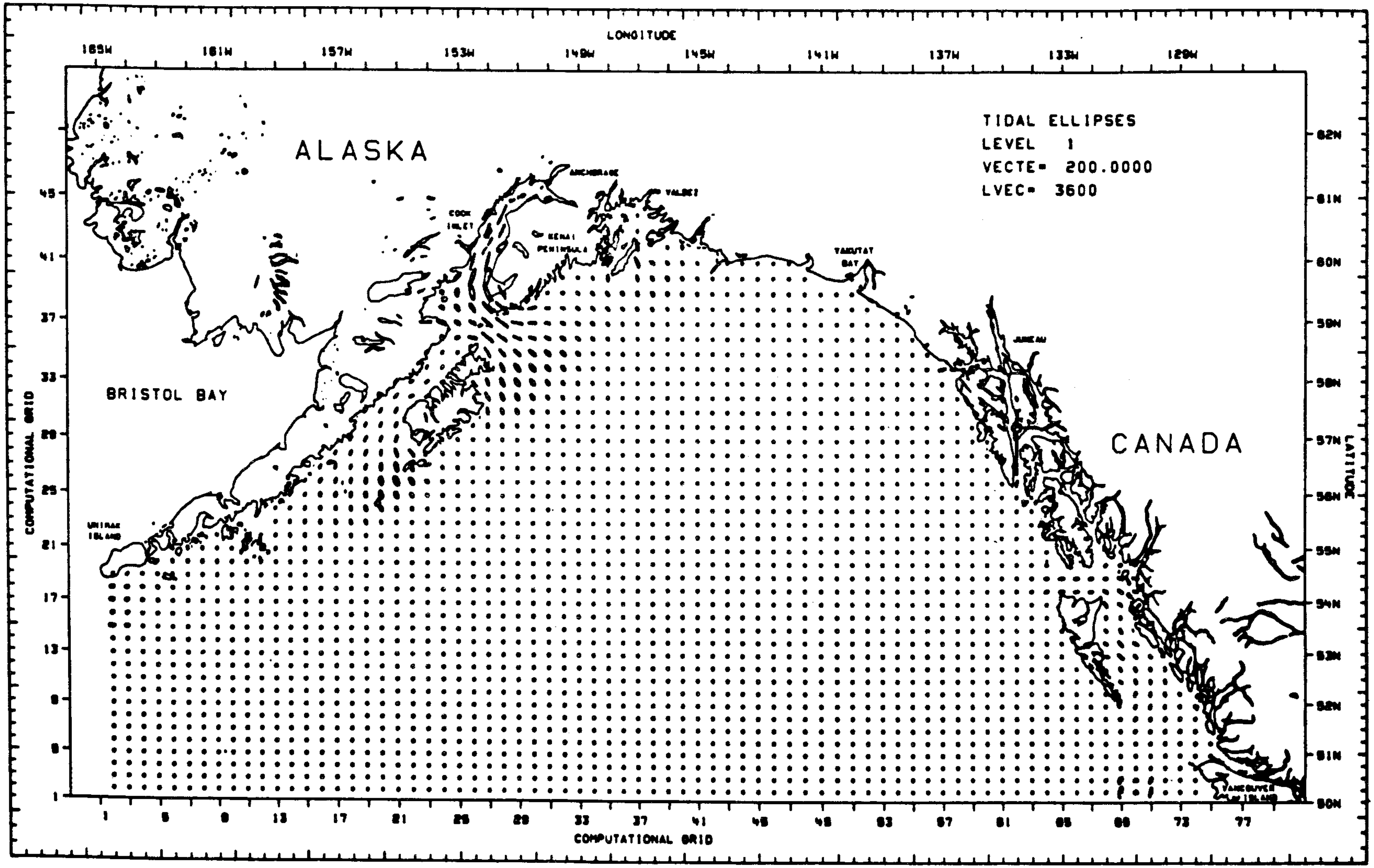

Fig. 3.12—Computed tidal ellipses (at 5 m level) in the Gulf of Alaska using a plotting scale of 200 cm/sec per grid spacing. Maximum tidal excursions are found in the middle of Cook Inlet where the tidal currents can reach 140 cm/sec in either direction. Currents over the shelf break near Kodiak are of elliptical rotary-type and can reach a maximum speed of 70 cm/sec.

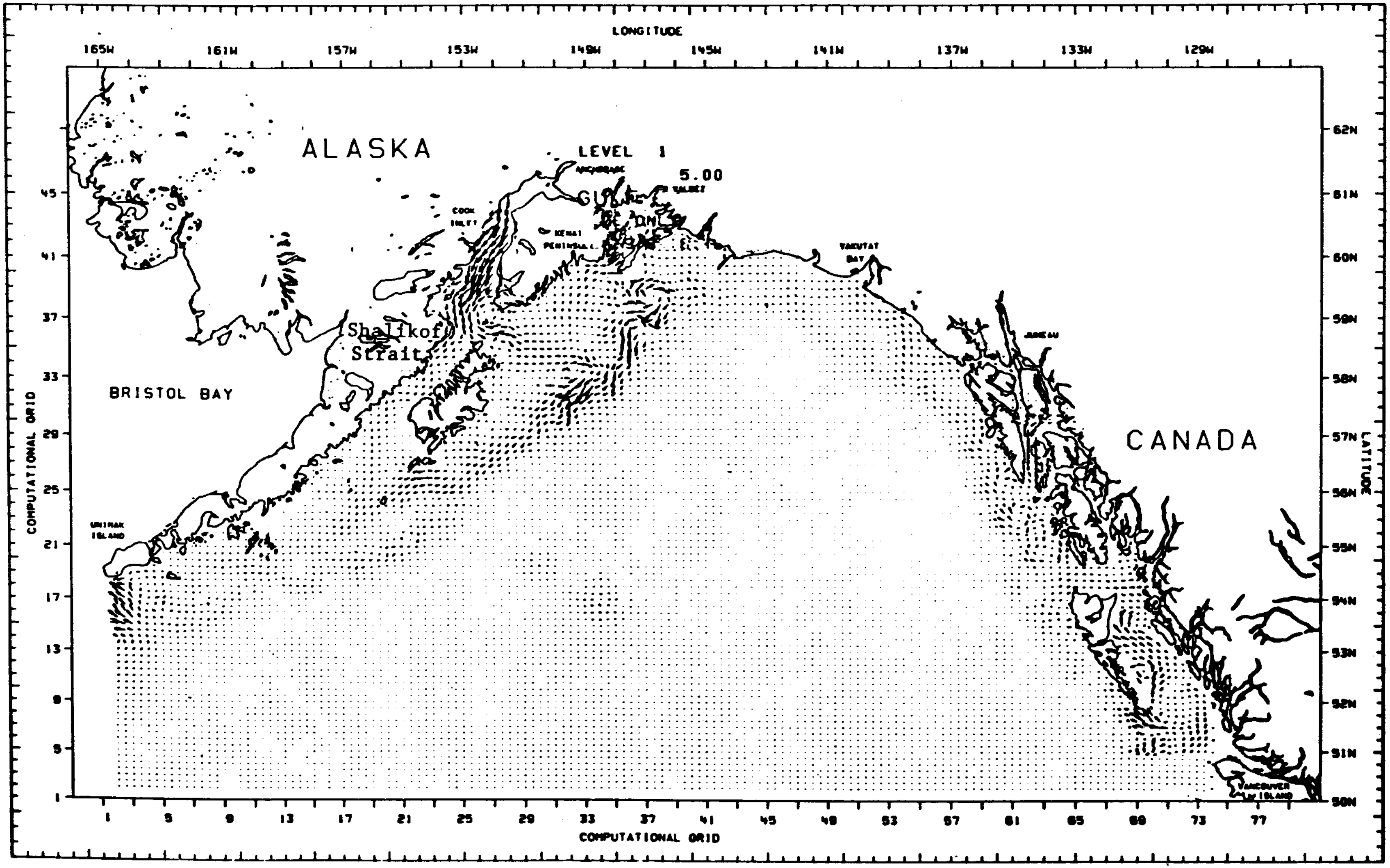

Fig. 3.13—Computed tidal residual circulation (at 5 m level) in the Gulf of Alaska using a plotting scale of 5 cm/sec per computational grid. Maximum residual current in the middle Cook Inlet can reach a speed of 7.5 cm/sec, which is approximately 5.5 percent of the local maximum tidal current. Over the shelf break and in the Shalikof Strait, residual currents flow primarily toward the southwest.

MODELING TIDES IN THE EASTERN BERING SEA

The propagation of tides in the study area is dominated by the bathymetry and to a certain extent is influenced by the vertical density structure. The bathymetric representation of the three-dimensional model is shown in Fig. 3.14. For the study of tide propagation during the summer when the deeper shelf waters are stratified, a simulation period in early August 1976 was selected. Figure 3.15 shows an instantaneous distribution of computed tidal currents and water levels plotted on a chart based upon the Mercator projection. The computed distributions reflect the conditions on August 2, 1976, at 6:00 A.M., but the simulation results do not reflect any influence of wind, as no inputs for the wind field were used. The figure shows conditions at ebb over the shelf break with falling water levels. The simulation results indicate rising water levels in the eastern part of Bristol Bay, in Norton Sound, and over most of the Chukchi Sea.

Figure 3.16 shows the co-tidal chart for the semidiurnal tidal component M2 obtained from a simulation of several days. Several amphidromic points will be noted. This chart is in agreement with a co-tidal chart of the M2 tide component compiled from field data by NOAA (Pearson et al., 1981a, 1981b) shown as Fig. 3.17. As to be expected the amplitudes in the model, which are the apparent amplitudes during the simulation period due to all semidiurnal constituents, are generally larger than shown in Fig. 3.17, which is only due to the M2 component.

The analysis of the semidiurnal component made from model simulations indicated two amphidromic points from which we found no previous reference in the literature, namely, one located at the opening of the Gulf of Anadyr, and the other between St. Lawrence Island and the Bering Strait.

The computed co-tidal chart for the diurnal tide component is shown in Fig. 3.18. On the shelf in the Bering Sea two counterclockwise amphidroms are found near the entrance of Bristol Bay and Norton Sound. This is in agreement with the co-tidal chart compiled by NOAA from field data (Fig. 3.19, Pearson et al., 1981a).

Co-tidal charts provide good insight into the up and down movement of the water surface, but they do not reveal comprehensive information on tidal currents. This information could be obtained by making charts of tidal ellipses such as shown in Fig. 3.20. In this graph, the end points of the computed current vectors in the second layer of the model are shown over a period of 12.5 hours of a simulation. It will be noted that in some parts of the system tidal ellipses are elongated, thus in those areas the tidal currents will be quite small during certain phases of a tidal cycle.

Results from a modeling also confirm two important tidal characteristics of the Bering Sea suggested by Harris (1904) based only on a small number of observations nearly 80 years ago. He suggested that after the tide enters from the Pacific the wave is retarded by the shallow shelf area while moving in a northeasterly direction. He also indicated that the shallow shelf section from Cape Navarin to the Pribilof Islands simply co-oscillates with the tide in the deep Bering Basin in the southwest. He continued to postulate that there would be a counterclockwise amphidrom at the opening of Norton Sound. His analysis, based on very limited field data, is remarkably in agreement with our findings and the field data collected by various surveys.

When comparing computed co-tidal charts with those derived from observed data it should be kept in mind that propagation of the tide is influenced by the vertical density structure. When a sharp pycnocline exists, the momentum transfer between the water

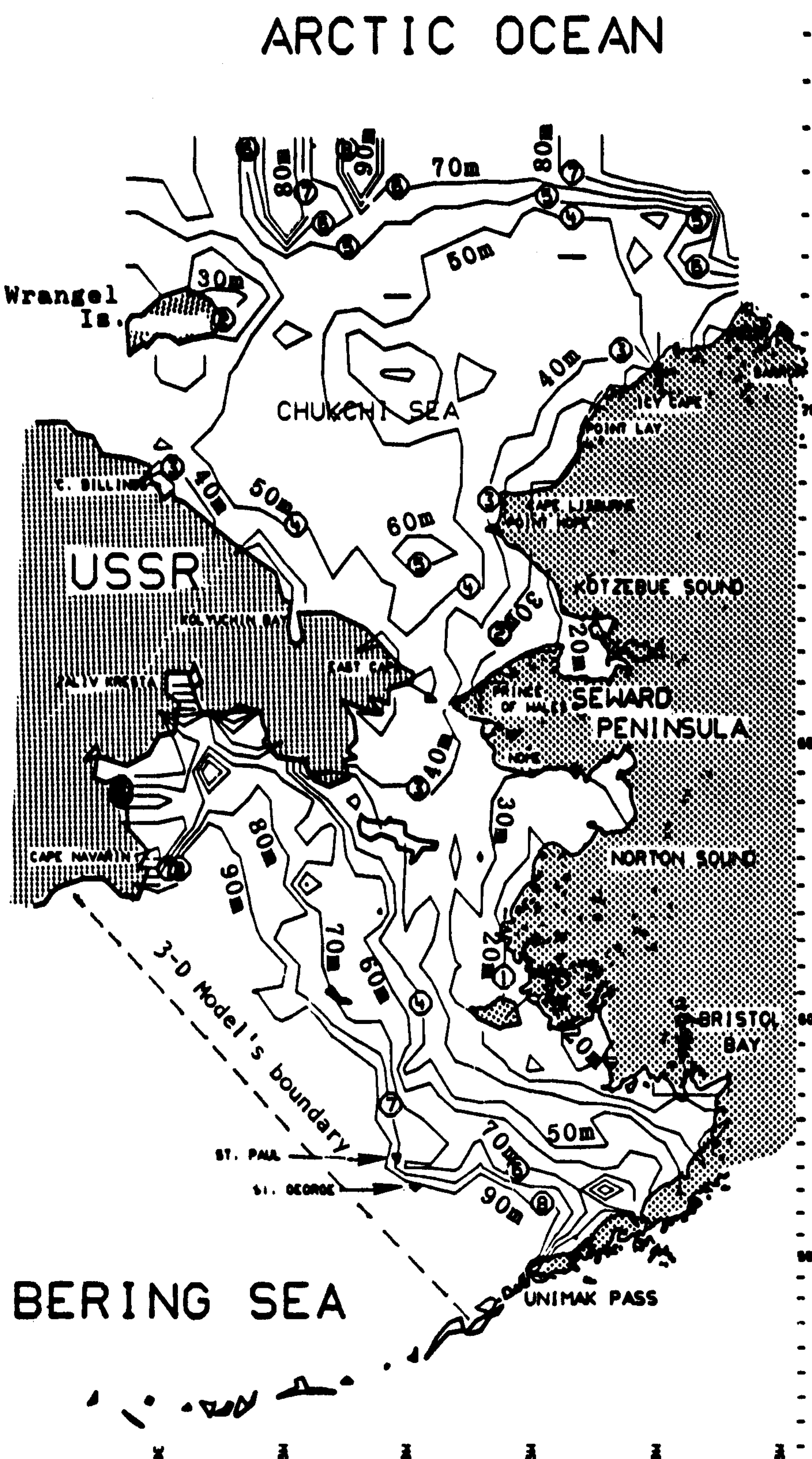

Fig. 3.14—Bathymetric schematization of the three-dimensional model of the Bering and Chukchi Seas.

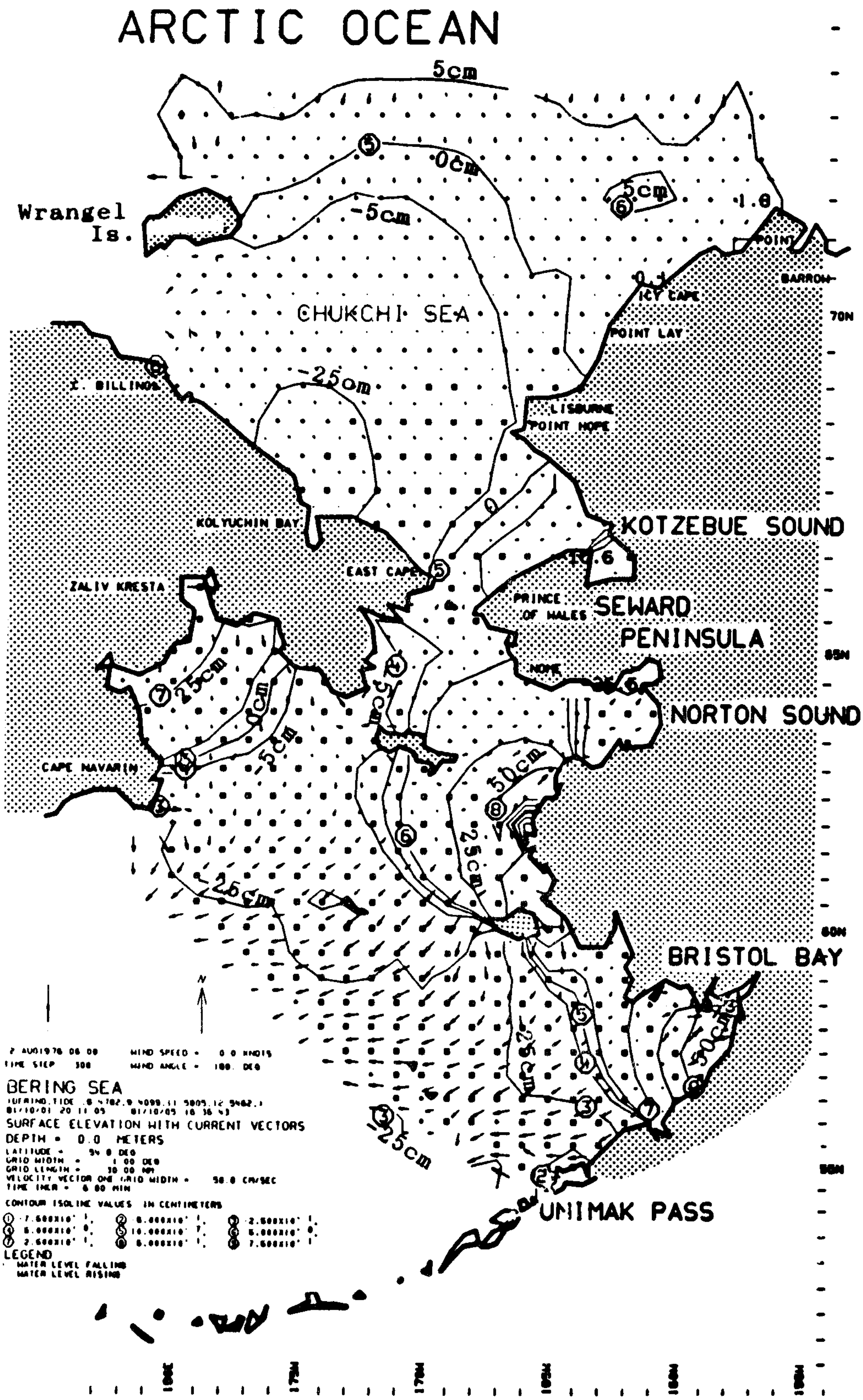

Fig. 3.15—Computed instantaneous tidal currents and water-level distributions in the Bering/Chukchi Sea system. + denotes that water level rises; □ indicates that local water level falls.

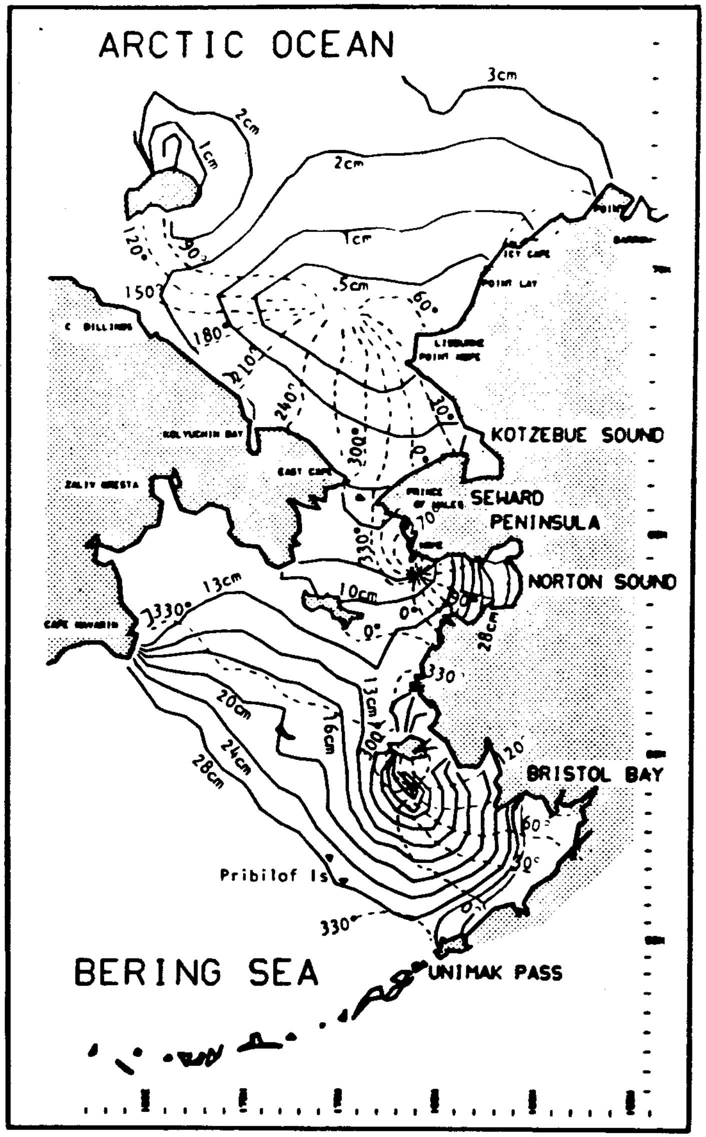

Fig. 3.16—Computed co-tidal chart for the semidiurnal tidal component using the three-dimensional model of the Bering/Chukchi Sea.

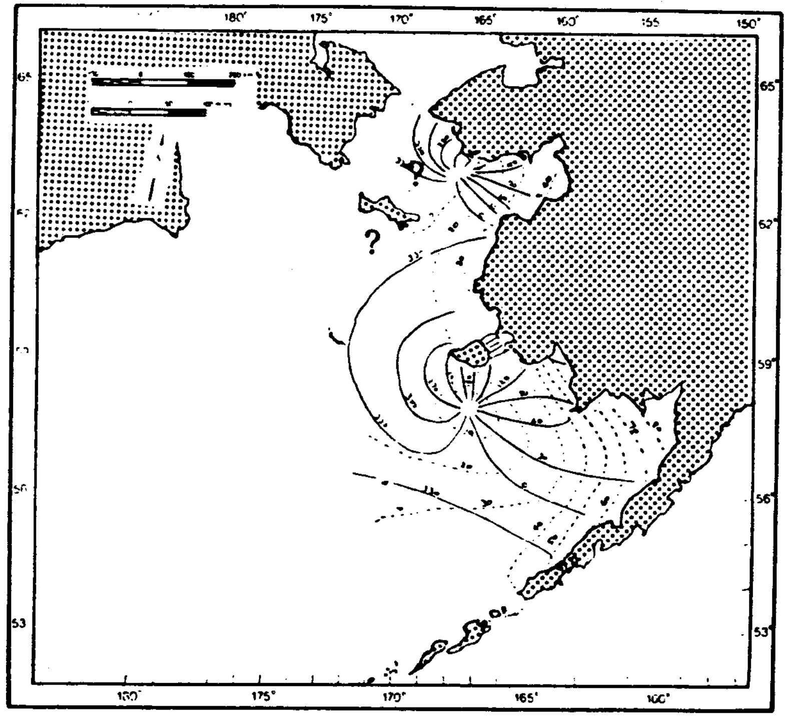

Fig. 3.17—Co-tidal chart for the semidiurnal tidal component M2 compiled by NOAA according to existing data (Pearson et al., 1981a).

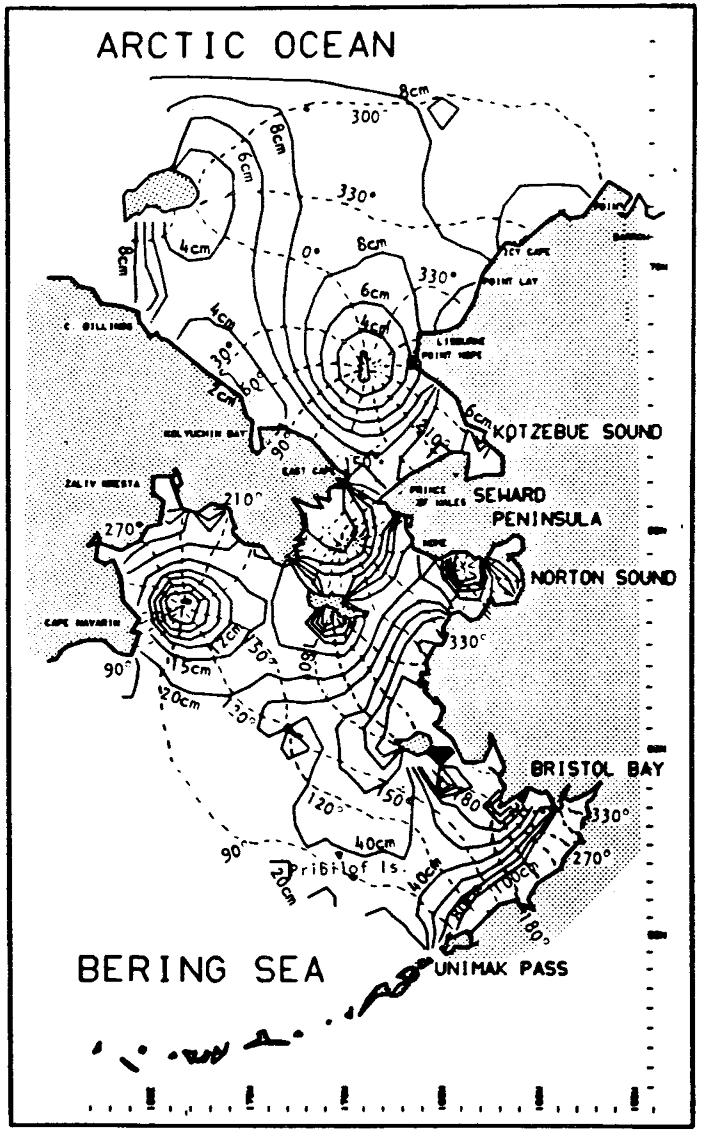

Fig. 3.18—Computed co-tidal chart for the diurnal tidal component using the three-dimensional model of the Bering/Chukchi Seas.

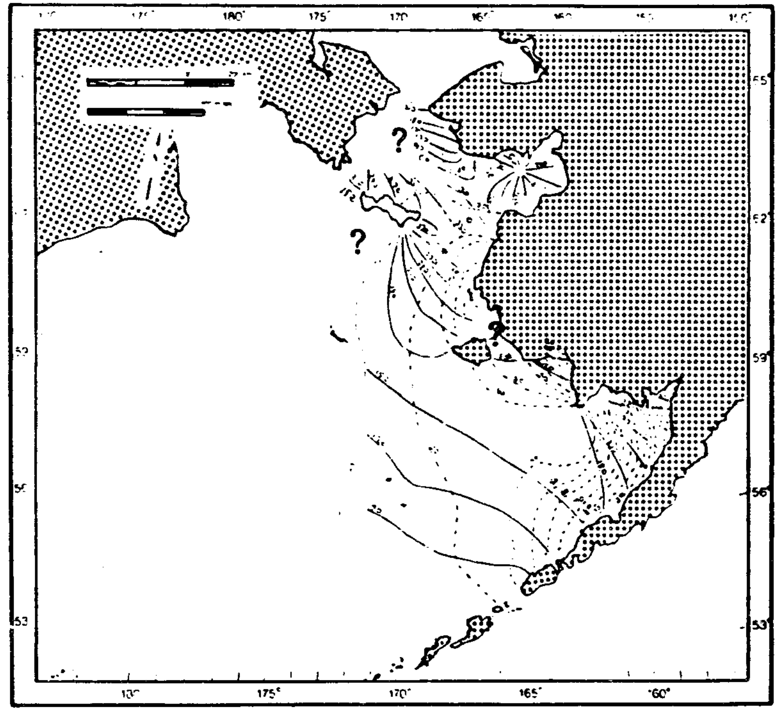

Fig. 3.19—Co-tidal chart for the diurnal tidal component (K1) compiled by NOAA according to existing data (Pearson et al., 1981a).

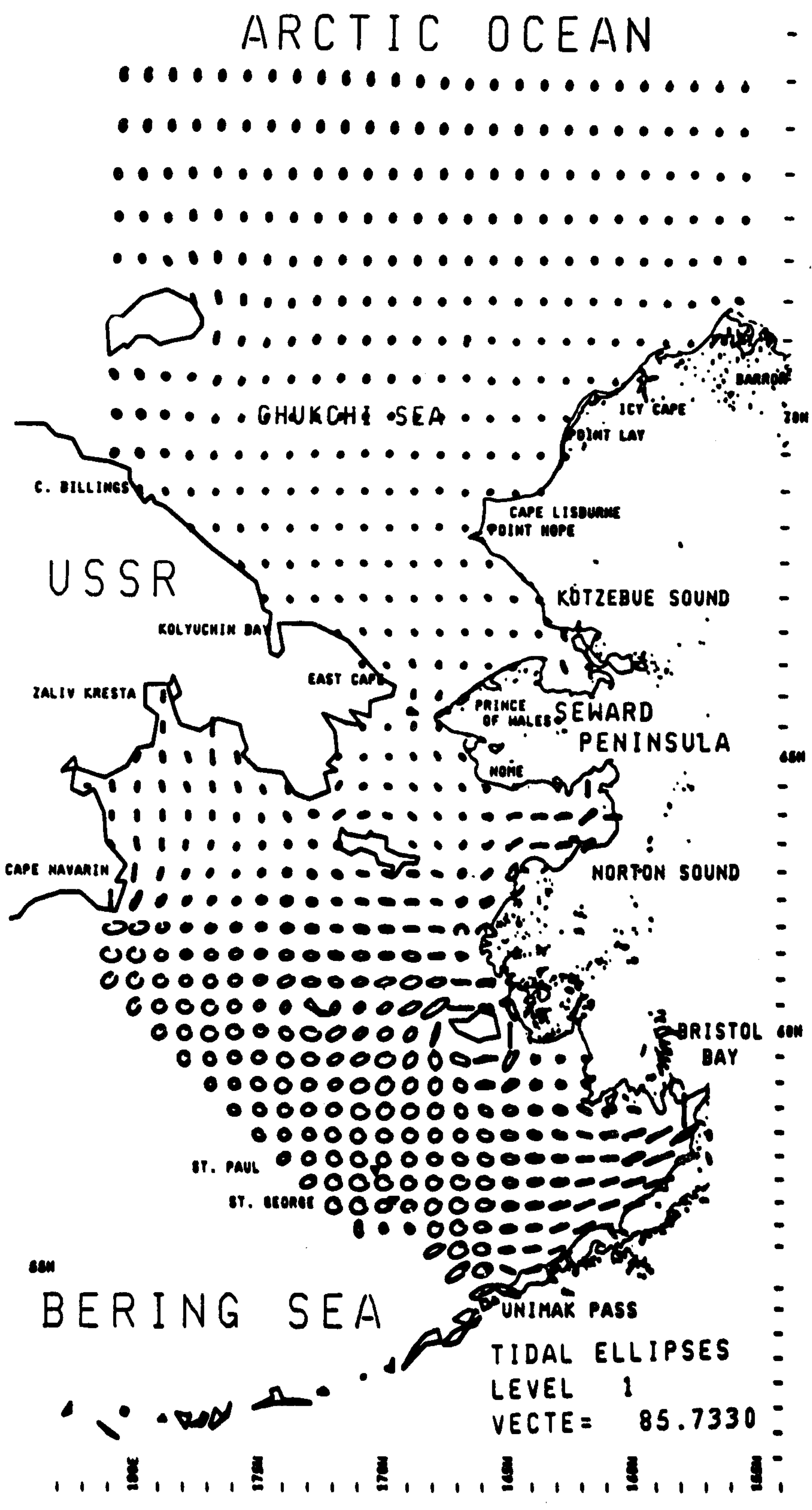

Fig. 3.20—Computed 12.5 hr tidal ellipses in the first layer (at 2.5 m level) using a plotting scale of 86 cm/sec per horizontal grid spacing.

masses above and underneath the pycnocline is reduced compared to the well-mixed situation. It is known that some of the amphidromic points in the Alaskan waters shift in position when the sea makes the transition from a well-mixed sea to a stratified sea. For this reason considerable effort was made to obtain temperature and salinity data that would be consistent with the periods that were simulated. Aspects of salinity and temperature distributions will be discussed at the end of this chapter.

MODELING TIDES IN THE CHUKCHI SEA

Unlike tides in the Bering Sea, tides in the Chukchi Sea are a subsystem of the Arctic tides that enter the shallow Chukchi shelf from the east. The propagation of tides in the Chukchi Sea is dominated by the bathymetry and coastal configuration, and to a certain extent is influenced by vertical density structure. The latter was known to cause shifting of the location of amphidromic points during summer when a strong pycnocline existed. Under an average summer condition, model results indicate that an amphidromic system exists in the southern Chukchi Sea for both diurnal and semidiurnal tides. The findings were reported in Liu and Leendertse (1982).

Tides in the Chukchi Sea are substantially weaker than in the Bering Sea. The presence of ice and the weather systems sometimes dominates local energetics. However, when the influence of the weather is weak, tides dominate the circulation pattern in the vicinity of the Bering Strait and the southern Chukchi Sea.

Connecting two vastly different tidal systems, dynamics of circulation near the Bering Strait have been a focal point of interest for many years. We conducted numerical experiments with the three-dimensional model of the Bering Sea and the Chukchi Sea by forcing it only with tide and baroclinic fields associated with the summer salinity/temperature distribution described in more detail at the end of this chapter.

The computational results from the experiment were analyzed and the computed currents are shown in Fig. 3.21. The east-west component of the velocities are predominantly eastward and the flow reverses only during a short period in the tidal cycle.

The north-south components of the velocities are nearly always directed toward the north. The maximum north-south velocity component is in the surface layer and is 22 cm/sec. The magnitude of the current at that time is approximately 23 cm/sec, and the direction is approximately 17° from the north. Higher modes (overtides) can be noticed in the computed currents. They appear mainly in the lower layers where frictional effects are strong and the velocities lag behind those in the upper layers. These characteristics are more obvious in the computed vertical velocity components (top graph, Fig. 3.22). Friction retards bottom currents and thus induces vertical mass transport.

Turbulence variation in the bottom layer leads to variation in the upper layers, as the momentum transfer is inefficient because of the vertical pycno-structure, as shown in the bottom graph of Fig. 3.22. Note that the greatest turbulence intensity exists in the bottom layer and it is represented by small squares.

From similar graphs for a coastal station near Point Lay (Figs. 3.23 and 3.24), it can be found that during flood tide, a bottom long shore tidal current of 7.8 cm/sec is flowing in a direction that is 17° from the north. At the same time, the surface current has a speed of 6.1 cm/sec and is flowing in a direction 31° from the north. During ebb tide a bottom current of 2.2 cm/sec exists, which is flowing 144° from the north, whereas the surface current is approximately 2 cm/sec to the south. Consequently, the direction of the net tidal transport is along the shore to the north.

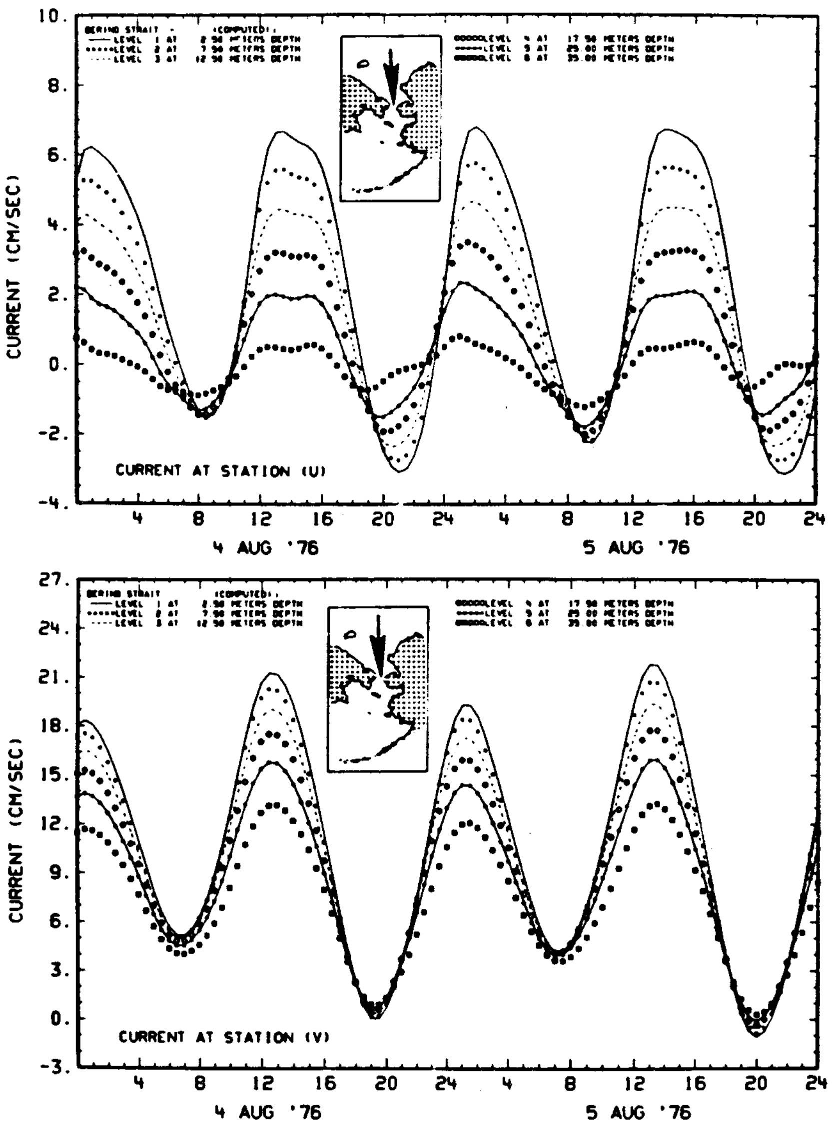

Fig. 3.21—Computed velocities (U = E/W, V = N/S components) in six representative layers at a station in the Bering Strait.

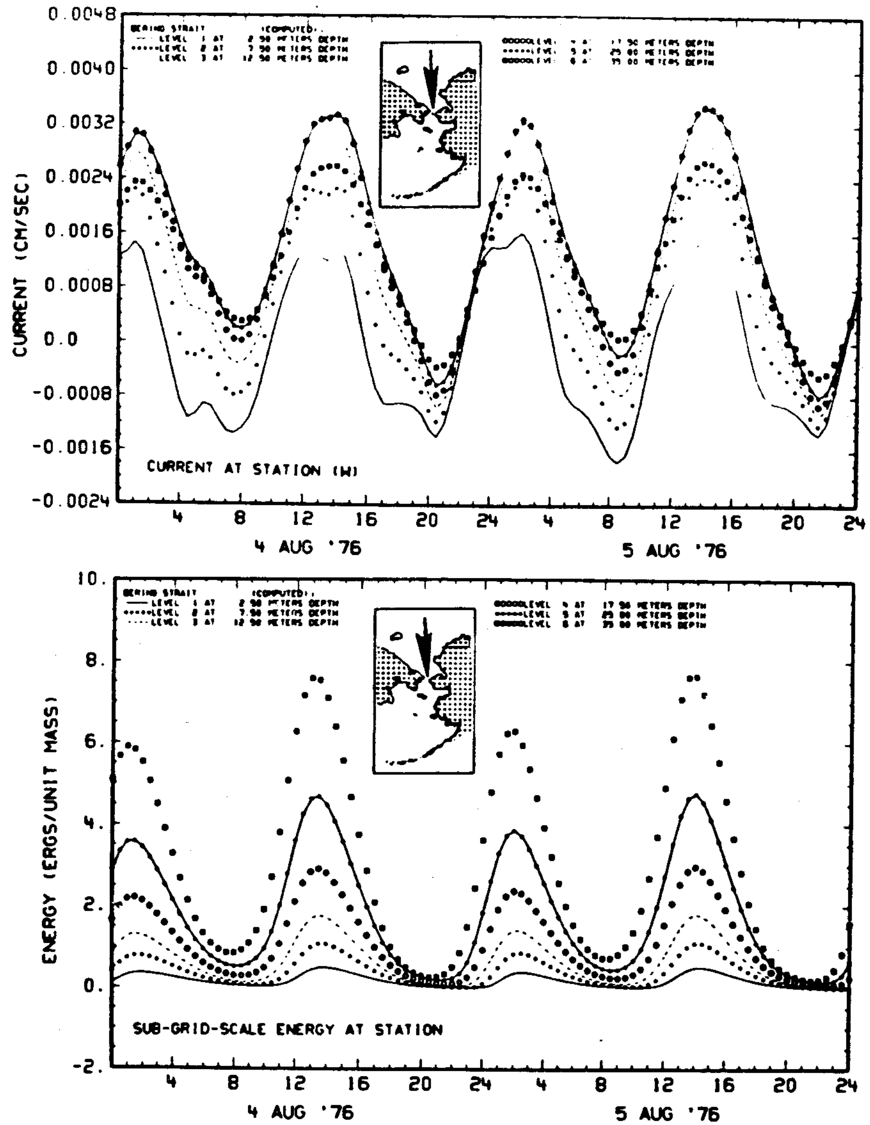

Fig. 3.22—Computed vertical velocity (w) and the turbulent energy intensities in six representative layers at a station in the Bering Strait.

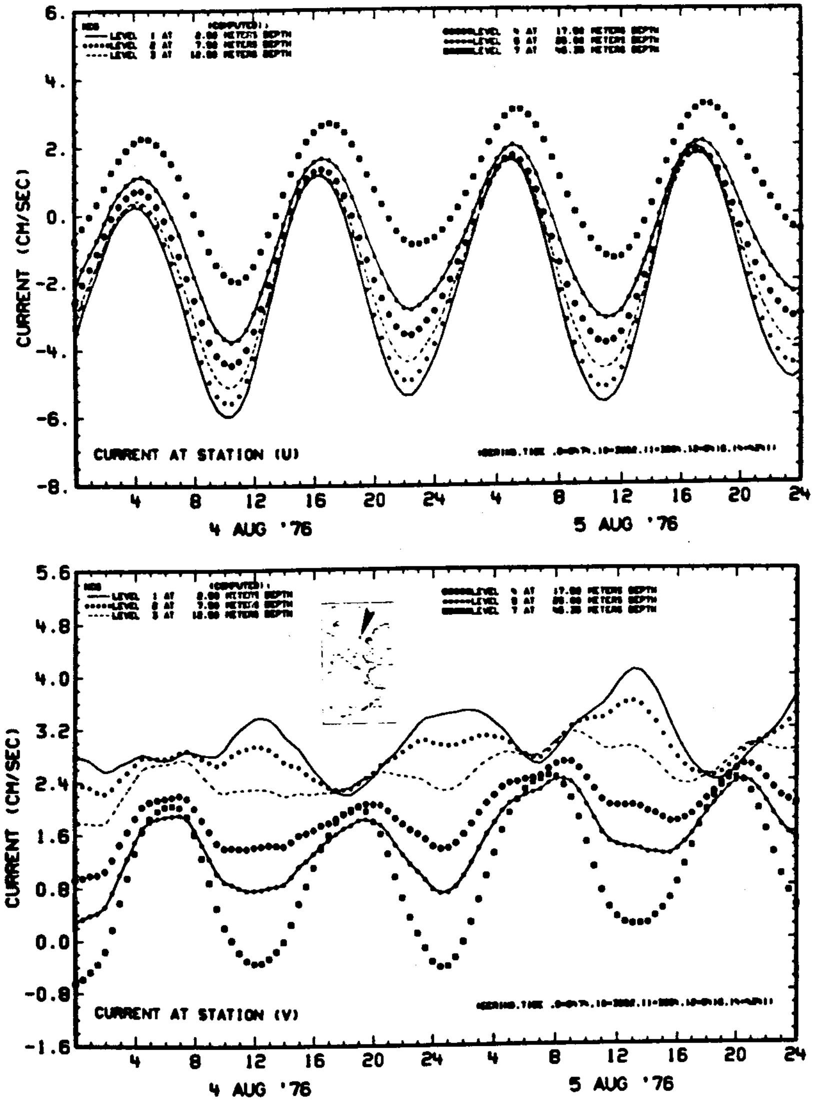

Fig. 3.23—Computed horizontal tidal velocity components (u = E/W, v = N/S) at station NC6.

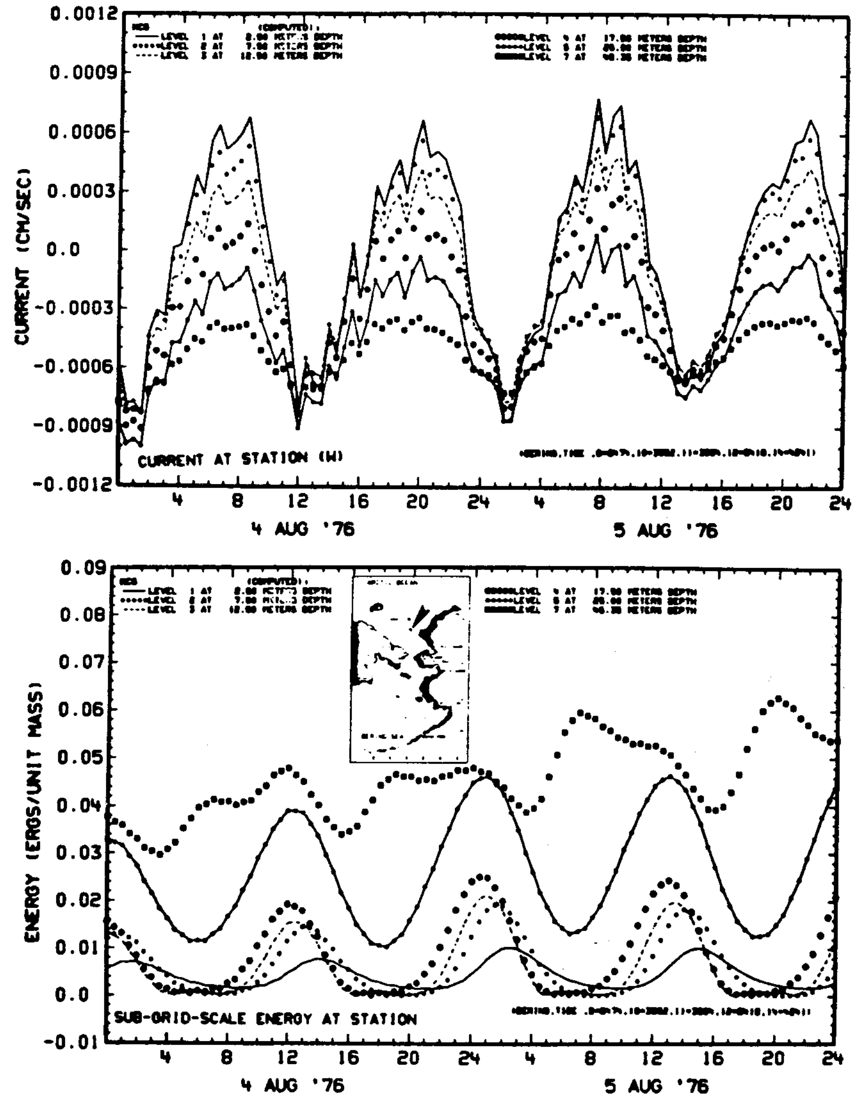

Fig. 3.24—Computed vertical tidal velocity component w and tide-induced sub-grid-scale energy densities at station NC6.

The simulation results of the two stations described above are characteristic for the model area.

MODELING TIDES IN THE BEAUFORT SEA

The propagation of tides in the Beaufort Sea is strongly influenced by the bathymetry. The tidal currents are mostly weak, and tidal currents of appreciable magnitude are present only near the large flat shelf area northwest of Point Barrow and in several embayments. The tidal amplitudes are also small and the maximum semidiurnal tide in the model area with an amplitude of approximately 10 cm is near the head of Mackenzie Bay.

Even though the magnitude of tides in the Beaufort Sea is small, compared to other modeled areas, the residual currents in many areas reach similar magnitudes to those in other areas and are more complicated. As these residuals are of considerable significance in modeling studies of the dispersion and transport of spilled oil, considerable effort was made to obtain a good representation of the tide.

In addition to the bathymetry, the very shallow pycnocline, ice coverage, and Coriolis effects associated with the high latitude influence the propagation of the tide. During most of the year the Beaufort Sea is covered with ice; only during the summer are there open areas close to shore. Thus ice had to be considered in all simulations.

The simulations with the model were made initially as a guide for the design of a field survey. From these simulations tidal charts were prepared from which the semidiurnal co-tidal chart is shown in Fig. 3.25. Several tide gauges were installed in the summer of 1983, and in 1984 results of the analysis of the tidal records obtained by Pitman (1984) became available. In the co-tidal chart, we have shown observed and computed semidiurnal tidal components at the location of the gauges. The agreement was good except near Hershel Island where the measured amplitude is 2 cm higher than the computed amplitude. This difference is very likely due to local effects; the computed amplitude is for the sea offshore, whereas the tide gauge was deployed behind a barrier island to protect it against ice scour.

In the literature we found another reference to tidal amplitudes in the Beaufort Sea (Kusunoki et al., 1962), namely, measurements obtained from the grounded Fletcher's Ice Island (T3). Observations made on this ice island are considered most suitable to study tides and storm surges, as the depth in the vicinity of the grounded island was very uniform. The location northwest of Point Barrow was far removed from land and thus was removed from shore effects. The agreement between this observation and our simulation was very good.

The simulations for summer conditions indicated that tidal currents near shore were highly influenced by shore effects, particularly where pack ice is present. This can be seen from the chart of tidal ellipses abstracted from a simulation and shown in Fig. 3.26. At those locations the fresh water beneath the ice and sharp pycnocline limits the vertical momentum transfer. The movement of ice is not in phase with the movement of the water underneath, and the nonlinear momentum transfer generates higher harmonics in the tide in addition to those generated by the shallowness of the coastal water. Later we will see that residual currents are generated in those regions. Note that tidal ellipses from Cape Halkett to Prudhoe Bay, in particular, have very unusual shapes.

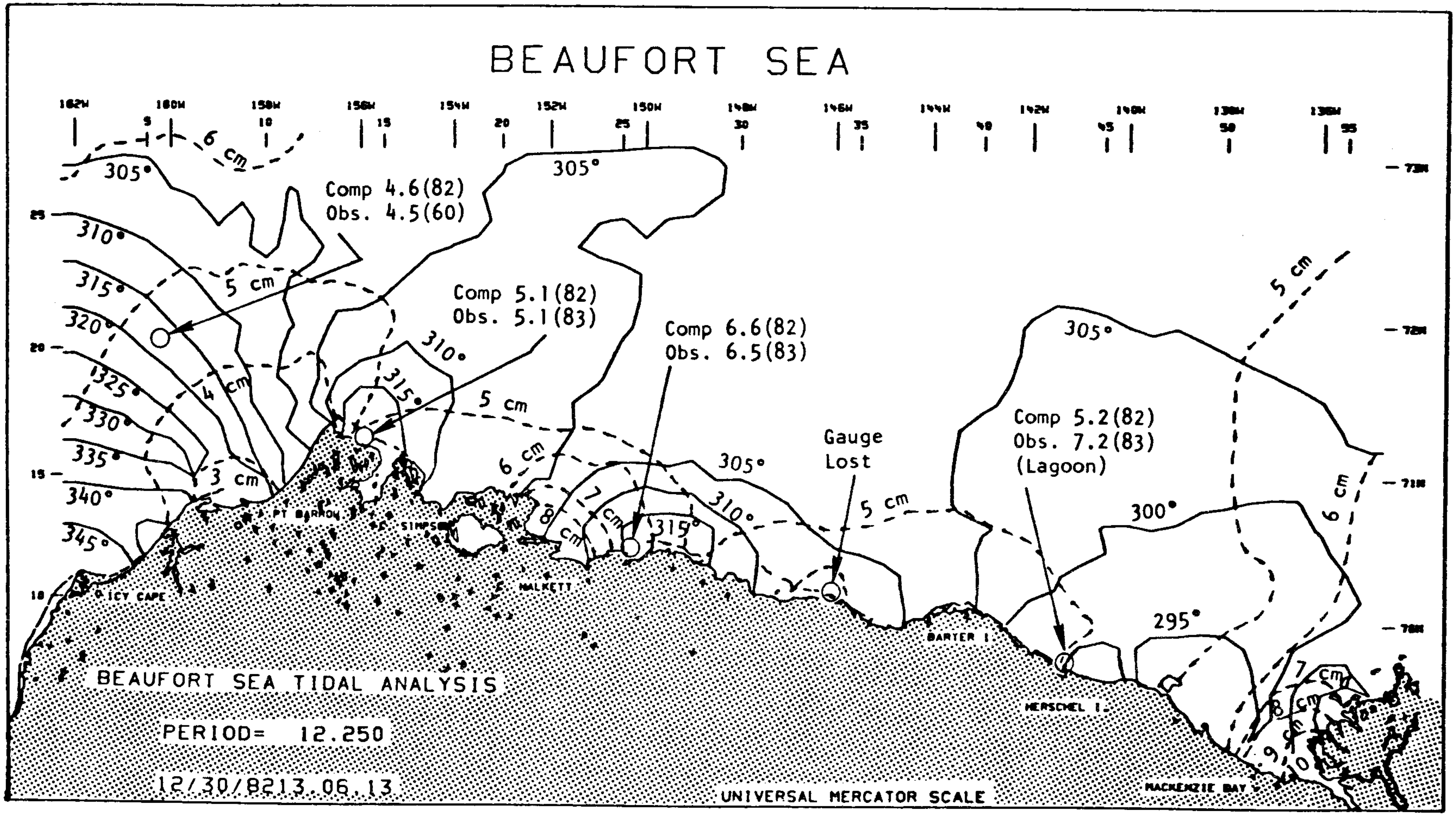

Fig. 3.25—Computed co-tidal chart for the semidiurnal component in the Beaufort Sea showing amplitudes in centimeters and Greenwich phase in degrees. Maximum amplitudes are located near Cape Halkett and Mackenzie Bay.

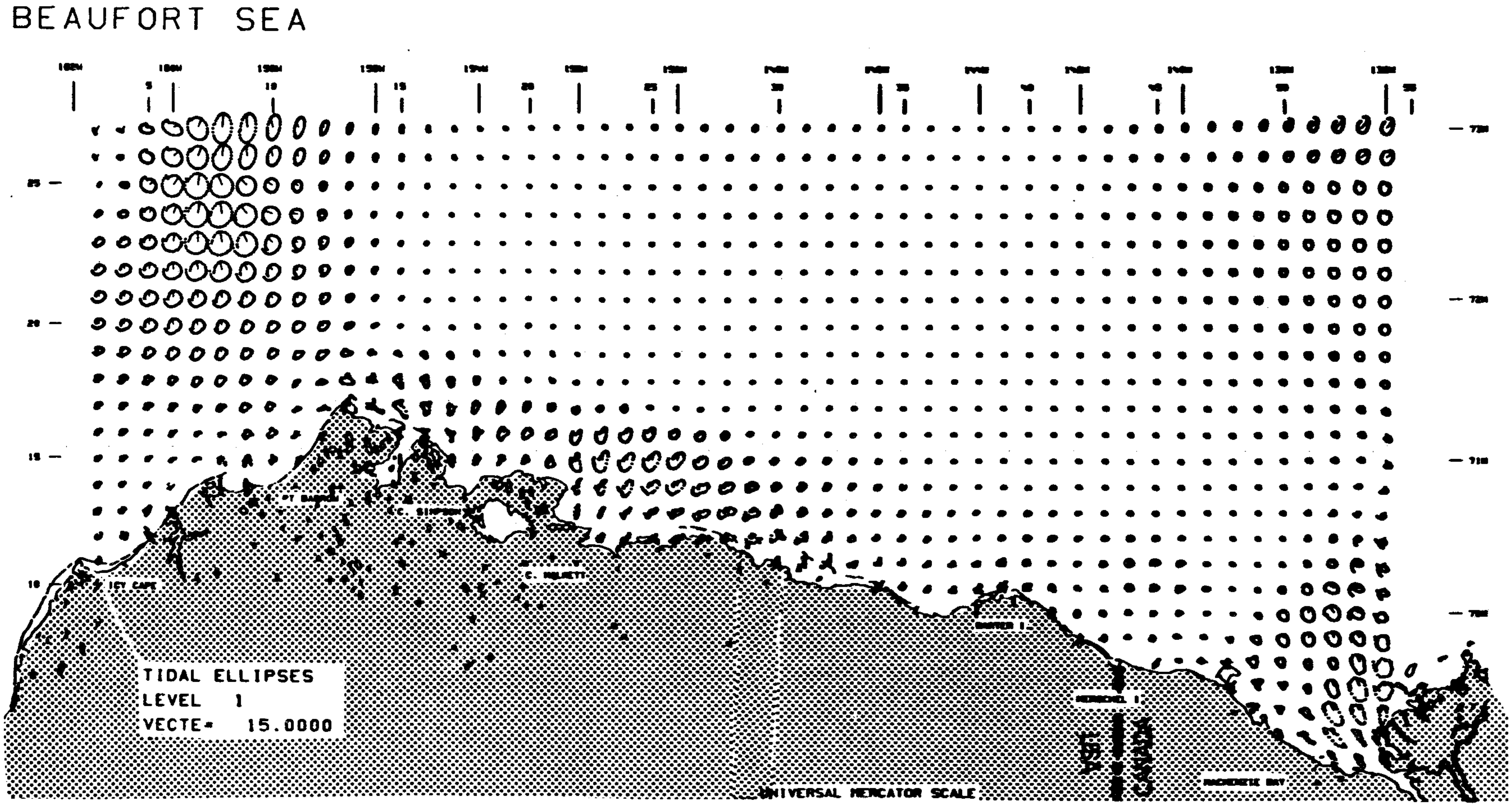

Fig. 3.26—Computed tidal current ellipses in the surface layer (at 2.5 m level) of the Beaufort Sea model with a plotting scale of 15 cm/sec per grid spacing. Magnitudes of tidal currents are inversely proportional to the local depth, whereas the shape of the tidal ellipses reflects the shore effects.

MODELING WIND-INDUCED CIRCULATIONS

Other than tides, winds are the next most important driving force in the coastal hydrodynamic process. If the area covered by the model is small, and if there is no need to take into account wind effects generated outside the model area, the computation of wind-induced flow is relatively straightforward. The wind field can be assumed to have the same speed and direction over an entire modeled area; however, when a large model area is involved, the wind field to be used varies in time and space.

For the study of the water movements resulting from wind in the eastern Bering Sea and the Chukchi Sea, the primary model contained the entire continental shelf. The need for a model of such a large area comes about because a storm passing through the southern Bering Sea may influence the hydrodynamics of the northern Bering Shelf, and vice versa. This became clearly evident when a 40-day current data series of a station in Norton Sound was analyzed.[1] Figures 3.27 and 3.28 show persistent nontidal oscillations in the current components after a numerical tidal eliminator was applied. The period of this oscillation is approximately 50 hours. This oscillation (seiching) of Norton Sound is generated by storms passing over the continental shelf. Such a storm passed over the recording station approximately 650 hours after the beginning of the record. The maximum nontidal current was approximately 30 cm/sec.

The passage of storms over the coastal waters of Alaska is very common, particularly over the eastern Bering Sea. The predominant direction of the cyclonic tracks is toward the northeast with an average passage time of one and a half to two days. Observation of such wind fields are generally difficult to obtain, as a dense network of weather stations is required for a good spatial resolution.

For the computation of wind-induced circulation with the three-dimensional model, the source terms in the turbulent energy balance equation and momentum equations are of major importance. The source for the energy balance equations is computed from the kinetic energy associated with the wind/wave field. For the case where the local water depth decreases, computations with the turbulent energy equation will then show that energy in the water column increases with a decrease in depth. Thus the model accounts for more intense mixing and dissipation, and larger bottom stress. When sufficient resolution is used in the model, these computations can even be extended up to the near-shore as all important physical processes are incorporated in the model formulation. Even though the model code is programmed to handle radiation boundary conditions, for the majority of the simulation, absorbing boundary conditions were imposed at the shelf break where water is much deeper than at the shelf.

Results of simulations with wind have been extensively used to determine the movement and dispersal of spilled oil, and these results will be presented in that context in Chapter 6. However, it seems appropriate to present some results and to illustrate the effects of the coastal configuration on wind drift in the eastern Chukchi Sea. Navigators in the eastern Chukchi Sea have noticed high currents in this area and have termed them the *coastal jets of the Chukchi Sea* (Wiseman and Rouse, 1980). To analyze this phenomenon, simulations were made with winds from the north as well as from the south, together with the tides. A wind speed of 10 knots was selected. After the run-in period of the simulation, we placed particles in the surface layer of the model at every grid point, followed these particles over a period of 48 hours, and made pathway plots of each particle.

---

[1] Original data were supplied by Dr. J. Schumacher of NOAA.

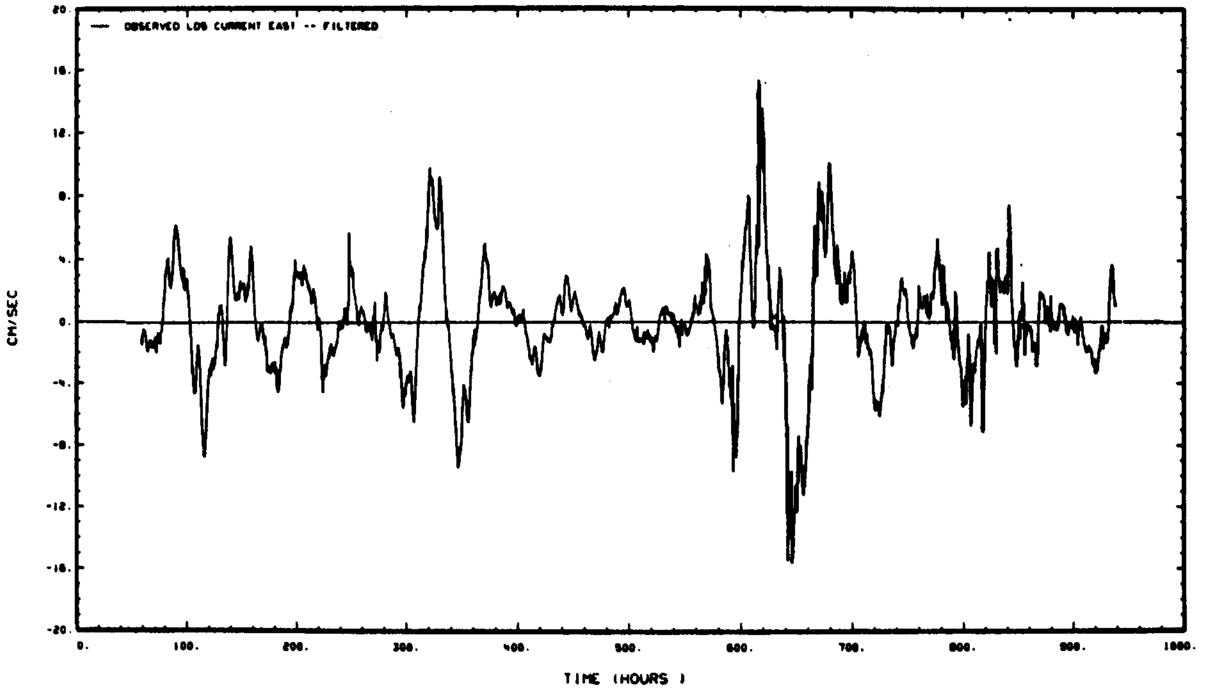

Fig. 3.27—Nontidal oscillations in the east-west velocity component of the observed currents at station LD-5 after applying the numerical filter which filters out energies in the primary and higher tidal modes.

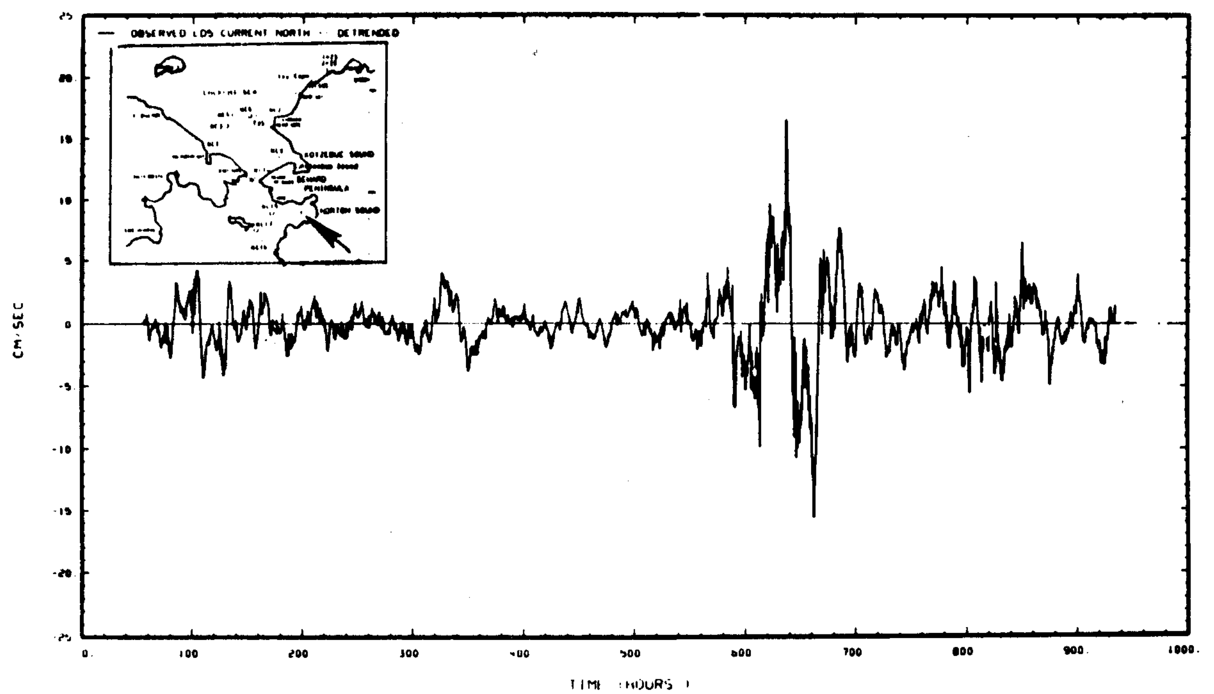

Fig. 3.28—Nontidal oscillations in the north-south velocity component of the observed currents at station LD-5 after applying the numerical filter which filters out energies in the primary and higher tidal modes.

When the wind blows from the south, areas with the largest particle displacements are in the Bering Strait and offshore Icy Cape (Fig. 3.29). However, when the wind direction is reversed and blowing from the north (Fig. 3.30) the area in the eastern Chukchi Sea with the largest displacement is still near Icy Cape. Note that the particle displacements in the Bering Strait, now small because of residuals, are in the opposite direction of the wind-generated current.

Figure 3.31 presents enlarged sections of water particle trajectories of the two previous figures. It is quite clear that a band of high speed coastal jet currents is present regardless of the wind direction. We will see below that this coastal jet would have a considerable effect on the movements of spilled oil in that area.

MODELING THE DENSITY FIELD AND THE RESIDUAL CIRCULATION

The hydrodynamic model used to compute the water motions contains the mathematical formulations for the evolvement of the salinity, temperature, and flow field in time. To start a simulation for a particular model area, the initial salinity and temperature fields are required. These data are furnished by the NODC project office. Figure 3.32 shows the salinity distribution in the surface layer of the model for the Bering Sea and the Chukchi Sea during a simulation of typical summer conditions. The lowest salinity (less than 20 g/kg) is located near the Yukon River Delta where fresh water from the river mixes with saline water of Norton Sound. Water of much higher salinity (approximately 29 g/kg) is found in the surface layer in the northwestern part of the Sound near Nome. Water in lower layers of the model have higher salinities, generally in the range of 29 to 34 g/kg.

In Fig. 3.33, the temperature distribution in the surface layer of the same simulation is shown. The highest temperatures are found in Norton Sound. At the head of the Sound (Norton Bay), summer temperatures can reach 14°C in the surface layer because of local solar heating. In the Chukchi Sea, temperatures vary over a large range in the surface layer for these summer conditions. In Kotzebue Sound, the temperature is 10°C and 2°C around Point Barrow.

The density structure in the vertical is as important as the horizontal distribution for its effects on the residual circulation. The vertical density structure is also important for dispersion processes on a relatively short time scale. To obtain an insight into the vertical distributions of salinity and temperature, cross-sectional graphs were made of simulation results. Figure 3.34 shows vertical salinity distributions through two sections of the model. Note that near the Bering Strait, water in the surface layer has a higher salinity than in the surface layers of the Bering Sea and Chukchi Sea. If we look at the east-west section at 70°N, it can be seen that near the Siberian coast, water has a much lower salinity than the sea near the Alaskan coast. The salinity distribution in this section shows that vertical salinity gradients are present in the whole section.

The graphs of the temperature distributions (Fig. 3.35) in the same vertical sections show the thermocline much more clearly than the graphs of the salinity distributions. This is due, in part, to the larger number of contour lines that are shown. In the longitudinal section, note that the temperatures decrease with higher latitudes, as was to be expected. The depth of the pycnocline is generally between 7 m and 15 m. This pycnocline is also present in the Chukchi Sea.

During summer several frontal systems are present. In the eastern Bering shelf area these frontal systems generally occur near the 50 m isobath. In the shallower area between

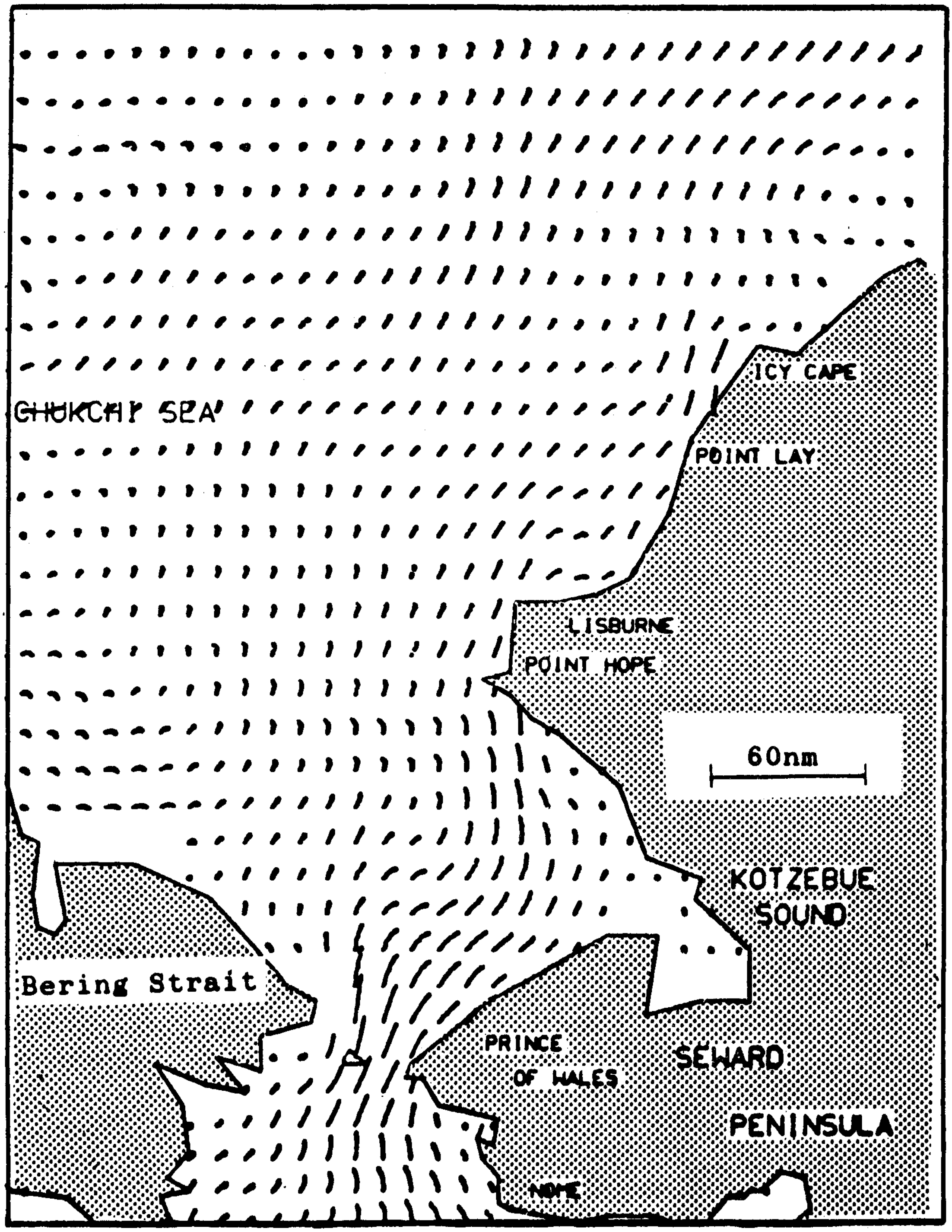

Fig. 3.29—Surface water particle trajectories in the Chukchi Sea induced by tide and 10 knot wind blowing from the south for 24 hours. Particles were traced for a total of 48 hours from the beginning to include the transient and inertial dynamics. Trajectories launched near the coastal areas between Point Lay and Icy Cape clearly indicate the development of coastal jets.

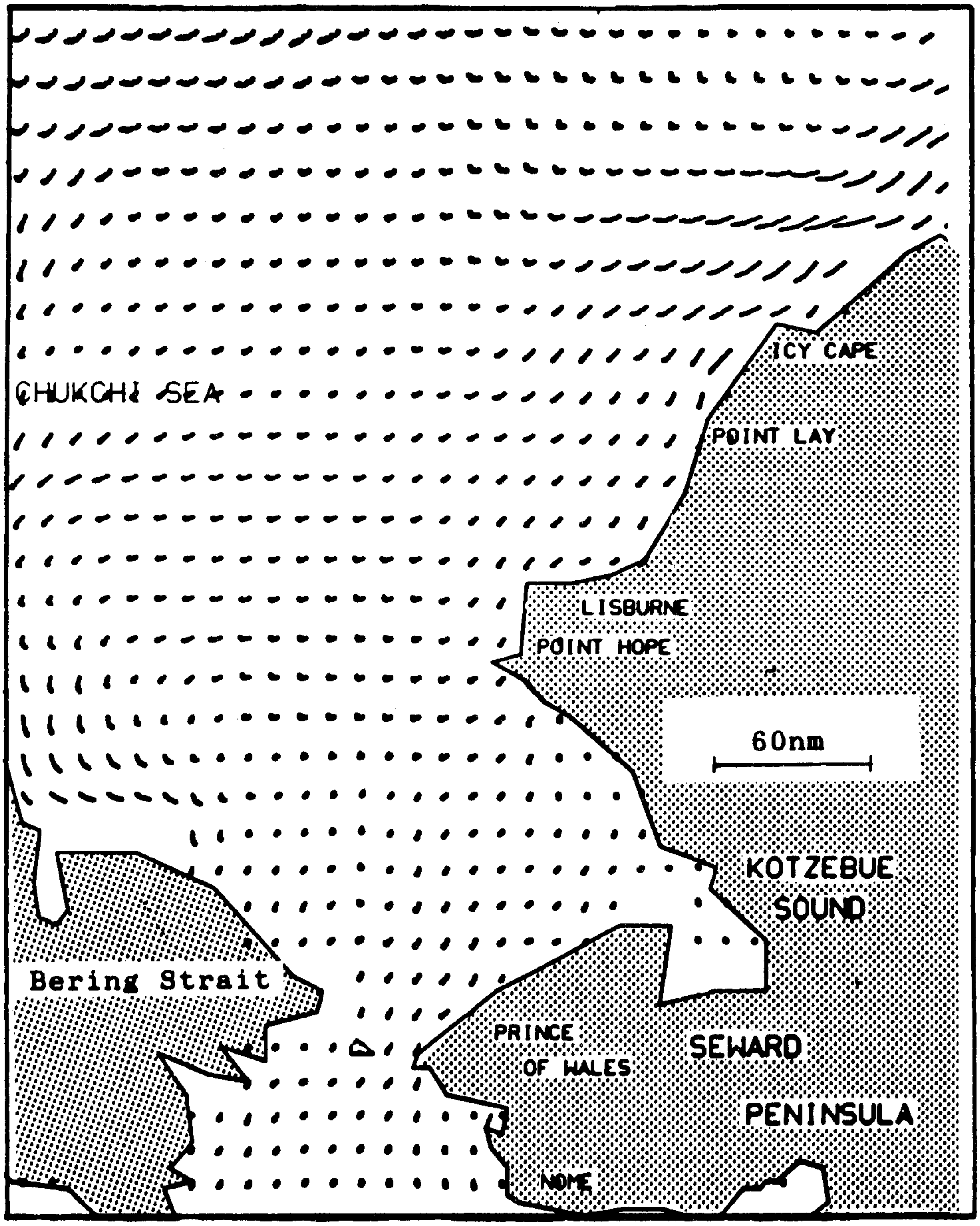

Fig. 3.30—Surface water particle trajectories in the Chukchi Sea induced by tide and 10 knot wind blowing from the north for 24 hours. Particles were traced for a total of 48 hours from the beginning to include the transient and inertial dynamics. Trajectories launched near the coastal areas between Point Lay and Icy Cape clearly indicate the development of coastal jets.

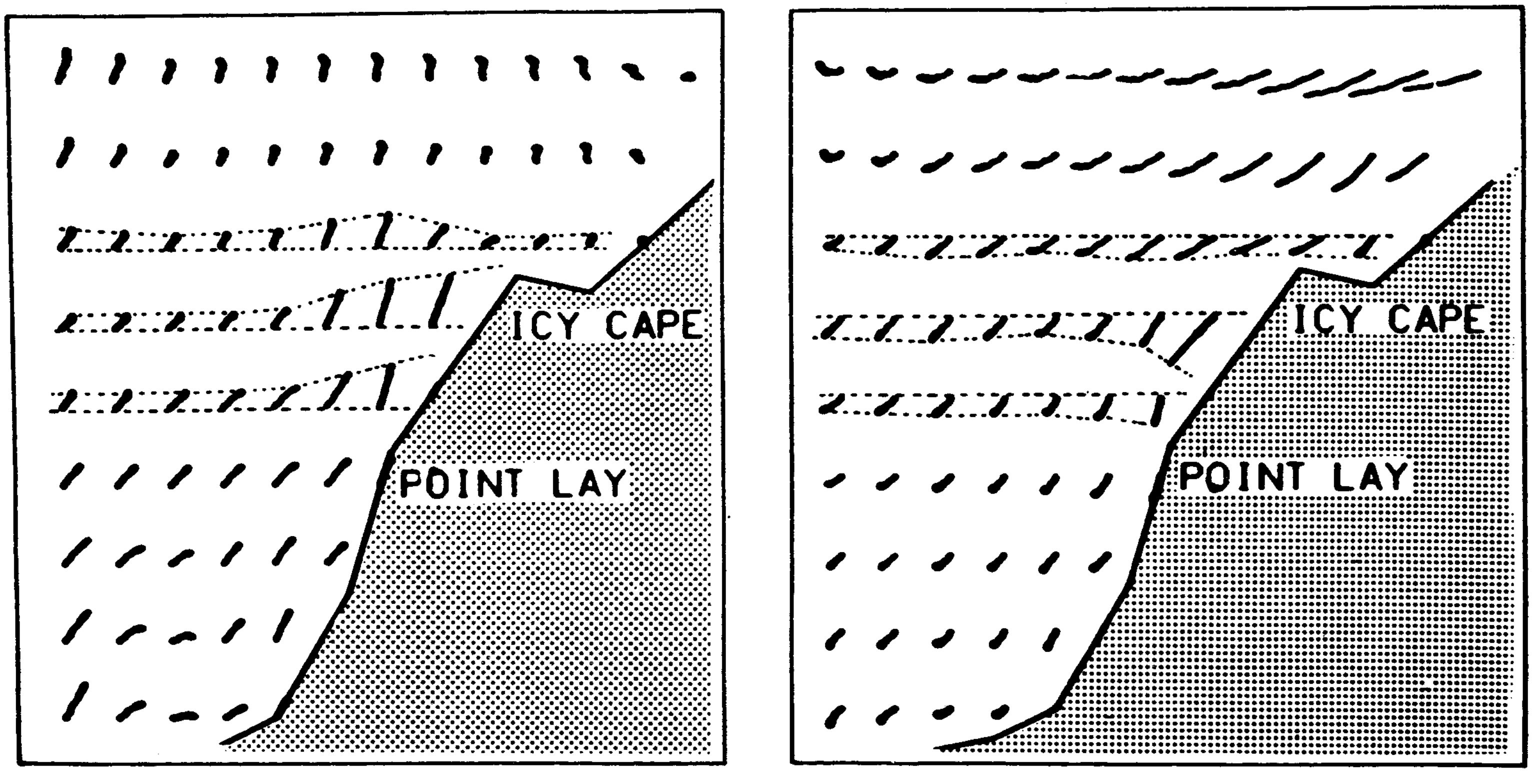

Fig. 3.31—Enlarged section of surface water particle trajectories near the coast between Point Lay and Icy Cape showing the coastal jet. The left shows the trajectories induced by tide and wind from the south (with water movements in the north to east directions); the right shows the trajectories induced by tide and wind from the north (with water movements in the west and south directions).

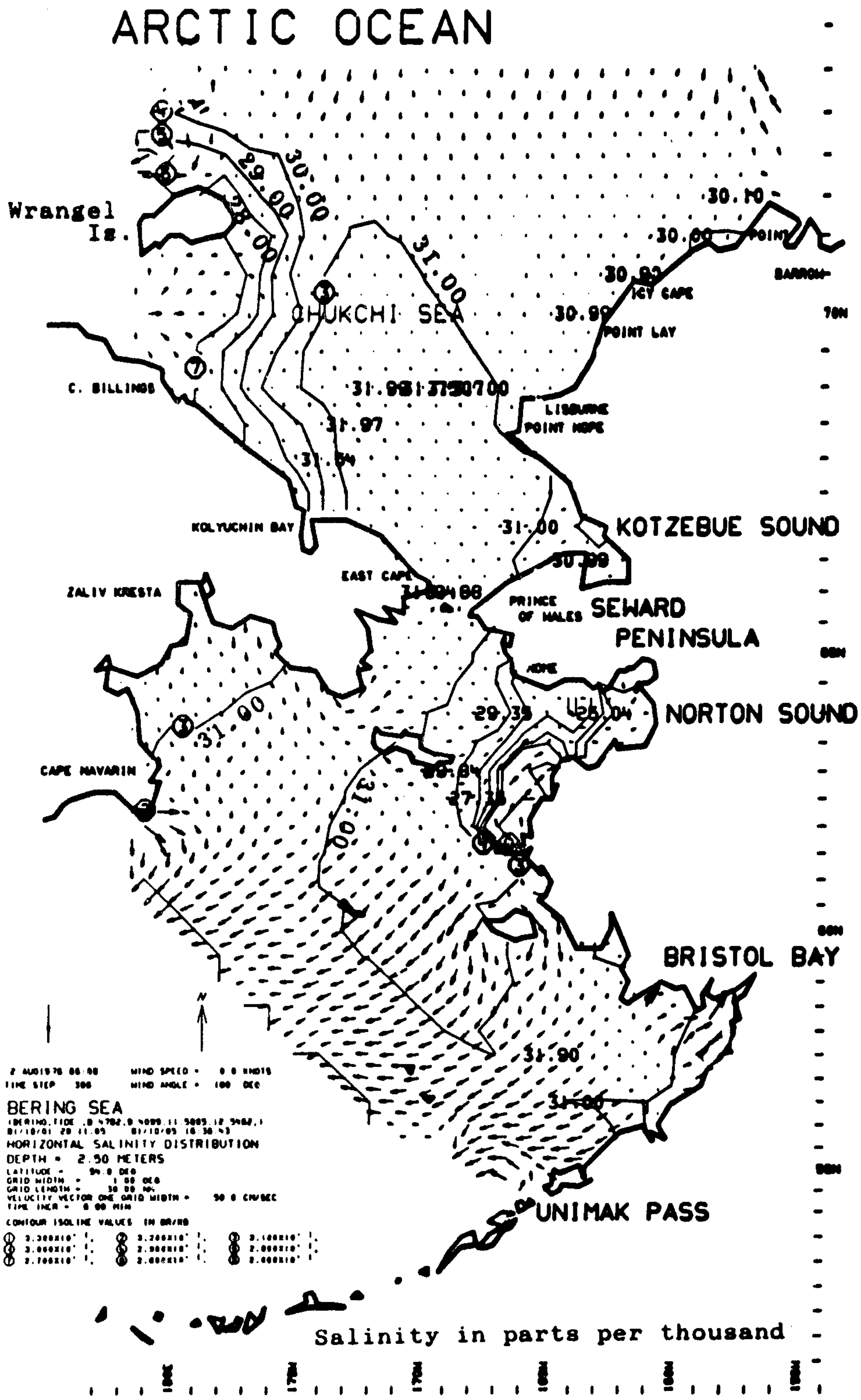

Fig. 3.32—Surface salinity distribution superimposed on the computed tidal circulation pattern at 1200 hours (Greenwich Mean Time) on August 2, 1976. Areas of low salinity are located near Yukon River and the eastern Siberian Shelf.

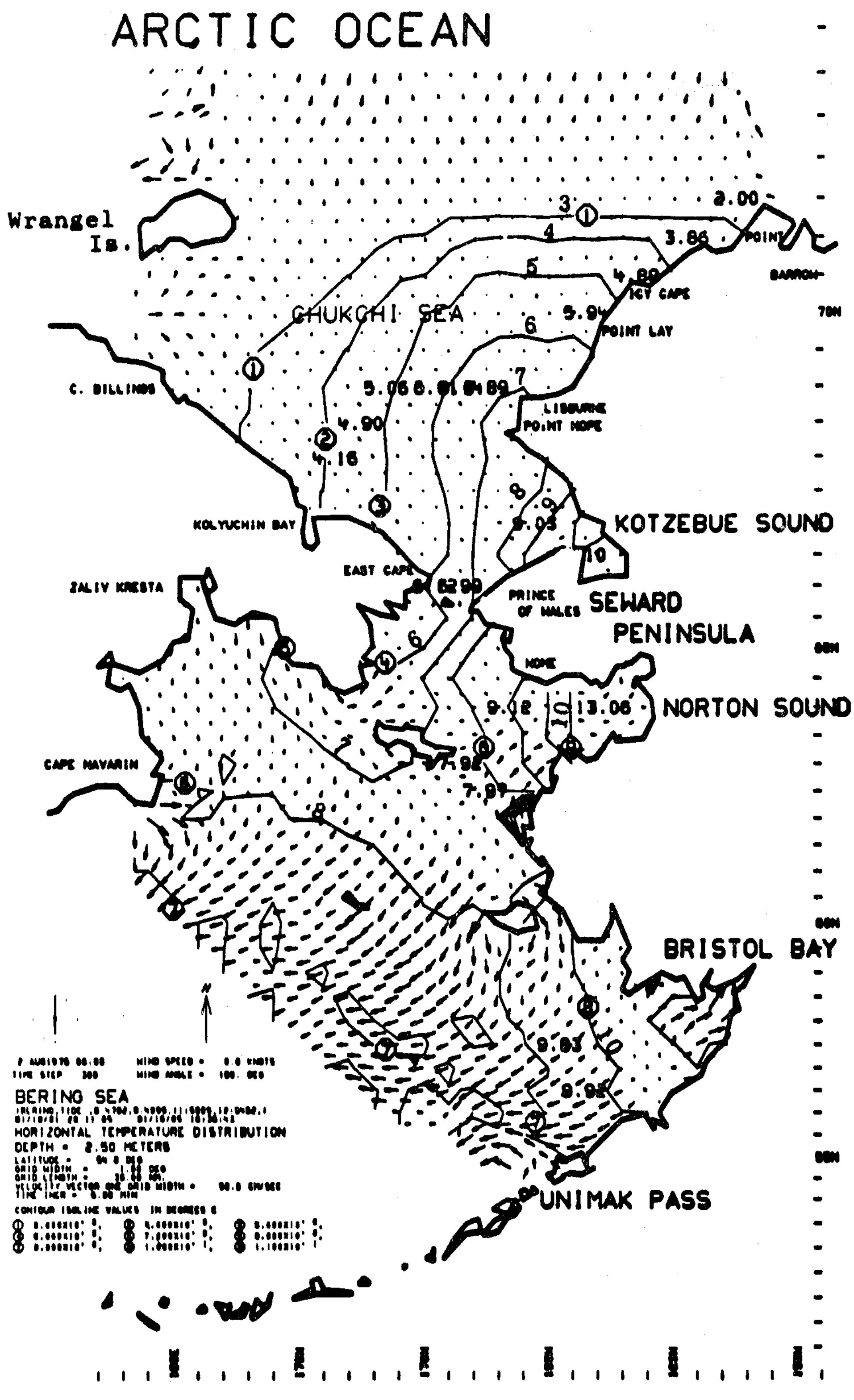

Fig. 3.33—Surface temperature distribution superimposed on the computed tidal flow pattern at 1200 hours (Greenwich Mean Time) on August 2, 1976. Areas of warmer temperature are generally located near Yukon Delta and the eastern shelf areas of the Bering and Chukchi Seas.

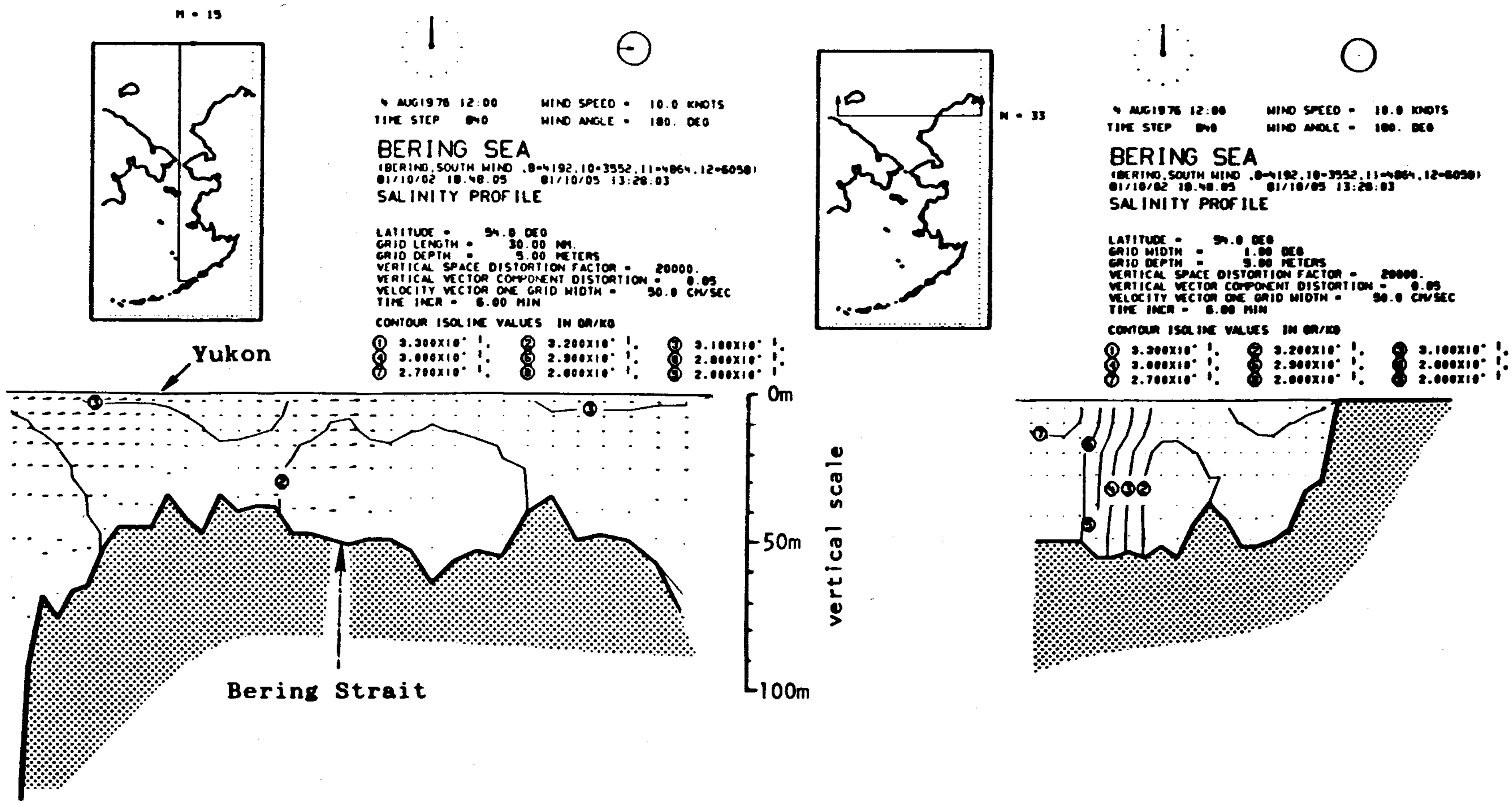

Fig. 3.34—Vertical salinity distributions through two cross-sections of the model. In the north/south section, the shallow pycnocline to the left is located near the Yukon Delta. Because of counterclockwise circulation within Norton Sound, the mixing causes deepening of the pycnocline before reaching the Bering Strait. In the east/west cross-section, fresher water is generally located near the Siberian shelf. The depth of pycnocline is approximately between 7 to 15 meters.

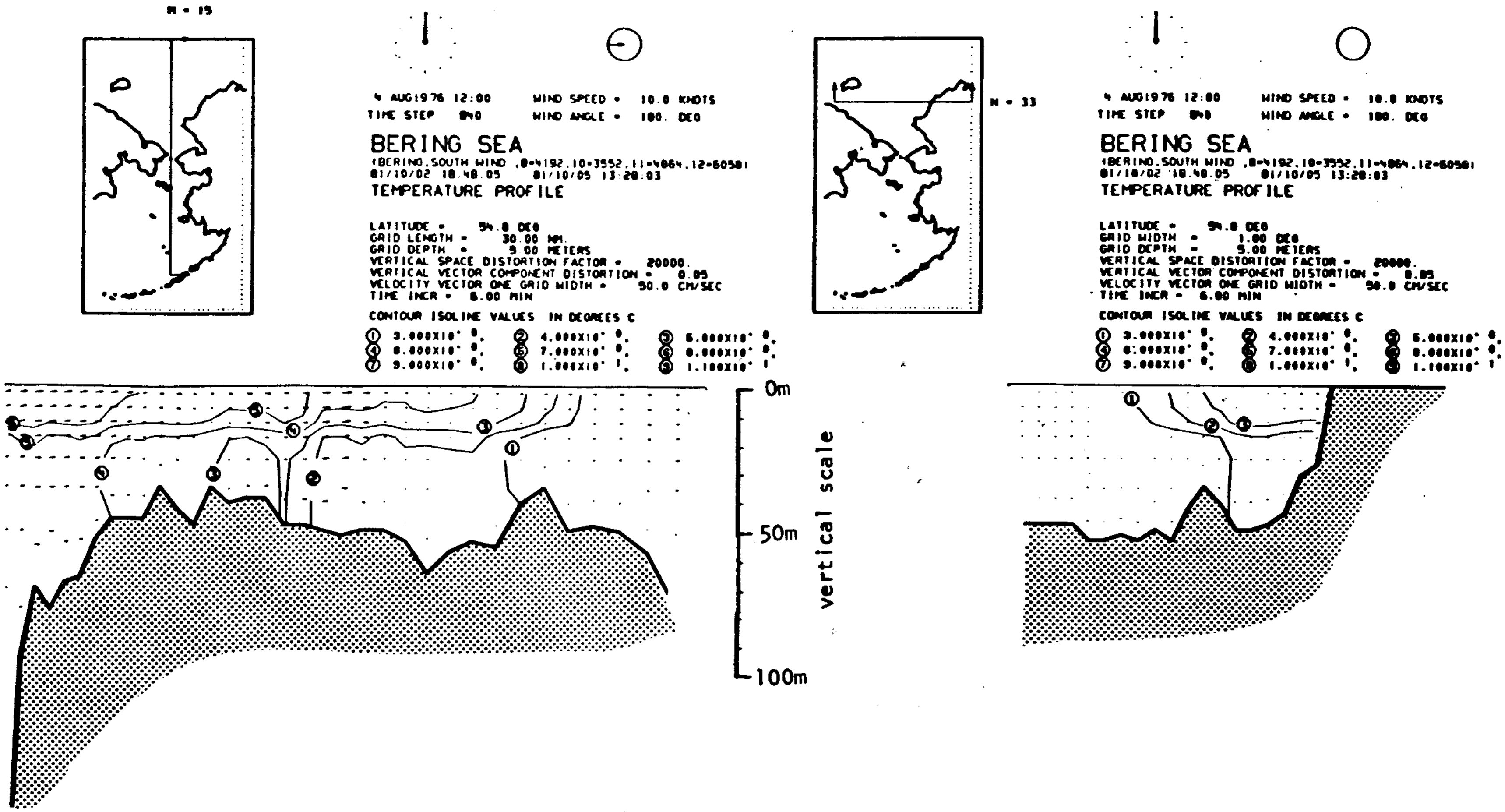

Fig. 3.35—Vertical temperature distributions through two cross-sections of the model.

50 m depth and the coast, water is well-mixed. A pycnocline exists in deeper water. The turbulence generated by tidal currents is not strong enough to mix water in the upper layer with water at a greater depth. The turbulence generated by wind causes the water above the pycnocline to be mixed and with a strong wind the pycnocline deepens. These effects can be seen very clearly in the salinity and temperature distributions in a vertical section of a submodel of the Bering Sea and Chukchi Sea model (Fig. 3.36).

The hydrographical structure of the Alaskan coastal waters is very complex, and many papers have been written on the subject (Mountain et al., 1976; Schumacher et al., 1979; Kinder et al., 1980; Coachman and Aagaard, 1981; Aagaard et al., 1981; Schumacher and Kinder, 1983; Salo et al., 1983; Reed and Schumacher, 1984). As the density field contributes considerably to the generation of the baroclinic currents and is very important for the dispersion computations of spilled oil, a major effort was made to obtain the appropriate salinity and temperature field for our studies and to have a good formulation of the turbulence closure computation when a pycnocline is present. It appears that in highly stratified regions, saltier water may sometimes stay on top of less saline water. In such a case the higher temperature more than compensates for the top-heavy distribution of the salinity. An example is shown by arrows in Fig. 3.36. In the absence of wind the layer can be temporarily stable until disturbed. Turner (1967) indicated that in nature in such a double diffusion convection case, salt fingers in the water column are formed. In principle the computation procedure is also able to model double diffusion convection instabilities, since different coefficients for the vertical diffusion transport in the mass balance equation of salt and heat are used, but we have not made an analysis of this phenomenon in our simulation results.

Now consider the propagation of tide in a homogeneous body of water where no density gradient exists. The bathymetry and bottom friction generate residual circulation through the nonlinear advective mechanisms in the equation of motion. The tidal residual in homogeneous water is different from the tidal residual of stratified water. In stratified water the vertical momentum transfer is suppressed, the vertical velocity profiles are different, and a different nonlinear advection and dissipation generates a different residual. Thus the seasonal change in the density structure produces a seasonal change in the tidal residual. The influence of the velocity distribution on the residual also shows near the vertical fronts that were discussed above. Near the front the water-level gradients are essentially the same, but the nonlinear processes that generate the residual are not the same. Consequently, a transition in the residual is generated that shows as a band of higher residual currents near the frontal area. Because the frontal area is located at the 50 m isobath, the residual more or less follows this isobath. A similar process exists near the shelf break. On the other hand, without tides the horizontal density gradient generates baroclinic circulation in seeking a geostrophic balance. Over the Alaskan coastal shelf, both tidal forces and density gradient are significant and dynamically coupled. One cannot, therefore, compute them separately.

It has been a useful analytical procedure to compute oceanic circulation using geostrophic balance according to the hydrographic data. Results from this type of diagnostic calculation would yield a pattern of currents relative to a "level of no motion" typically at 1200–1500 meter depths. The computed geostrophic currents represent the distance between the density (pressure) gradient and the Coriolis force. In the deep ocean when tidal currents are weak, the density-driven current is the primary circulation in the absence of local wind force.

However, over the shallow shelf of the Alaskan coastal waters a major portion of the kinetic energies are within tidal frequency bands (Mofjeld et al., 1984; Pearson et al., 1981a,

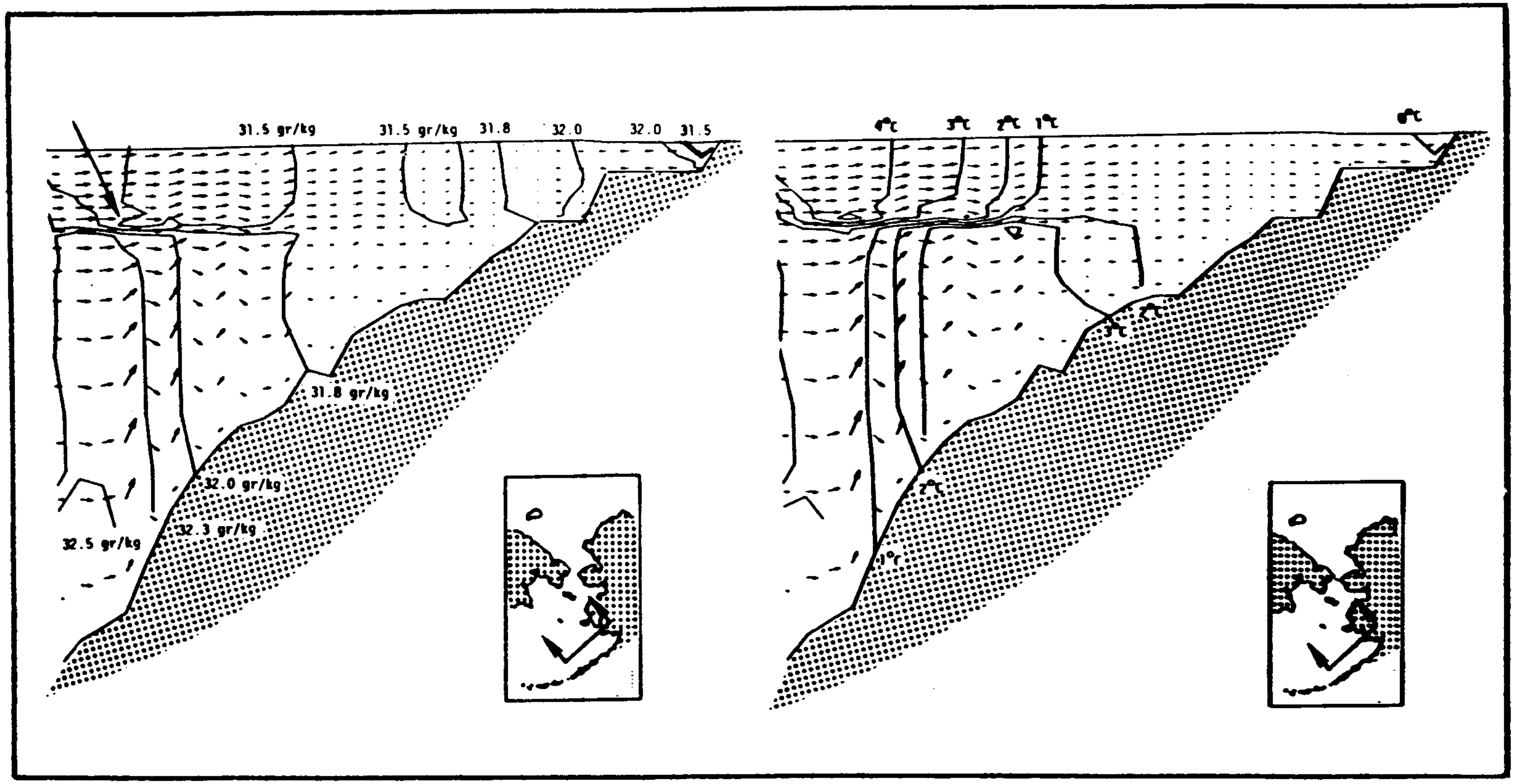

Fig. 3.36—Vertical distribution of salinity, temperature, and currents through a cross-section of the eastern Bering shelf showing the pycnocline, frontal structure, and local density instability where heavier water could stay above lighter water temporarily.

1981b). Consequently, in computing the density-induced circulation one has to include tides in the computation. If they are not included, the computed density currents are restrained by very weak bottom stress because of the quadratic relation between velocity and frictional dissipation. This would overestimate the density currents. Also, as a result, a deep-water density current when close to the shelf break, would extend over the shelf and the velocities gradually decrease landward. It is unlikely that any frontal eddies at the shelf break would be generated by the model. On the other hand, if tides are included in the computation, tidal currents are generated on the shelf, and these currents are damped by the bottom stress, which is much larger than in simulations without tide. The water movements on the shelf are then practically uncoupled from the density currents in the deep Bering basin, and sharp transitions are generated in the model.

Currents computed with tides and density field would include primarily baroclinic circulation with "tidal residuals" if energies at tidal frequencies are "filtered." The spin-up time required to establish a baroclinic balance is approximately five to ten days. This is reasonable when compared to the spin-up time required for the Atlantic Ocean (Anderson and Killworth, 1977), which takes between ten to 16 days.

At the beginning of our modeling study extensive field cruises were made to establish networks of conductivity, temperature, and depth (CTD) stations and to emplace current meters and bottom pressure recorders. The field studies were conducted by Drs. Kinder, Muench, Tripp, Schumacher, and Mofjeld (see the Bibliography). Because of practical difficulties, most of the gauge deployments were stopped at the shelf break, even though it had been requested to extend coverage further offshore into the deep Bering Basin. As compensation, more CTD profiles were cast near the shelf break. It was decided in a project technical review meeting to compute the baroclinic circulation over the shelf break using the three-dimensional model according to the CTD cast as mentioned above. The geostrophic currents at the northeast part of the Bering Basin were deduced from the 5500 hydrographic profiles (developed for the years 1874–1959, by Arsen'ev, 1967) and computed from a CTD cast made by a Japanese fishing fleet (Takenouti and Ohtani, 1974). The pattern was supplemented by the estimated transport computed from five CTD transects developed by Kinder et al. (1975). The net transport through the Unimak Pass was measured by Schumacher et al. (1982). Data groups were adapted for estimating the net circulation near the Bering Shelf break and this information is shown in Table 3.1. The general direction of geostrophic transport along the shelf break flows toward the northwest. This northwesterly flowing current along the shelf break has been called the "transverse current" by Russian oceanographers (e.g., Arsen'ev, 1965, Fig. 3.37) and the "Bering Slope currents" by American scientists (e.g., Kinder et al., 1975). This current is coupled with the cyclonic circulation in the eastern Bering Basin (Fig. 3.38 by Takenouti and Ohtani, 1974). Based on the measured density field and tidal forcing, a series of computations using three-dimensional dynamic computation were made in 1979 and 1980. The rationale to include tidal energy in the computation and then later filter it out was presented above. After filtering out the tidal components, the remaining baroclinic residual transport along the shelf break (with tidal residual also included) also flows toward the northwest, as shown in Fig. 3.39. (See also the Appendix.) Thus this agrees with the compiled data sets.

Furthermore, the baroclinic current tends to pass St. Lawrence Island not only through the western passage but is also to the south, passing through the eastern passage near Norton Sound. This computed pattern agrees with two earlier studies by the Russian and Japanese groups. For oil trajectory computations, baroclinic circulation near and beyond the shelf break was compiled from the sources listed in Table 3.1.

Table 3.1

DATA GROUPS ADAPTED FOR ESTIMATING THE NET CIRCULATION NEAR THE BERING SHELF BREAK AND THE UPDATING PROCESS

Data Group	Observation Period	Data Type	Author	Publication Date	Methods and Comments
1	1874–1959	CTD[a]	Arsen'ev	1967	Diagnostic comp. (Sparce data in the area of interest, qualitative.)
2	1959–1965	CTD	Takenouti and Ohtani	1974	Diagnostic comp.
3	8/2–13, 72	CTD	Kinder et al.	1975	Diagnostic comp.
4	8/14–21, 72	Drogue	Kinder et al.	1975	Parachute drogue at 150 m and 750 m
5	June 1976	CTD	Data: Kinder model: Liu and Leendertse	1977 1979	3-D dynamic computation (Liu and Leendertse, 1979) using this group of CTD casts
6	1981	Meter	Schumacher et al.	1982	Net flow through Unimak Pass
7	1982	Meter	Muench and Schumacher	1985	Marginal ice zone study
8	10/82–5/83	CTD meter	Muench and Schumacher	1985	Direct observation and diagnostic comp.
9	1983	CTD and drogue	Schumacher and Kinder	1983	Direct observation and inferred geostrophic flow
10	1982–1983	Drogue	Royer and Emery	1984	Window-shade drogue, broken (to give rough estimate at 30 m level).

[a]Conductivity, temperature, and depth.

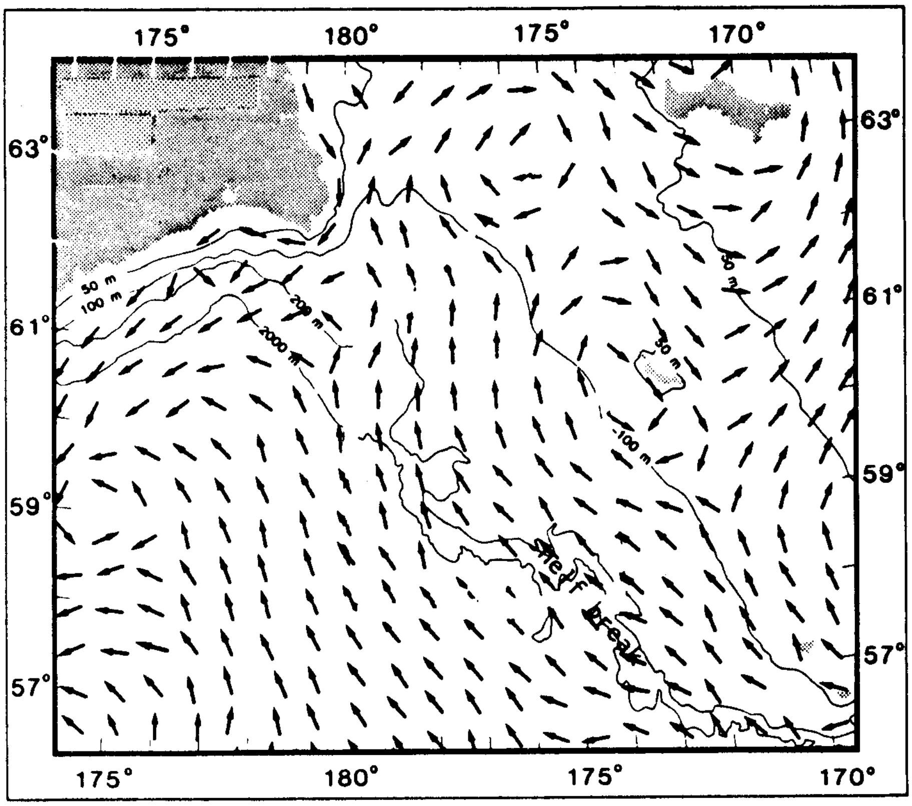

Fig. 3.37—Inferred geostrophic circulation pattern, based on 5500 hydrographic data, as reported by Arsen'ev (1967).

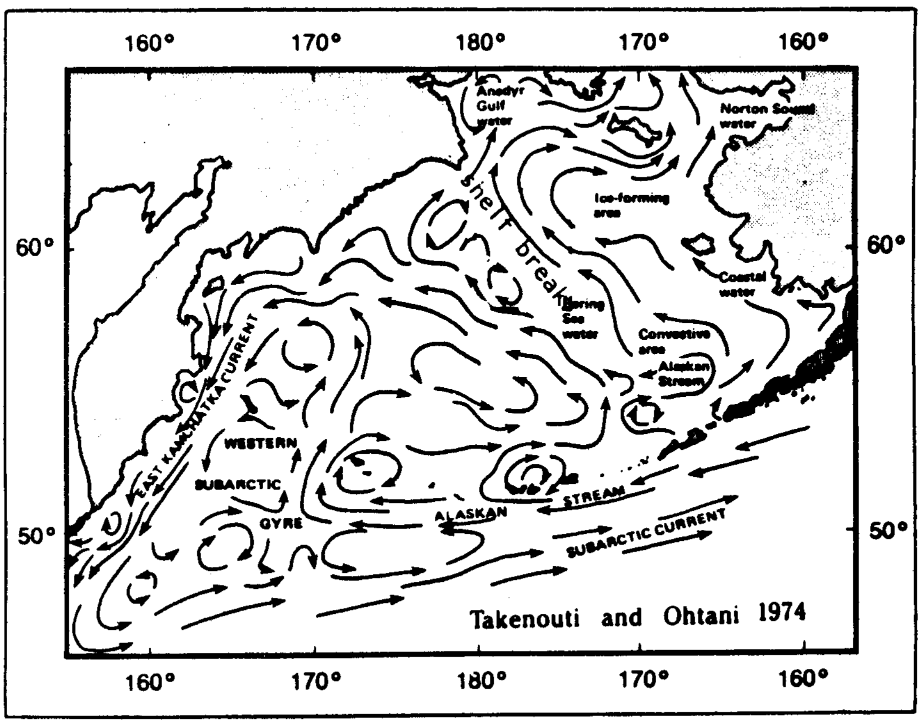

Fig. 3.38—Computed geostrophic circulation pattern based on a CTD cast by the Japanese fishing fleet, as reported by Takenouti and Ohtani (1974).

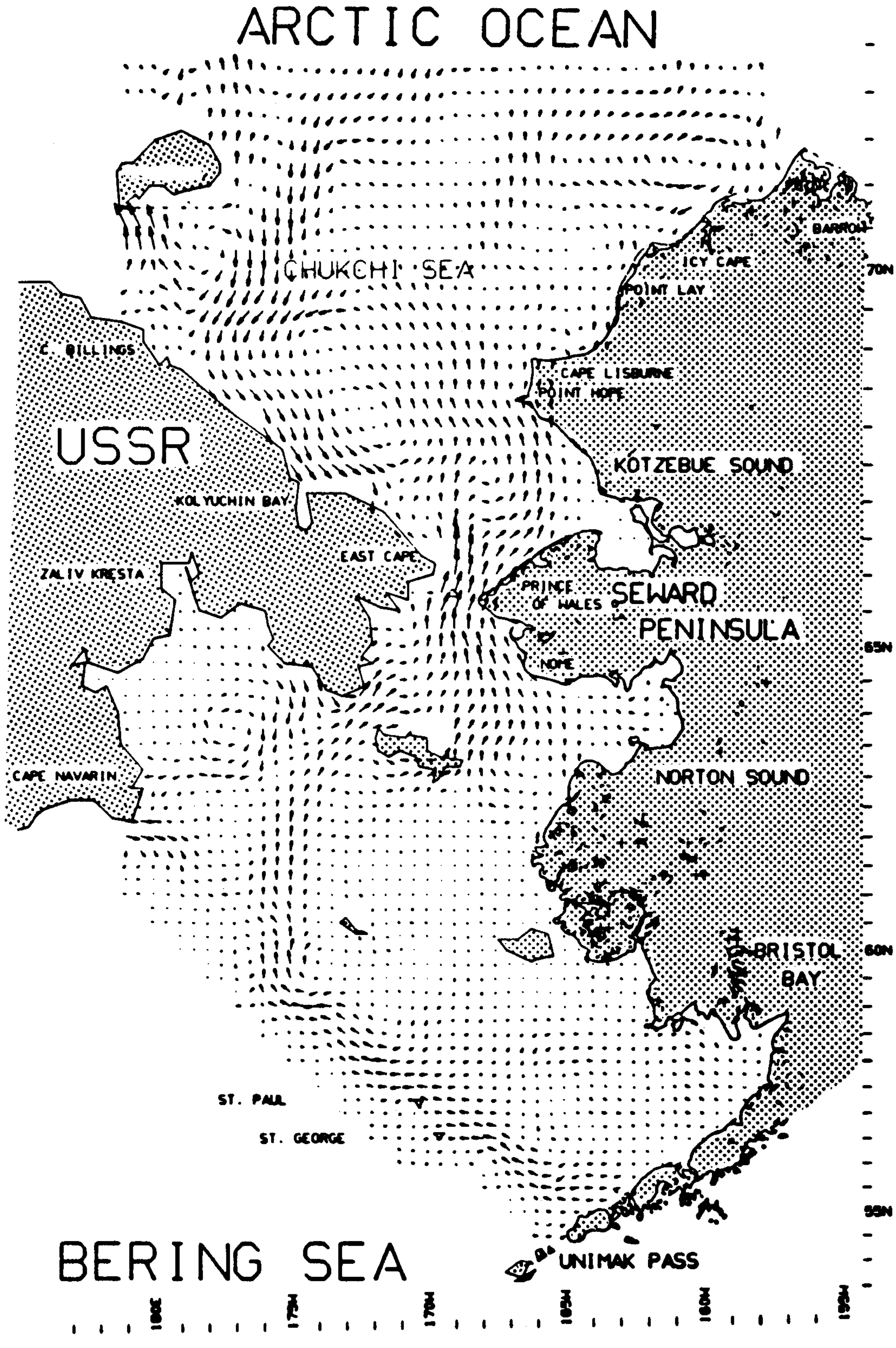

Fig. 3.39—Baroclinically induced residual currents at 5 m level after the initial 5-day spin-up. To reflect the realistic energy level over the continental shelf, astronomical tides are included in the computation and subsequently filtered with a two-dimensional numerical tidal eliminator.

Another noteworthy feature is the eddy structure west of Unimak Pass where an anticyclonic eddy is followed by a cyclonic eddy in the surface layer of a higher resolution model of Bristol Bay (Liu and Leendertse, 1979, e981a). Also of some interest is the baroclinic circulation near the Bering Strait (Fig. 3.40) where the computed surface pattern agrees extremely well with the observed long-term movement of water masses as compiled by Drury et al. (1981).

Even though the predominant transport through the Bering Strait is to the north, an atmospheric pressure difference across the Strait such as induced by a Siberian high or Bering cyclones could cause a temporary current reversal. Observed current through the Bering Strait with tidal bands filtered out (Fig. 3.41) reveals the northward transport with occasional reversals resulting from storms. The Bering and Chukchi Seas are relatively well studied in comparison with the Beaufort Sea, which is accessible for navigation only during a very short period in the summer, if conditions are favorable. Initial conditions were very difficult to obtain. A typical temperature distribution several meters under the water surface in the middle of the second layer of the model (7.5 m below the surface) is shown in Fig. 3.42. The water in a major part of the model is colder than 0°C.

From the simulations of the Beaufort Sea described earlier in this chapter, the density and tidal residual current field was determined by application of a low-pass filter on half-hourly data. Figure 3.43 shows this computed residual circulation. Even though the tides are weak in the Beaufort Sea, the combined density and tidal residual currents range between 2 to 6 cm/sec in a band near the Alaskan coast. Larger currents are found near the shallow areas around Mackenzie Bay and northeast of Point Barrow. The near-shore residual current for the Gulf of Alaska shelf is presented in Fig. 3.13. The offshore current (Alaskan stream) flows toward the southwest. Some field measurements have been made by Schumacher and Muench (1980).

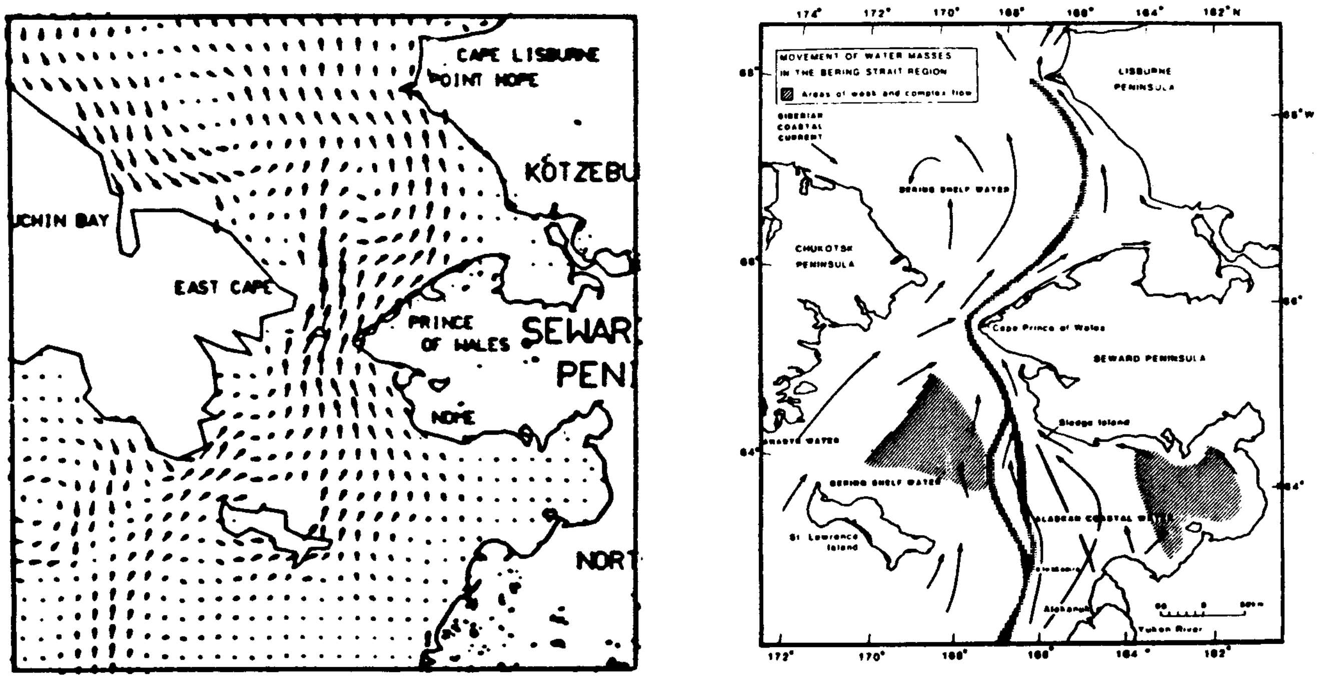

(A) (B)

Fig. 3.40—Comparison between (A), the computed long-term transport, and (B), observed long-term movement of water masses as compiled by Drury et al. (1981).

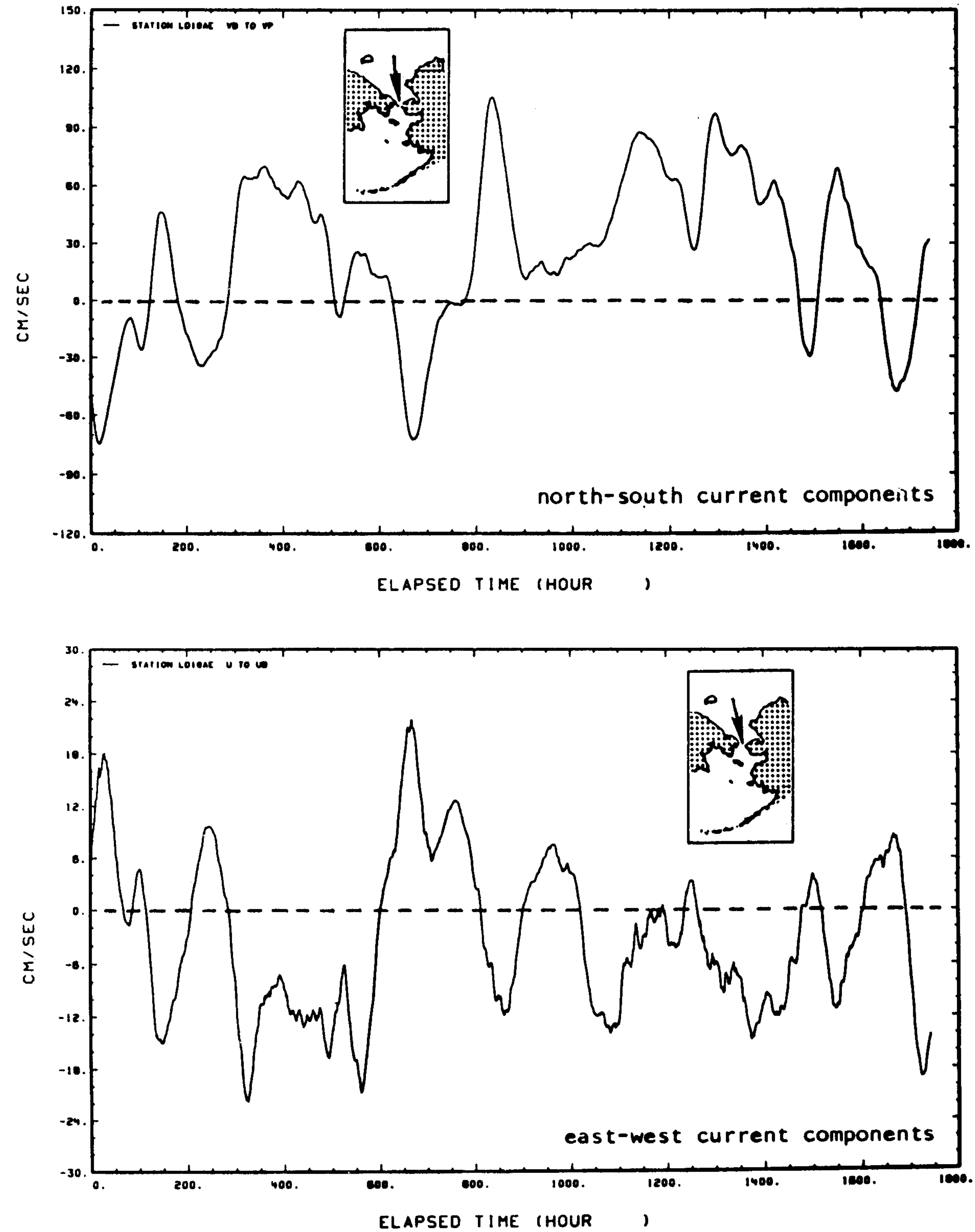

Fig. 3.41—Observed current components through the Bering Strait with the tidal bands filtered out. The general trend of northward flow is caused mainly by storm events and baroclinic and other residual transport. Sampling period covers November 4, 1982, through January 14, 1983 (by Dr. J. Schumacher of the PMEL, NOAA).

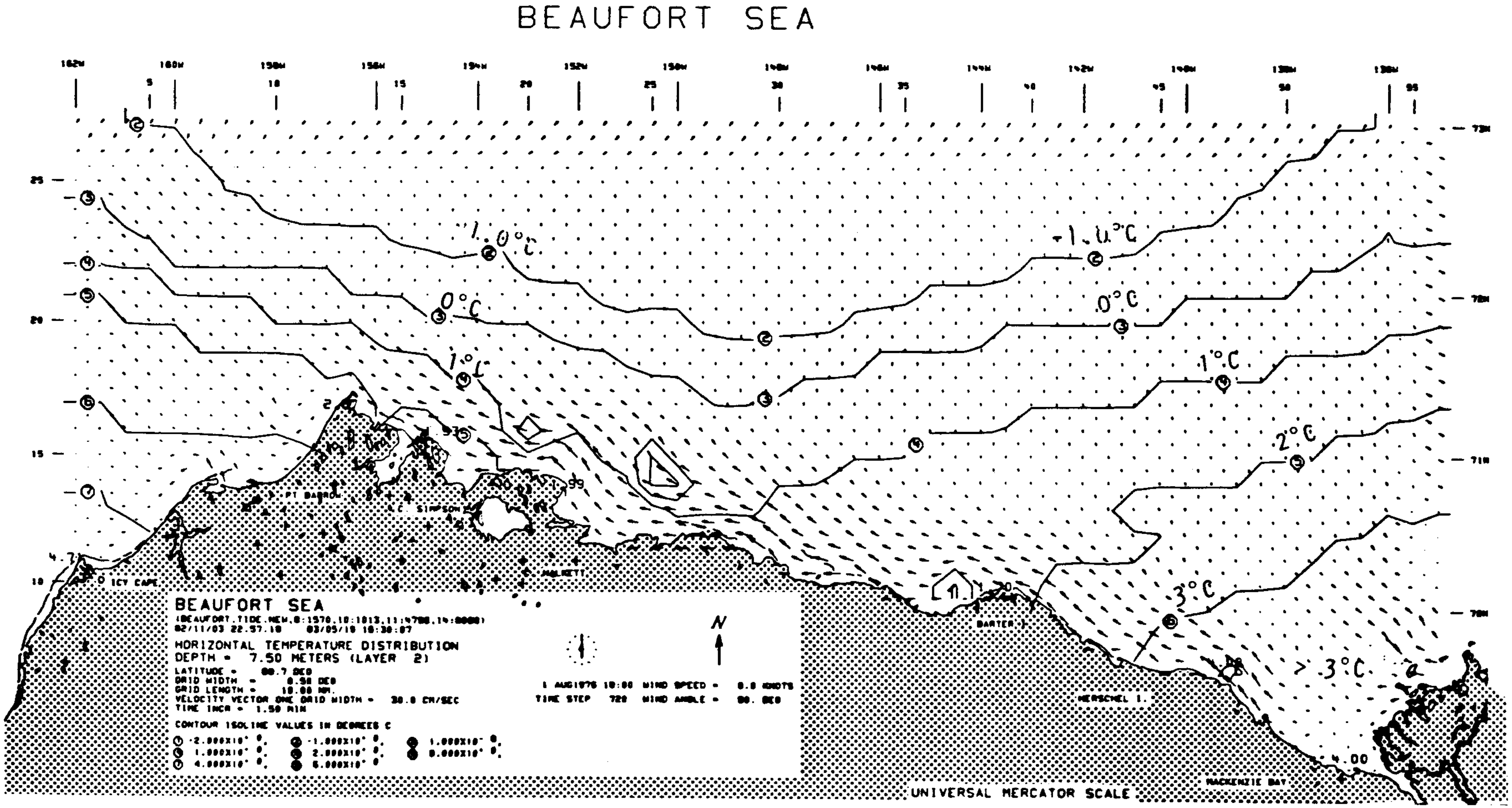

Fig. 3.42—Horizontal distribution of water temperature in the middle of the second layer (7.5 m level) of the Beaufort Sea model.

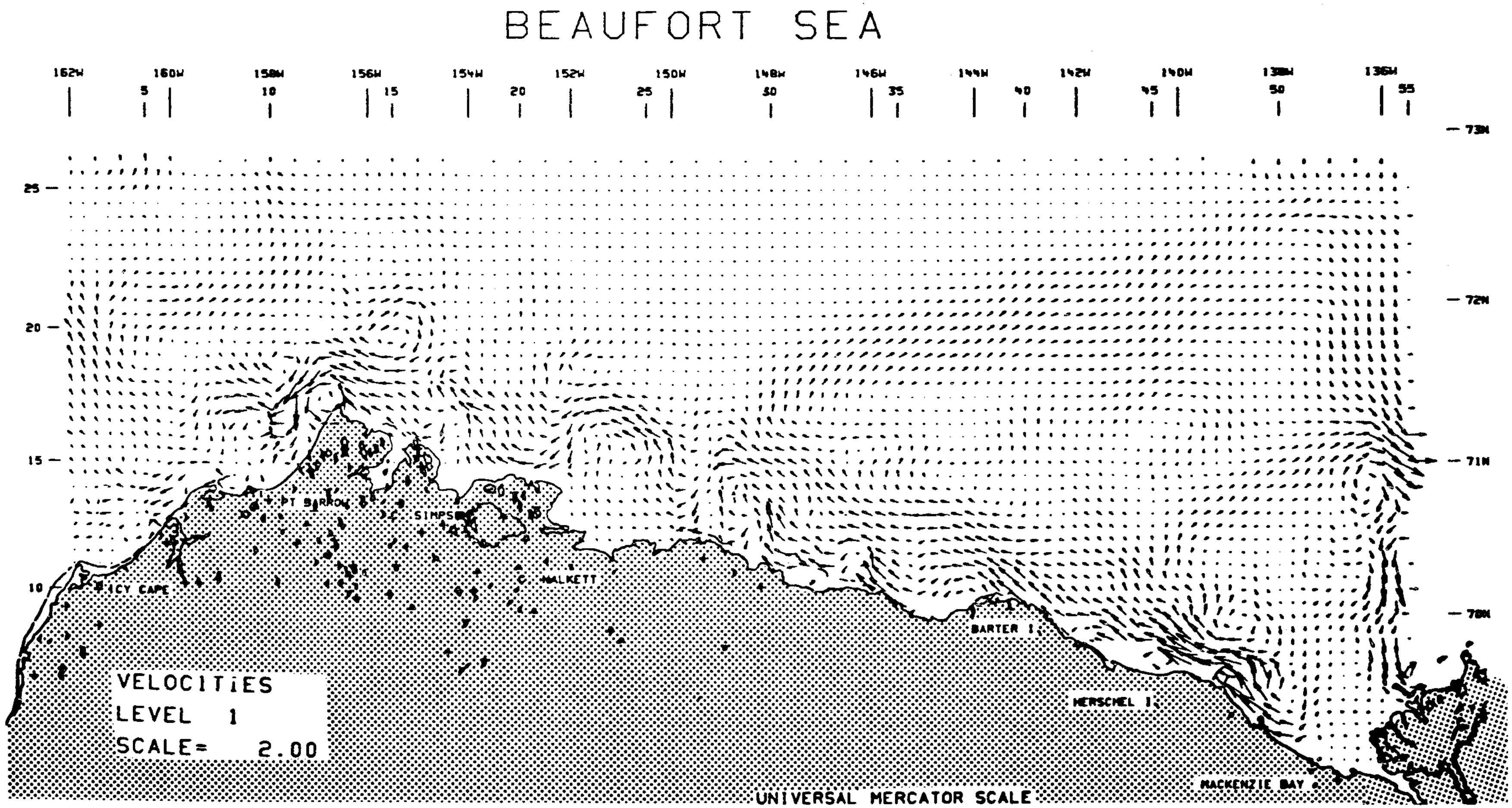

Fig. 3.43—Computed residual circulation in the surface layer with the plotting scale of 2 cm/sec per grid spacing.

4. MODELING WIND FIELDS

When an area in which the wind field is to be determined is small and located in the open ocean, a wind model is relatively simple to develop. Under such conditions a model can be built using random sampling according to a measured steady-state wind rose if observed data are available.

Another possibility is to use the mesoscale numerical weather model data to compute the wind field. Unfortunately, the strong winds of the extratropical cyclonic storms frequently occurring in this area cannot be simulated with this approach, which does not generate realistic winds in the computed wind fields. Therefore, the drift speed of the oil trajectories computed with this approach will also be inaccurate.

A high resolution of the wind field is required, as the area to be modeled is in one of two major extratropical depression tracks in the northern hemisphere, namely, the Aleutian Low, and the average radius of an Alaskan extratropical cyclone is about 500 km.

For example, when the sea-level pressure data from the National Center for Atmospheric Research (NCAR) are used, the spatial resolution is about 3.4° latitude (381 km) at 60°N (Overland et al., 1980; Macklin, 1984; Jenne, 1975; Holl, 1971), and a typical Alaskan extratropical cyclone would be represented by less than two grid points. With such a resolution realistic wind speeds cannot be generated, as the exponential pressure distribution within the cyclonic structure needs to be adequately resolved. Recent experiences (Dell'osso and Bengtsson, 1985) indicated that for large cyclones even with a fine mesh model, the computed cyclonic central pressure deficit is approximately 40 percent of the measured value.

Accurate modeling of the wind field of these depressions is very important, as high winds create large surface water movements, which are crucial in oil spill risk analysis. As the deterministic approach to obtain the time varying wind field is not feasible, a stochastic model was developed.

STOCHASTIC ANALYSIS OF REGIONAL WEATHER SYSTEM

Before entering the detailed computational methods it is perhaps more appropriate to give a general overview of the approach by which the wind data over the study area are analyzed and modeled. The basic approach involves three steps:

1. An analysis and determination of the baric types within the study area;
2. An assessment of measured weather elements at weather stations in relation to these baric types;
3. Computation of the circulation patterns belonging to the baric types by use of dynamic balances.[1]

These, in fact, constitute the three basic techniques of *synoptic climatology* (Barry and Perry, 1973). Because of the observed weather element whose probabilistic characteristic changes not only in space but also over time, the analysis is "stochastic" in nature.

[1]For oil spill trajectory computations, wind fields are required at intervals shorter than those at which the baric types are determined. These wind fields are obtained from dynamic balances of baric pressure fields obtained by interpolation of the two successive pressure fields.

In developing the model we first treat the weather system over the modeled area as a stochastic process whose evolution is represented by a series of transitions between certain "states" of the process. Previous analysis of the Alaskan weather system and of the Aleutian Low indicated that the residence time of a weather system is approximately between one to three days. It is plausible that the process is of the Markovian type. If one considers that the present weather state contains all essential elements that caused the weather to evolve from the previous state to the present state then the stochastic process is of the first order Markov type. It can be described or simulated if the probabilities of transition are known via the matrix of transitional probability

$$P\{p(ij)\} = \begin{bmatrix} p(1,1) & p(1,2) & \dots p(1,k) \\ p(2,1) & p(2,2) & \dots p(2,k) \\ \cdot & \cdot & \\ \cdot & \cdot & \\ \cdot & \cdot & \\ p(j,1) & p(j,2) & \dots p(j,k) \end{bmatrix} \tag{4.1}$$

$$0 \le p(ij) \le 1 \text{ and } \sum_{j=1}^{k} p(ij) = 1 \quad i = 1,2, \dots k$$

in which k represents the total number of possible outcomes, with p_{ij} denoting the probability from the weather state i evolved into the weather state j. Each weather state can represent, for example, an atmospheric pressure pattern over Alaska.

Also analyzed are the steady-state behavior of the process and the amount of occupation time of each weather state (within the state-space of the stochastic process).

The physical rationales behind the stochastic-synoptic approach are as follows:

1. Weather over a particular region, being a part of the global circulation system, possesses climatic characteristics unique to that area;
2. Governed by physical laws, the transition between one weather type to the next tends not to have an equally likely chance toward all possible types (i.e., it is not a purely random process). It must obey the dynamic elements associated with the evolutionary process;
3. The present weather state contains all essential elements that caused the weather to evolve from the previous state to the present state, thence to the next state.

The climatic characteristics of the Alaskan coastal area are unique. The climate is often dominated by low pressure centers over the Bering Sea and over the Gulf of Alaska, namely, the Aleutian Low. In an extensive effort, Putnins (1966) analyzed nearly 20 years of daily weather charts. As a result, he classified the baric pattern over Alaska into 22 types. In the classification, he also took into consideration the upper-level circulation. For each baric type, observed wind data at ground stations are summarized for each month. Raw data on the occurrence of each pressure type subsequently followed by another weather type are also tabulated. Transitional probability can then be calculated from these data.

In the classification of weather types by Putnins, surface pressures and upper-level pressures were used. To simplify the task, the original 22 weather types are condensed into 11 types for each season. Table 4.1 is an example of a transitional probability matrix tabulated in the form of a cumulative probability distribution. The transitional probability analyses are divided into spring/summer and fall/winter periods. Most pressure types exist in both seasons and 14 pressure types are considered. Altogether this covers approximately 98 percent of the original classification.

Tables 4.2 and 4.3 list the synoptic characteristics associated with each of the baric types. Figure 4.1 illustrates a typical type-1 summer baric pattern, whereas Fig. 4.2 shows a typical type-5 pattern.

For each weather type, speed and direction of the monthly mean value for each station are tabulated. Spatial interpolation between the stations are weighted according to the inverse square of the distances. Supplementary buoy data from the National Oceanic Data Center (NODC), as well as other triangulation analyses (Kozo, 1984), are also used.[2]

The variabilities of winds from the mean speed and direction associated with each pressure pattern are first analyzed at each individual station before spatial interpolation. The method to determine the statistical parameter of wind speed and direction needed for the simulation is described next.

MODELING WIND SPEED AND DIRECTION

The variability of wind speed from a given set of records is usually expressed in terms of its variance or standard deviation. The characteristic of wind speed variability is that it has a lower limit of zero. In the higher ranges, the variability decreases as the wind speed increases. This behavior is typically a physical process that fits an extreme-value probability distribution. Most commonly applied distributions in this class of problems are exponential, lognormal, Weibull, Rayleigh, and Gumbel probability distributions. For wind speed they are lognormal and Weibull distributions (Finzi et al., 1984; SethuRaman and Tichler, 1977; Kolmogorov, 1962; Oboukhov, 1962; Monin and Yaglom, 1975; Smith, 1971; Conradsen et al. 1984). The lognormal distribution was selected for the wind speed distribution not only because of its strong physical justification[3] but also for many of its convenient features—one of which is the ability to estimate its variance from the extreme value. In other words, we are able to estimate its standard deviation using its extreme value and the sample size. This was necessary because only the mean and maximum wind speed data were available from each of the ground stations during the 19-year period when data were used to derive the weather state transitional probability matrices. The procedure is as follows (see Table 4.4). For each weather station, the observed frequency of the maximum wind is computed from the number of wind speed observations associated with each weather type for that month. Frequency is simply the reciprocal of the total number of observations made during the 19-year period from the monthly station data.

By the nature of lognormal distribution, standardized units can be computed as shown in Table 4.4. The standardized normal units can be found in most mathematical tables (e.g.,

[2]Under contract from NOAA, Dr. Kozo has made special analyses to correlate wind parameters from coastal stations to offshore locations using buoy data. Results from these studies have been used extensively in the modeling work reported here.

[3]From a physical point of view, lognormality has been treated by Kolmogorov to "represent any essential positive characteristics" and became his third "well known hypothesis."

Table 4.1

CUMULATIVE DISTRIBUTION OF TRANSITIONAL PROBABILITY MATRIX ASSOCIATED WITH THE 11 WEATHER TYPES USED FOR SIMULATING OIL TRAJECTORIES, JUNE-AUGUST PERIOD

Weather Type	1	2	3	4	5	6	7	8	9	10	11
1	.6810	.7083	.7778	.8971	.9166	.9246	.9853	.9853	.9853	.9853	1.0000
2	.0195	.5135	.5663	.5749	.5901	.7391	.7391	.7391	.8560	.8560	1.0000
3	.2795	.4061	.8875	.9036	.9274	.9519	.9757	.9757	.9757	.9757	1.0000
4	.2610	.3586	.4397	.9158	.9995	.9995	1.0000	1.0000	1.0000	1.0000	1.0000
5	.4028	.4028	.4028	.4866	1.0000	1.0000	1.0000	1.0000	1.0000	1.0000	1.0000
6	.1701	.3351	.3544	.4069	.5188	.9020	.9020	.9020	.9020	.9020	1.0000
7	.3570	.4745	.5245	.5245	.5245	.5245	1.0000	1.0000	1.0000	1.0000	1.0000
8	.0000	.0555	.1111	.2061	.2061	.2894	.3310	.8208	1.0000	1.0000	1.0000
9	.0000	.1516	.1668	.1668	.1668	.3065	.3065	.3216	.9173	.9470	1.0000
10	.0000	.0000	.2500	.2500	.2500	.2500	.2500	.5000	.5000	1.0000	1.0000
11	.3895	.3895	.3895	.3895	.6006	.7434	.7434	.7434	.7434	.7434	1.0000

Table 4.2

SYNOPTIC CHARACTERISTICS FOR THE SUMMER BARIC TYPES

Type	Baric Characteristics
1	Entire area is dominated by a flat low with several centers over Alaska or near the coast
2	Low is at the east, plus a ridge over the Alaskan Peninsula
3	Low is stretched from the southwest toward the northeast. A high is located at the south or southeast of Alaska
4	Modeled area is part of the extensive low belt in the latitudinal direction
5	A pronounced low-pressure center occurs at the southwest of the Bering Sea moving toward the middle
6	A low is over Siberia
7	Low is centered over the Gulf of Alaska (southeast coast) plus a ridge over the northwest and north (over the Chukchi Sea)
8	A ridge dominates the Alaskan Peninsula, plus a low over the Gulf of Alaska
9	A high dominates the eastern section of Alaska
10	A trough from the east, plus a high over Siberia
11	Low in the west, plus a low over the Gulf of Alaska

Table 4.3

SYNOPTIC CHARACTERISTICS FOR THE WINTER BARIC TYPES

Type	Baric Characteristics
1	A flat low dominates the entire modeled area with several centers over Alaska or near the coast
2	Low is centered at the southeast coast, plus a ridge over the northwest and north (over the Chukchi Sea)
3	A belt of several lows occurs over the southern Bering Sea
4	A pronounced low-pressure center occurs at the southwest of the Bering Sea moving toward the middle
5	A high dominates the north over the Chukchi Sea
6	A high dominates the eastern Alaskan Peninsula
7	Dominated by a pronounced central low
8	Low at west plus a southern low over the Gulf of Alaska
9	Low is in east, plus a ridge over Alaska
10	Low centered at the southwest but stretched toward the northeast. A high is located at the south or southeast
11	Low centered at the southwest but stretched toward the northeast. A high is located at the south or southeast (over the Gulf of Alaska)

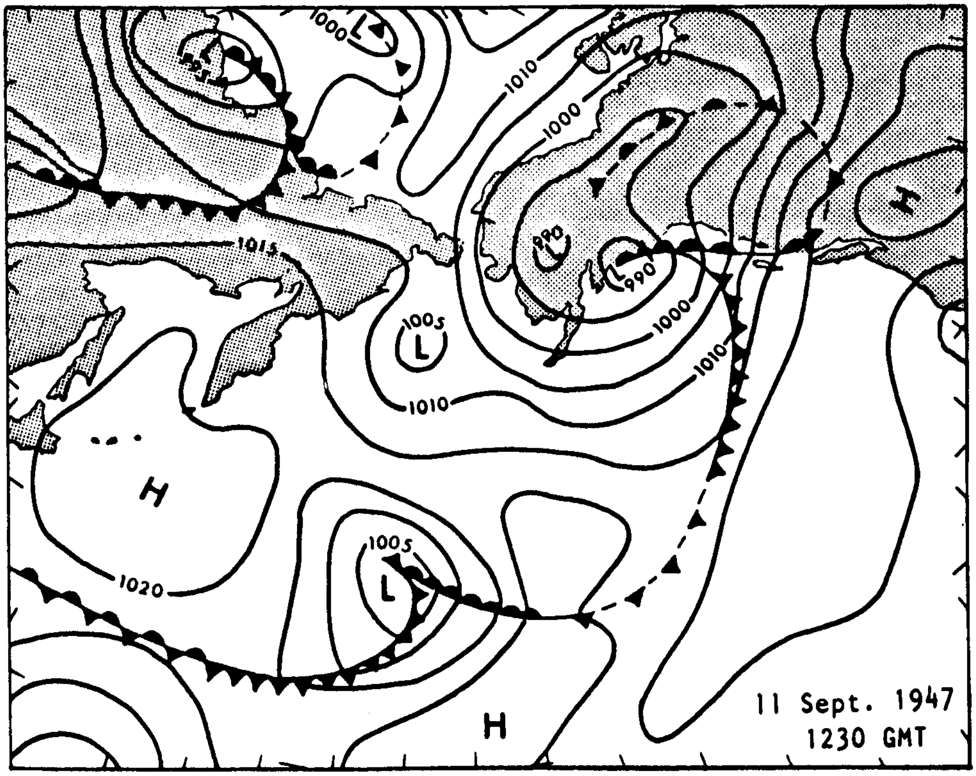

Fig. 4.1—Typical baric pattern where Alaska is dominated by a flat weak low with several centers over Alaska or near the coast.

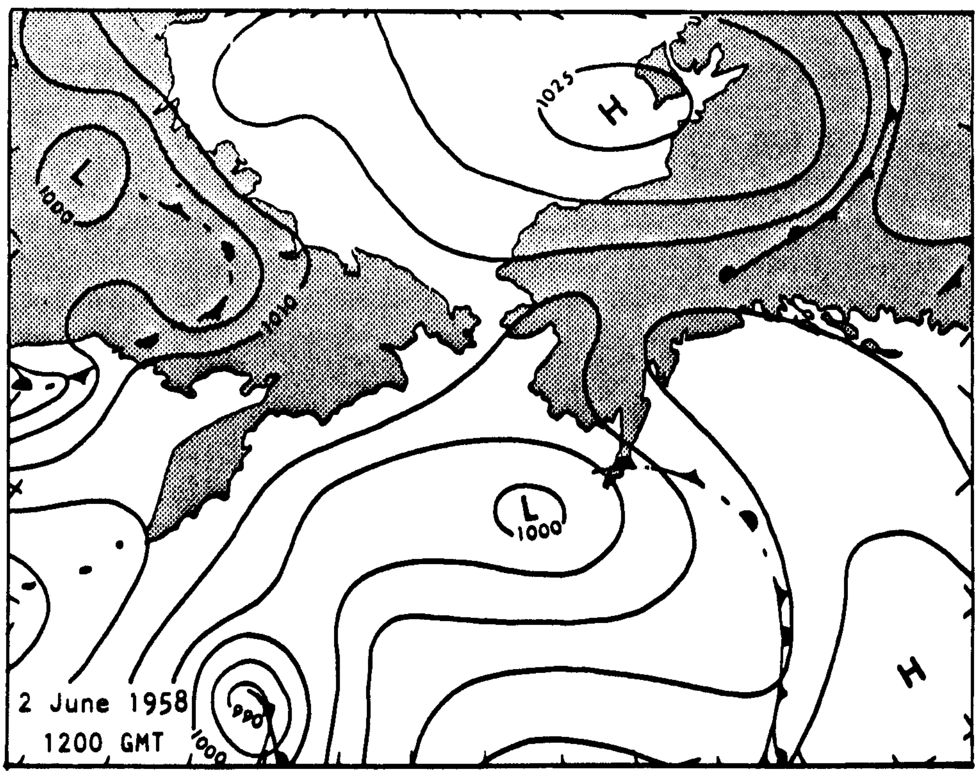

Fig. 4.2—Typical baric pattern where low is at the west over Siberia plus a ridge over Alaska.

Table 4.4

DETERMINATION OF STANDARD DEVIATION FOR WIND SPEED SIMULATION AT POINT BARROW FOR THE MONTH OF JANUARY (SAMPLE PERIOD, 19 YEARS)

Baric Type	Observed Frequency of Maximum Wind	Standardized $Z(q)$	Observed Wind: Direction (T)	Observed Wind: Deviation (2σ)	Observed Wind: Speed μ	(kn) Max.	Adjusted Marine Wind Speed: $ln(\mu)$	Adjusted Marine Wind Speed: $ln(max.)$	$\ln\sigma = [ln(max.) - ln(\sigma)]$ $Z(q)$	σ kn
1	0.00340	2.71	45	(90)	9	(28)	2.379	3.514	0.418	1.52
2	0.00393	2.66	225	(90)	7	(25)	2.128	3.401	0.478	1.61
3	0.00362	2.69	67.5	(90)	8	(25)	2.262	3.401	0.423	1.52
4	0.00363	2.69	90	(90)	13	(38)	2.747	3.820	0.399	1.49
5	0.00746	2.43	90	(90)	10	(34)	2.485	3.708	0.503	1.65
6	0.00216	2.86	101	(22.5)	10	(34)	2.485	3.708	0.427	1.53
7	0.00109	2.29	90	(45)	9	(34)	2.379	3.708	0.580	1.78
8	0.00387	2.66	270	(135)	8	(25)	2.262	3.401	0.428	1.53
9	0.00909	2.36	101	(67.5)	11	(33)	2.580	3.679	0.465	1.59
10	0.00704	2.46	90	(90)	11	(30)	2.580	3.583	0.407	1.50
11	0.00980	2.34	56	(112)	7	(27)	2.128	3.478	0.576	1.78

Abramowitz and Stegun, 1964). For better accuracy in the lower frequencies, tabulated values were obtained by rational approximation using Chebyshev polynomials (Hastings, 1955).

From the land-based station data, adjusting factors of 1.2 and 10° were used for marine wind speed and direction. These factors were determined from a field monitoring program relating land-based wind data (Nome) and the marine wind data (Norton Sound) carried out by the Pacific Marine Environmental Laboratory (PMEL, NOAA) (Overland, 1980).

As shown in Table 4.4, the standard deviation of wind speed is then computed by subtracting the logarithms of the maximum and the mean wind speed divided by the standardized normal units. The same procedure is used for each pressure pattern, each month, and each station.

To verify and adjust the probabilistic model of wind speed, data at Nome (from December 1, 1906, to December 31, 1980) were used and compared with the simulated data near Norton Sound. The simulated data were drawn at half-hour intervals. Each group of 1440 samples that represented a simulation period of 30 days was compared with the long-term monthly wind statistics. During this comparison, previously mentioned correlation factors between land-based wind data and marine wind conditions were considered. A total of 60 simulations were compared with the long-term data each of sample size 1440. The difference between the simulated wind speed and the observed wind speed for a winter period (December through May) was 3.0 percent too high. The difference for the summer period (June through September) was 3.7 percent too high. For the fall period (October through November) a simulated mean wind was 2.3 percent too low. These discrepancies were subsequently used for the final adjustments of mean wind speed for each of the weather types for that area.

In the case where a prevailing wind direction exists under a given pressure pattern, it is usually assumed that the prevailing direction is normally distributed with nonzero mean and a given variance (Riera et al., 1977; McWilliams and Sprevak, 1980, 1985). When winds are weak or from no prevailing direction, the distribution reduces to uniform distribution (McWilliams and Sprevak, 1980, 1985). In modeling wind direction, observed data of each weather type for that particular month were simulated with normal distribution. However, when data were categorized as "weak and variable," then a uniform distribution was used.

MODELING STORMS

In treating the Alaskan regional weather as a Markov stochastic process, we are, in essence, defining the weather and the regional wind field onto a finite set of stochastic states. Each state processes certain unique physical behavior characteristic of its baric pattern. The state of having an extratropical cyclone exist within a modeled area is one of the possible outcomes of the finite states of the stochastic weather system.

The principle of the computational procedure can be illustrated using a simple diagram (Fig. 4.3) in which the realization of a stochastic weather sequence is depicted. Starting from the lower left corner of the diagram, an initial state is selected from the steady-state probability distribution of all the weather types. Suppose the weather pattern type 4 is selected out of all possible outcomes. The next draw will be from the transitional matrix $P = (P_{ij})$. The probability of selecting a weather sequence 8 would be $p_{4,8}$, as shown in the diagram. The same weather type can also be selected at the probability $p_{2,2}$, which is the second diagonal element of the probability matrix. In the subsequent draws, solid lines represent outcomes of the random selection.

Suppose a type-5 weather pattern is selected. The sea-level pressure distribution associated with this particular weather type is a pronounced low pressure center occurring at the southwest of the Bering Sea moving toward the middle (Table 4.2). Under this condition, the simulation program would divert the computation to a subprogram handling the probabilistic simulation of a moving extratropical cyclone. In the subprogram, parameters associated with the cyclone are derived from synoptic analyses using a subset of the 19-year data from which the transitional matrices are derived. Essential parameters for the computation of a moving cyclonic wind field are, namely, the spatial distribution of the cyclogenetic process, the distribution of central pressure, the forwarding speed, and persistency. The last parameter would govern the number of consecutive weather states in which a cyclone exists until a cyclolytic process prevails. Under this condition a weather state that has the highest probability of following a cyclonic state is likely to be selected within the state transitional matrix.

To determine parameters of the Aleutian Low, several groups of climatological data were analyzed. For the frequency of occurrence, synoptic data between January 1966 and December 1974 (Brower et al., 1977) were used. Figure 4.4 gives the spatial distribution of cyclonic events in each subarea. The area west of 160°W and north of 50°N is classified as the southern Bering area, since its cyclonic flow dominates the entire southern Bering Sea. Figure 4.4 shows no major seasonal trend in the number of occurrences of the cyclonic activities over the modeled area. Table 4.5 gives the two-dimensional probability density function (*pdf* $\times$ 10000) of the occurrences over the computational grid for the weather simulation. The spatial resolution of the grid network is deemed necessary to provide an accurate wind field considering the pressure distribution of a typical extratropical cyclone.

For the probability distribution of the intensity, daily synoptic data for five years (1949–1953) were adapted. The original data were analyzed by Schutz (1975) for the climatological modeling work conducted at The RAND Corporation. In the analysis the normalized (using the *pdf* of the mean value = unity) frequency distribution of intensity based on synoptic characteristics of five-year January data is shown in Fig. 4.5. This sampling period is within the 19-year period when identical weather data were used to derive the weather state

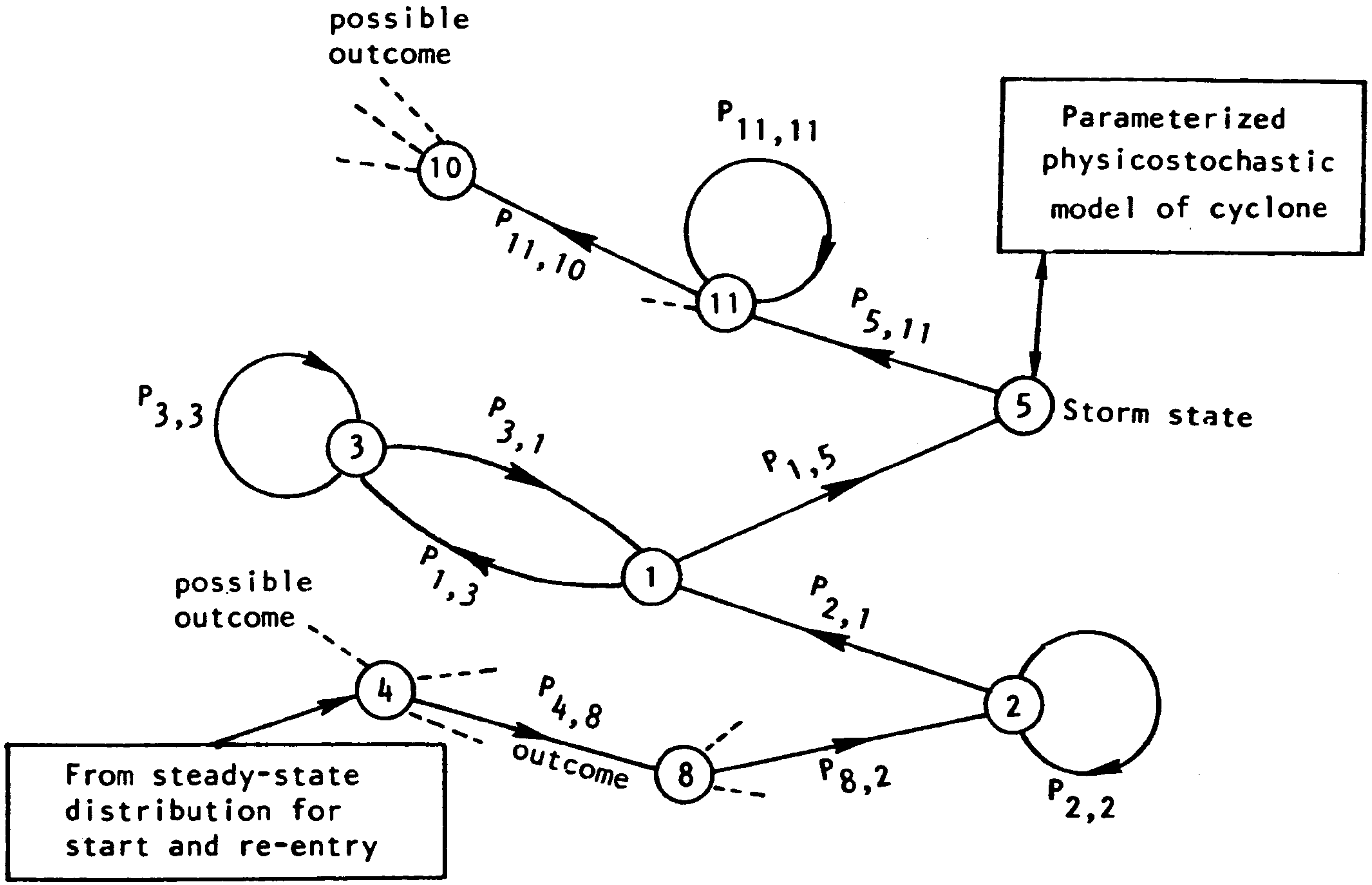

Fig 4.3—Abstract diagram showing transition of stochastic weather state in conjunction with the parameterized physicostochastic model of a cyclone.

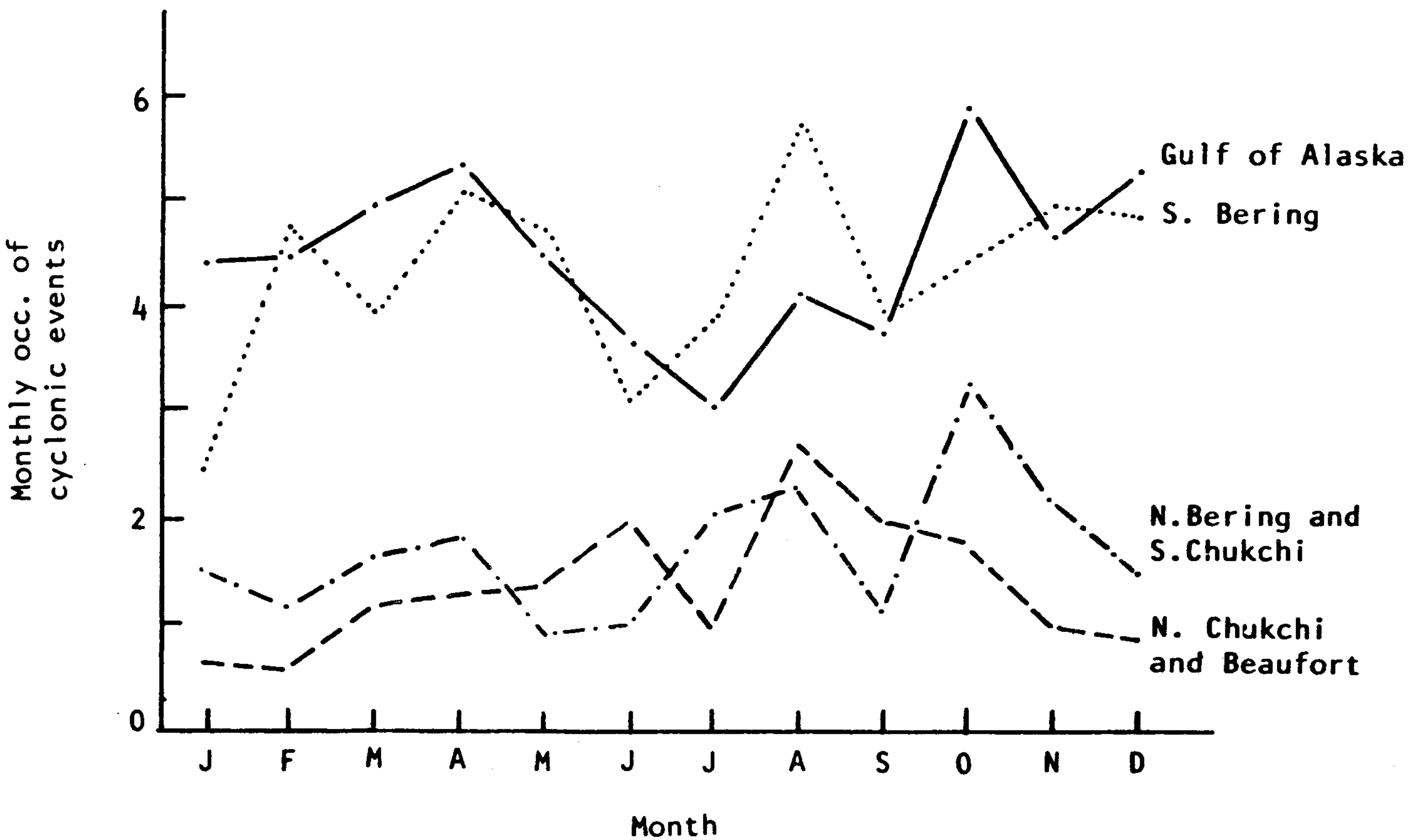

Fig. 4.4—Monthly occurrences of extra-tropical cyclones by subareas (January 1966 — December 1974).

Table 4.5

SPATIAL DISTRIBUTION OF PDF (x10000) OF LOW PRESSURE CENTERS

Latitude	180°W					170°W					160°W					150°W					140°W					130°W	Σ
80°N	1	0	0	0	1	1	1	1	1	3	1	1	1	2	0	1	1	2	0	3	1	1	0	0	0	0	23
	2	1	0	3	1	0	1	1	1	2	1	0	0	0	0	2	1	2	1	1	3	2	1	0	1	0	27
	1	1	1	2	0	2	0	2	0	0	0	2	3	0	0	1	4	1	0	1	2	1	1	1	1	0	27
	1	1	1	1	0	0	0	1	0	0	1	2	3	2	0	0	0	0	1	1	1	4	0	0	0	0	20
	1	1	1	2	0	1	1	2	3	2	1	2	0	2	0	0	0	1	1	1	1	1	2	0	0	0	26
	1	0	3	0	1	1	0	1	0	3	0	1	3	1	2	1	0	0	1	2	2	0	0	0	1	0	24
	1	1	1	2	2	2	1	0	0	0	0	0	0	2	1	0	0	1	1	2	3	1	3	1	0	2	27
	0	2	0	0	2	0	1	1	1	1	1	1	4	0	3	0	2	0	2	5	2	1	0	0	0	0	29
	2	0	1	1	1	1	1	3	2	1	2	2	0	4	2	2	2	1	3	1	3	2	2	1	0	0	40
	3	4	1	0	2	1	1	1	0	0	4	1	1	1	1	2	3	0	0	0	1	1	2	3	0	0	33
	1	1	1	2	2	3	3	1	3	2	4	0	1	4	2	2	0	3	2	1	3	1	1	2	1	0	46
	4	2	4	2	5	2	1	3	2	3	6	0	3	2	1	4	1	2	2	3	0	3	1	4	1	0	61
	4	3	1	2	3	4	6	2	2	4	1	2	2	3	1	1	6	3	3	2	4	3	2	4	5	0	73
	2	3	4	4	1	3	1	1	3	1	0	1	3	6	2	1	4	1	4	4	4	2	1	2	1	1	60
	4	5	3	3	7	2	3	3	3	2	3	5	2	2	0	6	1	1	3	3	2	5	4	0	1	0	73
70°N	6	1	5	5	3	1	5	3	6	2	4	2	2	3	0	2	1	4	2	4	2	3	4	5	3	0	78
	2	5	4	3	6	4	8	2	2	5	4	6	4	5	5	1	2	3	2	5	4	5	4	0	2	2	95
	1	2	3	6	4	6	8	2	8	6	2	4	5	3	3	5	2	5	4	6	8	7	6	0	4	0	110
	1	3	7	7	1	7	5	10	7	8	6	5	5	2	5	4	3	5	8	7	3	1	4	7	3	1	125
	6	7	8	2	6	6	5	1	6	4	4	0	6	3	4	7	5	5	3	7	3	5	10	4	6	0	123
	6	10	7	7	8	7	15	4	5	2	3	4	4	3	5	11	6	4	7	7	4	6	4	2	1	0	142
	2	4	12	4	10	9	12	7	8	6	10	6	3	2	7	5	5	3	3	7	7	8	6	6	7	2	161
	4	9	10	5	4	9	9	5	10	6	7	5	8	3	8	7	9	8	6	4	11	4	6	1	3	2	163
	9	7	7	5	9	4	5	8	3	9	7	5	6	6	8	5	7	7	17	8	5	4	5	8	4	1	169
	10	7	14	7	7	12	12	8	7	8	7	10	9	5	7	7	7	9	3	8	5	10	10	12	3	3	207
	10	4	10	6	6	6	3	4	8	6	4	8	8	10	8	5	13	9	3	5	14	8	10	13	6	3	190
	8	5	11	9	14	4	5	6	10	9	5	10	11	11	12	6	8	6	6	12	16	10	7	12	9	2	224
	6	9	14	12	18	8	14	13	13	7	6	12	17	3	12	10	10	9	11	6	11	12	12	10	9	2	266
	11	9	11	17	13	8	8	7	12	9	11	7	12	10	12	7	10	10	11	14	9	9	9	3	5	2	246
	9	8	14	19	9	10	8	6	16	5	17	7	9	2	8	3	8	10	10	10	13	12	9	8	4	4	238
60°N	7	9	11	11	14	13	16	15	11	9	12	14	12	10	14	9	11	12	9	5	15	15	8	4	8	1	275
	13	13	13	11	14	14	10	16	9	10	14	18	10	12	8	15	10	11	9	19	12	9	17	7	6	2	302
	11	14	17	11	13	14	14	16	15	14	12	7	8	11	17	16	14	15	8	8	16	5	18	15	8	1	318
	19	16	17	12	10	16	13	19	10	11	7	12	14	14	24	15	17	15	20	13	21	11	8	20	8	5	367
	13	14	20	26	14	17	18	20	14	10	19	15	22	12	10	16	14	14	18	12	13	20	14	12	11	1	389
	18	20	19	20	16	18	17	19	15	17	17	15	11	19	15	23	16	10	15	16	10	20	20	11	14	4	415
	21	12	18	26	22	19	22	10	17	19	19	17	17	7	15	15	19	19	18	19	21	12	17	12	16	3	432
	18	18	15	24	16	13	18	19	16	19	14	21	18	18	17	25	24	13	19	23	16	20	21	23	15	4	467
	12	21	19	24	23	16	21	24	27	13	16	17	17	15	17	24	25	23	34	25	21	24	18	14	13	0	503
	15	18	18	31	20	17	16	16	17	20	22	30	20	16	20	25	18	31	24	23	23	16	15	22	20	4	517
	21	20	34	20	21	22	19	28	23	23	13	22	18	15	11	17	26	19	24	30	24	16	17	8	18	5	514
	20	32	17	25	15	30	25	24	23	24	21	19	21	21	17	24	24	27	37	25	20	16	18	15	13	2	555
	20	18	20	20	28	28	15	21	21	22	23	16	31	27	26	20	20	29	26	22	22	25	23	10	16	11	560
	18	32	36	36	31	29	31	18	23	21	22	21	20	27	32	32	26	24	40	29	35	28	24	26	19	8	688
50°N	25	29	31	26	25	26	23	17	20	16	28	17	16	16	22	23	27	18	27	36	23	25	17	16	19	4	572
Σ	370	401	464	461	428	416	421	391	403	364	381	372	390	342	384	407	412	395	448	445	439	394	381	324	285	82	

transitional probability matrices as well as the wind statistics collected at all coastal stations. A mean value of 975.0 mb with a standard deviation of 10.66 mb was obtained from the synoptic analyses of the Aleutian Low.

The average forward speed and frequency of persistence of cyclones are shown in Fig. 4.6. Each 36-hour period is treated as a time unit that is subdivided into three 12-hour periods for the convenience of later convolution. From Fig. 4.6, the storm duration with the highest probability of occurrence is 1.0 to 2.0 days. This is followed by 3.0, 4.0, and 6.0 days, in a descending order.

The steady-state probability distribution of storm events can also be represented by transitional probability statistics in which a storm having longer persistence is equivalent to a "storm" weather state followed by another "storm" weather state. During a simulation, events like this are treated by continuing the storm track with new speed and direction sampled according to the observed statistical parameters associated with the Aleutian Low.

In certain aspects more refinements of the general approach are desirable. This usually requires more data as well as more detailed analyses. Dominant weather features like the persistent Aleutian Low make the synoptic weather analyses an effective way to simulate its behavior; without such prominent weather features this method would be less effective.

A unique weather feature in the modeled area is a pronounced low pressure center coexisting with a quasi-stationary Siberian High (Fig. 4.7). Because of the characteristic relationship between a pressure field and the veering angle of the surface wind field, the wind direction at sea level near the Bering Strait would have a direction of nearly due south. If a strong wind field persists long enough, a substantial amount of ice would migrate southward through the Bering Strait thus creating an "ice breakout" condition (Ahlnas and Wendler, 1979). As shown in Fig. 4.8 for a typical winter ice condition, under a wind stress of 0.5 pascal, it requires a fetch of 200 km to cause a breakout (Reiner, 1979). This corresponds approximately to a critical wind speed of 26 kn blowing over ice. Using 19-year observed wind data from the nearby weather station (Kotzebue) resulted in a probability of 2.3 events per each winter period (from November through June).

COMPUTING CYCLONIC SURFACE WIND

Surface wind speeds and directions associated with a cyclonic baric pattern are computed according to the following procedures. The pressure distribution in the cyclonic field is schematized with the pressures at the center and the outermost closed-isobar according to an exponential function often used to describe the cyclones.

The pressure at the center is selected at random according to the mean and the standard deviation associated with the Aleutian Low (Fig. 4.5). The outer pressure is selected by the long-term monthly average sea-level pressure in the modeled area (Fig. 4.9). The continuous pressure distribution is of the form:

$$P(r) = p_c + (p_n - p_c) \exp(-A/r^B) \tag{4.2}$$

where p_c is the central pressure and p_n is the ambient pressure. For the average extratropical cyclones in this area, the value of A is selected to be 30 nautical miles (i.e., 0.5° latitude). Slight modifications can be made because of the eccentricity associated with extratropical cyclones. But they were not implemented for the oil spill trajectory simulations.

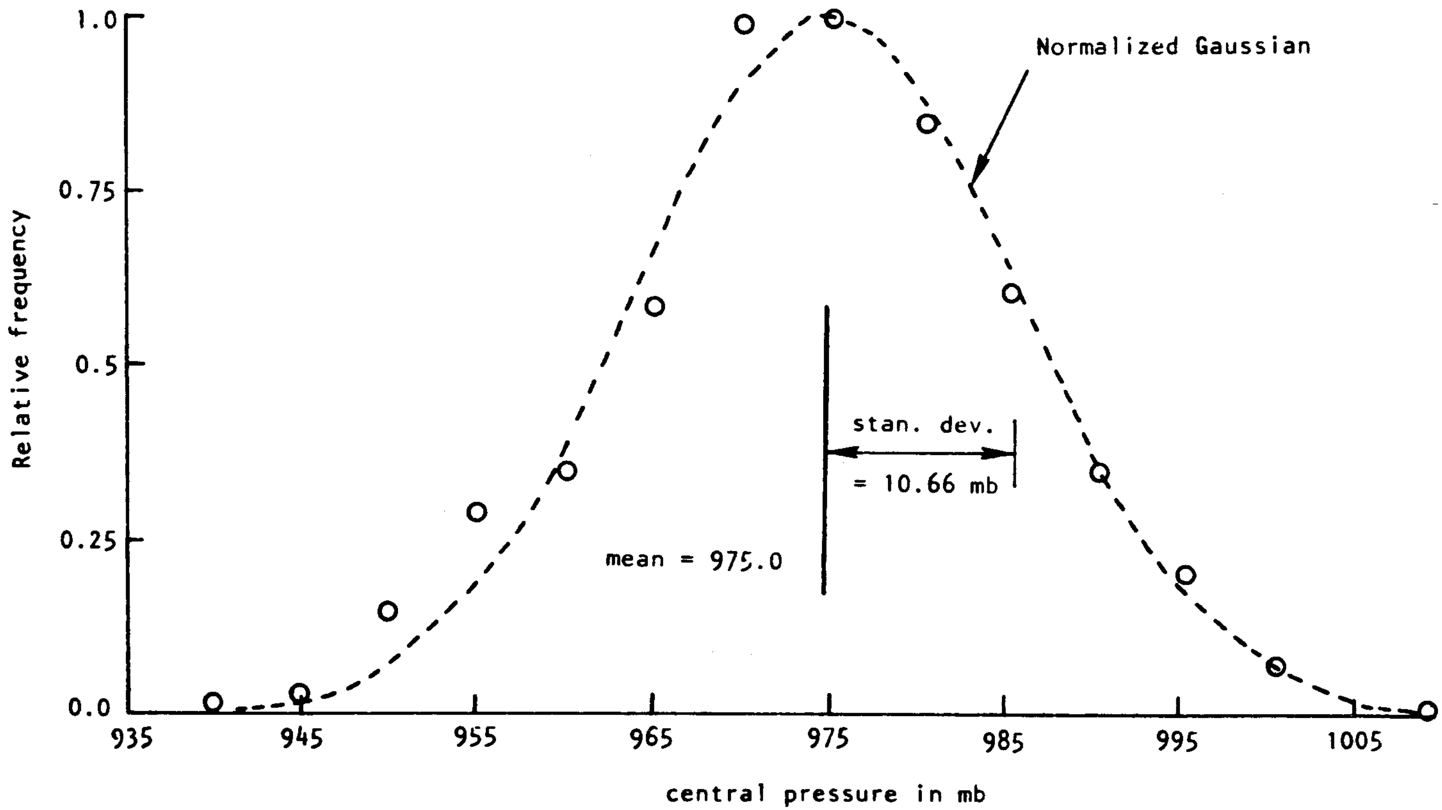

Fig. 4.5—Normalized frequency distribution of intensity based on synoptic characteristics of five-year January daily weather maps at 1230Z during 1949-1953. The sampling period is within the 19-year period when the identical weather charts were used for deriving the transition probability matrices. The original synoptic analyses were made by Schutz (1975).

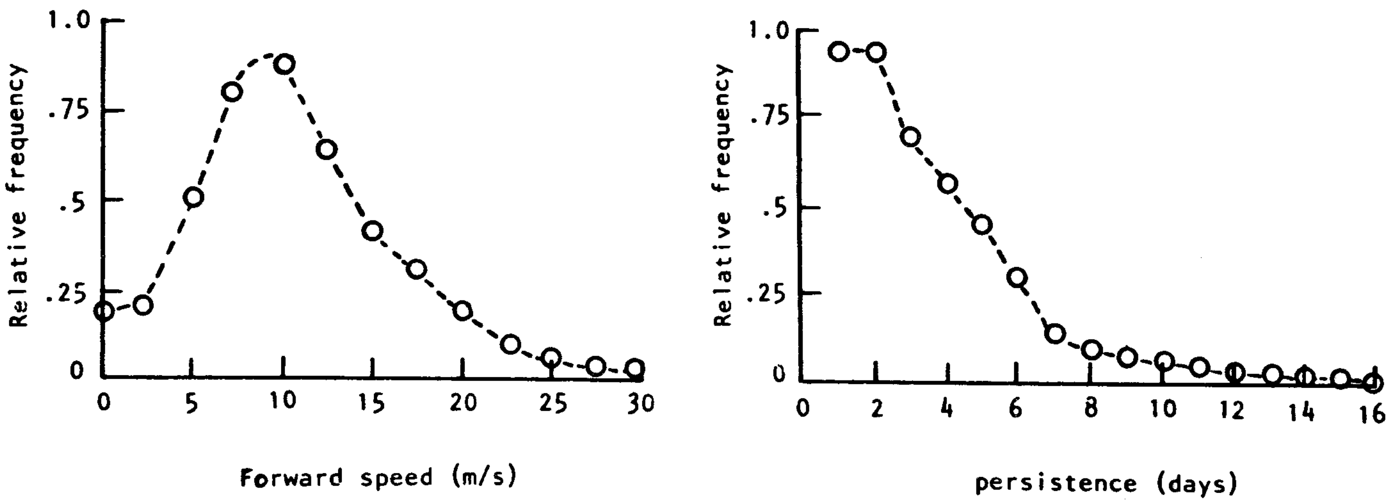

Fig. 4.6—Normalized frequency distribution of forward speed and persistence based on synoptic characteristics of five-year January daily weather maps at 1230Z during 1949-1953. The sampling period is within the 19-year period when the identical weather charts were used for deriving the transition probability matrices. The original synoptic analyses were made by Schutz (1975).

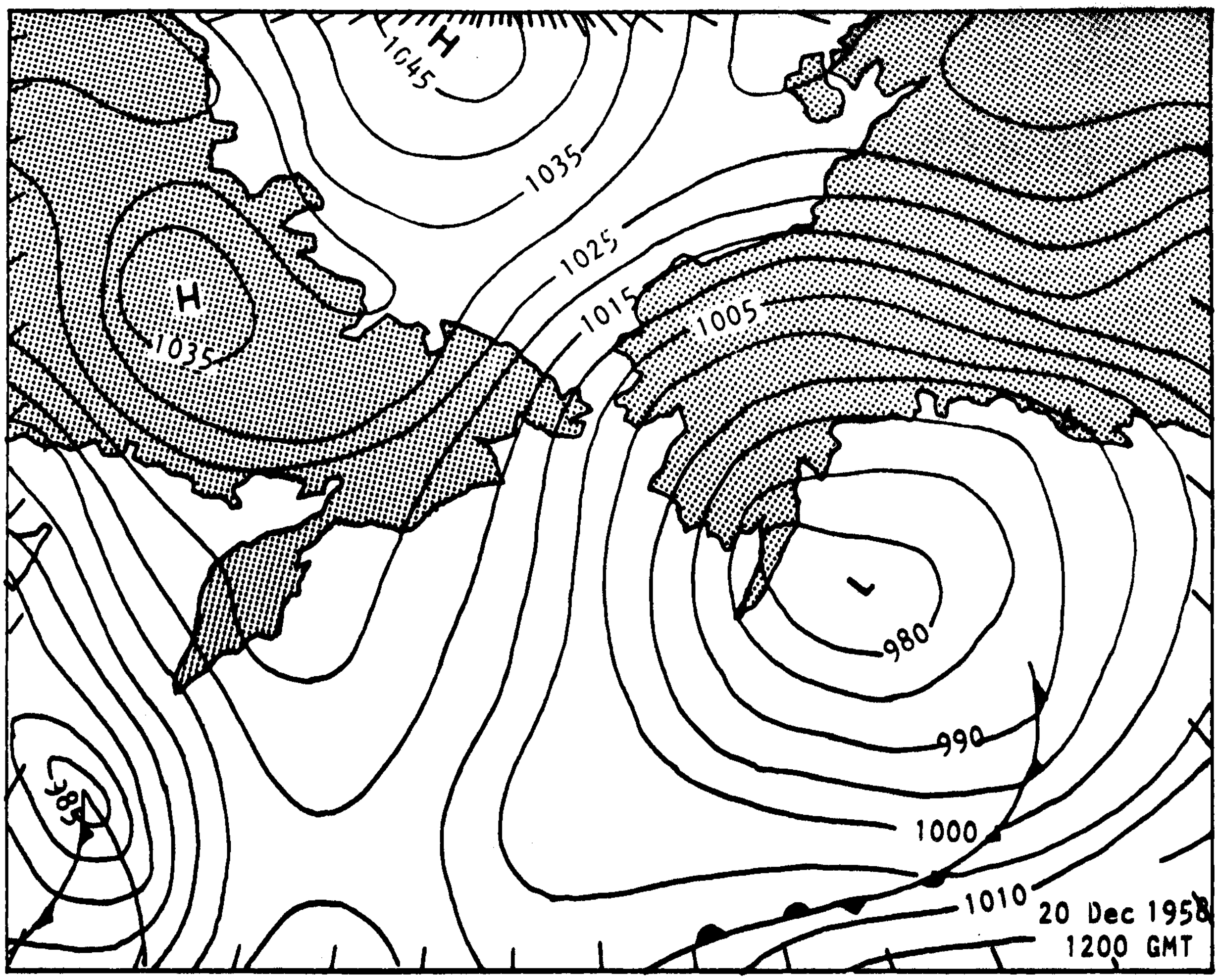

Fig. 4.7—Typical baric pattern where a pronounced low existed over the modeled area. In this case, the Eastern Low coexisted with a Siberian High. This pressure pattern creates strong southerly air flow near the Bering Strait and thus may induce an ice breakout through the Strait.

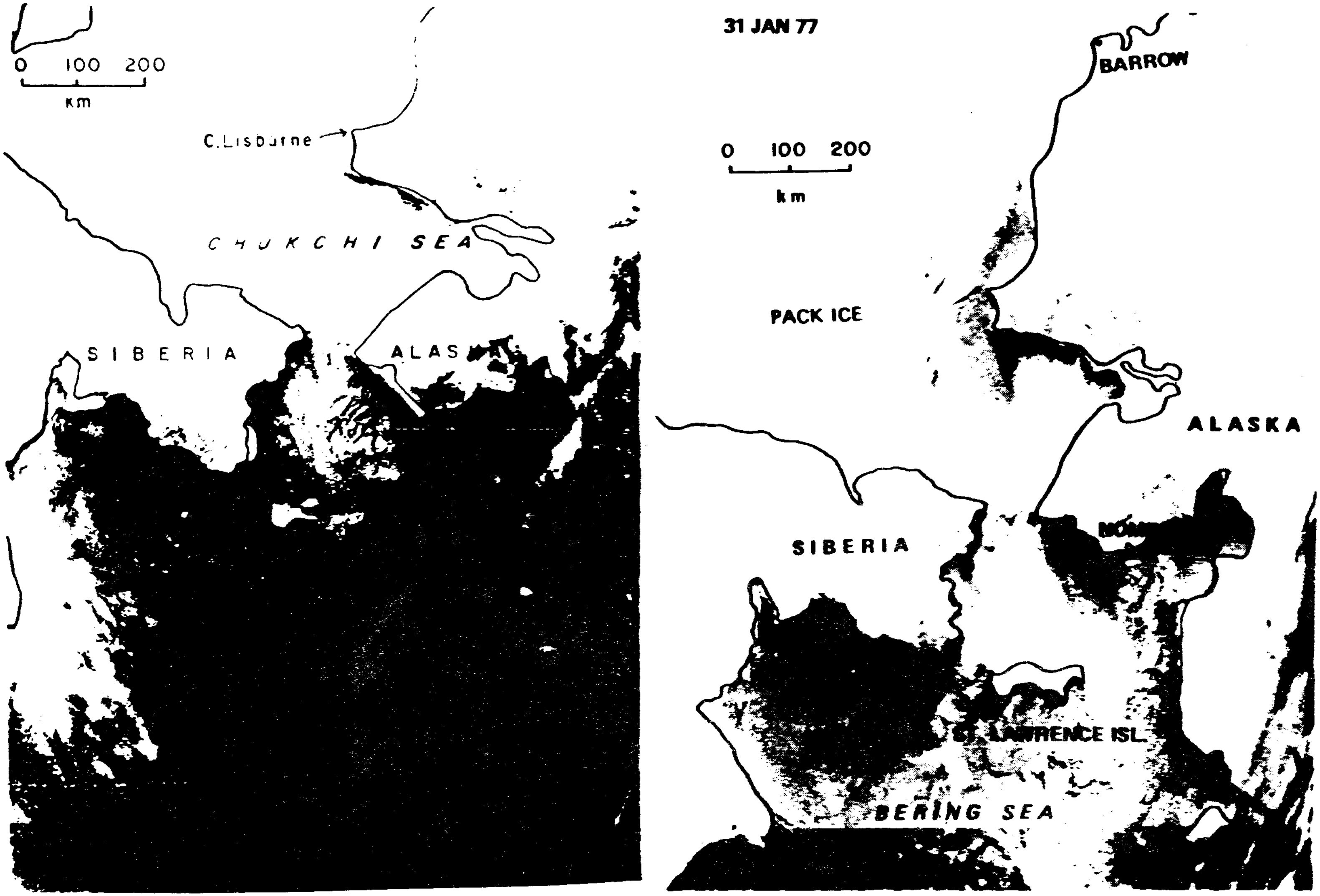

Fig. 4.8—Surface-temperature-enhanced infrared satellite (NOAA-5) images showing two events of ice breakout through the Bering Strait. The left is for March 20, 1978; the right is for January 31, 1977. Both were adapted from Ahlnas and Wendler (1979). These images imply that ice could pass either to the east or to the west of St. Lawrence Island.

The value of coefficient B is taken as 1.0. Higher values are often selected for a tropical cyclone. The average distance between the center and the outer closed isobar is approximately 5° latitude. The sea-level pressure at the outer closed isobar is obtained from the long-term monthly average SLP for the modeled area. The gradient wind speed is then computed using:

$$V_{gr}^2 + fr\ V_{gr} = \frac{r}{\rho_a}\frac{dp}{dr} \tag{4.3}$$

where f is the Coriolis parameter, r is radius, and dp/dr is the local pressure gradient. During the oil spill trajectory simulation, the wind field is computed every half hour. Finally, the computed gradient winds are adjusted for speeds and directions to obtain winds at sea surface (10 m level). For the adjustment, the method of Hesse (1974) and Hesse and Wagner (1971) was used. The method was selected because it was derived from extensive field data associated with the extratropical cyclones. For other models, the reader is referred to the work of Cardon (1969) and Brown and Liu (1982).

The bulk momentum transfer coefficients are computed according to the air-sea temperature difference (Fig. 4.10) and the results compiled by Kondo (1975) and Garratt (1977), and later the updated results were compiled by Wu (1982). The eccentricity associated with the extratropical cyclones was investigated. It was found, however, that synoptic analyses could not provide enough data to support a definite asymmetric parameter so that the gradient wind field can be modified. This aspect is worth further study.

With the methods described in this chapter, the stochastic model is tested by simulating 60 monthly cycles each having 1440 half-hourly wind data sets. For three stations in the modeled area, the frequency of occurrence of wind speeds at defined intervals from all the directions is plotted, as well as the percentage of occurrences from these directions. The three plots at the top of Fig. 4.11 are the direct outputs of the simulations. In this figure the observed data (obtained from Brower et al., 1977) are also plotted in a similar manner. The simulated and observed wind data are not directly comparable, as the model generates from 16 directions, whereas the compiled field data use only eight directions. It will be noted, however, that computations show good agreement with observations.

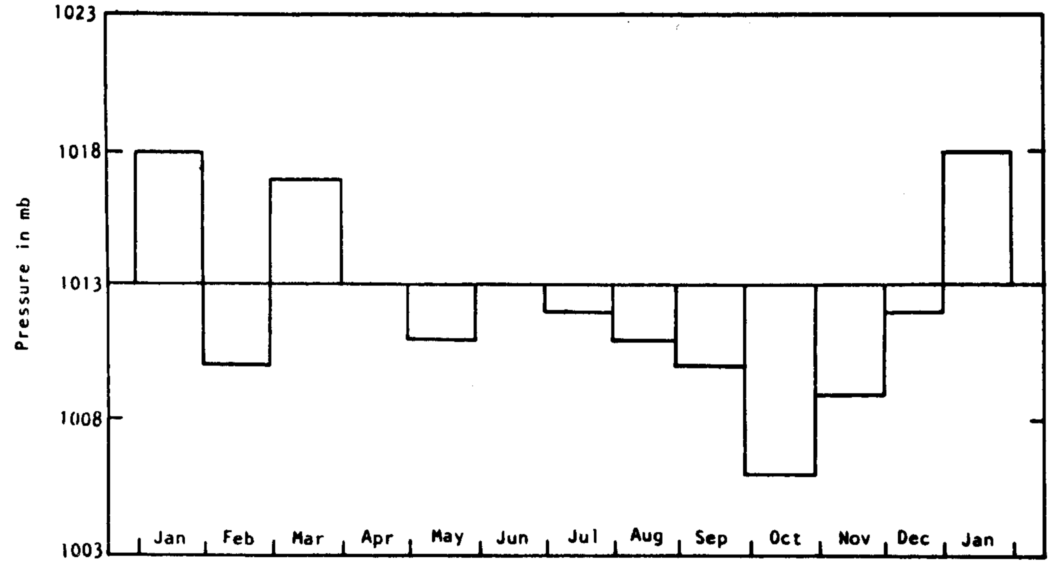

Fig. 4.9—Monthly Meridinal average sea-level pressure over the northern Bering Sea at 65°N latitude.

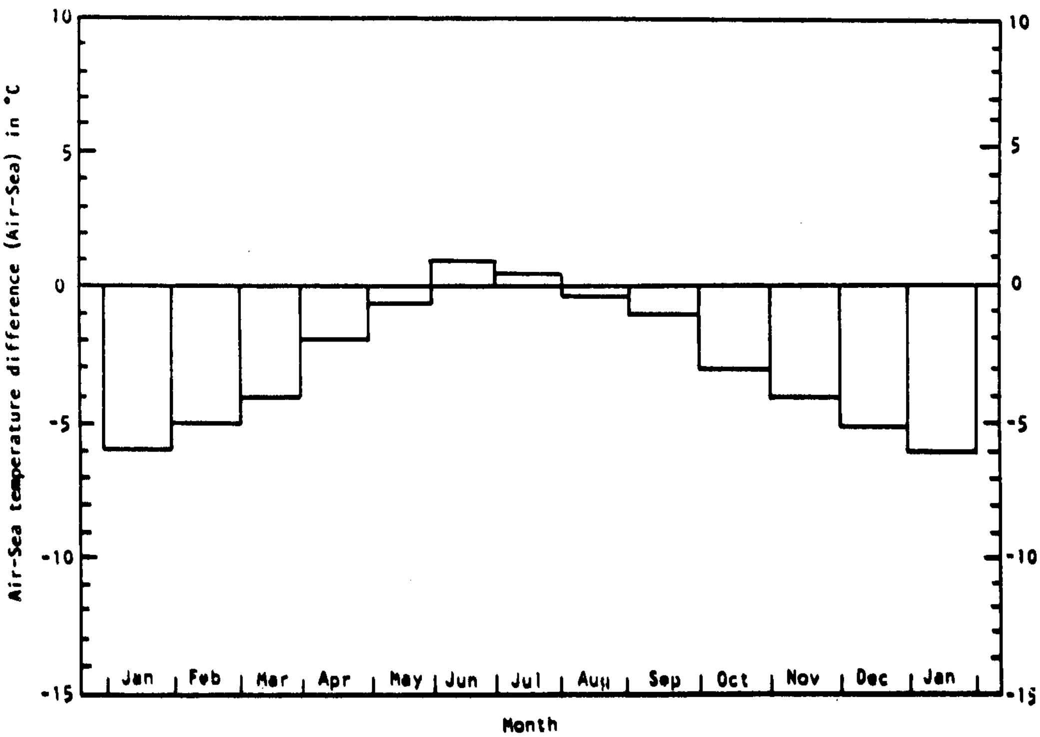

Fig. 4.10—Monthly average air-sea temperature difference over the eastern Bering Sea.

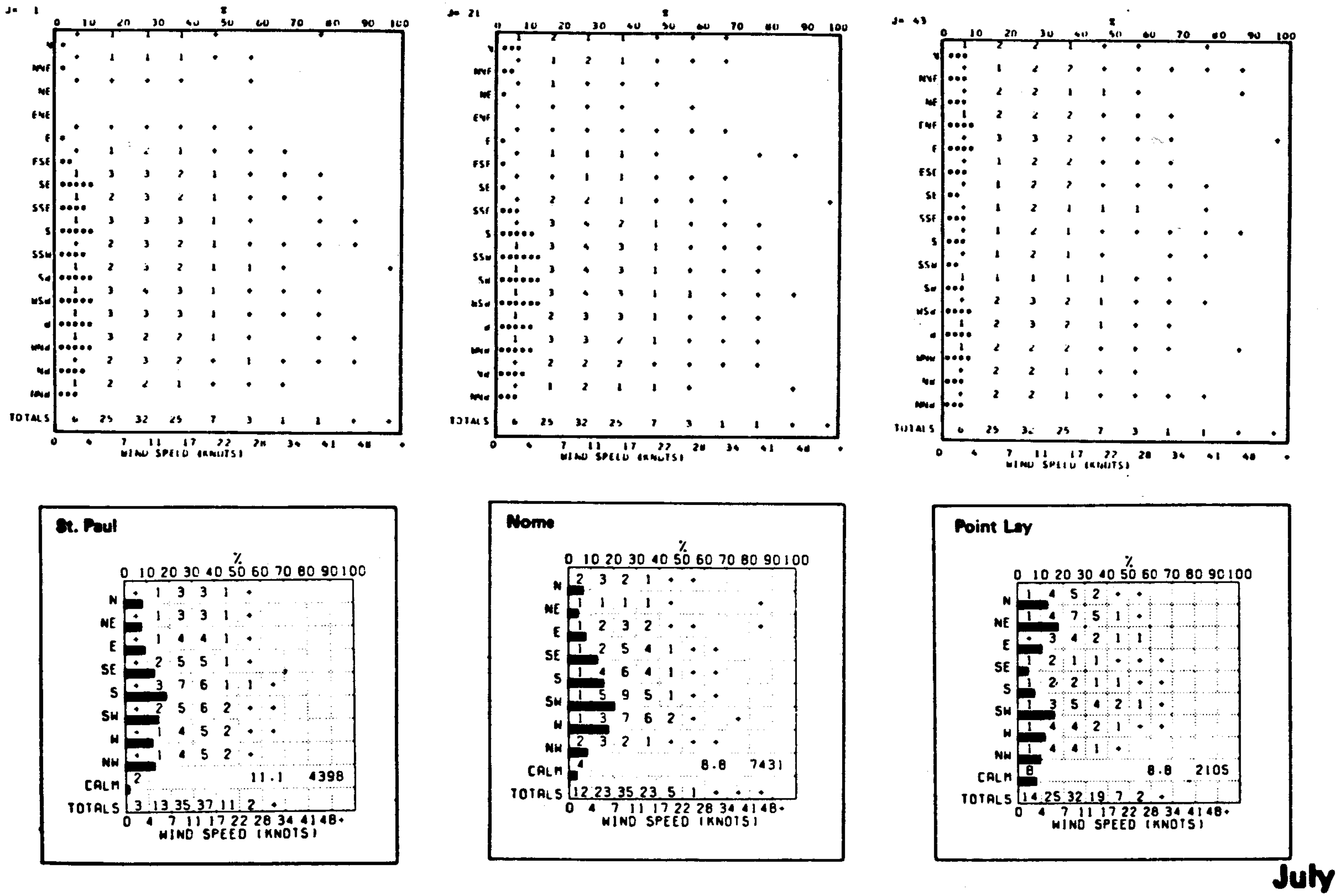

Fig. 4.11—Comparison between the observed wind roses at three land-based stations (Brower et al., 1977) for July, and typical marine winds at nearby locations obtained by long-term (2000) weather sequences interrupted by moving storms.

5. MODELING PACK ICE MOVEMENTS

OBJECTIVES

The primary objective of our study of pack ice movement in the Bering Sea, Chukchi Sea, and the Beaufort Sea is to provide information for an oil spill trajectory model. This model, described in the next chapter, simulates the movement of spilled oil. As spilled oil is trapped in or under the ice during winter and subsequently released during the spring/summer period, it is important in our overall modeling effort to establish ice pack movements. Consequently, our interest is centered around the movement of the ice pack rather than the mechanics of solid ice or shore-fast ice, which received considerable scientific attention some years ago (Parmerter and Coon, 1972; Hibler et al., 1972; Pritchard, 1975). This has been changed recently (Thorndike and Colony 1982; Pritchard, 1984). They have even shown that highly simplified free-drift ice computations can provide reasonable ice trajectories even in the Beaufort Sea during winter in areas other than the near-shore land-fast ice region. In the shore-fast region, ice moves vertically with tides, yet no major displacement in the horizontal direction occurs. Oil spill during winter would be released the following summer when the ice melted.

ICE CONDITIONS AND THE DYNAMICS OF ICE PACK

Within our modeled area, the Beaufort Sea is covered with ice almost the entire year with only seasonal variations in concentration. Only during summer are there open areas close to shore. Figure 5.1 shows the percentage of ice coverage during the summer as it is schematized in the five-layer Beaufort Sea model. The figure also shows the thickness of multiyear ice in the model. This thickness ranges from 1.7 m near the open area to nearly 3 m in the north. During winter the latitudinal variation in the thickness of pack ice ranges from approximately 1 meter to nearly 4 meters north of the 75° latitude. The ice cover contained, at that time, young ice (first year), and multiyear ice. The near-shore area, as well as the lagoons behind the barrier islands, are almost completely covered with shore-fast ice with minimum horizontal displacement throughout the entire winter season.

Outside the narrow shelf in deep water, most of the ice is pack ice, which drifts as a result of wind and current forcing. The mean annual net drifts vary from 0.4 to 4.8 km/day and move in a westerly direction, being part of the general circulation around the North Pole (Arctic Gyre). However, under storm conditions ice displacement can be considerable. Weeks and Weller (1984) reported that under winds of 90 km/hr, pack ice can move 40 km in five hours, suggesting a drift ratio of nearly 8.9 percent of the wind speed. Our model results sometimes show even higher drift speeds. For example, in an area southwest of Point Barrow, one simulation showed a drift speed of nearly 10 km/hr during very high winds in the vicinity.

High drift speed along the coastal areas between Point Barrow and the Bering Strait (except Kotzebue Sound, which is occupied by shore-fast ice) is attributable to two major causes. First, when the winter Siberian High is coupled to an easterly moving Aleutian Low, the direction and speed of the resulting air flow can cause ice movement in the eastern Chukchi Sea to reverse and break out of the Bering Strait to the south. Second, as we discussed

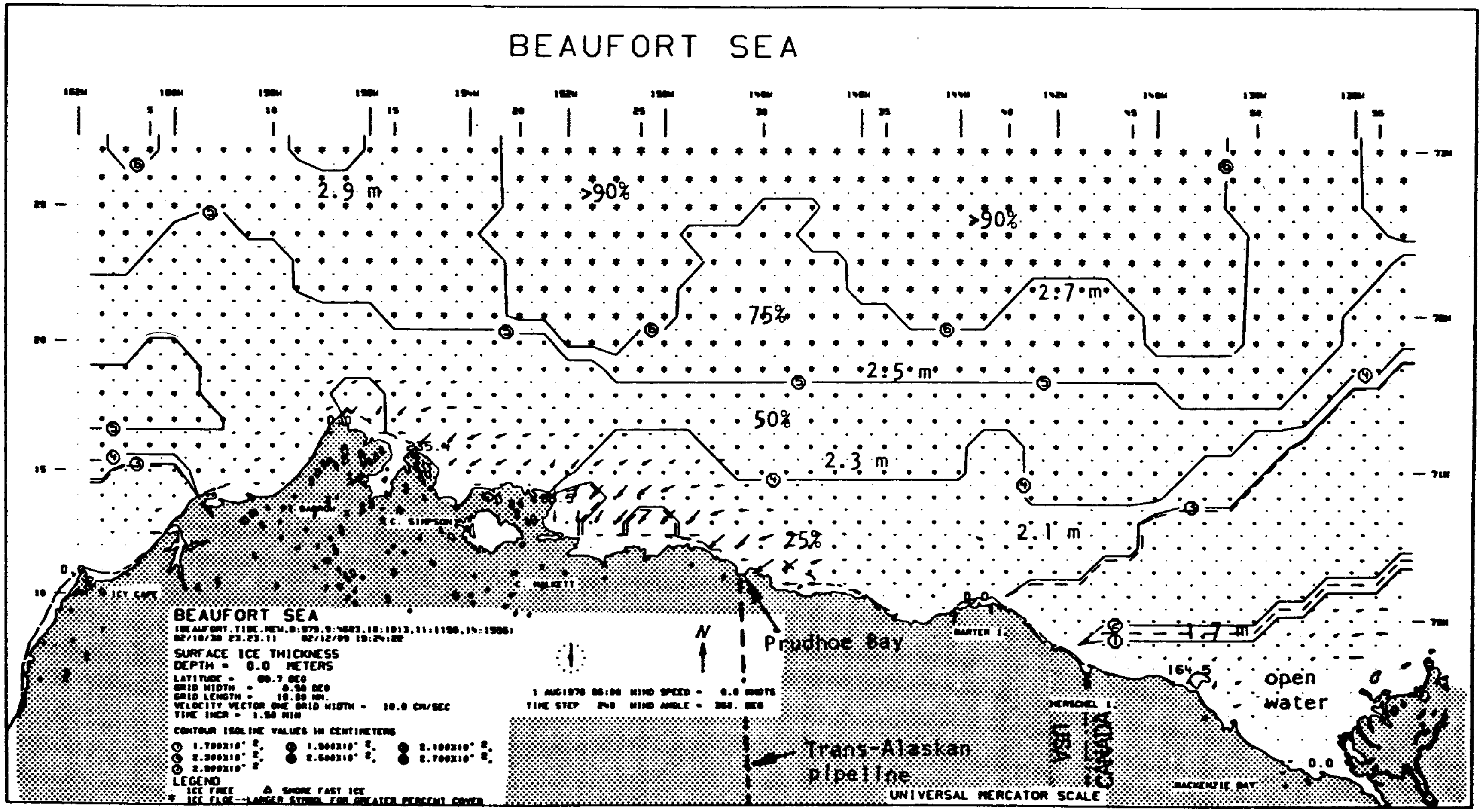

Fig. 5.1—Spatial distribution of ice concentration and thickness as compiled from existing data for the summer period.

above, because of the orientation of the coastline when the atmospheric pressure gradient creates a current reversal, coastal jets in that area would add a substantial advective component to the along-shore wind drift of ice pack.

The coverage of ice in the Bering Sea during winter is limited to the shelf area with interannual variability. The normal limit of ice during winter extends from Point Navarin southeast to the vicinity of Point Mueller. The thickness of pack ice varies considerably with larger thickness at higher latitudes. In the simulation with the Chukchi Sea/Bering Sea models of winter conditions, the ice thickness distribution shown in Fig. 5.2 was used.

During late fall when the predominant wind shifts from the southwest to the northeast, the surface cooling of water columns induces a strong vertical convective process over the eastern shelf area.

In the near-shore area, upwelling, associated with the northeasterly wind stress, reinforces this convective process. Accelerated by these two dynamic processes, temperatures of the homogeneous coastal water would reach the freezing point associated with its salinity (−1.65°C for a salinity of 32 g/kg at that point in time).

As ice is being formed, the freezing process releases a certain amount of salt—the amount is inversely proportional to the rate of freezing. However, this local process cannot continue indefinitely. The northeasterly wind, which produces ice through cooling, transports the locally produced young ice away from shore. This transport is not exactly with the prevailing wind but in a west southwesterly direction because of Coriolis effects.

As the ice factory of the Bering Sea, the northeastern coastal waters have higher salinity and lower temperatures than the deep Bering Basin near the end of the winter season. Near the shelf break, ice that has been formed near shore melts because of higher water temperatures and therefore leaves a layer of stable, fresher waters beneath the ice.

The dynamics of ice in the marginal ice zone are affected by the baroclinic field. Fresh water beneath the ice suppresses the generation of turbulence, therefore creating a discontinuity in the vertical shear coupling. This fresh water beneath the ice not only increases the drifting speed but also reduces the turning angle. In the marginal ice zone, ice also interacts with the short-wave field, reducing wave heights and the Stokes' transport.

In modeling the ice movements, we have tried to incorporate as much of the aforementioned dynamics as they have been understood since our modeling effort began in 1978. Wind stress and water/ice stress coefficients used in the model have been updated from published works (Ovsiyenko, 1976; Martin et al., 1978; Reynolds and Pease, 1982; Langleben, 1982; Macklin, 1983; Pease et al., 1983; Overland et al., 1984). The final drag coefficient used for the air/ice interface is 0.003 and the drag coefficient used for the ice/water interface is 0.018 with water velocity evaluated at the middle of the top layer. For the Bering Sea this is approximately 2.5 meters from the surface and 1.5 meter from the bottom of the ice.

COMPUTATIONAL FORMULAS AND DATA REQUIREMENTS

The computations of the movements of pack ice are based on the consideration of the change in momentum in the horizontal plane by wind stress at the upper surface, stress at the ice/water interface, Coriolis force, momentum transfer within the ice pack, thermodynamics, vertical stability associated with the growth/melting process, and the sea/surface tilt.

Since the model considers only the movements of pack ice, the size of an individual ice floe is assumed to be smaller than the computational grid size. Lacking actual field

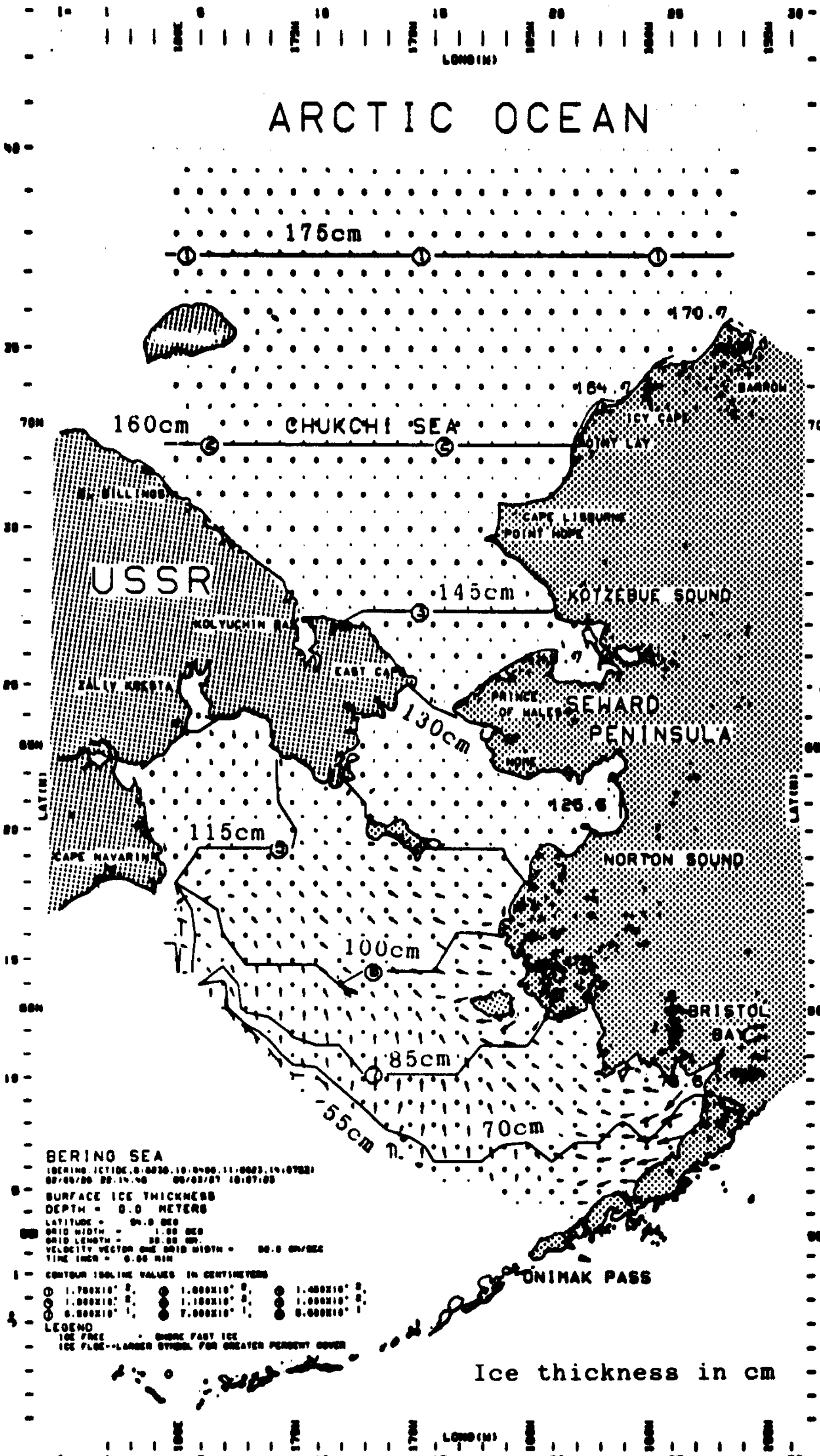

Fig. 5.2—Spatial distribution of average pack ice thickness in the Bering/Chukchi Sea model near the end of January.

measurements, we assume the vertical temperature gradient within the ice to be linear. The rate of momentum transfer within the pack ice in the computational grid is estimated as a function of ice concentration according to the four-third power law of the subgrid momentum transfer.

The balance of momentum for the ice in the horizontal direction, if written directly in finite difference form, is

$$\overline{\delta_t(\overline{H}^x u')}^t = -\delta_x\left(\overline{\overline{H}^x u'}^x\,\overline{u'}^x\right) - \delta_y\left(\overline{\overline{H}^y v'}^x\,\overline{u'}^y\right) + f\overline{H}^x\,\overline{v'}^{xy} - \frac{1}{\overline{\rho}^x}\,\overline{H}^x\delta_x p$$

$$+\frac{1}{\overline{\rho}^x}\left[C^*\rho_a W_a^2\sin\psi - \left(E_x'\delta_z\overline{u'}^{2t}\right)_{k-3/2} + \delta_x\left(HA_x'\delta_x u\right)_- + \delta_y\left(\overline{\overline{H}^x\,\overline{A_y'}^x}^y\,\delta_y u'\right)_-\right] \tag{5.1}$$

at $i+½$, j, l, n

$$\overline{\delta_t(\overline{H}^y v')}^t = -\delta_x\left(\overline{\overline{H}^x u'}^y\,\overline{v'}^x\right) - \delta_y\left(\overline{\overline{H}^y v'}^y\,\overline{v'}^y\right) - f\overline{H}^y\,\overline{u'}^{xy} - \frac{1}{\overline{\rho}^y}\,\overline{H}^y\delta_x p$$

$$+\frac{1}{\overline{\rho}^y}\left[C^*\rho_a W_a^2\cos\psi - \left(E_y'\delta_z\overline{v'}^{2t}\right)_{k-3/2} + \delta_x\left(\overline{\overline{H}^y\,\overline{A_x'}^y}^x\,\delta_x v\right)_- + \delta_y\left(HA_y'\delta_y v'\right)_-\right] \tag{5.2}$$

at i, $j+½$, l, n

where H = local ice thickness,
u' = ice velocity in x direction,
v' = ice velocity in y direction,
C^* = wind stress coefficient,
ρ_a = density of air,
ρ = density of ice,
W_a = wind speed,
ψ = wind angle from the y coordinate, and
f = Coriolis force term.

In these momentum equations, we have on the left side of the equals sign the change in momentum. The first two terms on the right are advection terms, the third term is the Coriolis force term, the fourth term is the pressure term, and the fifth, wind stress.

The sixth term represents the momentum transfer to the flowing water underneath the ice, and the last two terms give a rough approximation of shear between ice.[1]

With the last two terms we are able to couple part of the ice field to land by use of very high horizontal momentum exchange terms, or represent a certain area with unbroken thick ice coverage. In the latter case we have then assumed that in these areas ice does not elastically or plastically reform. This was recently found quite reasonable by Thorndike and Colony (1982) and by Pritchard (1984).

[1]A much more complicated formulation of the shear, similar to formulations in soil mechanics, was used initially. The use of that formulation required much computation and the results were nearly identical with the simple shear representation in Eq. (5.1) and (5.2).

Similar to the bottom stress of a fluid flow model, the momentum exchange coefficient at the bottom of the ice can be expressed:

$$E'_x = \frac{\rho g (\bar{h}^z)^2 \left[(\hat{\delta}_z u)^2_- + (\hat{\delta}_z \overline{v}^{xy})^2_- \right]^{1/2}}{(C_s)^2}$$

$$\text{at } i+\tfrac{1}{2},\ j,\ l,\ n \tag{5.3}$$

$$E'_y = \frac{\rho g (\bar{h}^z)^2 \left[(\hat{\delta}_z \overline{u}^{xy})^2_- + (\hat{\delta}_z v)^2_- \right]^{1/2}}{(C_s)^2}$$

$$\text{at } i,\ j+\tfrac{1}{2},\ l,\ n \tag{5.4}$$

where the density (ρ) and the thickness of the ice layer are computed locally by the parametric relationship presented later.

The Chezy coefficient (C_s) between the ice water interlayers is used not only for the momentum transfer computation but also for the computation of turbulence energy generation with respect to the transport of subgrid scale energy in the surface layer of water. In the computation of the ice cover model, a Chezy value of 420 cm$^{1/2}$/sec is used. This value was converted from the stress coefficient described above.

In the presence of ice, the local top-layer thickness for the water computation is adjusted according to ice displacement, which is also a function of local ice thickness and ice water density differences.

If ice is present in part of the modeled area, then the change of momentum is computed at the grid points as a function of the wind stress, stress at the ice water interface, Coriolis force, internal ice stress, and sea surface tilt.

The internal stress between ice floes is evaluated according to the degree of ice coverage by means of variable horizontal diffusion coefficients. Quantitatively, these coefficients range from one obtained by the four-thirds power law of the characteristic length scale (grid dimension) for the ice-free condition, to an arbitrarily large value for the fully covered condition. In the case of full coverage, shear stress terms at the ice water interface are reevaluated considering the random spacing of draft beneath the pressure ridges associated with the local ice thickness (Whittmann and Schule, 1966).

Before a simulation of winter conditions can be made with the three-dimensional model with ice cover, we need, in addition to the hydrodynamic forcing function at the open boundaries of the model, wind information and initial conditions such as ice thickness and ice coverage. Since it can be expected that very limited information about the ice thickness would be available during some winter periods, an initial ice thickness model is designed to estimate the ice thickness at the start of a simulation. Critical information to determine the ice thickness includes the average value of the total degree-days (below zero) at the starting time of the simulation and the spatial salinity distribution at the beginning of the winter season.

To initiate the ice simulation at each grid location, local water salinity is used to estimate the freezing point. This value is then stored for later use. The freezing point of sea water for various salinities can be estimated (Neumann and Pierson, 1966).

$$T_f = -0.003 - 0.527S_w - 0.00004S_w^2 \tag{5.5}$$

where s_w is the local sea water salinity.

From weather statistics, an averaged value of total degree-days (below zero) can be obtained that corresponds to the starting time of the simulation. From this information, the freezing point of sea water, depth, salinity, and initial temperature, and the "effective" local total degree-days below sea water freezing point can be computed. Once the freezing point has been reached, salt is rejected from the ice, thus it is no longer a function of local sea water but of the ambient freezing temperature. The relationship between the salt content and the ice temperature can be expressed as:

$$S_i = 2.3 - 0.1883T_a \tag{5.6}$$

T_i represents the ice temperature, which may be assumed to be the same as the ambient air temperature, T_a.

From the salinity of ice, the density of young ice is approximately:

$$\rho_i = 0.918 + 0.0008S_i \tag{5.7}$$

To estimate the local ice thickness, the local latent heat of fusion of ice, λ, can be computed also from the salinity of ice mentioned above.

$$\lambda_i = 80.0 - 4.267S_i \tag{5.8}$$

The initial local ice thickness at each grid location can be computed (in cgs units) according to:

$$H_i = \left[\frac{2\ell}{\lambda_i \rho_i}(D - T_f) \times 24 \times 3600\right]^{1/2} \tag{5.9}$$

where denotes the coefficient of thermoconductivity, which is approximately 0.0055 cal degree^{-1} sec^{-1}, and D represents the total degree-days below the freezing point locally. These data are obtained from Brower et al. (1977). During computation the formation and melting of ice are computed assuming linear vertical temperature gradient within ice:

$$\frac{\Delta h}{\Delta t} = -\frac{\ell}{\lambda_i \rho_i}\left[\frac{T_a - T_f}{h}\right] \tag{5.10}$$

The recursion formula in the finite-difference form is:

$$H^{n+1} = H^n \frac{\ell(T_a - T_f)(2\Delta t)}{\lambda_i \rho_i H^{n-1}} \tag{5.11}$$

In the subsequent computation the amount of salt rejection or formation is computed as the source or sink terms in the salt balance equation for the top-layer water simulation.

$$S = \left(H_i^{t+\Delta t} - H_i^{t-\Delta t}\right) \cdot \frac{\rho_i^t\, S_i^t \times 1000}{2\Delta t\, \rho_w^t\, H_w^t} \tag{5.12}$$

where ρ_w and H_w represent the density and surface layer thickness of water.

If ice is present at the model's open boundaries, then the nonlinear advection and diffusion terms are neglected in the momentum equation near the boundary in the same manner as is done in the flow computations. The same procedure is applied to all the internal open ice edges.

When land-fast ice exists in the model area we either assign locally an extremely large momentum diffusion coefficient or set locally the horizontal ice velocity components to zero. The vertical movements of land-fast ice are computed, however.

Sea ice distribution in the modeled area is expressed in Okta. By international agreement the Okta system is used to report the extent of the ice cover. An ice concentration of 1 Okta (one-eighth) or more, defines the edge of pack ice. Total ice coverage is 8 Oktas (Brower et al., 1977). More recent literature seems to report ice concentrations in the 0–10 system with a scale of 10 to represent full coverage. For example, charts issued by the Navy/NOAA Joint Ice Center are in the scale 10 system (Stringer et al., 1982).

For our model inputs we have adapted the Okta system, since the existing ice data at the beginning of our modeling effort were nearly all in Oktas. A value of 9 was created to denote a shore-fast ice zone. In the computation, the Okta scale is also used as a computational flag to classify approximately the type of ice, as well as a parameter for computing the horizontal momentum transfer within the ice pack.

The parametric relationship for the ice growth described here has been tested against the observed data at Norton Sound and Beaufort Sea (Stringer and Hufford, 1982; Stringer et al., 1982). Using typical values of degree days, the formula gives reasonable ice thickness for the entire winter season as compared with the local data.

ICE/WATER INTERACTION UNDER THE FORCES OF WIND AND CURRENTS

Pack ice moves because of the momentum transfer from currents underneath the ice to the ice mass, and because of the momentum transfer from wind to the ice. Ice motions are nonlinear functions in space and time because of nonlinear terms in the equations that describe the ice motions, Eqs. (5.1) and (5.2).

To test computational procedures and to understand the behavior of the system we were working with at that time, we made a number of experiments. One of these experiments is of particular importance, as it revealed considerable differences in the movement of ice in relation to the underlying water. The experiments were made with the submodel of Norton Sound for winter conditions typically occurring in March. Figure 5.3 shows the initial distribution of ice thickness. Open water exists in the northeast part of the bay where ice has been removed by the predominant wind from the north-northeast. The vertical water column is nearly homogeneous throughout the area except for the surface salt input associated with ice generation in the northeast part of the Sound. Other than in areas near the Yukon Delta and at the head of the Sound where shore-fast ice is found, Norton Sound is covered with ice floes that range in size from a few meters to one or two kilometers. The diurnal tide is dominant in the eastern part of the Sound, whereas in the western part of the model area, the semidiurnal tide is stronger. The thickness of the ice ranged from 0.8 to 1.05 meters.

To study the ice/water interaction, we exerted a constant wind of 18 knots from the north-northeast, the predominant wind for this month. Ice moves under the influence of wind and tide, and typical ice velocities are shown in Fig. 5.4. Note that the ice movements deviate considerably from the wind direction. The influence of the current stress and the stress exerted by the neighboring ice appears to be quite strong.

The velocity of the water in the top layer just underneath the ice is quite variable, as shown in Fig. 5.5. Near Kwikpak Pass the water velocity is nearly zero and, in this case, the direction of the ice movement is approximately 35° to the right of the direction of the wind. At this location the speed of ice is approximately 3.3 percent of the wind speed. However, a short distance away where larger water velocities exist, the speed of ice approaches 4.5 percent of the wind speed.

It will be noted also that the speed of ice near the shore-fast ice zones is reduced in comparison with its speed farther away. In many cases rotational effects in the ice movement may be observed near the boundary of land-fast ice. The model experiment also shows that shore-fast ice considerably reduces the water velocities in the layer immediately underneath the ice.

In a subsequent experiment we evaluated the movement of ice over a certain period. At the beginning of this experiment only the tidal motions were simulated until the starting transient had disappeared. Subsequently, the wind stress was applied over a 12-hour period and for the following 12 hours the wind was stopped again. The direction of the wind was from the northeast and the wind velocity was 10 knots.

To obtain insight into the transient effect of wind on the ice field, plots of ice displacements were made for a number of locations in the model. These pathways are shown in Fig. 5.6 and are the pathways resulting from a 12-hour period of wind followed by a 12-hour period without wind. The movement of the ice in the eastern Sound is influenced by the underlying diurnal tidal excursion, whereas in the southwestern part of the model the semidiurnal tide exerts the most influence. If we look at the movement over a 24-hour period, as shown in Fig. 5.7, it can be seen that the net displacement varies considerably over the area in displacement and in direction. The drift distance is typically from 6 to 9 km for this period in which the wind stress was applied for only 12 hours. To study the inertia component of the ice's movement, the wind stress is exerted only in the first 12 hours of the day simulated.

After this experiment, which was made in 1980, field data became available from sea/ice trajectories determined by Landsat imagery as shown in Fig. 5.8 (Stringer and Hufford, 1982). The daily movements of ice range from 7 km to 14.5 km, which is approximately twice the displacement during the 12-hour experiment; wind directions are quite well in agreement with those of our aforementioned simulation. Unfortunately, no wind data were obtained at stations in the Sound during that period. The wind conditions were typical for that season with air pressure difference between Point Barrow and Nome being 0.4 inches.

The comparison between the long-term observed ice trajectories and the simulated long-term trajectories under the areawide wind forcing is presented in the next chapter. It is our opinion that the long-term ice trajectories should be verified together with the wind model that will be used for the oil spill trajectory simulation.

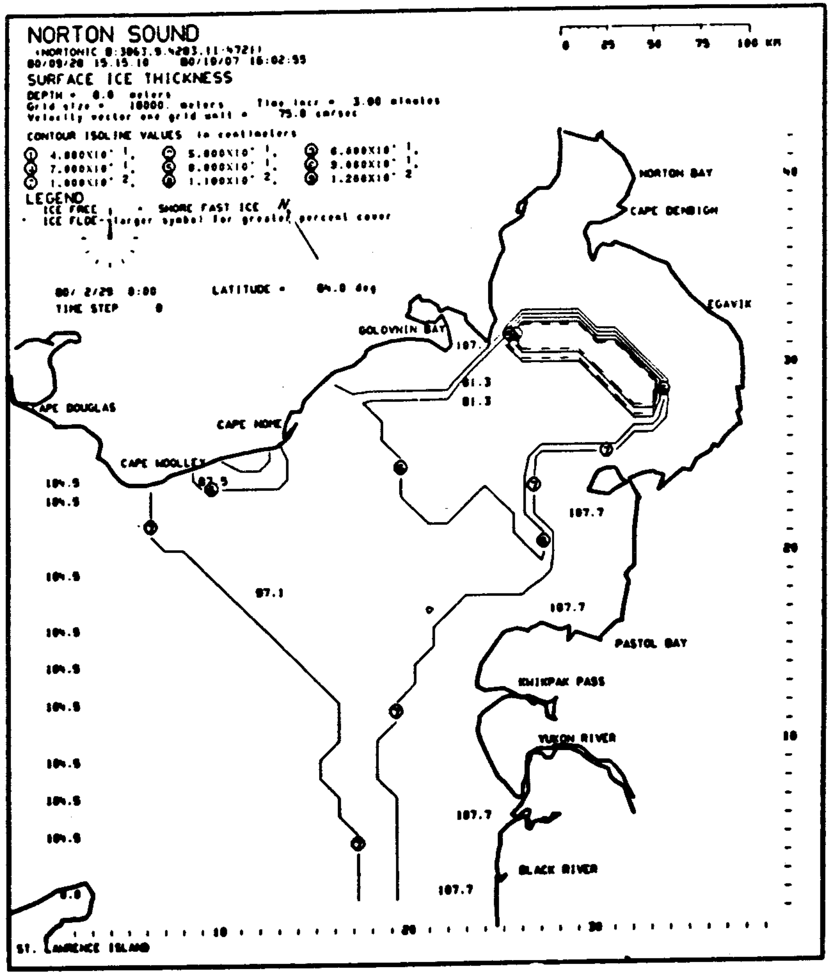

Fig. 5.3—Initial distribution of ice thickness. Area near the Yukon Delta and at the head of the Sound is covered by shore-fast ice. Areas near Golovin Bay and south of it are ice-producing areas.

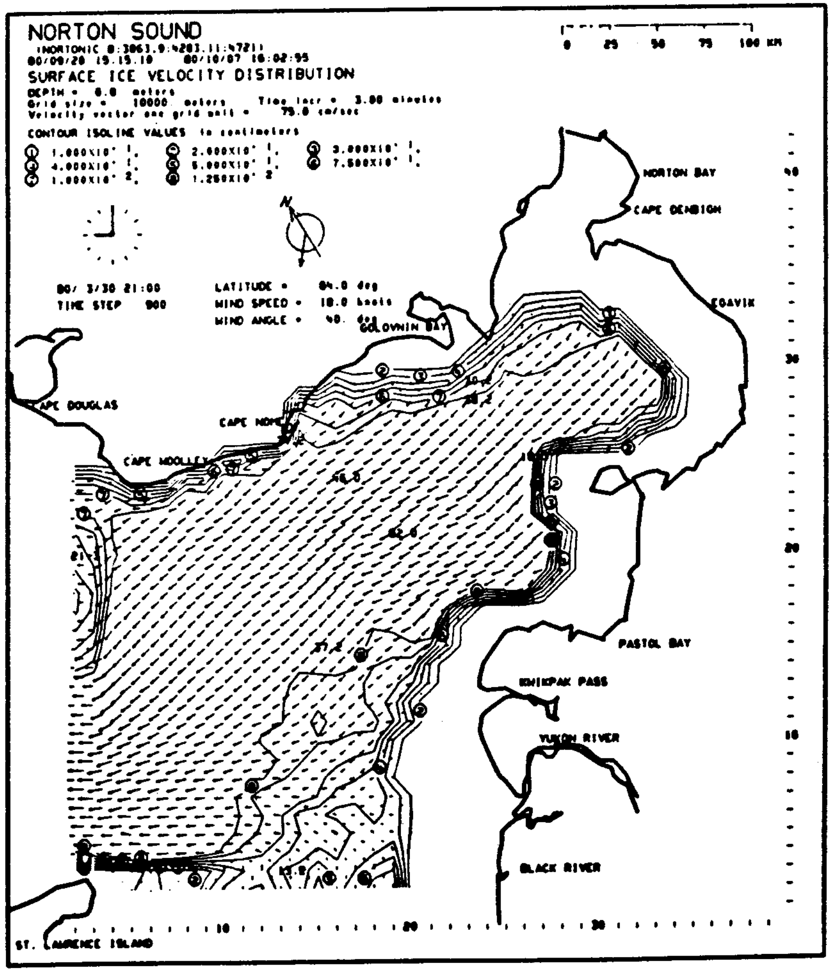

Fig. 5.4—Ice floe movement under northeast wind (10 kn) combined with tidal movement. Displacements immediately neighboring shore-fast ice zones are limited with rotational behavior induced by strong ice-ice interactions.

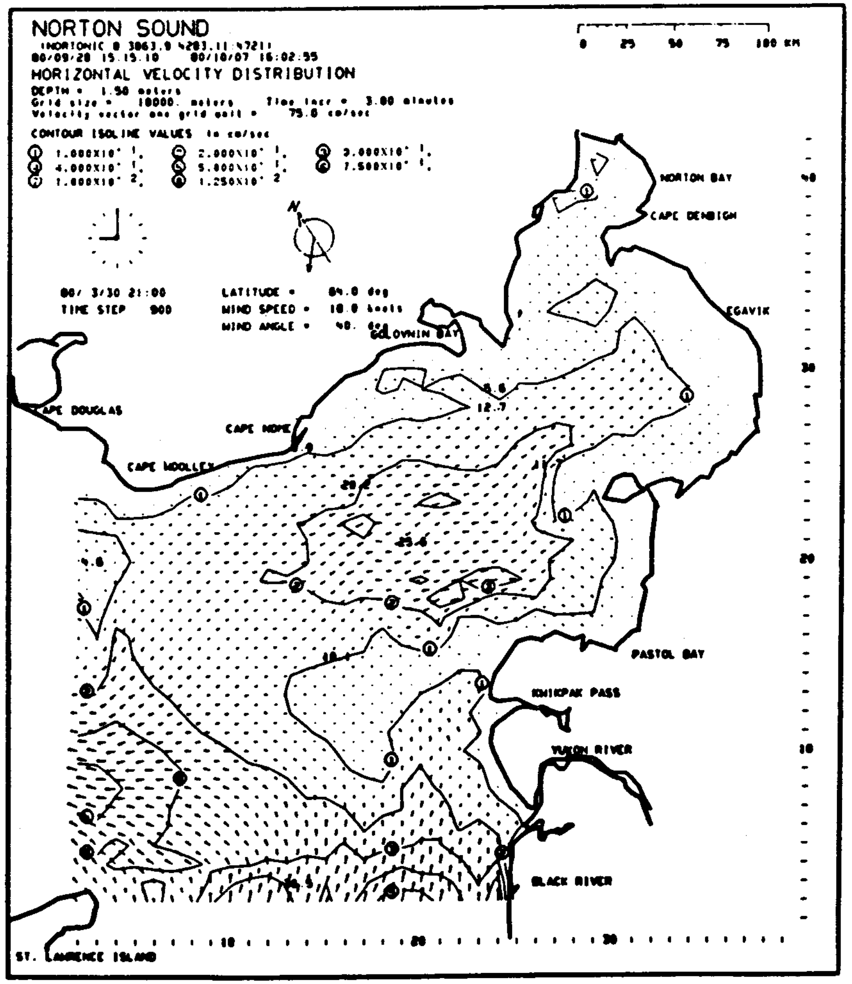

Fig. 5.5—Water movements beneath the ice. They are driven by tidal forces and wind stresses transmitted through the ice.

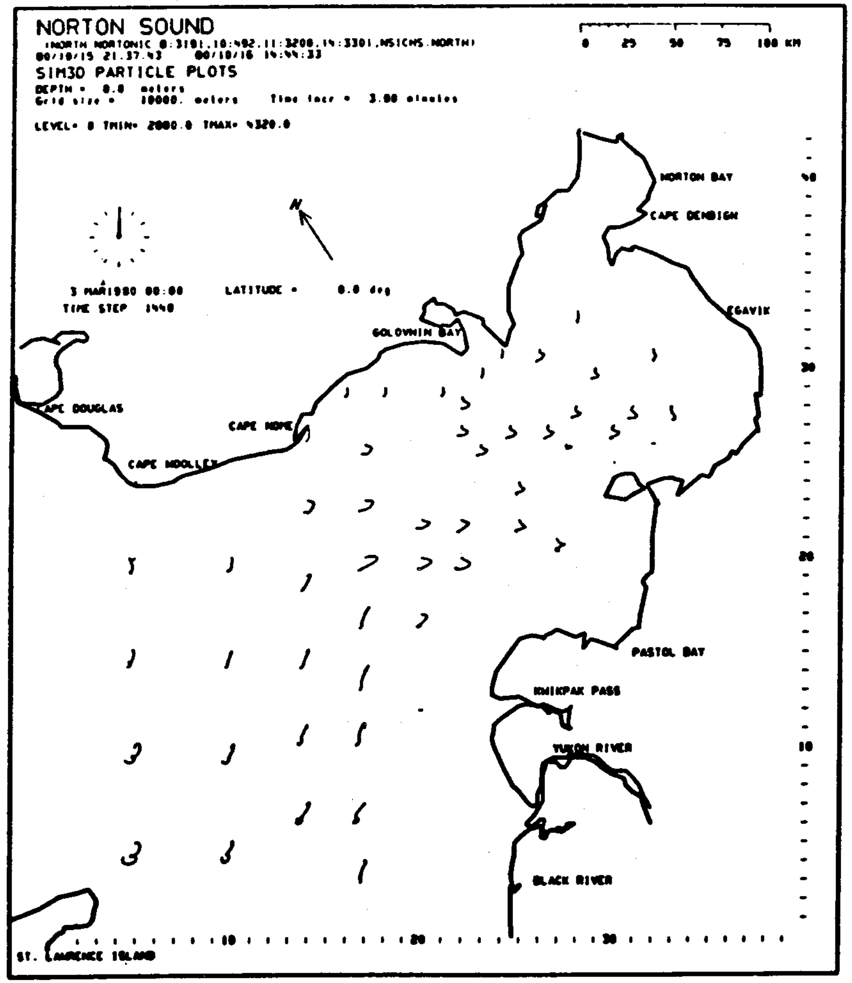

Fig. 5.6—24-hour ice trajectories, driven by tidal excursion and 10 kn wind from the northeast for the first 12 hours.

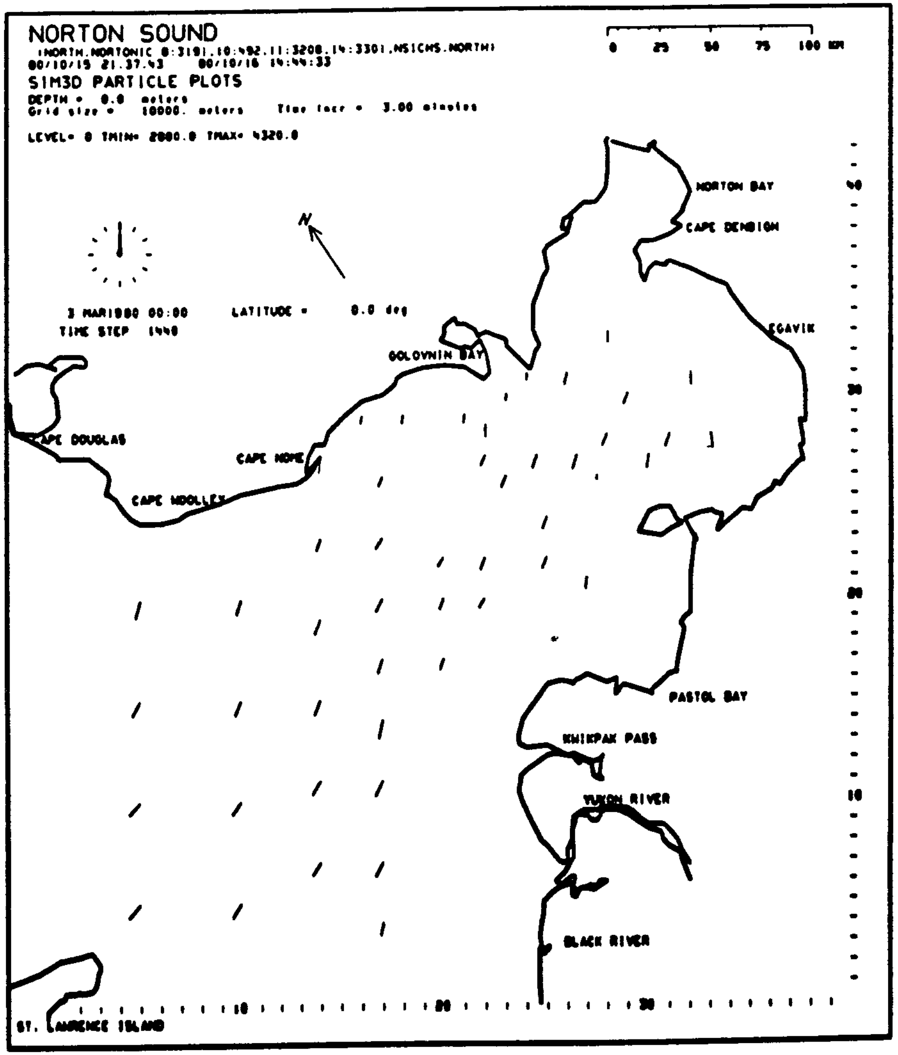

Fig. 5.7—24-hour net ice displacements, induced by tidal-residual current and 10 kn wind from the northeast for the first 12 hours. Daily displacements under 24-hour wind stress would be approximately twice the amount shown.

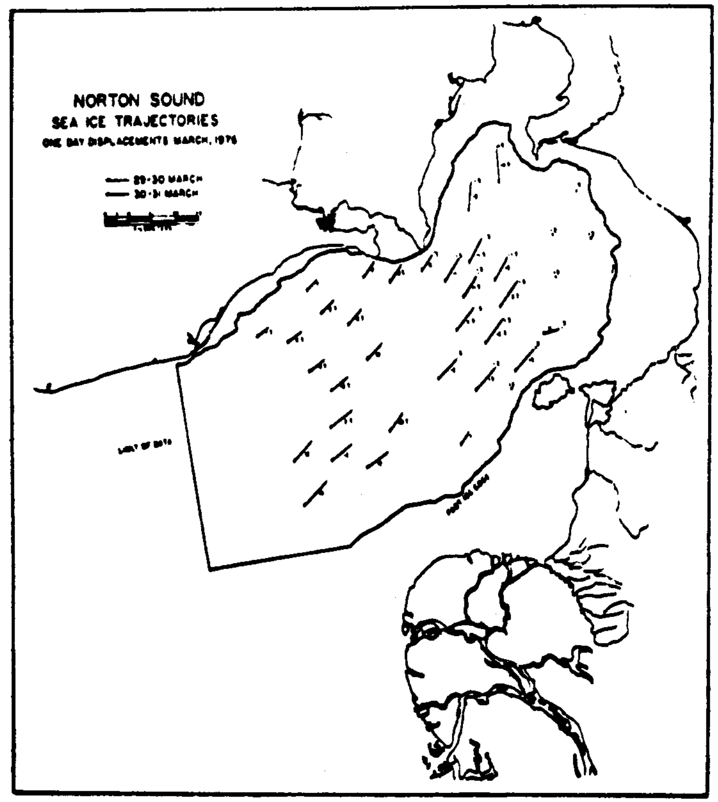

Fig. 5.8—Pattern of daily ice floe movement of 30-31 March 1976 (Stringer and Hufford, 1980) when the pressure difference between Barrow and Nome was approximately 0.4 inches.

6. MODELING OIL TRAJECTORIES

OBJECTIVES

Before decisions are made concerning which specific offshore areas to lease for exploration or exploitation, the responsible governmental agency (U.S. Department of Interior) must balance orderly resource development against the protection of human, marine, and coastal environments, to ensure that the public receives a fair return for these resources. In studies made for this purpose, the impact of hypothetical oil spills are considered. To assess the impact of these oil spills on resource areas, simulations of the pathways of oil spills are required for representative weather conditions for specified periods of the year. A relatively large number of simulations are required from each spill site to obtain sufficient data for statistical analysis.

Not only are oil spill pathways required for the impact analysis, in certain instances knowledge about the extent of oil spills is required as well as about the oil concentrations that would occur in the water column.

THE MODELING APPROACH FOR LONG DURATION WIND DRIVEN CURRENTS

As the three-dimensional models made of the different offshore areas of Alaska simulate the movements of water, and as a model is available to simulate wind sequences offshore, it would be logical to use these models in the computation of oil spill movements. To use these models effectively, we have developed a method to compute wind driven currents. This method retains the dynamic detail of the three-dimensional model and yet is approximately two orders of magnitude more efficient than the simulations with the three-dimensional model; it is called the "wind-driven response function method." In essence, the method extends the basic idea of the "drift ratio" between the wind speed and current speed except that the ratio changes in time and over space and is derived from the three-dimensional model.

The traditional, simple fixed drift-ratio method has many difficulties when applied in the Alaskan coastal waters. It is applicable only for cases of steady wind with constant speed blows over water with finite depth and with no boundaries. However, the concept of the "drift ratio" is a good one—but we need to include more dynamics in it.

In examining the fundamental dynamics of wind-driven currents, even under the assumption of steady (in time), constant (over space) wind and an infinitely long straight coastline, wind-driven currents over water of finite depth do vary both in direction and speed at the surface and at different levels to satisfy the law of conservation of mass. Using information on the distance from shore, wind direction, and local depth, Ekman (1905) worked out the variabilities of drift currents by using highly simplified terms in the equations of motion. On the other hand, to include more terms would require the solution of the complete three-dimensional model.

In our study, time-varying response functions under various wind conditions were developed using wind stress associated with the marine wind speed. Reverse procedures (convolution) were then used during the oil trajectory simulation; therefore, they are not linear with respect to local wind speed. Since the response functions for all layers are derived from the three-dimensional model, time-varying effects (such as a moving storm, deepening of a mixed layer, and inertia components) are included in the oil spill trajectory computation. The method is very efficient, however, the oil spill trajectory model was programmed so that the drift ratio and deflection angle from field observations under various conditions over an entire area can, as an option, still be used for the computation of oil movement.

Wind driven currents over stratified waters vary with the degree of vertical stability associated with the stratification. To illustrate this point we use a simple case where the time series of water movement at two nearby locations in Norton Sound is plotted (Fig. 6.1), and wind from the east is applied for a duration of 12 hours (close to the inertial period) over the water. The response of surface water at two nearby locations is not the same to satisfy the continuity principle of water within a bay. Response functions over the water column of the entire modeled area are calculated by the three-dimensional model.

To generate the complete set of response functions, five computer simulation runs are needed. One computer run is without wind but with tide. The other four computer runs are with tides and with wind from each of four directions. The four response functions set are derived from the difference between them and the one with tide as the only forcing function. The level of tidal currents at different areas produces variable wind responses under the same wind, so the tide has to be included when deriving wind response functions, otherwise they will be overestimated. This is why in a coastal area with strong tidal currents the drift ratio would be lower than in the open ocean because of the quadratic nature of the bottom friction.

When response functions are saved in discrete time intervals (30 minutes was used) the drift velocity at a certain time is computed by numerical convolution.

$$U_{ij}(n\,\Delta t) = \Delta t \sum_{k=0}^{n} (W^2) h_{ij}(n\,\Delta t - k\,\Delta t) \tag{6.1}$$

where W = wind speed from a certain direction,
U_{ijk} = velocity at a particular point (i, j, k), and
h_{ijk} = time domain response function between squared wind speed and velocity at point (k, j, k).

With this formula the velocity at point i, j, k can be determined if the wind speed from a specific direction is known, as well as the response function.

The same principle applies for complex wind scenarios, then the vectorial decomposition is involved.

COMPUTING OIL BEHAVIOR UNDER ICE

In the absence of a current, oil released in a water column will rise and be trapped underneath the ice. Under porous young ice during formation, oil will initially undergo a certain degree of vertical migration through the vertical brine channels. Most oil is initially in the form of droplets until a lateral slick is formed. The oil sheet tends to spread with an obtuse contact angle. For typical Alaska Prudhoe Bay crude oil, the average observed values of interfacial surface tension, density, and the contact angle are 31 dynes/cm, 0.911 g/cc, and 20°, respectively (Kovacs et al., 1980). The static thickness of the same oil is approximately

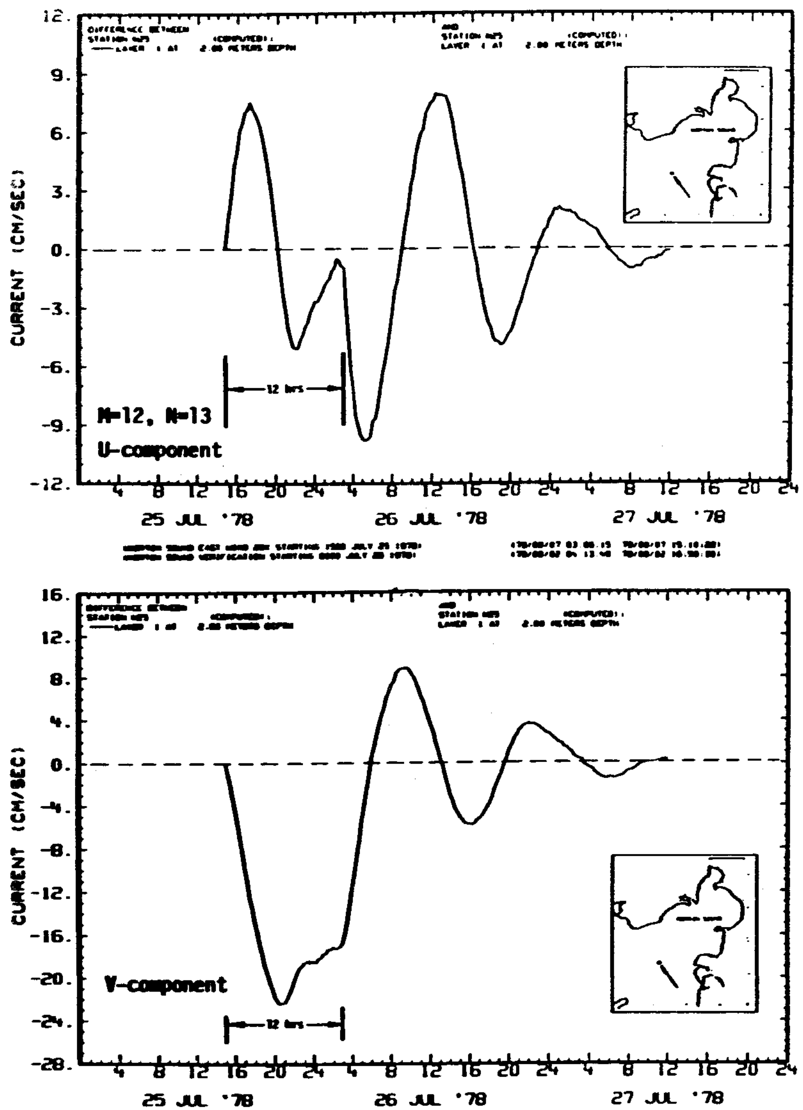

U- and V-components of the response function for the surface drift under easterly wind of 20 knots

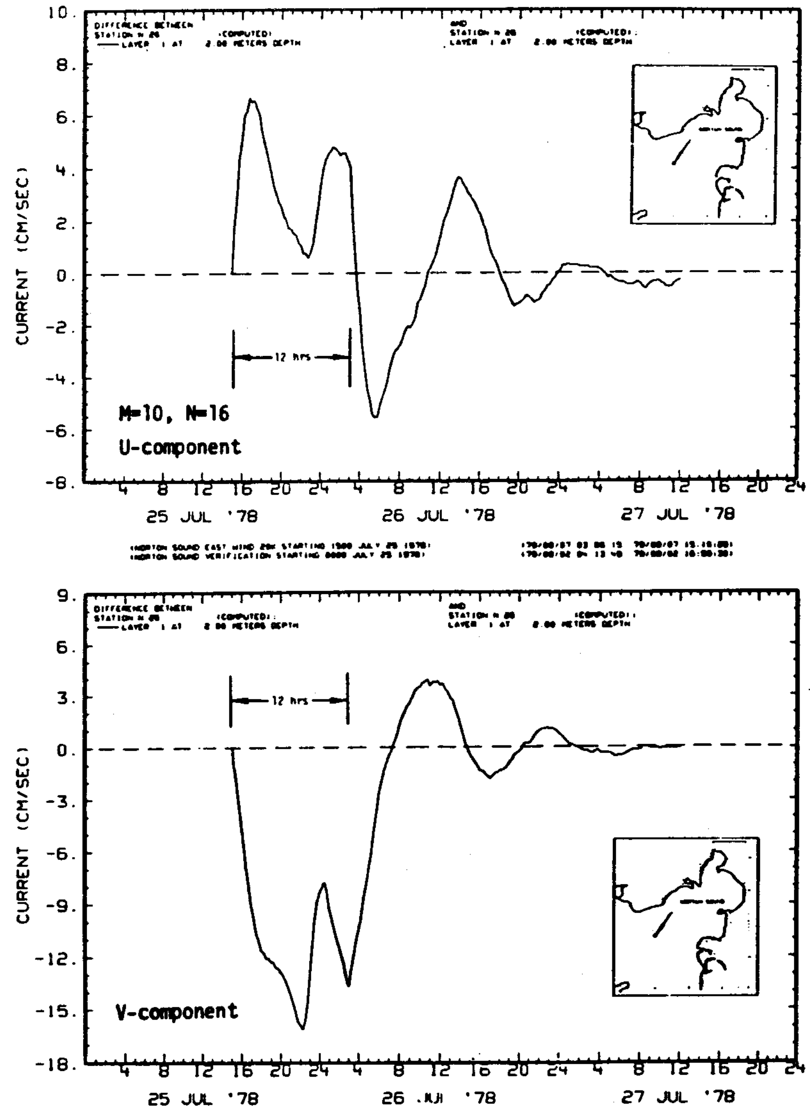

U- and V-components of the response function for the surface drift under easterly wind of 20 knots

Fig. 6.1—Response function components.

1.2 cm. Since the dynamic pressure exerted by a moving current on an oil slick of finite length tends to balance between the front and the back faces, the equilibrium thickness should be the same for both unaccelerated and static slicks.

The bottom roughness of ice not only determines the amount of oil that may be trapped beneath it, it also influences the speed of oil movement under moving currents. Using a radar echo sounding system, Cox et al. (1980) made extensive measurements of ice bottom morphology and found the standard variation of ice thickness to be 3.1 cm over a mean thickness of 1.53 m in an undeformed shore-fast ice zone near Prudhoe Bay. The thickness of ice was also found to be inversely proportional to the thickness of snow cover over it. The snow acts as an insulator that reduces heat exchange from the sea water through the ice to the atmosphere and thus retards the growth rate. Consequently, a substantial quantity of oil can be retained underneath the pack ice. Under weak currents, trapped oil will travel with the pack ice. The movement of oil under this condition would be identical to the computed movement of ice described above but the shear stress coefficients between water and ice are reduced.

Under strong "relative currents" (between water and ice), oil will travel at a speed different from the ice and currents. To compute the movement of oil under these conditions, in the three-dimensional model we adapted a method developed by Cox et al. (1980) with parameters evaluated from laboratory tests. This method involves the evaluation of a critical relative velocity between ice and water. Using ρ_w to represent the density of sea water in the surface layer of our computation, the critical velocity for the incipient motion with large roughness is approximately:

$$u_{\text{critical}} = 1.5 \left[\left(\frac{\rho_o + \rho_w}{\rho_o \rho_w} \right) \left\{ \sigma_{o/w} g (\rho_w - \rho_o) \right\}^{1/2} \right]^{1/2} \tag{6.2}$$

in which ρ_o, $\sigma_{o/w}$ are, respectively, the density of oil and the surface tension at the oil/water interface. With the aforementioned typical values observed in the Beaufort Sea, this critical value is approximately 21 cm/sec.

Equation (6.2) is developed considering the formation of Kelvin-Helmholtz type instability, which exerts a limit on the thickness of an oil slick near the head region. A multiplier of 1.5 on the right-hand side of Eq. (6.2) was used considering the actual velocity that would cause droplet tearing. Ultimate slick failure occurs at about twice the critical velocity.

According to Cox et al. (1980), the critical velocity at which oil begins to move relative to the water when the relative velocity between ice and water is:

$$u_{\text{oil}} = u_{\text{water}} \left[1 - \left[\frac{\kappa}{A F_\delta^2 + B} \right]^{1/2} \right] \tag{6.3}$$

where κ is the amplification factor and F_δ is a slick densimetric Froude number defined by:

$$F_\delta = \frac{u_{\text{water}}}{\sqrt{[(\rho_w - \rho_o)/\rho_w] g \delta}} \tag{6.4}$$

in which δ represents the equilibrium slick thickness.

Equation (6.3) is derived from the momentum balance between form drag, oil/water interfacial shear stress, and the retarding of oil/ice frictional force. Constants A and B in the equation contain the effects of frontal shear and plane shear, as well as the normal force from oil's buoyance against the ice. For the field conditions of the model areas, the values of these coefficients are 1.75 and 0.115. The amplification factor κ equals unity for a hydrodynamic smooth region and is greater than zero for rough surfaces. For the field conditions in the model areas, the factor was given a value of 1.105. To determine the equilibrium oil slick thickness from the density of the oil, we used an empirical relation. The empirical difference is:

$$\delta = 1.67 - 8.5\,(\rho_w - \rho_o)(\mathrm{cm}) \tag{6.5}$$

In the three-dimensional model the local density of water is evaluated by the equation of state of sea water. The density of oil can be computed by a table look-up procedure.

In our computation, the local density of sea water associated with the ice formation/salt rejection and advection was evaluated and updated. The results of oil movement beneath the ice under various wind conditions, in the form of response functions computed from the three-dimensional simulation, were recorded on magnetic tape as subsequent inputs to the oil spill trajectory computation.

We found that oil will generally move with ice except under two conditions that cause it to travel at a different speed. The first condition is beneath the shore-fast ice in an area where tidal currents are strong. The second condition is when pack ice is located very close to a passing storm center, when drifting ice abruptly changes direction. Under this condition a high relative velocity between the water and ice can be reached..

Because of the pronounced nonlinear vertical shear coupling, and at high latitude, the direction of an oil movement appears to be extremely variable. Therefore, the vertical shear coupling should be included in the computation even though spilled oil beneath the ice may not seem to be in constant motion with appreciable magnitude.

MODELING OIL SPILL TRAJECTORIES

Oil spill trajectory computations involve two parts—the first part calculates the movement of oil mainly by advective transport, and the second part calculates the movement of dispersive mechanisms, including weathering, diffusion, and dissolution processes. In this section we will describe the modeling of advective transport only.

Oil transported by advective mechanisms contains several major components. The method used to compute each component is as follows:

Oil Transport by Mean Wind Drift. During this computational step, oil movement resulting from wind stress at the surface layer and at different levels in the water column is calculated by the response function technique. The response function represents local advective transient response to a given wind stress. If a three-dimensional model is used to develop these response functions, the effects of transient inertia, bottom, shoreline, and vertical stratification are all included. The computed movement using this response technique gives only the movement near the middle of the surface layer (typically 5 meters) schematized in the 3D model. For the surface movement the results are extrapolated for speed and direction near the surface using an analytical solution of the Ekman type assuming constant density within that surface (mixed) layer.

Stokes' Transport. When wind blows over the water surface it generates Stokes' transport in addition to the mean wind-driven current. This transport is caused by the non-linear residual orbital motion associated with the local wind waves field. The magnitude of this transport is a function of the intensity and age of the wave field. The direction is nearly identical to the wave-propagating direction. In the oil spill trajectory model, a special subroutine is used to compute the direction and speed of this transport. According to measurements in the field and in the laboratory, Stokes' transport is approximately 1.6 percent of the local wind speed if the wave field is not limited by wind duration and fetch length. The wind used to compute the Stokes' transport is obtained from the wind field model described in Chapter 4.

Tidal and Baroclinic Residual Component over the Alaskan Outer Continental Shelf Area. Because of the complex tidal regime and density field, tidal residual and baroclinic circulation components are quite essential. We have discussed their dynamics in great detail in Chapter 3.

To simulate a number of trajectories with the trajectory model, many data are needed from other models that we have previously described. Figure 6.2 gives an overview of the data flow between these models. As illustrated in the diagram, when computing the oil movement, the oil/trajectory model plays the role of data synthesizer. As physical parameters involved in calculating oil movements are difficult and expensive to measure over the entire Alaskan waters, the model is programmed with flexibility in mind, so that any field data, if available, can be used to drive the model in its simplest mode. On the other hand, the trajectory model would link results from the other models. To perform this task, it contains the basic physical parameters of the entire lease area as well as the grid network of the entire model and submodels within the system.

During the study period, spill trajectory analyses were made on a lease-area basis. For each lease sale, approximately 30 to 40 launch points were selected by the Minerals Management Service according to the potential petroleum resource. The movements of oil were then tracked for a period of time, typically a month during the summer period, to as long as six months during winter.

From each launch location 40 to 60 trajectories are computed under different weather scenarios. For each trajectory, half-hourly positions are computed and landfall locations are recorded where possible. As described above, the wind-driven component of the oil movements is computed using the wind-driven response function technique through the convolution procedure. To maintain accuracy, each response function has half-hourly weighting elements for each wind direction, each computational grid, each layer, and each season. One magnetic tape is required to store all response functions from each of four wind directions. For the computation of oil spill trajectories, this information is transferred to disk storage.

Results from a typical simulation are presented in Fig. 6.3. In the figure, the computational grid of the three-dimensional model of the Beaufort Sea is superimposed over the oil trajectory model, which also covers the eastern portion of the Chukchi Sea. The response functions and net-current field over that area are averages obtained from the two models.

On top of the graph, computed 12-hour wind vectors sampled at Point Barrow are plotted. The mean winds and half-hourly varying winds from the simulation are also presented in the form of wind roses for speed and direction, also at Point Barrow. The wind direction rose represents the frequency of occurrence of wind direction toward which wind is blowing. A wind speed rose represents the average marine wind speed associated with each of the 16 wind directions mentioned above. The plotting scale of the highest speed in the rose is 12 knots as indicated under the rose.

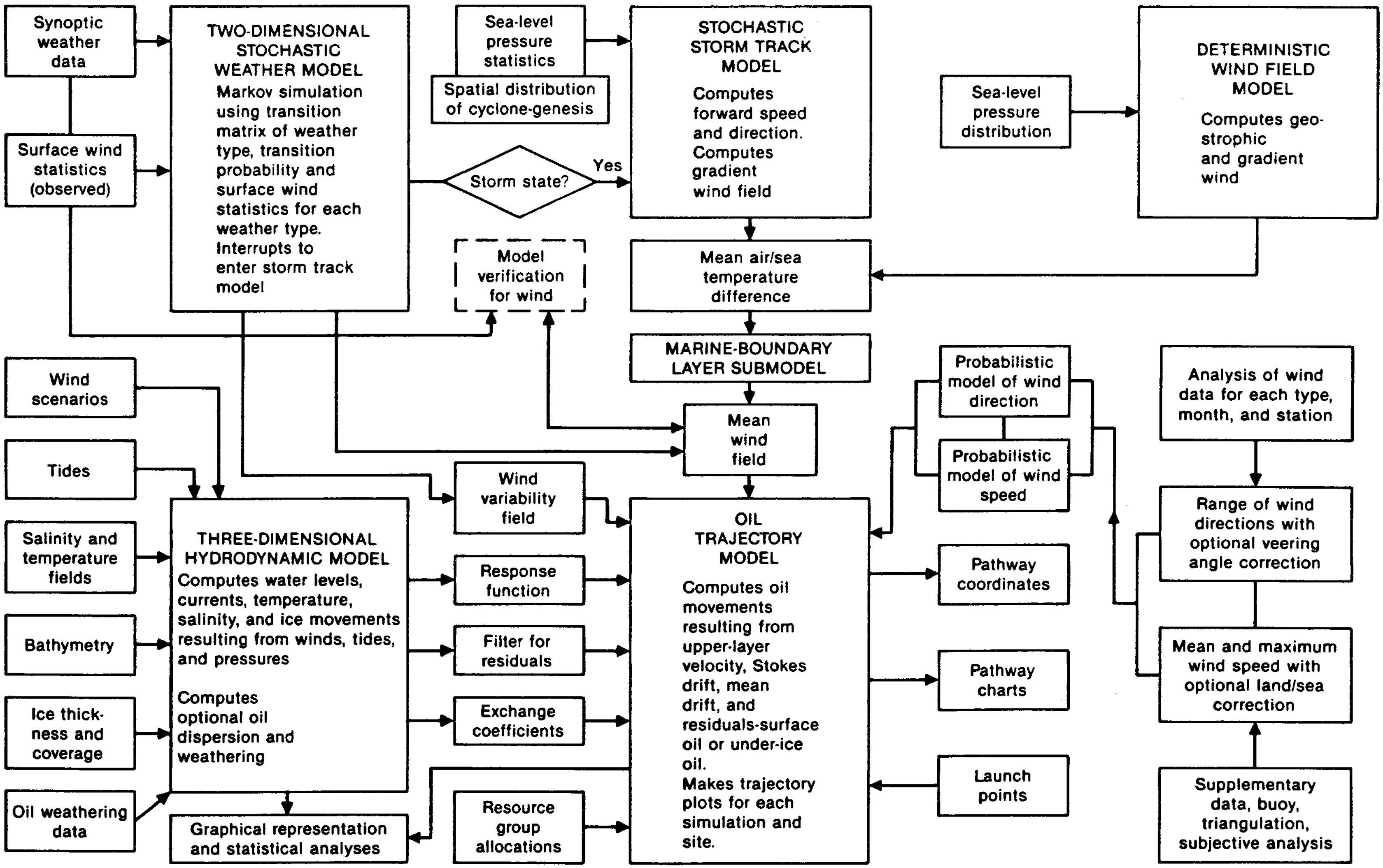

Fig. 6.2—Flow chart showing importance of both the three-dimensional hydrodynamic and the weather model to the oil-spill trajectory model. These parameters are difficult and expensive to measure over the entire coastal waters. Observed wind roses, if available, can still be used to drive the trajectory model in its simplest mode.

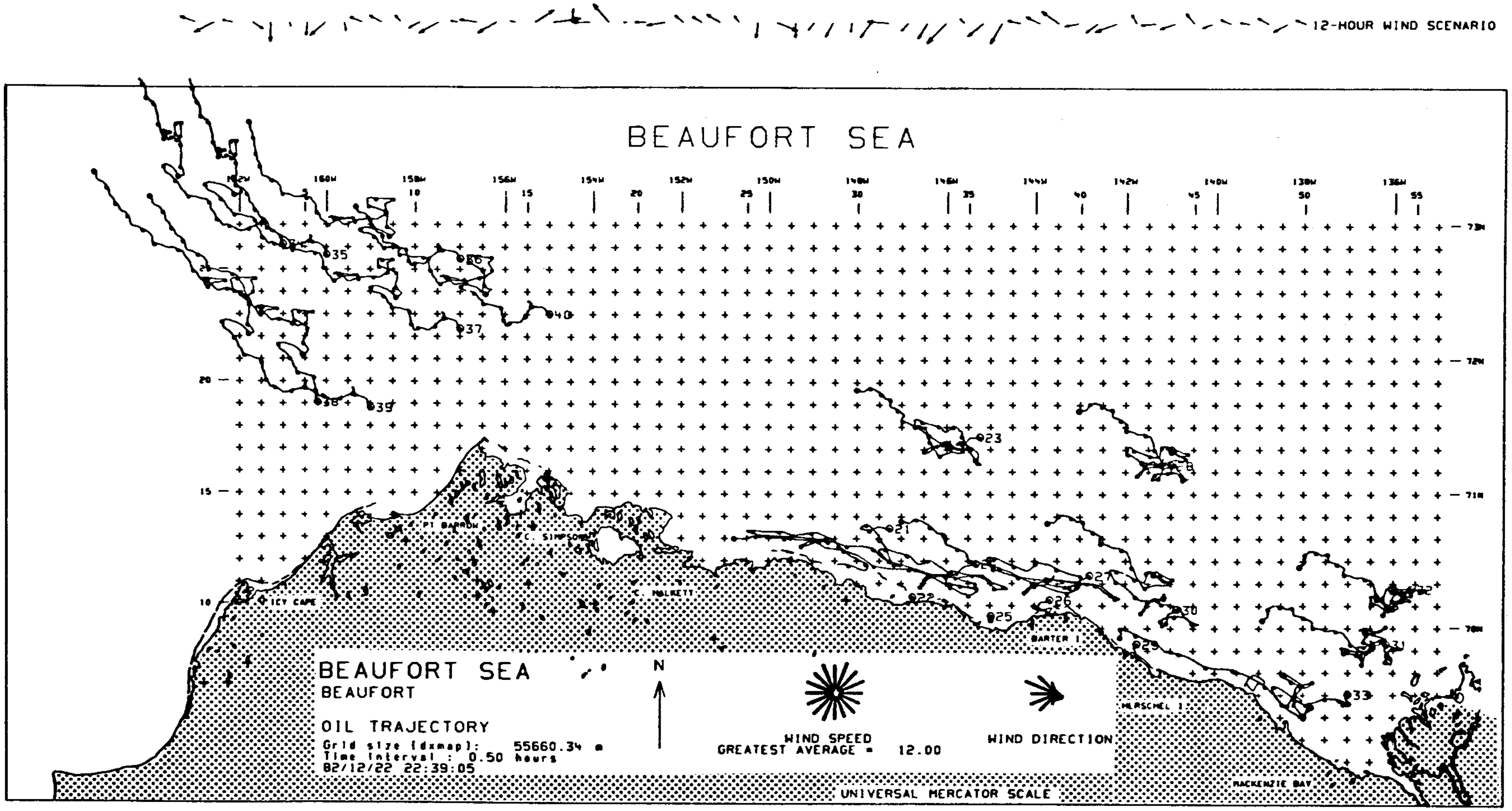

Fig. 6.3—Daily movements of oil originated from launch points 21 through 40.

Each dot in the oil trajectory represents daily displacement originating from the launch point, which is marked by a number. When examining the trajectories one would notice the following interesting aspects:

1. The predominant wind during a summer period is from the east-southeast.
2. Oil spilled closer to the shore travels faster, in a downwind position.
3. Oil spilled offshore moves in a more random direction and has a larger deflection angle. This can be attributed to the greater water depth and the existence of ice floes.
4. Oil spilled further offshore travels in a direction approximately the same as the Arctic Gyre (Colony and Thorndike, 1984, U.S. Coast Guard buoy data, Fig. 6.4). The simulation in Fig. 6.4 was made in December 1982.

The trajectories shown in Fig. 6.3 represent oil movements under a given 30-day weather scenario. In Fig. 6.5 comparison between satellite-tracked buoys (Murphy et al., 1981) and trajectories computed using the coupled trajectory-weather model is shown. During the summer period, the average observed movement of ice is approximately 140 nautical miles per month. The same is found in the computed monthly average displacement. The observed and the computed trajectory patterns in the Mackenzie Bay are quite irregular. This may be due, in part, to the cyclonic local eddy described above.

Without observed wind fields and the variability of winds, tracing the deterministic motion of a particular ice floe is not as desirable as comparing a group of observed trajectories to a group of computed trajectories using a weather model. The same weather model will be used for the statistical trajectory analyses below.

In the trajectories it can be seen that the impact of a moving storm can sometimes be seen as a loop in a trajectory. The size and shape of the loop vary because of their location relative to the moving storm.

The computed trajectories for the winter season have the similar direction of predominant movement. Figure 6.6 shows the general direction of movement launched from three selected points. The residence time within the modeled area is approximately two to three months. If all launch points for a given season are considered, one can assess the oil spill risk by counting the number of contact occurrences within each square area whose length is 10 nautical miles in the north-south direction (Fig. 6.7). In Fig. 6.7 the size of a circle represents the spatial distribution of landfall frequencies. If oil is trapped in a near-shore lagoon, a continuous contact is assumed for the remaining period. In preparing the map, analysis is made using two-hour counting method. Plotting scale for the circle is 21211, two-hour exposure periods equals one latitudinal grid spacing for the radius of the circle.

If the near-shore entrapments are excluded, a similar diagram (Fig. 6.8) gives the spatial distribution for the marine resource contact frequencies. In this case, each latitudinal grid spacing equals 1872 two-hour contact period for the radius of a circle. From graphs like Fig. 6.7 and 6.8, one would be able to obtain a general assessment of contact risk associated with the oil spill. However, sometimes it is more desirable to estimate the concentration of oil, if a contact is made.

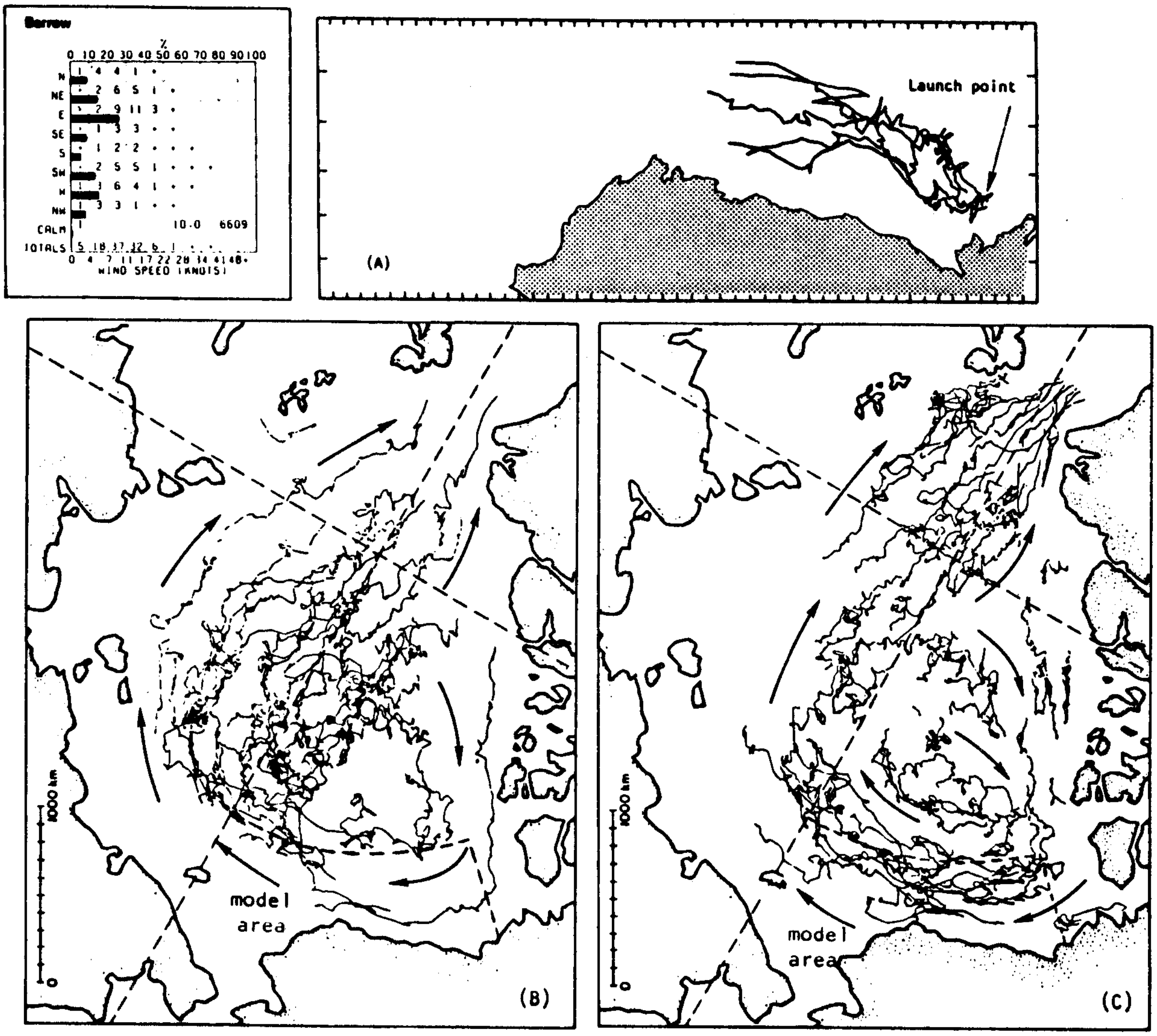

Fig. 6.4—Three groups of ice drift data. (A) Coast Guard drogues for 3 months during the summer of 1979; (B) composite trajectories compiled using data from 1893-1972 by Colony and Thorndike (1984); and (C) trajectories of automatic data buoys (1979-1982), also from Colony and Thorndike (1984).

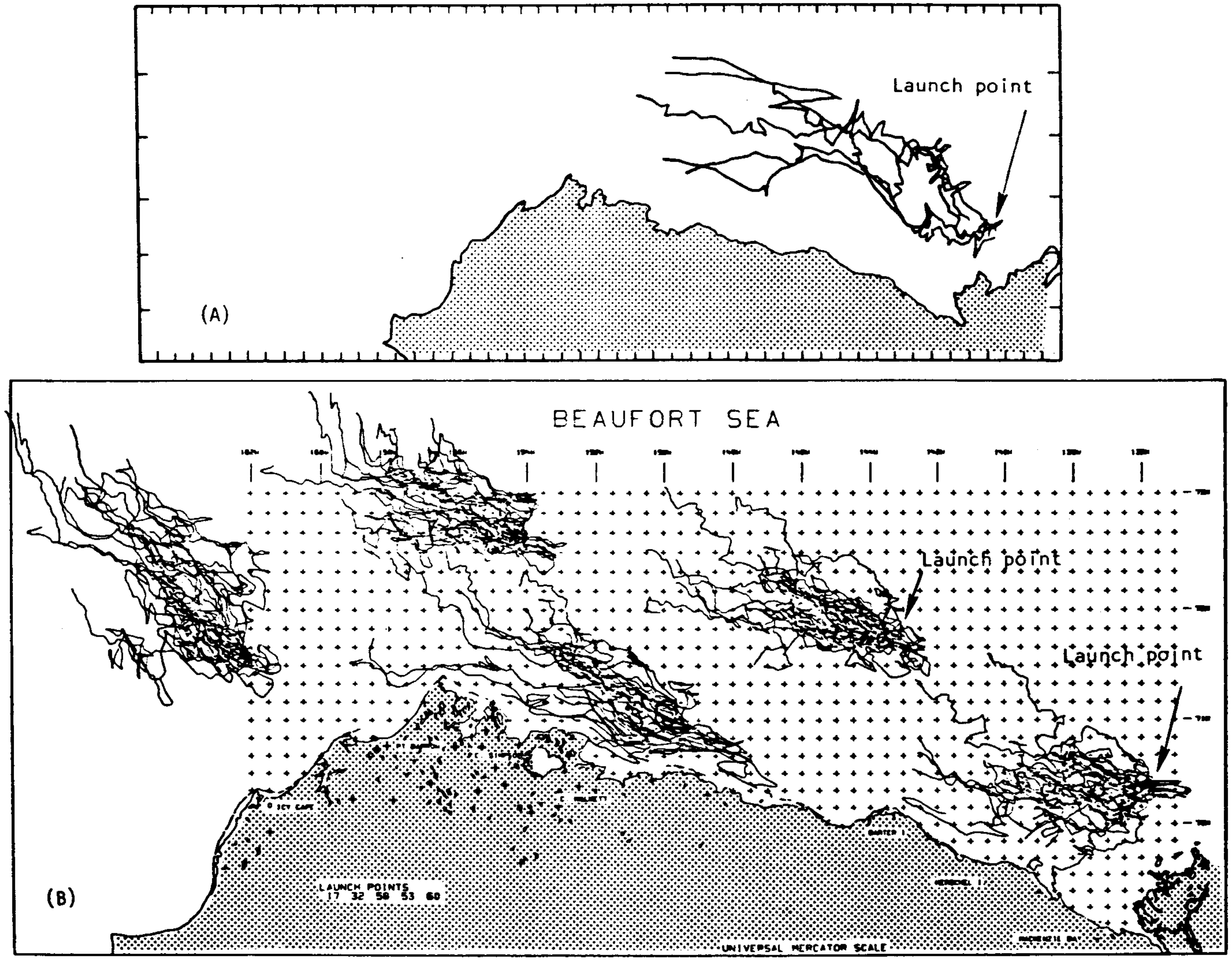

Fig. 6.5—Comparison between (A) trajectories of five satellite-tracked buoys deployed by the U.S. Coast Guard August to October, 1979, from eastern Mackenzie Bay, Canada, and (B) 30-day trajectories launched from five locations and computed by the RAND oil trajectory model and the two-dimensional stochastic weather simulation model.

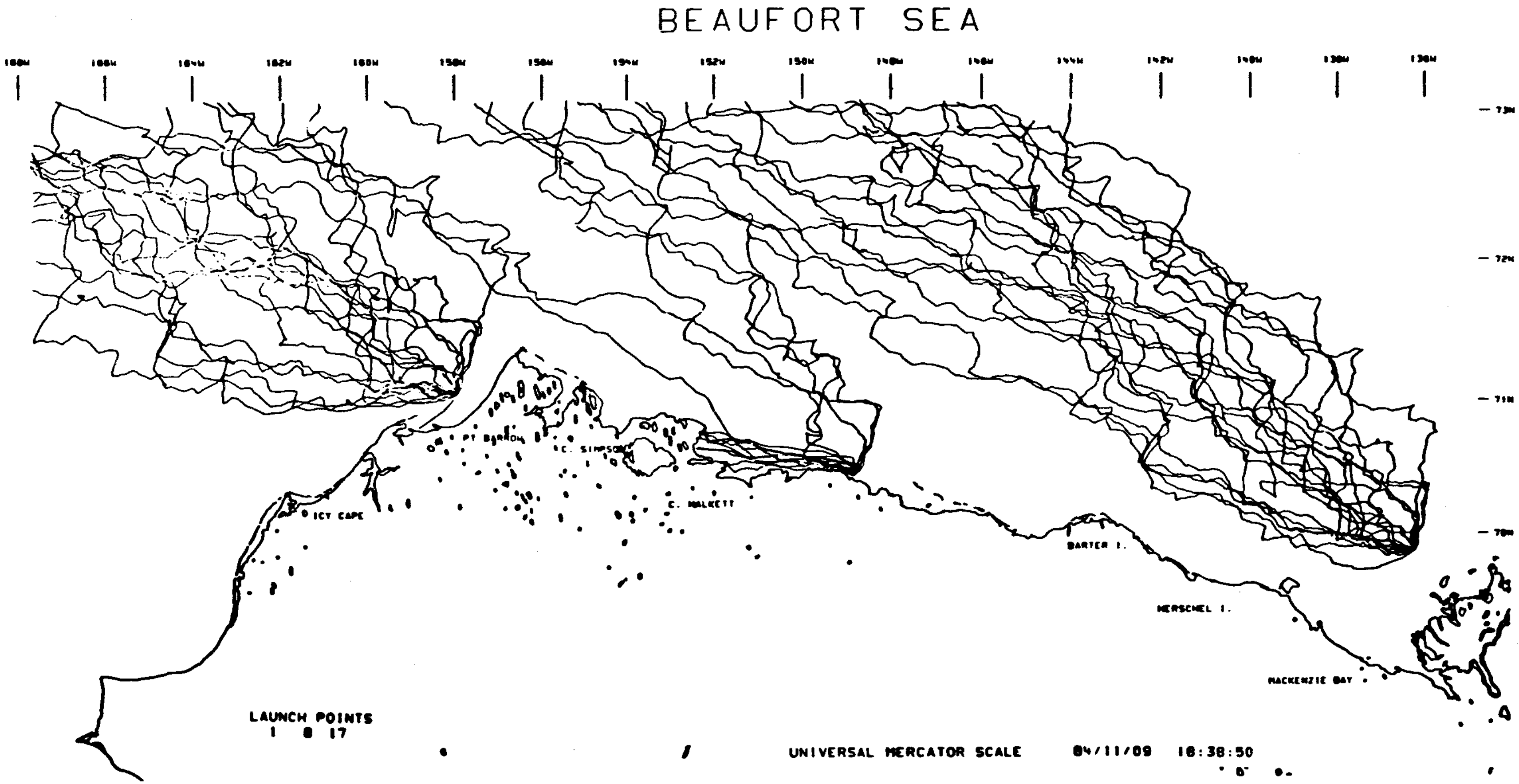

Fig. 6.6—Composite oil spill trajectory map showing the general direction of movements launched from stations 1, 8, and 17 during winter. The staggered launch scheme represents an equally likely chance of spill during the long winter period. The residence time within the modeled area is approximately two to three months.

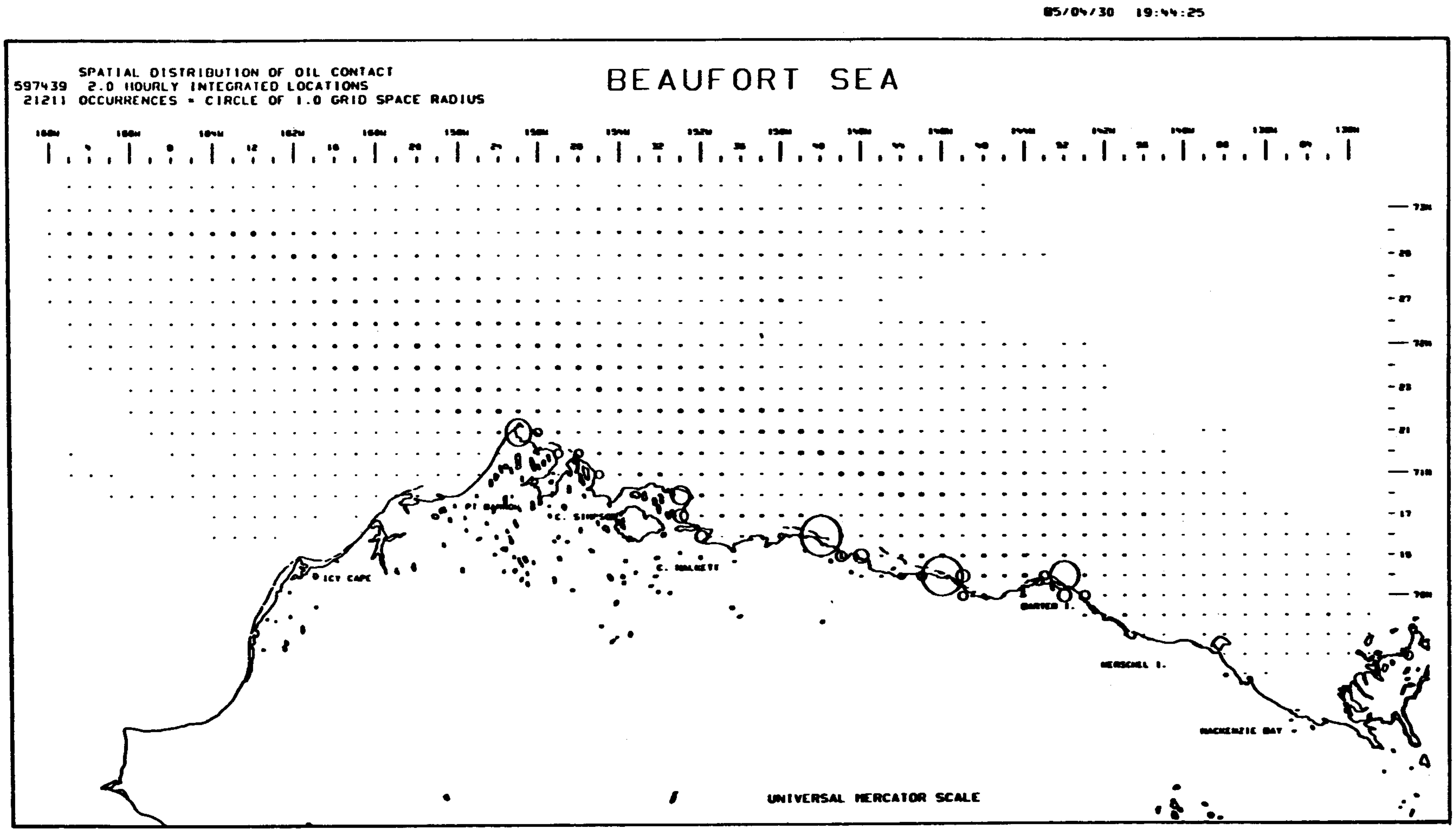

Fig. 6.7—Spatial distribution of oil contact frequencies. If oil is trapped in a near-shore lagoon, a continuous contact is assumed for the remaining period. Analysis is made using two-hour counting method. Plotting scale for the circle is 21211, two-hour exposure periods equal one latitudinal grid spacing for the radius of the circle.

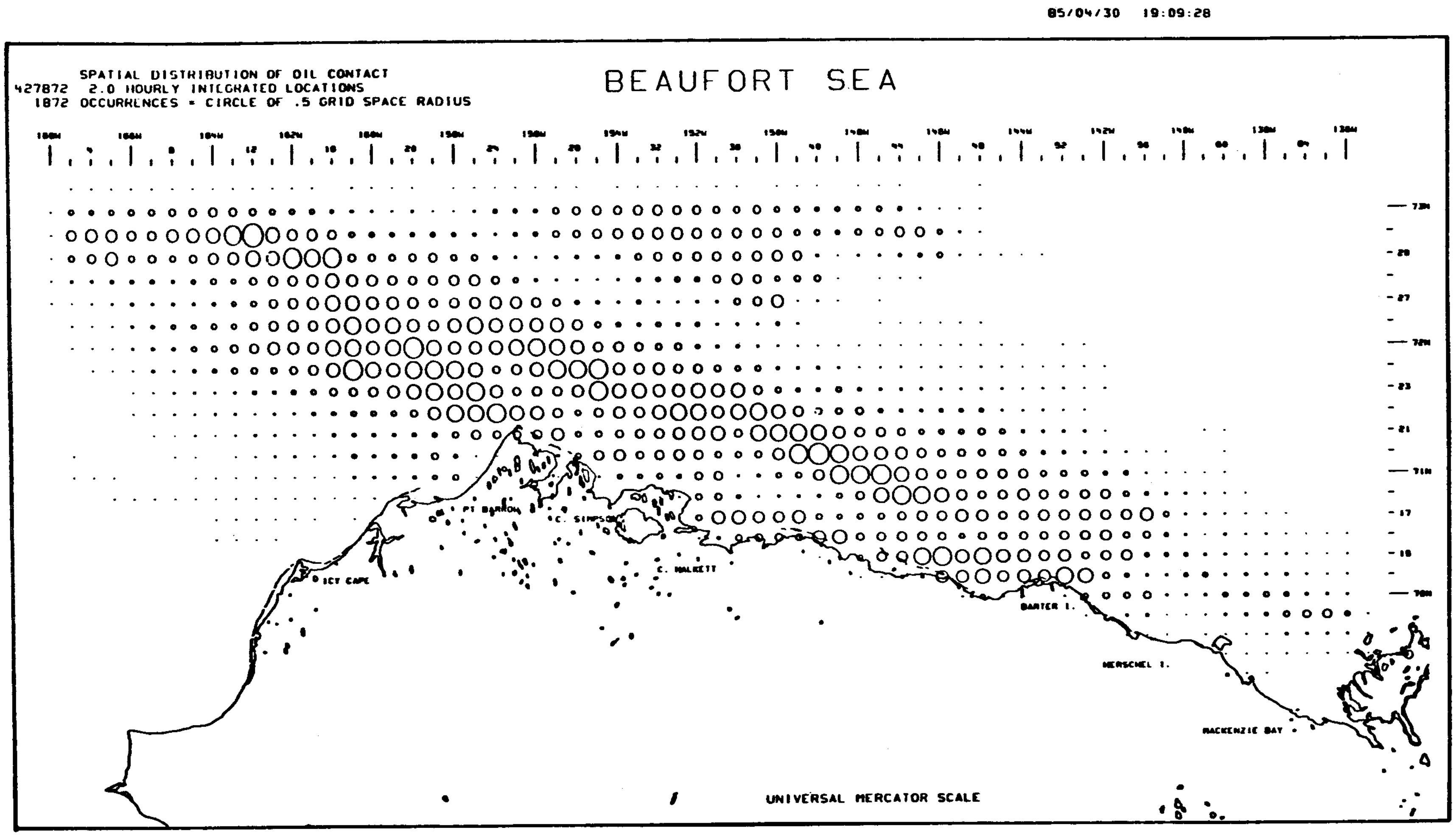

Fig. 6.8—Spatial distribution of oil contact frequencies excluding near-shore entrapments. Latitudinal grid spacing equals 1872 two-hour contact periods for the radius of a circle.

DETERMINING THE OIL CONCENTRATION FIELD

When released in water, fresh crude oil will undergo major changes in its composition while being transported and dispersed. The spreading of oil at the surface is mainly due to mechanisms associated with viscosity, surface tension, and inertia. As time progresses the major process responsible for the spreading of spilled oil are advection and turbulent dispersion. While oil is being advected and dispersed, its concentration decreases as a result of evaporation, photochemical degradation, and biodegradation. These processes are called weathering.

In modeling an oil concentration field, advection, dispersion, and weathering are considered as well as the transport of oil. The rates of evaporation and the bio- and photochemical degradation were evaluated under field conditions by other investigators (Payne et al., 1983). The oil decay rates for the simulation were estimated by these investigators on the basis of turbulence levels determined by means of the three-dimensional models for the different areas.

To illustrate the diffusion process induced by the turbulent oscillating flow, it is more convenient to demonstrate the magnitude of diffusion over the vertical plane in the absence of surface energy input from the wind. In other words, in this illustration the turbulence is generated primarily at the bottom by tide. To show the turbulent diffusion processes one hundred particles are released in each vertical layer near the Pribilof Island and half-hourly displacements are plotted there for a period of 24 hours (Fig. 6.9). The elevations for the eight layers are 2.5, 7.5, 12.5, 17.5, 25, 35, 85, and 240 meters, respectively.

In each layer the movements of particles are caused by advection and diffusion processes. For instance, the hourly displacement of the particle group in the first layer starts from the upper position, gradually moving with the tidal motion. As the group moves the distance between the particles increases because of the turbulent diffusion. In a stricter sense, the separation of particles is the combined result of diffusion and the nonuniformity of the current field. The combined process is called the turbulent dispersion. In shear flow, such as the one illustrated here, the major mechanism responsible for dilution of a soluble is dispersion. This is evident from the amount of dispersion experienced by the particle groups in the lower layers where the velocity gradient is much sharper than in the upper five layers. These five layers are located above the sharp pycnocline, which partially isolates the upward momentum transport.

Also of interest are the distances between the first and the last particle group within each layer. They represent the net displacement over a period of two days. The changes in net transport over the vertical are quite common in the coastal area, to satisfy the law of conservation of mass.

The example presented here illustrates the dispersion mechanism associated primarily with bottom stress and nonuniform velocity distribution. Dispersion effects can also be induced by shore line irregularity through the variability of the velocity field. For each of the large modeled areas, submodels are used to compute near-shore oil movements (Fig. 6.10). The turbulent diffusion coefficients averaged over ten tidal cycles, as computed by the three-dimensional model for each large area and for each layer, are stored on magnetic tapes. These diffusion coefficients became very useful for diffusion analysis in a limited near-shore area. Figure 6.11 represents the results of oil dispersion analysis in which crude oil is released instantaneously from five locations near the Bering Strait. Displacement of the one-part-per-billion concentration envelopes are plotted every five days. The influence of the

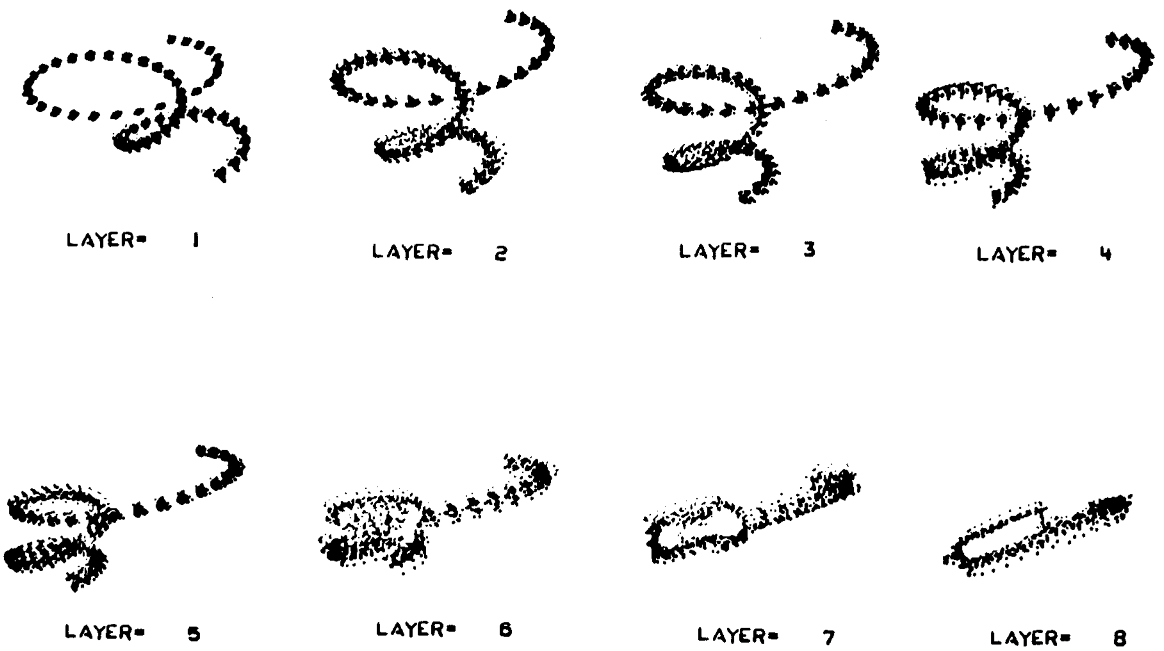

Fig. 6.9—Pathways of particle groups released in different layers of the model. Partially insulated by the pycnocline, 24-hour trajectories of particle groups released in the upper five layers experience less turbulent diffusion than the lower layers when the system is forced only with tidal energies.

shoreline and the variability of local advective/diffusive mechanisms (Fig. 6.11) are quite evident, as seen by the changing speed and direction of the oil movement.

Under a scenario of continuous release, the distribution of surface oil concentration is presented in Fig. 6.11. When oil moves through the Bering Strait, the strong local current tends to elongate the oil. Also notice the cumulation effects when the oil reaches the coastal area, where the on-shore current components drop and the along-shore currents strengthen. This near-shore effect tends to redirect the oil while slowing it down. The speed of an oil transport can be seen from the top diagram of Fig. 6.12, where daily displacements of the advancing plume are plotted. The daily traveling speed of oil is governed by the evolutionary weather state as well as the local circulation pattern.

To illustrate the effects of weather and local baroclinic circulation, a group of six trajectories are launched from five hypothetical spill locations in the Chukchi Sea/Barrow Arch lease area (Fig. 6.13). The net displacement for the northern trajectories during the eight-month period ranges between 3–5° latitude, which represents a daily movement of 1.4 to 2.31 km (Fig. 6.14). Oil launched near Point Hope travels substantially slower than its northern counterpart, which moves predominantly within the Arctic Gyre. The simulated direction and speed of ice movements within the Chukchi Sea agree with the observed values reported

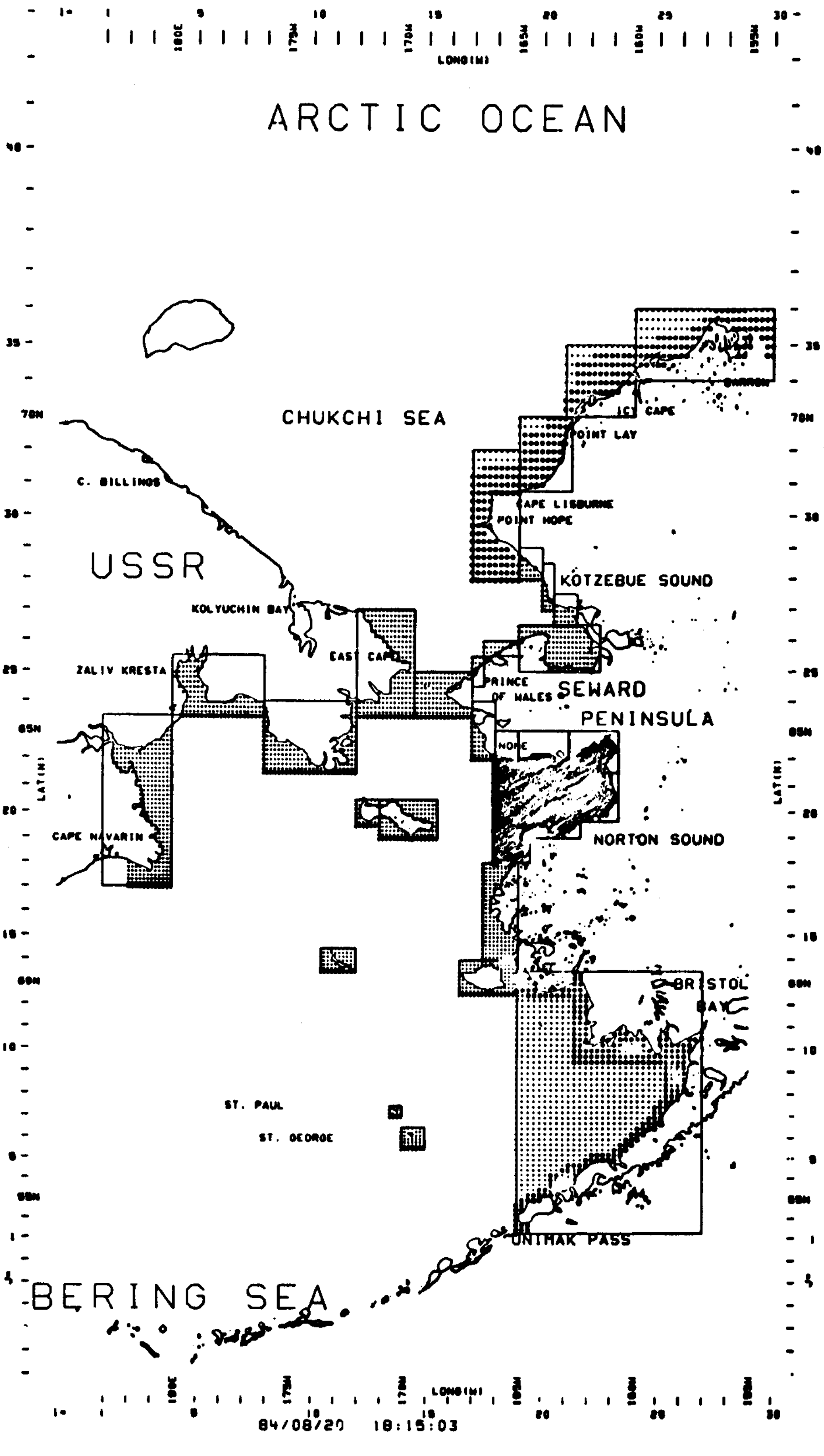

Fig. 6.10—Submodels are used to improve the near-shore resolution of the trajectory computation. The computational grids of the submodel are nested within the larger model's computational grid (Liu and Leendertse, 1984).

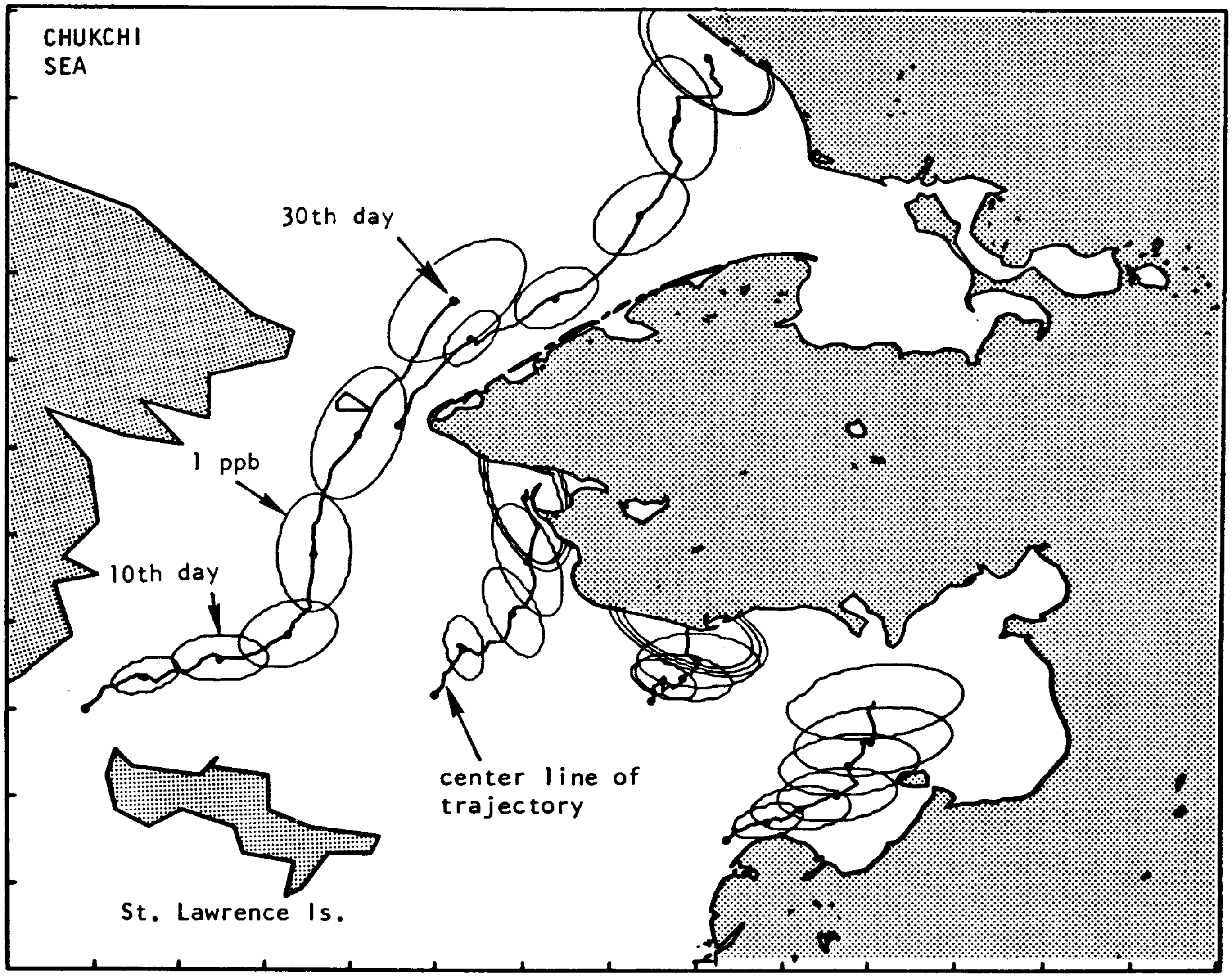

Fig. 6.11—Displacements of the one-part-per billion concentration envelope every five days for an instantaneous release of 700,000 barrels of crude oil from five hypothetical launch points during the summer. The variability of local advective and diffusive mechanisms is illustrated by the changing speed and direction of the oil's movements.

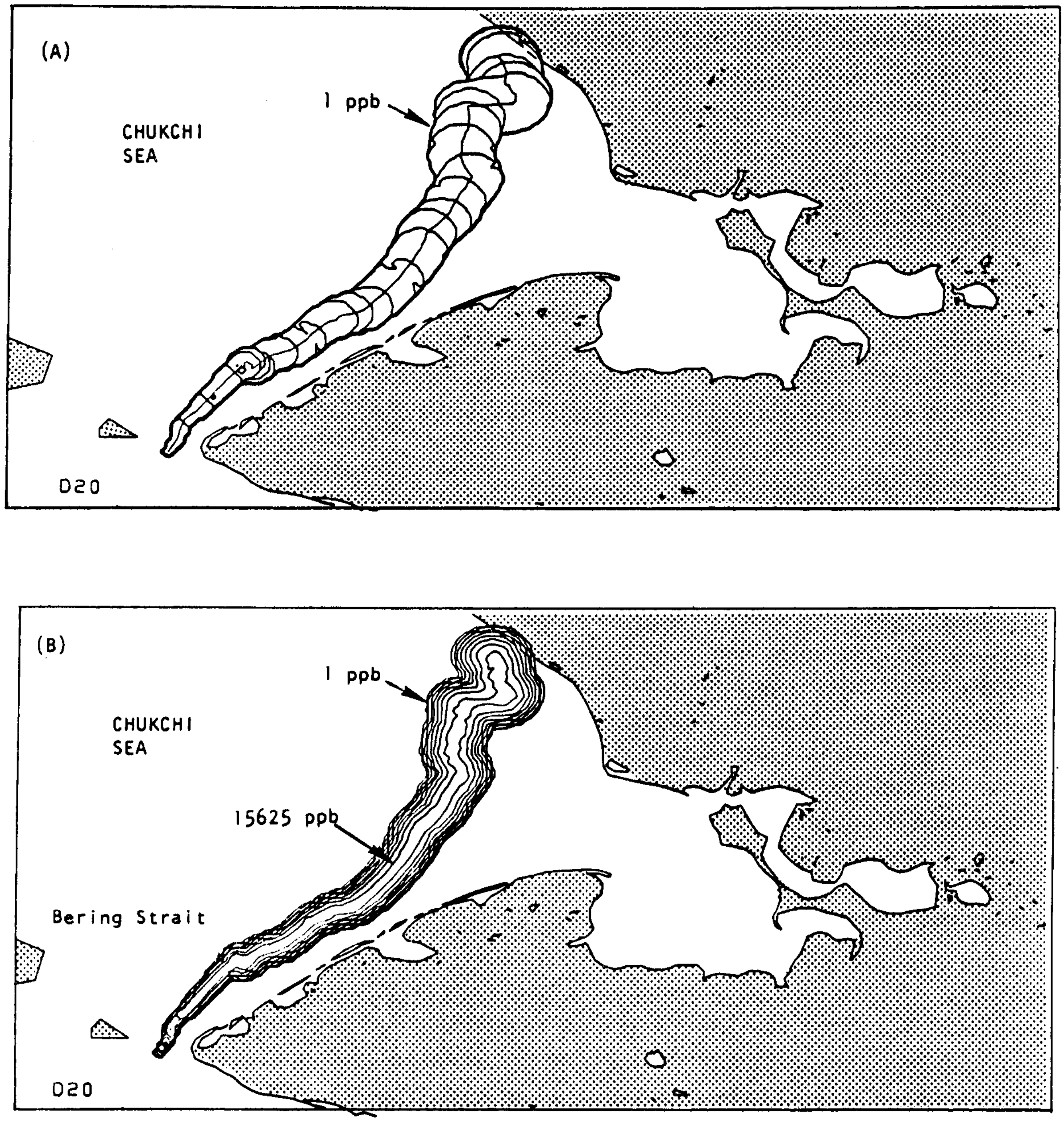

Fig. 6.12—Oil spill trajectory launched in the middle of the Bering Strait under a 30-day stochastic weather scenario during the summer. (A) illustrates the progressive daily displacements of the 1 part per billion concentration envelope for the continuous discharge of 2000 barrels of crude oil. The traveling speed of oil is governed by the evolutionary weather state as well as the local circulation pattern. (B) illustrates the concentration contour of the oil. Notice the cumulation effects when the oil reaches the coastal area where the on-shore current components drop and the along-shore currents strengthen. This near-shore effect tends to redirect the oil while slowing it down somewhat.

by Gordienko (1958), and Hibler (1979), who made computations using ice models including nonlinear plastic flow effects by means of viscous-plastic constitutive law.

Perhaps it is more illustrative to show and analyze a group of trajectories launched near an embayment so that the shore effects can be seen. The launch point is located between St. Lawrence Island and the Gulf of Anadyr, USSR (see thc insert map of Fig. 6.15). Twenty-one groups of 30-day oil spill trajectories are sampled every two hours. These sampled data are then analyzed for their direction and speed. For a 30-day duration there are 360 two-hour samples for current directions and speeds. Since the directions and speeds of currents at every two hours are located over a different area, local residual circulation and the relative distance from the shore-fast ice make the movement of oil contained in ice different from that of free-drifting pack ice. Consequently, there are more random ice motions under the local wind stress than the oil movements in the water column resulting from inertia and momentum filtering effects.

Figure 6.16 indicates that most oil spill trajectories move in a predominantly northwesterly direction. For the summer period (Fig. 6.16), however, most contacts are closer to the eastern shore. It should be noted that the plotting scale of Fig. 6.17 is four times that of the one shown in Fig. 6.16. The western Chukchi Sea receives much less impact during the summer season than in the winter period. On the average, oil travels a shorter distance and moves more randomly under the summer winds. During summer, winds have higher variabilities and, as a consequence, the inertial current components have a substantial contribution toward the overall current direction. The area of greatest impact is located near Icy Cape.

Another method using the oil spill trajectory simulation results is to trace back from a given marine resource contact location to the location of oil released. If the marine area is ecologically sensitive, then the area near the launch point should not be considered for oil exploration. This type of "trace-back" analysis was made, for example, for the Chukchi Sea lease area. Partial results for winter and summer are listed in Tables 6.1 and 6.2, respectively. The tables are for illustrative purposes only. For example, in Table 6.1, the location of the marine area is represented by the (I,J) grid of the model as listed in the first two columns in the table. The third column is the number of trajectories hitting this area during this period. The subsequent numbers are the launch points where the oil was released. In the first row of Table 6.1, at marine area I=3, J=17 as shown in Fig. 6.13, oil was released from stations J14, J15, J16, J20, and J36. The area is relatively safe during summer as indicated in Table 6.2 from the launch points considered for this particular simulation run. Analyses such as these are sometimes instrumental in marine pollution analysis where the location of a point source is to be selected to avoid a particular marine resource area.

The marine resource group risk exposure time can be evaluated by the spatial distribution of oil contact frequencies from the spill trajectories. In Fig. 6.17 the contact frequencies are plotted at each marine area with the size of circle proportional to the contact time.

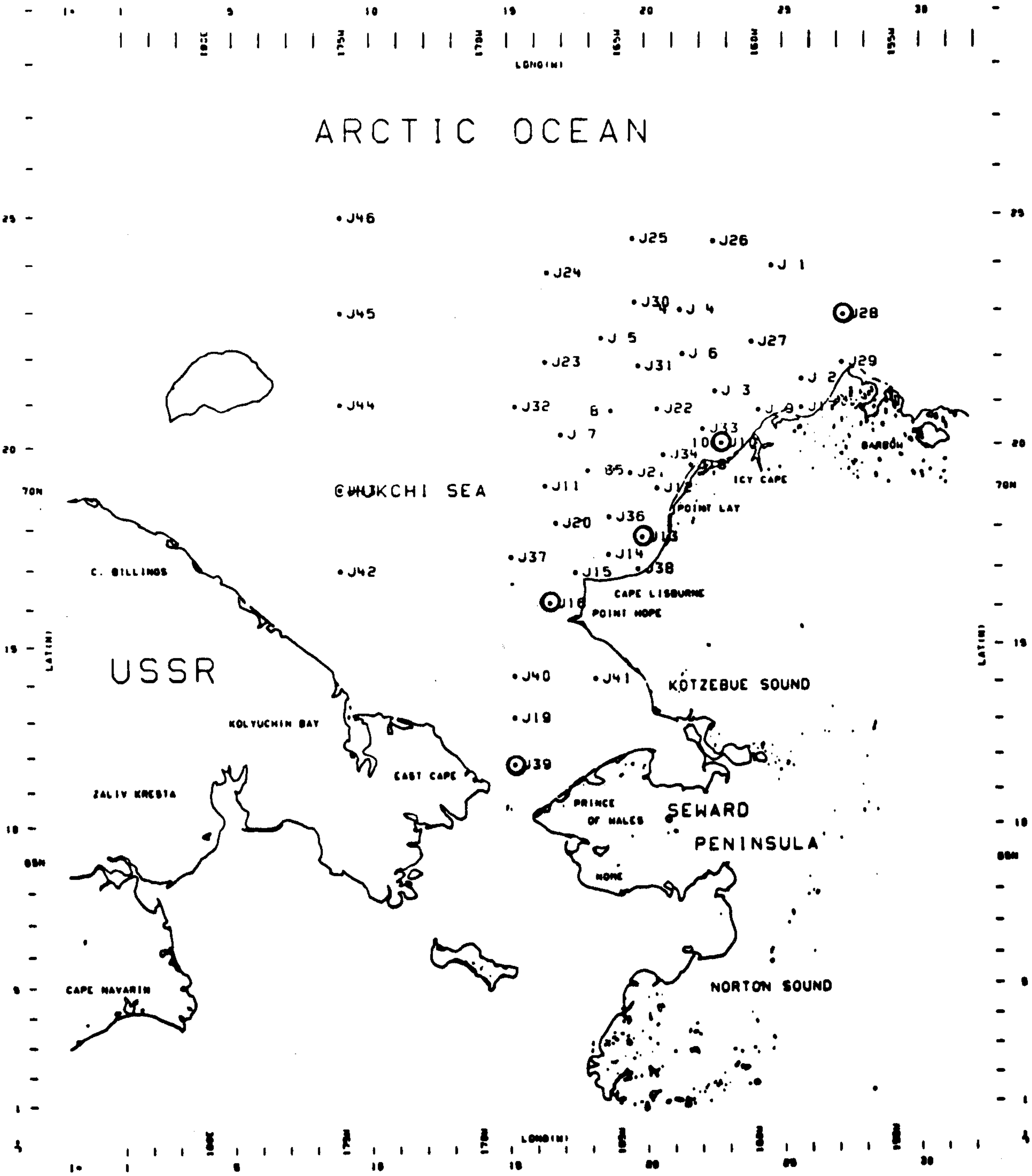

Fig. 6.13—Location of 46 launch points specified for the oil spill trajectory computation. Barrow Arch lease area (No. 109).

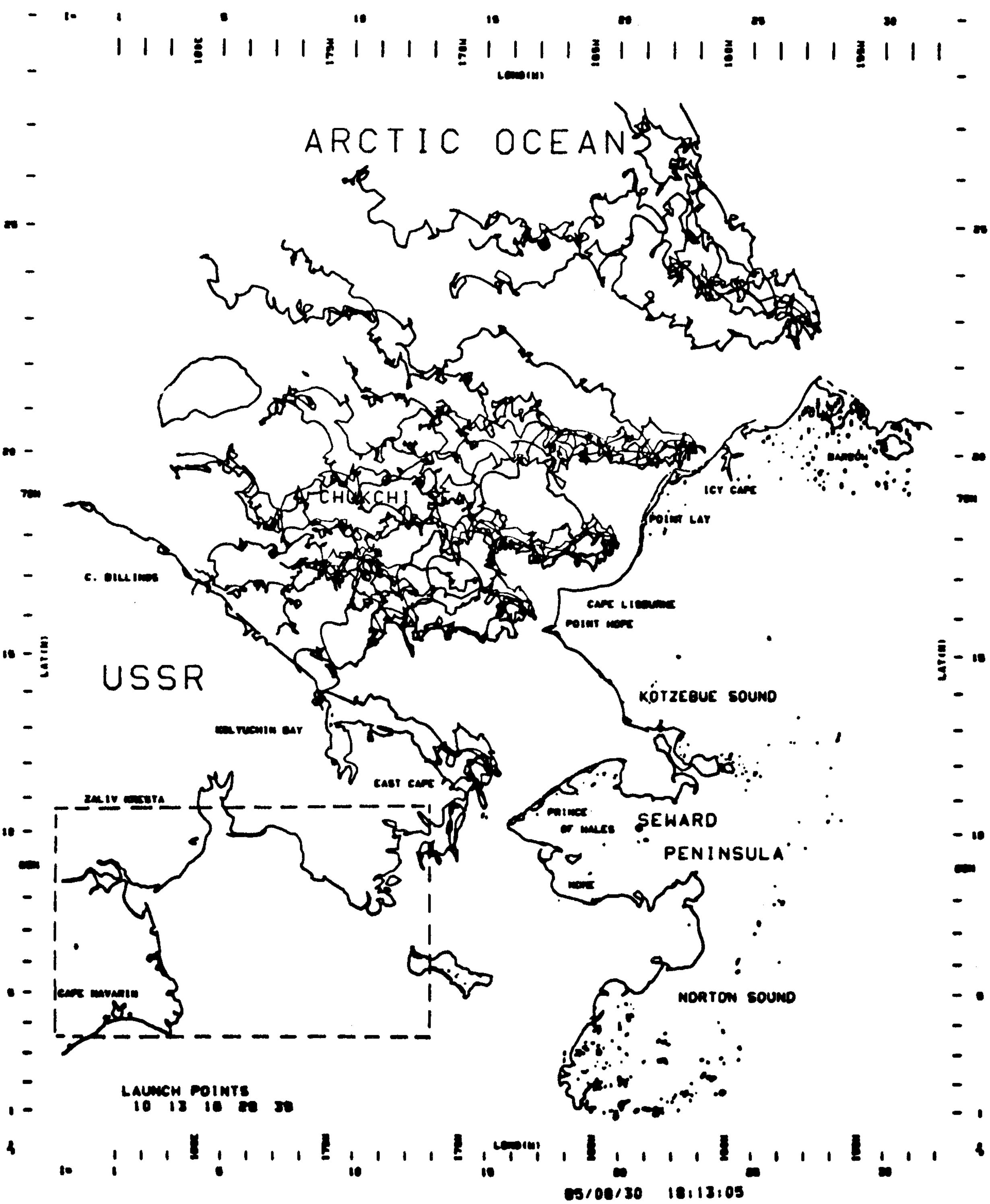

Fig. 6.14—Five sets of randomly selected trajectories from launch points 10, 13, 16, 28, and 39; under the staggered-launch mode, each spill has about equally likely chance of occurrence during the winter. Spill launched near the Bering Strait can move either south or north depending on the weather sequence.

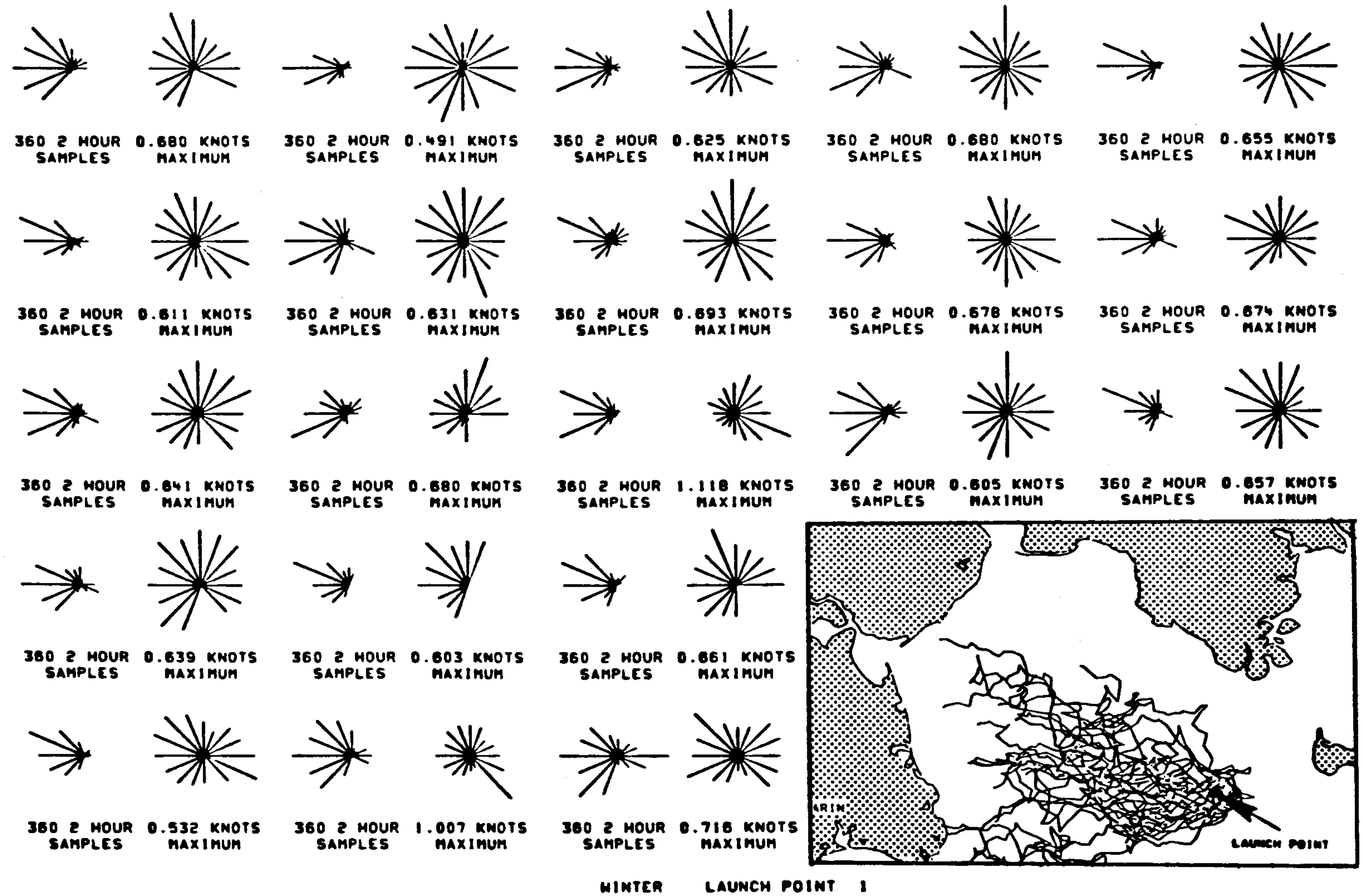

Fig. 6.15—Current roses analyzed from twenty-one 30-day oil spill trajectories for winter, launched near a point between St. Lawrence Island and the Gulf of Anadyr, USSR (see insert map). Local residual and the relative distance from the shore-fast ice make the oil containing ice move differently from the free-drifting pack ice. Consequently, there are more random ice motions under the local wind stress than the oil movements in the water column resulting from inertia and momentum filtering effects.

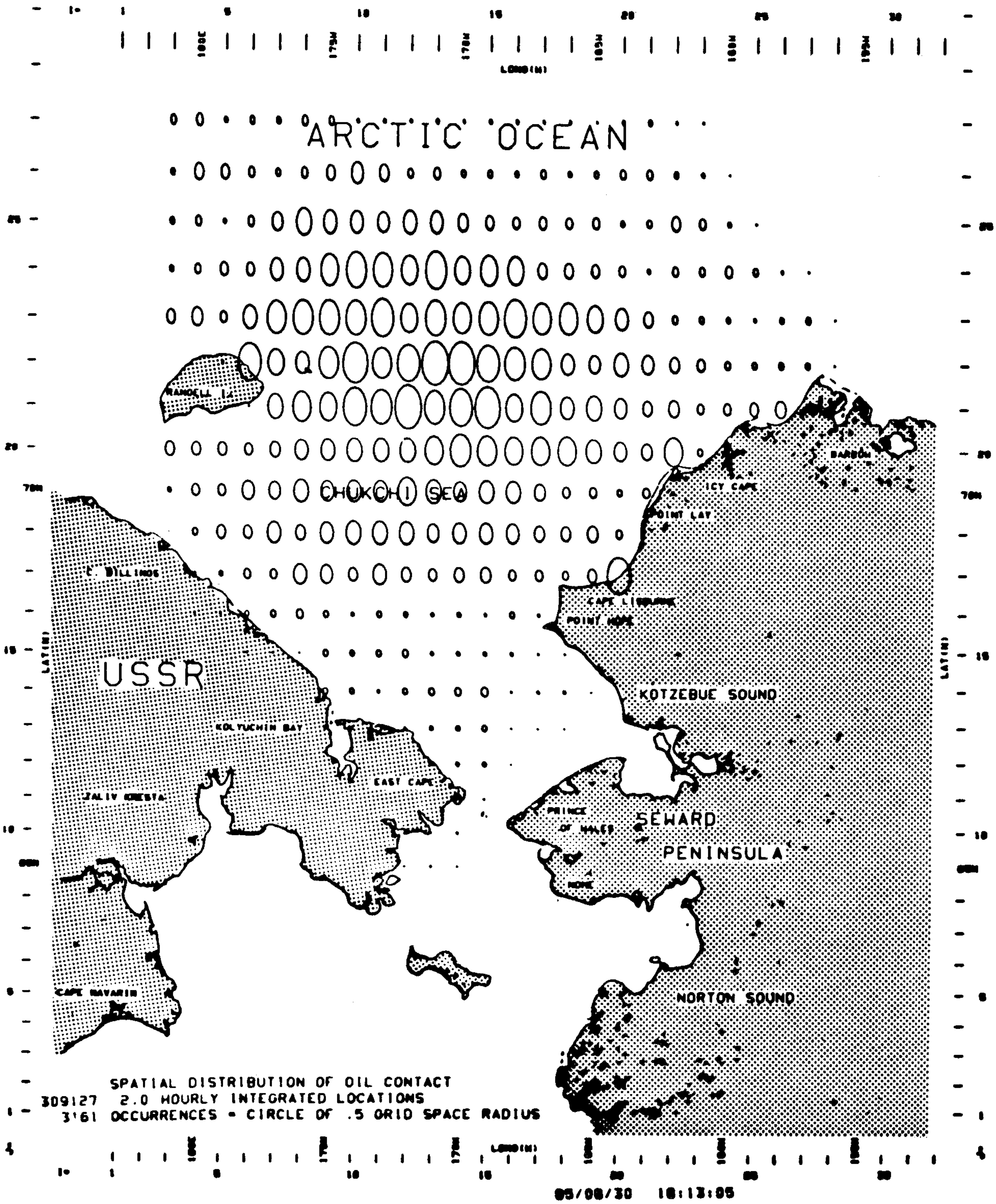

Fig. 6.16—Spatial distribution of oil contact frequencies during winter. Latitudinal grid spacing equals 3161 two-hour contact periods for the long axis of the ellipse.

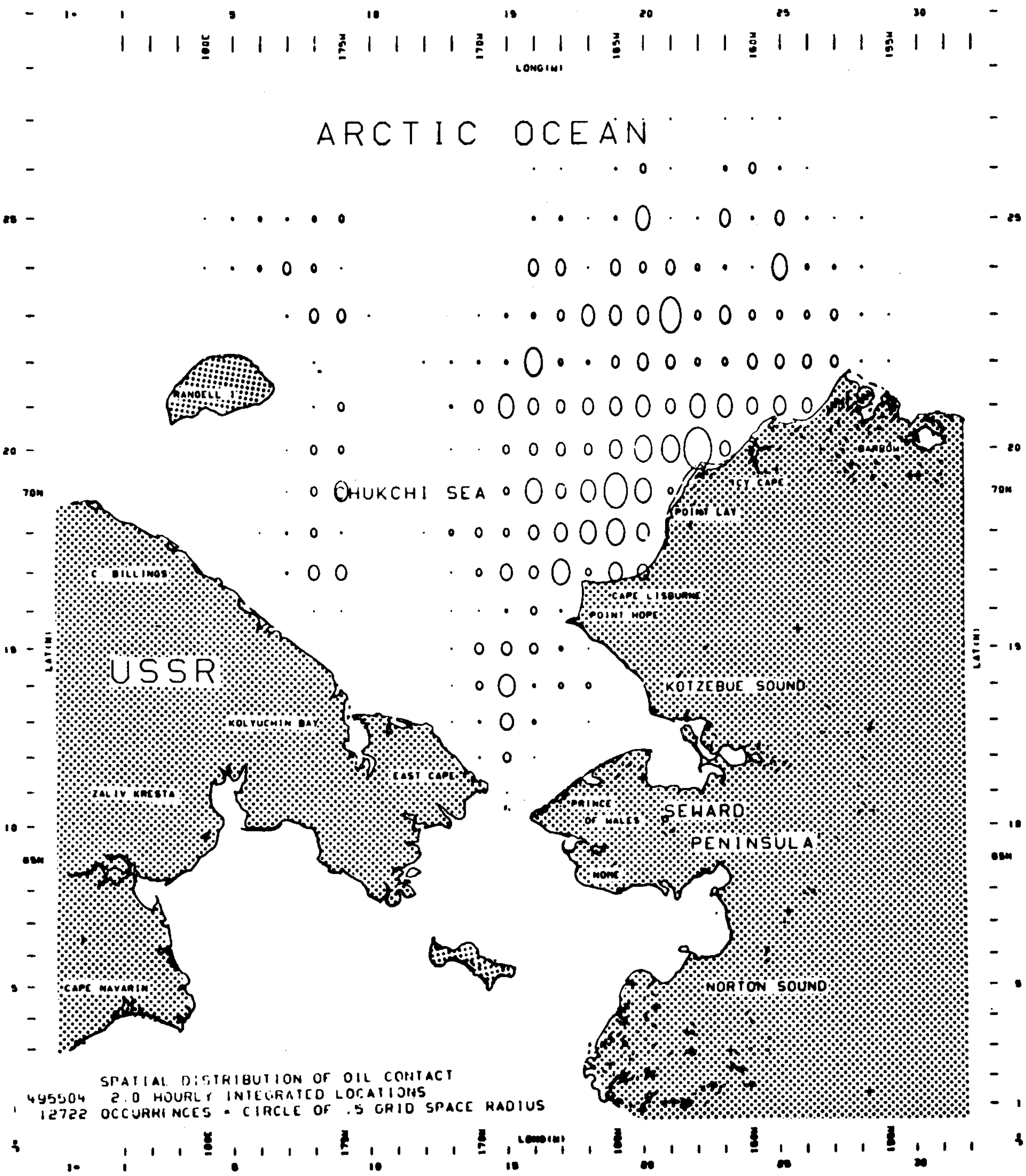

Fig. 6.17—Spatial distribution of oil contact frequencies during summer. Latitudinal grid spacing equals 12722 two-hour contact periods for the long axis of the ellipse.

Table 6.1

CHUKCHI SEA WINTER OIL SPILL TRAJECTORY ANALYSES (SALE 109). TABULATED "TRACE-BACK" OF OIL SPILL CONTACT BETWEEN CONTACT LOCATION AND LAUNCH POINT. "*" INDICATES LANDFALL AND "#" INDICATES TRAJECTORY MOVED OUT OF THE MODELED AREA

I	J	NO	LAUNCH POINTS TERMINATING AT (I,J)
3	17	9	*J14 *J15 *J15 *J16 *J16 *J16 *J20 *J36 *J36
3	18	8	J11 J14 J14 J15 J15 J37 J37 J37
3	19	28	J 7 J11 J12 J13 J13 J13 J13 J14 J14 J15 J16 J16 J20 J20 J20 J20 J21 J32 J32 J35 J35 J36 J36 J37 J37 J37 J37 J40
3	20	15	J 8 J 8 J12 J14 J15 J16 J20 J20 J20 J20 J23 J34 J36 J37 J37
3	21	1	*J11
3	23	16	J 2 J 5 J 5 J 7 J 8 J 8 J 8 J 9 J 9 J22 J23 J23 J30 J32 J34 J35
3	24	24	J 2 J 3 J 5 J 5 J 6 J 8 J11 J22 J22 J22 J23 J23 J23 J23 J24 J24 J25 J25 J30 J31 J32 J32 J32 J35
3	25	16	J 3 J 4 J 5 J 6 J 7 J 8 J23 J23 J23 J23 J24 J27 J30 J31 J31 J31
3	26	14	J 5 J 5 J 5 J 5 J 6 J 6 J24 J24 J24 J25 J25 J27 J30 J31
3	27	13	J 4 J 4 J 6 J24 J24 J24 J24 J27 J30 J30 J30 J30 J32
3	28	2	#J23 #J24
4	16	5	*J15 *J16 *J32 *J37 *J38
4	17	7	*J16 J16 *J19 J20 J36 *J37 *J41
4	18	10	J11 J12 J13 J15 J15 J23 J35 J37 J41 J41
4	19	9	J 7 J12 J14 J14 J21 J34 J35 J36 J36
4	20	6	J 5 J 7 J 8 J20 J33 J36
4	21	1	*J12
4	22	1	*J22
4	23	10	J 3 J 4 J 4 J 4 J12 J21 J21 J31 J32 *J33
4	24	10	J 6 J 6 J10 J17 J18 J25 J29 J31 J33 J34
4	25	9	J 2 J 4 J 5 J 8 J10 J22 J27 J30 J33
4	26	12	J 3 J 3 J 4 J 9 J24 J24 J25 J28 J29 J30 J31 J31
4	27	5	J 1 J 2 J 5 J 6 J25
4	28	1	#J26
5	16	16	*J 7 *J11 *J14 *J14 *J15 *J16 *J20 *J20 *J21 *J35 *J37 *J40 *J40 *J40 *J41 *J41
5	17	3	J15 *J16 J38
5	18	4	J 8 J15 J36 J38
5	19	4	J14 J21 J21 J31
5	20	6	J13 J18 J22 J34 J36 J37
5	21	9	*J11 *J13 *J15 *J20 *J21 *J22 *J23 *J33 *J38
5	22	39	*J 3 *J 3 *J 4 *J 5 *J 5 *J 6 *J 7 *J 7 *J 7 *J 8 *J 8 *J 8 *J 8 *J 8 *J 9 *J10 *J12 *J12 *J18 *J18 *J20 *J21 *J22 *J22 *J22 *J23 *J23 *J24 *J30 *J30 *J31 *J31 *J32 *J32 *J32 *J33 *J34 *J35 *J36
5	23	9	J 7 J 8 J 9 J12 *J25 J27 J30 J33 *J36
5	24	1	J23
5	25	2	J25 J33
5	26	6	J 4 J 9 J22 J26 J29 J30
5	27	2	J24 J26
5	28	4	#J 4 #J25 #J27 #J30
6	15	4	*J11 *J12 *J19 *J41
6	16	2	*J16 *J40
6	17	1	J14
6	18	2	J22 J40
6	19	4	J12 J14 J15 J16
6	20	4	J 6 J 9 J10 J13
6	21	75	*J 3 *J 3 *J 3 *J 3 *J 4 *J 5 *J 5 *J 6 *J 7 *J 7 *J 7 *J 7 *J 8 *J 9 *J 9 *J10 *J11 *J11 *J11 *J11 *J11 *J11 *J11 *J11 *J12 *J12 *J12 *J12 *J13 *J13 *J14 *J14 *J16 *J18 *J20 *J20 *J21 *J21 *J21 *J21 *J21 *J21 *J21 *J21 *J22 *J22 *J22 *J23 *J24 *J30 *J31 *J31 *J31 *J32 *J32 *J32 *J33 *J34 *J34 *J34 *J34 *J34 *J35 *J35 *J35 *J35 *J35 *J35 *J35 *J36 *J36 *J36 *J37 *J37 *J38
6	22	20	J 2 *J 6 J 6 *J 7 *J 7 *J 7 J 7 J10 J13 J14 *J15 J17 *J24 J31 *J32 *J32 *J32 J33 *J34 J34
6	23	6	J 3 J 4 J 9 J 9 J17 J27
6	24	7	J 2 J 5 J 6 J18 J18 J22 J32
6	25	2	J31 J34
6	26	3	J 3 J17 J23

Table 6.2

CHUKCHI SEA SUMMER OIL SPILL TRAJECTORY ANALYSES (SALE 109). TABULATED "TRACE-BACK" OF OIL SPILL CONTACT BETWEEN CONTACT LOCATION AND LAUNCH POINT. "*" INDICATES LANDFALL AND "#" INDICATES TRAJECTORY MOVED OUT OF THE MODELED AREA

I	J	NO	LAUNCH POINTS TERMINATING AT (I,J)
4	24	1	J45
4	25	1	J46
5	24	19	J45 J45 J45 J46 J46 J46 J46 J46 J46 J46 J46 J46 J46 J46 J46 J46 J46 J46 J46
5	25	8	J46 J46 J46 J46 J46 J46 J46 J46
6	18	1	J43
6	24	18	J45 J45 J45 J45 J45 J45 J45 J45 J45 J45 J45 J45 J45 J45 J45 J45 J46 J46
6	25	3	J46 J46 J46
7	17	13	J42 J42 J42 J42 J42 J42 J42 J42 J42 J42 J42 J43 J43
7	18	15	J43 J43 J43 J43 J43 J43 J43 J43 J43 J43 J43 J43 J43 J43 J44
7	19	1	J44
7	20	2	J44 J44
7	23	1	J45
7	24	4	J45 J45 J45 J45
8	17	16	J42 J42 J42 J42 J42 J42 J42 J42 J42 J42 J42 J42 J42 J42 J42 J42
8	18	11	J43 J43 J43 J43 J43 J43 J43 J43 J43 J43 J44
8	19	21	J43 J44 J44 J44 J44 J44 J44 J44 J44 J44 J44 J44 J44 J44 J44 J44 J44 J44 J44 J44 J44
8	20	1	J44
8	23	3	J45 J45 J45
8	24	2	J45 J45
9	16	2	J42 J42
9	17	1	J42
9	19	5	J43 J43 J44 J44 J44
9	20	1	J44
12	18	4	J37 J37 J37 J37
12	22	1	J32
13	13	3	J39 J39 J39
13	14	1	J19
13	15	1	J40
13	16	1	J40
13	17	4	J37 J37 J37 J37
13	18	17	J37 J37 J37 J37 J37 J37 J37 J37 J37 J37 J37 J37 J37 J37 J37 J37 J37
13	21	13	J32 J32 J32 J32 J32 J32 J32 J32 J32 J32 J32 J32 J32
13	22	7	J32 J32 J32 J32 J32 J32 J32
14	11	1	J39
14	12	3	J39 J39 J39
14	13	5	J39 J39 J39 J39 J39
14	14	22	J19 J19 J19 J19 J19 J19 J19 J19 J19 J19 J19 J19 J19 J19 J19 J19 J19 J39 J39 J39 J39 J40
14	15	29	J19 J19 J19 J19 J19 J19 J40 J40 J40 J40 J40 J40 J40 J40 J40 J40 J40 J40 J40 J40 J40 J40 J40 J40 J40 J40 J40 J40 J40
14	16	3	J16 J16 J40
14	17	20	J16 J16 J16 J16 J16 J16 J16 J16 J16 J16 J16 J16 J16 J16 J16 J16 J16 J16 J37 J37
14	18	3	J37 J37 J37
14	19	1	J20
14	20	1	J11
14	21	9	J 7 J 7 J 7 J 7 J32 J32 J32 J32 J32
14	22	5	J 7 J32 J32 J32 J32
14	23	2	J23 J23
15	13	4	J19 J39 J39 J39
15	14	10	J19 J19 J19 J39 J39 J39 J39 J39 J39 J41
15	15	10	J19 J19 J40 J40 J41 J41 J41 J41 J41 J41
15	16	5	J15 J40 J41 J41 J41
15	17	9	J15 J15 J16 J16 J16 J16 J16 J16 J16
15	18	11	J15 J15 J16 J16 J20 J20 J20 J20 J20 J20 J20
15	19	18	J11 J11 J11 J11 J20 J20 J20 J20 J20 J20 J20 J20 J20 J20 J20 J20 J20 J20
15	20	20	J 7 J11 J11 J11 J11 J11 J11 J11 J11 J11 J11 J11 J11 J11 J11 J11 J11 J11 J11 J11

7. CONCLUSIONS

This report presents the methodologies, data analyses, and the modeling efforts related to the hydrodynamic processes of the Alaskan coastal waters. The following conclusions were reached during the course of the study:

1. The hydrodynamic processes of the Alaskan coastal waters possess different characteristic scales both in time and over space, depending on their depth and the relative distance from the coast. This, when coupled with the shoreline configuration, requires nested models of various scale to resolve the dynamic process of our primary concern. Because of this, we have developed models that range in size from 1.5 million square kilometers (Gulf of Alaska model, 43,000 grid points) to lagoon models, which have grid spacings of only a few hundred meters.
2. In 1980 the results of the three-dimensional model of the Bering/Chukchi Sea indicated an amphidromic system in the lower Chukchi Sea. Its location varied slightly depending on the seasonal variability of ice coverage and the vertical stratification. The computational results are presented in Liu and Leendertse (1982).
3. The baroclinic spin-up time ranged from a few hours for a small coastal tidal model to more than ten days for a large model such as the Gulf of Alaska. For the eastern Bering shelf, which has an average depth of 75 meters, and over 90 percent of the energy is of tidal origin, the time to reach equilibrium is approximately five to seven days. The computed baroclinic circulation pattern over the shelf with the tidal bands filtered out agrees with the observed patterns.
4. A hydrodynamic model coupled to an areawide weather or wind model is required to simulate the complete water movements in the Alaskan coastal waters. At the present time, the global weather data grid network over the Alaskan area does not have enough resolution to compute realistic wind fields associated with a strong moving storm and cannot be used for accurate oil spill simulations.
5. A parametric wind model based upon statistical data can be used very effectively and with a high degree of accuracy as input for oil spill simulations.
6. In addition to the hydrodynamics computation algorithm, extensive software developments are required for the oil spill simulation and subsequent processing of results for impact assessments.
7. Short intervals are required for accurate computation of trajectories near shore locations. Also, the weathering of oil in the simulations requires a short time interval for accurate computation of oil concentrations. This is particularly true for the computation of weathering shortly after a release, as then the evaporation rates are high.
8. For oil spill impact risk analysis, not only is information about the trajectory required, but also information about the dispersion of oil. The computation of this dispersion requires a rather extensive computational effort.
9. Hydrodynamic models with much resolution of the pycnocline are required to properly model the physical processes in this stratification zone without appreciable numerical diffusion. Numerical models using vertical coordinate transformations appear to be insufficient for resolving the pycnocline.

10. Shear stress coefficients for the air/ice and ice/water interfaces should be calculated based on data using the exact model for which they will be used later, ideally for the areas with similar ice coverage. Otherwise, coefficients derived from models of lower dimensions would overestimate the amount of momentum transfer if they were used in a model of higher dimensions. Fewer terms are involved that represent the overall momentum transport process in the lower dimension models than in those with higher dimensions. The same is true for diffusion coefficients. Fitting the same data group, a one-dimensional model would result in higher diffusion coefficients than a two-dimensional model, as the latter has more terms to resolve the diffusive process.
11. At the present time, the available turbulence-closure schemes still need improvements when turbulence is strongly influenced by body forces acting in a preferred direction, such as the buoyancy forces. The ice melting process creates strong stratification in the Alaskan offshore waters; therefore, it is more difficult to simulate turbulent processes in these waters. More studies are needed to compute the dispersion in nonhomogeneous waters.
12. For the turbulence-closure computation in this modeling study, a parametric relationship considering energy transfer from the wind field is used as an input energy source term. The amount of energy input is evaluated according to the equilibrium condition considering the Miles-Phillip mechanism and uses shallow water wave/current data measured by our colleagues of the Netherlands Rijkswaterstaat. These data are measured over the southern North Sea under the influence of the Icelandic Low. Both the depth and wind conditions are quite similar to the oceanic conditions of the Alaskan shelf waters during an ice free condition. This is quite different from the traditional approach in which the upper boundary is treated as a moving or nonmoving wall like the bottom. It is the authors' belief that storm-induced surface diffusion and transport are extremely important in an oil spill risk analysis. The likelihood of a spill is much higher during storm conditions. The wall-generated turbulence does not behave the same as the storm generated surface turbulence. In the present k-ε formulation, there is little experimental information at the surface that could be used as the basis for specifying the length scale (Rodi, 1980). Certainly more research is needed in this area.
13. This study has developed a general data base on the tidal propagation and residual circulation pattern over the Alaskan coastal waters so that they can be used as boundary and initial conditions for the nested models of higher resolution. Baroclinic residual currents coexisted with the tidal energy over the broad Bering/Chukchi Sea shelf and results are tabulated in Tables A.1 through A.6. It is more economical and reliable to use the circulation produced in this manner than to have those small models generate baroclinic current fields themselves.

8. REFERENCES CITED

Aagaard, K., L. K. Coachman, and E. Carmarck, "On the Halocline of the Arctic Ocean," *Deep Sea Res.*, Vol. 28A, No. 6, 1981, pp. 529–545.

Abraham, G., "Jet Diffusion in Liquid of Greater Density," *J. of Hydraulic Div., Proc. Am. Soc. of Civil Engr.*, Vol. 86, HY6, 1960, pp. 1–3.

Abramowitz, M., and L. A. Stegun, *Handbook of Mathematical Functions*, National Bureau of Standards, Washington, D.C., 1964.

Ahlnas, K., and G. Wendler, "Sea Ice Observations by Satellite in the Bering, Chukchi, and Beaufort Sea," *Proc. Fifth Inter. Conf. Port and Ocean Eng. Under Arctic Conditions*, POAC 79, Trondheim, Norway, 1979, pp. 313–329.

Aitken, J., "On the Effects of Oil on a Stormy Sea," *Roy. Soc. Edinburgh*, Vol. 12, 1882, pp. 56–75.

Anderson, D.L.T., and P. D. Killworth, "Spin-Up of a Stratified Ocean with Topography," *Deep Sea Res.*, Vol. 24, 1977, pp. 709–732.

Arsen'ev, V. S., *Circulation in the Bering Sea*, No. 13, Akad. Nauka SSSR, Moscow, 1965, pp. 61–65.

Arsen'ev, V. S., *Currents and Water Masses of the Bering Sea*, Akad. Nauka SSSR, Moscow, 1967.

Barry, R. G., "Further Climatological Studies of Baffin Island, Northwest Territories," *Inland Water Directories*, Technical Report 65, Ottawa, Canada, 1972.

Barry, R. G., and A. H. Perry, *Synoptic Climatology*, Methnen and Co., Ltd, London, 1973.

Bowles, P., H. Bums, F. Hudswell, and R.T.P. Wipple, "Sea Disposal of Low Activity Effluent," *Second International Conference on the Peaceful Use of Atomic Energy*, United Nations, New York, 1958, p. 376.

Brower, W. A., H. F. Diaz, A. S. Prechtel, H. W. Searby, and J. L. Wise, *Climatic Atlas of the Outer Continental Shelf Waters and Coastal Regions of Alaska*, Publ. 8-77, AEIDIC, 1977.

Brown, B. G., R. W. Katz, and A. H. Murphy, "Time Series Models to Simulate and Forecast Wind Speed and Wind Power," *J. Climate and Appl. Meteor.*, Vol. 23, 1984, pp. 1184–1195.

Brown, R. A., and W. T. Liu, "An Operational Large-Scale Marine Planetary Boundary Layer Model," *J. Appl. Meteor.*, Vol. 21, 1982, pp. 261–269.

Cardon, V. J., *Specification of the Wind Distribution in the Marine Boundary Layer for Wave Forecasting*, New York University, Geophysical Sciences Lab, TR69–1, 1969.

Coachman, L. K., and K. Aagaard, "Reevaluation of Water Transports in the Vicinity of Bering Strait," in D. W. Hood and J. A. Calder (eds.), *The Eastern Bering Sea Shelf: Oceanography and Resources*, Vol. 1, University of Washington Press, Seattle, Washington, 1981, pp. 95–110.

Colony, R., and A. S. Thorndike, "Sea Ice Strain During 1979," *Sixth Intern. Conf. Port and Ocean Eng. Under Arctic Conditions*, POAC, Quebec, Canada, 1981.

Colony, R., and A. S. Thorndike, "A Estimate of the Main Field of Arctic Sea Ice Motion," *J. Geophys. Res.*, Vol. 89, No. 6, November 1984, pp. 10623–10629.

Conradsen, K., L. B. Nielsen, and L. P. Prahm, "Review of Weibull Statistics for Estimation of Wind Speed Distributions," *J. Climate and Appl. Meteor.*, Vol. 23, 1984, pp. 1173–1183.

Cox, J. C., L. A. Shultz, R. P. Johnson, and R. A. Sheley, "The Transport and Behavior of Oil Spilled In and Under Sea Ice," *Arctic Fac. Report*, No. 460C, 1980.

Danielsen, E. F., W. V. Burt, and M. Rattray, "Intensity and Frequency of Severe Storms in the Gulf of Alaska," *Trans. A.G.U.*, Vol. 38, No. 1, pp. 44–49.

Defant, A., *Physical Oceanography*, The MacMillian Co., New York, 1961.

Dell'osso, L., and L. Bengtsson, "Prediction of a Typhoon Using a Fine Mesh NWP Model," *Tellus*, Vol. 37A, 1985, pp. 97–105.

Drury, W. H., C. Ramsdell, and J. B. French, Jr., "Progress Report to NOAA/OCSEAP," Vol. 11, Anchorage, Alaska, 1981, pp. 175–487.

Dvoryaninov, G. S., and A. V. Prusov, "Theoretical Model of Mass Transport by Gravity and Tidal Waves," *Okeanologiya*, Vol. 18, No. 6, 1978, pp. 640–647.

Ekman, V. W., "On the Influence of the Earth's Rotation on Ocean Currents," *Ark. Math. Astr. Fysik.* Kong, Su. Vetenskap. Akad., Stockholm, Vol. 2, No. 11, 1905, p. 52.

Elliott, A. J., "Measurements of the Turbulence in an Abyssal Boundary Layer," *J. Phys. Ocean.*, Vol. 14, No. 11, 1984, pp. 1779–1786.

Essenwanger, O.M., "Analyzed Procedures for the Quality of Control of Meteorological Data," *Meteor. Monogr.*, Am. Meteor. Soc., No. 33, pp. 141–147.

Fan, L. N., and N. H. Brooks, *Numerical Solution of Turbulent Buoyant Jet Problems*, Keck Lab., Report No. KH-R-18, California Institute of Technology, 1969.

Favorite, F., "The Alaskan Stream," *Inter. N. Pac. Fish. Comm. Bull.*, Vol. 21, 1967, p. 20.

Favorite, F., A. J. Dodimimead, and K. Nasu, "Oceanography of the Subarctic Pacific Region," *Inter. N. Pac. Fish Comm. Bull.*, Vol. 33, 1976, p. 187.

Fay, J. A., and D. P. Hoult, "Physical Processes in the Spread of Oil on a Water Surface," U.S. Coast Guard R&D Report No. 714107/A/001, 1971.

Finzi, G., P. Bonelli, and G. Bacci, "A Statistic Model of Surface Wind for Air Quality Control Processes," *J. Climate and Appl. Meteor.*, Vol. 23, 1984, pp. 1354–1361.

Fisher N. I., Comment on "A Method for Estimating the Standard Deviation of Wind Directions," *J. Appl. Meteor.*, Vol. 22, 1983, p. 1971.

Fisher, N. I., and T. Lewis, "Estimating the Common Mean Direction of Several Circular or Spectral Distributions with Differing Dispersions," *BIOMETRIKA*, Vol. 70, 1983, pp. 333–341.

Franklin, B., "Of the Stilling of Waves by Means of Oil," in J. Sparks (ed.), *The Works of Benjamin Franklin*, Childs and Peterson Books, Philadelphia, Pennsylvania, 1840.

Gabriel, K. R., and J. Newmann, "On a Distribution of Weather Cycles by Lengths," *Quart. J. R. Meteor. Soc.*, Vol. 83, 1957, pp. 375-380.

Gabriel, K. R., and J. Newmann, "A Markov Chain Model for Daily Rainfall Occurrence at Tel Aviv," *Quart. J. R. Meteor. Soc.*, Vol. 88, 1962, pp. 90–95.

Garratt, J. R., "Review of Drag Coefficients over Oceans and Continents," *Mon. Wea. Rev.*, Vol. 105, 1977, pp. 915–929.

Gordienko, P., "Arctic Ice Drift," *Proc. Conf. on Arctic Sea Ice*, Published by the National Academy of Sciences and the National Research Council, Washington, D.C., 1958, pp. 210–220.

Gordon, R. L., "Internal Wave Climate near the Coast of Northwest Africa during JOINT-1," *Deep Sea Res.*, Vol. 25, 1978, pp. 625–643.

Harleman, D.R.F., and G. H. Jirka, "Buoyant Discharge from Submerged Multiport Diffusers," *Coastal Engineering*, Vol. 14, 1974, pp. 2180–2198.

Harris, R. A., *Manual of Tides*, Report of the Superintendent, U.S. Coast and Geodetic Survey, Washington, D.C, 1904, p. 313.

Hasting, C., *Approximations for Digital Computers*, Princeton University Press, 1955.

Heathershaw, A. D., "The Turbulent Structure of the Bottom Boundary Layer in a Tidal Current," *Geophys. J. Roy. Astron. Soc.*, Vol. 58, 1979, pp. 395–430.

Hesse, L., "On the Surface to Geostrophic Wind Relationship at Sea and the Stability of Dependence of the Resistance Law," *Beitr. Phys. Atmosph.*, Vol. 47, 1974, p. 45.

Hesse, L., and V. Wagner, "On the Relationship Between Geostrophic and Surface Wind at Sea," *Mon. Wea. Rev.*, Vol. 99, 1971, pp. 255–259.

Hibler, W. D. III., "A Dynamic Thermodynamic Sea Ice Model," *Phys. Oceano.*, Vol. 9, No. 7, 1979, pp. 815–846.

Hibler, W. D., W. F. Weeks, and S. J. Mock, "Statistical Aspects of Sea-Ice Ridge Distributions," *J. Geophys. Res.*, Vol. 77, No. 30, 1972, pp. 5954–5970.

Hinze, J. O., *Turbulence*, McGraw Hill, New York, 1959.

Hirst, E., "Buoyant Jets Discharged to Quiescent Stratified Ambients," *J. Geophys. Res.*, Vol. 76, No. 30, 1971.

Holl, M., and B. Mendenhall, "FIB-Fields by Information Bending," *Naval Fleet Numerical Weather Central.*, Proj. M-167, Final Report, 1971.

Holt, D. P., "Oil Spreading on the Sea," *Annual Review, Fluid Mechanics*, Vol. 4, 1972, pp. 341–368.

Hunt, J. N., and F. Johns, "Currents Induced by Tides and Gravity Waves," *Tellus*, Vol. 15, No. 4, 1963.

Ichiye, T., "The Theory of Turbulence," *Oceanographical Magazine*, Vol. 3, 1951, pp. 83–87.

Jenne, R. L., *Data Sets for Meteorological Research*, National Center for Atmospheric Research, Boulder, Colorado, TN/1A-111, 1975.

Johns, F., "On the Mass Transport Induced by Oscillatory Flow in a Turbulent Boundary Layer," *J. Fluid Mech.*, Vol. 43, Part 1, 1970.

Joppe, K., *Turbulence Models for Horizontal Layered Flow*, Delft Hydraulics Laboratory/Technological University, S656 (in Dutch), Delft, Netherlands, 1985.

Jowett, J., and D. Vere-Jones, "The Prediction of Point Processes," in P.A.W. Lewis (ed.), *Stochastic Point Processes*, J. Wiley Co., New York, 1972.

Kerr, R. A., "Fingers of Salt Help Mix the Sea," *Science*, Vol. 211, 1981, pp. 155–157.

Kinder, T. H., *The Hydrographic Structure over the Continental Shelf near Bristol Bay*, Department of Oceanography, University of Washington, Vol. 11, M77-3, 1977.

Kinder, T., L. K. Coachman, and J. A. Galt, "The Bering Slope Current System," *J. Phys. Oceano.*, Vol. 5, 1975, pp. 231–245.

Kinder, T., J. D. Schumacher, and D. V. Hansen, "Observation of a Baroclinic Eddy: An Example of Mesoscale Variability in the Bering Sea," *J. Phys. Oceano.*, Vol. 10, No. 8, 1980, pp. 1227–1245.

Kirstein, B. E., J. R. Payne, and R. T. Redding, *Multivariate Analysis of Petroleum Weathering in the Marine Environment Sub-Arctic*, NOAA, OCSEAP, Report No. 22, Anchorage, Alaska, 1984.

Klein, W. H., "Principal Tracks and Mean Frequencies of Cyclone and Anticyclones in the Northern Hemisphere," U.S. Weather Bureau, Research Paper No. 40, 1957.

Koh, R.C.Y., and N. H. Brooks, "Fluid Mechanics of Waste Water Disposal in the Ocean," *Annual Rev. of Fluid Mech., 1975.*

Kolmogoroff, A. N., "A Refinement of Previous Hypotheses Concerning the Local Structure of Turbulence in a Viscous Incompressible Fluid at High Reynolds Number," *J. Fluid Mech.*, Vol. 13, No. 1, 1962, pp. 82–85.

Kranenberg, C., "Wind-Induced Entrainment in a Stably-Stratified Fluid," *J. Fluid Mech.*, Vol. 145, 1984.

Kranenberg, C., *A K-Model for Stably-Stratified Turbulent Flow, Part 1, Formulation*, Report No. 4–85, Laboratory of Fluid Mechanics, Department of Civil Engineering, Delft University of Technology, Delft, Netherlands, 1985.

Kondo, J., "Air-Sea Bulk Transfer Coefficients in Diabatic Condition," *Boundary Layer Meteor.*, Vol. 9, 1975, pp. 91–112.

Kovacs, A., "Sea Ice Thickness Profiling and Under Ice Oil Entrapment," *Proc. Ninth Annual Offshore Tech. Conf.*, OTC, Houston, Texas, 1977, p. 2949.

Kovacs, A., "Oil Pooling Under Sea Ice," *Environmental Assessment of the Alaskan Continental Shelf*, Vol. 8, 1979, pp. 310–353.

Kovacs, A., R. M. Morey, and D. Cundy, "Oil Pooling Under Sea Ice," *Environmental Assessment of the Alaskan Continental Shelf, Annual Report*, Vol. 5, 1980, pp. 333–339.

Kozo, T., personal communication, 1984.

Kusunoki, K., J. Mugurama, and K. Higuchi, *Oceanographic Observations at Fletcher's Ice Island (T-3) in the Arctic Ocean in 1959–1960*, Sci. Report No. 4, AFCRL-62-479, GRD, Air Force Cambridge Research Laboratory, Bedford, Massachusetts, 1962.

Lamb, H., *Hydrodynamics*, Dover Publishing, New York, 1945.

Lambert, R. B., "On the Vertical Transport Due to Fingers in Double Diffusion Convection," *J. Fluid Mech.*, Vol. 54, 1972, pp. 627–640.

Langleben, M. P., "A Study of the Roughness Parameters of Sea Ice from Wind Profiles," *J. Geophys. Res.*, Vol. 77, No. 30, 1972, pp. 5935–5944.

Langleben, M. P., "Water Drag Coefficient of First-Year Sea Ice," *J. Geophys. Res.*, Vol. 87, No. C1, 1982, pp. 573–578.

Laufer, J., *The Structure of Turbulence in Fully Developed Pipe Flow*, National Advisory Commission on Aeronautics, TR-1174, Washington, D.C., 1954.

Launder, B. E., and D. B. Spalding, *Mathematical Models of Turbulence*, Academic Press, New York, 1972.

Leendertse, J. J., R. C. Alexander, and S. K. Liu, *A Three-Dimensional Model for Estuaries and Coastal Seas: Vol. 1, Principles of Computation*, The RAND Corporation, R-1417-OWRR, December 1973.

Leendertse, J. J., and S. K. Liu, *A Three-Dimensional Model for Estuaries and Coastal Seas: Vol. II, Aspects of Computation*, The RAND Corporation, R-1764-OWRT, June 1975.

Leendertse, J. J., and S. K. Liu, *A Three-Dimensional Model for Estuaries and Coastal Seas: Vol. IV, Turbulent Energy Computation*, The RAND Corporation, R-2187-OWRT, May 1977.

Linden, P. F., "On the Structure of Salt Fingers," *Deep Sea Res.*, Vol. 20, 1973, pp. 325–340.

List, E. J., and J. Imberger, "Turbulent Entrainment in Buoyant Jets and Plumes," *Proc. J. Hydro. Div.*, Vol. 99, 1973, p. 1461.

Liu, S. K., and A. B. Nelson, *A Three-Dimensional Model for Estuaries and Coastal Seas: Vol. V, Turbulent Energy Program*, The RAND Corporation, R-2188-OWRT, May 1977.

Liu, S. K., and J. J. Leendertse, "Multidimensional Numerical Models of Estuaries and Coastal Seas," *Advances in Hydroscience*, Vol. II, Academic Press, New York, 1978, pp. 95–164.

Liu, S. K., and J. J. Leendertse, *A Three-Dimensional Model for Estuaries and Coastal Seas: Vol. VI, Bristol Bay Simulations*, The RAND Corporation, R-2405-NOAA, September 1979.

Liu, S. K., and J. J. Leendertse, "A 3-D Oil Spill Model With and Without Ice Cover," *Mechanics of Oil Slicks*, Association Amicale des Ingenieurs, and International Association for Hydraulic Research, Paris, France, 1981a, pp. 247–265.

Liu, S. K., and J. J. Leendertse, "A Three-Dimensional Model of Norton Sound Under Ice Cover," *Proc. Sixth Inter. Conf. Port and Ocean Eng. Under Arctic Conditions*, POAC, Quebec, Canada, 1981b, pp. 433–443.

Liu, S. K., and J. J. Leendertse, "Three-Dimensional Model of Bering and Chukchi Sea," *Coastal Engineering*, Vol. 18, American Society of Civil Engineers, New York, 1982, pp. 598–616.

Liu, S. K., and J. J. Leendertse, "A Three-Dimensional Model of Beaufort Sea," *Coastal Engineering*, Vol. 19, American Society of Civil Engineering, New York, 1984.

Liu, S. K., and J. J. Leendertse, "A Three-Dimensional Model of the Gulf of Alaska," *Coastal Engineering*, American Society of Civil Engineering, New York, 1987.

Mackay, D., and Medir, "The Interfacial Behavior of Oil Under Ice," *Canadian J. of Chem. Engineering*, Vol. 54, February 1976.

Macklin, S. A., "Wind Drag Coefficient over First-Year Sea Ice in the Bering Sea," *J. Geophys. Res.*, Vol. 88, No. C5, 1983, pp. 2845–2852.

Macklin, S. A., C. H. Pease, and R. M. Reynolds, *Bering Air-Sea Ice Study* (BASICS), NOAA-ERL-PMEL-52, Seattle, Washington, 1984.

Macklin, S. A., R. L. Brown, J. Gray, and R. L. Lindsay, *METLIB-II—A Program Library for Calculating and Plotting Atmospheric and Oceanic Fields*, NOAA, ERL PMEL-54, Seattle, Washington, 1984.

Martin, S., *The Seasonal Variation of Oil Entrainment in First-Year Arctic Sea Ice, A Comparison of NORCOR/OCS Observations*, Department of Oceanology, University of Washington, March 1977.

Martin, S., P. Kauffman, and S. Soltar, *Field Report on March Field Traverse of Ice Temperature, Salinity and Thickness in Norton Sound*, Department of Oceanography, University of Washington, Special Report, September 1978.

McWilliams, B., and D. Sprevak, "The Estimation of the Parameters of the Distribution of Wind Speed and Direction," *Wind Engineering*, Vol. 4, No. 4, 1980, pp. 227–238.

McWilliams, B., and D. Sprevak, "Stochastic Model of Wind Speed and Direction," in O. D. Anderson (ed.), *Time Series Analysis: Theory and Practice*, Vol. 7, Elsevier Science Publisher, Amsterdam, Netherlands, 1985, pp. 195–203.

Mofjeld, H. O., "Effects of Vertical Viscosity on Kelvin Waves," *J. Phys. Oceano.*, Vol. 10, 1980, pp. 1040–1050.

Mofjeld, H. O., "Recent Observations of Tides and Tidal Currents from the Northeastern Bering Sea Shelf," PMEL/NOAA Technical Report, PMEL-57, Seattle, Washington, 1984.

Mofjeld, H. O., and J. D. Schumacher, "Residual Tidal Currents and Current Records from the Eastern Bering Sea Shelf," PMEL/NOAA, Seattle, Washington, 1983.

Mofjeld, H. O., and J. W. Lavelle, "Bottom Boundary Layer Studies in Tidally-Dominated Regimes," XVIII General Assembly of the Union of Geodesy and Geophysics, Hamburg, Federal Republic of Germany, IAPSO Programme and Abstracts, 1983.

Mofjeld, H. O., J. D. Schumacher, and D. J. Pashinski, *Theoretical and Observed Profiles of Tidal Currents at Two Sites on the Southeastern Bering Shelf*, NOAA Technical Memorandum, ERL PMEL-62, Seattle, Washington, 1984.

Monin, A. S., and A. M. Yaglom, "Statistical Fluid Mechanics," *Mechanics of Turbulence*, Vol. 2, Springer-Verlag, Berlin, 1975.

Mountain, D. G., L. K. Coachman, and K. Aagaard, "On the Flow Through Barrow Canyon," *J. Phys. Oceano.*, Vol. 6, 1976, pp. 461–470.

Muench, R. D., and K. Ahlnas, "Ice Movement and Distribution in the Bering Sea from March to June 1974," *J. Geophys. Res.*, Vol. 81, No. 24, 1976, pp. 4467–4476.

Muench, R. D., and J. D. Schumacher, *Physical Oceanographic and Meteorological Conditions in the Northwestern Gulf of Alaska*, NOAA Technical Memorandum ERL PMEL-22, Seattle, Washington, 1980.

Muench, R. D., J. D. Schumacher, and C. A. Pearson, *Circulation in the Lower Cook Inlet, Alaska*, NOAA Technical Memorandum ERL PMEL-28, Seattle, Washington, 1981.

Muench, R. D., and J. D. Schumacher, "On the Bering Sea Ice Edge Front," *J. Geo. Res.*, Vol. 90, No. C2, 1985, pp. 3185–3197.

Munk, W. H., G. C. Ewing, and R. R. Revelle, "Diffusion in Bikini Lagoon," *Trans. A.G.U.*, 1949, pp. 59–66.

Munk, W. H., and G. F. Carrier, "On the Wind-Driven Circulation in Ocean Basins of Various Shapes," *Tellus*, Vol. 2, 1950, pp. 158–167.

Murphy, D. L., P. A. Tebeau, and L. M. Lissuer, *Long-Term Movement of Satellite-Tracked Buoys in the Beaufort Sea*, Office of Research and Development, U.S. Department of Transportation, CG-D-48-82, 1981.

Murray, S. P., "Trajectories and Speeds of Wind-Driven Currents Near the Coast," *J. Phys. Oceano.*, Vol. 5, 1975, pp. 347–360.

Mysak, L. A., R. D. Muench, and J. D. Schumacher, "Baroclinic Instability in a Down Stream Varying Channel: Shelikof Strait, Alaska," *J. Phys. Oceano.*, Vol. 11, No. 7, 1981, pp. 950–969.

National Academy of Sciences, *Petroleum in the Marine Environment*, National Academy of Science, Washington, D.C., 1975.

Neumann, G., *Ocean Currents*, Elsevier Publishing Co., New York, 1968.

Neumann, G., and J. W. Pierson, Jr., *Principle of Physical Oceanography*, Prentice Hall, Englewood Cliffs, New Jersey, 1966.

Neyman, J., and E. L. Scott, "A Theory of the Spatial Distribution of Galaxies," *Astrophys. J.*, Vol. 116, 1952, pp. 144–163.

Niebauer, H. J., J. Roberts, and T. C. Royer, "Shelf Break Circulation in the Northern Gulf of Alaska," *J. Geophys. Res.*, Vol. 86, 1981, pp. 4231–4242.

Oboukhov, A. M., "Some Special Features of Atmospheric Turbulence," *J. Fluid Mechanics*, Vol. 13, No. 1, 1962.

Okubo, A., "Equation Describing the Diffusion of an Introduced Pollutant in a One-Dimensional Estuary," *Studies on Oceanography*, Tokyo, 1964, pp. 216–226.

Overland, J. E., R. A. Brown, and C. D. Mobley, *METLIB—A Program Library for Calculating and Plotting Marine Boundary Layer Wind Fields*, NOAA Technical Memorandum ERL PMEL-20, 1980.

Overland, J. E., "Progress Report on the Observed Wind over Norton Sound, Alaska to NOAA/OCSEAP," Anchorage, Alaska, 1980.

Overland, J. E., R. Reynolds, and C. H.Pease, "A Model of the Atmospheric Boundary Layer Over the Marginal Ice Zone," *J. Geophys. Res.*, Vol. 88, C5, 1983, pp. 2836–2840.

Overland, J. E., H. O. Mofjeld, and C. H. Pease, "Wind-Driven Ice Drift in a Shallow Sea," *J. Geophys. Res.*, Vol. 89, No. C4, 1984, pp. 6525–6531.

Ovsiyenko, S. N., "Numerical Modelling of the Drift of Ice," *Izvestiya, Atmo. and Oceanic Physics*, Vol. 12, No. 11, 1976, pp. 1201–1206.

Parmerter, R. R., and M. D. Coon, "Model of Pressure Ridge Formation in Sea Ice," *J. Geophys. Res.*, Vol. 77, No. 33, 1972, pp. 6565–6575.

Payne, J. R., *A Review of the Formation and Behavior of Water-in-Oil Emulsion (mousse) from Spilled Petroleum, and Tar Ball Distributions Chemistries and Fates in the World's Oceans*, National Academy of Sciences, Ocean Sciences Board Workshop, Clearwater Beach, Florida, 1981.

Payne, J. R., B.E. Kirstein, G. D. McNabb, J. L. Lamback, C. deOliveira, and W. Hom, "Multivariate Analysis of Petroleum Hydrocarbon Weathering in the Subarctic Environment," *Proc. 1983 Oil Spill Conference*, pp. 423–434.

Pearson, C. A., H. O. Mofjeld, and R. B. Tripp, "Tides of the Eastern Bering Sea Shelf," in D. W. Hood and J. A. Calder (eds.), *The Eastern Bering Sea Shelf: Oceanography and Resources*, Vol. 1, University of Washington Press, Seattle, Washington, 1981a, pp. 111–130.

Pearson, C. A., J. D. Schumacher, and R. D. Muench, "Effects of Wave-Induced Mooring Noise on Tidal and Low Frequency Current Observations," *Deep Sea Res.*, Vol. 28A, No. 10, 1981b, pp. 1223–1229.

Pease, C. H., S. A. Salo, and J. E. Overland, "Drag Measurements for the First-Year Ice over a Shallow Sea," *J. Geophys. Res.*, Vol. 88, C5, 1983, pp. 2853–2862.

Pease, C. H., and J. E. Overland, "An Atmospherically Driven Sea-Ice Model for the Bering Sea," *Am. J. of Glaciology*, Vol. 5, 1984, pp. 111–114.

Pitman, R. W., *Oceanographic Data from the Bering, Chukchi and Beaufort Sea*, Report to NOAA, WASC-83-00114, Brown and Caldwell, Anchorage, Alaska, 1984.

Plutchak, N. B., and R. L. Kolpack, "Numerical Simulation of Oil Spreading on Water," *Mechanics of Oil Slicks*, Int. Assoc. for Hydraulic Research, Paris, France, 1981.

Pritchard, R. S., "An Elastic-Plastic Constitutive Law for Sea Ice," *J. of Appl. Mechanics*, June 1975, pp. 379–384.

Pritchard, R. S., "Beaufort Sea Ice Motions," in P. W. Barnes, D. M. Schell, and E. Reimnitz, (eds.), *The Alaskan Beaufort Sea Ecosystem and Environments*, Academic Press, New York, 1984, pp. 95–113.

Putnins, P., "The Sequences of Baric Pressure Patterns over Alaska," *Studies on the Meteorology of Alaska*, Environmental Data Service, ESSA, Washington, D.C., 1966.

Reed, R. K., "Flow of the Alaskan Stream and Its Variations," *Deep Sea Res.*, Vol. 31, No. 4, 1984, pp. 369–386.

Reed, R. K., and J. D. Schumacher, "Additional Current Measurements in the Alaskan Stream Near Kodiak Island," *J. of Phys. Oceano.*, Vol. 14, No. 7, 1984, pp. 1239–1246.

Reiner, R. W., "Ice Breakout in the Bering Strait," M.S. Thesis, College of Engineering, University of Washington, Seattle, Washington, 1979.

Reynolds, M., and C. H. Pease, *Drift Characteristics of Northeastern Bering Sea During 1982*, NOAA, Tech. Memo ERL, PMEL-55, 1982.

Richardson, L. F., "Atmospheric Diffusion Shown on a Distance-Neighbor Graph," *Proc. Roy. Soc. London*, Vol. A110, pp. 709–727.

Richardson, L. F., and H. Stommel, "Note on Eddy Diffusion at Sea," *J. of Meteor.*, Vol. 5, pp. 234–240.

Riera, J. D., A. J. Viollaz, and J. C. Reimundin, "Some Recent Results on Probabilistic Models of Extreme Wind Speed," *J. of Indust. Aerodynamics*, Vol. 2, 1977, pp. 271–287.

Rodi, W., "Turbulence Models and Their Application in Hydraulics," *International Assoc. for Hydraulic Res.*, 1980.

Rodriguez, E., and R. E. Huschke, *The RAND Weather Data Bank (RAWDAB): An Evolving Base of Accessible Weather Data,* The RAND Corporation, R-1269-PR, March 1974.

Royer, T. C., and W. J. Emery, "Circulation in the Bering Sea 1982–83, Based on Satellite-Tracked Drifter Observations," *J. of Phys. Oceanography,* Vol. 14, 1984, pp. 1914–1920.

Salo, S. A., J. D. Schumacher, and L. K. Coachman, *Winter Currents on the Eastern Bering Sea Shelf,* NOAA/PMEL Technical Report, Seattle, Washington, 1983.

Schumacher, J. D., R. K. Reed, M. Grigsby, and D. Dreves, *Circulation and Hydrography Near Kodiak Island, September to November, 1977,* NOAA Technical Memorandum ERL PMEL-13, U.S. Government Printing Office, Washington, D.C., 1979-0-677-072/1279.

Schumacher, J. D., T. H. Kinder, D. J. Pashinski, and R. L. Charnell, "A Structure Front Over the Continental Shelf of the Eastern Bering Sea," *J. Phy. Oceano.,* Vol. 9, No. 1, 1979, pp. 79–87.

Schumacher, J. D., and R. D. Muench, *Physical Oceanography and Meteorological Conditions in the Northwest Gulf of Alaska,* NOAA, TM-ERL-PMEL-22, Seattle, Washington, October 1980.

Schumacher, J. D., and R. K. Reed, "Coastal Flow in the Northwest Gulf of Alaska: The Kenai Current," *J. Geo. Res.,* Vol. 85, No. C11, 1980, pp. 6680–6688.

Schumacher, J. D., C. A. Pearson, and J. E. Overland, "On Exchange of Water Between the Gulf of Alaska and the Bering Sea Through the Unimak Pass," *J. Geo. Res.,* Vol. 87, No. C7, 1982, pp. 5785–5795.

Schumacher, J. D., and T. H. Kinder, "Low Frequency Current Regimes over the Bering Sea Shelf," *J. Phys. Oceano.,* Vol. 13, 1983, pp. 607–623.

Schumacher, J. D., K. Aagaard, and R. B. Tripp, "Effects of a Shelf Polynya on Flow and Water Properties in the Northern Bering Sea," *J. Geo. Res.,* Vol. 88, No. C5, 1983, pp. 2723–2732.

Schumacher, J. D., S. A. Macklin, and L. S. Ineze, *Background and Research Plan for the Northwest Gulf of Alaska Fishery Oceanography Experiment,* Pacific Marine Environmental Lab., NOAA/PMEL-734, 1984, Seattle, Washington, 1984.

Schutz, C., *Synoptic Performance Characteristic of the Two-Level Atmospheric Model,* The RAND Corporation, R-1689-ARPA, August 1975.

Schutz, C., and W. L. Gates, *Global Climatic Data for Surface, 800MB, 400MB: January,* The RAND Corporation, R-915-ARPA, November 1971.

Schutz, C., and W. L. Gates, *Global Climatic Data for Surface, 800MB, 400MB: July,* The RAND Corporation, R-1029-ARPA, November 1972.

Schutz, C., and W. L. Gates, *Global Climatic Data for Surface, 800MB, 400MB: April,* The RAND Corporation, R-1317-ARPA, December 1973.

Schutz, C., and W. L. Gates, *Global Climatic Data for Surface, 800MB, 400MB: October,* The RAND Corporation, R-1425-ARPA, March 1974.

Schwiderski, E. W., *Global Ocean Tides,* TR-3866, Surface Weapons Center, Dahlgren, Virginia, 1978.

Semenov, Y. V., and B. M. Taran, "Numerical Model of the Wind Drift of Ice, Taking into Account the Appearance of Zones of Maximum Solidity," *Izvestiya, Atmo. and Oceanic Physics,* Vol. 18, No. 9, 1982, pp. 775–778.

SethuRaman, S., and J. Tichler, "Statistical Hypothesis Tests of Some Micrometeorological Observations," *J. Appl. Meteor.,* Vol. 16, No. 5, 1977, pp. 455–461.

Smith, O. E., "Application of Distribution Derived from the Bivariate Normal Density Function," *Probability and Statistics in Atmospheric Sciences,* Proc. of Int. Sym. held in Honolulu, Hawaii, 1971, p. 162–168.

Stern, M. E., "The 'Salt Fountain' and Thermohaline Convection," *Tellus*, Vol. 12, 1960, pp. 172–175.

Stern, M. E., and J. S. Turner, "Salt Fingering and Convective Layer," *Deep Sea Res.*, Vol. 16, 1969, pp. 497–511.

Stringer, W. J., and G. L. Hufford, "Interaction of Bering Sea and Norton Sound Pack Ice," *Arctic and Alpine Research*, Vol. 14, No. 2, 1982, pp. 149–156.

Stringer, W. J., and R. D. Henzler, "Norton Sound Ice Floe Trajectories Observed Between March 29 and 31, 1976," *Proc. Syn. Meeting, The Norton Sound Environment and Possible Consequences of Planned Oil and Gas Development*, NOAA, Anchorage, Alaska, February 1982.

Stringer, W. J., J. E. Groves, R. D. Henzler, L. K. Schreurs, and J. Zender-Romick, "Ice Concentration in the Eastern Beaufort Sea," *Geophys. Inst. Rep.*, University of Alaska, Fairbanks, Alaska, 1982.

Stroop, D. V., *Report on Oil Pollution Experiments, Behavior of Fuel Oil on the Surface of the Sea*, U.S. Department of Commerce, Bureau of Standards, Washington, D.C., 1927.

Sunderman, J., "The Semi-Diurnal Principal Lunar Tide M2 in the Bering Sea," *Deutsche Hydrographische Zeitschrift*, Vol. 30, 1977, pp. 91–101.

Tait, R. I., and M. R. Howe, "Thermocline Staircase," *Nature*, Vol. 231, 1971, pp. 178–179.

Takenouti, A. Y., and K. Ohtani, "Currents and Water Masses in the Bering Sea: A Review of Japanese Work," in D. W. Hood and E. J. Kelley (eds.), *Oceanography of the Bering Sea with Emphasis on Renewable Resources*, University of Washington, Seattle, Washington, 1974.

Thorndike, A. S., and R. Colony, "Sea Ice Motion in Response to Geostrophic Winds," *J. Geophys. Res.*, Vol. 87, No. C7, 1982, pp. 5845–5852.

Tripp, R. B., L. K. Coachman, K. Aagaard, and J. D. Schumacher, "Low Frequency Components of Flow in the Bering Strait System," American Geophysical Union Meeting, Seattle, Washington, September 1978.

Tuller, S. E., and A. C. Brett, "The Characteristics of Wind Velocity That Favor the Fitting of a Weibull Distribution in Wind Speed Analysis," *J. Climate and Appl. Meteor.*, Vol. 23, 1984, pp. 124–134.

Turner, J. S., "Salt Fingers Across a Density Interface," *Deep Sea Res.*, Vol. 14, 1967, pp. 599–611.

U.S. Navy Fleet Weather Facility, *Arctic Sea Ice Analyses 1972–1975*, Suitland, Maryland, 1979.

Uzuner, S., F. Weiskopf, J. Cox, and L. A. Schultz, *Transport of Oil Slicks Under a Uniform Smooth Ice Cover*, Environmental Protection Agency, Report No. EPA-600/3-79-041, Corvallis, Oregon, April 1979.

Van Bebber, W. J., "Die Zugstrassen der baromefrischen Minima nach den Bahnenkarten der Deutschen Seewarte fur den Zeitraum," *Met. Zeit., Vol. 8, 1891, pp. 361–366.*

Van Bebber, W. J., and W. Koppen, "The Isobaric Type of the North Atlantic Ocean and the Western Europe" (in German), *Arch. dtsch. Seewarte*, Hamburg, Vol. 18, 1895.

Verrall, K. A., and R. L. Williams, "A Method for Estimating the Standard Deviation of Wind Directions," *J. Appl. Meteor.*, Vol. 21, 1982, pp. 1922–1925.

Walter, B. A., J. E. Overland, and R. O. Gilmer, "Air-Ice Drag Coefficients for First Year Sea-Ice Derived from Aircraft Measurements," *J. Geophy. Res.*, Vol. 89, No. C3, 1984, pp. 3550–3560.

Weeks, W. F., and G. Weller, "Offshore Oil in the Alaskan Arctic," *Science*, Vol. 225, No. 4660, 1984, pp. 371–378.

Wiseman, W. J., and L. J. Rouse, Jr., "A Coastal Jet in the Chukchi Sea," *Arctic,* Vol. 33, 1980, pp. 21–29.

Whittmann, W., and J. J. Schule, "Comments on the Mass Budget of Arctic Pack Ice," in J. O. Fletcher (ed.), *Proc. of Symposium on Arctic Heating Budget and Atmospheric Circulation,* The RAND Corporation, RM-5233-NSF, December 1966.

Wu, J., "Wind Stress Coefficients over Sea Surface from Breeze to Hurricane," *J. Geophys. Res.,* Vol. 87, 1982, pp. 9704–9706.

Zeman, O., and J. L. Lumley, "Modeling Salt-Fingering Structures," *J. Mar. Res.,* Vol. 40, No. 2, 1982, pp. 315–330.

Zisman, W. A., "The Spreading of Oil on Water," *J. Chem. Physics,* Vol. 9, 1941, pp. 789–793.

Appendix

COMPUTED RESIDUAL CURRENTS IN THE BERING AND CHUKCHI SEAS

Table A.1

COMPUTED EAST-WEST COMPONENT OF TIDAL/BAROCLINIC RESIDUAL CURRENTS IN THE BERING AND CHUKCHI SEAS (cm/sec)

	181W 0.0'	180W 30.0'	180W 0.0'	179W 30.0'	179W 0.0'	178W 30.0'	178W 0.0'	177W 30.0'	177W 0.0'	176W 30.0'	176W 0.0'	175W 30.0'	175W 0.0'	174W 30.0'	174W 0.0'	173W 30.0'	173W 0.0'	172W 30.0'	172W 0.0'	171W 30.0'
72 0.0'N	-1.748	-2.152	-2.555	-1.368	-0.181	0.068	0.316	-0.913	-2.142	-1.826	-1.511	-1.828	-2.144	-1.114	-0.084	-1.058	-2.032	-1.921	-1.810	-1.624
71 45.0'N	-0.874	-1.076	-1.278	-0.684	-0.090	0.740	1.571	1.181	0.791	0.789	0.787	-0.373	-1.534	-1.754	-1.974	-1.786	-1.599	-1.502	-1.405	-1.266
71 30.0'N	0.0	0.0	0.0	0.0	0.0	1.413	2.825	3.274	3.723	3.404	3.085	1.081	-0.923	-2.393	-3.864	-2.515	-1.165	-1.083	-1.000	-0.908
71 15.0'N	0.0	0.0	0.0	0.0	0.0	0.706	1.413	1.503	1.594	1.506	1.419	0.151	-1.116	-1.871	-2.626	-2.010	-1.395	-1.178	-0.962	-0.893
71 0.0'N	0.0	0.0	0.0	0.0	0.0	0.0	0.0	-0.268	-0.535	-0.391	-0.247	-0.778	-1.310	-1.349	-1.388	-1.506	-1.624	-1.274	-0.924	-0.877
70 45.0'N	-3.963	-2.782	-1.601	-0.734	0.133	0.903	1.673	1.282	0.891	0.130	-0.630	-1.463	-2.297	-1.168	-0.039	-1.178	-2.316	-1.518	-0.720	-0.482
70 30.0'N	-7.925	-5.564	-3.202	-1.468	0.265	1.805	3.346	2.831	2.317	0.652	-1.013	-2.148	-3.283	-0.987	1.310	-0.849	-3.008	-1.762	-0.516	-0.088
70 15.0'N	-2.845	-3.102	-3.358	-2.883	-2.409	-1.609	-0.810	0.415	1.639	0.921	0.202	-0.107	-0.416	0.335	1.086	-0.307	-1.700	-1.719	-1.739	-0.772
70 0.0'N	2.234	-0.640	-3.514	-4.298	-5.082	-5.024	-4.965	-2.002	0.962	1.189	1.417	1.934	2.451	1.657	0.863	0.236	-0.391	-1.677	-2.962	-1.456
69 45.0'N	-0.406	-1.772	-3.137	-3.739	-4.341	-4.781	-5.221	-3.870	-2.520	-2.119	-1.718	-1.314	-0.911	-1.541	-2.172	-1.414	-0.656	-1.386	-2.115	-1.836
69 30.0'N	-3.046	-2.903	-2.761	-3.180	-3.599	-4.537	-5.476	-5.739	-6.002	-5.427	-4.852	-4.563	-4.273	-4.740	-5.206	-3.064	-0.922	-1.095	-1.269	-2.217
69 15.0'N	-1.523	-1.441	-1.360	-1.379	-1.398	-1.312	-1.226	-1.845	-2.464	-2.570	-2.677	-1.942	-1.207	-1.958	-2.709	-2.227	-1.744	-1.193	-0.641	-1.623
69 0.0'N	0.0	0.021	0.041	0.422	0.803	1.913	3.023	2.049	1.074	0.286	-0.502	0.679	1.860	0.824	-0.212	-1.389	-2.566	-1.290	-0.014	-1.030
68 45.0'N	0.0	0.010	0.021	0.211	0.401	2.334	4.266	3.910	3.554	2.087	0.620	1.075	1.530	0.891	0.252	-1.318	-2.888	-1.810	-0.732	-1.271
68 30.0'N	0.0	0.0	0.0	0.0	0.0	2.754	5.509	5.771	6.033	3.887	1.741	1.471	1.200	0.958	0.716	-1.247	-3.209	-2.330	-1.450	-1.511
68 15.0'N	0.0	0.0	0.0	0.0	0.0	1.377	2.754	2.885	3.017	3.486	3.955	2.397	0.839	1.736	2.633	0.662	-1.308	-0.976	-0.644	-1.087
68 0.0'N	0.0	0.0	0.0	0.0	0.0	0.0	0.0	0.0	0.0	3.085	6.169	3.323	0.478	2.514	4.551	2.571	0.592	0.377	0.161	-0.663
67 45.0'N	0.0	0.0	0.0	0.0	0.0	0.0	0.0	0.0	0.0	1.542	3.085	2.775	2.465	3.717	4.969	3.784	2.599	1.240	-0.120	0.186
67 30.0'N	0.0	0.0	0.0	0.0	0.0	0.0	0.0	0.0	0.0	0.0	0.0	2.226	4.452	4.920	5.388	4.997	4.607	2.102	-0.402	1.035
67 15.0'N	0.0	0.0	0.0	0.0	0.0	0.0	0.0	0.0	0.0	0.0	0.0	1.113	2.226	2.460	2.694	2.499	2.304	0.871	-0.562	0.181
67 0.0'N	0.0	0.0	0.0	0.0	0.0	0.0	0.0	0.0	0.0	0.0	0.0	0.0	0.0	0.0	0.0	0.0	0.0	-0.361	-0.722	-0.673
66 45.0'N	0.0	0.0	0.0	0.0	0.0	0.0	0.0	0.0	0.0	0.0	0.0	0.0	0.0	0.0	0.0	0.0	0.0	-0.181	-0.361	-1.289
66 30.0'N	0.0	0.0	0.0	0.0	0.0	0.0	0.0	0.0	0.0	0.0	0.0	0.0	0.0	0.0	0.0	0.0	0.0	0.0	0.0	-1.905
66 15.0'N	0.0	0.0	0.0	0.0	0.0	0.0	0.0	0.0	0.0	0.0	0.0	0.0	0.0	0.0	0.0	0.0	0.0	0.0	0.0	-0.952
66 0.0'N	0.0	0.0	0.0	0.0	0.0	0.0	0.0	0.0	0.0	0.0	0.0	0.0	0.0	0.0	0.0	0.0	0.0	0.0	0.0	0.0
65 45.0'N	0.0	0.0	0.0	0.0	0.0	0.0	0.0	0.0	0.0	0.0	0.0	0.0	0.0	0.0	0.0	0.0	0.0	0.0	0.0	-0.721
65 30.0'N	0.0	0.0	0.0	0.0	0.0	0.0	0.0	0.0	0.0	0.0	0.0	0.0	0.0	0.0	0.0	0.0	0.0	0.0	0.0	-0.441
65 15.0'N	0.0	-0.122	-0.245	0.132	0.508	0.529	0.549	0.334	0.119	0.059	0.0	0.0	0.0	0.0	0.0	0.0	0.0	0.561	1.122	1.308
65 0.0'N	0.0	-0.245	-0.490	0.264	1.017	1.057	1.097	0.667	0.237	0.119	0.0	0.0	0.0	0.0	0.0	0.0	0.0	1.122	2.244	3.056
64 45.0'N	0.188	0.057	-0.074	-0.095	-0.116	0.388	0.892	1.043	1.193	1.358	1.523	1.155	0.787	0.393	0.0	0.0	0.0	1.692	3.384	2.874
64 30.0'N	0.376	0.359	0.342	-0.453	-1.248	-0.281	0.686	1.418	2.149	2.597	3.046	2.310	1.574	0.787	0.0	0.0	0.0	2.262	4.524	2.692
64 15.0'N	0.006	0.289	0.573	0.465	0.356	1.395	2.434	1.804	1.173	0.976	0.780	0.169	-0.442	0.684	1.811	2.301	2.792	4.145	5.499	3.547
64 0.0'N	-0.364	0.220	0.805	1.382	1.960	3.071	4.182	2.190	0.197	-0.644	-1.486	-1.972	-2.459	0.582	3.622	4.603	5.584	6.028	6.473	4.402
63 45.0'N	0.050	0.701	1.352	1.022	0.691	0.138	-0.415	-0.152	0.111	-0.664	-1.439	-0.211	1.018	2.184	3.350	3.985	4.621	3.929	3.236	2.201
63 30.0'N	0.464	1.181	1.899	0.661	-0.577	-2.795	-5.012	-2.493	0.025	-0.684	-1.392	1.551	4.494	3.786	3.078	3.368	3.658	1.829	0.0	0.0
63 15.0'N	0.232	-0.682	-1.596	-1.161	-0.726	-2.800	-4.873	-3.121	-1.369	-0.889	-0.408	1.402	3.214	3.134	3.055	2.636	2.217	1.983	1.750	1.850
63 0.0'N	0.0	-2.546	-5.092	-2.984	-0.875	-2.805	-4.734	-3.749	-2.763	-1.094	0.575	1.254	1.933	2.483	3.032	1.903	0.775	2.137	3.500	3.699
62 45.0'N	0.0	-1.315	-2.631	-1.364	-0.097	-0.579	-1.060	-0.816	-0.571	0.265	1.102	1.312	1.521	1.773	2.026	1.542	1.059	1.889	2.719	2.781
62 30.0'N	0.0	-0.085	-0.169	0.256	0.681	1.648	2.614	2.118	1.621	1.625	1.628	1.369	1.109	1.064	1.019	1.182	1.344	1.641	1.938	1.862
62 15.0'N	4.113	3.393	2.673	2.138	1.603	1.283	0.962	0.994	1.027	0.713	0.399	1.193	1.987	1.848	1.709	1.575	1.442	1.525	1.608	1.592
62 0.0'N	8.225	6.870	5.515	4.020	2.526	0.918	-0.691	-0.129	0.432	-0.200	-0.831	1.016	2.864	2.631	2.398	1.969	1.540	1.408	1.277	1.321
61 45.0'N	5.127	4.519	3.910	3.105	2.299	1.358	0.418	1.060	1.701	0.352	-0.996	0.629	2.255	2.017	1.779	1.326	0.873	0.899	0.924	1.218
61 30.0'N	2.029	2.168	2.306	2.189	2.071	1.799	1.527	2.249	2.970	0.904	-1.162	0.242	1.646	1.403	1.160	0.684	0.207	0.389	0.572	1.115
61 15.0'N	1.099	1.378	1.657	1.898	2.140	1.772	1.404	1.950	2.496	0.512	-1.471	0.200	1.871	1.554	1.236	1.098	0.960	0.573	0.186	0.480
61 0.0'N	0.169	0.588	1.007	1.607	2.208	1.744	1.281	1.651	2.022	0.121	-1.781	0.158	2.096	1.704	1.313	1.513	1.713	0.757	-0.199	-0.156
60 45.0'N	0.085	0.058	0.030	0.526	1.021	0.636	0.251	0.573	0.896	-0.972	-2.840	-0.633	1.574	1.115	0.656	0.757	0.857	0.275	-0.307	-0.443
60 30.0'N	0.0	-0.473	-0.946	-0.556	-0.167	-0.472	-0.778	-0.504	-0.230	-2.065	-3.900	-1.424	1.052	0.526	0.0	0.0	0.0	-0.207	-0.414	-0.730
60 15.0'N	0.0	-0.236	-0.473	-0.417	-0.362	-0.362	-0.363	-0.161	0.041	-1.032	-2.106	0.218	2.542	1.558	0.575	0.627	0.679	0.728	0.777	0.302
60 0.0'N	0.0	0.0	0.0	-0.279	-0.557	-0.252	0.052	0.183	0.313	0.001	-0.312	1.860	4.031	2.590	1.149	1.253	1.358	1.663	1.969	1.334
59 45.0'N	0.0	0.0	0.0	-0.139	-0.279	-0.420	-0.561	0.649	1.259	-0.075	-2.008	-0.110	1.789	1.016	0.244	0.655	1.067	1.094	1.121	0.932
59 30.0'N	0.0	0.0	0.0	0.0	0.0	-0.588	-1.175	1.114	3.404	-0.150	-3.705	-2.079	-0.454	-0.558	-0.661	0.057	0.776	0.525	0.274	0.531
59 15.0'N	0.0	0.0	0.0	0.0	0.0	-0.294	-0.588	1.416	3.420	-0.283	-3.987	-3.616	-3.244	-3.581	-3.917	-1.853	0.211	0.467	0.723	0.425
59 0.0'N	0.0	0.0	0.0	0.0	0.0	0.0	0.0	1.718	3.437	-0.416	-4.269	-5.152	-6.035	-6.604	-7.173	-3.764	-0.354	0.409	1.172	0.319
58 45.0'N	0.0	0.0	0.0	0.0	0.0	0.0	0.0	0.859	1.718	-0.288	-2.293	-2.731	-3.169	-3.901	-4.634	-3.773	-2.912	-1.286	0.339	0.147
58 30.0'N	0.0	0.0	0.0	0.0	0.0	0.0	0.0	0.0	0.0	-0.159	-0.317	-0.310	-0.303	-1.199	-2.094	-3.782	-5.470	-2.982	-0.494	-0.026
58 15.0'N	0.0	0.0	0.0	0.0	0.0	0.0	0.0	0.0	0.0	-0.079	-0.159	-0.455	-0.751	-0.816	-0.882	-2.818	-4.754	-4.450	-4.145	-2.448
58 0.0'N	0.0	0.0	0.0	0.0	0.0	0.0	0.0	0.0	0.0	0.0	0.0	-0.599	-1.198	-0.434	0.331	-1.854	-4.039	-5.917	-7.796	-4.870
57 45.0'N	0.0	0.0	0.0	0.0	0.0	0.0	0.0	0.0	0.0	0.0	0.0	-0.300	-0.599	-0.441	-0.283	-1.252	-2.221	-3.673	-5.125	-4.048
57 30.0'N	0.0	0.0	0.0	0.0	0.0	0.0	0.0	0.0	0.0	0.0	0.0	0.0	0.0	-0.448	-0.896	-0.650	-0.403	-1.428	-2.454	-3.226
57 15.0'N	0.0	0.0	0.0	0.0	0.0	0.0	0.0	0.0	0.0	0.0	0.0	0.0	0.0	-0.224	-0.448	-0.528	-0.609	-0.988	-1.367	-1.577
57 0.0'N	0.0	0.0	0.0	0.0	0.0	0.0	0.0	0.0	0.0	0.0	0.0	0.0	0.0	0.0	0.0	-0.407	-0.814	-0.548	-0.281	0.071
56 45.0'N	0.0	0.0	0.0	0.0	0.0	0.0	0.0	0.0	0.0	0.0	0.0	0.0	0.0	0.0	0.0	-0.204	-0.407	-0.361	-0.315	0.184
56 30.0'N	0.0	0.0	0.0	0.0	0.0	0.0	0.0	0.0	0.0	0.0	0.0	0.0	0.0	0.0	0.0	0.0	0.0	-0.174	-0.348	-0.439
56 15.0'N	0.0	0.0	0.0	0.0	0.0	0.0	0.0	0.0	0.0	0.0	0.0	0.0	0.0	0.0	0.0	0.0	0.0	-0.087	-0.174	0.326
56 0.0'N	0.0	0.0	0.0	0.0	0.0	0.0	0.0	0.0	0.0	0.0	0.0	0.0	0.0	0.0	0.0	0.0	0.0	0.0	0.0	-0.213
55 45.0'N	0.0	0.0	0.0	0.0	0.0	0.0	0.0	0.0	0.0	0.0	0.0	0.0	0.0	0.0	0.0	0.0	0.0	0.0	0.0	-0.107
55 30.0'N	0.0	0.0	0.0	0.0	0.0	0.0	0.0	0.0	0.0	0.0	0.0	0.0	0.0	0.0	0.0	0.0	0.0	0.0	0.0	0.0
55 15.0'N	0.0	0.0	0.0	0.0	0.0	0.0	0.0	0.0	0.0	0.0	0.0	0.0	0.0	0.0	0.0	0.0	0.0	0.0	0.0	0.0
55 0.0'N	0.0	0.0	0.0	0.0	0.0	0.0	0.0	0.0	0.0	0.0	0.0	0.0	0.0	0.0	0.0	0.0	0.0	0.0	0.0	0.0

Table A.2

COMPUTED EAST-WEST COMPONENT OF TIDAL/BAROCLINIC RESIDUAL CURRENTS IN THE BERING AND CHUKCHI SEAS (cm/sec)

	171W 0.0'	170W 30.0'	170W 0.0'	169W 30.0'	169W 0.0'	168W 30.0'	168W 0.0'	167W 30.0'	167W 0.0'	166W 30.0'	166W 0.0'	165W 30.0'	165W 0.0'	164W 30.0'	164W 0.0'	163W 30.0'	163W 0.0'	162W 30.0'	162W 0.0'	161W 30.0'
72 0.0'N	-1.437	-1.266	-1.096	-0.587	-0.077	0.348	0.773	1.378	1.983	1.978	1.973	1.914	1.855	2.186	2.517	3.084	3.652	3.727	3.802	3.256
71 45.0'N	-1.127	-0.800	-0.473	-0.436	-0.399	-0.315	-0.231	0.149	0.529	1.458	2.386	2.168	1.950	2.165	2.381	2.546	2.711	2.736	2.760	2.658
71 30.0'N	-0.816	-0.333	0.151	-0.285	-0.720	-0.978	-1.236	-1.080	-0.924	0.938	2.800	2.422	2.045	2.144	2.244	2.008	1.771	1.744	1.717	2.059
71 15.0'N	-0.823	-0.474	-0.125	-0.365	-0.604	-0.232	0.140	-0.162	-0.464	0.016	0.496	-0.102	-0.701	-0.713	-0.724	-0.837	-0.949	-1.330	-1.712	-2.357
71 0.0'N	-0.829	-0.616	-0.402	-0.445	-0.488	0.514	1.515	0.756	-0.003	-0.906	-1.808	-2.627	-3.446	-3.570	-3.693	-3.681	-3.670	-4.405	-5.141	-6.773
70 45.0'N	-0.244	-0.327	-0.409	-0.309	-0.210	0.180	0.570	0.250	-0.070	-0.505	-0.939	-2.046	-3.154	-2.951	-2.749	-2.953	-3.157	-3.770	-4.383	-4.293
70 30.0'N	0.341	-0.038	-0.416	-0.174	0.068	-0.153	-0.374	-0.255	-0.136	-0.103	-0.071	-1.466	-2.861	-2.333	-1.805	-2.224	-2.644	-3.134	-3.625	-1.813
70 15.0'N	0.195	0.426	0.657	0.737	0.816	-0.144	-1.105	-1.442	-1.780	-1.291	-0.802	-0.753	-0.705	-0.533	-0.361	-0.841	-1.322	-1.567	-1.813	-0.906
70 0.0'N	0.050	0.890	1.731	1.647	1.564	-0.135	-1.835	-2.629	-3.424	-2.478	-1.532	-0.040	1.452	1.267	1.083	0.542	0.0	0.0	0.0	0.0
69 45.0'N	-1.557	-0.967	-0.378	-0.203	-0.028	-0.193	-0.359	-0.628	-0.896	-0.716	-0.536	0.095	0.725	0.481	0.236	0.118	0.0	0.0	0.0	0.0
69 30.0'N	-3.165	-2.825	-2.486	-2.052	-1.619	-0.251	1.117	1.374	1.631	1.046	0.461	0.230	-0.001	-0.306	-0.612	-0.306	0.0	0.0	0.0	0.0
69 15.0'N	-2.605	-2.527	-2.449	-2.364	-2.279	-0.909	0.462	0.342	0.221	0.619	1.017	0.925	0.833	0.263	-0.306	-0.153	0.0	0.0	0.0	0.0
69 0.0'N	-2.046	-2.229	-2.412	-2.676	-2.939	-1.566	-0.193	-0.691	-1.189	0.193	1.574	1.620	1.666	0.833	0.0	0.0	0.0	0.0	0.0	0.0
68 45.0'N	-1.809	-1.114	-0.419	-1.297	-2.176	-1.094	-0.012	0.055	0.121	0.454	0.787	0.810	0.833	0.417	0.0	0.0	0.0	0.0	0.0	0.0
68 30.0'N	-1.573	0.001	1.575	0.081	-1.413	-0.622	0.170	0.800	1.430	0.715	0.0	0.0	0.0	0.0	0.0	0.0	0.0	0.0	0.0	0.0
68 15.0'N	-1.530	-0.914	-0.298	-1.159	-2.020	-1.843	-1.666	-0.847	-0.029	-0.014	0.0	0.0	0.0	0.0	0.0	0.0	0.0	0.0	0.0	0.0
68 0.0'N	-1.487	-1.829	-2.171	-2.399	-2.627	-3.064	-3.501	-2.494	-1.488	-0.744	0.0	0.0	0.0	0.0	0.0	0.0	0.0	0.0	0.0	0.0
67 45.0'N	0.492	0.040	-0.411	-0.538	-0.665	-1.459	-2.253	-2.268	-2.282	-1.551	-0.819	-0.381	0.057	0.029	0.0	0.0	0.0	0.0	0.0	0.0
67 30.0'N	2.472	1.910	1.348	1.322	1.297	0.146	-1.006	-2.041	-3.077	-2.357	-1.638	-0.762	0.115	0.057	0.0	0.0	0.0	0.0	0.0	0.0
67 15.0'N	0.924	0.983	1.042	1.754	2.465	1.925	1.384	0.688	-0.008	-0.346	-0.683	-0.350	-0.016	0.043	0.102	0.051	0.0	0.0	0.0	0.0
67 0.0'N	-0.623	0.057	0.737	2.185	3.634	3.704	3.774	3.417	3.060	1.666	0.271	0.063	-0.146	0.028	0.203	0.102	0.0	0.0	0.0	0.0
66 45.0'N	-2.216	-2.114	-2.011	0.357	2.726	2.978	3.231	3.011	2.791	1.724	0.656	0.291	-0.073	0.014	0.102	0.085	0.068	0.034	0.0	0.0
66 30.0'N	-3.809	-4.284	-4.759	-1.470	1.819	2.253	2.688	2.605	2.523	1.781	1.040	0.520	0.0	0.0	0.0	0.068	0.135	0.068	0.0	0.0
66 15.0'N	-1.905	-2.142	-2.380	-0.426	1.527	2.253	2.978	2.120	1.261	0.891	0.520	0.260	0.0	0.0	0.0	0.034	0.068	0.034	0.0	0.0
66 0.0'N	0.0	0.0	0.0	0.617	1.235	2.252	3.269	1.634	0.0	0.0	0.0	0.0	0.0	0.0	0.0	0.0	0.0	0.0	0.0	0.0
65 45.0'N	-0.441	0.253	0.946	1.551	2.156	1.895	1.634	0.817	0.0	0.0	0.0	0.0	0.0	0.0	0.0	0.0	0.0	0.0	0.0	0.0
65 30.0'N	-0.882	0.505	1.892	2.484	3.076	1.538	0.0	0.0	0.0	0.0	0.0	0.0	0.0	0.0	0.0	0.0	0.0	0.0	0.0	0.0
65 15.0'N	1.493	2.011	2.529	1.665	0.802	-0.139	-1.080	-0.540	0.0	0.0	0.0	0.0	0.0	0.0	0.0	0.0	0.0	0.0	0.0	0.0
65 0.0'N	3.868	3.517	3.165	0.846	-1.473	-1.817	-2.161	-1.080	0.0	0.0	0.0	0.0	0.0	0.0	0.0	0.0	0.0	0.0	0.0	0.0
64 45.0'N	2.364	2.909	3.454	1.582	-0.291	-1.181	-2.071	-1.916	-1.761	-0.880	0.0	0.0	0.0	0.0	0.0	0.0	0.0	0.0	0.0	0.0
64 30.0'N	0.860	2.301	3.743	2.317	0.892	-0.544	-1.980	-2.751	-3.521	-1.761	0.0	0.0	0.0	0.0	0.0	0.0	0.0	0.0	0.0	0.0
64 15.0'N	1.596	1.599	1.603	1.098	0.593	-0.047	-0.686	-1.684	-2.683	-1.792	-0.901	-0.180	0.541	0.054	-0.432	-0.650	-0.867	-0.666	-0.464	-0.232
64 0.0'N	2.332	0.898	-0.536	-0.121	0.294	0.451	0.608	-0.618	-1.844	-1.824	-1.803	-0.361	1.082	0.109	-0.865	-1.299	-1.733	-1.331	-0.929	-0.464
63 45.0'N	1.166	0.449	-0.268	0.543	1.353	1.553	1.753	0.883	0.014	-0.249	-0.511	0.352	1.216	0.257	-0.702	-0.883	-1.064	-0.764	-0.464	-0.232
63 30.0'N	0.0	0.0	0.0	1.206	2.413	2.655	2.898	2.385	1.872	1.326	0.781	1.065	1.349	0.405	-0.540	-0.468	-0.395	-0.198	0.0	0.0
63 15.0'N	1.949	2.047	2.146	2.233	2.320	1.525	0.730	0.706	0.682	0.692	0.702	0.688	0.675	0.202	-0.270	-0.234	-0.198	-0.099	0.0	0.0
63 0.0'N	3.899	4.095	4.291	3.259	2.227	0.394	-1.439	-0.973	-0.507	0.057	0.622	0.311	0.0	0.0	0.0	0.0	0.0	0.0	0.0	0.0
62 45.0'N	2.842	2.477	2.112	1.877	1.642	-0.052	-1.745	-0.974	-0.202	0.054	0.311	0.155	0.0	0.0	0.0	0.0	0.0	0.0	0.0	0.0
62 30.0'N	1.786	0.859	-0.068	0.495	1.057	-0.497	-2.052	-0.975	0.103	0.051	0.0	0.0	0.0	0.0	0.0	0.0	0.0	0.0	0.0	0.0
62 15.0'N	1.576	0.752	-0.072	0.313	0.698	-0.173	-1.044	-0.252	0.539	0.270	0.0	0.0	0.0	0.0	0.0	0.0	0.0	0.0	0.0	0.0
62 0.0'N	1.365	0.644	-0.077	0.131	0.339	0.152	-0.036	0.470	0.976	0.488	0.0	0.0	0.0	0.0	0.0	0.0	0.0	0.0	0.0	0.0
61 45.0'N	1.512	1.022	0.532	0.458	0.384	0.396	0.407	0.448	0.488	0.244	0.0	0.0	0.0	0.0	0.0	0.0	0.0	0.0	0.0	0.0
61 30.0'N	1.659	1.400	1.141	0.785	0.430	0.640	0.850	0.425	0.0	0.0	0.0	0.0	0.0	0.0	0.0	0.0	0.0	0.0	0.0	0.0
61 15.0'N	0.773	0.965	1.156	1.052	0.948	0.869	0.789	0.351	-0.087	-0.044	0.0	0.0	0.0	0.0	0.0	0.0	0.0	0.0	0.0	0.0
61 0.0'N	-0.113	0.529	1.172	1.319	1.467	1.097	0.728	0.277	-0.174	-0.087	0.0	0.0	0.0	0.0	0.0	0.0	0.0	0.0	0.0	0.0
60 45.0'N	-0.579	0.044	0.668	0.768	0.868	0.581	0.294	0.200	0.107	0.254	0.402	0.201	0.0	0.0	0.0	0.0	0.0	0.0	0.0	0.0
60 30.0'N	-1.045	-0.441	0.164	0.217	0.269	0.065	-0.140	0.123	0.387	0.596	0.804	0.402	0.0	0.0	0.0	0.0	0.0	0.0	0.0	0.0
60 15.0'N	-0.173	-0.043	0.087	0.188	0.288	0.109	-0.070	0.062	0.194	0.298	0.402	0.201	0.0	0.0	0.0	0.0	0.0	0.0	0.0	0.0
60 0.0'N	0.699	0.355	0.010	0.158	0.307	0.153	0.0	0.0	0.0	0.0	0.0	0.0	0.0	0.0	0.0	0.0	0.0	0.0	0.0	0.0
59 45.0'N	0.743	0.511	0.279	0.388	0.497	0.423	0.349	0.391	0.433	0.419	0.405	0.353	0.301	0.234	0.166	0.065	-0.037	-0.018	0.0	0.0
59 30.0'N	0.788	0.668	0.548	0.618	0.688	0.693	0.697	0.781	0.865	0.837	0.809	0.706	0.603	0.468	0.333	0.130	-0.073	-0.037	0.0	0.0
59 15.0'N	0.127	0.342	0.557	0.442	0.328	0.431	0.534	0.603	0.671	0.528	0.384	0.679	0.974	0.833	0.693	0.542	0.391	0.195	0.0	0.0
59 0.0'N	-0.534	0.016	0.565	0.266	-0.032	0.169	0.372	0.425	0.478	0.219	-0.041	0.652	1.345	1.199	1.053	0.954	0.855	0.427	0.0	0.0
58 45.0'N	-0.046	0.175	0.397	0.129	-0.139	0.331	0.800	0.701	0.601	0.115	-0.371	0.022	0.414	0.490	0.566	0.662	0.759	0.162	-0.436	-0.455
58 30.0'N	0.441	0.335	0.229	-0.009	-0.246	0.492	1.229	0.977	0.725	0.012	-0.701	-0.609	-0.517	-0.219	0.079	0.371	0.663	-0.104	-0.871	-0.910
58 15.0'N	-0.752	-0.559	-0.366	-0.183	-0.000	0.270	0.540	0.859	1.177	0.149	-0.880	-0.998	-1.117	-0.706	-0.296	0.260	0.815	0.106	-0.602	-0.790
58 0.0'N	-1.944	-1.453	-0.961	-0.358	0.246	0.049	-0.149	0.740	1.629	0.285	-1.059	-1.387	-1.716	-1.193	-0.670	0.148	0.967	0.317	-0.333	-0.670
57 45.0'N	-2.971	-2.578	-2.185	-1.243	-0.300	-0.203	-0.105	0.771	1.648	1.240	0.832	-0.049	-0.931	-0.411	0.109	0.572	1.034	1.169	1.303	0.219
57 30.0'N	-3.998	-3.704	-3.409	-2.128	-0.846	-0.454	-0.062	0.803	1.667	2.195	2.724	1.289	-0.146	0.372	0.889	0.995	1.102	2.020	2.939	1.108
57 15.0'N	-1.788	-2.280	-2.773	-2.579	-2.385	-1.421	-0.458	0.449	1.356	1.848	2.340	1.558	0.777	0.690	0.604	0.590	0.577	1.279	1.980	0.861
57 0.0'N	0.423	-0.857	-2.137	-3.031	-3.925	-2.389	-0.853	0.096	1.046	1.501	1.957	1.828	1.700	1.009	0.318	0.186	0.053	0.537	1.021	0.613
56 45.0'N	-0.054	-0.746	-1.437	-2.405	-3.373	-3.325	-3.276	-1.295	0.685	1.732	2.778	2.193	1.609	1.031	0.452	0.434	0.416	0.482	0.549	0.451
56 30.0'N	-0.531	-0.634	-0.738	-1.780	-2.822	-4.260	-5.699	-2.687	0.325	1.962	3.599	2.559	1.518	1.052	0.586	0.682	0.779	0.427	0.076	0.288
56 15.0'N	-0.479	-0.682	-0.885	-0.439	0.007	-1.406	-2.819	-2.836	-2.854	-1.094	0.665	0.169	-0.327	-0.139	0.049	0.427	0.806	0.422	0.038	0.144
56 0.0'N	-0.427	-0.730	-1.032	0.902	2.836	1.449	0.061	-2.986	-6.032	-4.150	-2.269	-2.221	-2.173	-1.331	-0.489	0.172	0.833	0.417	0.0	0.0
55 45.0'N	-0.213	-0.365	-0.516	0.451	1.418	1.431	1.444	-1.714	-4.872	-4.442	-4.012	-3.590	-3.168	-2.715	-2.261	-0.922	0.417	0.208	0.0	0.0
55 30.0'N	0.0	0.0	0.0	0.0	0.0	1.414	2.828	-0.443	-3.713	-4.734	-5.755	-4.959	-4.164	-4.099	-4.034	-2.017	0.0	0.0	0.0	0.0
55 15.0'N	0.0	0.0	0.0	0.0	0.0	0.707	1.414	-0.391	-2.195	-2.980	-3.764	-3.060	-2.357	-2.187	-2.017	-1.009	0.0	0.0	0.0	0.0
55 0.0'N	0.0	0.0	0.0	0.0	0.0	0.0	0.0	-0.339	-0.678	-1.226	-1.773	-1.161	-0.549	-0.275	0.0	0.0	0.0	0.0	0.0	0.0

Table A.3

COMPUTED EAST-WEST COMPONENT OF TIDAL/BAROCLINIC RESIDUAL CURRENTS IN THE BERING AND CHUKCHI SEAS (cm/sec)

	161W 0.0'	160W 30.0'	160W 0.0'	159W 30.0'	159W 0.0'	158W 30.0'	158W 0.0'	157W 30.0'	157W 0.0'	156W 30.0'	156W 0.0'
72 0.0'N	2.709	2.661	2.612	2.052	1.492	0.769	0.047	-2.828	-5.703	-2.851	0.0
71 45.0'N	2.556	2.153	1.750	1.005	0.261	0.032	-0.197	-4.618	-9.040	-4.520	0.0
71 30.0'N	2.402	1.644	0.887	-0.041	-0.969	-0.705	-0.441	-6.409	******	-6.189	0.0
71 15.0'N	-3.002	-2.213	-1.423	-1.624	-1.825	-1.023	-0.220	-3.204	-6.189	-3.094	0.0
71 0.0'N	-8.406	-6.069	-3.732	-3.207	-2.681	-1.341	0.0	0.0	0.0	0.0	0.0
70 45.0'N	-4.203	-3.035	-1.866	-1.603	-1.341	-0.670	0.0	0.0	0.0	0.0	0.0
70 30.0'N	0.0	0.0	0.0	0.0	0.0	0.0	0.0	0.0	0.0	0.0	0.0
70 15.0'N	0.0	0.0	0.0	0.0	0.0	0.0	0.0	0.0	0.0	0.0	0.0
70 0.0'N	0.0	0.0	0.0	0.0	0.0	0.0	0.0	0.0	0.0	0.0	0.0
69 45.0'N	0.0	0.0	0.0	0.0	0.0	0.0	0.0	0.0	0.0	0.0	0.0
69 30.0'N	0.0	0.0	0.0	0.0	0.0	0.0	0.0	0.0	0.0	0.0	0.0
69 15.0'N	0.0	0.0	0.0	0.0	0.0	0.0	0.0	0.0	0.0	0.0	0.0
69 0.0'N	0.0	0.0	0.0	0.0	0.0	0.0	0.0	0.0	0.0	0.0	0.0
68 45.0'N	0.0	0.0	0.0	0.0	0.0	0.0	0.0	0.0	0.0	0.0	0.0
68 30.0'N	0.0	0.0	0.0	0.0	0.0	0.0	0.0	0.0	0.0	0.0	0.0
68 15.0'N	0.0	0.0	0.0	0.0	0.0	0.0	0.0	0.0	0.0	0.0	0.0
68 0.0'N	0.0	0.0	0.0	0.0	0.0	0.0	0.0	0.0	0.0	0.0	0.0
67 45.0'N	0.0	0.0	0.0	0.0	0.0	0.0	0.0	0.0	0.0	0.0	0.0
67 30.0'N	0.0	0.0	0.0	0.0	0.0	0.0	0.0	0.0	0.0	0.0	0.0
67 15.0'N	0.0	0.0	0.0	0.0	0.0	0.0	0.0	0.0	0.0	0.0	0.0
67 0.0'N	0.0	0.0	0.0	0.0	0.0	0.0	0.0	0.0	0.0	0.0	0.0
66 45.0'N	0.0	0.0	0.0	0.0	0.0	0.0	0.0	0.0	0.0	0.0	0.0
66 30.0'N	0.0	0.0	0.0	0.0	0.0	0.0	0.0	0.0	0.0	0.0	0.0
66 15.0'N	0.0	0.0	0.0	0.0	0.0	0.0	0.0	0.0	0.0	0.0	0.0
66 0.0'N	0.0	0.0	0.0	0.0	0.0	0.0	0.0	0.0	0.0	0.0	0.0
65 45.0'N	0.0	0.0	0.0	0.0	0.0	0.0	0.0	0.0	0.0	0.0	0.0
65 30.0'N	0.0	0.0	0.0	0.0	0.0	0.0	0.0	0.0	0.0	0.0	0.0
65 15.0'N	0.0	0.0	0.0	0.0	0.0	0.0	0.0	0.0	0.0	0.0	0.0
65 0.0'N	0.0	0.0	0.0	0.0	0.0	0.0	0.0	0.0	0.0	0.0	0.0
64 45.0'N	0.0	0.0	0.0	0.0	0.0	0.0	0.0	0.0	0.0	0.0	0.0
64 30.0'N	0.0	0.0	0.0	0.0	0.0	0.0	0.0	0.0	0.0	0.0	0.0
64 15.0'N	0.0	0.0	0.0	0.0	0.0	0.0	0.0	0.0	0.0	0.0	0.0
64 0.0'N	0.0	0.0	0.0	0.0	0.0	0.0	0.0	0.0	0.0	0.0	0.0
63 45.0'N	0.0	0.0	0.0	0.0	0.0	0.0	0.0	0.0	0.0	0.0	0.0
63 30.0'N	0.0	0.0	0.0	0.0	0.0	0.0	0.0	0.0	0.0	0.0	0.0
63 15.0'N	0.0	0.0	0.0	0.0	0.0	0.0	0.0	0.0	0.0	0.0	0.0
63 0.0'N	0.0	0.0	0.0	0.0	0.0	0.0	0.0	0.0	0.0	0.0	0.0
62 45.0'N	0.0	0.0	0.0	0.0	0.0	0.0	0.0	0.0	0.0	0.0	0.0
62 30.0'N	0.0	0.0	0.0	0.0	0.0	0.0	0.0	0.0	0.0	0.0	0.0
62 15.0'N	0.0	0.0	0.0	0.0	0.0	0.0	0.0	0.0	0.0	0.0	0.0
62 0.0'N	0.0	0.0	0.0	0.0	0.0	0.0	0.0	0.0	0.0	0.0	0.0
61 45.0'N	0.0	0.0	0.0	0.0	0.0	0.0	0.0	0.0	0.0	0.0	0.0
61 30.0'N	0.0	0.0	0.0	0.0	0.0	0.0	0.0	0.0	0.0	0.0	0.0
61 15.0'N	0.0	0.0	0.0	0.0	0.0	0.0	0.0	0.0	0.0	0.0	0.0
61 0.0'N	0.0	0.0	0.0	0.0	0.0	0.0	0.0	0.0	0.0	0.0	0.0
60 45.0'N	0.0	0.0	0.0	0.0	0.0	0.0	0.0	0.0	0.0	0.0	0.0
60 30.0'N	0.0	0.0	0.0	0.0	0.0	0.0	0.0	0.0	0.0	0.0	0.0
60 15.0'N	0.0	0.0	0.0	0.0	0.0	0.0	0.0	0.0	0.0	0.0	0.0
60 0.0'N	0.0	0.0	0.0	0.0	0.0	0.0	0.0	0.0	0.0	0.0	0.0
59 45.0'N	0.0	0.0	0.0	0.0	0.0	0.0	0.0	0.0	0.0	0.0	0.0
59 30.0'N	0.0	0.0	0.0	0.0	0.0	0.0	0.0	0.0	0.0	0.0	0.0
59 15.0'N	0.0	0.0	0.0	0.0	0.0	0.0	0.0	0.0	0.0	0.0	0.0
59 0.0'N	0.0	0.0	0.0	0.0	0.0	0.0	0.0	0.0	0.0	0.0	0.0
58 45.0'N	-0.474	-0.237	0.0	0.0	0.0	0.0	0.0	0.0	0.0	0.0	0.0
58 30.0'N	-0.949	-0.474	0.0	0.0	0.0	0.0	0.0	0.0	0.0	0.0	0.0
58 15.0'N	-0.978	-0.506	-0.033	0.015	0.062	0.031	0.0	0.0	0.0	0.0	0.0
58 0.0'N	-1.008	-0.537	-0.066	0.029	0.124	0.062	0.0	0.0	0.0	0.0	0.0
57 45.0'N	-0.865	-0.474	-0.083	0.148	0.379	0.202	0.024	0.012	0.0	0.0	0.0
57 30.0'N	-0.723	-0.412	-0.100	0.267	0.633	0.341	0.048	0.024	0.0	0.0	0.0
57 15.0'N	-0.259	-0.000	0.258	0.287	0.317	0.170	0.024	0.012	0.0	0.0	0.0
57 0.0'N	0.206	0.411	0.617	0.308	0.0	0.0	0.0	0.0	0.0	0.0	0.0
56 45.0'N	0.352	0.330	0.308	0.154	0.0	0.0	0.0	0.0	0.0	0.0	0.0
56 30.0'N	0.499	0.250	0.0	0.0	0.0	0.0	0.0	0.0	0.0	0.0	0.0
56 15.0'N	0.250	0.125	0.0	0.0	0.0	0.0	0.0	0.0	0.0	0.0	0.0
56 0.0'N	0.0	0.0	0.0	0.0	0.0	0.0	0.0	0.0	0.0	0.0	0.0
55 45.0'N	0.0	0.0	0.0	0.0	0.0	0.0	0.0	0.0	0.0	0.0	0.0
55 30.0'N	0.0	0.0	0.0	0.0	0.0	0.0	0.0	0.0	0.0	0.0	0.0
55 15.0'N	0.0	0.0	0.0	0.0	0.0	0.0	0.0	0.0	0.0	0.0	0.0
55 0.0'N	0.0	0.0	0.0	0.0	0.0	0.0	0.0	0.0	0.0	0.0	0.0

Table A.4

COMPUTED NORTH-SOUTH COMPONENT OF TIDAL/BAROCLINIC RESIDUAL CURRENTS IN THE BERING AND CHUKCHI SEAS (cm/sec)

	181W 0.0'	180W 30.0'	180W 0.0'	179W 30.0'	179W 0.0'	178W 30.0'	178W 0.0'	177W 30.0'	177W 0.0'	176W 30.0'	176W 0.0'	175W 30.0'	175W 0.0'	174W 30.0'	174W 0.0'	173W 30.0'	173W 0.0'	172W 30.0'	172W 0.0'	171W 30.0'
72 0.0'N	0.549	0.549	0.549	-1.815	-4.179	-0.615	2.950	4.257	5.564	3.800	2.035	1.378	0.722	-0.063	-0.847	-1.514	-2.181	-1.257	-0.333	-1.301
71 45.0'N	0.275	0.275	0.275	-0.907	-2.090	0.154	2.397	3.113	3.829	2.363	0.897	0.156	-0.586	-1.861	-3.137	-2.726	-2.316	-1.132	0.052	-0.647
71 30.0'N	0.0	0.0	0.0	0.0	0.0	0.922	1.844	1.969	2.095	0.927	-0.240	-1.067	-1.893	-3.660	-5.426	-3.939	-2.451	-1.006	0.438	0.007
71 15.0'N	0.0	0.0	0.0	0.0	0.0	0.461	0.922	2.898	4.874	3.077	1.280	-1.143	-3.566	-4.452	-5.338	-2.605	0.129	0.203	0.278	-0.064
71 0.0'N	0.0	0.0	0.0	0.0	0.0	0.0	0.0	3.826	7.652	5.226	2.800	-1.220	-5.239	-5.244	-5.250	-1.271	2.708	1.413	0.119	-0.136
70 45.0'N	0.0	0.0	0.0	0.0	0.0	0.0	0.0	1.554	3.109	0.259	-2.592	-4.819	-7.047	-5.744	-4.440	-1.653	1.135	0.961	0.788	0.228
70 30.0'N	0.0	0.0	0.0	0.0	0.0	0.0	0.0	-0.717	-1.435	-4.709	-7.983	-8.419	-8.855	-6.243	-3.630	-2.034	-0.438	0.510	1.457	0.593
70 15.0'N	3.995	3.995	3.995	2.672	1.349	1.046	0.743	-2.030	-4.803	-5.940	-7.078	-5.484	-3.890	-2.713	-1.536	-1.071	-0.605	0.527	1.660	1.141
70 0.0'N	7.990	7.990	7.990	5.344	2.698	2.092	1.486	-3.342	-8.170	-7.172	-6.173	-2.550	1.074	0.816	0.558	-0.107	-0.773	0.545	1.863	1.688
69 45.0'N	3.628	3.628	3.628	3.095	2.563	0.605	-1.352	-4.224	-7.095	-6.157	-5.218	-3.682	-2.146	-1.705	-1.265	-1.351	-1.437	-0.149	1.139	1.557
69 30.0'N	-0.734	-0.734	-0.734	0.847	2.427	-0.882	-4.191	-5.105	-6.020	-5.141	-4.262	-4.813	-5.365	-4.227	-3.089	-2.595	-2.102	-0.843	0.415	1.425
69 15.0'N	-0.367	-0.205	-0.043	0.142	0.328	-2.362	-5.051	-4.998	-4.944	-4.327	-3.710	-3.770	-3.830	-2.717	-1.605	-0.415	0.776	0.527	0.278	1.466
69 0.0'N	0.0	0.324	0.648	-0.562	-1.771	-3.842	-5.912	-4.890	-3.868	-3.513	-3.157	-2.726	-2.295	-1.208	-0.121	1.766	3.653	1.898	0.142	1.507
68 45.0'N	0.0	0.162	0.324	-0.281	-0.886	-2.921	-4.957	-4.288	-3.620	-2.129	-0.638	-0.690	-0.741	-0.470	-0.198	0.992	2.182	1.566	0.950	1.350
68 30.0'N	0.0	0.0	0.0	0.0	0.0	-2.001	-4.002	-3.687	-3.372	-0.745	1.881	1.347	0.813	0.268	-0.276	0.218	0.712	1.235	1.758	1.194
68 15.0'N	0.0	0.0	0.0	0.0	0.0	-1.000	-2.001	-1.843	-1.686	-2.365	-3.043	-1.930	-0.817	-1.826	-2.835	-1.224	0.387	1.171	1.956	1.897
68 0.0'N	0.0	0.0	0.0	0.0	0.0	0.0	0.0	0.0	0.0	-3.984	-7.967	-5.207	-2.447	-3.921	-5.395	-2.666	0.063	1.108	2.154	2.600
67 45.0'N	0.0	0.0	0.0	0.0	0.0	0.0	0.0	0.0	0.0	-1.992	-3.984	-3.430	-2.876	-3.787	-4.698	-2.843	-0.989	0.259	1.508	1.993
67 30.0'N	0.0	0.0	0.0	0.0	0.0	0.0	0.0	0.0	0.0	0.0	0.0	-1.652	-3.304	-3.653	-4.001	-3.021	-2.041	-0.590	0.861	1.387
67 15.0'N	0.0	0.0	0.0	0.0	0.0	0.0	0.0	0.0	0.0	0.0	0.0	-0.826	-1.652	-1.826	-2.000	-1.510	-1.020	-1.045	-1.069	0.913
67 0.0'N	0.0	0.0	0.0	0.0	0.0	0.0	0.0	0.0	0.0	0.0	0.0	0.0	0.0	0.0	0.0	0.0	0.0	-1.500	-3.000	0.439
66 45.0'N	0.0	0.0	0.0	0.0	0.0	0.0	0.0	0.0	0.0	0.0	0.0	0.0	0.0	0.0	0.0	0.0	0.0	-0.750	-1.500	1.041
66 30.0'N	0.0	0.0	0.0	0.0	0.0	0.0	0.0	0.0	0.0	0.0	0.0	0.0	0.0	0.0	0.0	0.0	0.0	0.0	0.0	1.643
66 15.0'N	0.0	0.0	0.0	0.0	0.0	0.0	0.0	0.0	0.0	0.0	0.0	0.0	0.0	0.0	0.0	0.0	0.0	0.0	0.0	0.822
66 0.0'N	0.0	0.0	0.0	0.0	0.0	0.0	0.0	0.0	0.0	0.0	0.0	0.0	0.0	0.0	0.0	0.0	0.0	0.0	0.0	0.0
65 45.0'N	0.0	0.0	0.0	-0.128	-0.255	-0.128	0.0	0.0	0.0	0.0	0.0	0.0	0.0	0.0	0.0	0.0	0.0	0.0	0.0	0.0
65 30.0'N	0.0	0.0	0.0	-0.255	-0.510	-0.255	0.0	0.0	0.0	0.0	0.0	0.0	0.0	0.0	0.0	0.0	0.0	0.0	0.0	0.0
65 15.0'N	0.0	0.0	0.0	-0.316	-0.632	-0.316	0.0	-0.022	-0.045	-0.022	0.0	0.0	0.0	0.0	0.0	0.0	0.0	0.0	0.0	0.024
65 0.0'N	0.0	0.0	0.0	-0.377	-0.754	-0.377	0.0	-0.045	-0.089	-0.045	0.0	0.0	0.0	0.0	0.0	0.0	0.0	0.0	0.0	0.049
64 45.0'N	0.0	-0.055	-0.109	-0.010	0.089	-0.105	-0.299	-0.373	-0.448	-0.477	-0.506	-0.253	0.0	0.0	0.0	0.0	0.0	0.443	0.886	0.853
64 30.0'N	0.0	-0.109	-0.219	0.356	0.931	0.167	-0.598	-0.702	-0.807	-0.909	-1.012	-0.506	0.0	0.0	0.0	0.0	0.0	0.886	1.772	1.657
64 15.0'N	0.172	-0.036	-0.243	0.084	0.412	-0.099	-0.609	-0.093	0.427	-0.251	-0.924	-2.168	-3.411	-2.732	-2.054	-1.027	0.0	2.138	4.277	3.111
64 0.0'N	0.344	0.038	-0.267	-0.188	-0.108	-0.364	-0.621	0.515	1.651	0.408	-0.836	-3.829	-6.822	-5.465	-4.107	-2.054	0.0	3.391	6.782	4.565
63 45.0'N	-0.193	0.050	0.292	0.441	0.590	0.973	1.357	1.090	0.824	-1.513	-3.851	-4.773	-5.695	-3.787	-1.878	0.485	2.847	3.479	4.111	2.642
63 30.0'N	-0.729	0.061	0.852	1.070	1.288	2.311	3.335	1.666	-0.003	-3.434	-6.865	-5.717	-4.569	-2.108	0.352	3.023	5.694	3.567	1.440	0.720
63 15.0'N	-0.364	0.955	2.274	1.346	0.417	0.515	0.612	-0.205	-1.023	-2.990	-4.958	-3.136	-1.314	0.748	2.809	3.044	3.280	1.633	-0.015	-0.007
63 0.0'N	0.0	1.848	3.696	1.622	-0.453	-1.281	-2.110	-2.076	-2.042	-2.546	-3.050	-0.554	1.941	3.603	5.265	3.065	0.866	-0.302	-1.469	-0.735
62 45.0'N	0.0	0.535	1.071	-0.374	-1.819	-1.561	-1.303	-0.515	0.274	-0.783	-1.840	0.095	2.031	2.699	3.367	1.461	-0.444	-0.689	-0.934	-0.088
62 30.0'N	0.0	-0.777	-1.555	-2.369	-3.184	-1.840	-0.496	1.047	2.589	0.980	-0.630	0.745	2.120	1.794	1.468	-0.143	-1.754	-1.076	-0.399	0.559
62 15.0'N	0.496	0.108	-0.281	-0.231	-0.180	0.199	0.578	0.533	0.489	0.456	0.424	2.141	3.858	2.736	1.615	0.294	-1.028	-0.386	0.255	0.550
62 0.0'N	0.993	0.993	0.993	1.908	2.823	2.237	1.651	0.019	-1.612	-0.067	1.478	3.536	5.595	3.679	1.762	0.730	-0.302	0.304	0.910	0.541
61 45.0'N	-1.272	-1.272	-1.272	-0.817	-0.362	-0.057	0.249	-0.609	-1.466	0.421	2.308	3.443	4.578	2.539	0.500	-0.019	-0.537	-0.010	0.518	-0.029
61 30.0'N	-3.536	-3.536	-3.536	-3.542	-3.548	-2.350	-1.153	-1.237	-1.321	0.909	3.139	3.350	3.560	1.399	-0.762	-0.767	-0.773	-0.324	0.126	-0.598
61 15.0'N	-2.173	-2.173	-2.173	-2.403	-2.633	-1.680	-0.727	-1.008	-1.288	0.938	3.165	3.581	3.997	1.860	-0.276	-0.611	-0.945	-0.475	-0.005	-0.194
61 0.0'N	-0.809	-0.809	-0.809	-1.263	-1.718	-1.009	-0.300	-0.778	-1.255	0.968	3.191	3.812	4.433	2.321	0.209	-0.454	-1.116	-0.626	-0.135	0.211
60 45.0'N	-0.405	-1.015	-1.625	-1.730	-1.835	-1.473	-1.111	-1.496	-1.882	0.205	2.292	3.245	4.199	2.068	-0.062	-0.310	-0.558	-0.596	-0.634	-0.324
60 30.0'N	0.0	-1.220	-2.441	-2.196	-1.952	-1.937	-1.921	-2.215	-2.509	-0.557	1.394	2.679	3.964	1.816	-0.333	-0.166	0.0	-0.567	-1.133	-0.859
60 15.0'N	0.0	-0.610	-1.220	-1.221	-1.223	-1.560	-1.898	-2.337	-2.776	-0.573	1.629	2.910	4.191	1.597	-0.998	-0.499	0.0	-0.603	-1.206	-0.791
60 0.0'N	0.0	0.0	0.0	-0.246	-0.493	-1.184	-1.874	-2.458	-3.042	-0.589	1.865	3.141	4.418	1.378	-1.663	-0.831	0.0	-0.639	-1.278	-0.722
59 45.0'N	0.0	0.0	0.0	-0.123	-0.246	-0.925	-1.603	-2.510	-3.417	-0.242	2.933	4.470	6.008	2.387	-1.234	-1.160	-1.085	-1.059	-1.033	-0.594
59 30.0'N	0.0	0.0	0.0	0.0	0.0	-0.666	-1.333	-2.562	-3.792	0.105	4.002	5.799	7.597	3.396	-0.806	-1.488	-2.170	-1.479	-0.788	-0.466
59 15.0'N	0.0	0.0	0.0	0.0	0.0	-0.333	-0.666	-1.412	-2.158	0.625	3.408	3.714	4.021	0.730	-2.560	-1.830	-1.100	-0.981	-0.863	-0.599
59 0.0'N	0.0	0.0	0.0	0.0	0.0	0.0	0.0	-0.262	-0.523	1.145	2.814	1.629	0.444	-1.935	-4.313	-2.171	-0.029	-0.483	-0.937	-0.732
58 45.0'N	0.0	0.0	0.0	0.0	0.0	0.0	0.0	-0.131	-0.262	0.183	0.628	0.865	1.102	-0.337	-1.776	-0.701	0.374	0.701	1.027	-0.434
58 30.0'N	0.0	0.0	0.0	0.0	0.0	0.0	0.0	0.0	0.0	-0.778	-1.557	0.102	1.761	1.261	0.761	0.769	0.778	1.884	2.991	-0.135
58 15.0'N	0.0	0.0	0.0	0.0	0.0	0.0	0.0	0.0	0.0	-0.389	-0.778	-0.330	0.118	0.052	-0.013	0.811	1.635	1.817	1.999	-0.292
58 0.0'N	0.0	0.0	0.0	0.0	0.0	0.0	0.0	0.0	0.0	0.0	0.0	-0.763	-1.526	-1.156	-0.787	0.853	2.493	1.750	1.008	-0.449
57 45.0'N	0.0	0.0	0.0	0.0	0.0	0.0	0.0	0.0	0.0	0.0	0.0	-0.381	-0.763	-0.672	-0.581	0.273	1.128	1.125	1.122	-0.375
57 30.0'N	0.0	0.0	0.0	0.0	0.0	0.0	0.0	0.0	0.0	0.0	0.0	0.0	0.0	-0.187	-0.374	-0.306	-0.238	0.499	1.236	-0.301
57 15.0'N	0.0	0.0	0.0	0.0	0.0	0.0	0.0	0.0	0.0	0.0	0.0	0.0	0.0	-0.094	-0.187	-0.263	-0.339	0.060	0.459	-0.381
57 0.0'N	0.0	0.0	0.0	0.0	0.0	0.0	0.0	0.0	0.0	0.0	0.0	0.0	0.0	0.0	0.0	-0.220	-0.440	-0.379	-0.318	-0.462
56 45.0'N	0.0	0.0	0.0	0.0	0.0	0.0	0.0	0.0	0.0	0.0	0.0	0.0	0.0	0.0	0.0	-0.110	-0.220	-0.365	-0.509	-0.585
56 30.0'N	0.0	0.0	0.0	0.0	0.0	0.0	0.0	0.0	0.0	0.0	0.0	0.0	0.0	0.0	0.0	0.0	0.0	-0.350	-0.700	-0.709
56 15.0'N	0.0	0.0	0.0	0.0	0.0	0.0	0.0	0.0	0.0	0.0	0.0	0.0	0.0	0.0	0.0	0.0	0.0	-0.175	-0.350	-0.597
56 0.0'N	0.0	0.0	0.0	0.0	0.0	0.0	0.0	0.0	0.0	0.0	0.0	0.0	0.0	0.0	0.0	0.0	0.0	0.0	0.0	-0.484
55 45.0'N	0.0	0.0	0.0	0.0	0.0	0.0	0.0	0.0	0.0	0.0	0.0	0.0	0.0	0.0	0.0	0.0	0.0	0.0	0.0	-0.242
55 30.0'N	0.0	0.0	0.0	0.0	0.0	0.0	0.0	0.0	0.0	0.0	0.0	0.0	0.0	0.0	0.0	0.0	0.0	0.0	0.0	0.0
55 15.0'N	0.0	0.0	0.0	0.0	0.0	0.0	0.0	0.0	0.0	0.0	0.0	0.0	0.0	0.0	0.0	0.0	0.0	0.0	0.0	0.0
55 0.0'N	0.0	0.0	0.0	0.0	0.0	0.0	0.0	0.0	0.0	0.0	0.0	0.0	0.0	0.0	0.0	0.0	0.0	0.0	0.0	0.0

Table A.5

COMPUTED NORTH-SOUTH COMPONENT OF TIDAL/BAROCLINIC RESIDUAL CURRENTS IN THE BERING AND CHUKCHI SEAS (cm/sec)

	171W 0.0'	170W 30.0'	170W 0.0'	169W 30.0'	169W 0.0'	168W 30.0'	168W 0.0'	167W 30.0'	167W 0.0'	166W 30.0'	166W 0.0'	165W 30.0'	165W 0.0'	164W 30.0'	164W 0.0'	163W 30.0'	163W 0.0'	162W 30.0'	162W 0.0'	161W 30.0'
72 0.0'N	-2.269	-1.847	-1.425	-0.818	-0.212	0.152	0.516	0.216	-0.084	0.334	0.751	0.848	0.944	0.882	0.820	0.871	0.922	1.561	2.200	2.177
71 45.0'N	-1.346	-1.230	-1.114	-0.389	0.336	0.445	0.554	0.829	1.103	1.325	1.546	1.206	0.865	1.137	1.409	1.395	1.380	1.824	2.268	2.162
71 30.0'N	-0.423	-0.614	-0.804	0.040	0.884	0.738	0.592	1.441	2.290	2.316	2.341	1.564	0.787	1.392	1.998	1.918	1.839	2.087	2.335	2.148
71 15.0'N	-0.407	-0.327	-0.246	0.322	0.890	0.507	0.124	1.539	2.955	3.131	3.307	2.123	0.939	1.487	2.035	2.052	2.070	2.247	2.424	2.220
71 0.0'N	-0.391	-0.040	0.311	0.604	0.897	0.276	-0.344	1.638	3.620	3.946	4.272	2.682	1.092	1.582	2.072	2.186	2.300	2.407	2.513	2.292
70 45.0'N	-0.331	0.253	0.838	0.643	0.447	0.735	1.022	2.922	4.821	3.623	2.424	0.766	-0.892	0.266	1.425	0.949	0.473	0.911	1.349	0.191
70 30.0'N	-0.272	0.547	1.365	0.681	-0.003	1.193	2.389	4.206	6.023	3.299	0.576	-1.151	-2.877	-1.049	0.779	-0.288	-1.355	-0.585	0.184	-1.910
70 15.0'N	0.621	0.727	0.834	0.456	0.077	1.579	3.080	3.339	3.599	1.052	-1.494	-1.981	-2.467	-0.530	1.406	1.010	0.614	0.353	0.092	-0.955
70 0.0'N	1.514	0.908	0.303	0.230	0.158	1.964	3.771	2.473	1.174	-1.195	-3.564	-2.810	-2.057	-0.012	2.033	2.308	2.583	1.291	0.0	0.0
69 45.0'N	1.974	1.993	2.011	1.274	0.537	1.006	1.476	1.226	0.976	0.138	-0.701	-0.757	-0.812	0.053	0.919	0.898	0.876	0.438	0.0	0.0
69 30.0'N	2.434	3.077	3.720	2.318	0.916	0.048	-0.820	-0.021	0.778	1.470	2.162	1.297	0.432	0.118	-0.196	-0.513	-0.830	-0.415	0.0	0.0
69 15.0'N	2.653	2.656	2.659	1.703	0.747	0.844	0.941	0.798	0.656	0.901	1.146	0.193	-0.761	0.320	1.401	0.493	-0.415	-0.208	0.0	0.0
69 0.0'N	2.871	2.234	1.597	1.087	0.577	1.640	2.702	1.618	0.534	0.332	0.131	-0.911	-1.953	0.523	2.999	1.499	0.0	0.0	0.0	0.0
68 45.0'N	1.751	1.483	1.216	1.729	2.241	3.017	3.792	2.038	0.284	1.000	1.716	0.370	-0.977	0.261	1.499	0.750	0.0	0.0	0.0	0.0
68 30.0'N	0.631	0.733	0.835	2.370	3.905	4.394	4.883	2.458	0.034	1.667	3.301	1.650	0.0	0.0	0.0	0.0	0.0	0.0	0.0	0.0
68 15.0'N	1.838	1.689	1.540	2.201	2.863	3.619	4.374	3.029	1.684	2.179	2.675	1.337	0.0	0.0	0.0	0.0	0.0	0.0	0.0	0.0
68 0.0'N	3.045	2.645	2.245	2.033	1.821	2.843	3.866	3.600	3.334	2.692	2.049	1.024	0.0	0.0	0.0	0.0	0.0	0.0	0.0	0.0
67 45.0'N	2.479	1.843	1.206	1.490	1.774	2.634	3.495	3.430	3.365	3.137	2.909	1.454	0.0	0.0	0.0	0.0	0.0	0.0	0.0	0.0
67 30.0'N	1.913	1.040	0.168	0.947	1.726	2.425	3.124	3.260	3.396	3.582	3.768	1.884	0.0	0.0	0.0	0.0	0.0	0.0	0.0	0.0
67 15.0'N	2.895	1.808	0.721	1.435	2.148	2.078	2.008	3.051	4.093	4.376	4.659	2.777	0.895	0.394	-0.108	-0.054	0.0	0.0	0.0	0.0
67 0.0'N	3.877	2.576	1.275	1.922	2.569	1.731	0.892	2.841	4.790	5.170	5.549	3.670	1.790	0.788	-0.215	-0.108	0.0	0.0	0.0	0.0
66 45.0'N	3.582	2.525	1.469	2.064	2.660	1.628	0.596	1.996	3.396	3.783	4.171	2.714	1.257	0.575	-0.107	-0.098	-0.089	-0.044	0.0	0.0
66 30.0'N	3.287	2.475	1.663	2.207	2.750	1.525	0.300	1.150	2.001	2.397	2.793	1.758	0.723	0.362	0.0	-0.089	-0.177	-0.089	0.0	0.0
66 15.0'N	1.643	1.237	0.832	3.986	7.141	4.780	2.420	2.406	2.392	1.894	1.396	0.879	0.362	0.181	0.0	-0.044	-0.089	-0.044	0.0	0.0
66 0.0'N	0.0	0.0	0.0	5.766	11.532	8.036	4.540	3.662	2.784	1.392	0.0	0.0	0.0	0.0	0.0	0.0	0.0	0.0	0.0	0.0
65 45.0'N	0.0	0.0	0.0	4.801	9.602	7.278	4.954	3.173	1.392	0.696	0.0	0.0	0.0	0.0	0.0	0.0	0.0	0.0	0.0	0.0
65 30.0'N	0.0	0.0	0.0	3.836	7.673	6.521	5.369	2.684	0.0	0.0	0.0	0.0	0.0	0.0	0.0	0.0	0.0	0.0	0.0	0.0
65 15.0'N	0.049	0.914	1.780	4.476	7.173	6.381	5.589	2.795	0.0	0.0	0.0	0.0	0.0	0.0	0.0	0.0	0.0	0.0	0.0	0.0
65 0.0'N	0.098	1.828	3.559	5.117	6.674	6.242	5.810	2.905	0.0	0.0	0.0	0.0	0.0	0.0	0.0	0.0	0.0	0.0	0.0	0.0
64 45.0'N	0.820	2.529	4.237	4.958	5.679	5.845	6.011	4.032	2.053	1.026	0.0	0.0	0.0	0.0	0.0	0.0	0.0	0.0	0.0	0.0
64 30.0'N	1.543	3.229	4.915	4.800	4.685	5.449	6.213	5.159	4.105	2.053	0.0	0.0	0.0	0.0	0.0	0.0	0.0	0.0	0.0	0.0
64 15.0'N	1.945	2.774	3.603	3.124	2.644	3.369	4.094	3.607	3.121	1.948	0.775	0.388	0.0	0.0	0.0	0.0	0.0	-0.530	-1.060	-0.530
64 0.0'N	2.348	2.319	2.291	1.447	0.603	1.289	1.974	2.056	2.137	1.844	1.550	0.775	0.0	0.0	0.0	0.0	0.0	-1.060	-2.120	-1.060
63 45.0'N	1.174	1.160	1.146	1.766	2.387	2.599	2.811	2.766	2.722	2.618	2.514	1.842	1.169	0.805	0.441	0.633	0.824	0.085	-0.653	-0.327
63 30.0'N	0.0	0.0	0.0	2.086	4.172	3.909	3.647	3.477	3.307	3.393	3.478	2.908	2.338	1.610	0.883	1.265	1.648	1.231	0.814	0.407
63 15.0'N	0.0	0.0	0.0	2.355	4.710	4.121	3.533	3.550	3.567	3.122	2.677	3.098	3.519	1.980	0.441	0.633	0.824	0.616	0.407	0.204
63 0.0'N	0.0	0.0	0.0	2.624	5.248	4.333	3.418	3.623	3.827	2.852	1.877	3.288	4.700	2.350	0.0	0.0	0.0	0.0	0.0	0.0
62 45.0'N	0.759	0.817	0.875	1.750	2.625	2.795	2.964	2.940	2.915	1.975	1.035	1.693	2.350	1.175	0.0	0.0	0.0	0.0	0.0	0.0
62 30.0'N	1.517	1.633	1.749	0.876	0.003	1.256	2.510	2.256	2.003	1.098	0.193	0.097	0.0	0.0	0.0	0.0	0.0	0.0	0.0	0.0
62 15.0'N	0.845	0.968	1.092	0.660	0.229	0.908	1.587	1.490	1.393	0.940	0.488	0.244	0.0	0.0	0.0	0.0	0.0	0.0	0.0	0.0
62 0.0'N	0.172	0.303	0.434	0.445	0.455	0.560	0.665	0.724	0.782	0.782	0.782	0.391	0.0	0.0	0.0	0.0	0.0	0.0	0.0	0.0
61 45.0'N	-0.575	-0.134	0.306	0.391	0.476	0.453	0.430	0.719	1.008	0.700	0.391	0.196	0.0	0.0	0.0	0.0	0.0	0.0	0.0	0.0
61 30.0'N	-1.322	-0.572	0.178	0.338	0.498	0.346	0.194	0.714	1.234	0.617	0.0	0.0	0.0	0.0	0.0	0.0	0.0	0.0	0.0	0.0
61 15.0'N	-0.383	-0.120	0.142	0.085	0.027	0.389	0.751	1.024	1.297	0.648	0.0	0.0	0.0	0.0	0.0	0.0	0.0	0.0	0.0	0.0
61 0.0'N	0.556	0.332	0.107	-0.168	-0.443	0.432	1.307	1.333	1.360	0.680	0.0	0.0	0.0	0.0	0.0	0.0	0.0	0.0	0.0	0.0
60 45.0'N	-0.015	-0.125	-0.235	-0.285	-0.334	0.273	0.880	0.751	0.621	0.249	-0.123	-0.062	0.0	0.0	0.0	0.0	0.0	0.0	0.0	0.0
60 30.0'N	-0.585	-0.582	-0.578	-0.402	-0.225	0.114	0.454	0.168	-0.117	-0.182	-0.246	-0.123	0.0	0.0	0.0	0.0	0.0	0.0	0.0	0.0
60 15.0'N	-0.376	-0.381	-0.386	-0.491	-0.597	-0.185	0.226	0.084	-0.059	-0.091	-0.123	-0.378	-0.633	-0.316	0.0	0.0	0.0	0.0	0.0	0.0
60 0.0'N	-0.166	-0.180	-0.194	-0.581	-0.968	-0.485	-0.002	-0.001	0.0	0.0	0.0	-0.633	-1.266	-0.633	0.0	0.0	0.0	0.0	0.0	0.0
59 45.0'N	-0.155	-0.351	-0.548	-0.742	-0.937	-0.753	-0.568	-0.284	0.0	0.0	0.0	-0.649	-1.297	-0.649	0.0	0.0	0.0	0.0	0.0	0.0
59 30.0'N	-0.144	-0.522	-0.901	-0.904	-0.906	-1.020	-1.134	-0.567	0.0	0.0	0.0	-0.665	-1.329	-0.665	0.0	0.0	0.0	0.0	0.0	0.0
59 15.0'N	-0.335	-0.627	-0.919	-1.043	-1.166	-1.266	-1.367	-0.808	-0.249	-0.095	0.060	-0.692	-1.444	-0.793	-0.142	-0.124	-0.106	-0.005	0.097	0.048
59 0.0'N	-0.527	-0.732	-0.938	-1.182	-1.426	-1.513	-1.599	-1.049	-0.499	-0.189	0.120	-0.719	-1.559	-0.921	-0.284	-0.248	-0.212	-0.009	0.193	0.097
58 45.0'N	-1.894	-1.782	-1.671	-1.515	-1.358	-1.400	-1.442	-1.033	-0.624	-0.424	-0.225	-0.652	-1.080	-0.635	-0.190	-0.153	-0.117	-0.193	-0.270	-0.135
58 30.0'N	-3.261	-2.833	-2.404	-1.848	-1.291	-1.288	-1.284	-1.016	-0.748	-0.659	-0.569	-0.586	-0.602	-0.349	-0.096	-0.059	-0.022	-0.377	-0.733	-0.367
58 15.0'N	-2.583	-2.180	-1.777	-1.544	-1.310	-1.252	-1.194	-1.382	-1.569	-1.832	-2.096	-1.538	-0.980	-0.745	-0.509	-0.642	-0.774	-1.012	-1.250	-0.617
58 0.0'N	-1.905	-1.528	-1.150	-1.240	-1.329	-1.217	-1.105	-1.747	-2.389	-3.006	-3.623	-2.491	-1.359	-1.141	-0.923	-1.224	-1.526	-1.647	-1.767	-0.866
57 45.0'N	-1.871	-1.873	-1.875	-1.278	-0.680	-0.842	-1.003	-1.473	-1.942	-2.240	-2.538	-1.926	-1.313	-0.623	0.067	-0.246	-0.559	-0.851	-1.144	-0.588
57 30.0'N	-1.838	-2.219	-2.601	-1.316	-0.031	-0.466	-0.901	-1.198	-1.496	-1.474	-1.453	-1.360	-1.268	-0.105	1.057	0.733	0.409	-0.056	-0.520	-0.309
57 15.0'N	-1.221	-0.976	-0.731	-0.602	-0.472	-0.431	-0.389	-0.706	-1.023	-1.363	-1.703	-1.192	-0.681	0.383	1.448	1.156	0.863	0.315	-0.233	0.216
57 0.0'N	-0.605	0.267	1.138	0.113	-0.913	-0.395	0.123	-0.214	-0.551	-1.252	-1.954	-1.025	-0.095	0.872	1.840	1.579	1.318	0.686	0.055	0.741
56 45.0'N	-0.662	-0.262	0.138	-0.089	-0.317	-0.051	0.214	0.142	0.069	-0.886	-1.841	-1.404	-0.968	-0.097	0.774	0.679	0.585	0.497	0.410	0.788
56 30.0'N	-0.719	-0.791	-0.862	-0.292	0.279	0.293	0.306	0.498	0.689	-0.519	-1.728	-1.784	-1.840	-1.066	-0.291	-0.220	-0.148	0.308	0.765	0.836
56 15.0'N	-0.843	-0.908	-0.974	-0.788	-0.602	-0.579	-0.557	0.534	1.625	1.221	0.817	-0.491	-1.800	-1.178	-0.557	-0.193	0.171	0.377	0.584	0.519
56 0.0'N	-0.968	-1.026	-1.085	-1.283	-1.482	-1.451	-1.420	0.571	2.562	2.962	3.363	0.801	-1.760	-1.291	-0.822	-0.167	0.489	0.447	0.404	0.202
55 45.0'N	-0.484	-0.513	-0.542	-0.642	-0.741	-0.658	-0.575	0.812	2.199	2.066	1.933	-0.947	-3.828	-2.334	-0.841	-0.643	-0.444	-0.121	0.202	0.101
55 30.0'N	0.0	0.0	0.0	0.0	0.0	0.135	0.271	1.054	1.837	1.170	0.504	-2.696	-5.895	-3.378	-0.860	-1.119	-1.377	-0.689	0.0	0.0
55 15.0'N	0.0	0.0	0.0	0.0	0.0	0.068	0.135	0.037	-0.061	0.348	0.756	-0.931	-2.618	-1.245	0.129	-0.280	-0.689	-0.344	0.0	0.0
55 0.0'N	0.0	0.0	0.0	0.0	0.0	0.0	0.0	-0.979	-1.958	-0.475	1.008	0.834	0.659	0.888	1.118	0.559	0.0	0.0	0.0	0.0

Table A.6

COMPUTED NORTH-SOUTH COMPONENT OF TIDAL/BAROCLINIC RESIDUAL CURRENTS IN THE BERING AND CHUKCHI SEAS (cm/sec)

	161W 0.0'	160W 30.0'	160W 0.0'	159W 30.0'	159W 0.0'	158W 30.0'	158W 0.0'	157W 30.0'	157W 0.0'	156W 30.0'	156W 0.0'
72 0.0'N	2.154	1.408	0.662	0.714	0.766	1.100	1.434	4.568	7.703	7.703	7.703
71 45.0'N	2.057	1.093	0.128	0.102	0.076	-0.366	-0.807	3.718	8.242	8.242	8.242
71 30.0'N	1.960	0.778	-0.405	-0.510	-0.614	-1.831	-3.048	2.867	8.782	8.782	8.782
71 15.0'N	2.015	0.516	-0.983	-1.497	-2.012	-2.529	-3.046	0.673	4.391	4.391	4.391
71 0.0'N	2.070	0.255	-1.560	-2.485	-3.410	-3.227	-3.044	-1.522	0.0	0.0	0.0
70 45.0'N	-0.967	-0.874	-0.780	-1.242	-1.705	-1.613	-1.522	-0.761	0.0	0.0	0.0
70 30.0'N	-4.004	-2.002	0.0	0.0	0.0	0.0	0.0	0.0	0.0	0.0	0.0
70 15.0'N	-2.002	-1.001	0.0	0.0	0.0	0.0	0.0	0.0	0.0	0.0	0.0
70 0.0'N	0.0	0.0	0.0	0.0	0.0	0.0	0.0	0.0	0.0	0.0	0.0
69 45.0'N	0.0	0.0	0.0	0.0	0.0	0.0	0.0	0.0	0.0	0.0	0.0
69 30.0'N	0.0	0.0	0.0	0.0	0.0	0.0	0.0	0.0	0.0	0.0	0.0
69 15.0'N	0.0	0.0	0.0	0.0	0.0	0.0	0.0	0.0	0.0	0.0	0.0
69 0.0'N	0.0	0.0	0.0	0.0	0.0	0.0	0.0	0.0	0.0	0.0	0.0
68 45.0'N	0.0	0.0	0.0	0.0	0.0	0.0	0.0	0.0	0.0	0.0	0.0
68 30.0'N	0.0	0.0	0.0	0.0	0.0	0.0	0.0	0.0	0.0	0.0	0.0
68 15.0'N	0.0	0.0	0.0	0.0	0.0	0.0	0.0	0.0	0.0	0.0	0.0
68 0.0'N	0.0	0.0	0.0	0.0	0.0	0.0	0.0	0.0	0.0	0.0	0.0
67 45.0'N	0.0	0.0	0.0	0.0	0.0	0.0	0.0	0.0	0.0	0.0	0.0
67 30.0'N	0.0	0.0	0.0	0.0	0.0	0.0	0.0	0.0	0.0	0.0	0.0
67 15.0'N	0.0	0.0	0.0	0.0	0.0	0.0	0.0	0.0	0.0	0.0	0.0
67 0.0'N	0.0	0.0	0.0	0.0	0.0	0.0	0.0	0.0	0.0	0.0	0.0
66 45.0'N	0.0	0.0	0.0	0.0	0.0	0.0	0.0	0.0	0.0	0.0	0.0
66 30.0'N	0.0	0.0	0.0	0.0	0.0	0.0	0.0	0.0	0.0	0.0	0.0
66 15.0'N	0.0	0.0	0.0	0.0	0.0	0.0	0.0	0.0	0.0	0.0	0.0
66 0.0'N	0.0	0.0	0.0	0.0	0.0	0.0	0.0	0.0	0.0	0.0	0.0
65 45.0'N	0.0	0.0	0.0	0.0	0.0	0.0	0.0	0.0	0.0	0.0	0.0
65 30.0'N	0.0	0.0	0.0	0.0	0.0	0.0	0.0	0.0	0.0	0.0	0.0
65 15.0'N	0.0	0.0	0.0	0.0	0.0	0.0	0.0	0.0	0.0	0.0	0.0
65 0.0'N	0.0	0.0	0.0	0.0	0.0	0.0	0.0	0.0	0.0	0.0	0.0
64 45.0'N	0.0	0.0	0.0	0.0	0.0	0.0	0.0	0.0	0.0	0.0	0.0
64 30.0'N	0.0	0.0	0.0	0.0	0.0	0.0	0.0	0.0	0.0	0.0	0.0
64 15.0'N	0.0	0.0	0.0	0.0	0.0	0.0	0.0	0.0	0.0	0.0	0.0
64 0.0'N	0.0	0.0	0.0	0.0	0.0	0.0	0.0	0.0	0.0	0.0	0.0
63 45.0'N	0.0	0.0	0.0	0.0	0.0	0.0	0.0	0.0	0.0	0.0	0.0
63 30.0'N	0.0	0.0	0.0	0.0	0.0	0.0	0.0	0.0	0.0	0.0	0.0
63 15.0'N	0.0	0.0	0.0	0.0	0.0	0.0	0.0	0.0	0.0	0.0	0.0
63 0.0'N	0.0	0.0	0.0	0.0	0.0	0.0	0.0	0.0	0.0	0.0	0.0
62 45.0'N	0.0	0.0	0.0	0.0	0.0	0.0	0.0	0.0	0.0	0.0	0.0
62 30.0'N	0.0	0.0	0.0	0.0	0.0	0.0	0.0	0.0	0.0	0.0	0.0
62 15.0'N	0.0	0.0	0.0	0.0	0.0	0.0	0.0	0.0	0.0	0.0	0.0
62 0.0'N	0.0	0.0	0.0	0.0	0.0	0.0	0.0	0.0	0.0	0.0	0.0
61 45.0'N	0.0	0.0	0.0	0.0	0.0	0.0	0.0	0.0	0.0	0.0	0.0
61 30.0'N	0.0	0.0	0.0	0.0	0.0	0.0	0.0	0.0	0.0	0.0	0.0
61 15.0'N	0.0	0.0	0.0	0.0	0.0	0.0	0.0	0.0	0.0	0.0	0.0
61 0.0'N	0.0	0.0	0.0	0.0	0.0	0.0	0.0	0.0	0.0	0.0	0.0
60 45.0'N	0.0	0.0	0.0	0.0	0.0	0.0	0.0	0.0	0.0	0.0	0.0
60 30.0'N	0.0	0.0	0.0	0.0	0.0	0.0	0.0	0.0	0.0	0.0	0.0
60 15.0'N	0.0	0.0	0.0	0.0	0.0	0.0	0.0	0.0	0.0	0.0	0.0
60 0.0'N	0.0	0.0	0.0	0.0	0.0	0.0	0.0	0.0	0.0	0.0	0.0
59 45.0'N	0.0	0.0	0.0	0.0	0.0	0.0	0.0	0.0	0.0	0.0	0.0
59 30.0'N	0.0	0.0	0.0	0.0	0.0	0.0	0.0	0.0	0.0	0.0	0.0
59 15.0'N	0.0	0.0	0.0	0.0	0.0	0.0	0.0	0.0	0.0	0.0	0.0
59 0.0'N	0.0	0.0	0.0	0.0	0.0	0.0	0.0	0.0	0.0	0.0	0.0
58 45.0'N	0.0	0.0	0.0	0.0	0.0	0.0	0.0	0.0	0.0	0.0	0.0
58 30.0'N	0.0	0.0	0.0	0.0	0.0	0.0	0.0	0.0	0.0	0.0	0.0
58 15.0'N	0.017	0.450	0.883	0.441	0.0	0.074	0.148	0.074	0.0	0.0	0.0
58 0.0'N	0.034	0.900	1.765	0.883	0.0	0.148	0.295	0.148	0.0	0.0	0.0
57 45.0'N	-0.031	0.983	1.997	1.265	0.533	0.348	0.163	0.089	0.016	0.008	0.0
57 30.0'N	-0.097	1.066	2.229	1.648	1.066	0.549	0.031	0.031	0.031	0.016	0.0
57 15.0'N	0.665	1.084	1.502	1.125	0.748	0.382	0.016	0.016	0.016	0.008	0.0
57 0.0'N	1.427	1.101	0.775	0.603	0.430	0.215	0.0	0.0	0.0	0.0	0.0
56 45.0'N	1.167	0.742	0.316	0.266	0.215	0.108	0.0	0.0	0.0	0.0	0.0
56 30.0'N	0.907	0.382	-0.143	-0.071	0.0	0.0	0.0	0.0	0.0	0.0	0.0
56 15.0'N	0.454	0.191	-0.071	-0.036	0.0	0.0	0.0	0.0	0.0	0.0	0.0
56 0.0'N	0.0	0.0	0.0	0.0	0.0	0.0	0.0	0.0	0.0	0.0	0.0
55 45.0'N	0.0	0.0	0.0	0.0	0.0	0.0	0.0	0.0	0.0	0.0	0.0
55 30.0'N	0.0	0.0	0.0	0.0	0.0	0.0	0.0	0.0	0.0	0.0	0.0
55 15.0'N	0.0	0.0	0.0	0.0	0.0	0.0	0.0	0.0	0.0	0.0	0.0
55 0.0'N	0.0	0.0	0.0	0.0	0.0	0.0	0.0	0.0	0.0	0.0	0.0

FINAL REPORT ON RESIDUAL TIDAL CURRENTS AND PROCESSING OF PRESSURE AND CURRENT RECORDS FROM THE EASTERN BERING SEA SHELF

by

Harold O. Mofjeld and James D. Schumacher

Pacific Marine Environmental Laboratory
National Oceanic and Atmospheric Administration
7600 Sand Point Way, N.E.
Seattle, Washington 98115

Final Report
Outer Continental Shelf Environmental Assessment Program
Research Unit 621

December 1983

ACKNOWLEDGMENTS

The research described in this report was supported by the Minerals Management Service through interagency agreement with the National Oceanic and Atmospheric Administration, under which a multiyear program responding to needs of petroleum development of the Alaskan Continental Shelf is managed by the Outer Continental Shelf Environmental Assessment Program (OCSEAP) Office. Support was also provided by NOAA's Environmental Research Laboratories.

The principal investigators thank the following people for their excellent support work: T. Jackson, W. Parker, and D. Pashinski for preparation of instruments and moorings; J. Blaha and T. Jackson for deployment and recovery of equipment; L. Long, S. Wright, P. Moen, D. Pashinski, and D. Kachel for processing of data; and J. Register and V. Curl for drafting. The authors also wish to thank J. W. Lavelle for helpful discussions on swell-induced boundary layers.

SUMMARY

Detailed observations of tidal current profiles were made at two sites on the Southeastern Bering Sea Shelf to study the vertical structure of tidal currents in two distinctly different tidal regimes. The rectilinear tidal currents at coastal station BBL1 were observed to have thick bottom boundary layers with significant variations in speed and phase extending well up into the water column. Comparison with a second order closure model indicates that the apparent bottom roughness was large at BBL1 during the period of observation. At middle shelf station BBL2, located between the Pribilof Islands and Nunivak Island, the rotary tidal currents had thin bottom boundary layers with a small apparent bottom roughness.

The difference in apparent bottom roughness at the two stations is probably due to the difference in weather during the periods of observation and/or the presence or absence of bedforms. The vertical structure of the tidal currents at the two stations is dominated by the strengths of the currents and the bottom roughness. The type of tidal wave is of secondary importance in determining the vertical heights of the bottom boundary layers.

Theoretical estimates of residual tidal currents generated by simple tidal waves fitted to the observed tidal currents at BBL1 and BBL2 indicate that the residual tidal currents have small speeds (<1 cm/s) in the absence of bottom topography. Near the Alaska Peninsula, tidal Kelvin waves generate a mass transport of approximately $2(10)^5$ m^3/s toward Kvichak Bay. At middle shelf station BBL2, the Sverdrup waves produce very small residual currents (<0.1 cm/s). Local topography could increase these currents to 1 cm/s if the local bottom slope is sufficiently large, as may occur near the 50-m isobath.

In addition to the observations over the Southeastern Bering Sea Shelf, observations were made of pressure and currents in the northern Bering Sea. Tidal harmonic constants from these long time-series will lead to improved cotidal charts for the Bering Sea. They will also be helpful in understanding the influence of ice on the tides and tidal currents of the Bering Sea.

TABLE OF CONTENTS

LIST OF FIGURES

LIST OF TABLES

INTRODUCTION

This is the final report for Research Unit 621 (originally RU 2016) which dealt with tidal motions on the Eastern Bering Sea Shelf. There were two primary goals of the work. The first was to make theoretical calculations to estimate locally generated residual tidal currents in two tidal regimes on the Southeastern Bering Sea Shelf. The second was to provide harmonic constants and time-series of pressure and currents from the Northern Bering Sea to be used in the calibration of the Model of Circulation and Oil Spill Trajectories under development at the RAND Corporation. In addition to these two goals, the Principal Investigators were asked to present a description of tidal motions and oceanography in the Navarin Basin. This summary was presented at the Physical Oceanography Workshop held in September 1982.

The theoretical study of residual tidal currents was intended to look at the contribution such currents make to the mean circulation on the Eastern Bering Sea Shelf. The focus was on estimates of residual currents generated by simple theoretical waves that mimic the tides and tidal currents in the coastal and middle shelf regimes. The waves were assumed to be propagating on a shelf of constant depth. Bottom topography can enhance the residual currents. To check into this possibility, some simple computations involving topography are presented in this report.

The research on residual tidal currents was partly supported by the Pacific Marine Environmental Laboratory which funded two bottom boundary layer experiments (two moorings each) and one additional mooring. The observed currents from the experiments were used to calibrate theoretical profiles of tidal currents which were in turn used to compute the residual currents. The experiments consisted of deploying moorings at each site for several weeks with a high density of current meters near the bottom to resolve the bottom boundary layer in detail. One site, BBL1 (also called TP-3), was located near the Alaska Peninsula where the tidal currents are relatively strong and rectilinear. The other site, BBL2, was located in the middle shelf regime between Nunivak Island and the Pribilof Islands where the tidal currents have smaller speeds and broad current ellipses. Both sites were occupied during May 1981. The time-series of currents were obtained from the coastal station, BBL1, for May 1981, but the mooring at the midshelf station, BBL2, was lost during the recovery oepration. A new mooring was deployed at BBL2 during August-September 1982 and time-series were successfully obtained.

Seven pressure and current moorings in the Northern Bering Sea were requested by the RAND Corporation to provide boundary conditions and interior test points for an expanded circulation model of the Eastern Bering Sea Shelf. The moorings were deployed during October-November 1981 and recovered during June 1982. The time-series have been analyzed for tides and tidal currents and the resulting harmonic constants are tabulated in this report. Copies of the time-series have been sent to the RAND Corporation. An additional mooring (NC17C) was deployed in support of ice research at PMEL; harmonic constants from the resulting time-series are also presented in this report.

This report first deals with tidal current profiles and the calculations of locally generated residual tidal currents on the

Southeastern Bering Sea Shelf. Descriptions are included of the observations at the two sites where the model was applied, the formulation of the model and method of solution, the fit of the model to the observed harmonic constants, and the predictions of residual currents with a discussion of topographic effects. The report concludes with a description of the observations on the Northern Bering Sea Shelf, a brief summary of the method of tidal analysis, and tables of the resulting harmonic constants.

Detailed profiles of tidal currents were measured at two stations (Fig. 1) on the southeastern Bering Sea Shelf. Station BBL1 (56°19'N, 161°33'W; 63m depth) was deployed about 50km northwest of Port Moller. The tidal currents (Fig. 2) in this coastal region are relatively strong and flow parallel to the general trend of the adjacent coast. Station BBL2 (57°37'N, 167°45'W; 69m depth) was deployed in the mid-shelf region (Fig. 1) about 130 km northeast of the Pribilof Island where the tidal currents (Fig. 2) are characterized by broad tidal ellipses.

Two moorings were deployed at each station. At BBL1 Neil-Brown acoustic current meters were placed on one mooring at heights of 14, 35, 44, 49 and 59m above the bottom. On a shorter mooring were Aanderaa current meters at heights of 1, 3 and 5m. At BBL2 Neil-Brown acoustic current meters were used throughout. Meters were placed at heights of 5, 15 and 30m on one mooring and 1, 3, 5m on the other.

The two stations were occupied during different years. BBL1 yielded time series of currents over the period 15 May 81-30 May 81 while the current records at BBL2 span the period 28 July 82-5 August 82. A mooring was deployed at BBL2 during 1981 but it was lost during the recovery operation.

The current records were analyzed for tidal currents using the response method. This method finds the relative amplitudes and phases of the tidal constituents with respect to a reference series. The relative quantities are combined with the harmonic constants for the reference series to produce harmonic constants for the observed series. The analyses are performed on the east and north components of the currents and the resulting harmonic

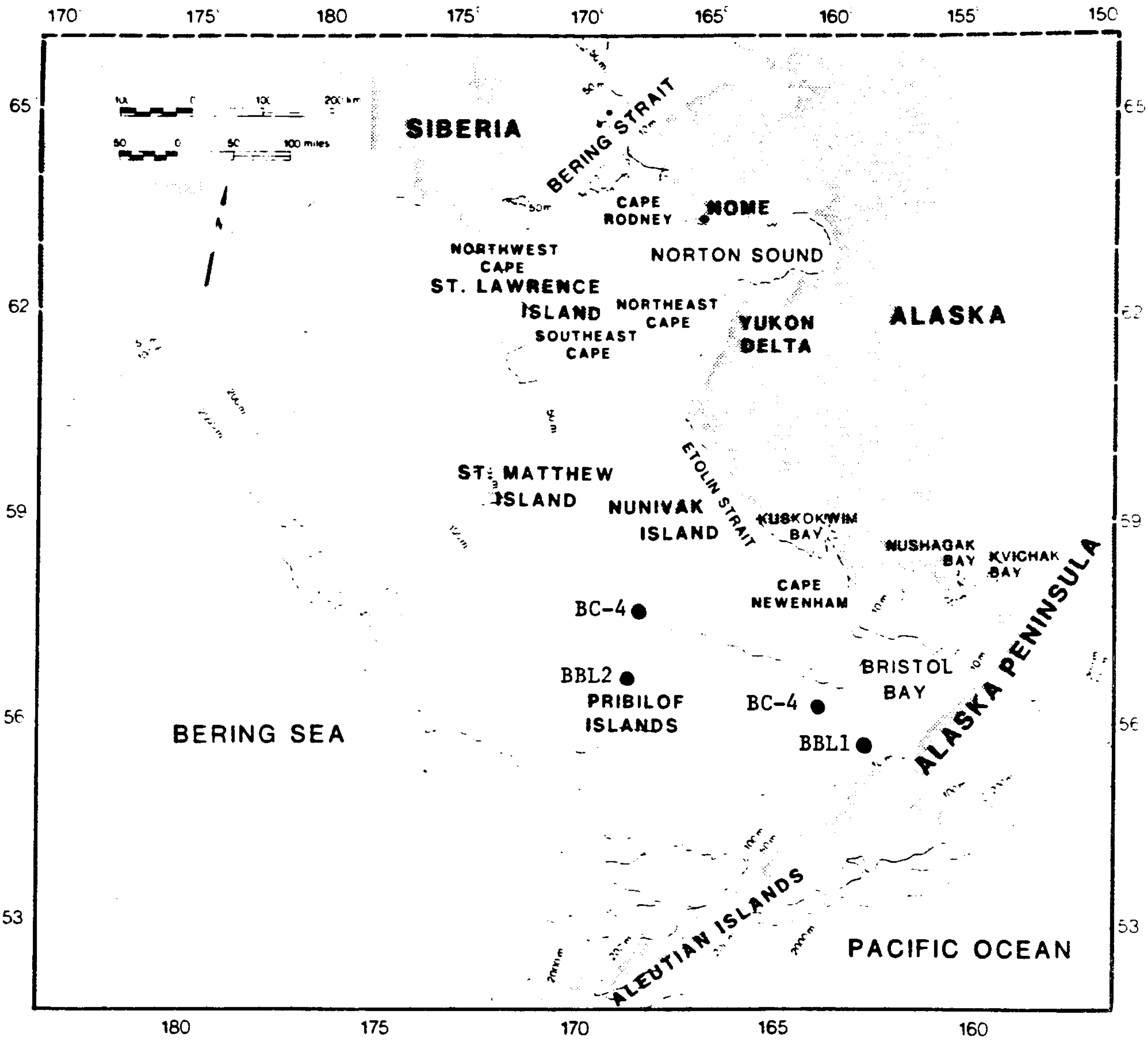

Figure 1. Chart of the Eastern Bering Sea Shelf showing the location of bottom boundary layer stations BBL1 and BBL2 and their corresponding reference stations BC-2 and BC-4 for response tidal analyses.

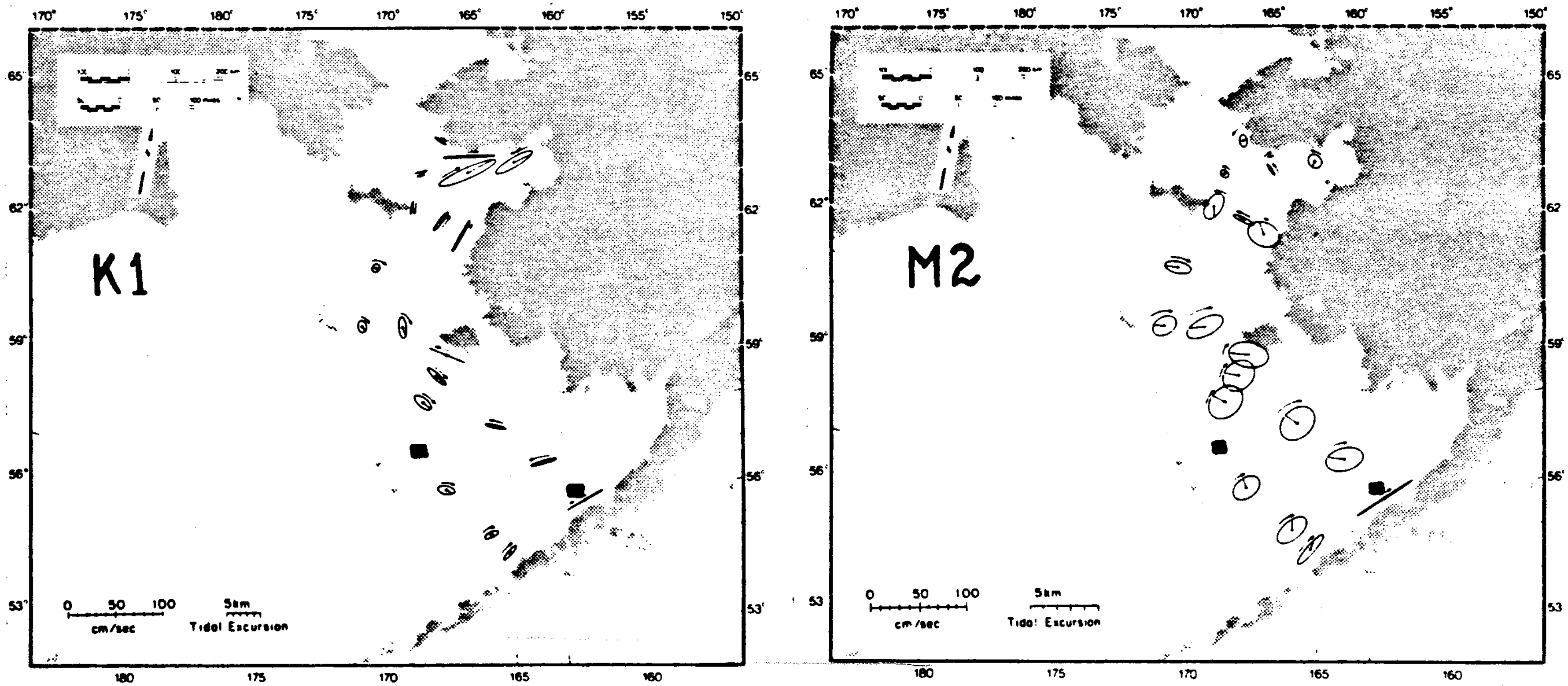

Figure 2. Observed M2 and K1 tidal ellipses on the Eastern Bering Sea Shelf. Arrows outside the ellipses show the sense of rotation of the velocity vectors with time. Lines from the centers of the ellipses show the velocity vector at the time of Greenwich transit for that tidal constituent. From Pearson, Mofjeld and Tripp (1981).

constants are then converted into the parameter of the tidal ellipses. Because the current records are short, one complex weight per tidal band was used in the correlations between the observed and reference series. This choice for the number of complex weights is equivalent to the assumption that the internal relationships of the tidal constituents within a given tidal band are the same in the observed and reference series. It is therefore important that the observed and reference series have similar tidal characteristics.

The response method provides an estimate for the accuracy of the harmonic constants of the east and north components. The estimate is obtained by comparing the residual variance (left in each tidal band after analysis) with the predicted variance. If the ratio of residual to predicted variance is small, the analysis has succeeded in explaining a large part of the tidal signal. A large residual variance indicates that much tidal variance remains after analysis and that the estimated harmonic constants may not accurately represent those at the station. Large residual variances may be caused by a number of problems including a small tidal signal, a poor choice of reference series, an incorrect time base for the reference or observed series and faulty current sensors.

The results of the tidal analysis on the current records from BBL1 are given in Tables 1-6. The reference series was the predicted tide at BC-2 (57°04'N, 163°22'W) based on the tidal harmonic constants shown in Table 1. The current harmonic constants of the major tidal constituents O1, K1, N2 and M2 for BBL1 are shown in Table 2. Ordinarily S2 would be included in such a list but it is a minor constituent in the Bering Sea (Pearson, Tripp and Mofjeld, 1981). The tidal analyses were performed over the full length (378 hours) of each acoustic current meter record. Table 3 shows that the

Table 1. Reference tidal harmonic constants from BC-2 (57°04'N, 163°22'W) used in the response analyses of the coastal station BBL1.

Constit.	Period (hours)	Amplitude (cm)	Greenwich Phase Lag (°G)	Amplitude Ratio	Relative Phase Lag (°)
Q1	26.87	3.7	351	0.131	-22
O1	25.82	19.0	358	0.671	-15
M1	24.84	1.1	6	0.039	-7
P1	24.07	9.3	11	0.329	-2
K1	23.93	28.3	13	1.000	0
J1	23.10	1.7	19	0.060	6
OO1	22.31	1.0	25	0.035	12
2N2	12.91	2.0	47	0.044	-110
μ2	12.87	1.8	47	0.040	-110
N2	12.66	14.7	102	0.325	-55
ν2	12.63	2.8	109	0.062	-48
M2	12.42	45.2	157	1.000	0
L2	12.19	0.6	153	0.013	-4
(T2)[1]	(12.02)	(0.1)	(350)	(0.002)	(193)
S2	12.00	0.5	343	0.011	186
K2	11.97	0.1	343	0.002	186

[1] not used in response analyses

Table 2. Current harmonic constants for O1, K1, N2, M2 from the acoustic current meter data at the coastal station BBL1 (56°19'N, 161°33'W; 63 m depth) obtained by the response method (1 complex weight per tidal band; 378 hour series length) with predicted tides at BC-2 (Table 1) as the reference.

		Amplitudes		Greenwich	Orientation of	Sense of
	Height	Major	Minor	Phase Lag[1]	Major Axis	Rotation[2]
Constit.	(m)	(cm/s)	(cm/s)	(°G)	(°True)	
O1	59	15.90	0.39	290.3	77.3	C
	49	15.03	0.18	293.5	76.0	CC
	44	13.62	0.12	298.1	71.1	CC
	35	13.37	0.26	300.4	71.9	CC
	14	12.33	1.04	307.7	60.1	CC
K1	59	23.68	0.58	305.3	77.3	C
	49	22.38	0.27	308.5	76.0	CC
	44	20.29	0.18	313.1	71.1	CC
	35	19.92	0.39	315.4	71.9	CC
	14	18.36	1.55	322.7	60.1	CC
N2	59	12.90	0.72	116.9	64.7	C
	49	11.96	0.61	117.8	64.9	C
	44	11.05	0.69	119.4	62.9	C
	35	11.04	0.54	114.5	67.0	C
	14	8.67	1.55	95.0	80.8	CC
M2	59	39.67	2.22	171.9	64.7	C
	49	36.76	1.88	172.8	64.9	C
	44	33.98	2.13	174.4	62.9	C
	35	33.97	1.67	169.5	67.0	C
	14	26.69	4.77	150.0	80.8	CC

[1]Major Axis [2] C = Clockwise
CC = Counterclockwise

Table 3. Reductions in variance as a result of response tidal analyses applied to the acoustic current meter data at the coastal station BBL1. Small residual variances and reductions near 100% indicate that almost all the variance in a given tidal band is accounted for by the predicted tidal currents resulting from the response method.

Component	Tidal Band	Height (m)	Variance Predicted $(cm/s)^2$	Variance Residual $(cm/s)^2$	Reduction in Variance (%)
East	Diurnal	59	438.34	24.84	94.33
		49	387.40	13.26	96.58
		44	302.74	9.82	96.76
		35	294.42	10.97	96.27
		14	208.32	3.50	98.32
North	Diurnal	59	22.60	5.00	77.88
		49	24.06	2.36	90.19
		44	35.33	3.09	91.25
		35	31.50	2.23	92.92
		14	70.30	3.74	96.68
East	Semi-diurnal	59	385.08	6.37	98.35
		49	331.60	6.26	98.11
		44	273.61	5.13	98.13
		35	292.17	2.96	98.99
		14	207.34	7.40	96.43
North	Semi-diurnal	59	86.89	1.29	98.52
		49	73.45	2.62	96.43
		44	72.91	1.77	97.57
		35	53.50	1.55	97.10
		14	12.09	0.81	93.30

Table 4. Current harmonic constants for O1, K1, N2, M2 from the near-bottom Aanderaa current meter data at the coastal station BBL1 (56°19'N, 161°33'W; 63 m depth) obtained by the response method (1 complex weight per tidal band) applied to 3-day segments with predicted tides at BC-2 (Table 4) as the reference. The procedure for estimating the harmonic constants of other constituents is the same as that given in Table 2.

Constit.	Height (m)	Segments	Amplitudes Major (cm/s)	Minor (cm/s)	Greenwich Phase Lag (°G)	Orientation of Major Axis (°True)	Sense of Rotation
K1	5	1	16.86	3.49	144.0	238.9	CC
		2	16.76	5.66	146.7	229.8	CC
		3	13.13	3.08	137.9	228.7	CC
		4	15.59	3.27	130.5	227.4	CC
		5	19.41	3.81	138.5	231.1	CC
K1	3	1	15.21	4.60	141.3	237.8	CC
		2	15.30	5.59	145.8	235.2	CC
		3	13.30	3.18	136.4	236.1	CC
		4	15.05	3.22	133.8	232.5	CC
		5	15.74	3.84	111.2	237.3	CC
K1	1	1	13.77	4.20	140.8	237.1	CC
		2	13.51	5.01	119.6	236.0	CC
		3	6.75	2.27	173.3	215.2	CC
		4	11.65	1.45	180.9	228.8	CC
M2	5	1	15.70	3.82	334.4	249.4	CC
		2	21.91	7.34	320.0	258.9	CC
		3	19.34	4.99	322.5	251.3	CC
		4	22.40	6.81	311.8	262.7	CC
		5	25.38	5.57	322.3	253.6	CC
M2	3	1	21.73	7.17	326.3	261.9	CC
		2	20.44	6.94	320.3	263.5	CC
		3	18.58	5.50	323.6	256.5	CC
		4	22.35	7.36	314.1	269.0	CC
		5	16.40	3.96	259.7	255.0	CC
M2	1	1	19.69	6.89	326.5	262.7	CC
		2	14.18	5.22	283.1	260.3	CC
		3	9.05	6.53	166.9	238.6	CC
		4	21.52	6.20	53.7	265.3	CC

Table 5. Reductions in variance for the diurnal band as a result of response analyses applied to 3-day segments of the near-bottom Aanderaa current meter data at the coastal station BBL1.

Component	Tidal Band	Height (m)	Segment	Variance Predicted $(cm/s)^2$	Variance Residual $(cm/s)^2$	Reduction in Variance (%)
East	Diurnal	5	1	41.80	3.59	91.41
			2	117.35	11.15	90.50
			3	111.65	2.36	97.89
			4	129.67	0.31	99.76
			5	76.14	2.62	96.56
North	Diurnal	5	1	17.14	0.35	97.96
			2	96.37	3.78	96.08
			3	87.76	3.69	95.80
			4	103.87	0.17	99.84
			5	36.77	1.78	95.16
East	Diurnal	3	1	29.17	1.34	95.14
			2	112.12	9.51	91.52
			3	137.94	0.44	99.68
			4	136.85	0.44	99.68
			5	56.13	6.17	89.01
North	Diurnal	3	1	15.63	0.36	97.70
			2	69.26	6.34	90.85
			3	68.37	6.03	91.18
			4	81.37	0.04	99.95
			5	19.92	1.10	94.48
East	Diurnal	1	1	23.41	0.91	96.11
			2	92.60	2.35	97.46
			3	22.21	11.85	46.65
			4	83.89	1.50	98.21
North	Diurnal	1	1	13.25	0.39	97.06
			2	53.56	3.65	93.19
			3	35.89	9.50	73.53
			4	56.44	0.29	99.49

Table 6. Reduction in variance for the semidiurnal band as a result of response and analyses applied to 3-day segments of the near-bottom Aanderaa current meter data at the coastal station BBL1.

Component	Tidal Band	Height (m)	Segment	Variance Predicted $(cm/s)^2$	Variance Residual $(cm/s)^2$	Reduction in Variance (%)
East	Semi-diurnal	5	1	81.47	0.42	99.48
			2	109.59	4.51	95.88
			3	81.27	3.74	95.40
			4	146.23	0.71	99.51
			5	260.38	1.09	99.58
North	Semi-diurnal	5	1	15.94	0.14	99.12
			2	16.89	8.19	51.51
			3	15.88	2.23	85.96
			4	20.31	0.29	98.57
			5	38.37	1.31	96.59
East	Semi-diurnal	3	1	175.73	0.17	99.90
			2	97.43	3.23	96.68
			3	79.05	0.42	99.47
			4	147.75	0.70	99.53
			5	111.30	54.72	50.84
North	Semi-diurnal	3	1	21.96	0.21	99.04
			2	13.10	7.23	44.81
			3	12.89	0.89	93.10
			4	19.96	0.31	98.45
			5	16.20	5.19	67.96
East	Semi-diurnal	1	1	144.75	0.30	99.79
			2	44.16	19.44	55.98
			3	18.53	12.90	30.38
			4	140.62	1.98	98.59
North	Semi-diurnal	1	1	19.50	0.12	99.38
			2	7.52	7.52	0.00
			3	13.37	4.64	65.30
			4	14.30	1.78	87.55

reductions in variance were quite good and the harmonic constants can therefore be expected to represent accurately those at BBL1. The Aanderaa records at BBL1 suffered from speed and time base problems. It was convenient to analyze the Aanderaa records in 3-day segments to isolate these problems. The most reliable harmonic constants were assumed to be those for which there was an excellent reduction in variance although the phase may still be in error due to time base problems earlier in the records. The harmonic constants for the Aanderaa records at BBL1 are given in Table 4 and the reductions in variance in Table 5 and 6.

The results of the analyses for the middle shelf station BBL2 are given in Table 7-9. The reference series was the predicted tidal current at BC-4 (58°37'N, 168°14'W) based on the harmonic constants for BC-4 in Table 7. The values for the 30m height (Table 8) are in parentheses because of a possible defect in the current record. After recovery it was discovered that the corresponding current meter had lost an acoustic mirror in the current sensor. A comparison of results (Table 8) for the 30m height with the results at other heights reveals significant differences. There were two current meters deployed at the 5m height, one on each mooring. From Table 8 it can be seen that the differences in amplitudes for the two current meters at the 5m height is significantly less than the differences between heights. It appears then that the amplitude profile is well-resolved at BBL2. This is partially true for the phase lags and orientations (Table 8). The orientation at the 1m height may have been contaminated by magnetic interference from the steel anchor because both M2 and K1 show the same deviation in direction at the 1 m height relative to the directions measured above.

Table 7. Reference current harmonic constants from BC-4 (58°37'N, 168°14'W) used in the response tidal analyses of the current data from the middle shelf station BBL2.

Constit.	Period (hours)	Amplitude (cm/s)	Greenwich Phase Lag (°G)	Amplitude Ratio	Relative Phase Lag (°)
Q1	26.87	1.3	320	0.111	-30
O1	25.82	7.4	330	0.632	-20
M1	24.84	0.4	340	0.034	-10
P1	24.07	3.8	348	0.325	-2
K1	23.93	11.7	350	1.000	0
J1	23.10	0.7	0	0.060	10
OO1	22.31	0.4	10	0.034	20
2N2	12.91	1.8	332	0.066	-146
μ2	12.87	1.6	342	0.059	-136
N2	12.66	9.6	45	0.352	-73
ν2	12.63	1.0	55	0.037	-63
M2	12.42	27.3	118	1.000	0
L2	12.19	0.4	191	0.015	73
T2	12.02	0.1	249	0.004	131
S2	12.00	1.5	254	0.055	136
K2	11.97	0.4	265	0.015	147

Table 8. Current harmonic constants for O1, K1, N2, M2 from the current meter data at the middle shelf station BBL2 (57°37'N, 167°45'W; 69m depth) obtained by the response method (1 complex weight per tidal band; 207 hour series length) with predicted tidal currents at BC-4 (Table 1) as the reference. The labels (8201) and (8202) on the values for the height of 5m refer to the two moorings at the station.

Constit.	Height (m)	Amplitudes Major (cm/s)	Minor (cm/s)	Greenich Phase Lag[1] (°G)	Orientation of Major Axis (°True)	Sense of Rotation[2]
O1	30	(7.0)	(1.3)	(140.8)	(285.1)	c
	15	7.3	3.3	133.8	293.6	c
(8201)	5	7.5	2.9	133.8	298.5	c
(8202)	5	7.3	2.8	133.3	295.5	c
	3	5.8	2.7	132.8	298.2	c
	1	5.7	2.3	132.2	289.7	c
K1	30	(11.1)	(2.0)	(160.8)	(285.1)	c
	15	11.5	5.2	153.8	293.6	c
(8201)	5	11.8	4.6	153.8	298.5	c
(8202)	5	11.6	4.4	152.3	295.5	c
	3	9.2	4.2	152.8	298.2	c
	1	9.0	3.7	152.2	289.7	c
N2	30	(7.9)	(6.0)	(16.2)	(28.9)	c
	15	7.8	5.9	19.2	43.2	c
(8201)	5	7.6	5.9	12.0	40.5	c
(8202)	5	7.5	5.8	14.6	43.5	c
	3	6.2	4.7	14.6	42.9	c
	1	5.8	4.4	12.1	33.7	c
M2	30	(22.6)	(17.2)	(89.2)	(28.9)	c
	15	22.1	16.9	92.2	43.2	c
(8201)	5	21.5	16.9	85.0	40.5	c
(8202)	5	21.2	16.4	87.6	43.5	c
	3	17.6	13.3	87.6	42.9	c
	1	16.5	12.5	85.1	33.7	c

[1] Major Axis
[2] c=clockwise

The reductions in variance (Table 9) for BBL2 are quite good with the exception of the 30m record. This is further evidence of a problem in this record. The reductions in variance (Table 9) for BBL2 are better than those (Table 3) for BBL1. One reason for this difference may be the choice of reference series. Predicted tidal currents from a nearby station were used as the reference series for BBL2 whereas predicted tides were used for BBL1. For the middle shelf station BBL2, tidal currents were chosen for the reference because of tidal amphidrome regions (Fig. 3) of a small tidal amplitudes and rapidly changing phase near the station. Tides were chosen as the reference for the coastal station BBL1 because it is located in a relatively simple tidal regime where the tides and tidal currents have similar characteristics. In such a regime it is often preferable to use tides for the reference because their harmonic constants are better determined due to a superior signal-to-noise ratio in the observations. The reference tidal station BC-2 (Fig. 1) is about 130km to the northwest of BBL1. This may be a sufficient distance for differences to appear in the tidal characteristics. Besides the influence of the reference series or the reduction in variance, the background noise level may also be a factor. The observations at BBL1 were made in May which is a stormier period than late July to early August when the BBL2 observations were made. Whatever the reasons for the differences in the reduction in variance between BBL1 and BBL2, the reductions are quite good for both station and we may assume that the associated harmonic constants are adequate to calibrate the profile model.

Table 9. Reductions in variance as a result of response tidal analyses applied to the current time series at the middle shelf station BBL2. Small residual variances and reductions near 100% indicate that almost all the variance in a given tidal band is accounted for by the predicted tidal currents resulting from the response method. The labels (8201) and (8202) and the values for the height of 5m refer to the two moorings at the station.

Component	Tidal Band	Height (m)	Variance Predicted $(cm/s)^2$	Variance Residual $(cm/s)^2$	Reduction in Variance ($^o/o$)
East	Diurnal	30	104.23	2.20	97.89
		15	98.20	0.05	99.95
	(8201)	5	97.28	0.09	99.91
	(8202)	5	97.50	0.12	99.88
		3	60.37	0.02	99.97
		1	63.50	0.03	99.95
North	Diurnal	30	9.80	1.06	89.18
		15	40.84	0.10	99.76
	(8201)	5	44.32	0.07	99.84
	(8202)	5	38.16	0.15	99.61
		3	30.11	0.07	99.77
		1	19.70	0.06	99.70
East	Semi-Diurnal	30	164.36	2.60	98.42
		15	182.31	1.58	99.13
	(8201)	5	170.19	1.13	99.34
	(8202)	5	168.44	1.54	99.09
		3	111.48	0.71	99.36
		1	88.95	0.61	99.31
North	Semi-Diurnal	30	224.42	3.17	98.59
		15	185.33	1.98	98.93
	(8201)	5	183.19	1.97	98.92
	(8202)	5	173.20	2.28	98.68
		3	116.92	1.25	98.93
		1	111.72	1.23	98.90

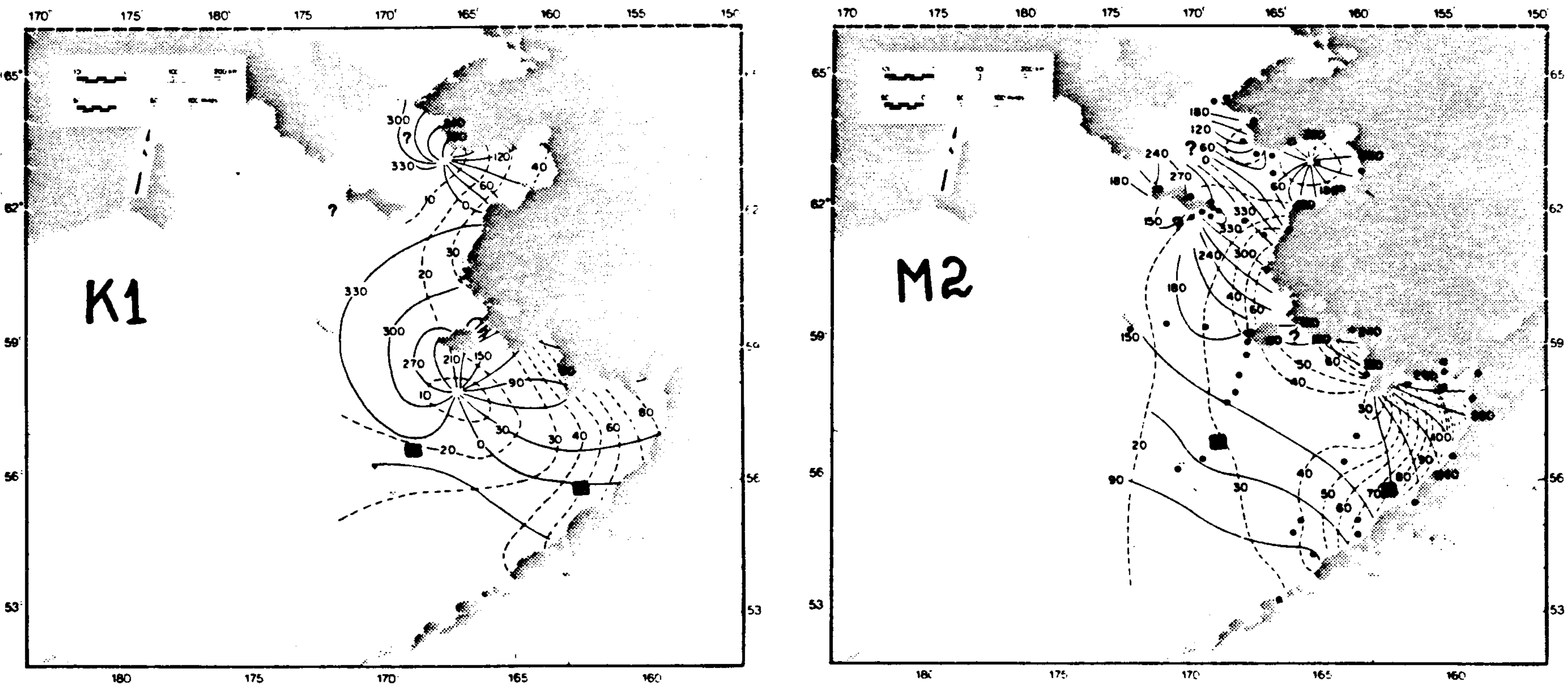

Figure 3. Empirical M2 and K1 cotidal charts for the Eastern Bering Sea Shelf. Solid lines are cophase lines and are labelled in degrees elapsed since Greenwich transit of the tidal constituent. Dashed lines are coamplitude lines and are labelled in centimeters of seawater. Dots in the M2 chart show the locations of observations used in the construction of the cotidal charts. Solid squares show the location of the bottom boundary layer stations BBL1 and BBL2. From Pearson, Mofjeld and Tripp (1981).

THEORETICAL FORMULATION

Tidal Currents

The theoretical profiles of tidal currents and locally-generated residual tidal currents are obtained by solving a set of differential equations. The currents are described in terms of their east u and north v components. Under the assumptions that the tidal motion are driven by horizontal pressure gradients and that these gradients are independent of depth (long-waves unaffected by baroclinicity), the tidal pressure is described entirely by the sea surface displacement η_s. As discussed by Mofjeld (1980), the tides and tidal currents satisfy the linearized equations of motion

$$\frac{\partial u}{\partial t} - fv = -g \frac{\partial \eta_s}{\partial x} + \frac{\partial}{\partial z} \left(A \frac{\partial u}{\partial z}\right) \qquad (1)$$

$$\frac{\partial v}{\partial t} + fu = -g \frac{\partial \eta_s}{\partial y} + \frac{\partial}{\partial z} \left(A \frac{\partial v}{\partial z}\right) \qquad (2)$$

$$\frac{\partial \eta_s}{\partial t} + \int_{z_o}^{H} \left(\frac{\partial u}{\partial x} + \frac{\partial v}{\partial y}\right) dz = 0 \qquad (3)$$

with time t, east-and north-and vertical coordinates x, y, z, Coriolis parameter f, acceleration of gravity g, eddy viscosity A, bottom roughness length z_o and mean depth H.

At the bottom, friction causes the tidal currents to be zero

$$u, v = 0 \quad \text{at} \quad z = z_o \qquad (4)$$

At the surface, the stress is assumed to be zero which is equivalent to requiring that the vertical gradients of velocity be zero

$$\frac{\partial u}{\partial z} , \frac{\partial v}{\partial z} = 0 \quad \text{at } z = H \tag{5}$$

This surface condition precludes the presence of floating ice of sufficient rigidity to produce major drag on the water. The present study focuses on the bottom boundary layers during the summer when the bottom boundary layer observations were taken. Pearson, Mofjeld and Tripp (1981) observed tidal currents on the eastern Bering Sea Shelf which apparently change significantly between ice-free and ice-covered conditions. However, the influence of ice on tidal currents is beyond the scope of the proposed work.

The eddy viscosity is given by

$$A = \ell^2 \left[\left(\frac{\partial u}{\partial z}\right)^2 + \left(\frac{\partial v}{\partial z}\right)^2 \right]^{\frac{1}{2}} \tag{6}$$

where the mixing length ℓ is taken the form

$$\ell = kz/(1 + kz/\ell_o) \tag{7}$$

which is recommended for boundary layers by Mellor and Yamada (1974, 1982). Well-above the bottom, the mixing length ℓ reaches its asympotic value ℓ_o which is assumed to be determined by the vertical scale of the turbulent intensity q

$$\ell_o = \gamma \int_{z_o}^{H} zq\,dz / \int_{z_o}^{H} q\,dz \tag{8}$$

As found by Mofjeld and Lavelle (1984), the appropriate value of γ is 0.2. This value was arrived at through matching this Level II model to the similarity theory of Businger and Arya (1974) for the steady Ekman layer as well as through a fit of the model to observed M2 tidal currents in Admirality Inlet, Washington.

The turbulent intensity (square root of the turbulent energy density) is given by a local balance between shear production and viscous dissipation (Level II model)

$$0 = - (A \frac{\partial u}{\partial z})\frac{\partial u}{\partial z} - (-A \frac{\partial v}{\partial z})\frac{\partial v}{\partial z} - \frac{q^3}{c\ell} \qquad (9)$$

As shown by Mofjeld and Lavelle (1984), the velocity components u, v and eddy viscosity A are independent of the dissipation constant c while the turbulent intensity q has a weak $c^{1/3}$ dependence. In the calculations, c was set equal to 12.0. Because we are considering the bottom boundary layer away from sources of stratified water such as the shelfbreak or the pycnocline, stratification is neglected in equation (9). This is a simplified form of the turbulent energy equation used in the three-dimensional RAND model described by Liu and Leenderstre (1978, 1979).

In the original proposal for RU621, the eddy viscosity was to be the linear-times-exponential form advocated by Businger and Arya (1974) for the steady Ekman layer. The form (6) was adopted instead because of an ambiguity that arises in the Businger-Arya form when it is applied to tidal currents in high-latitude regions like the Bering Sea.

In the Level II model of tidal currents, it is assumed that the eddy viscosity is independent of time. This is because the observations to which the model will be compared are the major harmonic constants which are a part of the total tidal signal that is affected by the time-average of eddy viscosity. The time-dependence in the eddy viscosity gives rise to higher frequency tidal constituents not resolved in the observations. A discussion of how the time-dependence of the eddy viscosity affects rectilinear tidal currents (Kelvin wave-like) is given by Lavelle and Mofjeld (1983). Rotary tidal constituents with broad ellipses such as those in the mid-shelf region of the Eastern Bering Sea Shelf show little change in speed over the tidal cycle and the eddy viscosity due to a given tidal constituent is relatively independent of time.

In the Level II model, we allow the four largest tidal constituents O1, K1, N2 and M2 to contribute to the eddy viscosity. Because of the short length and noise content of the bottom boundary layer observations, each tidal band has to be considered as a unit (1 complex weight per band) in the response tidal analyses. Hence the comparison of the Level II model and observations can be made with the largest constituents in the principal bands: M2 for the semidiurnal band and K1 for the diurnal band.

Following the standard procedure developed by Sverdrup (1927) and discussed by Mofjeld (1980) components of a given tidal constituent may be written as a sum of clockwise q and counterclockwise r rotating components

$$u = (q + r)/2 \quad , \quad v = (q - r)/2i \tag{10}$$

The horizontal equation of motion (1) and (2) for the rotating components (Mofjeld, 1980) are most conveniently written in terms of velocity defects q', r'

$$q = Q(1 - q') \quad , \quad r = R(1 - r') \tag{11}$$

$$\frac{\partial}{\partial z}\left(A \frac{\partial q'}{\partial z}\right) + i(\omega - f)q' = 0, \quad \frac{\partial}{\partial z}\left(A \frac{\partial r'}{\partial z}\right) + i(\omega + f)r' = 0 \tag{12}$$

with

$$q', r' = 1 \text{ at } z = z_o \quad ; \quad \frac{\partial q'}{\partial z} \; , \; \frac{\partial r'}{\partial z} = 0 \quad \text{at } z = H \tag{13}$$

where the amplitudes of the rotating components q, r are given by depth-independent amplitudes Q,R that satisfy the relations derived from the momentum equations (1) and (2)

$$Q = -ig(\frac{\partial\eta_s}{\partial x} + i\frac{\partial\eta_s}{\partial y})/(\omega-f) \quad , \quad R = -ig(\frac{\partial\eta_s}{\partial x} - i\frac{\partial\eta_s}{\partial y})/(\omega+f) \qquad (14)$$

We shall assume that the tides and tidal currents at the two selected sites are simple tidal waves. As we shall see, these assumptions work well for the tidal currents at these two bottom boundary layer stations.

For a planar wave

$$\eta_s = \eta_o \exp[i(k_x x + k_y y - \omega t)] \qquad (15)$$

the dispersion relation for these waves (Mofjeld, 1980) relating the wavenumber components to the angular frequency ω is obtained by substituting (11)-(14) into the equation of continuity (3)

$$k_x^2 + k_y^2 = (\omega^2 - f^2)/gH_e \qquad (16)$$

The equivalent depth H_e is given by

$$H_e = H-z_o + \frac{i}{2\omega}\left[(\frac{\omega+f}{\omega-f})\, A\frac{\partial q'}{\partial z} + (\frac{\omega-f}{\omega+f})\, A\frac{\partial r'}{\partial z}\right]_{z=z_o} \qquad (17)$$

One more condition is needed between the wavenumber components. For the Sverdrup wave, we rotate the coordinate system so that the negative y-axis is parallel to the direction of propagation. The midshelf station is far enough from lateral boundaries that the wave can be considered independent of the x-direction.

$$k_x = 0 \text{ for the Sverdrup waves} \qquad (18)$$

As we shall see later, the observed relationship between the tides and tidal currents in the mid-shelf region indicate that the tidal motions there are combinations of incident and reflected Sverdrup waves. In looking at the tidal currents alone, we can use the same condition (18) on k_x. The effect of having a super-position of Sverdrup waves is to have partial cancellation of the residual currents.

The coastal Kelvin wave has a component of velocity transport in the bottom boundary layer in the direction perpendicular to the coast. This transport component must be balanced (Mofjeld, 1980) by a compensating transport in the rest of the water column because there can be no net transport through the coast

$$\int_{z_o}^{H} u \, dz = 0 \tag{19}$$

where the Kelvin wave is assumed to propagating in the negative y-direction. This condition produces an equation between the wavenumber components

$$H_e k_x + i \, \Gamma \, k_y = 0 \quad \text{for the Kelvin waves} \tag{20}$$

where

$$\Gamma = H - z_o + \frac{i}{2\omega} \left[\left(\frac{\omega+f}{\omega-f}\right) A\frac{\partial q'}{\partial z} - \left(\frac{\omega-f}{\omega+f}\right) A\frac{\partial r'}{\partial z} \right]_{z=z_o} \tag{21}$$

At the bottom, the magnitude of the stress exerted by the water on the bottom is assumed to be of the form

$$u_*^2 = A\left[\left(\frac{\partial u}{\partial z}\right)^2 + \left(\frac{\partial v}{\partial z}\right)^2\right]^{\frac{1}{2}} \quad \text{at } z=z_o \tag{22}$$

where u_* is a time-independent friction velocity defined as the square root of the kinematic stress. In the expression (22), the shears $\frac{\partial u}{\partial z}$ and $\frac{\partial v}{\partial z}$ are sums over four tidal constituents O1, K1, N2 and M2. This sum produces the upper limit on u_* based on these four constituents since cancelling is not allowed between the constituents and the contribution of a given constituent is $2^{\frac{1}{2}}$ times the time-average for that constituent. An adjustment of the bottom roughness z_o can be used to compensate for the factor $2^{\frac{1}{2}}$. This overestimate for the four constituents tends to compensate for the contributions to u_* that are not made by neglected constituents. The details of cancellation between constituents is beyond this analysis.

To compute the residual currents, it is necessary to have profiles of the vertical velocity and displacement. The vertical displacement η at a height z is given by

$$\eta = \eta_s \ (z_e/H_e) \tag{23}$$

where

$$z_e = (z-z_o) + \frac{i}{2\omega} \left[\left(\frac{\omega+f}{\omega-f}\right) A\frac{\partial q'}{\partial z} + \left(\frac{\omega-f}{\omega+f}\right) A\frac{\partial r'}{\partial z}\right]_{z=z_o}^{z} \tag{24}$$

for a tidal constituent with angular frequency ω. The vertical velocity w for the same constituent is given by

$$w = -i\omega\eta \tag{25}$$

The equations (1)-(25) are solved numerically using a fourth-order Runge-Kutta scheme. The integration is performed downward from the surface and renormalized to match the boundary conditions at the bottom. A variable grid is used to provide high resolution near the bottom. The value of the height z at each grid point are given by the implicit equation

$$s = az + b \log(z) + c \tag{26}$$

where s is the index of the grid point and the constants a, b, c are such that half the grid points lie between z=1m and the bottom $z=z_o$; s=1 at $z=z_o$ and s=2001 at z=H. The grid has a total of 1000 intervals divided into two subintervals each. The formula (26) is used when s is an odd number. For s even, z is halfway between adjacent values of z as required by the Runge-Kutta scheme.

Using an initial profile of viscosity based on a linear-times-exponential Businger-Arya form, profiles of velocity and an initial estimate of the friction velocity u_* are obtained. A new profile of viscosity is then computed and hence a new value for u_*. The procedure is continued until the values of u_* from successive interations differ by less than $1.0(10)^{-3}$cm/s. Instabilities in the interation scheme are avoided by setting the viscosity profile equal to the mean of the two previous profiles.

Residual Currents

The residual tidal currents are assumed here to be generated locally over a horizontal bottom (residual tidal currents generated over a sloping bottom are discussed briefly in the Results of Modeling Section). There are three kinds of residual currents: Eulerian currents, Stokes drifts and Lagrangian currents. Eulerian currents are generated by divergences in the tidal Reynolds stresses. These are the residual currents that can be directly sensed by current meters as mean currents. The Stokes drifts arise from spatial variations in the tidal currents that cause a given water parcel to end up at a different location at the end of a tidal cycle than where it began. The Lagrangian currents are the sums of the Eulerian currents and the Stokes drift. They represent the total mass transport induced by the tides and tidal currents.

We assume that the Eulerian currents components u_E, v_E satisfy the equations

$$-fv_E = -\sum_n (\overline{u_n \frac{\partial u_n}{\partial x}} + \overline{v_n \frac{\partial u_n}{\partial z}} + \overline{w_n \frac{\partial u_n}{\partial z}}) + \frac{\partial}{\partial z} (A\frac{\partial u_E}{\partial z}) \tag{27}$$

$$fu_E = -\sum_n (\overline{u_n \frac{\partial v_n}{\partial x}} + \overline{v_n \frac{\partial v_n}{\partial z}} + \overline{w_n \frac{\partial v_n}{\partial z}}) + \frac{\partial}{\partial z} (A\frac{\partial v_E}{\partial z}) \tag{28}$$

where the summation is over the four tidal constituents O1, K1, N2 and M2 and the overbars denote time-averages. In (27) and (28), each tidal constituent contributes individually to the total Eulerian current without cross-modulation with the other constituents. We are therefore excluding low-frequency oscillations of fortnightly (two-week) periods generated by the non-linear interaction of the tidal constituents. The viscosity is that computed by the profile model for the tidal constituents.

The Eulerian currents are subject to the same boundary conditions as the tidal currents: zero velocity at the bottom

$$u_E,\ v_E = 0 \quad \text{at} \quad z = z_o \tag{29}$$

and zero shear at the surface

$$\frac{\partial u_E}{\partial z}\ ,\ \frac{\partial v_E}{\partial z} = 0 \quad \text{at } z = H \tag{30}$$

We write the total Stokes drift as a sum of contributions from the individual constituents

$$u_S = \sum_n (\overline{\Delta X_n \frac{\partial u_n}{\partial x}} + \overline{\Delta Y_n \frac{\partial u_n}{\partial y}} + \overline{\eta_n \frac{\partial u_n}{\partial z}}) \tag{31}$$

$$v_S = \sum_n \left(\overline{\Delta X_n \frac{\partial v_n}{\partial x}} + \overline{\Delta Y_n \frac{\partial v_n}{\partial y}} + \overline{\eta_n \frac{\partial v_n}{\partial z}}\right) \tag{32}$$

where the horizontal displacements ΔX_n and ΔY_n are time-integrals of the horizontal velocity components

$$\Delta X_n = iu_n/\omega_n \quad , \quad \Delta Y_n = iv_n/\omega_n \tag{33}$$

A derivation of the formulas for the Stokes drift is given by Longuet-Higgins (1969).

The total mass transport is given by the sum of the Eulerian currents and the Stokes drifts. These Lagrangian currents are written simply as

$$u_L = u_E + u_S \quad , \quad v_L = v_E + v_S \tag{34}$$

CALIBRATION OF THE PROFILE MODEL

The model was tuned to observations in two steps. The first step was to choose the type of theoretical tidal wave that best resembled the observed tides and tidal currents at a given station. The second step was to fit the theoretical profiles of that wave to the observed tidal ellipses by varying parameters in the model.

Wave Type

The appropriate type of tidal wave for each station was determined from the observed distributions of tidal currents (Fig. 2) and tides (Fig. 3). The coastal station BBL1 (56°19'N, 161°33'W) is located (Fig. 1) near the Alaska Peninsula where the tidal ellipses (Tables 2 and 4, Figs. 2 and 4) are narrow and oriented parallel to the adjacent coast. The tidal amplitudes (Fig. 3) decrease seaward from the Alaska Peninsula, and the phase lags increase with distance away from the shelfbreak. The characteristics of the tidal ellipses and distribution of tides suggest that the tidal motions at BBL1 are associated with Kelvin waves (Pearson, Mofjeld and Tripp, 1981) trapped to the Alaska Peninsula and propagating away from their source in the deep basin of the Bering Sea.

BBL2 (57°37'N, 167°45'W) was deployed in the middle shelf regime where the tidal ellipses (Figs. 2 and 4) are broad. The major axes of the M2 ellipses are oriented toward the northeast while the major axis of the narrower K1 ellipses are oriented toward the northwest. The amplitudes of tides (Fig. 3) are relatively uniform near BBL2. The M2 cophase lines (Fig. 3) are oriented toward the northwest over this regime although the M2 phase tends to be relatively constant in the region located northeast of BBL2. The K1 cophase

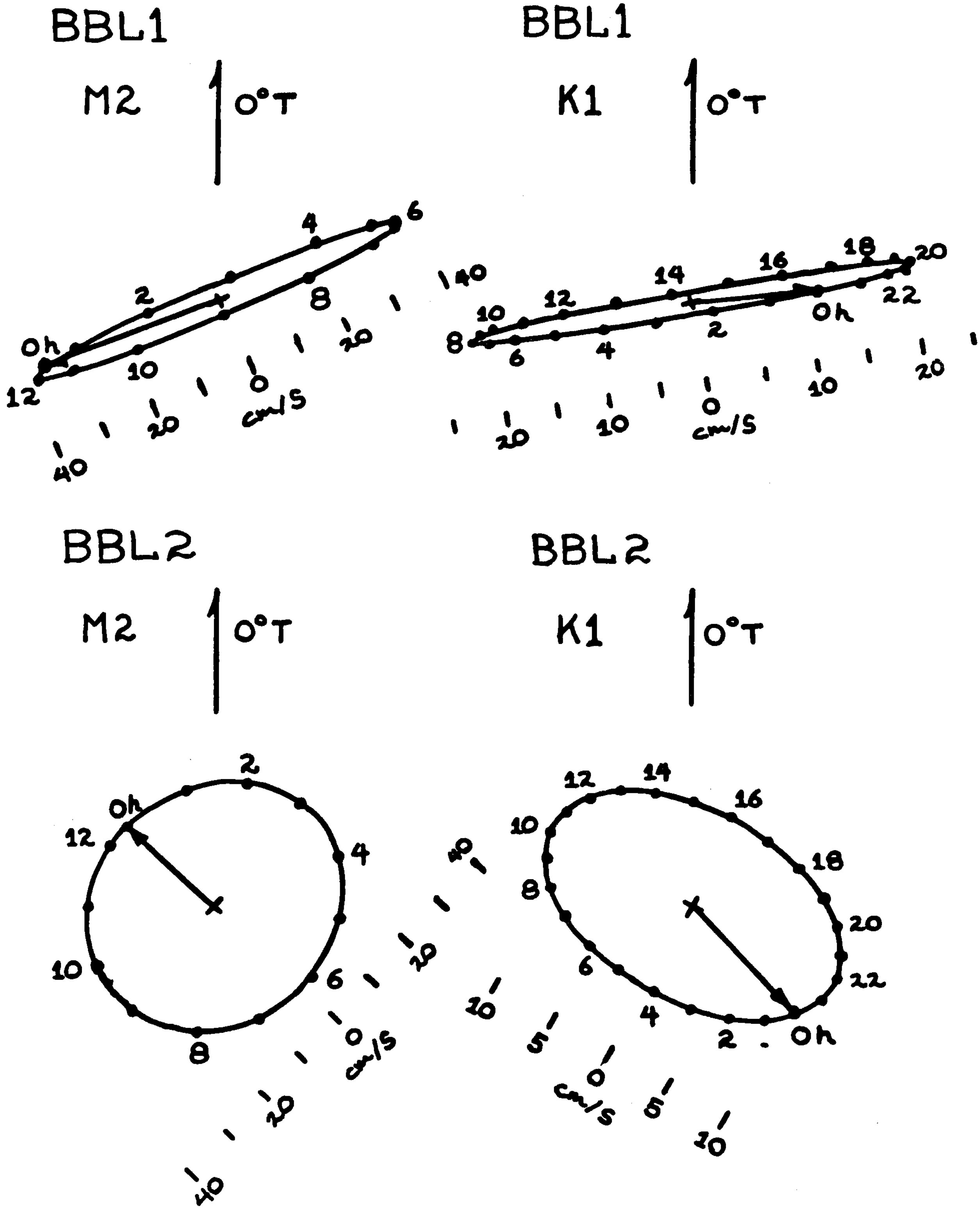

Figure 4. Representative M2 and K1 tidal ellipses at bottom boundary layer stations BBL1 and BBL2. Dots on the ellipses show the tips of the velocity vectors are at hourly intervals and are labelled in hours elapsed since Greenwich transit for the tidal constituent. The orientation is relative to true north (0°T), and amplitude scales are shown in cm/s.

lines (Fig. 3) form a more complicated pattern. Near BBL2, a K1 cophase line is shown (Fig. 3) oriented toward the northwest, but the cophase lines to the north and east help form the radiating pattern of the K1 amphidrome located south of Nunivak Island.

The tidal ellipses and tides around BBL2 suggest that the tidal motions are due in part to Sverdrup waves propagating from the deep basin. Other waves suppliment the tidal motions as well. In the case of M2, the relatively constant phase (Fig. 3) to the northeast of BBL2 suggests that the incident Sverdrup wave reflects at the coast of Alaska. The northeastward progression of M2 phase lag (Fig. 3) on the outer shelf indicates that the incident M2 wave amplitude is larger than that of the reflected M2 wave near BBL2.

The K1 tidal motions at BBL2 are also due to a combination of waves. One K1 wave is that incident from the deep basin. It and the other waves form the amphidromic system (Fig. 3) south of Nunivak Island. The mid-shelf station BBL2 appears (Fig. 3) to be in the transition between the other shelf regime dominated by the incident K1 Sverdrup wave and the inner region of the K1 amphidromic system.

In choosing the appropriate wave type, it is helpful to compare quantitatively the observed tidal currents with those inferred from the tides using formulas based on inviscid theoretical waves. If the inferred current harmonic constants resemble closely the observed values at BBL1 and BBL2, then the tidal currents can be represented by a single wave of the appropriate type for each tidal constituent.

The comparison for K1 and M2 is presented in Table 10. In general, there is good agreement (Table 10d) between the inferred and observed values. For BBL1, the Kelvin wave formulas (Table 10a) yield narrow ellipses with amplitudes and orientation similar to the observations. The M2 phase lags

Table 10. Comparison of inviscid Kelvin waves at BBL1 and inviscid Sverdrup waves at BBL2 with observed K1 and M2 current harmonic constants above the bottom boundary layers. Theoretical currents are inferred from the tidal harmonic constants (Fig. 3).

a. Theoretical relations between the tide η and tidal currents with tidal amplitude η and phase lag η°

Wave Type	Amplitude Major	Amplitude Minor	Phase Lag	Orientation of Major Axis[1]	Sense of Rotation
Kelvin	$\sqrt{g/H}$	0	η	Perpendic.	—
K1 Sverdrup	$\dfrac{\sqrt{g/H}}{(f^2/\omega^2 - 1)^{1/2}}$	$\dfrac{\omega}{f}$ x Major	$\eta + 180^\circ$	Parallel	C
M2 Sverdrup	$\dfrac{\sqrt{g/H}}{(1 - f^2/\omega^2)^{1/2}}$	$\dfrac{f}{\omega}$ x Major	η	Perpendic.	C

[1] Relative to the local cophase lines of the tide

b. Tidal harmonic constants (from Fig. 3)

Station	Constit.	Amplitude (cm)	Greenwich Phase Lag (° G)	Orientation of cophase lines[2] (° True)
BBL1	K1	51	358	330
	M2	80	180	330
BBL2	K1	20	335	310
	M2	31	135	290

[2]For BBL1, perpendicular to the general trend of the adjacent coast

c. Parameters used in theoretical relations

$g = 9.8\ m/s^2$ $\quad \omega(K1) = 7.29(10)^{-5}\ s^{-1}$ $\quad \omega(M2) = 1.405(10)^{-4}\ s^{-1}$

Station	Depth H (m)	$\sqrt{g/h}$ (s^{-1})	Latitude (°N)	f (s^{-1})
BBL1	63	0.394	56°19'	$1.213(10)^{-4}$
BBL2	69	0.377	57°37'	$1.231(10)^{-4}$

Table 10

d. Current harmonic constants

Constit.	Amplitude Major (cm/s)	Amplitude Minor (cm/s)	Amp. Ratio	Greenwich Phase Lag (°G)	Phase Diff. (°)	Orientation (°True)	Sense of Rotation
Station BBL1							
K1 (Obs.)	22	0.3	0.01	310	48	76	cc
K1 (Kelvin)	20	0	0	358		60	--
M2 (Obs.)	37	2	0.05	173	7	64	c
M2 (Kelvin)	32	0	0	180		60	--
Station BBL2							
K1 (Obs.)	12	5	0.42	154	1	298	c
K1 (Sverd.)	6	4	0.59	155		(290)	c
M2 (Obs.)	22	17	0.77	92	43	42	c
M2 (Sverd.)	24	21	0.88	135		40	c

agree, but the observed K1 phase lag is 48° earlier than the phase lag based on the assumption that the K1 current is in phase with the K1 tide. The K1 currents must therefore be the sum of at least two waves. From the K1 tidal distribution in Fig. 3, it seems that the K1 tides at BBL1 are under the influence of the K1 amphidromic system. In particular, the K1 distributions to the north and northeast of BBL1 form the classic pattern of a Kelvin wave propagating around an embayment. The K1 phase difference (Table 10d) at BBL1 indicates that the influence of the K1 motion propagating northwestward along the northeast coast extends to BBL1. This is not the case for the M2 tide (Fig. 3) where the influence of the virtual (on land) amphidrome extends only as far as Kvichak Bay.

The quantitative comparison (Table 10d) between Sverdrup and observed tidal currents at the mid-shelf station BBL2 reveals generally good agreement with some important exceptions. As with the theoretical currents at BBL1, the theoretical estimates of the tides (Table 10c) from the cotidal charts in Figure 3. Different formulas are used for K1 and M2 because Sverdrup waves change character as the frequency passes through the inertial frequency f.

The M2 Sverdrup amplitudes (Table 10d) at the middle shelf station are in good agreement with the observations except that the amplitude ratio of minor to major axes is somewhat larger for the M2 Sverdrup wave (0.88) than for the observed K1 current (0.77). The inferred K1 current has an amplitude (6 cm/s) along the major axis which is half the observed value (12 cm/s). This discrepancy may be due to the inference of the K1 amphidromic system (Fig. 3) near BBL2 since regions within such systems can have much larger currents than those inferred from the local tides under the assumption that the currents are due to a single wave. The amplitude ratio (0.59) of the K1 Sverdrup wave is larger than that observed (0.42).

Turning to the phase lags (Table 10d) at BBL2, there is excellent agreement between the K1 Sverdrup and observed phase lags. Evidently, the phase lag of K1 at the mid-shelf station BBL2 is controlled by the incident K1 Sverdrup wave even though the K1 amplitude at BBL2 is strongly affected by the K1 amphidromic system. It appears that BBL2 is located in the transition between two K1 tidal regimes - one dominated by the incident K1 Sverdrup wave and the other associated with the K1 amphidromic system (Fig. 3) to the east and north of BBL2. The M2 phase lags (Table 10d) at BBL2 show less agreement. The earlier M2 phase lag of 43° in the observations relative to the theory suggests that there is a reflected Sverdrup wave at BBL2 propagating southwestward from the Alaskan coast, in addition to the incident M2 Sverdrup wave from the deep basin. If the two waves had equal amplitudes, the M2 current observations would lead those based on the local tide by 90°. The fact that the actual M2 phase lead is 43° suggests that the incident M2 Sverdrup wave is dominant but that the reflected wave is significant.

The theoretical orientations (Table 10d) of the tidal ellipses at BBL2 agree relatively well with those observed. The assumption that the theoretical K1 and M2 tidal currents are associated with Sverdrup waves also produces the large difference in orientation observed (Fig. 2) between these tidal constituents. The theoretical and observed orientations are consistent with those for the mid-shelf region. The major axes of the M2 ellipses are oriented toward the northeast, which is parallel to the direction of propagation for the M2 wave incident from the deep basin. The K1 ellipses are oriented to the northwest, which is perpendicular to the incident direction of the K1 wave.

The simple theory predicts the correct clockwise rotation is expected in the middle shelf region where the Coriolis effect can accelerate moving water to the right without the inhibiting influence of a nearby coast.

The comparison of simple waves with the observed tidal currents is helpful in understanding the tidal dynamics at the two stations and in contrasting the differences in the tidal currents at the coastal (BBL1) and middle shelf (BBL2) stations. It also serves to show that the simple Kelvin and Sverdrup waves explain many of the observed tidal features but that there are some differences between the tidal currents predicted from the tides using these waves and the currents observed at the stations. This will be important to keep in mind when we interpret the residual tidal currents based on the waves.

Fit of Model Parameters

Having chosen the wave type for each station, we proceed to fit theoretical profiles of currents to the observed profiles of tidal ellipses for the K1 and M2 tidal constituents. The tides do not play a direct role in the calibration of the profile model as they did in the discussion on wave type. Instead, the model is fitted directly to the observed tidal ellipses. There are several parameters in the model that can be adjusted. The amplitude, phase lag and orientiation of K1 and M2 currents can be varied at one height in the water column. The bottom roughness length z_o can also be varied. The model then produces continuous profiles over the entire water column which pass through the values at the reference height. The amplitude ratio of minor to major axes is determined by the frequency of the tidal constituent, the Coriolis parameter f and the wave type.

The strength of the viscosity is determined in part by the bottom roughness length z_o which is adjusted to match the shear profiles in the bottom boundary layer. Changing the amplitudes of the tidal currents also changes the profile of viscosity. Fitting the model to the observations becomes an iterative process in which the constituent parameters and roughness length z_o are adjusted in turn. The result of the fit at each station is a compromise between matching the vertical profiles of amplitude, phase lag and orientation. We have placed primary emphasis on matching the amplitude profiles.

The theoretical K1 and M2 profiles for the coastal station BBL1 are shown in Fig. 5 together with the observed values from Tables 2 and 4. Not all the observed values were plotted for the near-bottom meters at 1, 3 and 5 m heights; only those values in Table 4 were used which corresponded to relatively good reductions in variance. Nevertheless, there is still considerable scatter in the near-bottom observations.

The profile model reproduces several of the features seen in the observations. These include the shapes of the amplitude profiles and the height at which the sense of rotation switches for M2 from counterclockwise below to clockwise above. The observed sense of rotation for K1 is not statistically significant at mid-depth because of noise affecting the small K1 amplitudes along the minor axis.

The fit of the profile model to the observed amplitude profiles required at the coastal station BBL1 a large viscosity (Fig. 7a). This in turn requires an unusually large value for the roughness length z_o = 1.0 cm; the implied vertical scale of the roughness elements is then 30 cm. One explanation for such a large z_o has to do with the effect of surface swell on the bottom boundary layer.

As pointed out by Grant (private communication), surface swell create a thin boundary layer just above the bottom which has the same effect on low-frequency motions like tidal currents as enhanced bottom roughness. If the large apparent roughness at BBL1 were due to surface swell, the roughness and hence the profiles of tidal currents would depend on the intensity of the swell which varies through the seasons of the year. Whether this is true cannot be demonstrated in the observations at BBL1 since no swell measurements were made during the period of observation at BBL1. It is known from shipboard observations however that the current observations at BBL1 were taken during a stormy period. Another explanation for the large roughness is that there were bedforms at the surface of the bottom sediment with amplitudes of the order of 30 cm. It is not known whether substantial bedforms existed at BBL1 during the period of observation.

The theoretical profiles (Fig. 5) of phase lag at BBL1 do not match the details of the observations. The theoretical K1 phase lag is essentially constant over the water column except for a small decrease (~3°) from the 20 m height to the bottom. The observed K1 phase lag has much more structure over the water column. The observed phase lag increase by 16° from the surface to the 14 m height and then decreases by ~6° from that height to the bottom. Crean (private communication) has found from 3-dimensional tidal models of the Straits of Juan de Fuca-Georgia that non-linear interactions between the tidal constituents can induce large vertical variations (as much as 100°) in K1 phase lag. It may be that the vertical structure (Fig. 5) of K1 phase lag at BBL1 is controlled by non-linear interaction not included in the profile model. The theoretical profile (Fig. 5) of M2 phase lag shows the correct tendency for earlier (smaller) phase lag moving downward in the water column but the theoretical profile underestimates the total phase shift, a factor of about 2 (11° versus 24°).

The K1 orientations (Fig. 5) of the model and observations agree rather well at BBL1. Both show a counterclockwise rotation of K1 ellipses moving downward from the surface. The theoretical profile (~17°) does underestimate the observed change (~24°) over the water column. The theoretical M2 profile of orientation is a poor match to the observations. The theory predicts a small (7°) counterclockwise rotation with depth whereas the observations indicate a clockwise rotation of ~16°. We have no explanation for this discrepancy in M2 orientation at this time; possible explanations may be related to topographic and non-linear effects which are not included in the model.

Turning to the fit (Fig. 6) of the profile model to the observations at the middle shelf station BBL2, we see that the reliable observations (Table 8) are confined to the bottom 15 m of the water column. It isn't possible to check the model well-above the bottom boundary layer as is the case for the coastal station BBL1.

The near-bottom profiles (Fig. 6) of amplitude for the model can be matched relatively easily to the observations at BBL2. The major increases in amplitude occur closer to the bottom than is the case (Fig. 5) for the coastal station BBL1. This is suprising because a Sverdrup wave regime such as that at the middle shelf station BBL2 should have a relatively thick bottom boundary layer due to the dominance of the clockwise-rotating velocity components. For the same profile of viscosity, the Kelvin waves would have a thinner bottom boundary layer. The key to the difference is amplitude profiles between the two stations BBL1 and BBL2 must lie in the differences in viscosity (Fig. 7). To fit the amplitude observations (Fig. 6) at BBL2 requires a small value of the bottom roughness length z_o (0.001 cm). This small value of z_o combines with the relatively smaller current amplitudes at

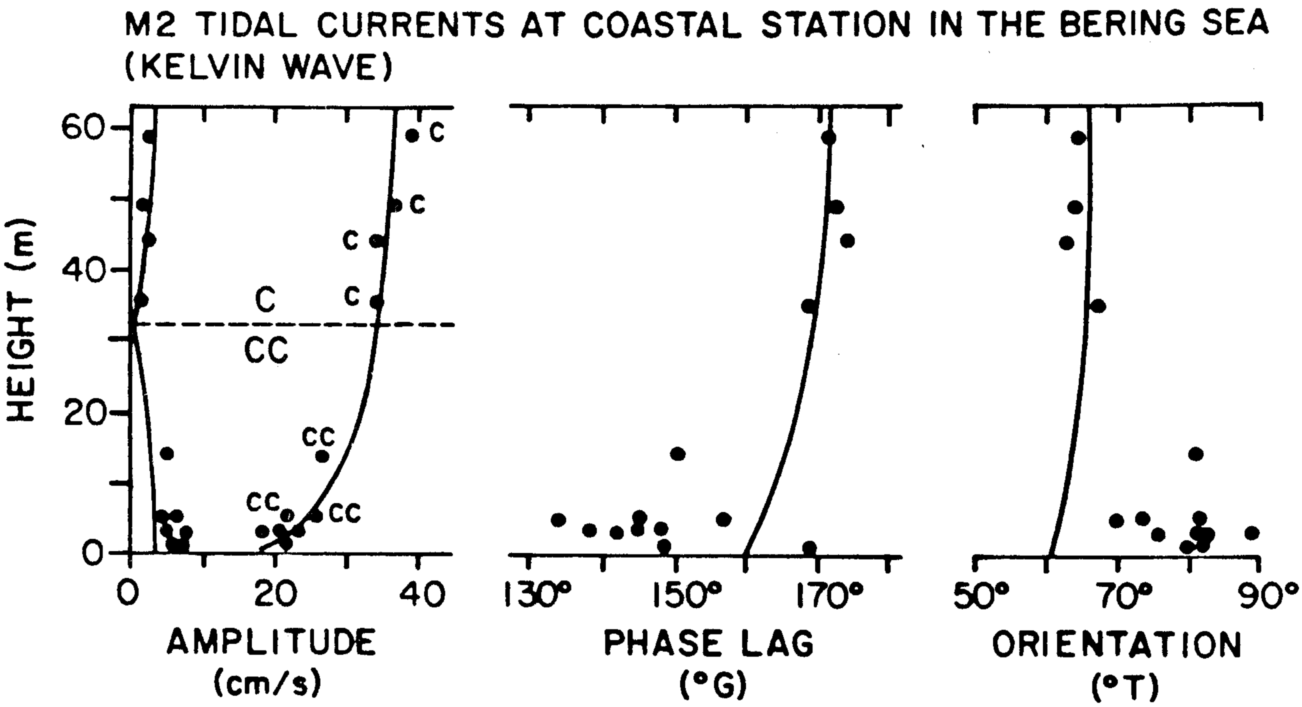

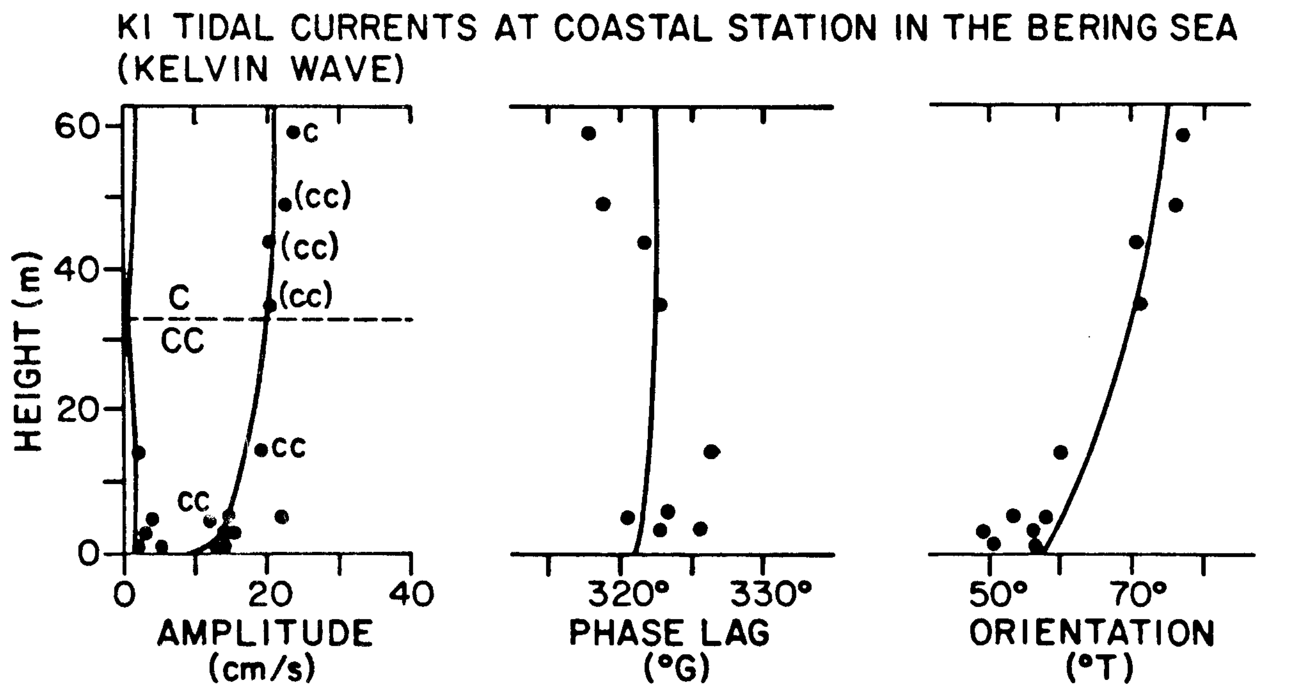

Figure 5. Fit (solid lines) for BBL1 of the profile model to observed M2 and K1 tidal ellipse elements (dots): amplitudes along the major and minor axes, Greenwich phase lag and orientation. The symbols c and cc refer to clockwise and counterclockwise senses of rotation respectively. The dashed lines show the location in the water column where the profile model predicts the transition from clockwise to counterclockwise rotation.

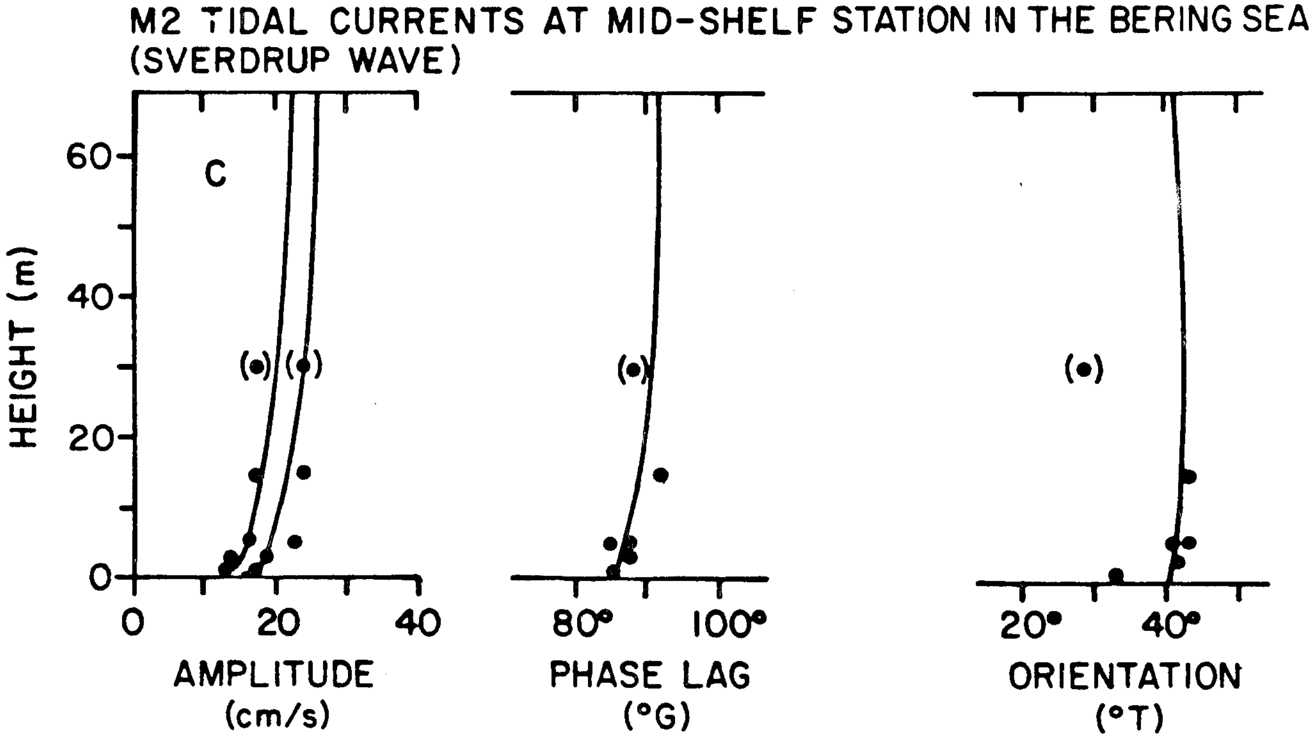

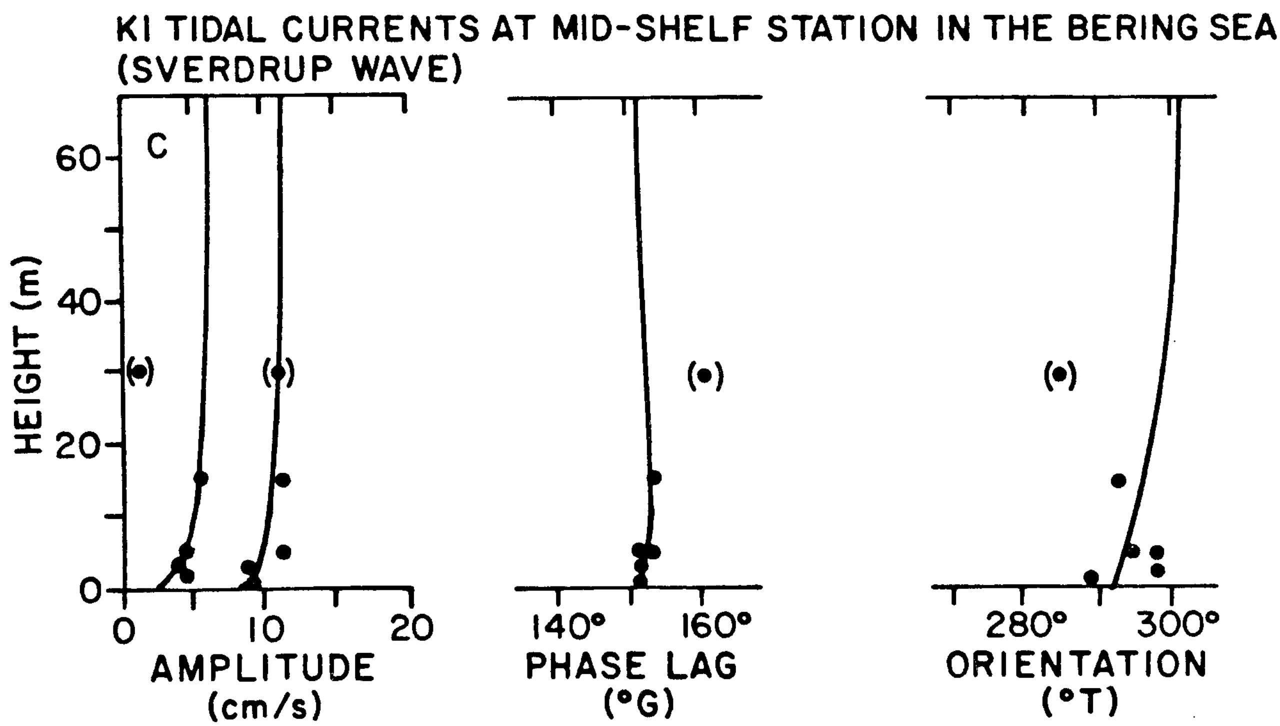

Figure 6. Fit (solid lines) for BBL2 of the profile model to observed M2 and K1 tidal ellipse elements (lines and dots defined in Fig. 5). The symbol c near the amplitude curves indicates that the sense of rotation is clockwise for both the theoretical and observed ellipses. The observed values at the 30 m height are in parentheses because the current meter was defective.

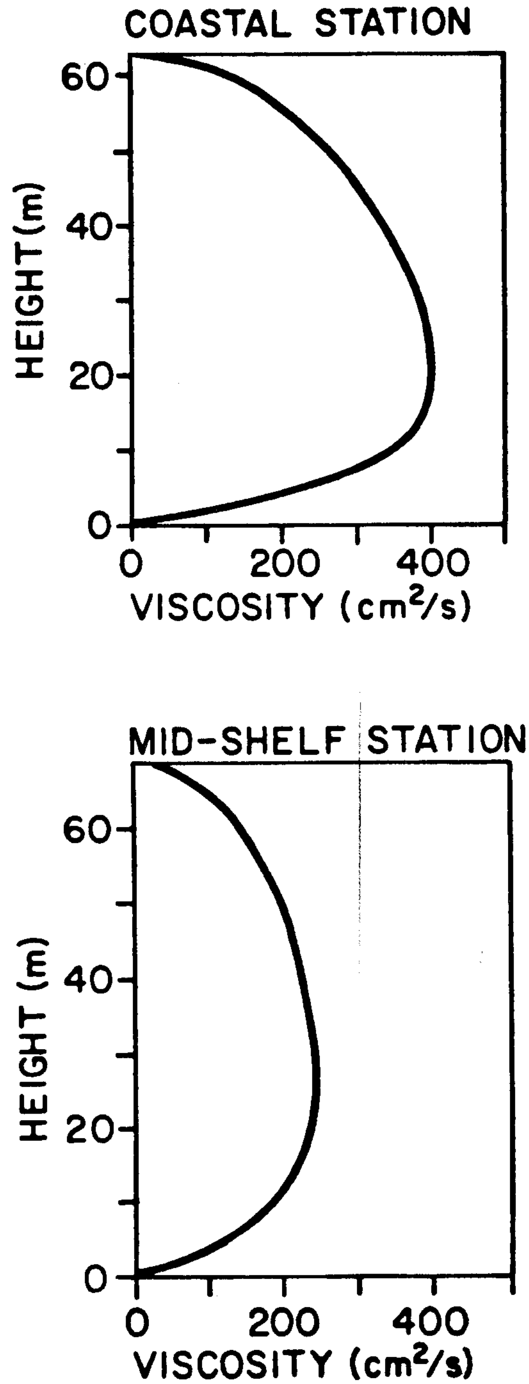

Figure 7. Theoretical profiles of eddy viscosity corresponding to fits (Figs. 5 and 6) of the profile model to the observed tidal currents at BBL1 and BBL2. These viscosities are sums of those generated by the major tidal constituents O1, K1, N2 and M2.

BBL2 to produce a less intense viscosity (Fig. 7) than at BBL1. The difference in viscosity between the two stations is sufficient to overcome the opposing tendency due to the differences in wave type. One reason for this smaller z_o inferred at BBL2 may be that the observations were taken at a quieter time of year (late August-early September) for surface swell than was the case at BBL1 (May). Shipboard observations suggest that this was indeed the case.

Tidal theory predicts that an M2 Sverdrup wave at high latitude should have nearly circular ellipses and thicker bottom boundary layers than K1. At the middle shelf station BBL2, the K1 ellipses (Fig.6) are narrower (smaller relative amplitude along the minor axes) and the K1 bottom boundary layer thinner than is the case for the M2 ellipses at BBL2. The direct fit (Fig. 6) of the profile model to K1 currents matches the amplitude ratios of the K1 Sverdrup wave and observations (though this did not occur when the K1 Sverdrup currents were computed from the local K1 tide).

The theoretical and observed phase lags (Fig. 6) agree well at BBL2. They show that the K1 phase lag is nearly constant over depth while the M2 phase lag is smaller (~6°) than that above the bottom boundary layer. The observations of K1 orientation at BBL2 shows considerable scatter, and it is difficult to test the validity of the counterclockwise trend of the theoretical K1 orientation. The observed K1 and M2 orientation at the 1 m height deviate in the same way and by the same amount from the corresponding observations at 3 and 5 m. This may be due to the effect of the steel anchor and its associated magnetic field on the magnetic compass of the current meter at the 1 m height. If the observed orientation at 1 m are rejected, the theoretical K1 profile of orientation has the wrong trend with height. This is a tenuous finding because it is based in large part on the single value at the 15 m height.

A few summary remarks seem appropriate for this section. Matching the profile model to the observations at BBL1 and BBL2 was done in two steps. The first step was to identify the best wave type for each station. This was relatively easy because the station locations were purposely chosen to lie in tidal current regimes that resembled either the Kelvin or the Sverdrup waves. The study of how the local tides relate to the tidal currents showed the similarities of the observations to the simple waves as well as the differences between the actual currents and those based on this simple theory. Fitting the model to the observed profiles of K1 and M2 currents was the second step. There are actually relatively few parameters to adjust in the model. One of these is the bottom roughness parameter which turned out to be quite different at the two stations. The reasons for the difference is a matter of speculation. The inability of the model to reproduce some of the profiles of the tidal ellipse parameters shows that there are processes at work which are not included in the model. To understand the tidal currents in detail will require a more complete model that includes non-linear interactions between the tidal constituents and bottom topography.

RESIDUAL TIDAL CURRENTS

The residual tidal currents computed from the profile model represent only part of the residual flow induced by tidal motions. They are that part generated locally by simple wave analogs propagating over a horizontal bottom. The computations do not take into account non-linear interactions between tidal constituents, effects of topography nor residual tidal currents generated in other tidal regimes that flow into the region. The model also ignores the difference between the actual tidal motions and those due to the simple Kelvin and Sverdrup waves. Even though the profile model cannot produce realistic estimates of the *complete* residual tidal currents, it allows considerable insight into the processes that give rise to the residual currents and shows the differences between the two tidal regimes where the observations were made. It also shows that the mass transport generated by tidal currents can be quite different from a simple time-average of local currents.

It is helpful to first consider residual currents based on waves without friction. Simple expressions (Table 11b) can be written for these waves which show explicitly the relative importance of wave type, amplitude, frequency and total depth in determining the speed and direction of the residual currents. Estimates (Table 11c) from these expressions are consistent with the residual tidal currents (Figs. 8 and 9) above the bottom boundary layer based on waves subject to viscosity.

The inviscid Kelvin waves at the coastal station BBL1 each generate a Stokes drift (Table 11) in the direction of propagation but their Eulerian current has zero speed. The quadratic dependence (Table 11b) of the Stokes drift on amplitude causes the largest constituent M2 to dominate the residual

Table 11. Theoretical estimates of K1 and M2 residual tidal currents at the coastal station BBL1 and middle shelf station BBL2 based on inviscid Kelvin and Sverdrup waves, respectively. The currents are independent of height.

a. Theoretical Equations (propagation in the y-direction)

	Stokes	Eulerian	Lagrangian
x-component	$u_S = \overline{\Delta Y \frac{\partial u}{\partial y}}$	$fu_E = -\overline{v \frac{\partial v}{\partial y}}$	$u_L = u_S + u_E$
y-component	$v_S = \overline{\Delta Y \frac{\partial v}{\partial y}}$	$-fv_E = -\overline{v \frac{\partial u}{\partial y}}$	$v_L = v_S + v_E$

b. Theoretical Expressions

Wave Type	Stokes Speed	Stokes Dir.	Eulerian Speed	Eulerian Dir.	Lagrangian Speed	Lagrangian Dir.
K1 & M2 Kelvin	$V^2/2C_o$	0°	0°	0°	←Vector Sum	
K1 Sverdrup	$(1-\omega^2/f^2)^{\frac{1}{2}} V^2/2C_o$	-90°	$\frac{\omega^2}{f^2}$ Stokes	90°	←Vector Sum	
M2 Sverdrup	$(1-f^2/\omega^2)^{\frac{1}{2}} V^2/2C_o$	0°	Stokes	180°	←Vector Sum	

V = Amplitude along major axis; direction is relative to propagation direction

$C_o = \sqrt{gH}$

c. Estimates of Residual Tidal Currents (Observed parameters from Table 10)

Sta.	Constit.	Stokes Speed (cm/s)	Stokes Dir. (T°)	Eulerian Speed (cm/s)	Eulerian Dir. (T°)	Lagrangian Speed (cm/s)	Lagrangian Dir. (°T)
BBL1	K1 (Kelvin)	0.10	76	0	-	0.10	76
	M2 (Kelvin)	0.28	64	0	-	0.28	64
BBL2	K1 (Sver.)	0.022	298	0.008	118	0.014	298
	M2 (Sver.)	0.045	42	0.045	222	0	-

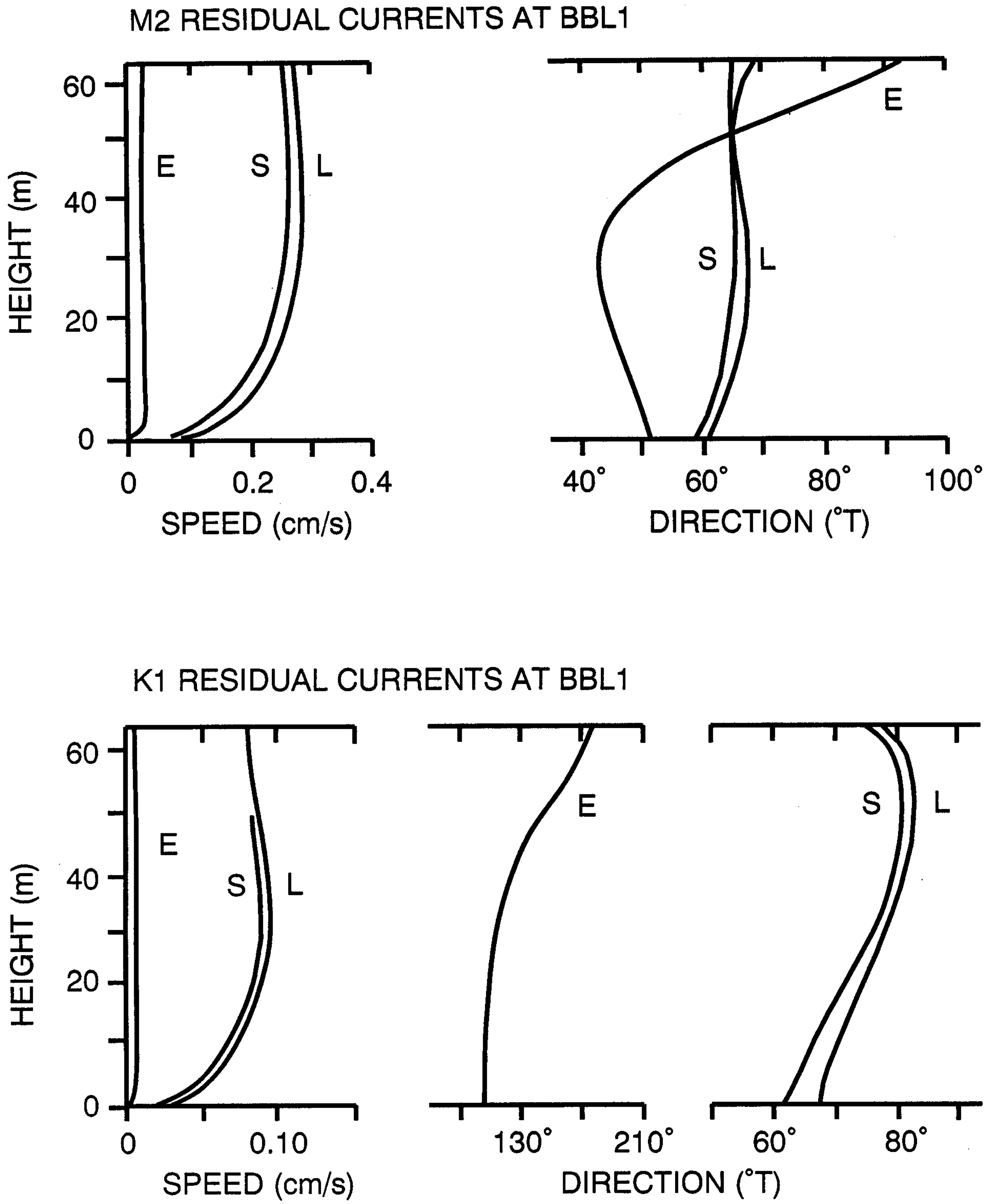

Figure 8. Theoretical M2 and K1 residual currents at BBL1 computed with the profile model. Shown are profiles of Eulerian current E, the Stokes drift S and the Lagrangian current L.

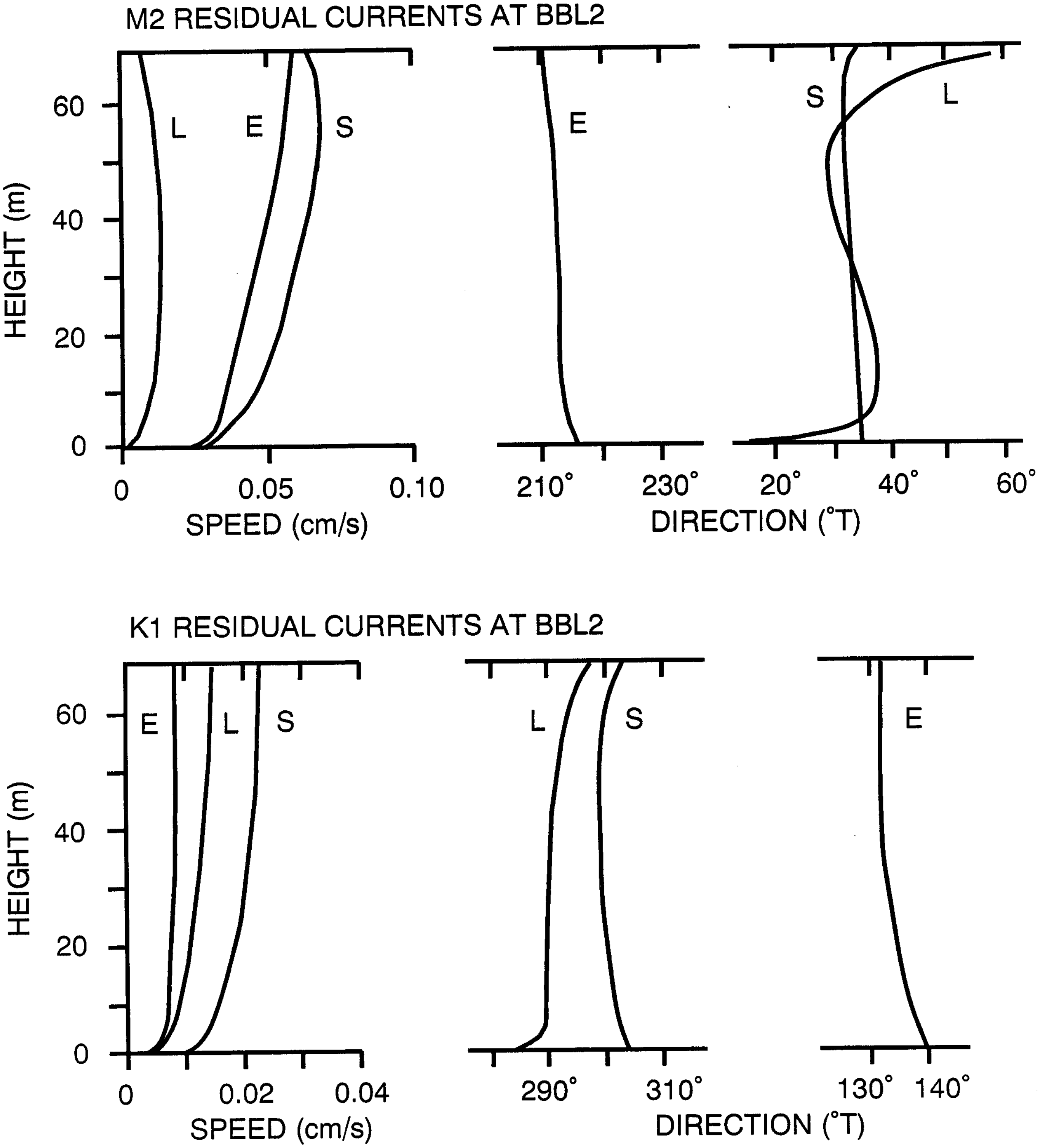

Figure 9. Theoretical M2 and K1 residual currents at BBL2 computed with the profile model. Shown are profiles of Eulerian current E, Stokes drift S and Lagrangian current L.

currents (Table 11c). At BBL1, the estimated residual currents are on the order of a few tenths of a cm/s. The magnitudes of these currents can be expected to increase shoreward from this station because the current amplitudes of Kelvin waves increase and the phase speed c_o decreases. Conversely, the residual currents should decrease seaward of BBL1.

At the middle shelf station BBL2, inviscid Sverdrup waves produce non-zero Eulerian currents (Table 11) in addition to the Stokes drift. Indeed, the M2 Eulerian current is equal in speed but opposite the direction to the M2 Stokes drift. As a result, the net M2 Lagrangian current has a net zero speed; this is also true for the other semidiurnal constituents. As for the other diurnal constituents, the K1 residual current (Table 11) at BBL2 are dominated by the Stokes drift with a smaller contribution due to the Eulerian current. The directions of the K1 residual currents are perpendicular to the direction of propagation.

There are several reasons that the Stokes drifts and Lagrangian currents (Table 11) are smaller at the Mid-Shelf Station BBL2 than at the coastal station BBL1. The most important of these is that the tidal current amplitudes (Table 10) are smaller at BBL2. Of next importance is that M2 Sverdrup waves have smaller tides (vertical excursions) than Kelvin waves for the same tidal current amplitude and this produces smaller Stokes drifts. Finally, the water depth is greater at BBL2 which produces a larger phase speed and hence smaller residual currents. The K1 waves at BBL1 and BBL2 are quite different. There is a propagating Kelvin wave at BBL1 and an evancescent (spatially decaying) Sverdrup wave at BBL2. The differences in K1 residual currents at the two stations are a reflection of this as well as the differences in amplitude and water depth at the two stations.

Vertical viscosity modifies the residual tidal currents. At the coastal station BBL1, the residual currents (Figs. 8 and 10) are still dominated by the Stokes drift with a very small Eulerian current (<0.03 cm/s) induced by dissipation along the direction of propagation. Because the tidal currents (Fig. 5) with friction vary in amplitude and orientation over the water column, the speeds and directions of the residual currents are also functions of height. The decrease in tidal currents near the bottom are responsible for the corresponding decrease (Figs. 8 and 10) in Stokes drift and Lagrangian current.

Based on a sum of contributions from the four major tidal constituents O1, K1, N2 and M2, the total Lagrangian currents at BBL1 has a maximum speed of about 0.4 cm/s and a direction along the coast away from the shelfbreak. This is probably an accurate estimate of the Stokes drift at BBL1 because the tidal currents flow parallel to isobaths with little topographic generation of residual currents. Sündermann (1977) found from a vertically-integrated model of M2 in the Bering Sea that Kvichak Bay is a major source of Eulerian residual flow for the Eastern Bering Sea Shelf. This outflowing Eulerian current represents the conversion of the incoming M2 Stokes drift.

The Stokes transport due to the M2 Kelvin wave near the Alaska peninsula can be estimated by integrating the inviscid expression $v_S = V^2/2c_o$ in the seaward direction. We assume that amplitude V of the M2 tidal current decays exponentially with offshore distance with a decay distance c_o/f = 205 km and that the M2 amplitude equals the observed value (Table 10) at BBL1. The Stokes transport due to the M2 Kelvin wave is then approximately $HV_o^2/f = 1.0\ (10)^5 m^3/s$ where H is 63 m and the current amplitude V_o at the coast is 44 cm/s based on an offshore distance of 37 km for the location of BBL1. The corresponding K1 Stokes transport is $0.4\ (10)^5 m^3/s$. The total Stokes

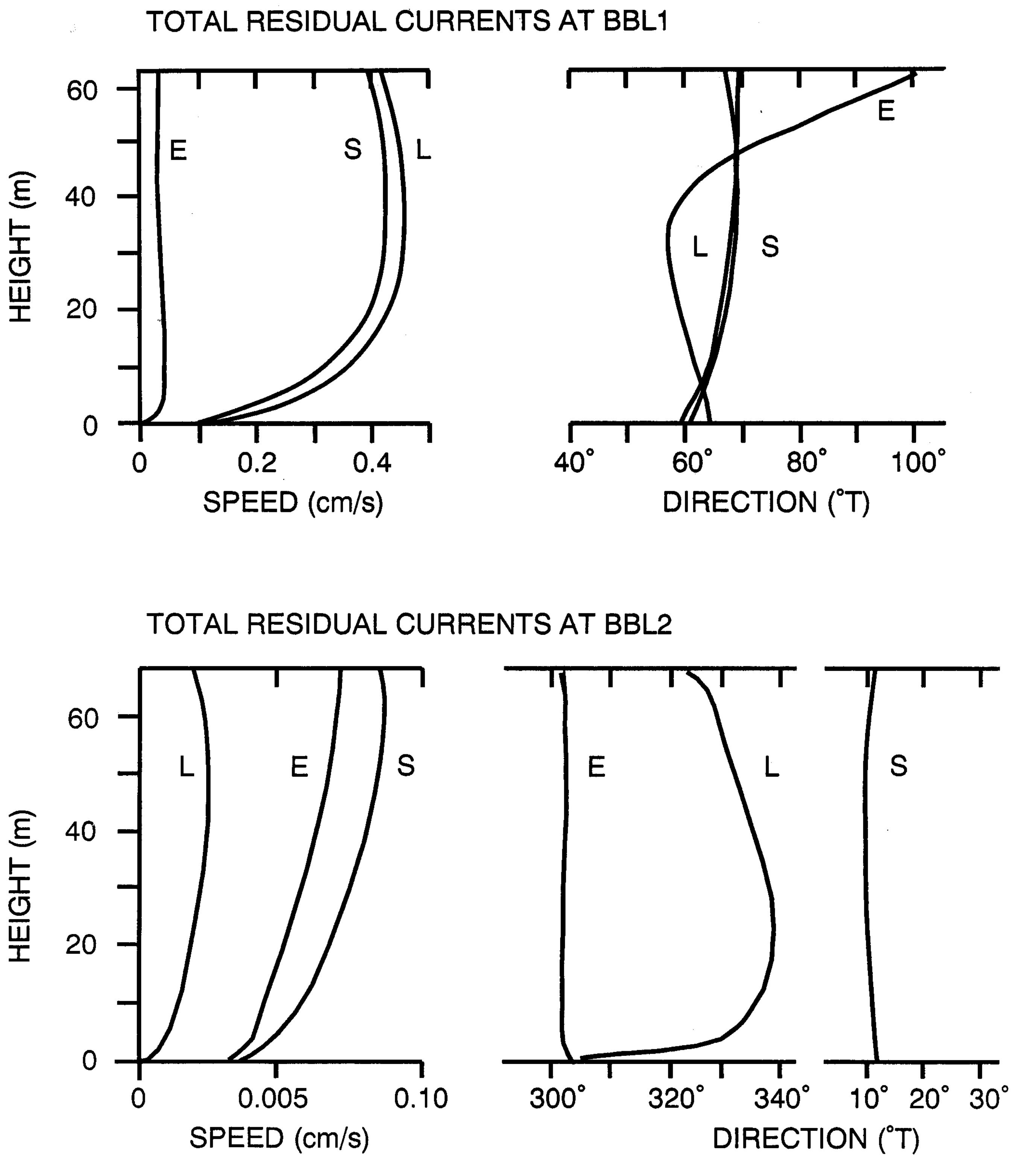

Figure 10. Total residual currents at BBL1 and BBL2 obtained by summing the contributions of the major tidal constituents O1, K1, N2 and M2. Shown are profiles of Eulerian current E, Stokes drift S and Lagrangian current L.

transport in this region is about 1.7 $(10)^5 m^3/s$ based on the sum of O1, K1, N2 and M2 Stokes drifts. This transport is along the Alaska Peninsula toward the northeast. The corresponding Stokes drift speed decays seaward with a decay distance 102 km equal to half that of the inviscid Kelvin waves. The Stokes transport is therefore confined to a coastal band about twice the decay distance of the Stokes drift speed or 205 km.

Vertical viscosity also affects the theoretical residual currents (Figs. 9 and 10) at the middle shelf station BBL2, but the general characteristics of these currents are the same as those (Table 11) without friction. There is still the tendency for the M2 Eulerian current to cancel the M2 Stokes drift, producing a small M2 Lagrangian current. The K1 residual current (Fig. 9) at BBL2 is dominated by the Stokes drift with a direction (~300°T) perpendicular to the direction of wave propagation. As with the inviscid currents, the total residual currents (Fig. 10) at BBL2 have considerably speeds than those at the coastal station BBL1 because the tidal current amplitudes are less at BBL2, the wave type is Sverdrup and the water depth is greater than at BBL1. The maximum speed (Fig. 10) of the total Lagrangian current computed for BBL2 is only 0.02 cm/s which is a factor of 20 smaller than that at the Coastal Station BBL1.

The residual currents at the middle shelf station BBL2 are probably enhanced by topographically generated currents. A rough estimate of the M2 topographic currents can be obtained from the formulas.

$$u_S = 0 \ , \ v_S = - \frac{\alpha}{H} \frac{f}{\omega^2} \frac{V^2}{2} \ , \ u_E = - \frac{\alpha}{fH} \frac{V^2}{2} \ , \ v_E = 0 \qquad (35)$$

where α is the local slope of the bottom and the M2 wave is assumed to be propagating into shallow water. The formulas (35) are derived from the equations in Table 11 under the assumption that the decrease in depth in the direction of propagation causes an increase in tidal current amplitude sufficient to conserve the instantaneous tidal transport. For a representative bottom slope $\alpha \doteq 2(10)^{-4}$ and M2 parameters for Table 10, the M2 topographic residual current at BBL2 has a speed of 0.07 cm/s and a direction of 280°T. The topographic Stokes drift and Eulerian current do not cancel. Hence, the topographic current is comparable in magnitude with the M2 Stokes drift (Table 11) derived earlier and is larger than the Lagrangian current. Both topographic currents are small (<0.1 cm/s). They can however be larger where local topographic features produce larger bottom slopes (Schumacher and Kinder, 1983). The direction of this flow would be toward the west if isobaths are oriented toward the northwest.

The theoretical residual currents discussed in this section are helpful in understanding the generation of residual currents. They are however based on many assumptions. The Stokes drifts do represent the local residual currents of this type but the theoretical Eulerian currents should include currents flowing past the observation point from other tidal regimes. A model of the entire Eastern Bering Sea Shelf is required to do this adequately. From the vertically integrated model by Sündermann (1977) for M2 in the Bering Sea, it appears that the M2 Eulerian residual current (Fig. 10) is small (<1 cm/s) at the two stations BBL1 and BBL2. In this model, the only significant Eularian current flow is along the coast of Alaska toward the northwest. This current is primarily due to shoreward M2 Stokes drift of the M2 Kelvin wave propagating along the Alaska Peninsula (Fig. 3). This drift is converted into the Eulerian current in the shallow embayments of Bristol Bay.

PROCESSING OF CURRENT AND PRESSURE TIME-SERIES FROM THE NORTHERN BERING SEA SHELF

The second part of the work proposed for RU621 consisted of processing current and pressure time-series obtained during the period October 1981 to August 1982 on the northern Bering Sea Shelf. Information is presented in Figure 11 and Table 12 on the locations, times and depths of the time-series. The current observations were made with Aanderaa RCM-4 current meters deployed on taut-wire moorings with sub-surface floats placed deep enough to avoid winter ice. The pressure time-series were obtained with Aanderaa TG-3A pressure gages firmly attached to bottom anchors during the periods of observation. The time-series were processed using the standard procedures described by Kachel (1984). Copies of the processed data have been sent to the Rand Corporation for use in calibrating and testing the circulation model.

The time-series were analyzed for tidal motions with overlapping 29-day harmonic analyses with start times spaced every 15 days. The resulting harmonic constants were averaged for each major tidal constituent (O1, K1, N2, M2 and S2). The means and standard deviations are presented in Table 13 for currents and Table 14 for pressure. The harmonic constants are consistent with those reported by Pearson, Mofjeld and Tripp (1981) for those stations (LD14A, NC17C, LD10AW and LD10AE) for which previous information from surrounding stations are available. The harmonic constants from the western stations (LD13A, LD15A, LD16A and NC19C) are consistent with extrapolation of the cotidal charts of Pearson, Mofjeld and Tripp (1981). These cotidal charts can now be substantially improved with the use of these new observations.

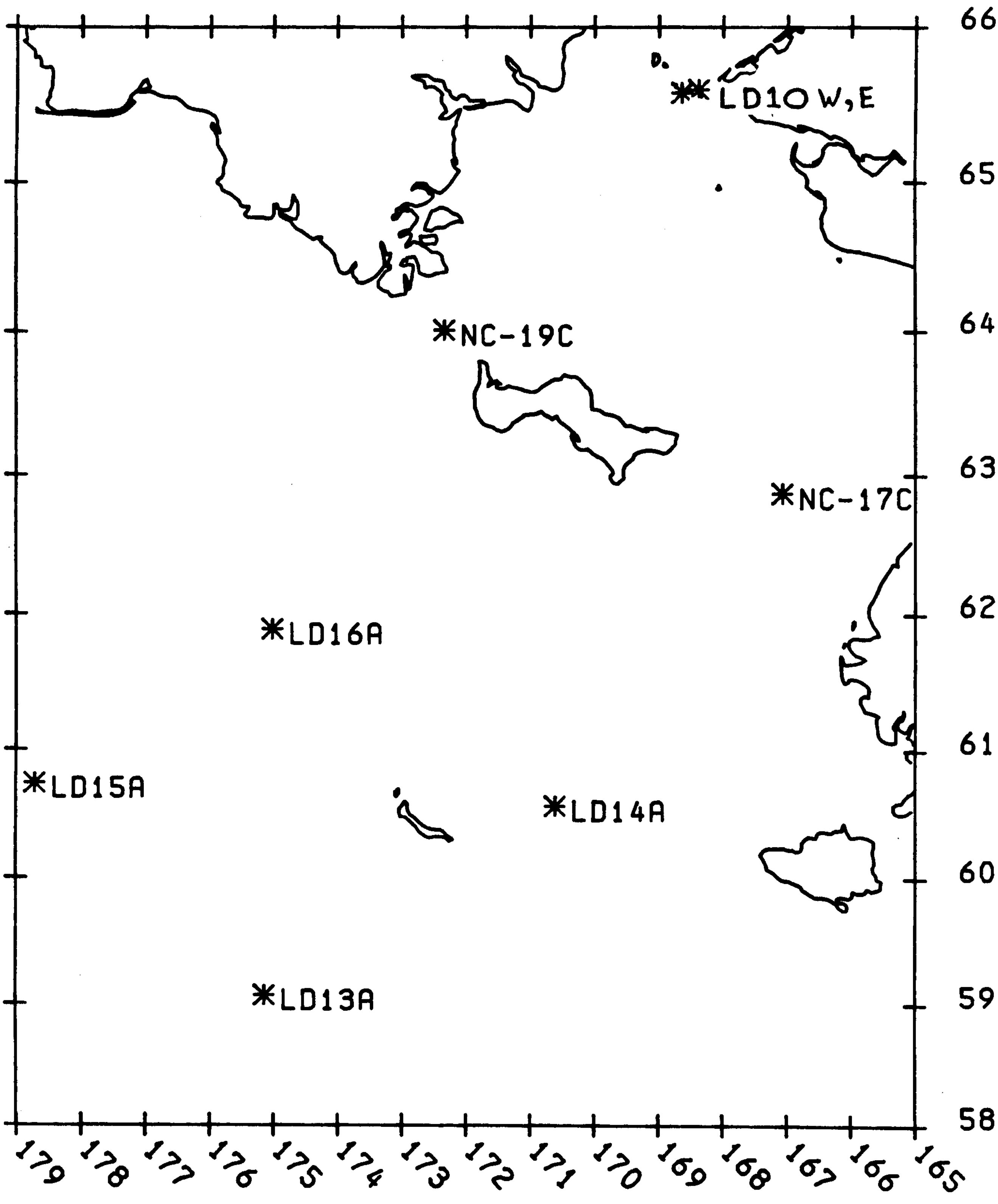

Figure 11. Locations of current and pressure stations occupied during 1981–1982 in the northern Bering Sea Shelf as part of RU 621.

Table 12. Current and pressure stations deployed during 1981-1982 on the northern Bering Sea Shelf.

Current Records

Sta.	Latitude (N)	Longitude (W)	Instrument Depth (m)	Total Depth (m)	1981 Start Date (JD)[1]	1982 End Date (JD)[1]	Duration (days)
LD14A	60°34.2	170°36.2	37	57	304	215	276
NC17C[2]	62°52.6	167°03.6	18	28	305	094	154
NC19C	64°00.4	172°19.6	35	55	306	015	74
LD10AW	65°35.0	168°38.0	30	50	306	213	272
LD10AE	65°36.0	168°21.8	29	49	306	213	272

Pressure Records

Sta.	Latitude (N)	Longitude (W)	Instrument Depth (m)	Total Depth (m)	1981 Start Date (JD)[1]	1982 End Date (JD)[1]	Duration (days)
LD13A	59°04.1	175°08.0	129	130	308	209	266
LD14A	60°34.2	170°36.2	56	57	304	215	276
LD15A	60°44.3	178°42.5	195	196	307	209	267
NC17C[2]	62°52.6	167°03.6	27	28	305	214	274
LD16A	61°53.2	175°00.1	79	80	307	211	269
NC19C	64°00.4	172°19.6	54	55	306	162	220
LD10AW	65°35.0	168°38.0	49	50	306	213	272
LD10AE	65°36.0	168°21.8	48	49	306	213	272

[1] Julian Day
[2] PMEL-funded

Table 13. Current harmonic constants for stations (Table 12) deployed during 1981-1982 on the northern Bering Sea Shelf. Means and standard deviations σ of overlapping 29-day harmonic analyses.

Station	Constit.	H_{max} Mean (cm/s)	H_{max} σ (cm/s)	H_{min} Mean (cm/s)	H_{min} σ (cm/s)	Direction Mean (°T)	Direction σ (°)	Phase Mean (°G)	Phase σ (°)	Rot.
LD14A	O1	4.6	0.7	2.5	0.4	162	9	3	10	c
	K1	6.8	0.3	4.5	0.4	358	6	216	6	c
	N2	5.3	1.1	3.3	0.8	71	6	95	11	c
	M2	18.2	0.8	12.7	0.8	65	2	152	2	c
	S2	2.2	0.3	1.4	0.4	68	15	220	26	c
NC17C	O1	6.8	0.5	0.7	0.3	44	4	272	6	cc
	K1	11.1	0.7	0.5	0.5	46	1	318	3	cc
	N2	3.0	0.7	0.8	0.5	314	9	5	10	cc
	M2	9.7	1.3	2.1	1.0	309	2	61	3	cc
	S2	1.4	0.3	0.2	0.3	309	31	136	14	cc
NC19C	O1	2.5	1.2	0.9	0.5	60	4	339	3	c
	K1	5.9	0.2	0.1	0.1	65	2	1	7	cc
	N2	2.5	0.3	0.7	0.3	75	5	145	5	c
	M2	10.0	0.7	2.5	0.2	63	1	211	2	c
	S2	2.1	0.1	0.6	0.4	75	12	296	15	c
LD10AW	O1	1.9	0.6	0.2	0.4	353	20	64	54	cc
	K1	2.1	1.0	0.02	0.3	7	14	24	38	c
	N2	1.1	0.3	0.1	0.3	0	17	30	30	c
	M2	3.4	0.4	0.5	0.6	355	7	149	12	c
	S2	0.7	0.3	0.1	0.2	7	24	206	25	c
LD10AE	O1	2.0	0.5	0.2	0.6	50	47	28	47	c
	K1	1.9	0.3	0.3	0.3	13	33	40	16	cc
	N2	1.6	0.4	0.05	0.3	357	20	97	23	c
	M2	4.2	0.5	0.2	0.5	0	6	161	5	c
	S2	1.1	0.2	0.1	0.4	75	45	148	88	c

Table 14. Pressure[1] harmonic constants for stations (Table 12) deployed during 1981-1982 on the northern Bering Sea Shelf. Means and standard deviations σ of overlapping 29-day harmonic analyses.

Station	Constit.	Amp Mean (mbar)	Amp σ (mbar)	Phase Mean (°G)	Phase σ (°)	Station	Constit.	Amp Mean (mbar)	Amp σ (mbar)	Phase Mean (°G)	Phase σ (°)
LD13A	01	23.3	0.3	318	1	LD14A	01	9.1	0.7	304	4
	K1	35.2	1.4	334	1		K1	17.3	0.7	322	1
	N2	6.6	0.7	60	5		N2	6.9	0.6	132	7
	M2	22.8	0.2	106	1		M2	22.1	0.8	180	1
	S2	2.0	0.5	197	11		S2	2.3	0.4	263	7
LD15A	01	26.0	0.3	317	1	NC17C	01	10.2	0.7	306	7
	K1	38.7	1.2	334	1		K1	18.6	1.1	346	5
	N2	5.7	0.6	42	5		N2	7.9	0.8	281	12
	M2	21.6	0.2	87	1		M2	25.7	1.2	336	7
	S2	2.7	0.3	166	6		S2	3.0	0.7	53	13
LD16A	01	12.2	0.8	325	3	NC19C	01	5.7	0.6	304	10
	K1	19.6	0.9	341	1		K1	10.0	0.6	329	3
	N2	4.7	0.6	99	7		N2	6.2	0.5	118	7
	M2	16.9	0.4	145	1		M2	23.7	0.9	172	1
	S2	2.1	0.3	226	5		S2	2.7	0.4	252	14
LD10AW	01	1.4	0.6	357	37	LD10AE	01	1.4	0.6	328	74
	K1	2.7	0.7	359	28		K1	2.7	0.8	346	35
	N2	2.4	0.5	128	13		N2	2.4	0.4	104	18
	M2	7.7	1.4	202	9		M2	7.6	1.3	180	12
	S2	1.5	0.7	312	38		S2	1.4	0.7	276	38

[1] Multiply pressure amplitudes (mbar) by 0.993 to obtain tidal height amplitudes in centimeters of seawater.

REFERENCES CITED

Businger, J.A., and S.P.S. Arya, 1974: Height of the mixed layer in the stably stratified planetary boundary layer. Advances in Geophysics, 18A, Academic Press, 73-92.

Defant, A., 1961: Physical Oceanography, Vol. II. Pergamon Press, 598 pp.

Kachel, D.G., 1984: Guide to Processing System for Oceanographic Data. NOAA Technical Memo. (in preparation).

Liu, S.K., and J.J. Leenderste, 1978: Three-dimensional subgridscale-energy model of the eastern Bering Sea. Proc. XVI Coast. Eng. Conf., Amer. Soc. Civil Eng.

Liu, S.K., and J.J. Leenderste, 1979: A Three-Dimensional Model for Estuaries and Coastal Seas: VI Bristol Bay Simulations. The Rand Corp., R-2405-NOAA.

Longuet-Higgins, M.S., 1969: On the transport of mass by time-varying currents. Deep-Sea Res., 16, 431-447.

Mellor, G.L., and T. Yamada, 1974: A hierarchy of turbulence closure models for planetary boundary layers. J. Atmos. Sci., 31, 1791-1806.

Mellor, G.L., and T. Yamada, 1982: Development of a turbulence closure model for geophysical fluid problems. Rev. Geophys. Space Phys., 20, 851-875.

Mofjeld, H.O., 1980: Effects of vertical viscosity on Kelvin waves. J. Phys. Oceanogr., 10, 1040-1050.

Mofjeld, H.O., and J.W. Lavelle, 1983: Bottom boundary layer studies in tidally-dominated regimes. XVIII General Assembly of the Union of Geodesy and Geophysics, Hamburg FRG, IUGG-IAPSO Programme and Abstracts.

Mofjeld, H.O., and J.W. Lavelle, 1984: Setting the length scale in a second-order closure model of the unstratified bottom boundary layer. J. Geophys. Rev., in press.

Pearson, C.A., H.O. Mofjeld and R.B. Tripp, 1981: The tides of the Eastern Bering Sea Shelf. In: The Eastern Bering Sea Shelf: Oceanography and Resources. D.H. Hood and J.A. Calder, Eds., University of Washington Press, 111-130, 625 pp.

Roach, A., J.D. Schumacher, K. Aagaard and R.B. Tripp, 1984: Interannual variations of transport through the Bering Strait. Ocean Sciences Meeting, New Orleans, Abstracts.

Schumacher, J.D., and T.H. Kinder, 1983: Low-frequency current regimes over the Bering Sea Shelf. J. Phys. Oceanogr., 13, 607-623.

Sündermann, J., 1977: The semidiurnal principal lunar tide M2 in the Bering Sea. Deutsche Hydrog. Zeitschrift, 30, 91-101.

Sverdrup, H.U., 1927: Dynamics of tides on the North Siberian Shelf. Geofis. Publ., 4, 75 pp.

NORTHEAST GULF OF ALASKA PROGRAM

by

R. D. Muench, J. D. Schumacher,
S. P. Hayes, and R. L. Charnell

Pacific Marine Environmental Laboratory
National Oceanic and Atmospheric Administration
7600 Sand Point Way, N.E.
Seattle, Washington 98115

Final Report
Outer Continental Shelf Environmental Assessment Program
Research Unit 138

October 1978

PREFACE

Commencing in 1974, the Pacific Marine Environmental Laboratory, NOAA, has been investigating physical oceanographic processes on the continental shelf in the northern Gulf of Alaska. The work has been funded by the Bureau of Land Management as part of the Alaskan Outer Continental Shelf Environmental Assessment Program. The initial phases of this effort addressed processes in the northeastern gulf, in particular the shelf region adjacent to Icy and Yakutat bays. Geographical emphasis has shifted westward with time; the program currently emphasizes the northwest Gulf of Alaska with stress on the region surrounding Kodiak Island. Initially, the program was concerned primarily with obtaining moored current and bottom pressure measurements with only minor attention to coincident conductivity and temperatures versus depth (CTD) and other data. More recently, the program has shifted emphasis to include collection of CTD data along with ancillary information such as that obtained from satellite-tracked drifters, drift cards and environmental buoys.

The field program in the northeastern gulf was completed in summer 1977 while that in the western section is continuing. However, based on our observations, it is evident that the Gulf of Alaska continental shelf can be divided oceanographically at Middleton Island into an eastern and western regime. The northeastern gulf is a region of relatively broad, diffuse westerly flow. The western gulf, particularly the region off Kodiak Island is characterized by a narrow, high-speed boundary flow, the Alaskan Stream. In addition to the difference in major current regimes, the shelf is narrower off Yakutat and Icy bays than off Kodiak Island and bottom topography is somewhat more irregular, though considerable topographic irregularities also exist off Kodiak Island. We would *a priori* expect shelf circulation off Kodiak Island to be more heavily influenced by shelf break circulation than in the northeastern gulf because of the more intense shelf break current in the former location. Conversely, local meteorological effects and freshwater input might be expected to have relatively greater effect on shelf circulation in the northeastern gulf.

In view of the oceanographic differences between the two regions, we can present in this final report an independent synopsis of the results of the northeast Gulf of Alaska field program without loss of understanding. The stress will be measured currents and bottom pressures, consistent with the major thrust of our field effort.

These will be related to regional circulation where possible, and to coincident temperature, salinity and weather data where appropriate. It is hoped that the end product will provide a useful working document both for environmental planning and for future, more focused, scientific endeavors in the region.

TABLE OF CONTENTS

TABLE OF CONTENTS (continued)

LIST OF FIGURES

LIST OF FIGURES (continued)

LIST OF FIGURES (continued)

LIST OF TABLES

1. INTRODUCTION

Circulation in the Gulf of Alaska comprises a subarctic gyre in the North Pacific Ocean. It is characterized by a cyclonic (anticlockwise) mean circulation driven by the large-scale atmospheric flow. In the continental shelf region of the northeast gulf (Figure 1.1), we expect to see also the effects of local wind-driven circulation, freshwater input and heating and cooling in generating currents. In addition, we must consider the role of complex geography and bottom topography in modifying currents. This report addresses circulation in the northeast Gulf of Alaska from within this framework.

1.1 History of Oceanographic Research

Taken within the context of large-scale oceanic circulation, the Gulf of Alaska gyre has been indirectly discussed by various researchers (c.f. Munk, 1950, Carrier and Robinson, 1962, and numerous others). These studies, which are largely theoretical, established that the gyre is driven by regional wind-stress and that as a consequence of the earth's rotation westward intensification of the Alaskan Stream must occur off Kodiak Island. Within this context, the westward shelf break flow observed in the northeast Gulf of Alaska is simply the northern arm of a cyclonic circulation encompassing the entire gulf.

Research on the northern portion of the Gulf of Alaska has been severly hampered in the past by lack of field data. One of the earliest works was that of McEwen, Thompson and Van Cleve (1930), who used temperature and salinity data obtained along sections normal to the coast from Cape Cleare and Yakutat Bay to discuss regional temperature and salinity structure and currents over the shelf and shelf break. Not until some three decades later, with increased interest in the regional fisheries potential, did significant additional field work occur. The resulting manuscripts used temperature and salinity data to address large scale circulation in the Alaskan Stream southwest of Kodiak Island and westward along the Aleutian Chain, rather than in the northeastern gulf (e.g., Favorite, 1967). Drift-card studies were an exception, however, and provided qualitative support for cyclonic circulation in the Gulf of Alaska and a westerly flow south of the Aleutians (Favorite, 1964; Favorite and Fisk, 1971). An excellent oceanographic summary of the subarctic Pacific covering research through about 1972, including a thorough reference list, has been prepared by Favorite, Dodimead and Nasu (1976). As in prior work they discuss primarily larger-scale features and details in the northwest gulf, but find insufficient data to address details in the northeast gulf.

Following inception of the BLM-sponsored Outer Continental Shelf Environmental Assessment Program in 1974, data were acquired from the northeast Gulf of Alaska which were sufficient to describe regional oceanographic conditions. The first resultant work was a

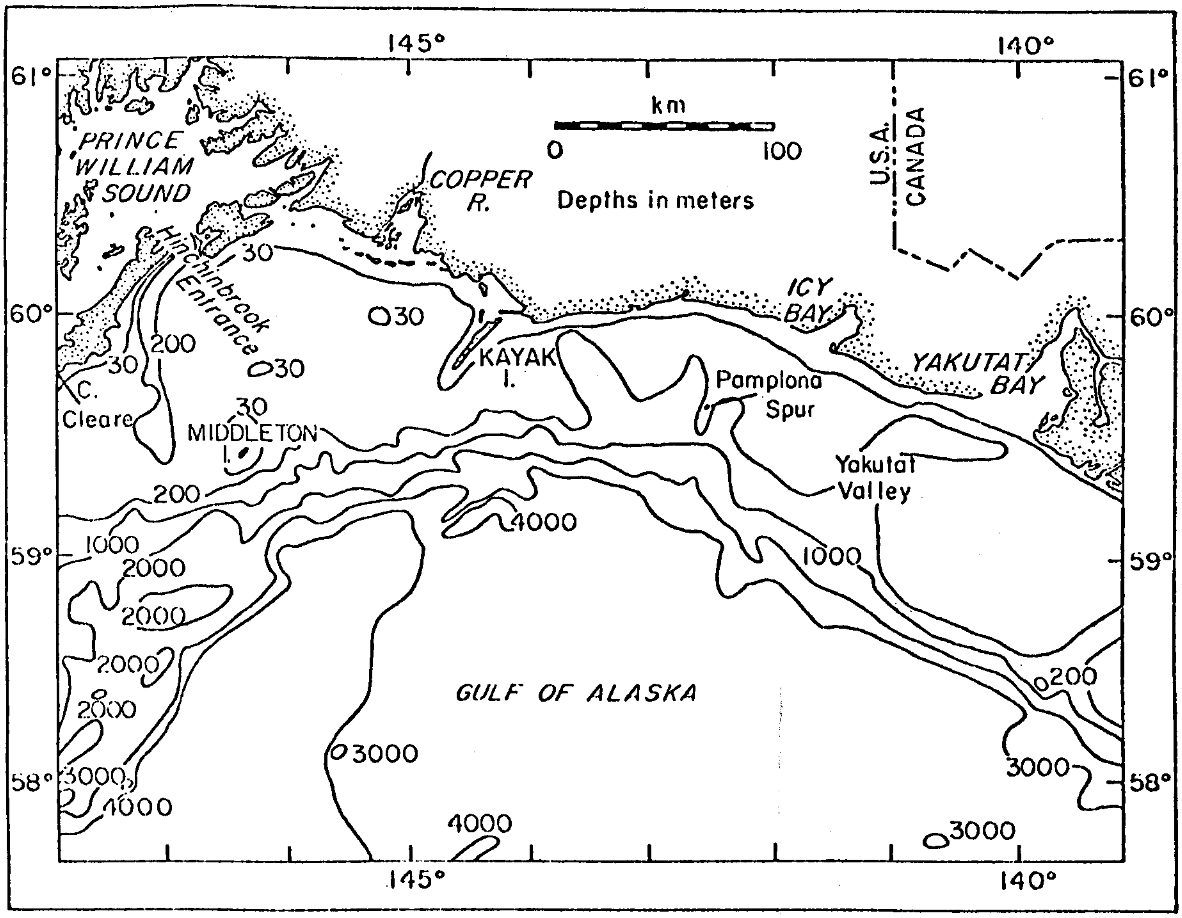

Figure 1.1 - Geographical location in the northeast Gulf of Alaska.

characterization of seasonal variations in the water column in the northern gulf based on time series observations from a single oceanographic station in the northern central gulf (Royer, 1975). Galt and Royer (in press) used current and hydrographic data to discuss large-scale current, temperature and salinity distributions in the northern gulf. Royer and Muench (1977) discussed some large-scale features in the surface temperature distribution and related these to the regional circulation and to vertical mixing regimes on the shelf. Hayes and Schumacher (1976), Hayes (1978), and Holbrook and Halpern (1977) have described and discussed variations in winds, currents and bottom pressures on the shelf off Icy Bay during the period February-May 1975.

1.2 Geographical Setting

The northern Gulf of Alaska is characterized by an arcuate, east-west trending coastline indented with several embayments, the largest of which are Yakutat and Icy bays and Prince William Sound (Figure 1.1). Kayak Island provides an effective southward-extending promontory, more like a peninsula than an island, while Middleton Island occupies the center of a shoal region south of Prince William Sound. The coastline between Yakutat Bay and Kayak Island is characterized by numerous glacial streams which contribute freshwater to the marine system during summer. A major concentrated freshwater source, the Copper River, is present between Kayak Island and Prince William Sound.

Topography adjacent to the coast is generally rugged, with elevations greater than 3,000 m and long, steep-sided valleys which serve to channel strong winter drainage winds. Such valleys are located, for example, at the heads of Yakutat and Icy bays. The Copper River valley also serves as a route for drainage winds. Discussion of the shelf in relation to Prince William Sound is not included in this report; we have chosen the western boundary of our study area to lie along a line between Hinchinbrook Entrance and Middleton Island and the eastern boundary to lie roughly normal to the coastline at Yakutat Bay.

Bathymetrically, the region is complex. The shelf is bounded roughly by the 200 m isobath, seaward of which bottom depths drop off steeply to 3,000-4,000 m. Shelf width is about 50 km between Yakutat Bay and Kayak Island and increases to nearly 100 km west of Kayak Island. The shelf between Yakutat Bay and Kayak Island is marked by major irregularities in the form of valleys and ridges normal to the coastline. The most obvious such features are Yakutat Valley and Pamplona Spur. West of Kayak Island the shelf attains a generally more uniform topography and is somewhat shallower over much of its extent as indicated by the shoal areas (depths of less than 30 m) including that surrounding Middleton Island.

1.3 Oceanographic and Meteorological Setting

Since we are concerned in this report with observed circulation, this section will be limited to a brief discussion of those factors which might be expected to directly affect the circulation. In general, we can expect circulation in any shelf region to be affected by both the offshore or shelf break current, via lateral momentum transfer onto the shelf, and by local forcing due to winds and fresh-water input as it affects the baroclinic field. We discuss the former factor first.

1.3.1 Regional oceanographic process

Gulf of Alaska circulation is a subarctic gyre within the North Pacific Ocean. Water for this circulation comes from the North Pacific Drift, which flows easterly from the vicinity of Japan and splits into two branches west of Vancouver Island. The south-flowing branch parallels the coast to become the California Current, while the northerly flowing branch follows the coastline and eventually becomes the Alaskan Current. The lower latitude origin of this water gives rise to characteristic temperature and salinity features which have been discussed by Royer (1975), Royer and Muench (1977) and Galt and Royer (in press). These features include subsurface warm and cold cores, both of which are generated at mid-latitudes and sink beneath the high latitude layer of less saline, less dense water which is locally formed in the northern Gulf of Alaska. The temperature maximum can, if we neglect the effects of diffusion, be used to trace the path of flow followed by the shelf break current in our study region (Figure 1.2).

While temperature and salinity distributions can be used to trace flow path, obtaining estimates of current speed proves more difficult. We approach it indirectly, using the known fact that the subarctic gyre derives its energy from the regional atmospheric circulation. Ingraham, Bakun and Favorite (1976) have computed mean monthly wind stress curls over the Gulf of Alaska for the period 1950-1976 and used these to compute total wind-driven water transport according to the method of Sverdrup (1947). This method yields a northward transport throughout the gulf which is dynamically constrained to exit the northern gulf as a concentrated stream along the northwestern boundary (cf Welander, 1959, for a discussion of the dynamics of this mechanism). We recognize this concentrated flow as the Alaskan Stream southeast of Kodiak Island. Mean winter flow streamlines computed using the wind stress curl by Ingraham *et al.* (1976) are shown in Figure 1.3. It is immediately apparent that our study region in the northeast gulf lies east of the area where appreciable intensification would be expected to occur. Therefore, while there is a westerly flow, current speeds and volume transports would be expected to be a factor of two or three less than computed for the Alaskan Stream farther west. This conclusion is qualitatively supported by the theoretical work of Thomson (1972).

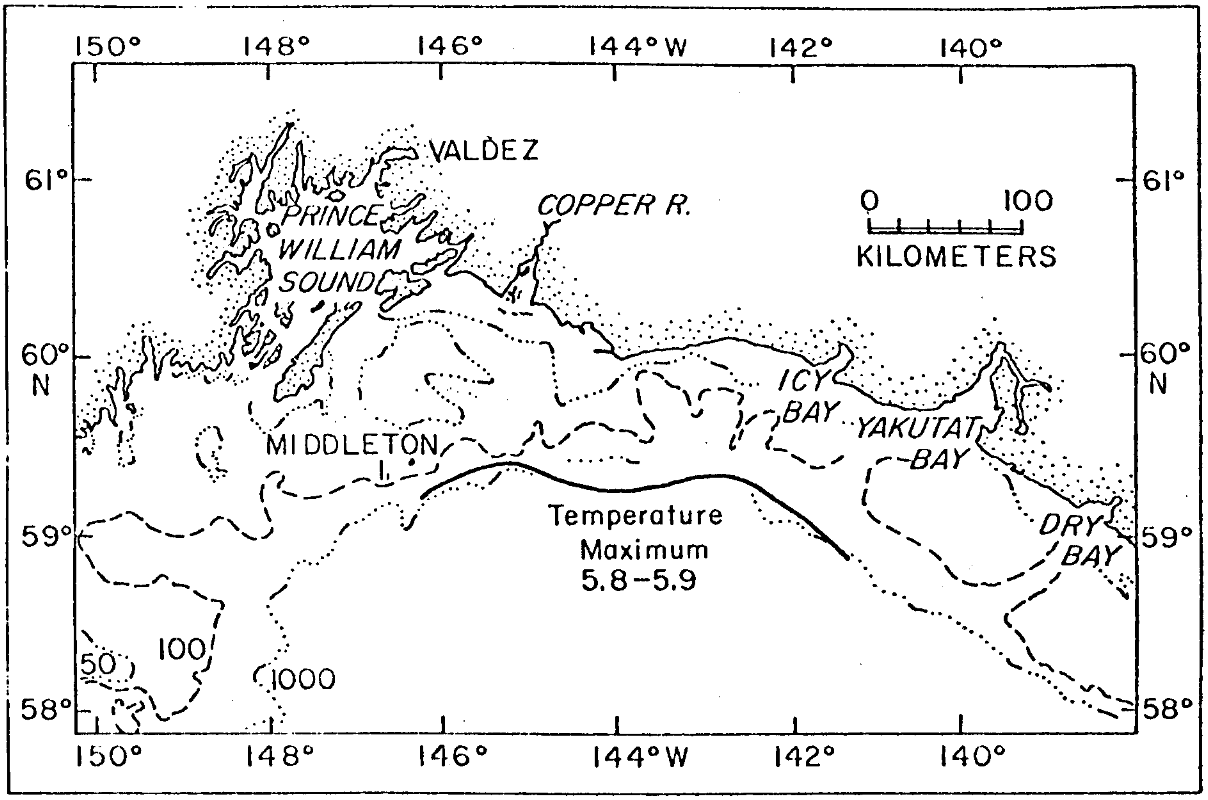

Figure 1.2 - Axis of subsurface temperature maximum used as an indicator of flow streamlines in the Alaska Current in the northeast Gulf of Alaska (from Galt and Royer, in press).

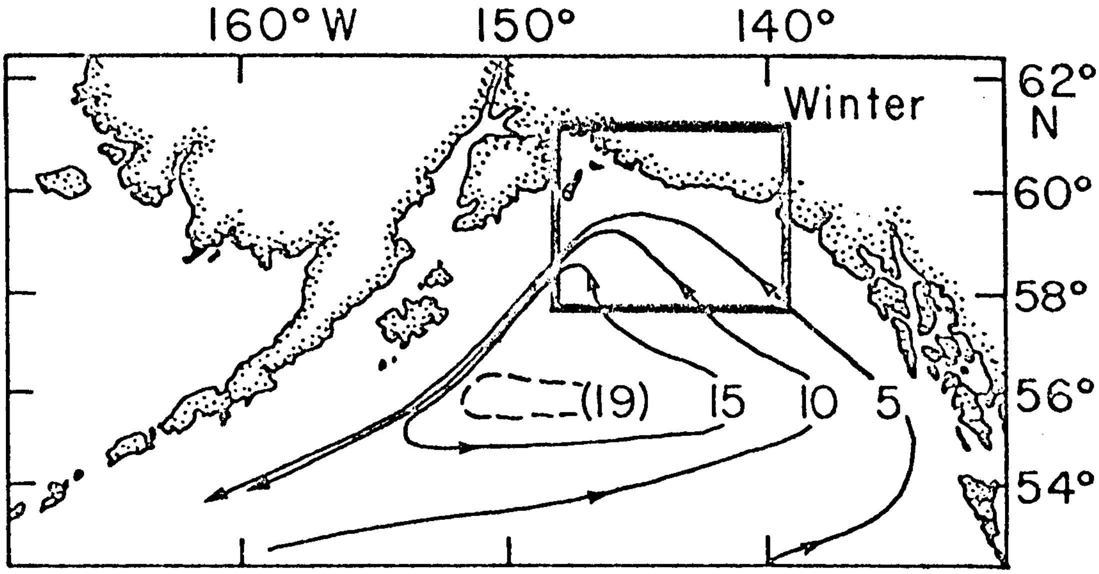

Figure 1.3 - Schematic showing winter water transport in million cubic meters per second computed from wind stress curl (from Ingraham et al., 1976). Rectangle shows our study region, approximately the area included in Figure 1.1.

Computed summer transports were, as opposed to winter transports, virtually zero. This is a consequence of decay of the Aleutian Low atmospheric pressure system during summer and concurrent loss of the wind stress and was also noted, using sealevel data, by Reid and Mantyla (1976). Ingraham *et al*. (1976) also noted considerable year-to-year variability in winter transport; values varied from as low as about 9 x $10^6 m^3 s^{-1}$ (in 1963) to as high as 25 x $10^6 m^3 s^{-1}$ (in 1969). We therefore, can expect considerable interyear variability in current speeds along the shelf break in our study region, as well as large intrayear differences.

The method of averaging used by Ingraham *et al*. (1976) in computing wind stress curl likely biased the computed transport toward the low side. Aagaard (1970) carried out wind-driven transport calculations for the Norwegian Sea, following the procedure of Fofonoff (1960), and analyzed the effect which varying the wind stress averaging period had upon computed transports. He found that the six-hourly mean wind stress curl yielded transports some four times greater than monthly mean curls, and attributed the difference to the importance of wind stress variability in affecting transport. Since the Gulf of Alaska is characterized by highly variable winter winds, it seems likely that the actual transports are larger than those computed by Ingraham *et al*. (1976).

Shelf break flow in the northern Gulf of Alaska gyre is important to continental shelf flow only inasmuch as energy from this flow is transferred onto the continental shelf. Since, by conservation of potential vorticity, flow will tend to follow isobaths and hence follow the shelf break, indirect means of transferring energy to the shelf must be found. One probability is that a longshore sea level slope connected with the longshore mean flow generates nearshore currents, in similar fashion to that discussed in the Gulf of Maine by Csanady (1974). Another is simply lateral friction transfer of mean flow energy onto the shelf; this might be manifested in the form of eddy-like features splitting off from the current and migrating shoreward as they dissipate energy along their paths as observed for the Florida Current (Lee, 1975). This process, discussed by Csanady (1975), would result in transfer of kinetic energy onto the shelf from the shelf break currents. A considerable volume of material has been written on lateral momentum transfer, and it is not our intention to dwell on this here but rather to emphasize that such processes exist and can be considered significant in the northeast gulf.

1.3.2 Local or shelf oceanographic processes

The study of shelf dynamics currently comprises one of the most active fields in physical oceanographic research. It is this field which deals with processes affecting circulation on the continental shelves. We make no attempt here to present a thorough discussion and bibliography addressing shelf processes; such a task would indeed be monumental. Instead, we present a brief discussion of those processes which *a priori* may be important to coastal circulation in our study region. We will neglect more esoteric concepts, particularly those whose importance has not been demonstrated by field observations in other regions.

Local winds are a mechanism of major importance for generation of currents on continental shelves. This must be judged especially true in the northern Gulf of Alaska, due to the severity of winter storms transiting the region. Mooers (1976) has given a useful summary of information concerning wind-driven currents on the continental shelves, including a set of references complete up to that date. He classifies locally wind-driven shelf motions as free and forced waves (continental shelf waves) and transient responses (storm surges). A discussion of coastal upwelling/downwelling regimes is included, along with discussion of near-surface and bottom mixed-layer development. All of these phenomena would be expected to occur along the shelf in the northeast gulf. Royer (1975) has characterized the northern Gulf of Alaska shelf as a region of coastal downwelling during winter due to prevailing easterly winds. During summer the wind field relaxes and a weak upwelling tendency is present. More recent observational and theoretical material has enriched our general knowledge of wind-driven shelf waves (Clarke, 1977; Brooks and Mooers, 1977).

The presence of lateral and vertical current shear, in conjunction with density gradients, can lead to certain types of instabilities which are revealed in the current records as periodic motions. Such motions have been detected in the Norwegian current by Mysak and Schott (1978), and we expect similar effects in the northeast gulf, an oceanographically similar region. In addition, the westerly-flowing current must interact with the local bathymetry. There is evidence in satellite imagery, for example, that lee vortices form on the downstream (west) side of Kayak Island (Muench and Schmidt, 1975). It is also likely that the current is perturbed as it passes over the irregular transverse ridge and valley shelf topography between Yakutat Bay and Kayak Island.

Considerable freshwater input to the northeast gulf coastal region occurs during early summer due to snow melt. A second runoff peak occurs in autumn due to local storms which can generate large amounts of precipitation. The resultant low salinity layer is advected westward along the coast (Muench and Schmidt, 1975), and contributes to baroclinicity there. Cessation of most of this freshwater input during winter, coupled with wind and thermohaline mixing, reduces baroclinicity and leads to vertically-uniform temperature, salinity structure on the shelf (Royer, 1975).

1.3.3 Meteorological conditions.

Meteorological conditions over the shelf region of the northeast Gulf of Alaska are subject to strong annual variation. During winter, atmospheric circulation over the Gulf of Alaska is dominated by a low pressure trough, the Aleutian Low. This trough effectively comprises a trajectory for severe cyclonic winter storms which originate to the west along the Aleutian Islands then migrate northeastward as they intensify. Typically, migration speeds are 12-25 m sec^{-1}. Wind speeds during passage of these cyclonic storms can be high; over about a 15 year period, speeds greater than 48 knots occurred for 1% of the time during November-February in the coastal region off Yakutat (Brower *et al.*, 1977). Though statistics are not complete, the time scales of these storms appear to be of order 5-7 days. During winter the coastal waters will, therefore, be subjected to sequential events of strong easterly winds which, average over periods of a month or more, yield a mean easterly wind stress.

During summer, the Aleutian Low dissipates largely and is displaced by an atmospheric high pressure system, the North Pacific High. While low pressure systems migrate eastward through the system, as in winter, they do not tend to intensify. As a result, winds over the shelf are generally weak and variable, though there is a net eastward component. As in winter, the wind field is event-dominated.

Recent research on near-coastal meteorology in the northeast gulf has clarified the role of the coastal mountain ranges and valleys in directing near-coastal winds (Reynolds *et al.*, in press). The mountains are sufficiently high that they cause bunching of the isobars. This leads to alignment of winds into a direction parallel to the coastline, an effect which has been observed in extreme cases to extend as far as 100 km offshore. Caution must therefore be used when using computed geostrophic winds such as those from Bakun (1975) in the region adjacent to this mountainous coast.

Reynolds *et al.*, have also investigated the effects of drainage, or katabatic, winds which are funneled seaward through the valleys in the coastal topography. These drainage winds may flow seaward as far as about 25 km, and can comprise considerable perturbations on the large-scale wind field within the coastal region. Particularly low temperatures can occur during these localized wind events, due to the continental source of air masses. Mean monthly winter temperatures in the coastal region off Icy Bay and Yakutat vary from a minimum of about -10°C to a maximum of about +8°C (in February-March; from Brower *et al.*, 1977).

As a general summary, we can say that winds over the shelf in the northeast gulf are easterly in winter, westerly and weak in summer, and dominated by events. Topographic effects can become significant in the near-coastal regions, therefore, geostrophic winds must be used with caution in such areas.

2. OBSERVATIONAL PROGRAM

In an ideal world, we could recreate the ocean in a computer model and generate the oceanic velocity fields from first principals. However, the real ocean is so rich in variability that *a priori* modeling is impractical. Rather, observational results must be accumulated and events documented in order that the models may be guided into correct approximations. In this manner, models may be used to extend observational results so that we may predict what will probably happen in a given situation.

The experimental program discussed here was designed with this philosphy in mind. The immenseness of the continental shelf in the Gulf of Alaska defies saturation of measurements. Instead, the program provided coverage sufficient to establish statistics of the velocity field at a few points (61 and 62). This was supplemented by process-oriented studies in areas which were selected so that either generic dynamics (Icy Bay Experiment) or site specific problems (west of Kayak Island) could be studied. The dynamical studies related velocity field to wind forcing, bathymetry, sea surface slope, and density field. The process experiments are required in order to interpret statistical observations.

2.1 The Overall Mooring Program

Current meter station locations are shown in Figure 2.1. Aanderaa RCM-4 current meters were used on taut wire moorings with an anchor and acoustic release at the bottom and 1,000-lb subsurface buoyancy float above the top current meter (Figure 2.2). A summary of location, duration and depth of each station's current meters is given in Table 2.1.

Current data were resolved into north and east components and low-pass filtered to remove high-frequency noise. Two new data series were then produced using a Lanczos filter (cf. Charnell and Krancus, 1976). The first series was filtered such that over 99% of the amplitude was passed at periods greater than 5 hours, 50% at 2.86 hours, and less than 0.5% at 2 hours. The second series, filtered to remove most of the tidal energy, passed over 99% of the amplitude at periods of over 55 hours, 50% at 35 hours, and less than 0.5% at 25 hours. This was resampled at 6-hour intervals and was used for examining non-tidal circulation.

Temperature and salinity data were collected using Plessey model 9040 CTD systems with model 8400 data loggers. This system sampled twice per second for simultaneous values of conductivity, temperature and depth. Data were recorded during the down cast using a lowering rate of 30 m min^{-1}. Nansen bottle samples were taken at each station to provide temperature and salinity calibration data. The data were averaged to provide 1-m temperature and salinity values from which the other parameters were then computed.

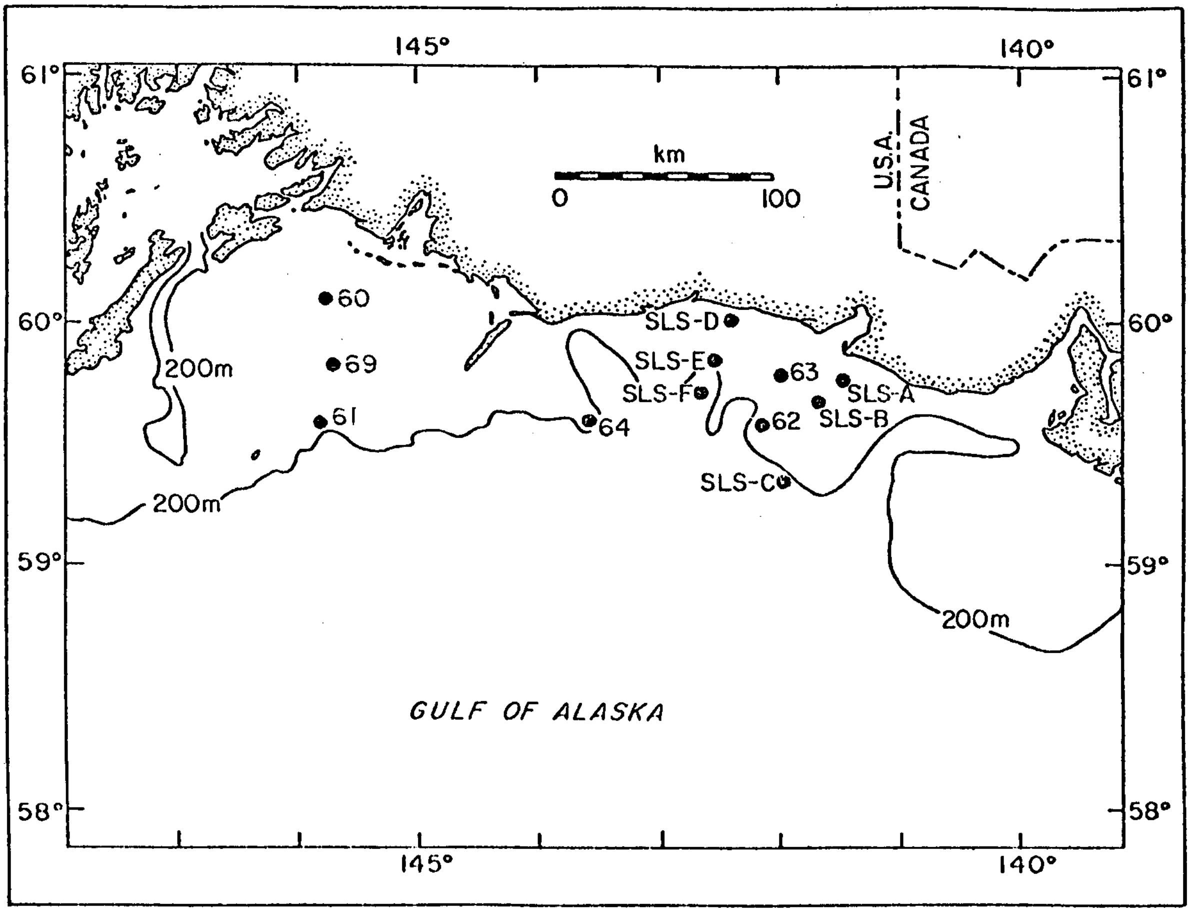

Figure 2.1 - Locations of current meter moorings in the northeast Gulf of Alaska.

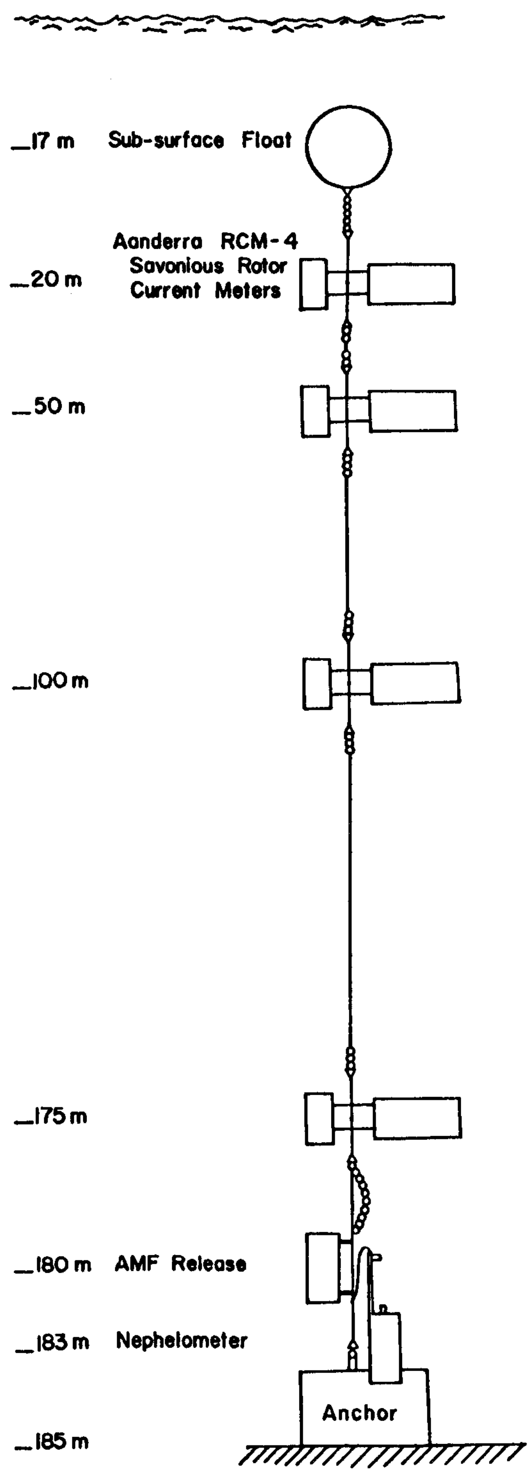

Figure 2.2 - Schematic diagram showing configuration of current moorings used in the northeast Gulf of Alaska (from Feely et al., 1978). Where pressure gauges were used, they replaced the nephelometer.

TABLE 2.1 Northeast Gulf of Alaska mooring deployment information

Sta. No.	LAT(N)	LONG(W)	DATES	Instr. Ser. No.	Instr. Depth
60A	$60^{o}05.4'$	$145^{o}50.7'$	7/2/74-9/3/74		
			"	625	20
			7/2/74-9/1/74	412	30
			7/2/74-8/29/74	392	50
			7/2/74-9/3/74	624	90
B	$60^{o}07.3'$	$145^{o}46.1'$	3/2/76-5/18/76		
			"	1815	20
			"	1451	50
			"	600	100
C	$60^{o}07.8'$	$145^{o}48.7'$	5/18/76-8/19/76		
			"	1679	20
			"	1675	50
			"	1676	90
61A	$59^{o}34.0'$	$145^{o}47.0'$	8/16/74-11/20/74		
			"	604	20
			"	601	30
			"	711	50
			"	603	100
B	$59^{o}33.9'$	$145^{o}53.0'$	3/11/76-5/17/76		
			"	1454	20
			"	1835	50
			"	1667	100
			3/11/76-3/23/76	1668	162
C	$59^{o}32.6'$	$145^{o}49.7'$	5/18/76-8/19/76		
			"	1687	20
			5/18/76-8/2/76	1804	50
			5/18/76-8/19/76	1805	90
			"	1807	163
62A	$59^{o}34.0'$	$142^{o}10.5'$	8/17/74-2/1/75		
			"	598A	20
			8/17/74-10/4/74	617A	50
			8/17/74-11/13/74	616A	100
			8/17/74-2/1/75	600A	178

TABLE 2.1 (cont'd)

Sta. No.	LAT(N)	LONG(W)	DATES	Instr. Ser. No.	Instr. Depth
62B	59°34.0'	145°13.5'	2/2/75-4/27/75		
			"	603B	20
			"	602A	50
			"	604A	100
			"	645B	184
C	59°33.6'	142°11.7'	4/28/75-6/4/75		
			"	598	20
			"	1451B	30
			"	1454A	50
			"	1455	100
			"	1456A	180
D	59°33.0'	142°05.3'	6/5/75-9/18/75		
			6/5/75-7/12/75	601	20 (Part I)
			8/2/75-9/18/75	601	20 (Part II)
			6/5/75-9/18/75	603	50
			"	1452	100
			"	602	178
E	59°33.0'	142°05.3'	9/19/75-11/20/75		
			"	1682	20
			"	1681	50
			"	1680	100
			"	1679	180
F	59°34.7'	142°11.4'	11/21/75-3/5/76		
				1811*	20
			11/21/75-3/5/76	1810	50
			"	1809	100
			11/21/75-12/15/75	1807	180
			"		
G	59°35.6'	142°06.0'	3/6/76-5/16/76		
			"	1683	20
			"	1684	50
			"	1669	100
H	59°37.6'	142°06.2'	5/16/76-8/21/76		
			"	1809	20
			"	1810	50
			"	1811	100
			"	1814	170

* Recording tape was installed improperly in meter, with backing contacting the recording head rather than the oxide side of the tape. Translation has not yet occurred due to weak recorded signal.

TABLE 2.1 (cont'd)

Sta. No.	LAT(N)	LONG(W)	DATES	Instr. Ser. No.	Instr. Depth
62I	59°38.1'	142°05.0'	8/22/76-10/21/76		
			"	1812	20
			"	1977	50
			"	2252	100
			"	2258	180
J	59°38.1'	142°06.1'	10/21/76-3/15/77		
			"	1805	50
			"	1804	100
K	59°38.3'	142°06.1'	3/16/77-6/8/77		
			3/17/77-6/8/77	1678	20
			"	1685	50
			3/17/77-5/22/77	1673	100
			3/17/77-6/8/77	1818	178
L	59°38.5'	142°07.0'	6/8/77-9/11/77		
			"	2160	20
			"	1987	50
			"	1833	100
			"	1804	180
63	59°46.6'	141°59.2'	2/2/75-2/21/75		
			"		3
63½	59°46.7'	141°59.1'	2/3/75-5/10/75		
			"		100
64	59°35.5'	143°36.6'	4/28/75-6/11/75		
			"	625A	20
			"	412B	30
			"	392A	50
			"	624B	114
69A	59°50.1'	145°41.9'	3/3/76-5/17/76		
			"	604	20
			"	1670	50
B	59°49.2'	145°43.3'	5/18/76-8/19/76		
			"	1824	20
			"	1828	50
			"	1829	87

TABLE 2.1 (cont'd)

Sta. No.	LAT(N)	LONG(W)	DATES	Instr. Ser. No.	Instr. Depth
SLSA					
#19	59°46.0'	141°29.0'	10/22/76-3/17/77		
			"	1824	20
			"	1810	40
SLSB					
#5	59°40.2'	141°39.7'	11/21/75-3/3/76		
			"	1830	50
			"	1828	75
#8	59°39.5'	141°39.2'	3/3/76-5/14/76		
			"	1672	49
			3/8/76-5/13/76	1673	74
#14	59°40.0'	141°40.0'	5/14/76-10/21/76		
			5/15/76-9/22/76	1833	50
			5/15/76-9/24/76	1830	77
#20	59°40.0'	141°40.0'	10/21/76-5/17/77		
			10/21/76-3/16/77	1675	50
			"	1828	75
SLSC					
#9	59°18.8'	142°01.6'	3/7/76-5/13/76		
			"	1677	51
			"	1987	100
			"	1988	240
#21	59°20.0'	142°07.0'	10/22/76-3/16/77		
			"	1811	100
SLSD					
#16	59°59.0'	142°19.0'	8/21/76-3/15/77		
			8/21/76-11/6/76	603	22
			8/21/76-3/14/77	1453	42
SLSE					
#17	59°49.5'	142°31.3'	8/21/76-3/15/77		
			8/21/76-2/24/77	1452	45
			"	1686	70
WIST I	59°47.5'	141°36.7'	3/17/77-6/8/77		
			"	1680	45
			3/17/77-5/19/77	1681	51
WIST II	59°39.9'	141°40.6'	3/18/77-6/8/77	598	58
			"	1812	83
			"	1813	98
			"	1817	105

2.2 Icy Bay Experiment

The plan for the Icy Bay experiment was to measure bottom pressure at six locations A-F (Figure 2.1) and to measure currents at several depths at B, C, and 62. These measurements span the continental shelf from the 50 m isobath to the shelf break at 250 m. Due to mooring and equipment failures, a complete data set was not obtained. Figure 2.4 lists the records analyzed from each location. In brief, 6 month (March-August) current records at B and 62 and pressure records at B, D, E, and F were obtained. Shorter current records (March-May) were obtained at C. In addition to the moored measurements, CTD stations were taken along the two lines A-C, D-F when instruments were deployed and recovered.

Instrumentation and processing used to measure the pressure fluctuation are described by Hayes *et al.*, (1978). The pressure gauge consisted of a 400 psia full-scale quartz pressure transducer manufactured by Paroscientific Corporation in Redmond, Washington, a temperature sensor, and a digital recording system. The gauges continuously averaged pressure and recorded at 15-min intervals. Temperature corrections were applied to account for the temperature coefficient of the pressure transducer. Final data series were low-pass filtered using the tidal eliminator filter of Godin (1972).

2.3 Kayak Island Experiment

The current meter mooring 60, 61 and 69 were deployed west of Kayak Island to study the complex flow downstream of this island. The full mooring set was in place from May to October 1976. It provided current meter data at 20 m, 50 m, 90 (or 100) m, and at the shelf break (station 61) 163 m. Earlier observations consisted of a winter deployment at 61. These moored observations were supplemented by CTD sections taken on deployment and recovery cruises.

2.4 Current Observations

Aanderaa current meters were used for the current measurements. Data were reduced using programs described by Charnell and Krancus (1976).

Moorings at B and C (cf. Figure 2.1) had the uppermost flotation at 45 m depth. This flotation was situated well below the surface in order to minimize contamination due to surface waves (Halpern and Pillsbury, 1976). However, mooring 62 which had a current meter at 20 m depth had flotation 17 m below the surface. There is some evidence that during high wind periods this record may be unreliable. Figure 2.3 shows unfiltered kinetic energy spectra of the current data at 50 m depth on B, C, and 62 for the period 15 March-15 April and on B and 62 for the period 15 July-15 August. Note the order of magnitude difference in the high-frequency energy level between B and 62 during the first period. In summer when winds were generally lighter, the high-frequency spectral levels

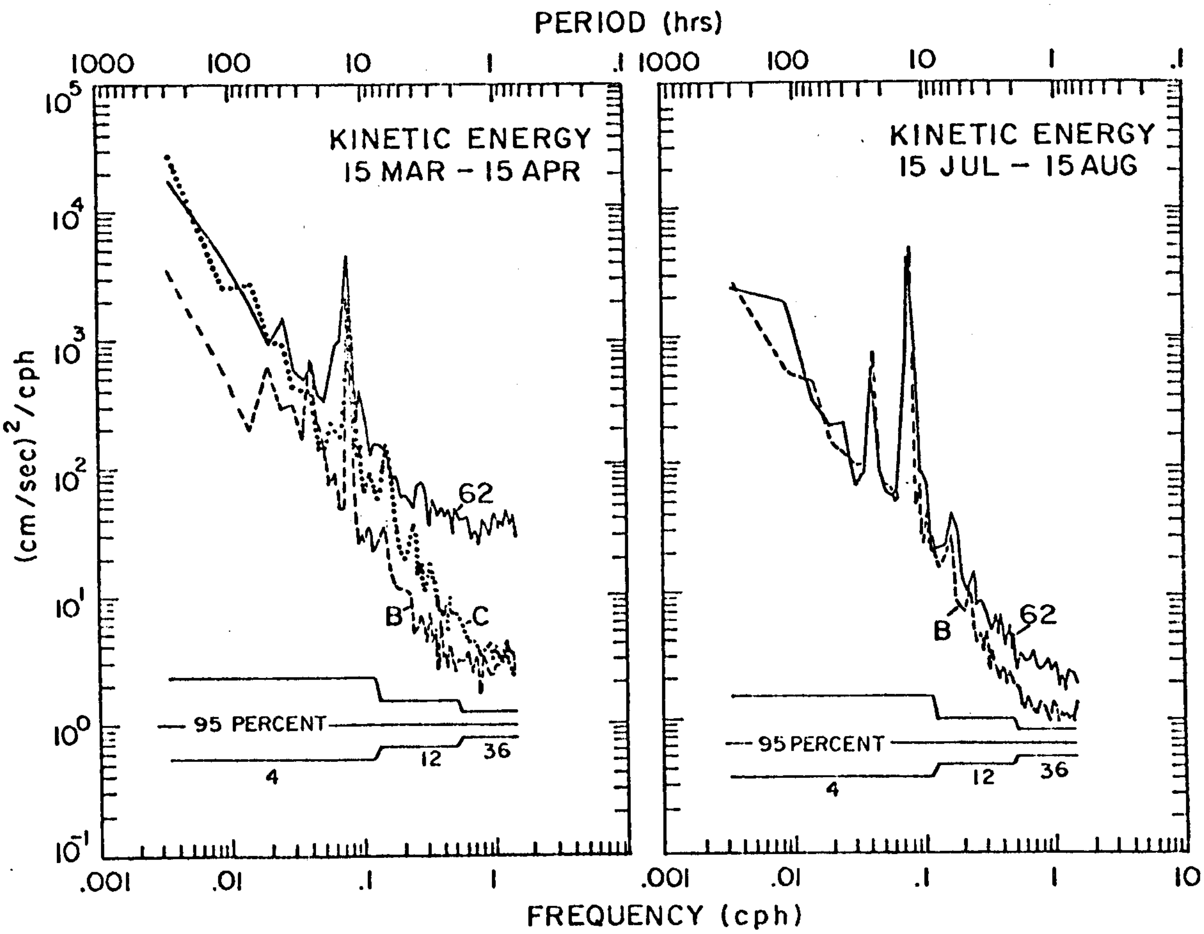

Figure 2.3 - Comparison of the kinetic energy spectra at locations 62, B, and C in spring and at B and 62 in summer. Moorings B and C had upper flotation at 45 m, mooring 62 had flotation at 17 m.

more clearly agreed. The high spectral energy observed in March is similar to that commonly seen when comparing current records obtained on moorings contaminated with high-frequency noise (Halpern and Pillsbury, 1976; Gould and Sambuco, 1975). Since we have no direct, nearby comparison, we cannot ascertain whether the low-frequency oscillations are also erroneous. However, results observed in mooring intercomparison experiments indicate that caution is advisable when interpreting speed data from station 62.

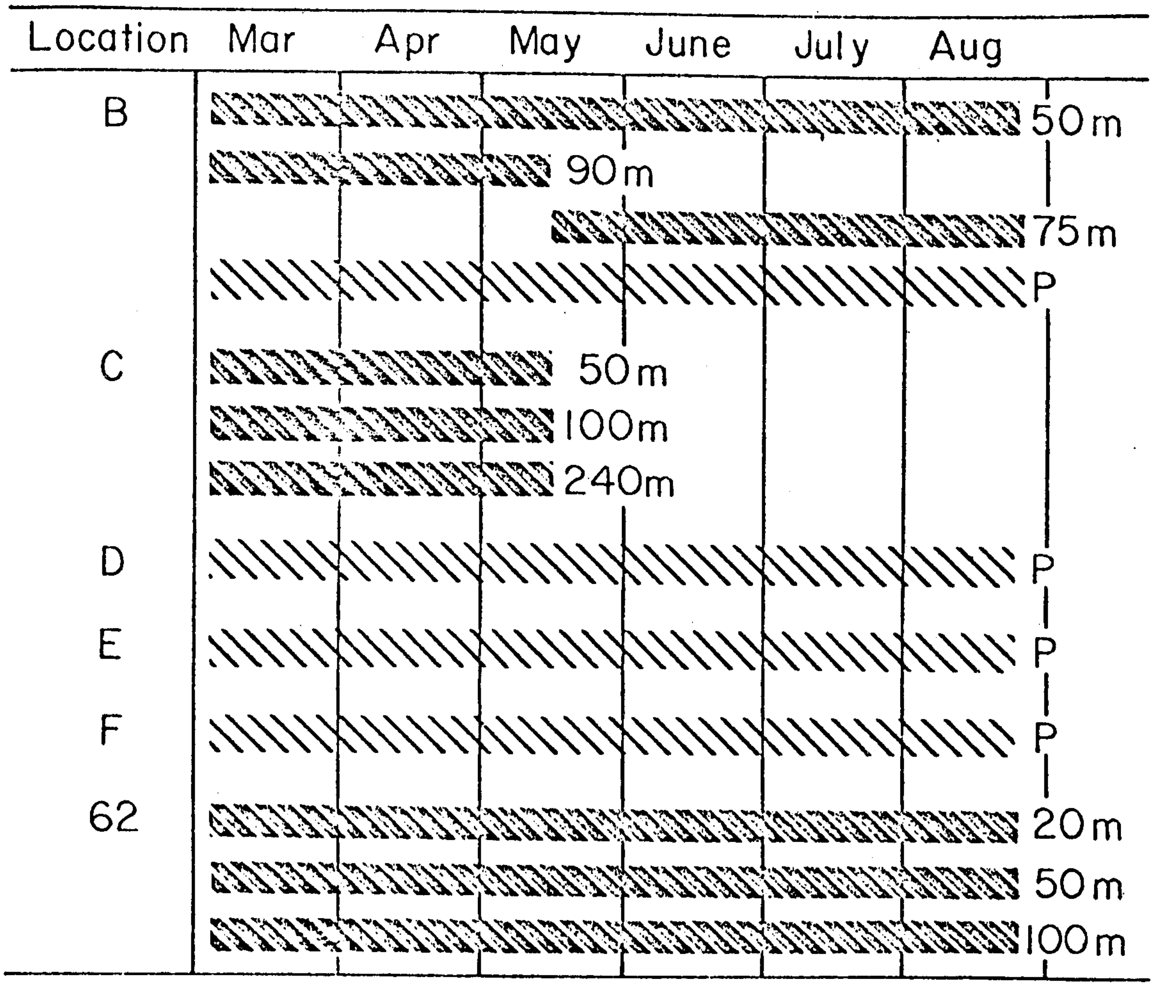

Figure 2.4 - Duration of data records at each location for the Icy Bay experiment. Current moorings are solid bars; pressure gauges are hatched.

3. LONG PERIOD TIME VARIATION IN CURRENTS

A major objective of the regional observation program was to obtain a long-term current time series from the seaward boundary of potential lease sites, i.e. the continental shelf edge. This mooring, 62, was designed with current meters located 20, 50, 100 and 180 m below the surface and was moored near the shelf-break (190 m depth) off Icy Bay (see Figure 2.1). Time distribution of current observation at different depths is depicted in Figure 3.1. In this Section, we describe this shelf break current on a variety of time scales and examine its variability. The next section (4) extrapolates the measurements in order to estimate extreme currents.

Monthly averaged currents are shown in Figure 3.2. These vectors were constructed from all speed and direction data from either a 15 min, 20 min or 30 min sample interval which were obtained during a given month. Two prominent features of flow were a persistent net drift toward the northwest (approximately longshore) and a strong seasonal speed variation. The vectors exhibited negligible directional shear except at the deepest observation level. The tendency for the net flow to veer to the right at the lowest observation level suggests bathymetric steering was important. This effect has been reported (Kundu and Allen, 1976) for flow over the continental shelf off the Oregon coast. A seasonal speed trend was present in all the records and was strongest at the upper level (20 m). During winter (approximately October through April) speeds at 20 m were typically 25 to 35 cm/s, decreasing in summer to 10 to 15 cm/s. Consistent net drift toward the northwest, with seasonally modulated speeds is characteristic of shelf edge flow in the Icy Bay region. Only one month (June 1976) was an exception to this generalization.

For periods less than a month, however, directional variability was a feature of the records. Hayes and Schumacher (1977) reported "eddy-like" features with a period of 1.5 to 3 days and an extended period (~12 days) during June 1976 when flow was reversed, i.e. towards the southeast. Variability at these time scales would have a significant impact on pollutant transport. Using a PVD presentation, we preserve the time history of the extended current reversal in Figure 3.3. This diagram was constructed from 2.86 hour filtered data resampled at 1 hour intervals. Between 17-20 May, there was an offshore pulse, followed by 15 days of predominantly longshelf flow with a small onshelf component. From 4-7 June, flow was onshelf, followed by three days of flow toward the southeast, and then onshelf flow for 2.5 days shifting to approximately southeasterly flow for 6 days, ending 19 June. The mean flow for the record segment described thus far was directed towards 030°T, which was substantially different than any of the monthly averaged flow vectors shown in Figure 3.2. The remainder of this current record indicated four more distinguishable direction changes between 19 June and 5 July. Each of these events were low speed (5 cm/s) and persisted for periods of approximately 3 days. The remainder of this record showed predominantly longshelf flow (13 cm/s) with a smaller (2 cm/s) offshelf component and was typical of summer flow.

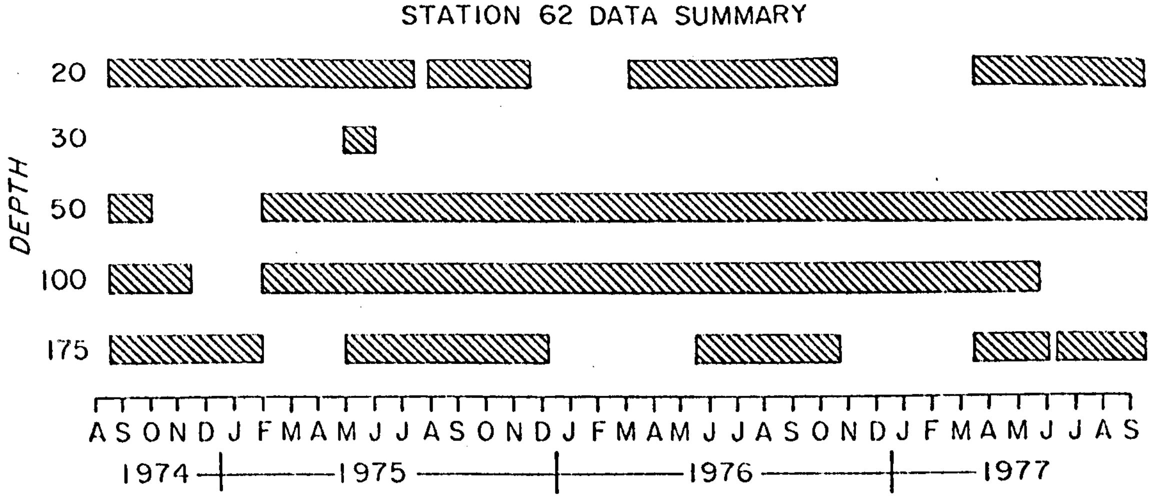

Figure 3.1 - Time distribution of current observations at different depths at station 62.

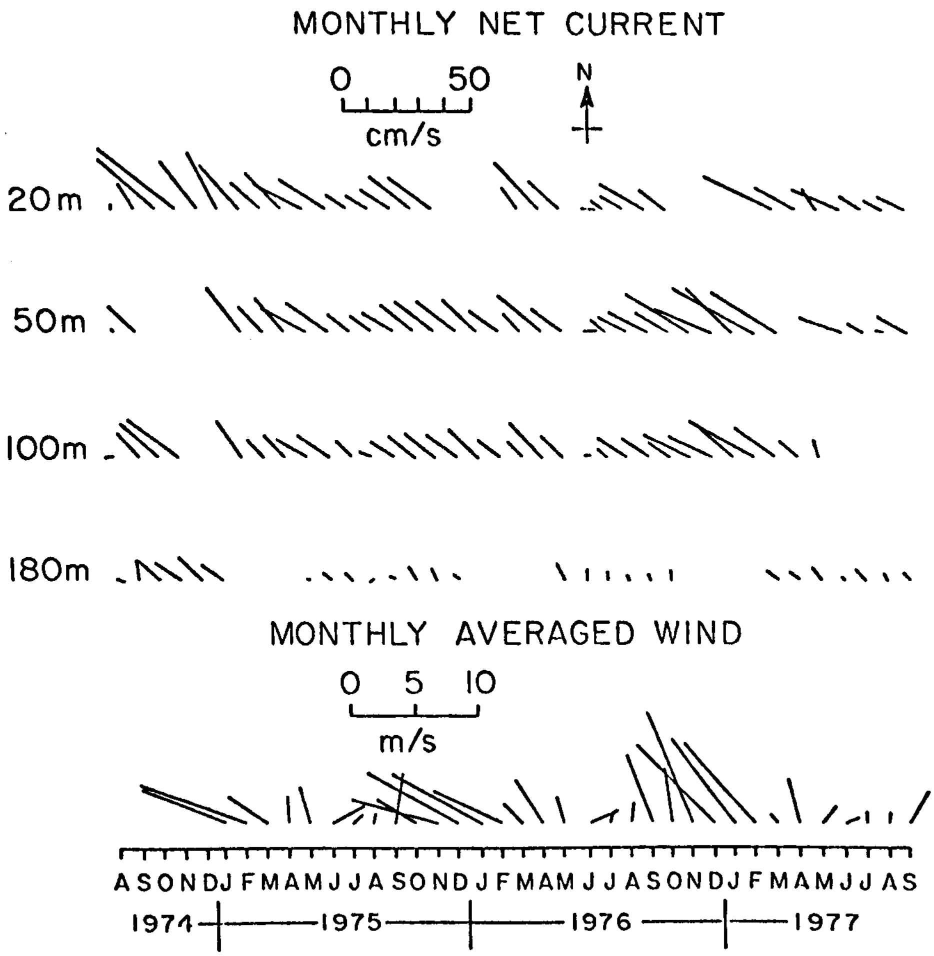

Figure 3.2 - Monthly mean vector-averaged currents at station 62 (upper) and monthly mean averaged Bakun winds at the same location.

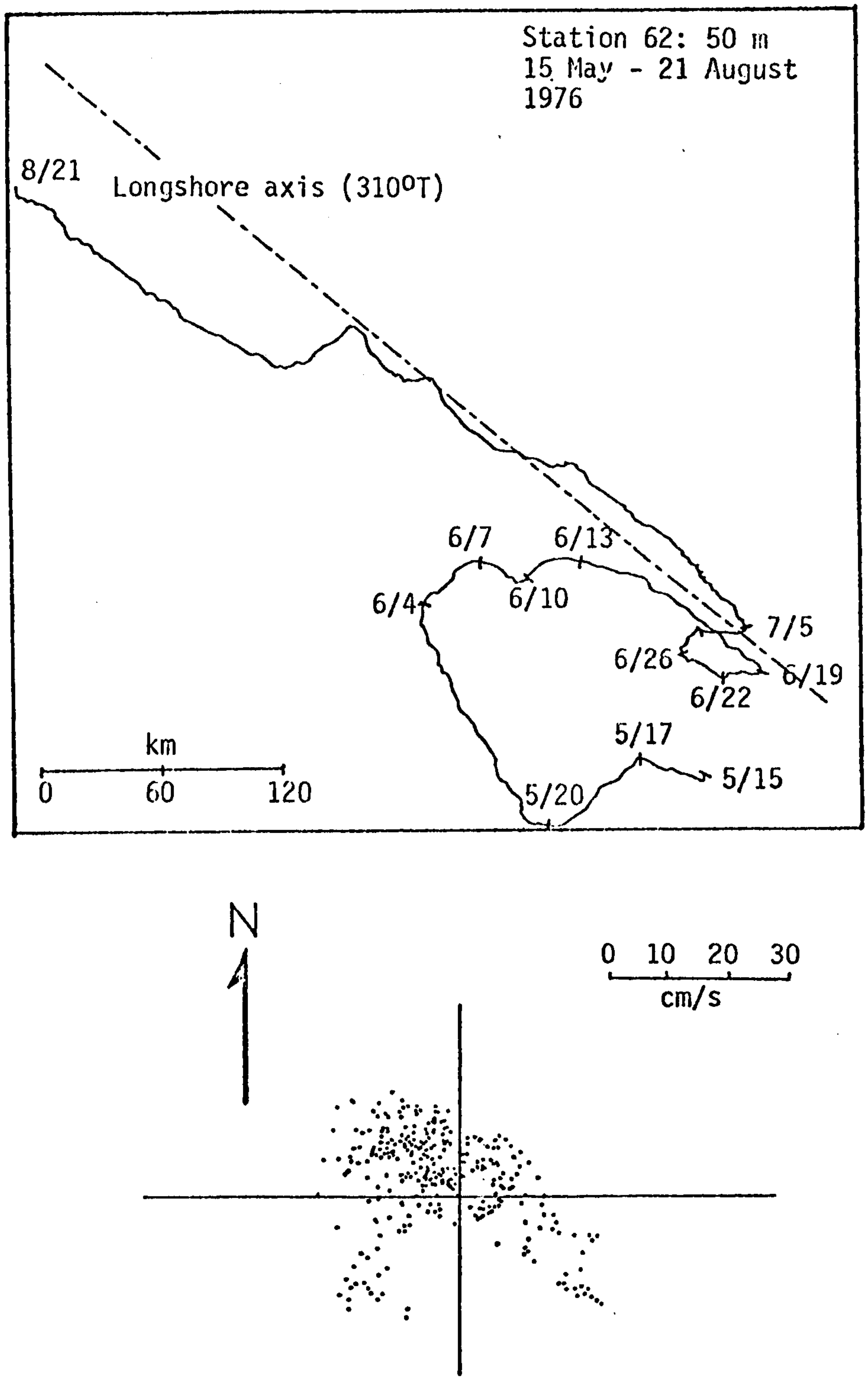

Figure 3.3 - Progressive vector diagram and scatter plot for station 62 during summer.

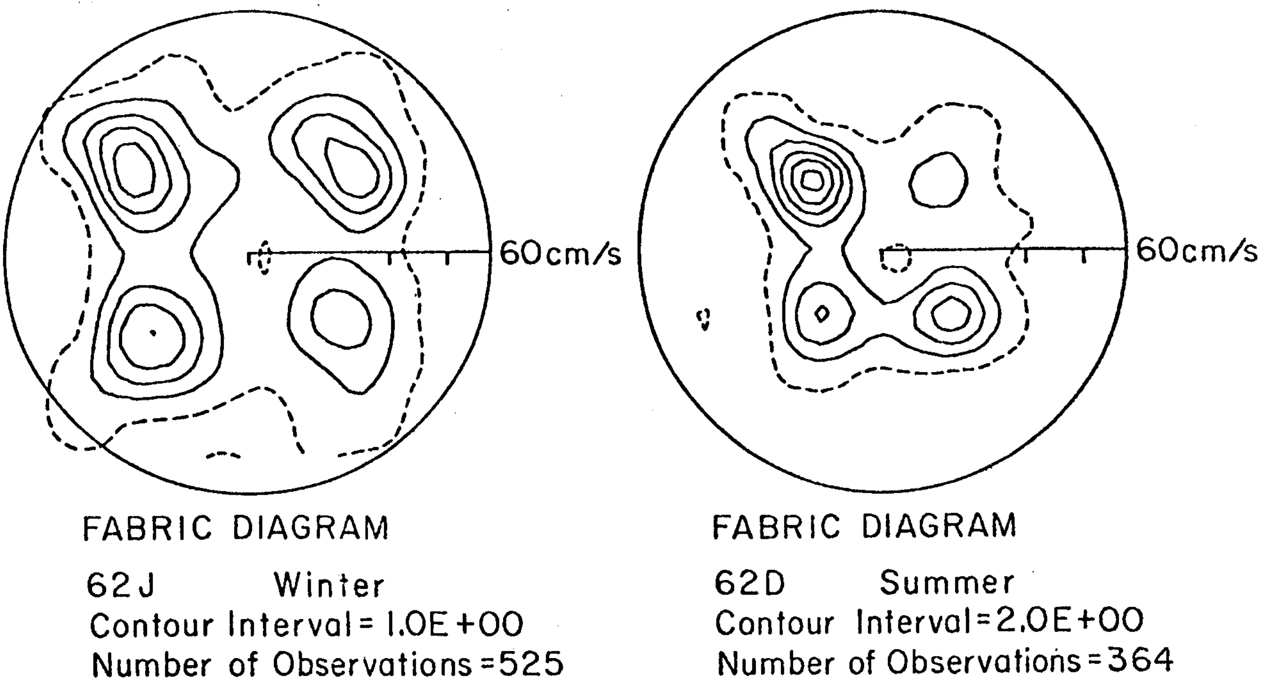

Figure 3.4 - Fabric diagrams showing directional trends in representative winter and summer current records at station 62.

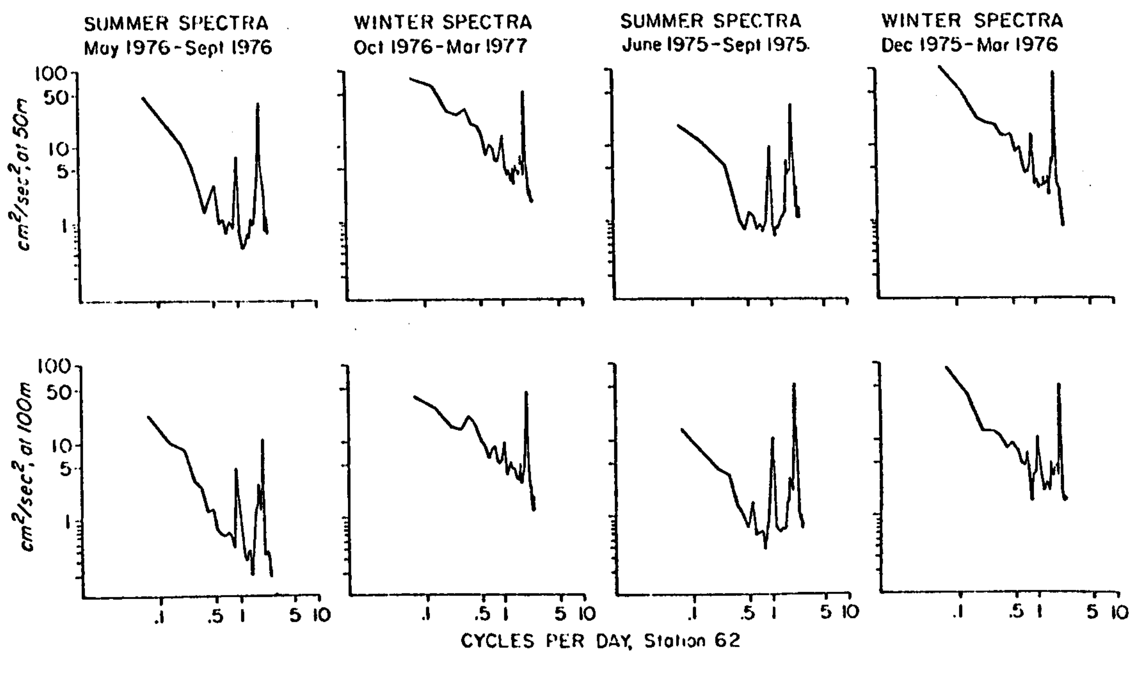

Figure 3.5 - Kinetic energy spectra for winter and summer observations at two depths at station 62.

We present the same record as above in a scatter diagram format in Figure 3.3. This plot was constructed from low-pass (35 hr) filtered data which was resampled at 6 hour intervals. The degree of variability is clearly shown in this format, although time history is lost. The record mean (5 cm/s at 315°T) was substantially less than the scatter and we note that the strongest speeds (30 cm/s) were directed toward the southeast. Another method of showing the variability of the current is the fabric diagram (Davis and Ekern, 1976). We apply this technique to the current records from 50 m depth during a winter and summer (62D) observation period (Fig. 3.4). The contours represent the density of observations by speed and direction. We note a higher density of contours in the northwest quadrant, but it is not dominant. The observations tend to be partitioned into longshelf and cross-shelf domains. The northeast quadrant contained a higher portion of observations during winter than during summer, reflecting seasonal onshore Ekman transport.

The partition of kinetic energy is shown in the spectral energy density diagrams (Figure 3.5) representing winter and summer regimes at 50 m and 100 m depths. During both regimes, semi-diurnal and diurnal tides dominated the short period (less than 30 hr) spectra. Using records from 62J and 62D as representative of winter and summer conditions, respectively, we note that the record variance increased by a factor of six between summer and winter. During summer, variance at the tidal frequencies accounted for approximately 60% of the total, while the variance for periods longer than 30 hours accounted for approximately 35% of the total. The remainder of the variance was contained in short period motions. In contrast, 70% of the total variance during winter was contained in the low frequency bands, with tidal frequency bands accounting for approximately 25% of the total. Thus, the seasonal trend established by the monthly averaged vectors is also apparent in the kinetic energy spectra.

In Figure 3.6, we present the average of the speeds squared as a further measure of kinetic energy, with envelopes of standard deviation calculated during each months averaging. Again, winter flow is shown to be more energetic than that measured during summer. The wide envelopes of the standard deviation suggest that mean flow was not an expected or common value. In fact, we emphasize that kinetic energy and vector components were highly variable, and that standard deviation sometimes exceeded the mean. To demonstrate this fact, we present a plot of the standard deviation as a percentage of the mean kinetic energy for the 100 m record (Fig. 3.7). In this presentation there was no seasonal trend, which suggests that flow was not consistently more uniform during one time of the year as opposed to another time.

The kinetic energy of the large-scale wind field in the vicinity of Icy Bay is shown in Figure 3.8. The wind data shown here were calculated on a 3° grid from atmospheric pressure data using a geostrophic approach. The seasonal nature of the wind signal appears well

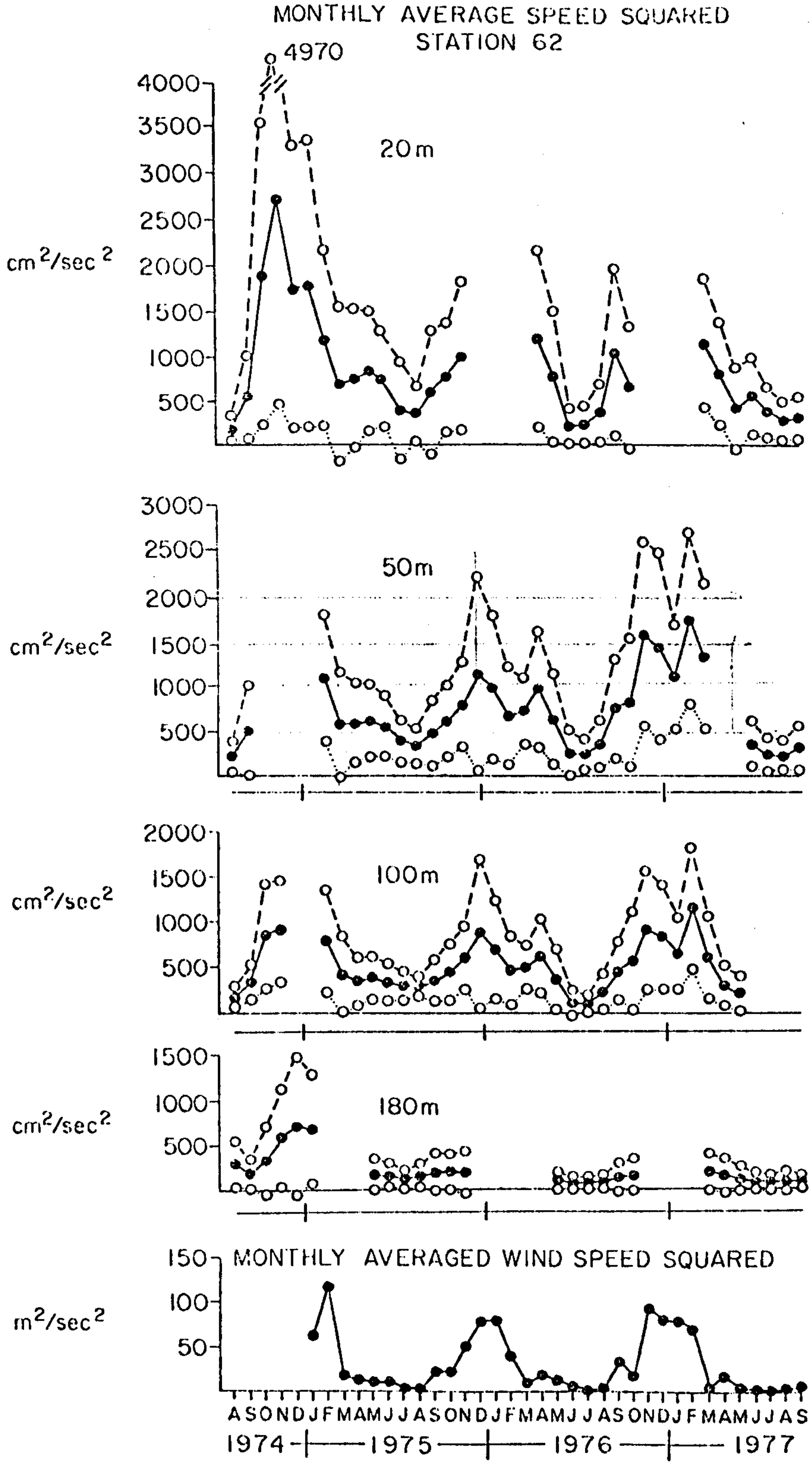

Figure 3.6 - Average of current and geostrophic wind speecs squared, showing standard deviation as envelopes.

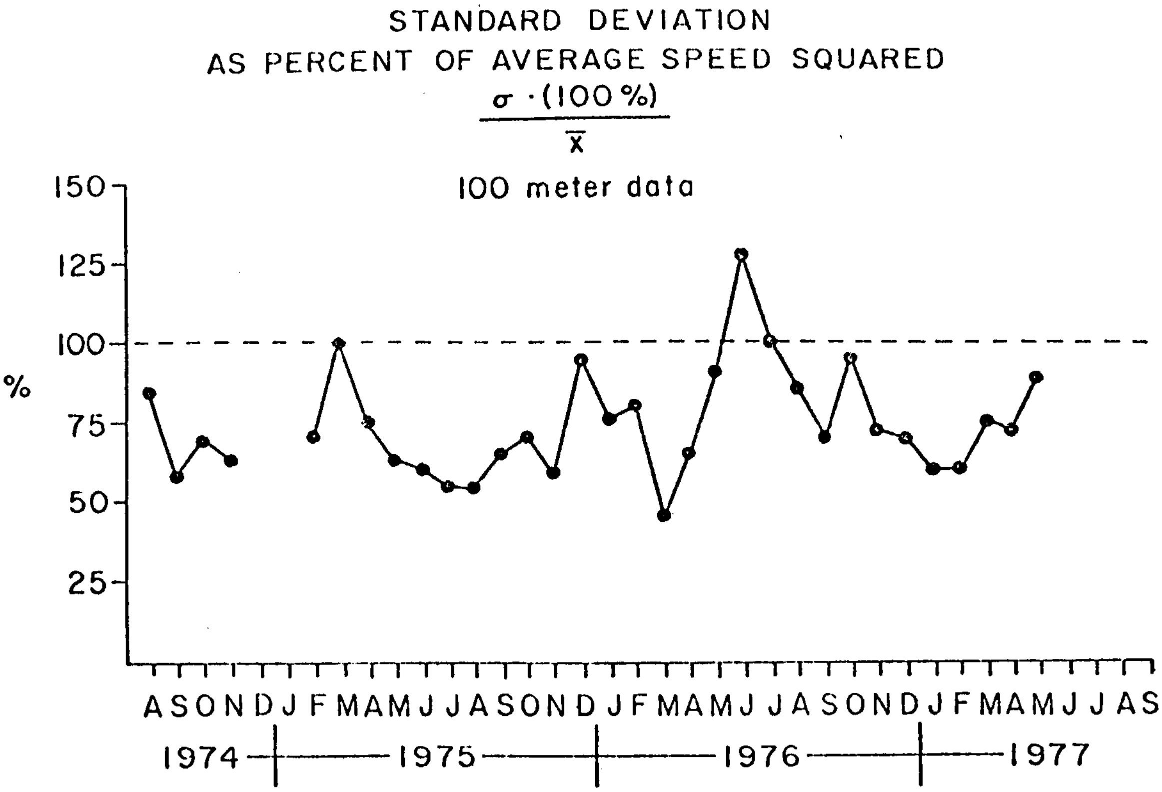

Figure 3.7 - Standard deviation of currents as percent of average speed squared, plotted vs. time.

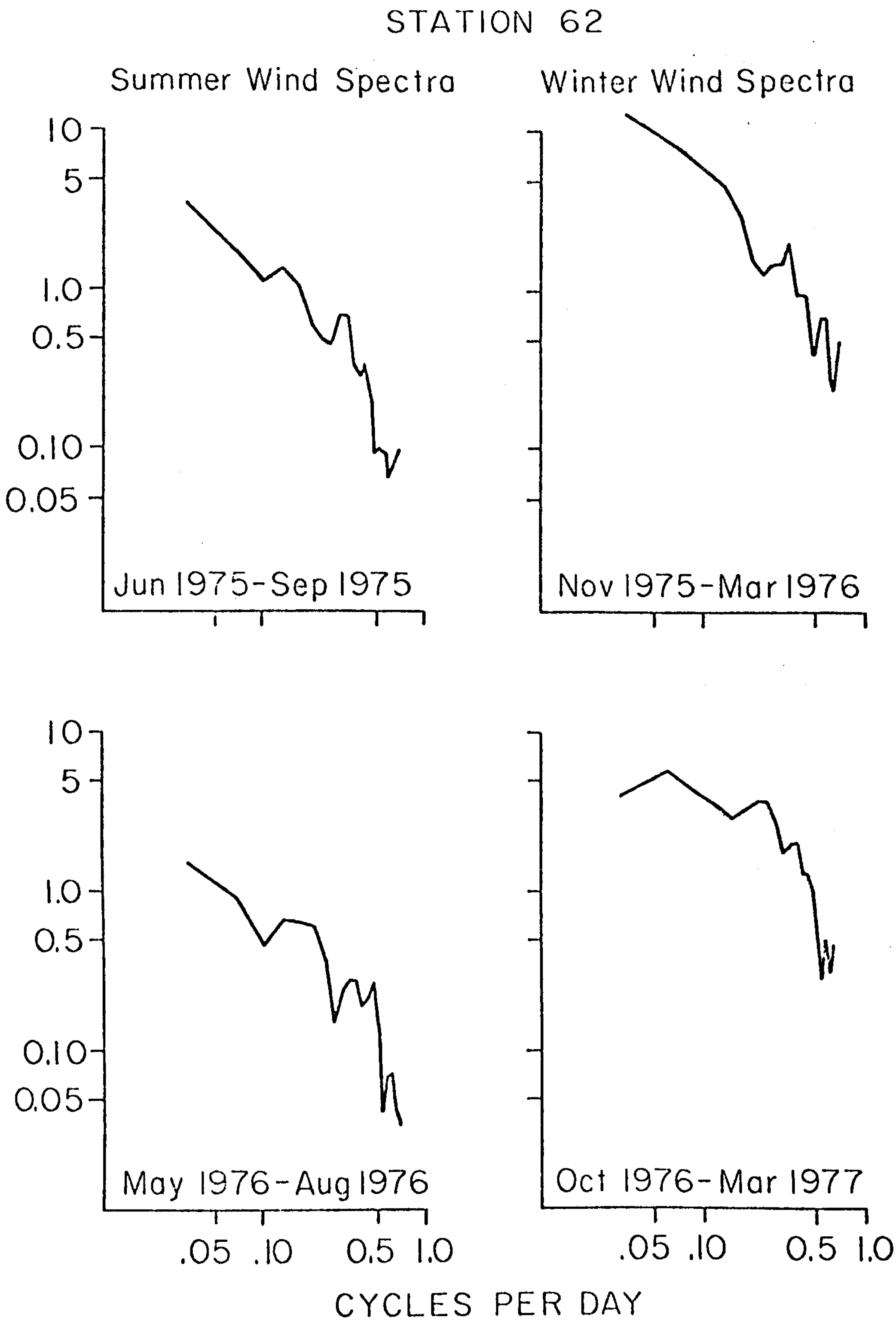

Figure 3.8 - Kinetic energy spectra for geostrophic winds at station 62.

correlated with that of the current kinetic energy. The monthly mean current was found to be correlated to the monthly mean wind speed with $r = 0.80$ at the 95% level. Clearly the winter intensification of the current along the shelf was due in large part to the intensification of the wind field.

In summary, we have shown that on time-scales of a month or more, flow was consistently toward the northwest with a seasonal trend in the speed: higher speeds obtained during winter and were two to three times greater than in summer. No consistent directional shear was evident between the 20 m and 100 m observations, and the kinetic energies at these depths were consistent. The response of the currents to seasonal influences was quite uniform throughout the water column. Only one month out of thirty deviated dramatically from this rather consistent picture. The observed variation in the monthly averaged currents and kinetic energy clearly coincided with the seasonal signal in the wind field. For time scales of the order of months, flow at the shelf-break off Icy Bay was well organized; however, for time scales between tidal periods and 15 days flow was observed to be quite variable. Over half of the sub-tidal frequency variance occurred in periods between 1.5 and 7.5 days. Such variability is clearly shown in current fabric diagrams.

4. EXTREME VALUE ANALYSIS APPLIED TO CURRENT DATA

The station 62 record was further analyzed in an attempt to describe extreme events. This analysis, while admittedly crude, provides an indication of maximum speeds likely in the vicinity of the shelf break.

4.1 Introduction

The 50 m and 100 m records at station 62 were continuous over 31 months, from February 1975 to September 1977. Figure 4.1 shows 5-day mean speeds over the August 1974 through May 1976 period. The 5-day mean speeds for the 20 m observations ranged from 9-57 cm sec^{-1} while for the 180 m observation the mean ranged from 8-28 cm sec^{-1}. The data clearly show marked seasonal behavior of flow associated with annual variation in storm activity described by Royer (1975). Data from the 50 and 100 m levels show an increase in the very low frequency flow from a mean of about 15 cm sec^{-1} in summer to a mean of over 25 cm sec^{-1} in winter; variation about this mean in winter is considerably higher than during the summer. This low frequency flow is due to the effect of the Alaskan Stream on shelf water. Response of shelf water to the passage of storm events during winter at this site is the subject of Hayes and Schumacher (1976).

The ensemble averaged energy spectra for available data at each of the four depths are shown in Figure 4.2. Tidal and inertial periods are indicated. Data from all levels show marked tidal peaks. However, the proportion of diurnal tidal energy is barely above background energy at the 20 meter level but increase with depth. Only the 20 m data show significant energy at the inertial frequency, though most of this occurred during the winter of 1974-75 when records from other levels were incomplete.

Local topography controls the direction of flow, which tends to parallel isobaths at this location. While there are seasonal as well as higher frequency variations in these trends the mean is stable and variations small. Generally, flow strongly adheres to this bathymetric constraint and tends to have a mean direction of around 315°T. Variation of maximum flow about this axis is apparently quite low since mean speeds along this axis for the 50 m data are only 5 percent less than those using mean speed alone. This directional stability allows analysis of extreme flow events to be carried out on a scalar rather than a vector quantity; consequently, subsequent discussion is related to extreme speeds.

4.2 Extreme Speed Analysis

It is desirable to summarize these data in some manner that allows a characterization of significant flow events. A promising technique is that of extreme value analysis. This technique has been used successfully on other environmental data sets and has a large volume

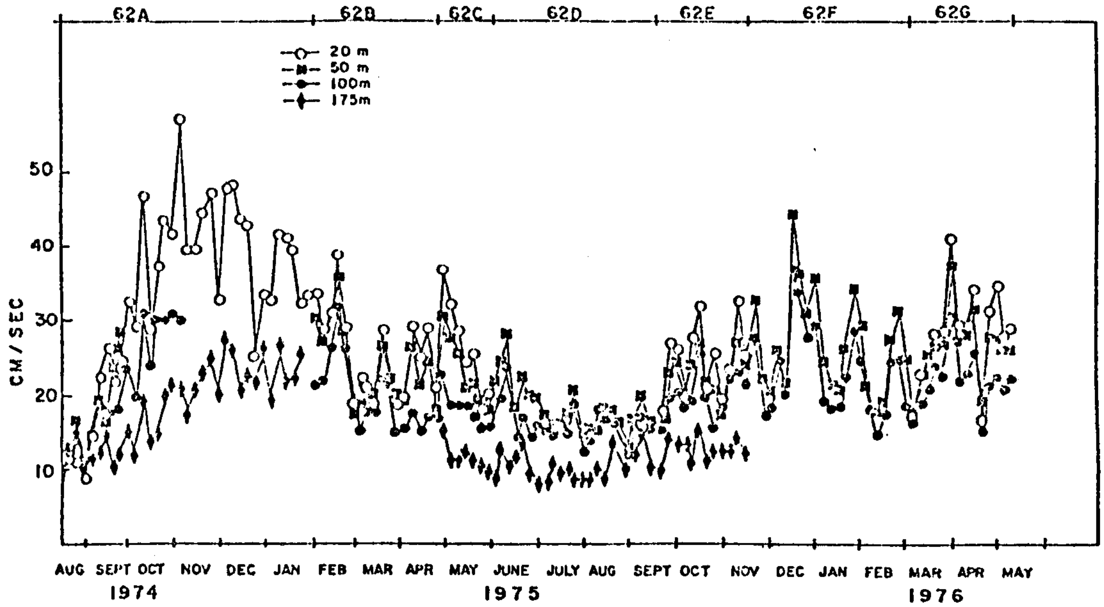

Figure 4.1 - Five-day speeds for data from station 62 from August 1974 through May 1976. Data from the 50-m and 100-m current meters were continuous from February 1975 through May 1976. Mean speeds were higher in winter than in summer.

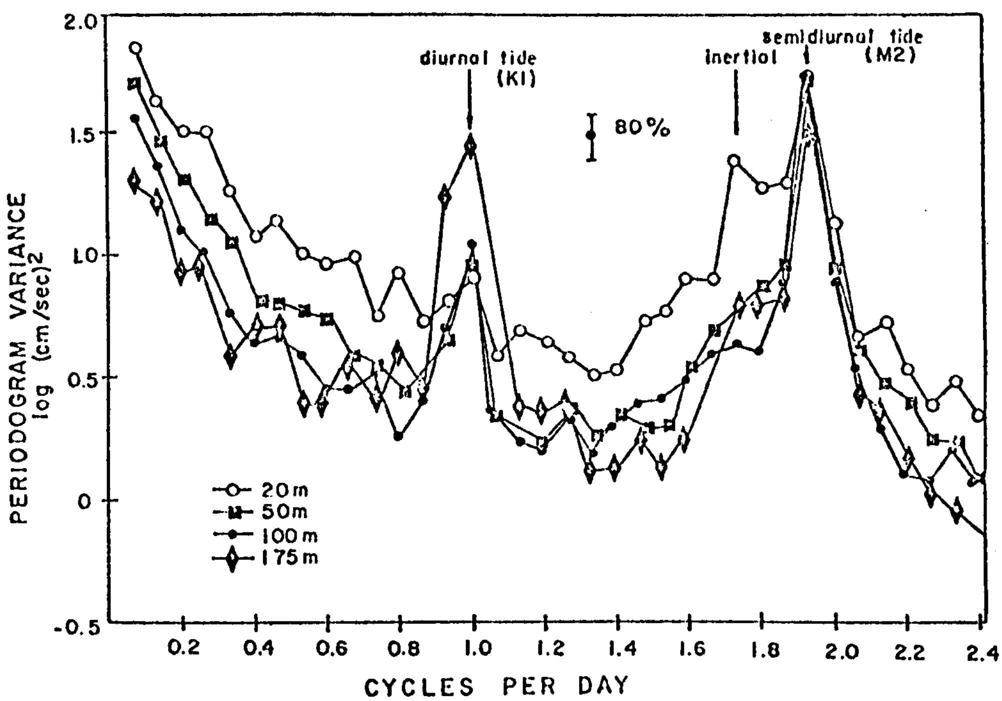

Figure 4.2 - Ensemble averaged energy spectra for the station 62 data. Tidal and inertial frequencies are denoted. Energy is given by logarithm of periodogram variance.

of literature describing its application. Gumbel (1954) presents the technique in detail and can be used readily for application. The theory supposes that magnitude of extreme flow events increases with the logarithm (ln) of observation time. Such a distribution fit through observed data allows defination of a return period for extreme values. This concept does not state that the specific value is the largest value to be obtained at a certain time, but only that it is the most probable largest value to be obtained within a certain time and gives limits within which this value may be expected to lie, with a certain probability.

The procedure is to section the record into N segments of length ΔT, select the largest value of each segment and order the new set by increasing magnitude. For this new data set a mean cumulative probability function, $P(s_m)$, is calculated for each ranked speed, s_m:

$$P(s_m) = \frac{m}{M+1} \tag{4.1}$$

The probability of the m^{th} speed equaling or exceeding other speeds of the set thus is equal to $P(s_m)$. A return period, T_R, may be defined for the m^{th} speed as:

$$T_R(s_m) = \frac{\Delta T}{(1-P(s_m))} \tag{4.2}$$

Significance of the return period is such that on the average, a speed s_m or greater will occur once every $T_R(s_m)$ days. Assuming the data follow the proposed logarithmic distribution, extreme speeds should vary linearly with a logarithmic function of $P(s_m)$. Gumbel's model for the logarithmic function is called the reduced variate, Y:

$$Y = \ln(-\ln(P(s))) \tag{4.3}$$

A straight line can be fit through these data using least squares methods; from the equation for that line, expected extreme speed as a function of return period and segment length can be calculated:

$$s = A+B \cdot Y = A+B \cdot (-\ln(-\ln(1-\Delta T/T_R))) \tag{4.4}$$

A measure of the fit of these data to the probability distribution can be determined from the calculated linear correlation coefficient, r. The percentage of total variation of the expected speeds that is accounted for by the linear relationship with observed speeds can be estimated as $100r^2$. Further, the confidence intervals can be computed using Student's t distribution. For our data, the confidence interval was chosen for a 95% significance level.

There are several restrictions to the technique that require attention and make interpretation for a small data set, such as represented by the Alaska current meter data, somewhat tentative. Application of statistical theory of extreme values is ideally suited to a large data set covering many years, such as occurrence of flood conditions in streams. For the Alaska current meter data we have 2.5 years of data with many storm events producing extreme flows during that period. The question immediately arises about representativeness of the extremes in this period. While conclusions based on 2.5 years of data offer guidelines, it must be remembered that additional data may modify actual values somewhat. Since obtaining long time series of current meter data is at best difficult, it is worth stretching this technique to the limit to examine typical ranges likely to be encountered in further observations.

Another important restriction is that the data extremes represent independent events. Since extremes are likely to result from storm events, this restriction can be ameliorated by examining extremes in segments of the record coincident with storm frequency. Major storm activity in the Gulf of Alaska is most likely to occur during winter, October through March, so we use data only from that time period to eliminate seasonal variability. Therefore, 6 months of winter extreme speed data represents a full year. Major storm activity during this period is reported to have an average period at roughly 5 days (Hayes and Schumacher, 1976), while tides have a spring-neap cycle of 15 days. To eliminate short period variability, we have chosen a segment length of 30 days.

With these restrictions in mind, extreme value analysis was applied to the Gulf of Alaska data. Figure 4.3 shows speed data for levels 50 m and 100 m of station 62 in such a representation. Extreme values are along the ordinate with return period in years along the abscissa. The fit of each line has a correlation greater than 0.96.

If one remembers the limitations imposed by representativeness of the sample and proper interpretation of the return period concept it is possible to extrapolate these data and estimate the extreme values likely to occur over longer periods. For example, data at the 50 m level suggest that with a return period of 5 years we are likely to observe an extreme speed of around 100 cm sec^{-1} within $\pm$ 6 cm sec^{-1}. Similarly, extreme speed at 100 m is likely to be 89 cm sec^{-1} $\pm$ 4 cm sec^{-1} for the same period of 5 years.

Webster (1969) suggested that the mean vertical speed profile has a power law dependence on depth. Were this situation universal, extreme speeds might similarly show this power law dependence. Using this assumption, and extrapolating the 5 year projections of the 50 and 100 meter depths, we might expect a 5 year speed of about 125 cm sec^{-1} at the 10 m level. This would be a lower bound, since it does not include wind effect in the Ekman layer.

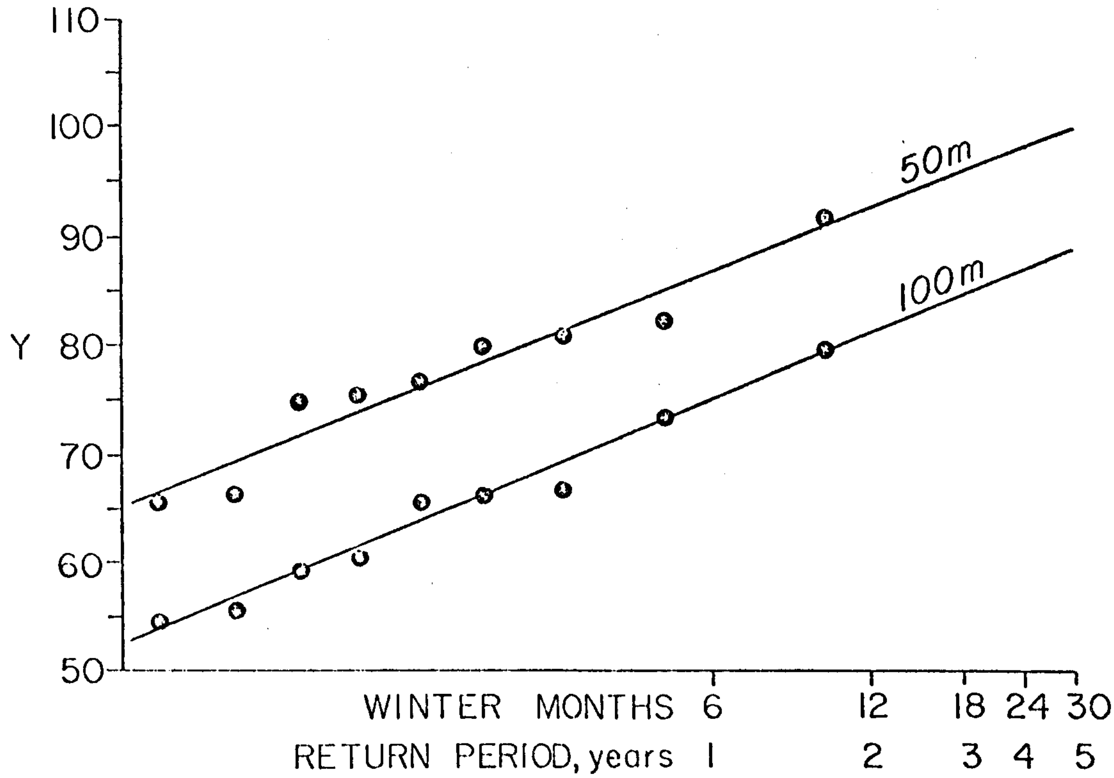

Figure 4.3 - Plot of projected extreme values Y vs. time at station 62.

4.3 Summary

We have carried out an analysis of projected maximum current speeds at 50 m and 100 m depths at station 62 using the technique of extreme value analysis. This has resulted in estimated maximum current speeds, over a five year period, of about 100 cm sec^{-1} at 50 m and 89 cm sec^{-1} at 100 m. It must be stressed that *these are estimates only*, due to the short (relative to inter-year variability) sampling period and resulting uncertainty as to whether or not the sampled data represent "normal" conditions.

5. CURRENT, BOTTOM PRESSURE, AND WIND CORRELATIONS OFF ICY BAY

In the previous two sections (3 and 4), we have examined time variations at a single location in the northeast gulf; station 62. It is now appropriate to examine circulation in the region surrounding this mooring, in order to place the behavior of currents at station 62 in perspective within a larger scale oceanographic milieu. In this section an analysis of the Icy Bay data set acquired during March-August 1976 is presented. The measurements consisted of moored current meter arrays, including station 62 (cf. Figure 5.1), moored bottom pressure gages, and geostrophic and observed coastal winds. The area included in this analysis is that bounded by the lines connecting moorings SLS A-F (Figure 5.1).

5.1 Introduction

The Icy Bay Experiment was designed to describe low-frequency ($f < .025$ cph or periods >1.7 days) velocity fluctuations and their relation to bottom pressure and wind variability. In addition to characterizing velocity and pressure fields across the shelf, the usefulness of long- and cross-shelf measurements of bottom pressure in interpretation of the flow field are considered. Several recent studies (Beardsley and Butman, 1974; Smith, 1974; Hayes and Schumacher, 1976) have noted close correlation between long-shelf current fluctuations and sea level measured at a nearby tide gage or bottom-moored pressure gage. A possible interpretation of this result is that much of the low-frequency variability is quasi-barotropic. If so, then direct measurement of cross-shelf bottom pressure gradient fluctuations can provide a time series of barotropic transport.

Allen and Kundu (1977) recently reviewed some dynamical features common to many time-dependent shelf circulation models. In the absence of forcing, equations for the depth integrated velocity components may be written:

$$v_t + fu = -gp_y \qquad (1)$$

$$fv = gp_x \qquad (2)$$

The coordinate system is shown in Figure 5.1; u is the cross-shelf velocity component shoreward, and v is longshore velocity to the northwest. Subscripts denote differentiation. In the longshore direction, velocity is geostrophically balanced; in the cross-shelf equations the acceleration term may be important. If baroclinic effects are small, then the bottom pressure gradients across and along the shelf approximate P_x and P_y. Velocity and pressure time series will be used to test equations (1) and (2).

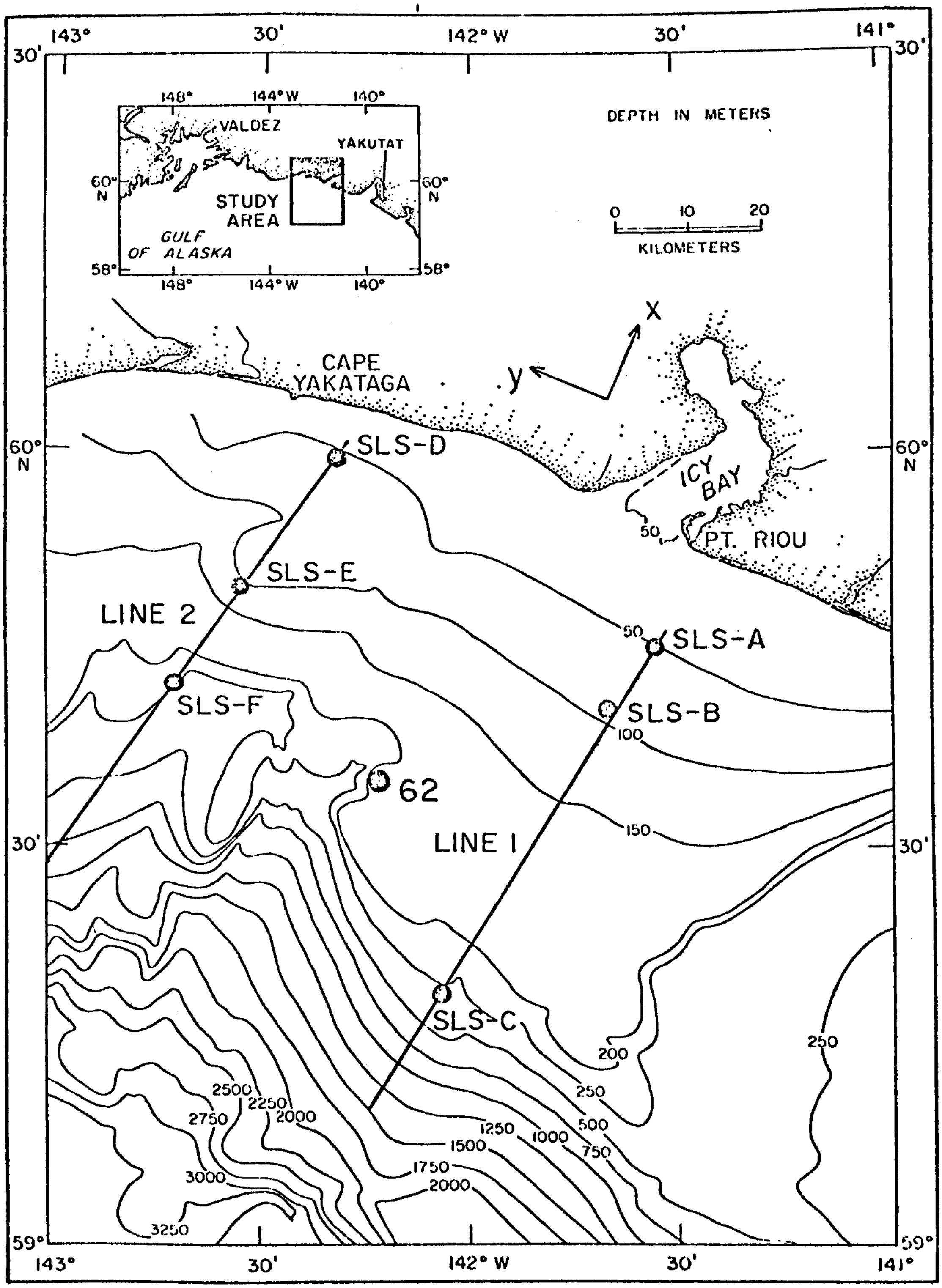

Figure 5.1 - Location of the experiment off Icy Bay, Alaska. The coordinate system indicates the alongshore direction, y, and cross-shelf direction, x.

5.2 Observations

5.2.1 Hydrographic observations

Temperature and salinity data were obtained from hydrographic sections made during March, May and August as discussed in section 2. Additional sections from Royer (1977) provided data in February, April and September. Representative density sections for winter, spring and summer are shown in Figure 5.2. The February and May sections show weak vertical stratification and downwelling. By summer, a shallow seasonal pycnocline had developed. Figure 5.3 compares temperature, salinity and density stratification at the three depth contours where bottom pressure measurements were made. Through May, little vertical gradient was observed at the 50 and 100 m locations. Salinity stratification largely determines the density gradient, and temperature gradient can be of either sign. At 50 m the temperature increased 3.2° from March to May. This increase was probably due to advection rather than seasonal heating. In August, a seasonal thermocline was seen at all locations. However, at 50 m, effects of river runoff produced a shallow, cold, low-salinity layer.

Surface water near the shelf break had a seasonal structure similar to that on the shelf. However, at about 150 m the permanent halocline of the Gulf of Alaska gyre occurs. This halocline can be expected to isolate deep from surface flow. Temperature in the halocline is variable and has been used as a water mass tracer (Royer, 1975).

5.2.2 Wind observations

Measurements of surface wind over the Northeast Gulf of Alaska region are available from Yakutat and as geostrophic winds calculated from 6-hourly synoptic surface atmospheric pressure analyses produced by Fleet Numerical Weather Central (Bakun, 1975). Yakutat winds are not representative of oceanic winds because of the mountainous coastal topography (Hayes and Schumacher, 1976; Reynolds *et al.*, 1976). The FNWC winds have received considerable attention recently (Hickey, 1977; Halpern and Holbrook, 1978). In the vicinity of Icy Bay the coastal mountains form a barrier to storms propagating to the northeast; the resultant packing of isobars may yield actual winds which are stronger than those inferred from large-scale (3° grid) pressure gradients used by FNWC. In addition, katabatic winds which blow offshore from the coastal glaciers have been observed near Icy Bay by Reynolds and Walter (1976). Such winds are not included in the FNWC calculation. With these reservations, the FNWC winds are presented in Figure 5.4. The wind vectors have been lowpass filtered (40-hr cutoff) and rotated into approximate onshore and longshore axes. Visually, the record can be divided into a spring period (March-May) when the wind is large and variable with a significant longshore component toward the west and a summer period (June-August) when the wind is smaller and often has an eastward longshore component. The vector mean wind

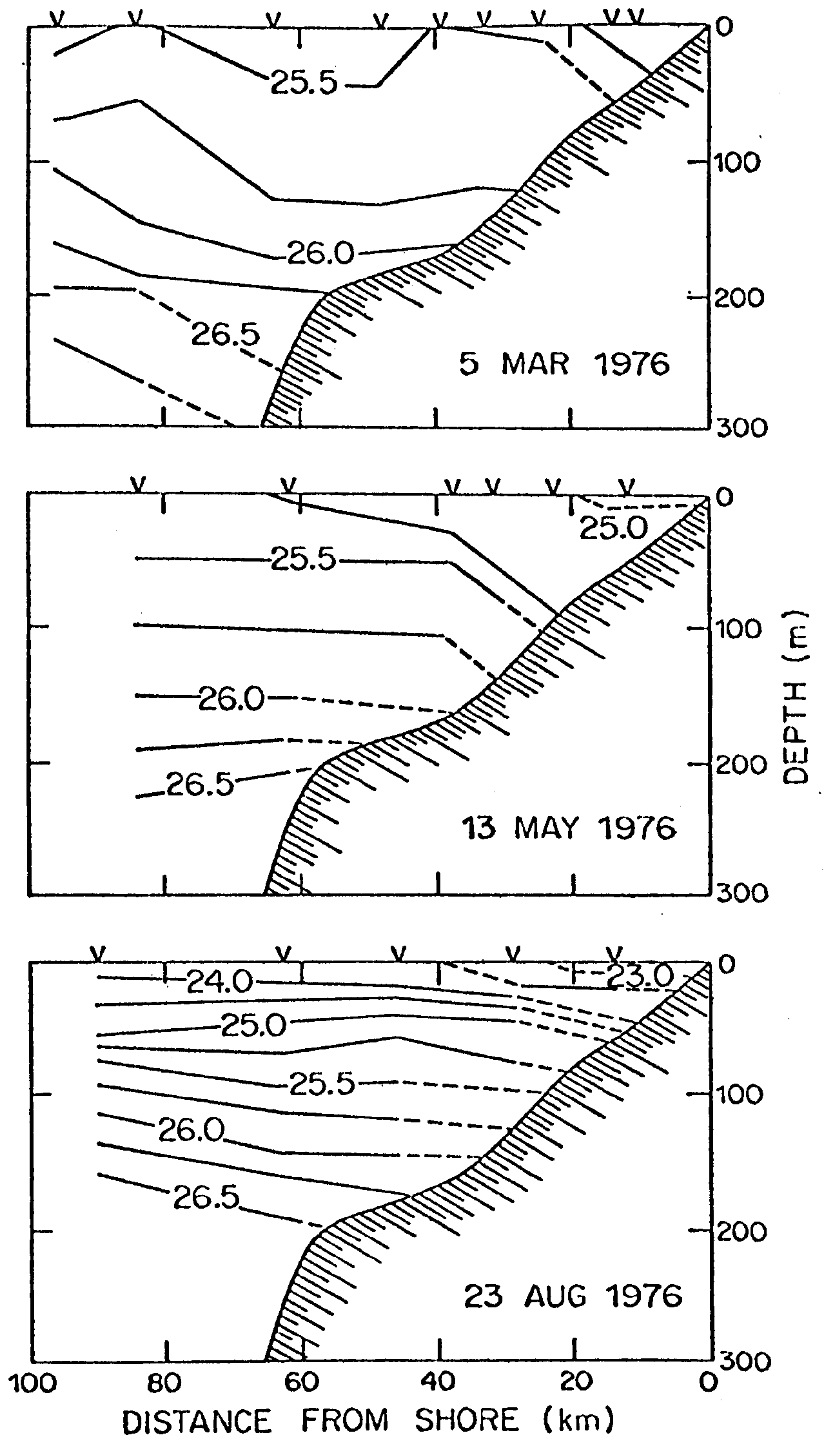

Figure 5.2 - Typical cross-shelf density sections for February, May and August.

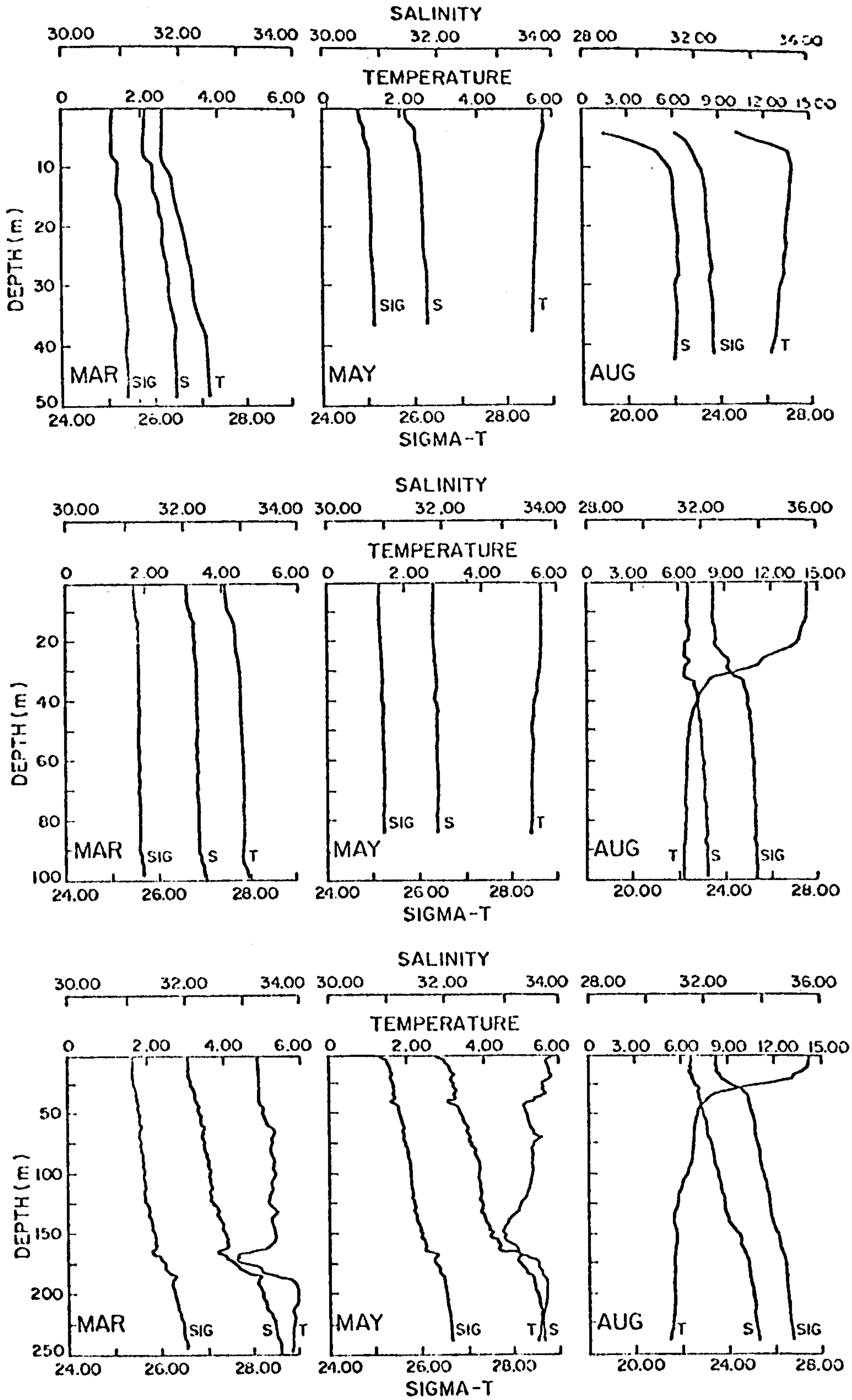

Figure 5.3 - Seasonal variation of the temperature, salinity, and sigma-t profiles at the three depths where bottom pressure was measured.

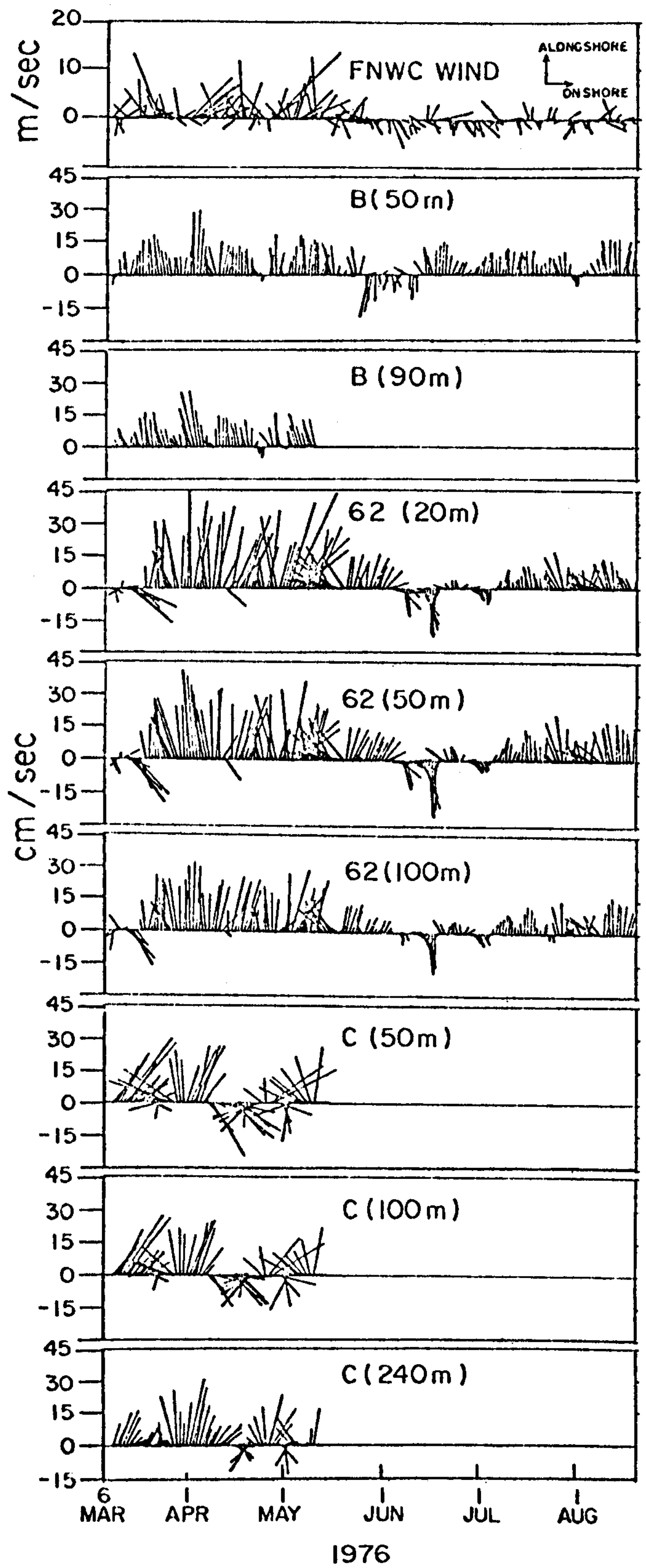

Figure 5.4 - FNWC vector time series for the calculated wind and measured currents. All vectors have been low-pass filtered and rotated into alongshore and onshore axes as discussed in the text.

speed was 5.8 m/s in spring and 2.9 m/s in summer. This variation is typical of seasonal wind patterns as described by Ingraham *et al.* (1976).

5.2.3 Bottom pressure observations

The low-pass filtered (0.025 cph cutoff) time series of atmospheric pressure at Yakutat, adjusted sea level (atmospheric pressure in millibars added to sea level in centimeters) at Yakutat, and bottom pressure at sites B, D, E, and F are shown in Figure 5.5. Mean pressure calculated over the record length was subtracted from each time series. At site B, the total record was constructed by joining records from two consecutive deployments; at other locations the data are continuous measurements by a single gage.

In Table 5.1 the mean trend and detrended variance are given for filtered bottom pressure records. Adjusted sea level from Yakutat was not included in this table because tide gage data from the Yakutat station had numerous gaps. However, the Yakutat series was similar visually to bottom pressure recorded at site D. Mean trend, based on least squares linear regression, varied between sites. At the 100 m isobath (sites B and E) the trend was negligible; however, at 50 m (D) and 250 m (F) the trend was about 1 cm/mo. These trends were not constant throughout the record.

The measured bottom pressure is composed of several terms related by the equation:

$$P_B = \bar{P} + P_a + g\int_0^H \rho^1(z,t)dz + \rho_o g\eta \qquad (3)$$

$\bar{P}$, mean pressure at the mean depth H of the gage, can be ignored since we are only concerned with time-dependent pressure. P_a, the atmospheric pressure, is often assumed to be compensated for by the inverse barometer effect (i.e., an equivalent change in sea level). However, if sea level compensation is depth-dependent, then atmospheric pressure fluctuations will produce changes in the bottom pressure gradient. Such an effect is difficult to isolate, since winds accompanying the changes in P_a are expected to dominate (Buchwald and Adams, 1968). The third term in (3) represents the density effect. Local changes in the density distribution could affect the measurement of bottom pressure. Finally, the last term represents pressure changed due to sea level variation η. Using equations (1) and (2), this term can be related to the barotropic current. Thus, before assigning dynamical significance to the measured bottom pressure gradient, the influence of all other terms must be considered.

The observed trends can be compared with water density variations at each site. CTD casts near each mooring showed an increase in dynamic height from spring (February-April) to summer (August-September) of 12.5 cm, 6.6 cm, and 4.8 cm at the 50, 100 and 250 m isobaths, respectively. If sea level were constant over this period,

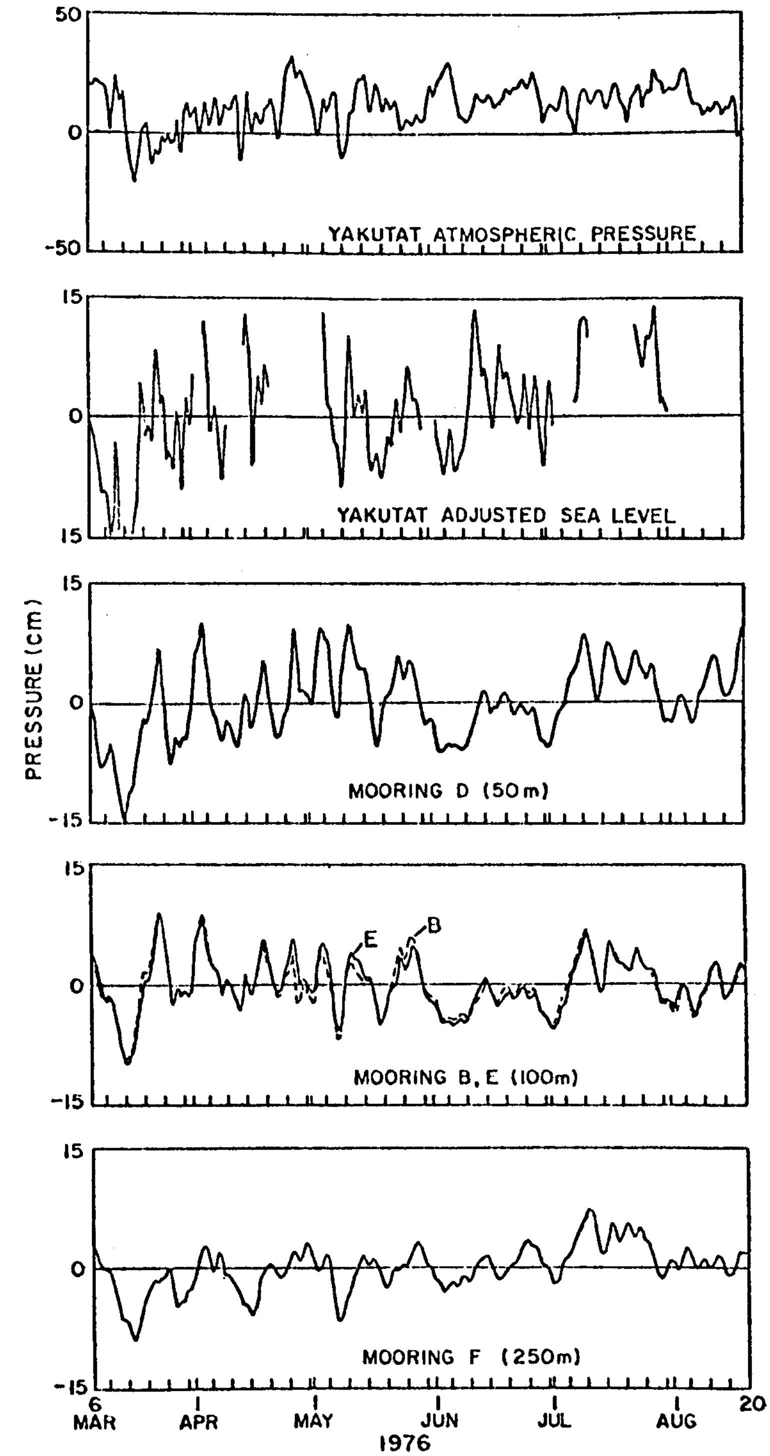

Figure 5.5 - Time series of atmospheric pressure and adjusted sea level at Yakutat and of bottom pressure at B, D, E, and F. All records have been low-pass filtered. The gaps in adjusted sea level are caused by missing tide gauge data. It is assumed that 1 cm = 1 mb.

Table 5.1 - Statistics of bottom pressure for the period 6 March-20 August 1976. The variance was calculated after removing the linear trend.

Location	Variance (cm^2)	Trend (cm/mo)
B	11	0.04
D	19	0.99
E	11	0.05
F	5.8	0.93

then bottom pressure at each site would show a decrease comparable to the dynamic height increase. None of the bottom pressure records show such a decrease, thus shallow water density changes do not appear important in local sealevel variations.

Reid and Mantyla (1976) found good agreement between seasonal changes in Yakutat adjusted sea level and deep water density variations off the continental shelf. Based on historical data, monthly mean adjusted sea level at Yakutat increased by 5 cm between April and August. This change is similar to the pressure trend observed at 50 and 250 m. Using CTD observations in 1,500 m of water, we calculated a spring-summer change in dynamic height between 1,000 dbar and 50, 100 and 250 dbar surfaces to be 6.2, 5.1, and 4.2 dyn cm, respectively. These observations support the conclusion of Reid and Mantyla (1976) that seasonal sea-level changes observed on the shelf are related to the deep water density field.

Bottom pressure variance across the shelf varies inversely with water depth H (Fig. 5.6). If one assumes that bottom pressure fluctuations represent sealevel oscillations associated with a nondivergent wave, then the inverse relation of pressure variance with depth implies that the depth-integrated horizontal kinetic energy is constant across the shelf, i.e., $V \sim H^{-1/2}$. As pointed out by Kundu and Allen (1975), theories of continental shelf waves lead to such a velocity-depth relationship.

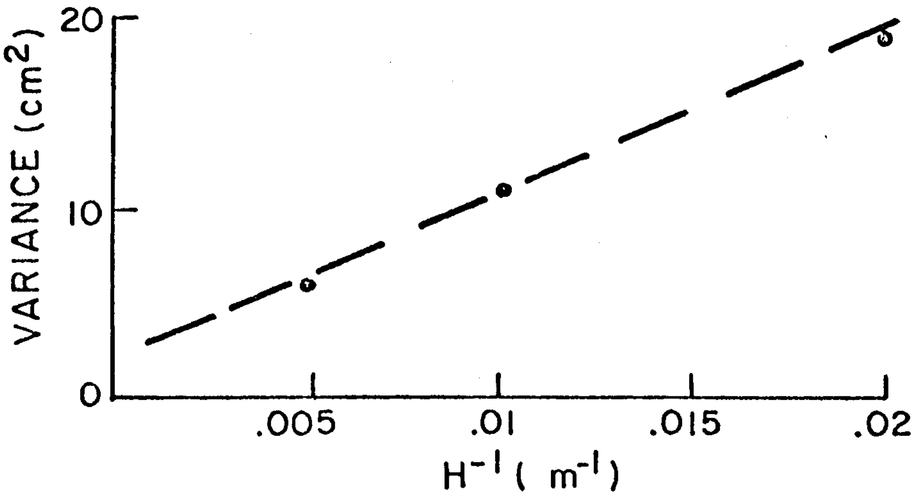

Figure 5.6 - Low-frequency bottom pressure variance plotted as an inverse function of water depth H. A linear trend was removed from the time series before computing variance.

5.3 Analysis

5.3.1 Current time series, vertical and cross-shelf structure

Current vectors were rotated into an approximate cross-shelf (u) and along-shelf (v) coordinate system determined from principal axes of the data (Fofonoff, 1969), local bathymetry, and the mean velocity vector. The principal axes were significant (based on the stability of the ellipse; Gonella, 1972) at the 50 m and deeper current meters on B and 62. At C only the near-bottom (240 m) current record had a stable axis. At all locations the principal axis of the deepest current record was within 10° of the orientation of the local bathymetry. This direction was therefore chosen as the alongshore coordinate, and current vectors at all depths were rotated accordingly. For the three locations, B, C, and 62, the alongshore axes were 300°T, 300°T and 310°T, respectively.

The rotated velocity time series were filtered using a tidal eliminator filter (Godin, 1972). This filter was chosen since it removed the strong tidal component seen in the pressure records. However, its half-power point is at a period of about 72 hours. Therefore, in calculating spectra or coherence the unfiltered time series are used and only the low-frequency (<.025 cph) estimates are presented. Filtered data are used in time series plots and correlation function calculations.

Figure 5.4 shows the low-pass filtered vector time series of the velocity observations considered here. The data have been subsampled to give daily values. Statistical characteristics of these records are given in Table 5.2. In all cases a bar indicated mean value over the length of the series, while a prime refers to time-dependent velocity with frequencies below .025 cph. Mean kinetic energy (per unit mass) $\overline{KE}$ is defined as $\frac{1}{2}(\overline{u}^2 + \overline{v}^2)$ and eddy kinetic energy $KE' = \frac{1}{2}(u'^2 + v'^2)$. In referring to velocity series a subscript indicates mooring location, and depth of the current meter is given in parentheses.

Mean velocity at all locations is predominantly longshore. The shear in this component is small; the largest velocity difference (5 cm/s) occurred between $\overline{v}_{62}$ (20) and $\overline{v}_{62}$ (100) during spring. In the cross-shelf direction, vertical structure during March-May was consistent with downwelling circulation. On the shelf at B and 62, the near-surface current $\overline{u}_{62}$ (20 M) was onshore and the near-bottom current $\overline{u}_B$ (90) was offshore. However, at the shelf break (C) flow at all depths was onshore which may indicate that the downwelling circulation did not extend this far offshore. Cross-shelf flow was small at all locations, and a slight error in assigning axis orientation could affect this interpretation.

In summer, the seasonal thermocline could support larger mean shear. If such shear occurred, it must be above 20 m, since in the mean there was negligible gradient between the 20 and 100 m currents in May-August. The dominant difference between spring and summer was a reduction in mean flow speed. At B, the mean speed dropped by a factor of 2, at 62 it dropped by a factor of 4. (However, mooring motion may affect this result.)

Vertical structure of the time-dependent velocity components varied across the shelf. At B and at 62, the rms speeds had little vertical structure; however, at C these rms speeds decreased from 21 cm/s at 50 m to 11.5 cm/s at 240 m. Presumably, shear across the permanent pycnocline is responsible for this decrease. Linear cross-correlation between longshore velocities at different depths show high correlations at B and 62. For the spring period (March-May) the correlation coefficient 0.95 between v_B (50) and v_B (90) and 0.93 between v_{62} (20) and v_{62} (100) was not significantly reduced (0.88). At C, the correlation between velocity components was less than observed on the shelf (0.71 between v_C (50) and v_C (240)); however, the nature of the flow at the shelf break makes the correlation of the rectilinear components less useful.

Figure 5.4 shows a clear difference in the current field as we proceed across the shelf. At the 100 m isobath, mean flow and low-frequency oscillations were largely parallel to the coast. At the 250 m isobath the flow was still predominantly longshore, but there was significant cross-shelf flow. Even the near-bottom current meter (240 m depth) showed this effect. There is little visual correlation between velocity at B and C; however, B and 62 appear related both to each other and to the wind.

Table 5.2 - Statistics of velocity time series. Overbars indicate mean values, u' and v' are the standard deviations of these components. Standard error estimates on the mean values, $\overline{KE}$ and KE' are discussed in the text.

Location	Date	Depth (m)	$\overline{u}$ (cm/s)	$\overline{v}$ (cm/s)	u' (cm/s)	v' (cm/s)	$\overline{KE}$ $(cm/s)^2$	KE' $(cm/s)^2$
B	7 Mar-14 May	50	.1±.5	11.1±1.4	2.6	7.3	62	30
		90	-1.6±.3	8.8±1.1	1.4	6.0	40	19
	15 May-20 Aug	50	.1±.7	4.9±1.2	4.1	7.7	12	38
	7 Mar-20 Aug	50	.1±.2	7.2± .9	2.0	7.6	26	31
C	9 Mar-13 May	50	3.2±3.7	5.6±3.7	14.9	14.8	21	221
		100	2.9±3.0	5.6±3.3	12.2	13.1	40	160
		240	2.2±1.4	7.1±2.5	5.5	10.1	28	66
62	7 Mar-14 May	20	4.6±1.9	19.5±3.3	9.0	15.9	201	167
		50	0.5±1.7	16.9±3.1	8.0	14.8	143	142
		100	1.2±1.2	14.0±2.5	6.0	11.8	99	87
	15 May-20 Aug	20	-.1±1.1	3.8±1.6	6.5	9.1	7.2	62
		50	.2±1.2	5.2±1.8	6.6	10.0	14.1	72
		100	.4±.6	4.2±1.3	3.7	7.6	8.9	36
	7 Mar-20 Aug	20	1.6±1.0	9.9±1.8	7.1	13.6	50	117
		50	.4±.9	10.1±1.7	6.5	12.9	51	104
		100	.9±.5	8.4±1.4	4.0	10.2	36	60

The statistics in Table 5.2 characterize cross-shelf variations. In spring at the 50 m depth, $\bar{V}$ increased from B (11 cm/s) to 62 (17 cm/s) and then decreased at C to 6 cm/s. In view of possible contamination of the record at 62 by surface waves, we cannot be certain of the relatively high mean velocity (30 cm/s) to C (22 cm/s). Also, the balance between contribution from longshore and cross-shelf fluctuations changed; at B the alongshelf fluctuations dominated, whereas at C the two components contributed equally. Flow 10 m off the bottom had less cross-shelf variability; however, KE' still increased by a factor of 3.5 between B and C.

In order to compare time scales of low-frequency velocity fluctuations, auto-correlation functions were calculated. The low-pass filtered velocity time series were used with a time step Δt of 4 hours. Results for sites B and C are shown in Figure 5.7. The integral time scale T_{ij} for each velocity series was estimated from the equation:

$$T_{ij} = \sum_{n=-N}^{N} r_i(n\Delta t)\, r_j\, (n\Delta t) \qquad (4)$$

(Allen and Kundu, 1977), where r_i (t) and r_j (t) are the autocorrelation function for series i and j. N was chosen to be 8 days so that the contribution to T from n>N was negligible. The integral time scale determines the time required to obtain independent measurements. At 50 m, v' had a time scale of about 2.5 days at B and 4 days at C. Similarly, the u' time scale increased at the shelf break. Figure 5.7 also shows the autocorrelation functions for the near-bottom currents at the two locations. Although details vary, motions at C had longer time scales than those at B.

Having established T for each velocity series, root-mean-square error in the mean velocities can be estimated from:

$$\sigma_1 = \sigma/(\tfrac{\tau}{T})^{\frac{1}{2}} \qquad (5)$$

(Kundu and Allen, 1975), where σ_1 is the rms error of the mean and σ is the standard deviation of the time series of length τ. Integral time scales of 2.5, 3 and 4 days at B, 62, and C were used to obtain the error limits shown in Table 5.2. These error limits indicate that the differences in $\bar{V}$ at B, c and 62 (during spring) are probably not due to random fluctuations.

Spectral decomposition of the kinetic energy is shown in Figure 5.8 for the 50 m velocity at B, c and 62 in spring. As expected, at the lowest frequency the energy density at the 100 m isobath (B) was an order of magnitude smaller than that observed near the shelf break (C). At higher frequencies the spectra at C falls rapidly with insignificant peaks. However, at B there is a significant energy density peak at about 0.017 cph (60 hr. period).

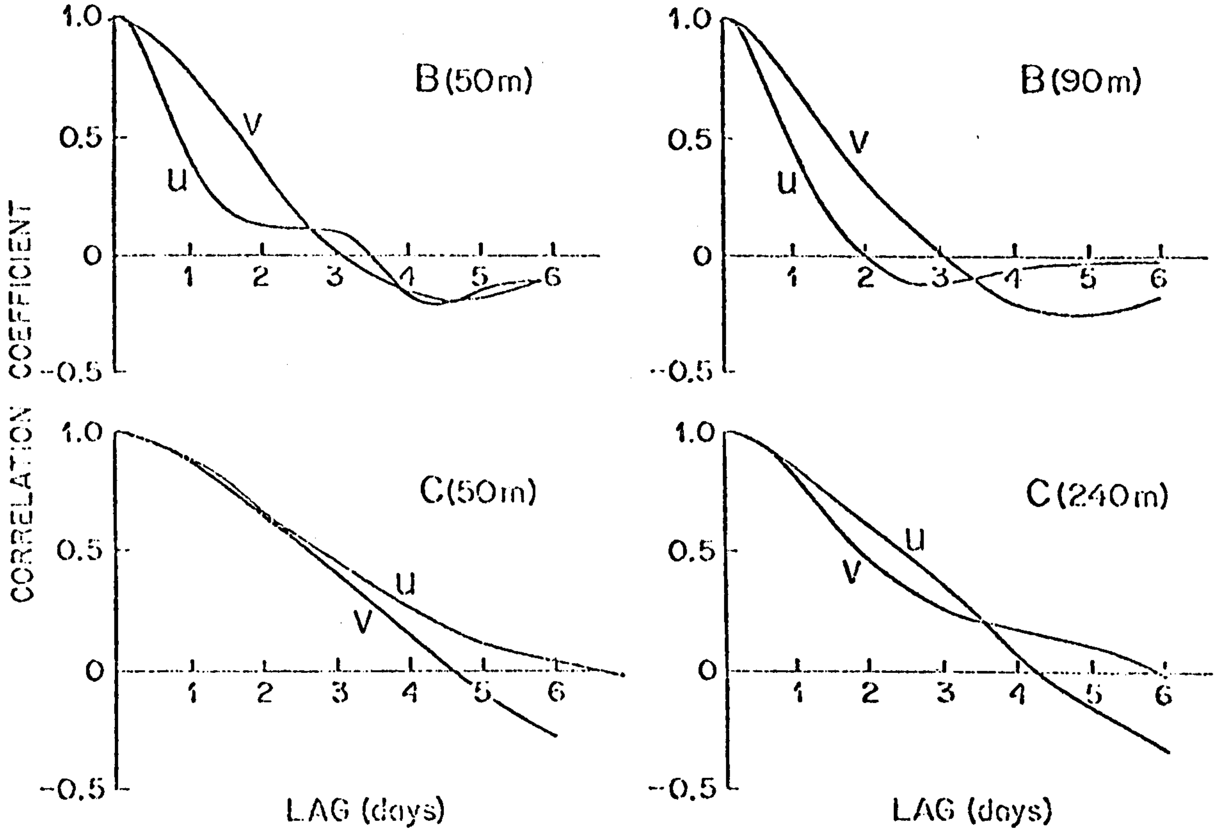

Figure 5.7 - Autocorrelation functions of the low-pass filtered velocity components at B and C. Results for records at 50 m depth and at 10 m above the bottom are shown in each case.

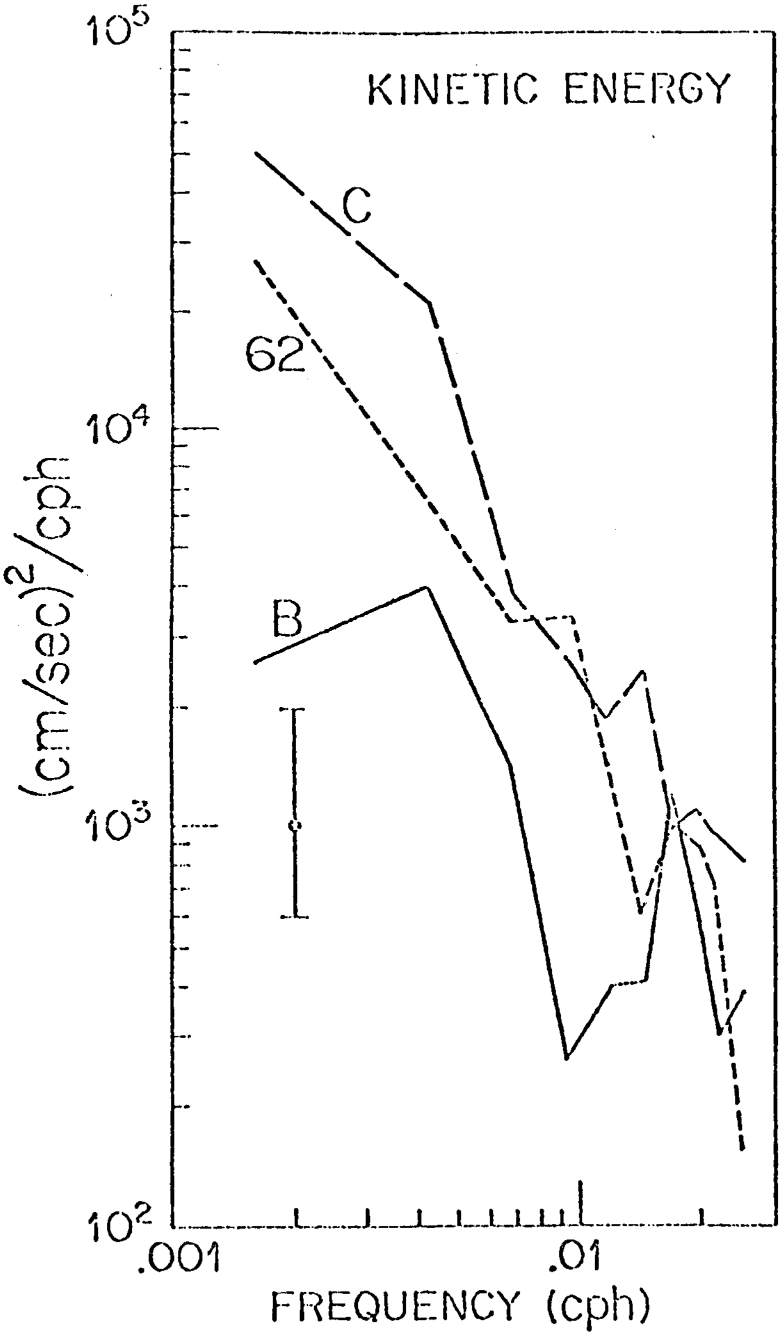

Figure 5.8 - Kinetic energy spectra of the low-frequency fluctuation at B, C, and 62 for the period 15 March - 15 May.

Spectra at B and C are further compared in Figure 5.9 where rectilinear and rotary spectra are shown. At B the low-frequency flow paralleled the isobath so that the v spectra exceed the u spectra; at C the flow was rotary with a clockwise rotation. Near-bottom kinetic energy spectra are similar to those shown even though the 240 m velocity at C was more nearly aligned with the bathymetry. Clockwise polarization was still observed. These spectra indicate that flow on the shelf was directly steered by the bathymetry, while at the shelf break where the bottom gradient is greater, the flow was rotary.

Cross-correlations for currents at the three sites were computed, but were not large for any of the series. In spring, 50 m cross-correlation coefficients were $r_u = .2$, $r_v = .4$ between B and 62 and $r_u = .1$, $r_v = .3$ between B and C; subscript indicates the velocity component. Similar results were observed between near-bottom currents at B and C. Based on a joint time scale of about 3 days, the 10% significance level for these correlations is about .35. Therefore, observed correlations are at best marginally significant. The change in polarization of the flow across the shelf may have resulted in small correlation of u and v components even if rotary components were coherent. To test this, rotary coherence between the velocity series, independent of the coordinate system, was computed (Mooers, 1973). To obtain a measure of overall coherence, spectral estimates with periods greater than 3 days were ensemble-averaged. These coherence estimates have a 95% confidence level for zero coherence of 0.40 (Carter *et al.*, 1973). In spring at the 50 m level the counterclockwise (C_+) and, clockwise (C_-) coherences were $C_+ = .50$, $C_- = .19$ between B and C; $C_+ = .49$, $C_- = .35$ between B and 62; and $C_+ = .23$, $C_- = .06$ between 62 and C. Thus, the dominant clockwise oscillations observed at C (Figure 5.9) apparently did not propagate onto the shelf. These oscillations were coherent and had no phase shift in the vertical ($C_+ = .25$, $C_- = .86, \phi \doteq 3^\circ$ between 50 and 240 m). The motions at C apparently represented quasi-barotropic motions along the shelf break.

5.3.2 Pressure time series, spectra and correlations

Low-frequency (<.025 cph) spectral estimates of the unfiltered pressure records are shown in Figure 5.10. At the lowest frequencies these spectra are similar; they have a weak slope up to about .003 cph and then a sharp falloff (ω^{-3}) with frequency. This frequency dependence is stronger than that observed for kinetic energy (Fig. 5.8). Pressure spectra at sites D (50 m) and E (100 m) show a significant peak at 0.017-0.020 cph (60-50 hr. period). This peak is not seen in the shelf break record at C (250 m). A similar peak was noted in the velocity spectra at B (Fig. 5.8). In the frequency band of this spectral peak, pressure variance across the shelf fell more rapidly than H^{-1}. The ratios of variance estimates at the 100 m and 250 m isobath to the 50 m variance were 0.55 and 0.15. This rapid falloff is consistent with an exponential depth dependence.

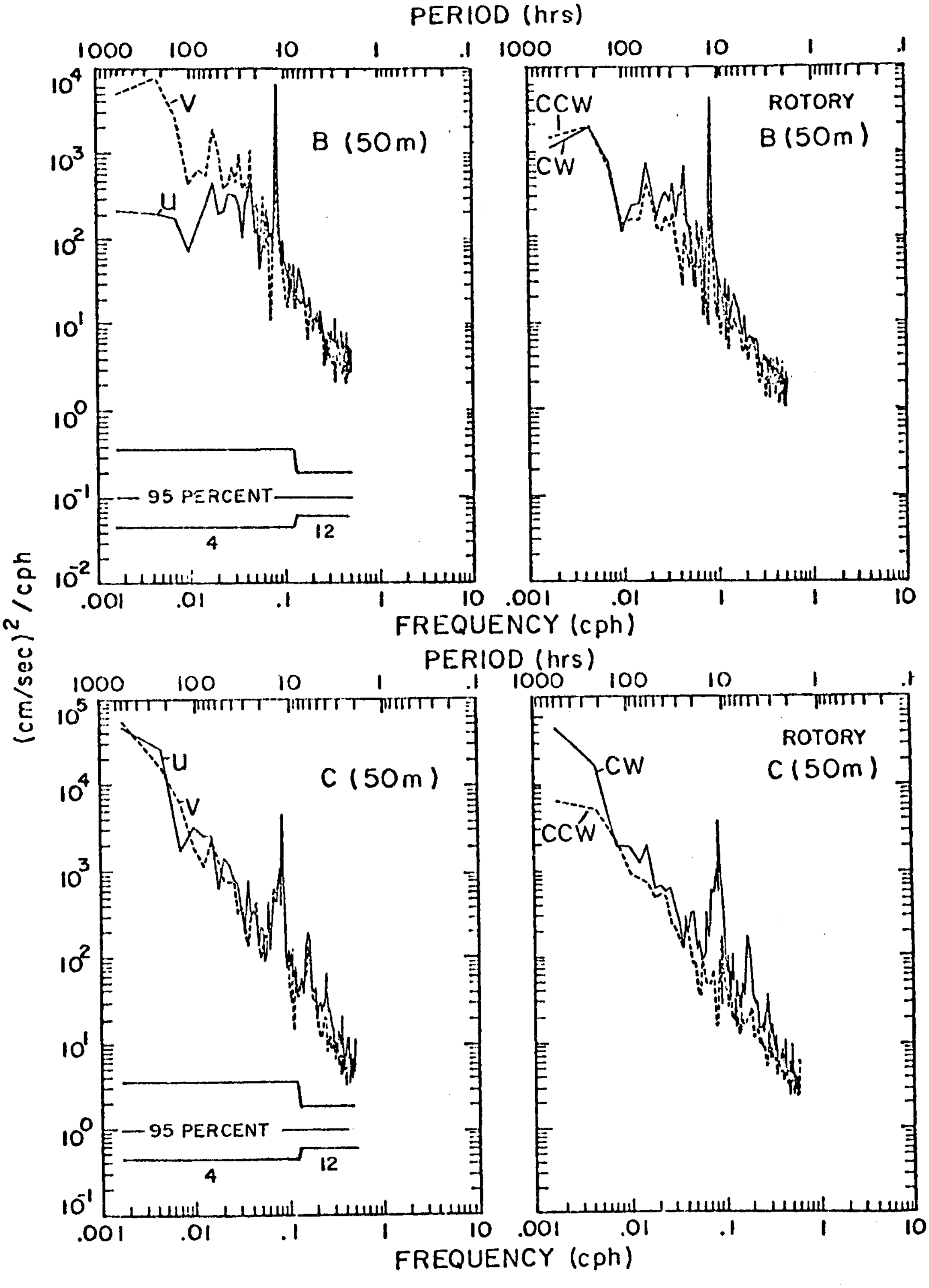

Figure 5.9 - Rectilinear and rotary kinetic energy spectra at the 50-m depth at locations B and C.

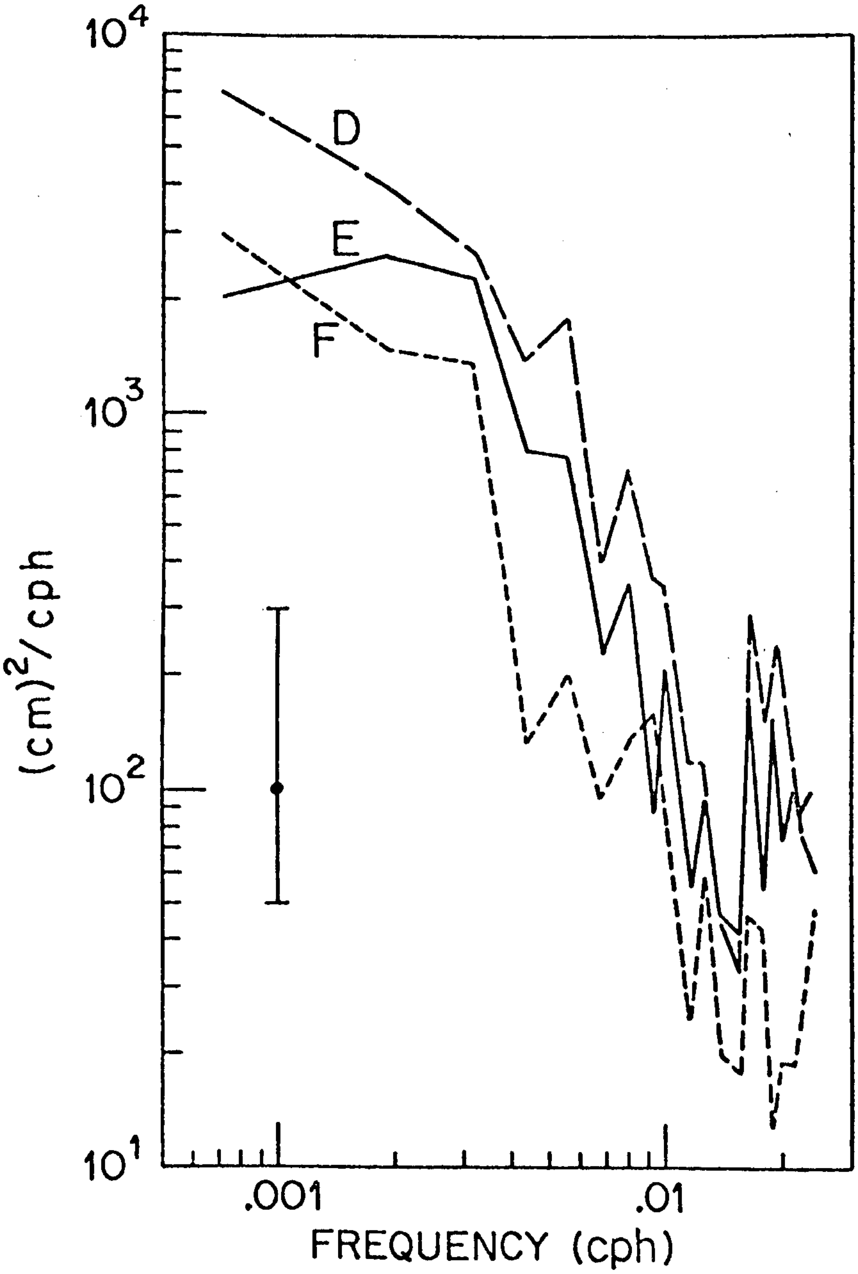

Figure 5.10 - Spectra of bottom pressure records at sites D, E, and F. The error bars indicate 95% confidence interval.

Pressure records may be compared in both cross-shelf and long-shelf directions. The pressure field has a larger cross-shelf coherence scale than velocity. The cross-correlation coefficient between 50 m and 250 m records was 0.59. This larger scale could reflect pressure fluctuations unrelated to shelf effects, such as a seasonal variance associated with changes in deep water structure of the Alaska Current. Though the data records presented here are probably highly influenced by shelf circulation, the 250 m record should reflect to some degree off-shelf pressure fluctuations. Except for the .017 cph energy peak, pressure variance spectra are similar at all locations and offer little hope of separating shelf effects on the basis of frequency (Fig. 5.10). However, coherence between locations D and F shows that only the lower frequency variance ($f < .006$ cph) is significantly coherent across the shelf (Fig. 5.11). This suggests that oscillations with periods longer than about 7 days are more likely associated with off-shelf (or, in any case, very broad) current structures.

The single pressure comparison obtained in the along-shelf direction indicated high coherence. Time series at sites B and E are nearly identical; the cross-correlation coefficient at 100 m depth is 0.98. A phase lag of 2 hours suggests propagation from E to B, counter to the direction expected for free shelf waves. It may be related to the eastward propagation of most storm systems.

5.3.3 Velocity-pressure correlations

Comparison of variations in bottom pressure gradients and currents can provide information on dynamical balances in the equations of motion (1) and (2). We first consider the velocity field. Accelerations u_t and v_t were calculated from the low-pass filtered time series using a central difference approximation with a time increment of 12 hours. The rms longshore velocity term, fv, exceeded acceleration by a factor of 20 for both the 50 m current at B and the 100 m. Thus neglect of u_t in equation (1) is reasonable. In equation (2) the rms value of fu exceeded rms v_t by factors of 5 and 10 at sites B and 62, respectively; cross-shelf velocity dominates, but acceleration terms may not be negligible.

Table 5.3 compares longshore velocity with the pressure time series. Cross-correlation coefficients have been calculated between longshore velocity measurements at four currents meters (B (50 m), 62 (100 m), C (100 m and 240 M)) and bottom pressure and bottom pressure gradients. Correlations using low-pass filtered data are presented for three periods: the total record, spring (15 March-15 May), and summer (15 June-15 August). The 5% significance level for the correlation coefficient was estimated using integral time scales defined by auto-correlation functions of the component series (equation (4)). For the total record the 5% signigicance level was 0.25; for each subinterval it was 0.45.

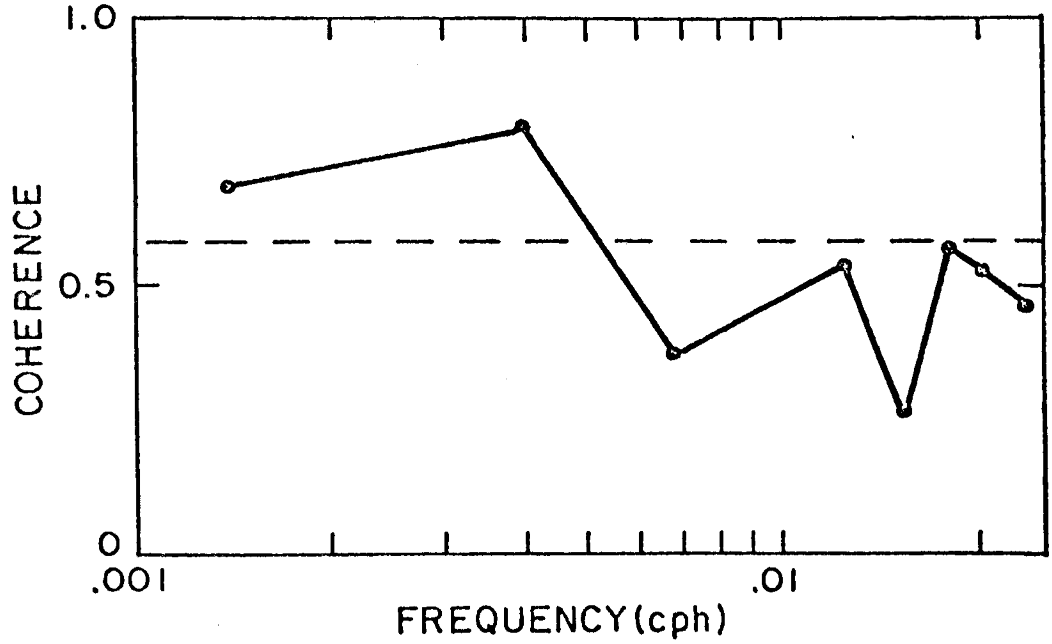

Figure 5.11 - Coherence between bottom pressure measured at sites D (50-m depth) and F (250-m depth). The dashed line indicates the 95% confidence level for zero coherence.

Table 5.3 - Linear correlation coefficients between velocity and pressure or pressure gradient. The 5% level of significance is approximately 0.45 for the 2-month pieces and 0.25 for the total record.

Velocity	Pressure	7 Mar-14 May	15 June-15 Aug	7 Mar-15 Aug
B-50 m	P_D	0.52	0.56	0.47
	P_E	0.33	0.35	0.36
	P_F	0.02	-0.02	0.08
	P_D-P_E	0.52	0.87	0.49
	P_D-P_F	0.63	0.68	0.56
	P_E-P_F	0.54	0.45	0.47
C-100 m	P_D	0.01	-	-
	P_E	-0.08	-	-
	P_F	-0.04	-	-
	P_D-P_E	0.14	-	-
	P_D-P_F	0.05	-	-
	P_E-P_F	-0.08	-	-
C-240 m	P_D	0.21	-	-
	P_E	0.25	-	-
	P_F	0.27	-	-
	P_D-P_E	0.05	-	-
	P_D-P_F	0.09	-	-
	P_E-P_F	0.12	-	-
62-100 m	P_D	0.75	0.39	0.61
	P_E	0.77	0.41	0.58
	P_F	0.32	0.13	0.18
	P_D-P_E	0.40	0.11	0.41
	P_D-P_F	0.68	0.41	0.63
	P_E-P_F	0.77	0.74	0.67

Results can be summarized by considering the largest velocity-pressure correlations. At the 100 m contour (B) for the total record interval, the highest correlation (0.56) was with the pressure gradient estimated over the entire shelf (P_D - P_F). This correlation was better than that obtained with the pressure measurement at 50 m alone (P_D). In spring, similar results were obtained. However, during summer a distinct improvement in correlation was found when the 50 m velocity at B was compared to the pressure gradient between the 50 and 100 m isobaths (P_D - P_E). This correlation (.87) was the highest observed. At the 180 m isobath (62) the best correlation (.67) for the total record was with the pressure gradient between the 100 m and 250 m isobaths. Again, this pressure gradient correlation was only slightly better than the correlation (.61) with the single pressure measurement at 50 m. During spring, results were similar. The summer period was characterized by poor correlation with individual pressure measurements, but correlation with the pressure gradient between 100 m and 250 m isobaths was large (.74). Finally, at the 250 m isobath (C) correlations for all pressure-velocity combinations were below the 5% significance level.

The seasonal pattern of pressure-velocity correlations suggest that the pressure field across the shelf is simpler in spring than in summer. During March-May, correlations using a single pressure measurement on the shelf were almost as high as those which involved pressure gradient measurements. Thus, in spring a reasonable model for the pressure-velocity relation is a linear sealevel slope across the shelf with little or no response at the shelf break. The slight enhancement of the correlation at 62 (180 m depth) when the outer shelf pressure gradient (P (100m)-P (250m)) is used indicates that this model is not entirely adequate and that there is some difference in shallow water sea level response. During summer, individual pressure measurements gave lower correlations with velocity than did pressure gradients. Also, the difference between pressure gradients measured over the inner (P (50 m)-P (100 m)) and outer (P (100 m)-P 250 m)) shelf region was large. The interior gradient correlated with velocity at 62 ($r = 0.63$).

Summer stratification contributes to increased complexity of the pressure field. For example, the pressure gradient between 50 m and 100 m isobaths includes a cross-shelf density gradient term as well as the sea surface gradient. Variations in this density gradient term reflect baroclinic velocity fluctuations which would be observed by the current meter at the 50 m level at B. To measure these baroclinic effects the shear in v was correlated with the pressure gradients. No significant correlations were found. However, since we expect the barotropic term to dominate both velocity and pressure fluctuations, the small correlation coefficients do not necessarily preclude baroclinic effects.

In summary, comparison of the longshore velocity and pressure measurements indicates that on the continental shelf 50-70% of the current variance can be accounted for by equation (1). At the shelf break, current and bottom pressure are uncorrelated. The cross-shelf velocity coherence and these pressure-velocity correlations show that the shelf break separates the circulation into two distince regimes.

With the present data a definitive test of equation (2) is not possible. Figure 5.12 shows v_t, fu and P estimated from the 50 m velocity at B and the long-shelf pressure difference between B and E. Although there are periods when v, or fu appear correlated with P, the overall correlations are not significant. Similarly, the sum, v_t + fu, is not correlated with pressure difference $P_E - P_B$. This lack of correlation is not surprising considering the small magnitude of the quantities. Errors in axis orientation could contaminate the u series: density and local topography could influence the longshelf pressure gradient.

5.3.4 Wind correlations

Wind has been neglected in the above discussions. We expect, particularly in spring, that atmospheric forcing will be important both in driving currents and in setting up sea level slope. FNWC calculated winds and observed winds and pressure at Yakutat are used to investigate the gross features of the response.

A wind energy spectrum for the March-August period (Fig. 5.13) was calculated after detrending the time series by joining the end points (Frankignoul, 1974). At the 95% confidence limit no significant peaks were observed. The energy density had a frequency dependence of about ω^{-1} at low frequencies. This frequency dependence and the energy level are similar to the wind spectrum presented by Hayes and Schumacher (1976). However, the latter spectrum had significant structure near .02 cph.

Variations in atmospheric pressure P_a exceeded variations in any of the bottom pressure series (Fig. 5.5). The low-frequency variance in P_a was 81 cm^2, a factor of 4 greater than the bottom pressure variance at D. The inverted barometer effect has been shown to reduce bottom pressure fluctuation in the deep ocean (Brown *et al.*, 1975) and at the shelf break (Beardsley *et al.*, 1977). Here we see that the reduction in bottom pressure variance occurs across the shelf. In addition, linear correlation between bottom pressure fluctuations and P_a was insignificant at all sites (r = -.13, -.14, -.18 between P_A and P_D, P_E, P_F). We thus feel confident in neglecting the contribution of the atmospheric pressure term in equation (3).

Table 5.4 shows correlation coefficients between wind and current or pressure measurements over the 6-month record. At both B and 62, longshore current components are significantly correlated with longshore wind, but cross-shelf wind and current components are uncorrelated. No significant correlation of wind and current at C was found. These velocity correlations substantiate what is clear from the time series plots (Fig. 5.4); longshore shelf flow is related to longshore winds, but flow at the shelf break is not.

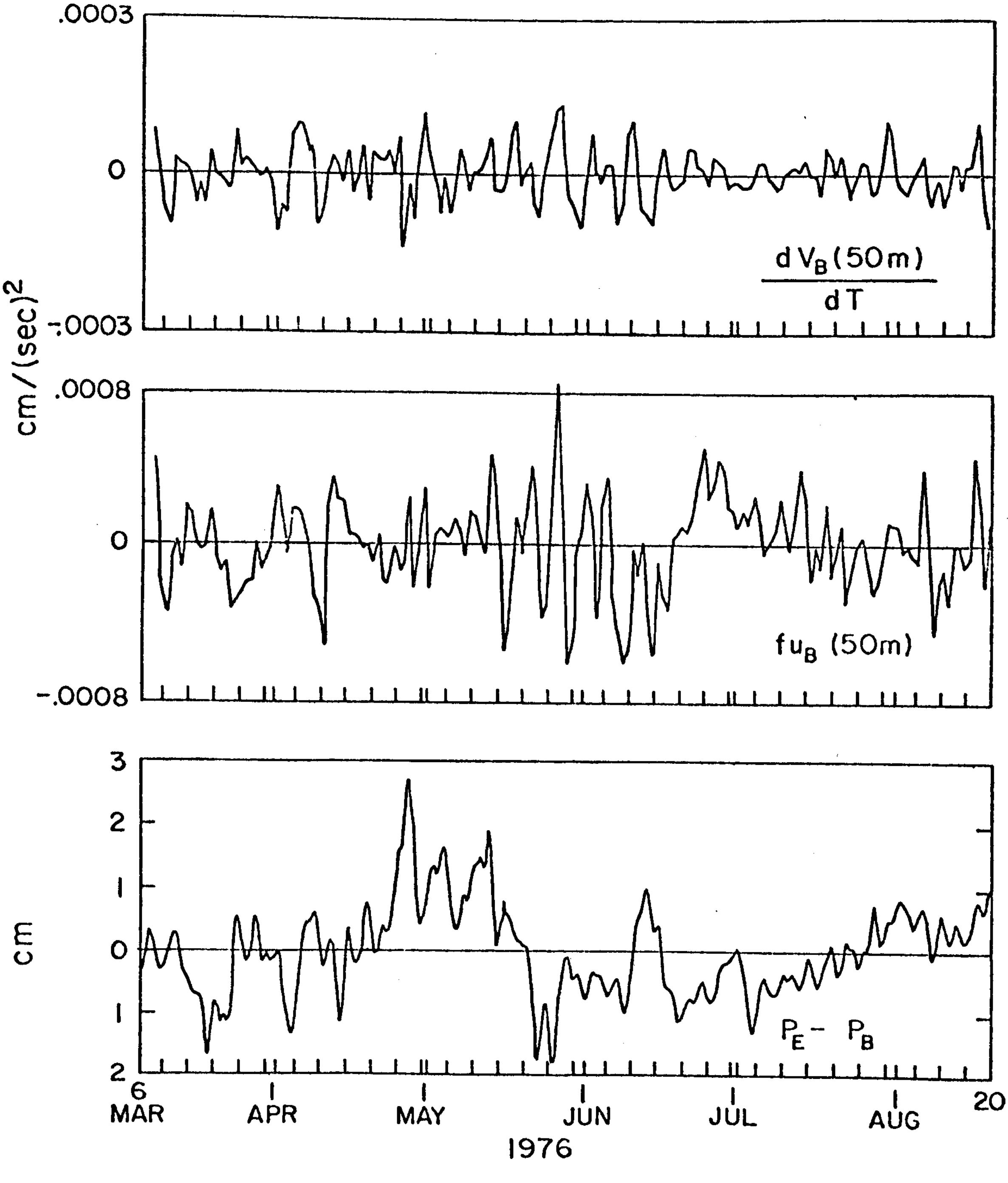

Figure 5.12 - Acceleration of the alongshore velocity compared with the cross-shelf velocity and the alongshelf bottom pressure difference. Measurements were made at the 100-m isobath. Velocity records are from 50-m depth; f is the Coriolis parameter.

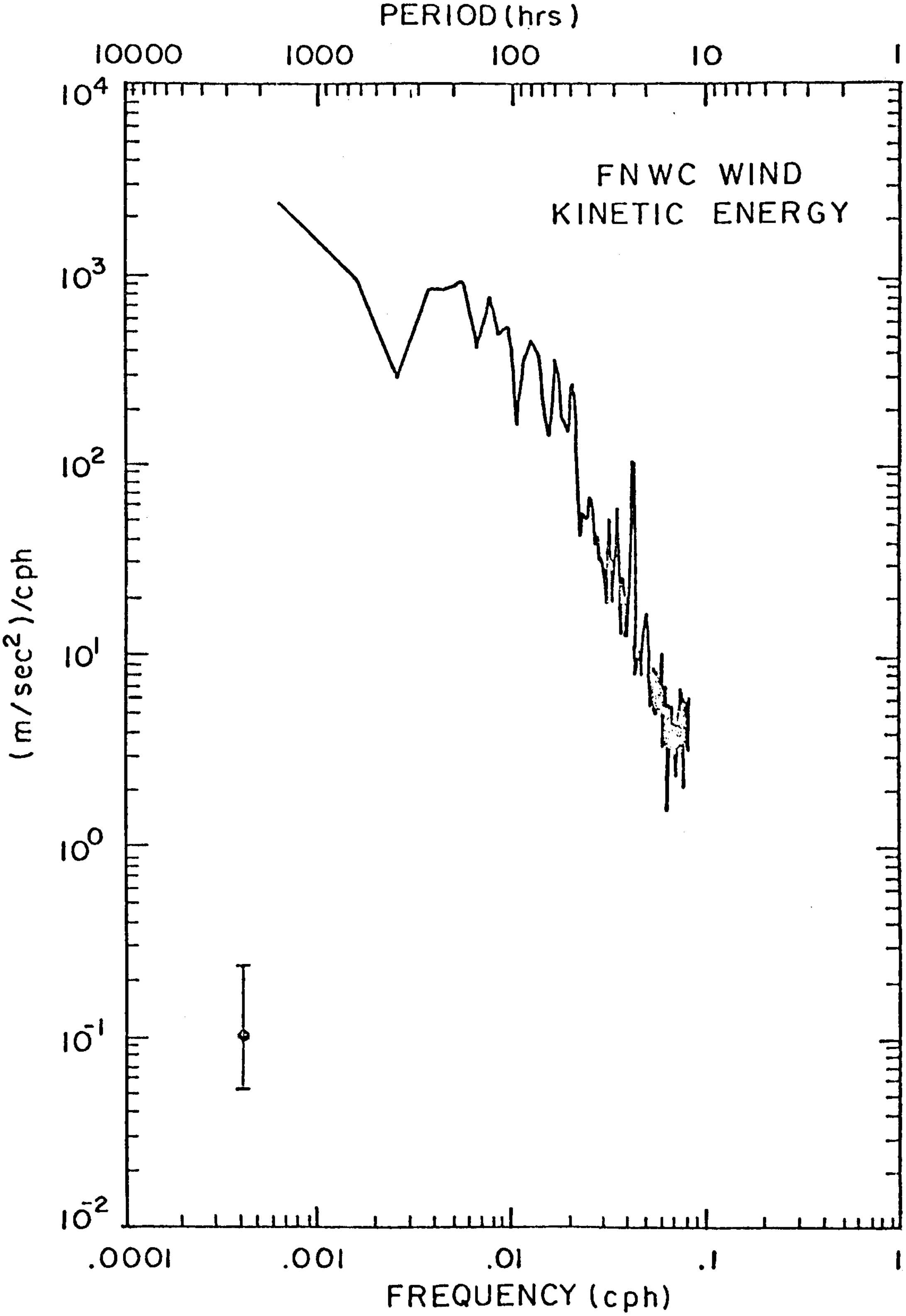

Figure 5.13 - Kinetic energy spectrum of the FNWC wind. The error bars indicate 95% confidence interval.

Table 5.4 - Linear correlation coefficients between wind components and velocity or pressure series.

Series	u_{wind}	v_{wind}
u_B (50 m)	0.10	-0.03
v_B (50 m)	0.27	0.51
u_{62} (100 m)	-0.12	0.20
v_{62} (100 m)	0.08	0.52
$P_D - P_E$	0.33	0.15
$P_E - P_F$	0.05	0.63

The pressure gradient correlations suggest an interesting difference in response across the shelf. On the inner shelf (between 50 m and 100 m isobaths) pressure gradient was significantly correlated (assuming a 5% significance level of 0.25) with onshore wind; on the outer shelf (between 100 and 250 m isobaths) the significant correlation was with the longshore wind. This relationship is further described by binning the pressure differences according to the component wind speed using 2 m/s bins. Resulting scatter diagrams between pressure difference and wind (Fig. 5.14) show a clear tendency for shallow water to respond to onshore wind while deep water responds to longshore winds. This relationship is consistent with simple dynamical ideas. In deep water the Ekman response produces onshore transport accompanying an longshore wind (Ekman, 1905). If however, Ekman depth is equal to or less than water depth, direct wind setup becomes more important (Welander, 1957). It must be kept in mind that wind estimates are crude, particularly for the onshore component. Until more accurate measured winds are available in conjunction with bottom shelf pressure gradient measurements, distinctions between inner and outer shelf response to wind forcing must be treated with caution.

5.4 Discussion and Summary

This section has focussed upon low-frequency ($f<0.025$ cph) variations in current and bottom pressure on the continental shelf in the Northeast Gulf of Alaska. The analysis has shown:

(1) Flow on the shelf differed from flow at the shelf break. At the 100 m contour, mean and fluctuating velocity components were aligned with bathymetry and depth dependence was small. At the 350 m contour,

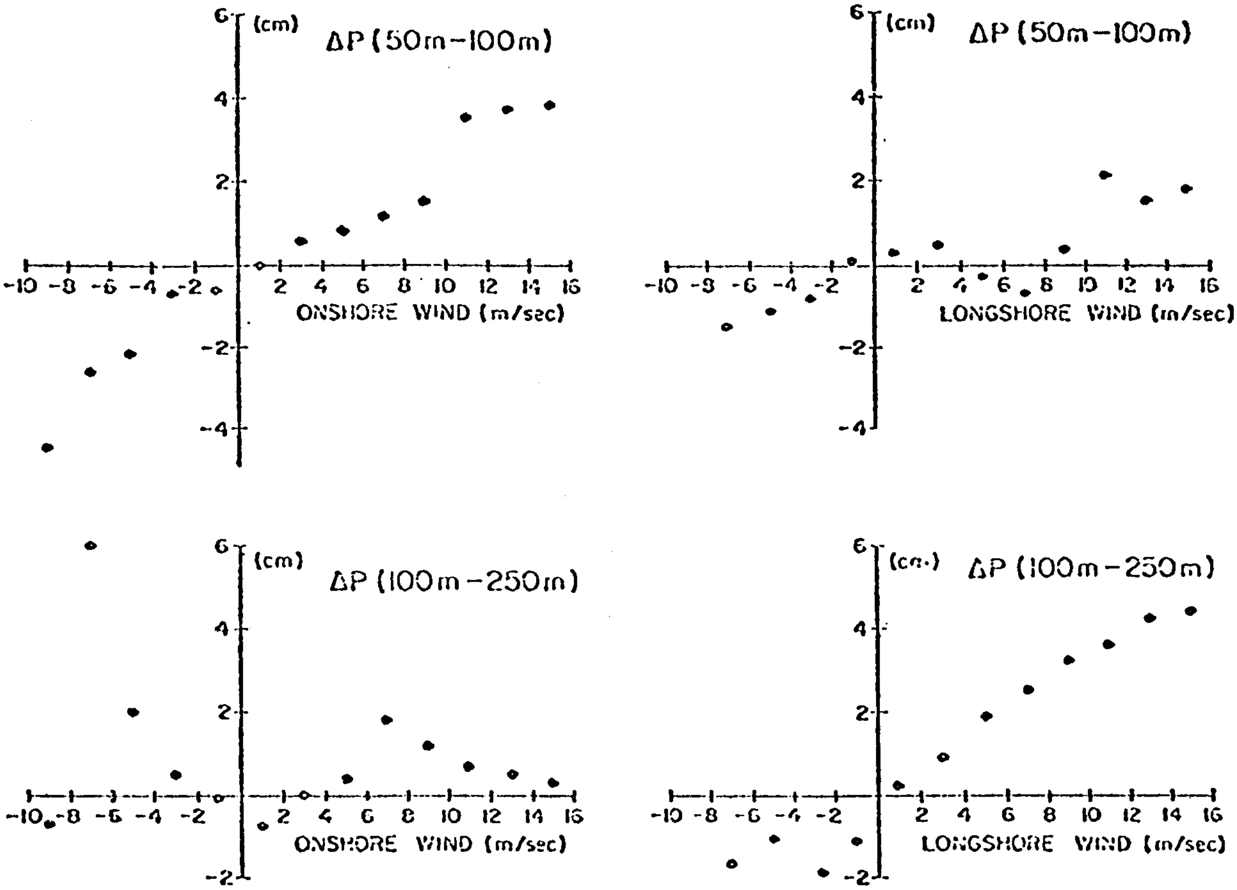

Figure 5.14 - Cross-shelf pressure gradient between indicated depth contours versus onshore and alongshore wind.

mean longshore flow was reduced by 50%, fluctuating components were rotary and largely anticyclonic, and eddy kinetic energy increased by a factor of 7. These anticyclonic low-frequency motions were vertically coherent, but did not propagate onto the shelf. In general, cross-shelf coherence between all velocity series was small.

(2) The bottom pressure field across the shelf was more coherent than the velocity. Along the 100 m isobath the correlation coefficient was 0.98 for a separation of 50 km and the pressure differences did not exceed 3 cm. Cross-sheld bottom pressure variance was an inverse function of water depth. The correlation coefficient of 0.59 between pressure measurements at 50 m and 250 m isobaths indicates large cross-shelf scales for a significant

fraction of the variance. These larger scale fluctuations were predominantly low-frequency (periods greater than 7 days) motions.

(3) On shelf, the 50 m and 100 m isobath bottom pressure variance and 100 m horizontal kinetic energy spectra had a significant peak at about 0.017 cph. Station separation was not sufficient to observe propagation (if any). The oscillations may be a local forced response.

(4) On the continental shelf, bottom pressure and velocity correlations can be interpreted in terms of a simple geostrophic barotropic model. Alongshore velocity fluctuations were balanced by cross-shelf bottom pressure gradients. However, cross-shelf velocity and alongshelf pressure gradients were too small to permit a test of this component equation. Alongshore current-cross-shelf pressure correlations were simpler in spring than in summer. In the former case, a single nearshore pressure measurement was representative of the sea level slope across the shelf. In summer, possibly because of increased baroclinicity, pressure gradient measurements enhanced the velocity correlation.

(5) The contribution of atmospheric pressure to the bottom pressure changes can be neglected even in water depths of 50 m.

(6) Simple dynamical models describe features of the sea level response to wind forcing. In shallow depths, sea level slope responded directly to onshore winds; in deeper water only the alongshore wind component caused setup. This depth-dependent response can be expected to yield a near-shore coastal current which differs from the current over the outer shelf.

Low-frequency variance on the continental shelf has been shown to correlate with the wind. The Alaska Current is an additional, potentially important, source. Royer and Muench (1977) noted temperature structures in this current which they interpreted as anticlyclonic eddies with spatial scales of tens of kilometers. These eddies could correspond to the anticyclonic flow observed at the shelf break. As discussed above, this flow does not propagate onto the shelf. A possible explanation for this result is provided by the theory for topographic Rossby wave transmission across an exponential shelf break (Kroll and Niiler, 1976). By choosing exponential shapes which fit the Northeast Gulf of Alaska shelf and shelf break, we calculated that the maximum transmission coefficient for low-frequency (~.014 cph) waves corresponds to a longshore wavelength of 400 km. Ignoring friction, this transmission coefficient is a broad function of longshore wavelength; however, the coefficient does indicate that small-scale waves (~50 km) will tend to be reflected at the shelf break. Thus, assuming scales similar to those noted by Royer and Muench, the observed lack of cross-shelf current coherence is expected. In order to improve our understanding of the relative importance of various low-frequency sources better spatial resolution of the current field and direct nearby wind measurements are required.

6. CURRENTS WEST OF KAYAK ISLAND

In the preceding sections of this report, attention has been focused primarily on circulation in that portion of the northeast gulf east of Kayak Island. In this section, we devote attention to the region between Kayak Island and an imaginary north-south line across the shelf from about Hinchinbrook Entrance to Middleton Island. We expect *a priori* that circulation here will be affected by the presence of Kayak Island on the upstream side (relative to flow in the Alaska Current) and by summer freshwater influx from the Copper River.

6.1 Introduction

General circulation over the shelf west of Kayak Island may be classified as highly complex. The visible surface manifestation of this complexity, as indicated by surface suspended sediments on ERTS satellite imagery (Muench and Schmidt, 1975), was a series of vortex-like features suggesting an anticyclonic flow tendency on the downstream or western side of Kayak Island and extending several hundred kilometers southwest from the island. This complexity was also reflected in the trajectories of four satellite-tracked drifters drogued at 30-50 m depths in the region during summer 1975 (Fig. 6.1). These drifters suggested existence of an eastward counterflow directly downstream from Kayak Island and a westerly near-shore flow. One drifter, #1174, executed several circular loops 30-40 km in diameter just west of Kayak Island, suggesting presence of an eddy-like feature. Since the other drifters did not duplicate this track, the eddy was likely a transient feature associated with vortex shedding on the downstream side of the island.

6.2 Observations

In an effort to better define circulation west of Kayak Island, current meter mooring 60, 61 and 69 were deployed during March-October 1976 (cf. Table 2.1, Section 2). We note that mooring 61, at the shelf break, had in addition been deployed during the previous winter. At each mooring, currents were measured at depths of 20 m, 50 m, 90 (or 100) m and, at the shelf break station 61, 163 m. Data acquired were therefore adequate for estimating cross-shelf and vertical distribution of currents spanning winter-summer (March-August) 1976. Based on the above discussions dealing with time variability, it appears that 1976 was not an unusual year in terms of currents, with the possible exception of the current reversal at station 62 during June 1976. With this caveat, we proceed.

Time-series current data can be conveniently presented as vectors showing mean velocity during the measurement period, upon which are superposed bars indicating variance in low-pass filtered current speed both parallel and normal to the mean flow direction. This presentation is used for selected March-August 1976 data (Fig. 6.2) and is the basis for the following discussion. We present only the 20 m data, which were generally representative of deeper motions,

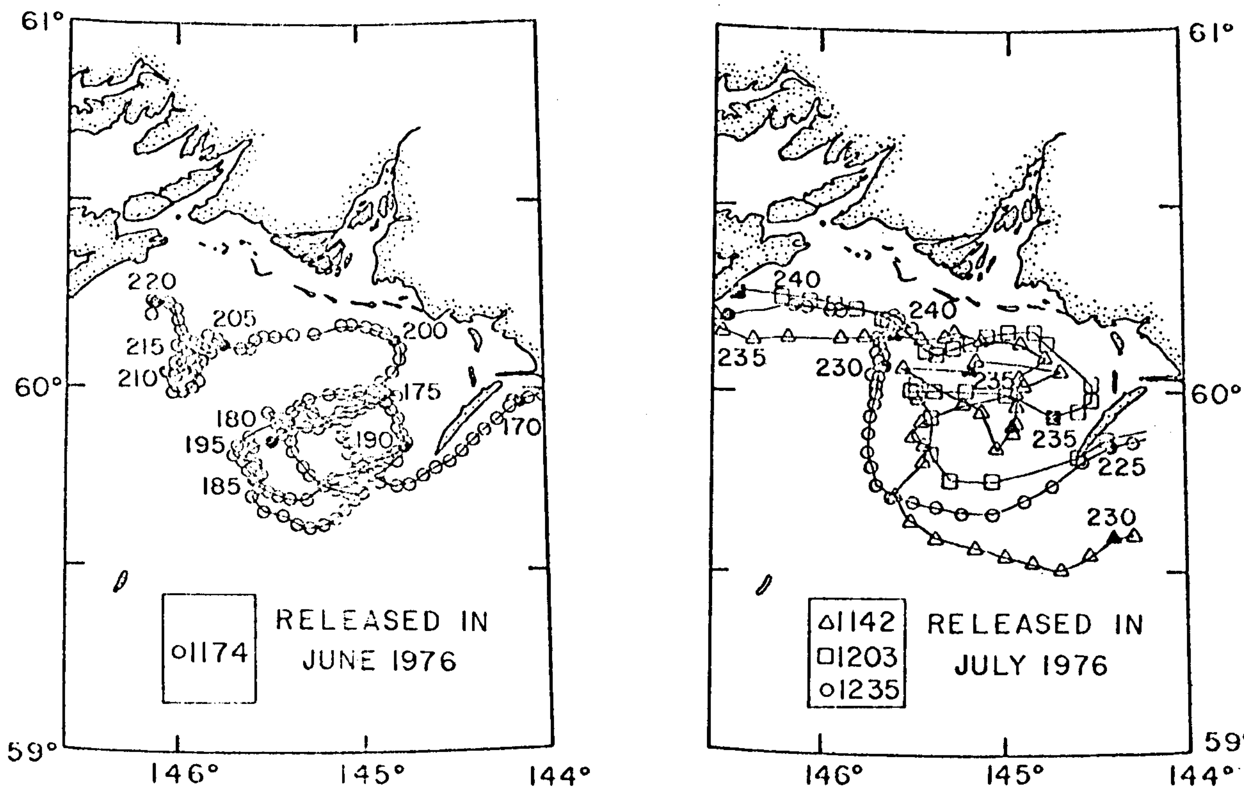

Figure 6.1 - Satellite-tracked drifter trajectories west of Kayak Island in summer 1976.

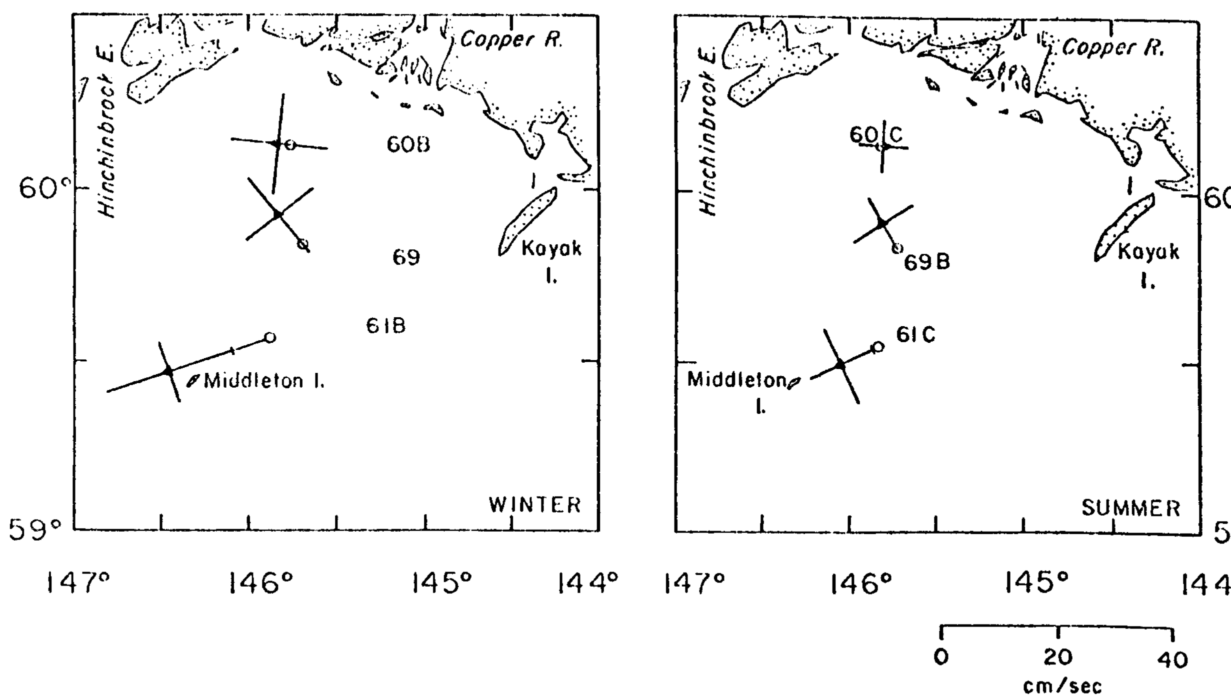

Figure 6.2 - Arrows indicate mean current vectors, while cross-bars indicate variance, at three locations west of Kayak Island during winter and summer 1976.

for stations 60, 61 and 69. Mean flow at the shelf break station 61 reflected the influence of westward longshelf flow due to the Alaska Current, being directed westward. Mean speed was greater during the winter than during summer, as was the variability, noted also for station 62 off Icy Bay (cf. Section 3). The relatively constant direction of flow at station 61 reflected the role of bathymetry in steering water motion; flow paralleled isobaths at the shelf break. Currents at 50 m paralleled those at 20 m and have similar speeds. Flow at 100 m was about 45° to the left of the 20 m and 50 m flow during both winter and summer, while speeds were lower than at shallower depths. Referral to the bathymetry (Fig.1.1) suggests that bathymetric steering was more effective in controlling current direction at deeper levels. An alternative possibility is that an offshore flow component was present at depth, at least during winter, in response to the known tendency for winter coastal downwelling which would require an onshore near-surface flow and a compensating offshore deep flow (Royer, 1975). Offshore near-bottom flow in this region was also reported by Feely *et al.* (in press), based on near-bottom suspended sediment transport. Such causal factors are impossible to assess here, given the local flow complexity and small number of observations. We also note, *en passant*, that a portion of the flow variability at 20 m was likely due to wave noise acting on the 17 m deep subsurface float with consequent transfer of energy to the uppermost current meter. This would have been particularly likely during winter, when sea state is at its highest in the northern gulf (cf. Section 2).

At station 69, approximately 25 km shoreward of station 61 and at the same latitude as the western tip is Kayak Island, the mean flow lacked any significant winter-summer speed variation, such as observed at stations 61 and 62 along the shelf break. Current direction at station 69 was consistently northwesterly toward Hinchinbrook Entrance at both 20 m and 50 m depths. This northwesterly flow tendency agrees qualitatively with the trajectories of the satellite-tracked drouges (cf. Figure 6.1) in that same area. Apparently this region is one of persistent shoreward cross-shelf flow. This is probably a consequence of the pressure gradients set up by intrusion of Kayak Island into the regional westerly flow and is thus a normal situation.

Currents at station 60, that nearest the coastline, were highly variable and exhibited only a weak mean flow with current speeds of order 2 cm sec^{-1} or less. During the spring-summer period, however, flow was easterly. This change in direction was of the proper sense to result from local winter-summer wind variations; winter easterly winds would have driven a westward flow, with the converse true in summer.

Relative variability in the 20 m deep currents at stations 60, 61 and 69 is qualitatively shown by progressive vector diagrams for the summer 1976 period (May-October). While currents at stations

61C and 69B show some fluctuation, the overall direction of flow was consistent. Such was not the case at station 60C. One way in which current variability can be addressed quantitatively is by use of rotary spectra (Mooers, 1973), which give an indication both of the frequency components and of the rotational sense (if any) of the motion. Spectra for the 100 m deep records at stations 60B and 61B during winter (March-May 1976) are typical and are shown as an example (Fig. 6.3). Both spectra contain a clearly defined semi-diurnal tidal peak with no other significant peaks. At near-coastal station 60B, the total variance was only about 20% of that at station 61B at the shelf break. At station 61B some 65% of a total variance of 597 $cm^2 sec^{-2}$ was contained in periods between 12.00 and 12.86 hours, with about 30% in periods between 1.25 and 15 days. Tidal energy at station 60B, like overall energy, was lower than at station 61B. The overall correlation between the two data sets indicates that, at the 95% significance level, only flow at the semi-diurnal tidal frequency was correlated.

While the hydrographic structure of the water can be used to give an indication of large-scale, long time period motions, it will generally not reflect the shorter period flow fluctuations which characterize currents in the northeast gulf shelf region. With this limitation in mind, we present vertical sections showing density distribution along a transect normal to the coastline just downstream from Kayak Island (Figure 6.4). These sections clearly show evolution of vertical stratification during winter-summer 1976. Using;

$$\Delta\sigma_t = \sigma_{t_{15}} - \sigma_t$$

as a measure of vertical stratification, there was an increase of σ_t from ~0.5 to 2.0. This can be attributed primarily to freshwater addition consequent to summer snowmelt in the continental interior, while some of the change is due to temperature increase from isolation.

In addition to the change in stratification, the vertical density sections show a consistent pattern which must reflect long period flow. The sloping isopycnals indicate a westward baroclinic flow at the shelf break, an eastward counter-flow in the center of the section due west of the southern tip of Kayak Island and a weak westward coastal flow which was best defined during October. Since the current moorings were located west of the sections, a direct comparison between density structure and measured currents was not possible. We note, however, that the persistent westward shelf break flow suggested by the density field is consistent with the westerly flow observed at station 61. Comparison between density distribution and the drifters (cf. Fig. 6.1) is however more satisfying; drift trajectories on the downstream side of Kayak Island generally agreed well with the currents deduced from density distributions.

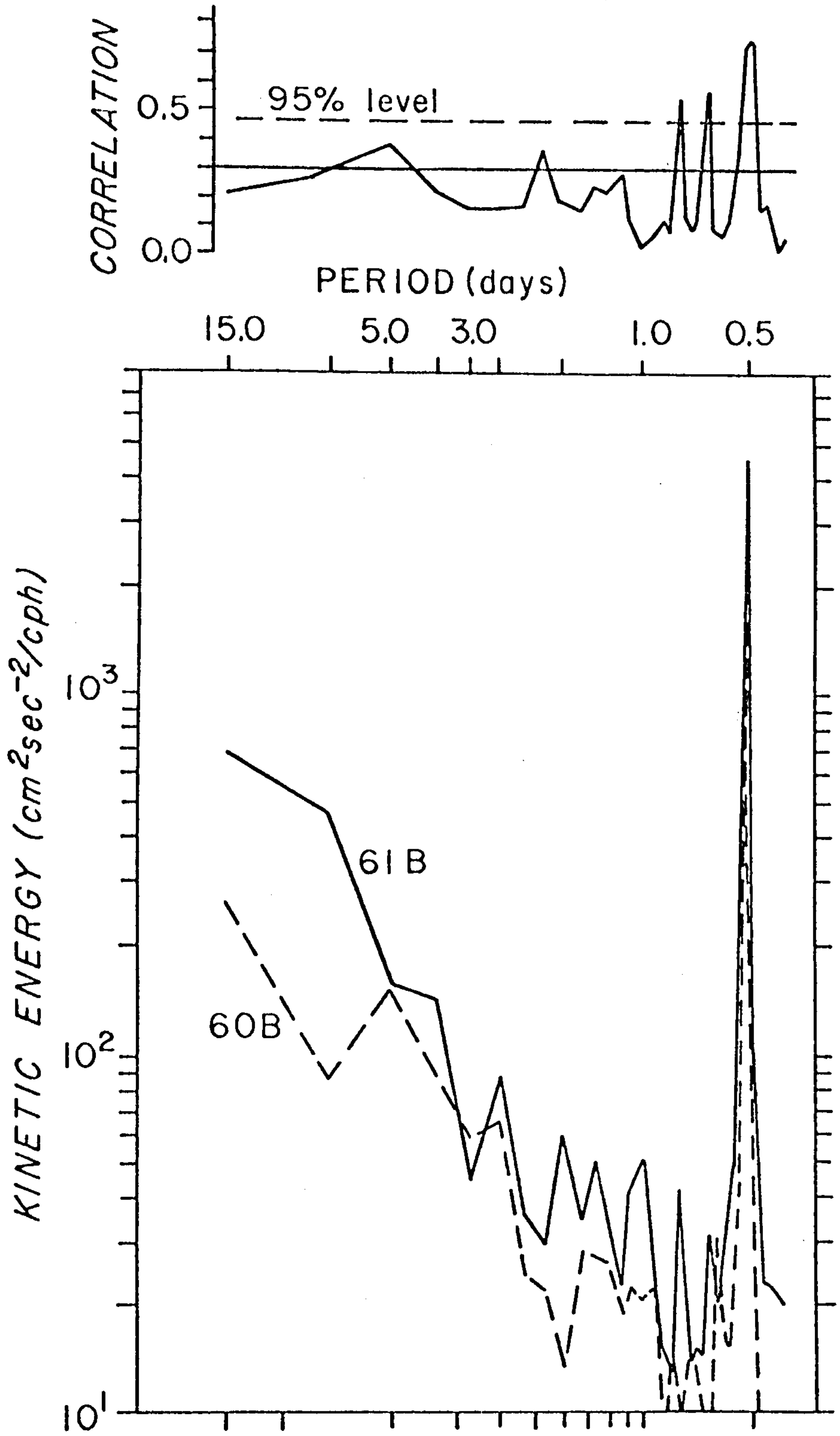

Figure 6.3 - Kinetic energy spectra and rotary correlations for 100 m winter current records at stations 60 and 61 west of Kayak Island.

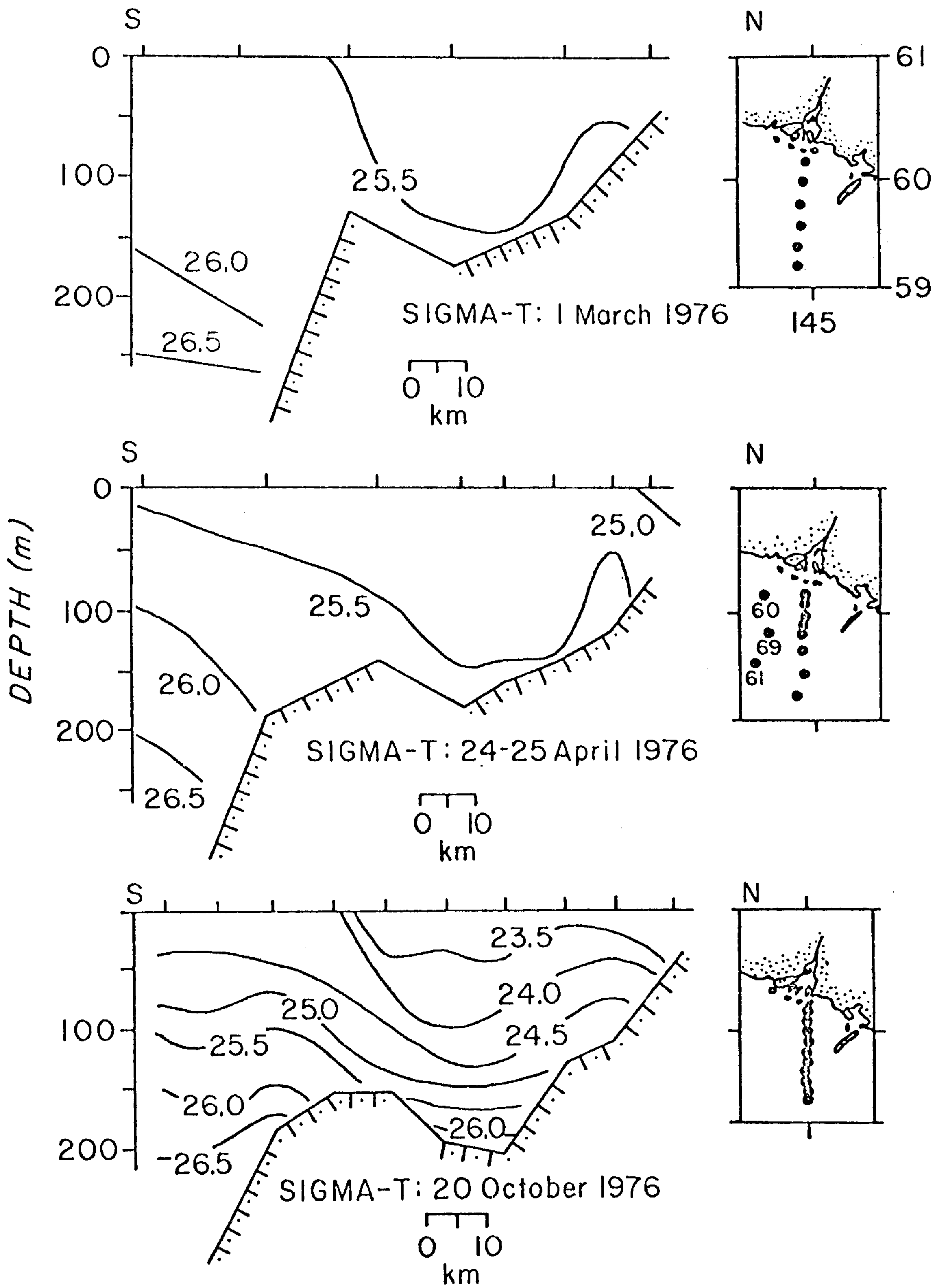

Figure 6.4 - Vertical distribution of density (as sigma-t) west of Kayak Island for three periods in 1976.

6.3 Conclusions

Our measurements have substantiated that there was a persistent westerly shelf break flow southwest of the southern tip of Kayak Island. Typical observed mean flow speeds were approximately 10-15 cm sec^{-1}, and were higher during winter than in summer. These compare well with speed estimates south-southwest of Kayak Island of 17-23 cm sec^{-1} based on buoy drift (Feely *et al.*, in press). Speed variability was also greater during winter. These seasonal variations are due to variations in the regional wind field, which drives the mean flow, and in the local winds which contribute to the shorter period fluctuations.

Shoreward from the shelf break, lee effects on the downstream side of Kayak Island confuse the flow field. Our moorings were too far west to aid in defining an easterly counterflow which was suggested both by drifter trajectories and by the density field. This counterflow has a consequence of pressure gradients established in the water by the blocking effect of Kayak Island, which protrudes southward into the westerly flow. The westerly coastal flow was likely contributed to, in addition, by a coastal low density wedge due to freshwater input. Current measurements in the lee of the island showed large variability which, in the case of the mooring nearest the coast (60) was considerably larger than the mean flow; mean flow at that location must be considered to have little real physical meaning.

The mid-shelf current station, 69, showed persistent shoreward flow which agreed qualitatively with the drogue trajectories. Since this flow persisted through winter-summer, it appears to be a permanent feature.

In summary, the shelf region west of Kayak Island was characterized by a westerly net flow which was greatest at the shelf edge. Flow variability increased shoreward, as mean flow decreased. The overall flow pattern was considerably more complex than to the east of Kayak Island, due to the blocking effect of the island itself.

7. DISCUSSION AND SUMMARY

Time series current data were obtained from moorings situated in the northeast Gulf of Alaska between Yakutat and Prince William Sound over periods varying from several months to about 2.5 years. These data show the major regional flow characteristic to be a westward mean current extending over the width of the shelf. This flow persisted throughout the year, but speeds were greater during winter than in summer.

The winter speed increase is due to winter increase in regional wind stress curl over the Gulf of Alaska. The Aleutian Low pressure system intensifies during winter, leading to migration of cyclonic storms over the gulf and consequent generation of large positive wind stress curls. This leads to increased cyclonic transport in the Gulf of Alaska gyre with a concurrent increase in westerly flow within the Alaska Current along the northeast gulf shelf break. The westerly flow on the shelf results from lateral transfer of momentum from the shelf break flow and from longshore sealevel slope set up by the shelf break flow. This shelf flow is abetted by local wind forcing and modified by local bathymetric effects, resulting in considerable complexity at the scales which we are considering.

7.1 Spatial Variability

Given a generalized westerly flow on the shelf, more detailed features can be discussed in terms of both spatial and temporal variability. The former will be addressed first. Spatial variations in currents in the northeast gulf are due primarily to constraints imposed by local bottom and coastline topography and, in some cases, to local winds. We first address the topographic, or non time-variant, effects.

The northeast Gulf of Alaska continental shelf can be divided into two segments, which have different physical oceanographic characteristics, by the southward extending promontory formed by Kayak Island. East of this island the shelf is relatively narrow, deep and broken by major bathymetric irregularities in the form of transverse troughs and ridges. West of the island the shelf is broader, shallower and, with the exception of a deep hole just west of Kayak Island, more regular in depth. The width differences in particular are pertinent to continental shelf physical processes. On broad shelves current regimes connected with the shelf break occur independently from the coastal current regimes; on narrow shelves the coastal and shelf break current systems merge and can generate considerable complexity.

Part of the difference in flow regimes between those regions east and west of Kayak Island requires consideration of the larger scale topography of the northern Gulf of Alaska. The northern coastline of the gulf is arcuate, curving in direction from northwesterly-southeasterly through east-west to southwesterly-northeasterly. Large-scale oceanic dynamics require that the Alaska Current intensify, due to this coastline configuration, as it flows westward. While the major intensification occurs to the west of our immediate study area, off Kodiak Island, it is likely that the shelf break flow west of Kayak Island may be stronger than that east of the island. Our observations are, however, insufficient to make conclusive statements about this hypothetical longshore flow variability. A cross-shelf flow west of Kayak Island might, in fact, tend to divert flow from the shelf break current and hence tend to mask this effect.

Currents on the shelf east of Kayak Island were westerly across the entire width of the shelf. At the shelf break, some anticyclonic rotary motions were present, probably due at least in part to the shear zone on the landward side of the Alaska Current. On the shelf itself, currents tended to parallel the local isobaths more closely and lacked the rotary component. West of Kayak Island, the flow was considerably more complex. While westerly flow was observed at the shelf break, as expected due to presence there of the Alaska Current, flows north of the shelf break were characterized by dominant shoreward components through the observation period and vertically through the water column. With the exception of the shelf break observations, currents west of the island showed considerably greater variability in speed and direction than east of the island. This increased complexity west of the island is due to lee effects from Kayak Island, which extends southward and blocks the flow along the shelf. This blocking leads to several features. One of the more obvious effects was vortex shedding in the downstream direction. These vortices were at times manifested as transient eddy-like features appearing first downstream from the island then propagating westward with the mean flow as they decayed. These features were observed both in satellite imagery and in satellite-tracked drifter trajectories.

A second effect of Kayak Island was to establish by its blocking effect a hypothetical (we have not observed it directly) mean sea-level slope leading to an easterly mean counterflow in the lee of the island. This counterflow was observed in drifter trajectories and as a persistent feature in the baroclinic (density) field. An easterly flow requires by volume continuity a compensating westerly flow, and there are two possible choices for such a counterflow. One option would be entrainment into the westerly flow off the southern end of Kayak Island, closing an anticyclonic eddy there. A second option would be inclusion in a westerly coastal flow. Such a coastal flow was observed in drifter trajectories and in the baroclinic field during late summer. The coastal flow appears to be in large part due to presence of a 5-10 km wide freshwater wedge consequent to freshwater input from the Copper River, so would be expected to be a seasonally appearing feature. The spring density section did not indicate presence of such a feature, and no drifter data were obtained during winter to verify its absence. We hypothesize that it may not be present during winter, or would be in greatly reduced form if present.

The strong shoreward component of flow observed at the mid-shelf current mooring west of Kayak Island and indicated also by one of the drifter paths is of uncertain origin. This flow was apparently too far west to reflect the counterflow behind Kayak Island, but it is likely that it reflected the perturbing influence of the island on westward flow.

7.2 Time Variations

It is apparent from examination of the long time series current record obtained from station 62 that time variability is a major factor to consider in any discussion of flow on the northeast Gulf of Alaska continental shelf. Standard deviations were at times larger than mean flow, particularly during summer when mean flow was weakest. Time variations can be subdivided and discussed according to the dominant time scales ranging from seasonal down to 5-7 day scales typical of synoptic weather patterns.

Seasonal variations are the most obvious both as to nature and source, therefore are easiest to characterize. They are manifested both as variations in the mean flow itself and as variations in intensity of perturbations upon the mean flow. Seasonal variations in mean flow were readily observable from the monthly means computed for station 62 (Section 3), and were also evident as differences between mean values computed for summer versus winter moorings at other locations (Sections 5 and 6). Seasonal variations in flow variability are reflected on the plots of variance (as mean speed squared) against time of year at station 62; the winter increase in variability was considerable, and was due to the effects on the water column of severe cyclonic storms migrating eastward through the system. It must be noted that, while the record from station 62 was long enough to qualitatively identify seasonal variation, the record was not long enough to statistically define the annual cycles. Since there was no reason to believe that the years sampled were abnormal, the variations observed are probably representative.

Shorter term fluctuations in current speed and direction, those which contribute to the large variability about the mean at station 62, are due to variations in local wind forcing and to interaction of the mean flow with topographic features such as Kayak Island and the ridges and troughs which cross the shelf transversly off Icy Bay. East of Kayak Island the flow regime is more heavily controlled by the westerly shelf break flow than west of the island because the shelf is narrower in the former location and also because the blocking action of the island itself influences downstream flow. Short-term (2-10 days) flow fluctuations east of the island are largely due to fluctuations in local wind forcing (Section 5), though some portion of the variability reflected fluctuations in the shelf break flow due in turn to offshelf disturbances.

West of Kayak Island, fluctuations were large relative to the mean flow. Due to the greater width of the shelf, local winds can be expected to play a larger role in driving variable currents relative to the shelf break-driven mean flow. Fluctuations downstream from the island would also reflect the effects of vortex shedding from the interaction of the island with the westerly flow, i.e., a topographic effect. Wind observations west of Kayak Island were inadequate for comparison with currents. It is therefore impossible to assess quantitatively the relative importance of local winds and topography upon flow variability west of Kayak Island.

Based on the foregoing, it is apparent that the concept of a "mean current" is a statistical entity which does not necessarily have any physical significance. This is due to the observation that the mean current was, in many cases, considerably less than the fluctuations about the mean. This was particularly true during summer, when the concept of mean current would have had little meaning if taken within a predictive context, and at current stations closer to the coast and farther from the shelf break.

The northern Gulf of Alaska coastal region has been characterized as a coastal upwelling regime during summer which reverses during winter to a downwelling regime. These are driven by the regional wind field. The current measurements off Icy Bay indicate that this was true some of the time during late winter-summer. There was a bimodality in the flow, however, which indicated that currents could be off- or onshore depending upon the particular wind event. As on other shelf regions, upwelling phenomena tend to occur as discrete events with periods of relaxation in between. Therefore, while the "mean" seasonal characterization might accurately be an upwelling or downwelling regime, the instantaneous situation at a given time can be quite otherwise in much the same way in which instantaneous currents need not bear any relation to mean currents. The topographic complexities west of Kayak Island make it difficult to determine whether upwelling or downwelling were in fact operative mechanisms. Near-bottom flow on the central shelf tended to be offshore, which would have supported a downwelling regime, but there did not appear to be a shoreward near-surface flow, necessary by continuity to maintain such a regime. The mid-shelf shoreward flow at station 60 downstream from Kayak Island extended through the water column. This barotropic feature was apparently a consequence of extension of Kayak Island southward into the westerly flow and was not related to wind-driven upwelling or downwelling. We conclude by characterizing the flow in the shelf region west of Kayak Island as generally northwesterly but with numerous temporal and spatial variations, large relative to the mean, superposed upon this flow.

When considering near-shore regions, it is necessary to take into consideration the rapid response of nearshore waters to local wind events. In light of the strong katabatic winds which occur in coastal regions of Alaska during winter, nearshore dynamics would be highly influenced by these outbreaks. Since such winds are not necessarily related to the regional wind field, they must be considered on a case by case basis when addressing the response of near-coastal waters.

Tidal currents have not been specifically addressed in this report except inasmuch as their presence has been noted as peaks on the energy spectra. Tidal currents represent fluctuations having time scales of a day or less, considerably shorter than those connected with meteorological forcing. In terms of trajectories for either water parcels or pollutants, they represent a mechanism for dispersion rather than for advection, taken in comparison with other advective terms such as instantaneous non-tidal flow.

7.3 Summary

Major features observed in the current distribution on the northeast Gulf of Alaska shelf can be summarized:

- Flow at the shelf break was westerly, with mean speeds on the order of 15 cm sec^{-1}. Large variations are however superposed on this mean speed and, coupled with directional variability, can lead to flow reversals.

- Westerly flow was strongest and most persistent at the shelf break. Nearer the coast, westerly flow weakened and directional variability became greater.

- Currents on the downstream (west) side of Kayak Island showed a mid-shelf eastward counterflow which appeared to be a permanent feature. During mid-late summer, a westerly near-coastal flow was observed shoreward of the counterflow. On one occasion, the westward shelf break flow interacted with the easterly counterflow to form a transient eddy-like feature on the downstream side of the island. West of this flow-counterflow system, flow across mid-shelf was northwesterly through the water column.

- Flow variability was larger relative to a weak mean flow during summer. During winter the mean flow was stronger and variability, while larger than during summer, was smaller relative to mean flow. The larger mean flow during winter was due to regional wind stress acting on the Gulf of Alaska gyre. The large winter variability was due to local winds acting on the shelf waters.

- Flow variability west of Kayak Island was due in part to vortex shedding off the southern tip of the island where it impinges into the westerly shelf break current.

- In all parts of the study region, flow variability was appreciable relative to, and at times larger than, mean flow. This was true with respect to both speed and direction. Mean flow figures must therefore be used with considerable circumspection when applied in a predictive sense.

8. REFERENCES CITED

Aagaard, K. 1970. Wind-driven transports in the Greenland and Norwegian seas. Deep-Sea Res., 17, 281-291.

Allen, J.S., and P.K. Kundu 1977. On the momentum, vorticity, and mass balance off the Oregon coast. J. Phys. Oceanogr. (In press).

Bakun, A. 1975. Wind-driven convergence-divergence of surface waters in the Gulf of Alaska. (Abstract) EOS Trans. Am. Geophys. Union, 56, 1008.

Beardsley, R.C., and B. Butman 1974. Circulation on the New England continental shelf: Response to strong winter storms. Geophys. Res. Lett., 1, 181-184.

Beardsley, R.C.,H. Hofjeld, M. Wimbush, C.N. Flagg, and J.A. Vermersch, Jr. 1977. Ocean tides and weather-induced bottom pressure fluctuations in the middle-Atlantic bight. J. Geophys. Res., 82, 3175-3182.

Brooks, D.A. and C.N.K. Mooers 1977. Wind-forced continental shelf waves in the Florida Current. Jour. Geophys. Res., 82, 2569-2576.

Brower, W.A., Jr., H.F. Diaz, A.S. Prechtel, H.W. Searby, and J.L. Wise 1977. Climatic atlas of the outer continental shelf waters and coastal regions of Alaska; Volume I - Gulf of Alaska. AEIDC Pub. B-77, Anchorage, Alaska, 439 pp.

Brown, W., W. Munk, F. Snodgrass, H. Mofjeld, and B. Zetler 1975. mode bottom experiment. J. Phys. Oceanogr., 5, 75-85

Buchwald, V.T. and J.L. Adams 1968. The propagation of continental shelf waves. Proc. R. Soc. London, A305, 235-250.

Carrier, G.F. and A.R. Robinson 1962. On the theory of the wind-driven ocean circulation. Jour. Fluid Mech., 12, 49-80.

Carter, G.C., C.H. Knapp and A.H. Nuttal 1973. Statistics of the estimate of the magnitude-coherence function. IEEE Trans. Audio Electro-acoust., AU-21, 383-389.

Charnell, R.L. and G.A. Krancus 1976. A processing system for Aanderaa current meter data. NOAA Tech. Memo. ERL PMEL-6, Seattle, Washington, 49 pp.

Clarke, A.J. 1977. Observational and numerical evidence for wind-forced coastal trapped long waves. Jour. Phys. Oceanog., 7, 231-247.

Csanady, G.T. 1974. Barotropic currents over the continental shelf. Jour. Phys. Oceanog., 4, 357-371.

Csanady, G.T. 1975. Lateral momentum flux in boundary currents. Jour. Phys. Oceanog., 5, 705-717.

Danielson, E.F., W.V. Burt and M. Rattray, Jr. 1957. Intensity and frequency of severe storms in the Gulf of Alaska. EOS Trans. Am. Geophys. Union, 38, 44-49.

Dodimead, A.J., F. Favorite and T. Hirano 1963. Salmon of the North Pacific Ocean region. Bull. 13, Inst. N. Pac. Fish. Comm., Vancouver, B.C., 195 pp.

Dodimead, A.J. and G.L. Pickard 1967. Annual changes in the oceanic-coastal waters of the eastern subarctic Pacific, J. Fish. Res. Bd. Canada, 24, 2207-2227.

Ekman, V.W. 1905. On the influence of the earth's rotation on ocean currents. Arkiv for Matematik, Astron. ock Fys., 2, 1-52.

Favorite, F. 1964. Drift bottle experiments in the northern North Pacific Ocean, 1962-1964. Jour. Oceanog. Soc. Japan, 20, 160-167.

Favorite, F. 1967. The Alaskan Stream. Int. N. Pac. Fish. Comm. Bull. 21, 1-20.

Favorite, F. and D.M. Fisk 1971. Drift bottle experiments in the north Pacific Ocean and Bering Sea 1957-60, 1962, 1966 and 1970. U.S.Dept. Comm., NOAA/NMFS Data Rep. 67, 20 pp.

Favorite, F. 1974. Flow into the Bering Sea through Aleutian passes, Oceanography of the Bering Sea. occas. Publ. 2, Inst. of Mar. Sci., Univ. of Alaska, Fairbanks, 623 pp.

Favorite, F, A.J. Dodimead and K. Nasu 1976. Oceanography of the subarctic Pacific region, 1960-71. INPFC Bull. No. 33, Vancouver, B.C., 187 pp.

Feely, R.A., E.T. Baker, J.D. Schumacher and G.J. Massoth 1978. Processes affecting the distribution and transport of suspended matter in the northeast Gulf of Alaska. Deep-Sea Res., 25, in press.

Fofonoff, N.P. 1960. Transport computations for the North Pacific Ocean. Ms. Rep. Ser., Fish. Res. Bd. Canada, 77, 87 pp.

Fofonoff, N.P. 1969. Spectral characteristics of internal waves in the ocean. Deep-Sea Res., 16, 59-71.

Frankignoul, C. 1974. A cautionary note on the spectral analysis of short internal wave records. J. Geophys. Res., 79, 3459-3462.

Galt, J.A. and T.C. Royer (in press). Physical oceanography and dynamics of the NE Gulf of Alaska. In; Proc. Symp. on Science Resources and Technology in the Gulf of Alaska, AINA.

Godin, G. 1972. The Analysis of Tides. Univ. of Toronto Press, Toronto, 264, pp.

Gonella, J. 1972. A rotary-component method for analyzing meteorological and oceanographic vector time series. Deep-Sea Res., 19, 833-846.

Gould, W.J. and E. Sambuco 1975. The effects of mooring type on measured values of ocean currents. Deep-Sea Res., 22, 55-62.

Gumbel, E.J. 1954. Statistical theory of extreme values and some practical applications, NBS Applied Mathematics Series, 33, 51 pp.

Halpern, D. and R.D. Pillsbury 1976. Influence of surface waves on subsurface current measurements in shallow water. Limnol. and Oceanogr., 21, 611-616.

Halpern, D. and J.R. Holbrook 1978. Moored near-surface current measurements during February 1975 on the Gulf of Alaska outer continental shelf. J. Geophys. Res. (in press).

Hayes, S.P. and J.D. Schumacher 1976. Description of wind, current and bottom pressure variations on the continental shelf in the northeast Gulf of Alaska from February to May 1975. Jour. Geophys. Res., 81, 6411-6519.

Hayes, S.P., J. Glenn and N. Soreide 1978. A shallow water pressure-temperature gage (PTG): Design, calibration and operation. NOAA Tech. Memo. (in press).

Hickey, B.M. 1977. The use of a numerical model as a diagnostic tool to interpret current and density measurements from the Washington shelf. EOS Trans. Am. Geophys. Union, 58, 1158.

Holbrook, J.R. and D. Halpern 1977. A compilation of wind, current, bottom-pressure and STD/CTD measurements in the northeast Gulf of Alaska, February-May 1975. NOAA Tech. Memo. ERL/PMEL-10.

Ingraham, W.J., Jr., A. Bakun and F. Favorite 1976. Physical oceanography of the Gulf of Alaska. Northwest Fish. Ctr. Processed Rep., July 1976, 132 pp.

Kroll, J. and P.P. Niiler 1976. The transmission and decay of barotropic topographic Rossby waves incident on a continental shelf. J. Phys. Oceanogr., 6, 432-450.

Kundu, P.K. and J.S. Allen 1975. Three dimensional structure of low frequency current fluctuations near the Oregon coast. J. Phys. Oceanogr., 6, 181-199.

Lee, T.N. 1976. Florida Current spin-off eddies. Deep-Sea Res., 22, 753-765.

McEwen, G.F., T.G. Thompson and R. Van Cleve 1930. Hydrographic sections and calculated currents in the Gulf of Alaska, 1927 to 1928. Rep. Int. Fish. Comm., 4, 36 pp.

Mooers. C.N.K. 1973. A technique for the cross-spectrum analysis of complex-valued time series with emphasis on properties of polarized components and rotational invariants. Deep-Sea Res., 20, 1129-1141.

Mooers, C.N.K. 1976. Wind-driven currents on the continental margin. In: Marine Sediment Transport and Environmental Management (Stanley and Swift, Eds.), John Wiley, N.Y., 29-52.

Muench, R.D. and G.M. Schmidt 1975. Variations in the hydrographic structure of Prince William Sound. Univ. of Alaska Sea Grant Rep. R75-1, 135 pp.

Munk, W.H. 1950. On the wind-driven ocean circulation. Jour. Met., 7, 79-93.

Munk, W.H. and G.F. Carrier 1950. The wind-driven circulation in ocean basins of various shapes. Tellus, 2, 158-167.

Mysak, L.A. and F. Schott 1977. Evidence for baroclinic instability of the Norweigian Current. Jour. Geophys. Res., 82, 2087-2095.

Reid, J.L. and A.W. Mantyla 1976. The effect of the geostrophic flow upon coastal sea elevations in the northern North Pacific Ocean. Jour. Geophys. Res., 81, 3100-3110.

Reynolds, R.M. and B.A. Walter 1976. A study of convective activity in the Bering Sea and air-mass modification on the southern Alaska Coast. Bull. Am. Meteorol. Soc., 56, 139.

Royer, T.C. 1975. Seasonal variation of waters in the northern Gulf of Alaska. Deep-Sea Res., 403-416.

Royer, T.C. and R.D. Muench 1977. On the ocean temperature distribution in the Gulf of Alaska, 1974-1975. Jour. Phys. Oceanog., 7, 92-99.

Royer, T.C. 1977. Hydrographic data report, Northeast Gulf of Alaska, July 1975-June 1976. Univ. of Alaska, Fairbanks.

Smith, R.L. 1974. A description of current, wind and sea level variations during coastal upwelling off the Oregon coast, July-August 1972. J. Geophys. Res., 79, 435-443.

Sverdrup, H.U. 1947. Wind-driven currents in a baroclinic ocean; with application to the equatorial currents of the eastern Pacific. Proc. Nat'l Acad. Sci., 33, 318-326.

Thomson, R.E. 1972. On the Alaskan Stream. Jour. Phys. Oceanog., 2, 363-371.

Webster, F. 1969. Vertical profiles of horizontal ocean currents. Deep-Sea Res., 16, 85-98.

Welander, P. 1957. Wind action on a shallow sea: Some generalizations on Ekman's theory. Tellus, 9, 45-52.

Welander, P. 1959. On the vertically integrated mass transport in the oceans. In: The Atmosphere and The Sea In Motion (Bolin, Ed.), Oxford, N.Y., 95-101.

TRANSPORT PROCESSES IN THE NORTH ALEUTIAN SHELF

by

James D. Schumacher

Pacific Marine Environmental Laboratory
National Oceanic and Atmospheric Administration
7600 Sand Point Way, N.E.
Seattle, Washington 98115

Final Report
Outer Continental Shelf Environmental Assessment Program
Research Unit 549

August 1982

ACKNOWLEDGMENTS

I acknowledge the aid of a large number of persons, not only in the preparation of this document but in carrying out the field work and processing which have led to its existence. Of these, special thanks must go to the complement of the research vessels *Discoverer, Surveyor,* and *Thompson* (R. B. Tripp, chief scientist) for laboring under less than ideal conditions to carry out field operations. Lynn Long, Sharon Wright, Gini May, Lt. Paul Moen, and Phyllis Hutchens of NOAA/PMEL are due thanks for their help in processing the data and preparing this document.

This study was supported in part by the Bureau of Land Management through interagency agreement with the National Oceanic and Atmospheric Administration, under which a multiyear program responding to needs of petroleum development of the Alaskan continental shelf has been managed by the Outer Continental Shelf Environmental Assessment Program (OCSEAP) Office, Juneau, Alaska.

TABLE OF CONTENTS

LIST OF FIGURES

LIST OF FIGURES (continued)

LIST OF FIGURES (continued)

LIST OF TABLES

1. INTRODUCTION

The general objective of research unit 549, Transport Processes in the North Aleutian Shelf, is to provide oceanographic data and interpretation of such in Unimak Pass and a portion of the southeastern Bering Sea shelf along the Alaska Peninsula (Figure 1). The results of this study provide input to oil trajectory modeling and a characterization of the physical environment. This, together with other studies, permits an estimation of fate and impact of petroleum resource development in the proposed north Aleutian Shelf lease area.

In this report, we first describe the regional setting, including a review of previous oceanographic studies. We then discuss methods of observation and analysis. Results are discussed in Section 4, where they are treated separately for Unimak Pass and the north Aleutian Shelf. The major features are summarized in Section 5, Summary and Conclusions.

2. SETTING

2.1 Geography

The Alaska Peninsula (Figure 1) extends about 700 km (∿157°W to 165°W) from the mainland to Unimak Pass and is oriented southwestward. The northern coast contains several major embayments; Bechevin Bay and Isanotski Strait which separate Unimak Island from the peninsula; Izembek/Moffet Lagoon located north of Cold Bay; the Nelson Lagoon, Herendeen Bay, Port Moller complex and Port Heiden. These indentations in an otherwise relatively strait coastline are accompanied by passages across the peninsula which break the rugged orographic contours. Such features permit local winds to become down gradient rather than geostrophic and hence can dramatically modify local winds over length scales of up to 30 km offshore.

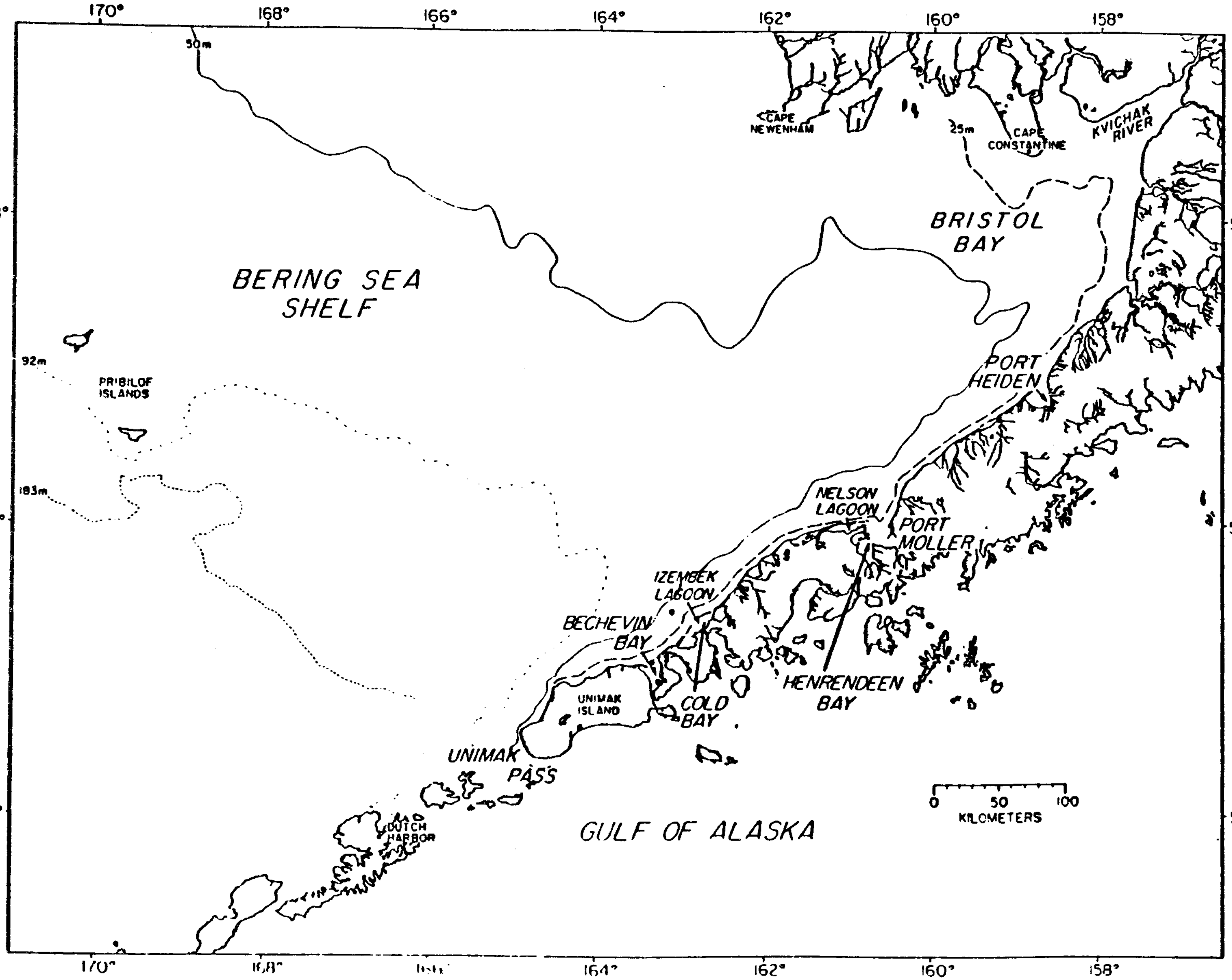

Figure 1. - Geomorphology of the southeastern Bering Sea shelf, including the study area.

Unimak Pass is the eastern most passage of significant cross-section ($\sim 10^6 m^2$) between the Bering Sea and the Gulf of Alaska. Complex orographic and bathymetric contours are typical in the vicinity of Unimak Pass. At the narrowest location (Scotch Cap to Ugamak Island) which we call the Pass proper, it is 19 km wide and has an average depth of ~55 m with an along-pass axis of 285°T. Complexity also exists due to the presence of the Krenitzin Islands southwest of Unimak Island and the passes between these islands and Unimak Pass proper. On the Krenitzen Islands, there are many peaks in excess of 800 m and elevations up to 2500 m exits on the western end of Unimak Island.

Bathymetry along the remainder of the study area is less complex, the 50-m isobath generally trends toward ~60°N from the northern coast of Unimak Island to about 159°W, where it becomes nearly orthogonal to the coastline. The shelf shoreward of the 50-m isobath is generally 20 to 30 km wide west of Nelson Lagoon where it becomes ~40 km in width and then is constricted to 20 km just east of Port Moller. From Port Mollar to Port Heiden, the width of the coastal region gradually broadens to 40 km. Seaward of the 50-m isobath, depths increase monotonically to greater than 100 m off Unimak Island, however, the 92-m isobath becomes nearly orthogonal to the peninsulas east of Cold Bay. Isobaths up to 80-m parallel the 50-m isobath and form a trench-like feature which extends into Kvichak Bay. This feature, which is most pronounced east of Port Moller, results in depths greater than 25 m to just east of Cape Constantine.

2.2 Physical Properties

Kinder and Schumacher (1981a) characterized this region of the shelf in terms of hydrographic properties and structure; along most of the peninsula the germane domains are the coastal and the middle shelf. The coastal domain (away from the direct influence of freshwater addition) is typically well mixed and lies shoreward of the 50-m isobath. The middle shelf domain generally is two-layered and lies seaward of the 50 m isobath. Separating these domains is a structural front (Schumacher et al., 1979) where a transition between well-mixed and two-layered vertical structure occurs. A typical width of the front is about 5 to 10 km. Geopotential contours across the front suggest baroclinic flow into Bristol Bay with surface speeds of 0.02-0.05 ms^{-1}. During winter, waters in the middle shelf are mixed to the bottom so that structural differences between domains are slight; however, fresher water remains in the coastal domain and cross-shelf density gradients persist.

Sources of fresh or less saline water include ice melt, local addition from rivers and, as will be shown later, flow of Kenai Current water through Unimak Pass. Recent studies of sea ice climatology include Webster (1979), Overland and Pease (1981), and Pease, Schoenberg and Overland (1982). The average progression (50% probability) of ice extent during the growth season (Figure 2: from Pease, Schoenberg and Overland 1982) indicates that ice growth occurs in northern Bristol Bay by December and progresses to maximum extent by March with ice covering much of Bristol Bay and extending along the peninsula to about 160°W. However, during extreme ice years, e.g. winter 1975-76, ice covered most of the north Aleutian shelf westward to Unimak Island. Local (rather than transported) ice production occurs along the northern shore of

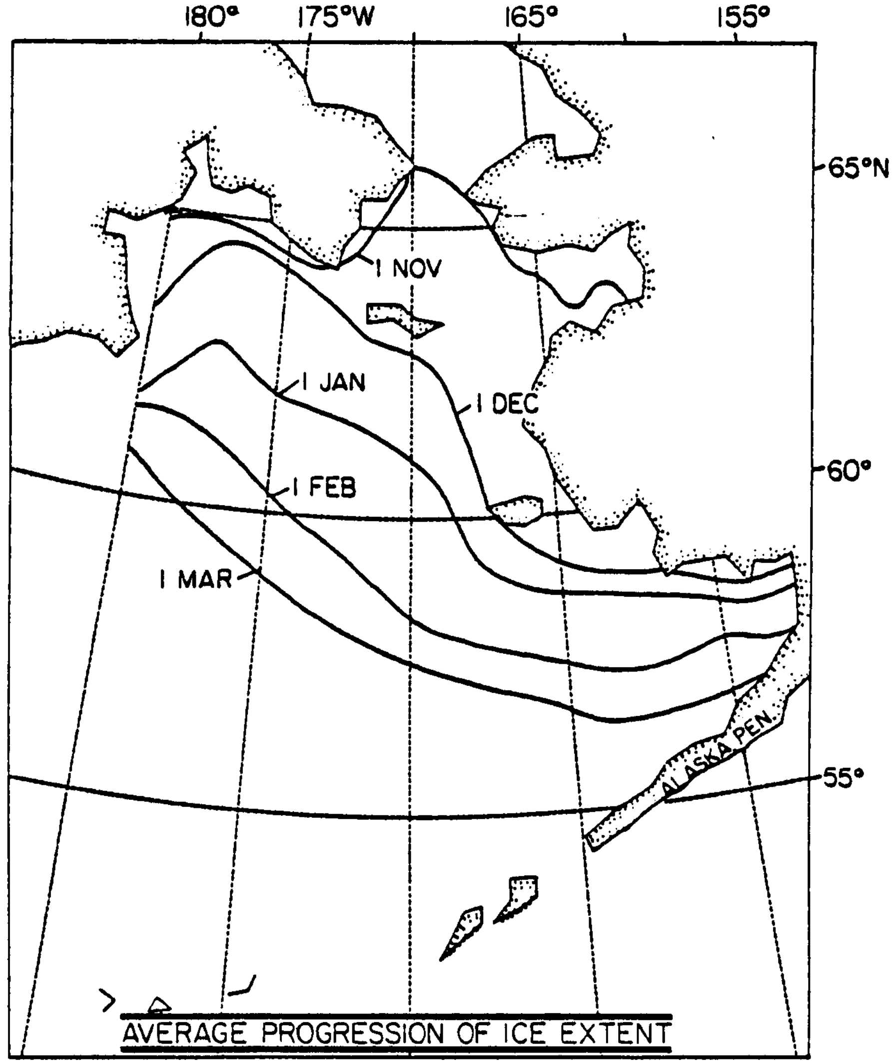

Figure 2. - Average progression (50% probability) of ice extent during the growth season, based on 1972-79 ice extents (from Pease et al., 1982).

Bristol Bay, and perhaps to a limited extent within the Port Moller system. Although there are no major rivers along the peninsula, rainfall is substantial. Brower, et al. (1977) show a decrease from ~3.2 m at ~158°W to 0.8 m at 162.5°W (Cold Bay). Just north of the eastern end of the Peninsula, the Kvichack River enters Bristol Bay. Seifert and Kane (1977) indicate that this river has a basin area of 16,800 km^2 and an average annual flow of 1.84×10^5 m^3 s^{-1}. Hydrographs indicate that mean daily discharge can vary by a factor of three between wet and dry years and that the greatest monthly discharge occurs in October (1,700 m^3 s^{-1}) with the minimum in April (~283 $m^3 s^{-1}$). However, a clear freeze cycle is not detectable, so that during winter discharge does not cease.

2.3 Circulation and tides

Since there are abundant fisheries (including Alaskan King Crab, Halibut, and Salmon) in the north Aleutian shelf region, much of the early (pre-1975) oceanography was in support of these resources. Although only a few, short-term (~4 days) current observations were made in the past (Reed, 1971), there exists the supposition that waters of the Gulf of Alaska enter the Bering Sea through Unimak Pass; general inflow vectors appear on large scale circulation schemes (e.g., Hughes, Coachman and Aagaard, 1974; Takenouti and Ohtani, 1974; and Favorite, Dodimead and Nasu, 1976). This belief is based on mariner's reports as given in The Coast Pilot, drift bottle studies (Thompson and Van Cleve, 1936; Favorite and Fisk, 1971) and on hydrographic data. The inflow of water through Unimak Pass has also been inferred in studies of lateral water mass interactions on the southeastern Bering Sea shelf (Coachman and Charnell, 1977: Coachman and Charnell, 1979).

Circulation along the peninsula is less well known. Kinder and Schumacher (1981b) present limited current meter data which suggests flow along the 50-m isobath into Bristol Bay. Schumacher and Pearson (1981) present drift card and radar tracked drogue data which support the inference of inflow in the vicinity of the 50-m isobath.

Tides constitute more than 90% of the horizontal kenetic energy (Kinder and Schumacher, 1981a) and are important to mixing and through interaction with bathymetry and/or relative sea level changes versus mean depth, to the generation of residual flow. Pearson, Mofjeld and Tripp (1981) described the tides over the north Aleutian shelf. The tide enters the Bering Sea through the central and western Aleutian Island passes and progresses as a free wave to the shelf. Largest tidal amplitudes are found over the southeastern shelf region, especially along the Alaska Peninsula and interior Bristol Bay. Each semidiurnal tide propagates as a Kelvin wave along the Alaska Peninsula but appears to be converted on reflection in interior Bristol Bay to a Sverdrup wave. In general, tidal ellipses are oriented along isobaths and are nearly rectilinear.

2.4 Climatology

A major influence of the general atmospheric circulation on the area is the region of low pressure normally located in the vicinity of the Aleutian chain, referred to as the Aleutian Low. On monthly mean pressure charts (e.g. Brower, et al. 1977) this appears as a low-pressure cell normally oriented with the major axis in an east-west direction. This is a statistical low, indicating only that pressures are generally lower along the major axis as a result of the passage of low-pressure centers or storms. Storms are most frequent in this area and are more intense than in adjacent regions. The most frequent trajectory of these storms is along the Aleutian Islands and into the Gulf of Alaska in winter, and along the same general path in the west but curving northward into the Bering Sea in summer (Overland, 1981). The monthly frequency of low-pressure centers in the southern Bering Sea is slightly higher in winter (generally four to five) than in summer (three to four), with winter storms being more intense. Climatology of the southern Bering Sea can be characterized by a progression of storms rather than fixed weather types (Overland, 1981) and the presence of mountain passes will further complicate local wind characteristics.

3. METHODS

3.1 Current and Bottom Pressure

Most of our measurements were made using RCM-4 Aanderaa recording current meters on taut-wire moorings. Typical instrument placement was 20 m below the surface and 10 m above the bottom. Where water depths were less than 35 m, a singe RCM-4 was located at 10 m above the bottom. The subsurface flotation was usually at 18 m depth, and exerted about 1000 lb (1 lb = 4.45N) buoyancy. Sampling interval was 30 minutes. Aanderaa RCM-4 current meters record speed by summing the number of rotor turns for (in our case) 15, or 30-min intervals. Direction is recorded at the time of sampling by measuring compass and vane orientation. Therefore, speed recorded at time t_n is integrated over $\Delta t = t_n$ t_{n-1}, while direction is instantaneous at time t_n. Speed at t_n and t_{n-1} were averaged before converting to east and north components of velocity at time t_n. These components were then low-pass filtered (filter half-amplitude response was at a period of 2.9 hr) and a second-order polynomial was used to interpolate the observations to whole hours. We estimate that directions were accurate to ±5° and speeds to ±1 cm/sec, exclusive of rotor pumping mooring motion, or fouling. A summary of meter location, depth and obstruction period is given in Appendix A. Note that on most of the Transport Processes (TP) moorings, one of the RCM-4's was fitted with a transmissometer.

It is well known that mechanical current meters such as the RCM-4 may give erroneous speeds because of effects from either mooring motion or high frequency water motion (e.g. Quadfasel and Schott, 1979, give several references). Pearson, Schumacher, and Muench (1981) have examined the performances of moorings like ours on the Alaskan shelves, and they found speed differences at tidal frequencies of $\leq$ 10% when windy and calm seasons were compared, however, during storms erroneous speeds do occur. Extrapolating their results to lower frequencies, we believe that the effects of mooring motion and rotor pumping were minor and that errors were probably limited to a few percent increase of the speeds of low frequency flows (which were usually strongest during windy periods).

At some locations along the Alaska Penninsula, Neil Brown accoustical (ACM) current meters were used because biological fouling was a problem for mechanical rotors (Schumacher and Pearson, 1980). The ACM's emit continuous high frequency acoustic signals which are phase advanced or delayed as they travel with or against the current. The relative phase is converted to a voltage which is directly proportional to the water velocity. Currents are measured along two right angle horizontal paths. At a pre-determined interval, in this case one minute, the component velocities are averaged and recorded. Ten minute segments of the original one minute sample interval data were averaged.

In order to characterize the bottom pressure field and to estimate sea level changes, Aanderaa TG-2 or TG-3 pressure gauges were deployed on all of moorings. These instruments were located in a cage welded to the anchor, thereby eliminating any possible noise due to mooring motion. Sampling intervals varied between 15 and 30 minutes.

Data from the current meters and pressure gauges are processed in a similar manner. The original series are converted to engineering units, and time base is checked by comparing field logs to the number of records. Excessive values are removed by determining the standard deviation (σ) of consecutive one-thousand record segments and eliminating values greater than six σ from the segment mean. A tidal analysis is then performed on the edited data set to check consistency of tidal amplitudes and phases.

Two sets of time-series are produced from edited current and pressure observations using a Lanczos filter [cf. Charnel and Krancus, 1976]. The first set is filtered so that over 99% of the amplitude was passed at periods greater than 5 hr, 50% at 2.9 hr, and less than 0.5% at 2.0 hr. These sets are used to determine tidal constituents and spectral estimates. The second sets are filtered to remove most of the tidal energy; the filter passed 99% of the amplitude at periods greater than 55 hr, 50% at 35 hr, and less than 0.5% at periods less than 25 hr. These sets are resampled at 6 hr intervals for use in examining subtidal current and pressure.

3.2 Hydrographic Data

Conductivity and temperature versus depth (CTD) data were obtained during three cruises conducted by NOAA's Pacific Marine Environmental Laboratory and one "ship of opportunity" cruise (Appendix A). The CTD systems sampled five times per second during the down-cast (lowering rate of 30 m/min). Nansen bottle samples were taken at most stations to provide temperature and salinity calibration. Data from monotonically increasing depth were "despiked" to eliminate excessive values and were averaged over 1-m intervals to produce temperature and salinity values from which density and geopotential anomaly were computed.

3.3 Wind Observations

Because orography can effect large-scale geostrophic winds (Livingstone and Royer, 1980), a meteorological station was established near Lagoon Point and was maintained throughout the current meter observation period. The wind sensor was located about 7 m above ground level. The ensuing parameters are recorded like the Aanderaa RCM-4 and are processed similarly. We also have surface wind time series over the mooring period which were computed by Fleet Numerical Weather Central from 6 hr synoptic surface pressure maps, using a 3° grid mesh and interpolated at 57°N, 163.5°W. The surface winds were estimated by rotating computed geostrophic wind by 15°to the left and reducing it in magnitude by 30% (Bakun, 1973). Climatological data from Brower, *et al*. (1977) was also used.

4. RESULTS

4.1. The Unimak Pass Experiment

Three current meter/pressure gauge moorings (Figure 3) were deployed in and on either end of Unimak Pass to describe currents and evaluate forcing

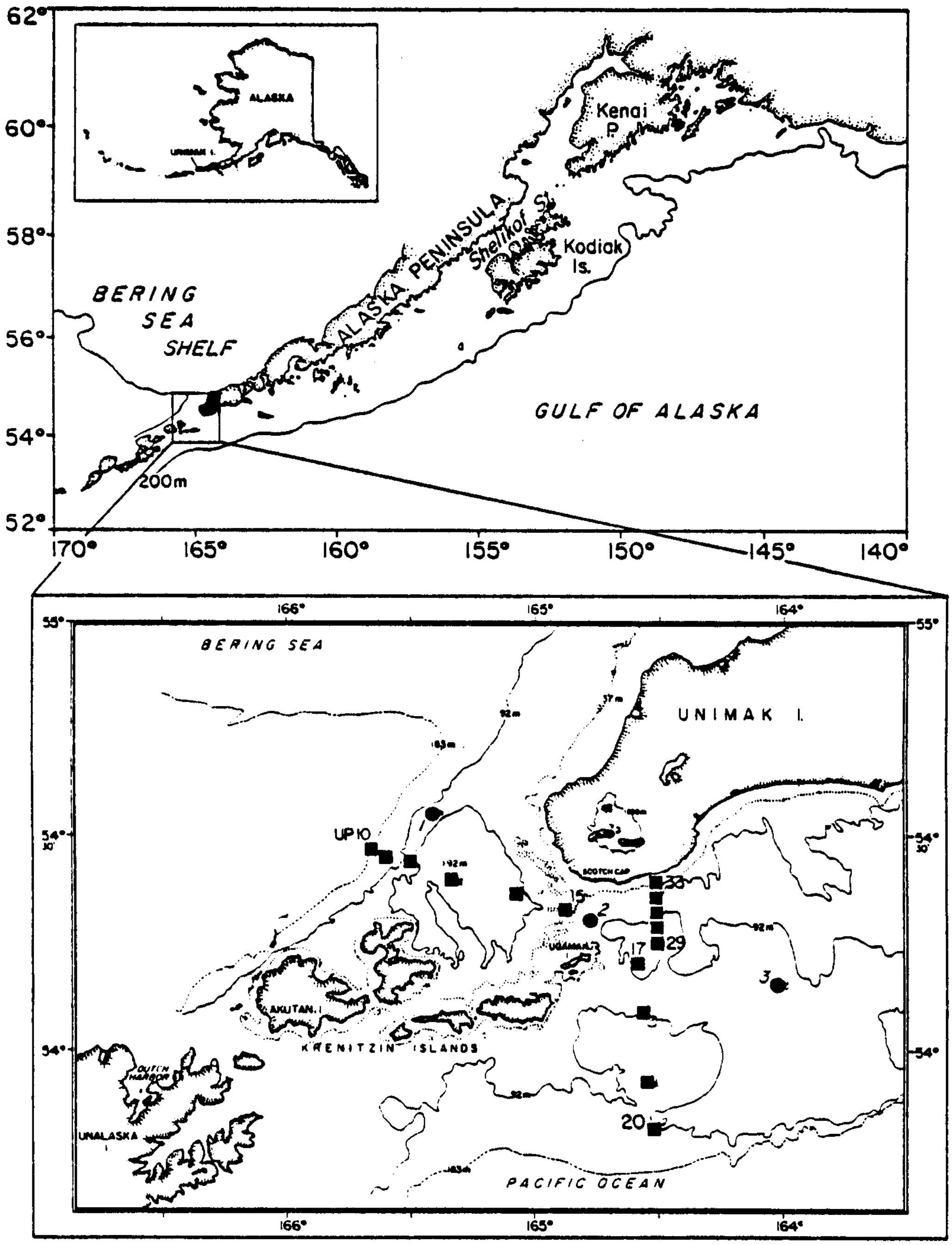

Figure 3. - Geographic setting showing (a) the Gulf of Alaska and Bering Sea shelves and (b) a detailed view of the Unimak Pass study area with some orographic features and the location of current meter and pressure gauge moorings (dots) and CTD stations (squares). Depth contours (given in meters) were constructed from the 20 (dotted line), 50, and 100 fathom isobaths.

mechanisms. Each mooring consisted of two Aanderaa RCM-4 current meters separated by ~1 m and located 20 m above the bottom and an Aanderaa TG-3 pressure gauge. Such redundancy of current meters increases the probability of recovering at least one data set per mooring (one meter did fail).

From 11 March 1980 to 15 August 1980, the atmospheric pressure gradient across Unimak Pass was determined using the National Meteorological Center's twice daily sea level pressure analyses for the Northern Hemisphere. Each map was quality checked for station accuracy and pressure analysis, and then a pressure gradient vector was determined for 54°N, 165°W and recorded in terms of direction from true north and magnitude in mb/1° latitude. Wind time series over the mooring period were computed by Fleet Numerical Weather Central from 6 h synoptic surface pressure maps, using a 3° grid mesh and interpolated at 54°N, 163°W.

4.1.1. Introduction

Straits or passes which connect large bodies of water are a common geographical feature throughout the world and water transported through the straits can have a profound impact on oceanographic characteristics in the surrounding bodies of water. In his review of currents in a strait, Defant (1961) discusses the oceanography of several well-known examples and notes that the dynamic cause of currents in these straits lies in the density difference between the adjacent bodies of water. While mean flow generally may be driven by such differences, shorter period (two to ten days) fluctuations are driven by barotropic sea level differences along the strait. These, in turn, can be produced by large-scale meteorological forcing which results in sea level changes at the coast. Examples of passages where such forcing was observed include the English Channel (Bowden, 1956), the Bering Strait (Coachman and Aagaard, 1981) and the Strait of Belle Isle (Garrett and Toulany, 1981: Garrett and Petrie, 1981).

We present results from current, bottom pressure and hydrographic data which support the supposition of inflow to the Bering Sea, however, the waters are from the shelf of the Gulf of Alaska and not the Alaska Stream. Further, both driving mechanisms noted above are operative; the mean flow was related to a baroclinic coastal current along the southern side of the Alaska Penisula and fluctuations were related to an along pass bottom pressure difference generated by sea level changes mainly over the Gulf of Alaska shelf.

4.1.2 Low Frequency and Mean Current

The 35 hr filtered current meter data are shown as scatter diagrams (Figure 4A) and progressive vector diagrams (PVD's, Figure 4B). The scatter diagrams depict the distribution of the 6-hourly current vectors and thus provide a visualization of variance about axes, while PVD's emphasize the time-dependent nature of the low frequency flow. In the Bering Sea (UP1) about 50% of the vectors were in the northwest quadrant with a mean speed of about 15 cm/s. There were, however pulses toward the south with magnitudes of 15 to 20 cm/s. Currents at UP2 tended to parallel the isobaths in the pass and about 75% of the observations indicated flow from the Gulf of Alaska shelf into the Bering Sea. Maximum pulses (60 to 75 cm/s) prevailed over tidal current reversals. On the Gulf shelf (UP3), flow was highly variable in direction with a slight westward tendency. The strongest flows were 15 to

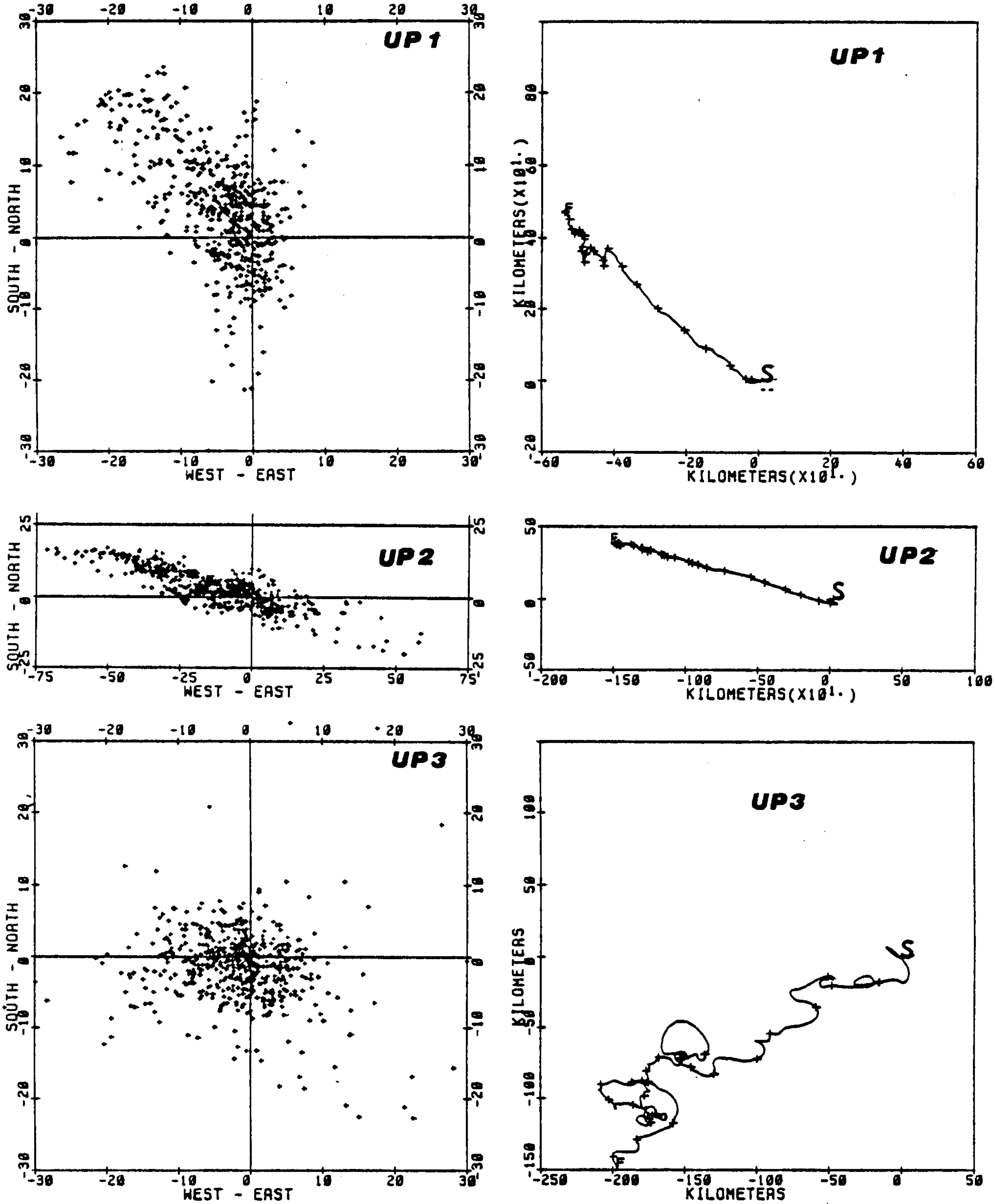

Figure 4. - Results from 35-hr filtered current data presented as scatter plots and progressive vector diagrams (S represents the start of the record, and the crosses are at 5-day intervals). Note the different speed and length scales.

30 cm/s toward the southeast. The PVD's (Figure 4B) show similar flow features, however, the 5-day time ticks suggest that two distinct levels of current magnitude occurred during the observation period: the strongest flow existed during approximately the first seventy days while flow was markedly less during the last half of the current records.

In Figure 5, we present plots of the 35 hr filtered currents and bottom pressure for each of the mornings, the UP3-UP1 bottom pressure difference (ΔP), the atmospheric pressure gradient, and the geostrophic (Bakun) winds. The currents are resolved along the axis of greatest variance (defined by the principal eigenvector of the orthogonal velocity component covariance matrix computed for the entire record) which also corresponds to flow through the pass. The atmospheric pressure gradient is resolved along an axis of 165°T approximately normal to the Gulf of Alaska coastline. The winds are resolved along 255°, parallel to the Alaska Peninsula.

A characteristic common among all the time-series was a transition from a period of large fluctuations to one of lesser variance which occurred about halfway through the records. Analysis of the atmospheric pressure gradient series showed that while the direction of the principal axis remained constant toward 336°T (i.e. higher pressure over the Gulf of Alaska), magnitude increased during the second half by a factor of two and variance decreased. A dramatic change also occurred in winds with alongshore magnitude increasing from -1.7 m/s in the first period to -3.5 m/s in the later period. This suggests a four-fold increase in wind stress and enhanced coastal divergence along the Gulf side of the Alaska Peninsula. These results are consistent with the establishment of high pressure over the north Pacific Ocean which is a summer climatological feature (Brower, *et. al.*, 1977). Thus, that component

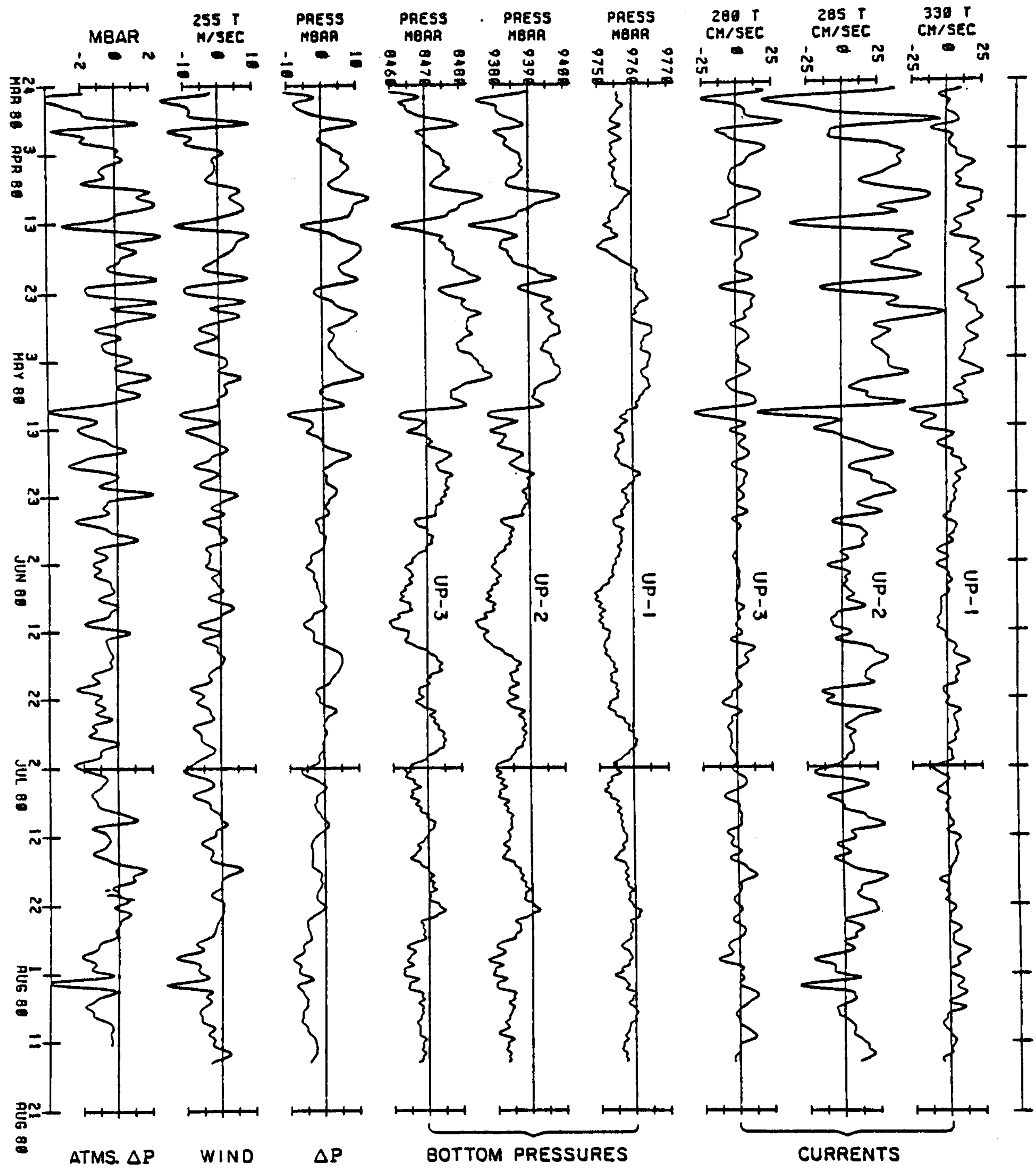

Figure 5. - Current vector time-series (35-hr filtered data) of current, bottom pressure, bottom pressure difference between UP3 and UP1 (Δ1P), alongshore geostrophic wind, and atmospheric pressure gradient (ATMS ΔP in mbar/°lat.).

of current which is a local response to meteorological forcing will also undergo a seasonal change.

A seasonal signal exhibiting less energy during summer was evident in current and wind time-series from both the northwest (Schumacher and Reed, 1980) and northeast Gulf of Alaska (Lagerloef, Muench, and Schumacher, 1981) and from the southeastern Bering Sea (Kinder and Schumacher, 1981a). As will be discussed later, an important aspect of flow through Unimak Pass is a non-locally generated coastal current which has a seasonal signal linked to fresh water discharge (Royer, 1981). Although our records are too short to unequivocally define the amplitude and phase of a seasonal signal in flow through the pass, we clearly have observed a marked change between first and second halves of the records. The impact of this difference on mean current is given in TABLE 1. The first half of the records (26 March to 3 June 1980) is called spring and the second half summer because the derived winds during this time were very similar to climatological mean winds and hence reflect a seasonal signal.

Within Unimak Pass vector mean speed decreased by a factor of three between first and second halves, while direction remained nearly constant. The error estimate is a measure of statistical significance for the vector mean; the values in TABLE 3 are twice the RMS error estimate and thus are analogous to a 95% confidence interval. Using this measure, mean flow in the pass was always significant while on the shelves adjacent to the pass there was significant mean flow only during spring.

4.1.3 Time-Series Relations:

We consider the correlations given in TABLE 2 in the context of a simple conceptual model of low frequency currents as follows: 1) currents in Unimak

Table 1. - Current and wind during first (spring) and second (summer) halves of the observations.

Record	Observation Period	Vector Mean Speed (cm/s: °T)	Error Estimate[1] (cm/s)	Variance (cm^2/s^2)
UP1	spring	9.8 : 306	± 6.6	14.1
	summer	2.2 : 334	± 2.2	8.9
UP2	spring	19.3 : 285	± 9.2	37.4
	summer	6.0 : 282	± 4.6	13.1
UP3	spring	3.2 : 240	± 2.4	41.0
	summer	1.0 : 198	± 1.2	12.4
Geostrophic Wind	spring	2.3×10^2 : 030	± 2.6	18.1×10^4
	summer	3.8×10^2 : 048	± 1.6	11.6×10^4

[1] Estimate of Error = $2\sigma/(\ell/\tau)^{\frac{1}{2}}$, where σ is the standard deviation along the vector mean speed axis, ℓ is the record length and τ is the integral time scale or area under the autocorrelation function (Allen and Kundu, 1978).

Pass are driven by the pressure difference on either side of the pass, 2) the pressure difference is produced by sea level changes which can occur along the coast on both sides of the pass, and 3) currents observed on the adjacent shelves respresent a barotropic reponse to pressure gradients rather than an Ekman layer response. All of the observed currents were collected at least 47 m below the surface. As noted by Winant (1980), conventional estimates of the thickness of the Ekman layer are about 40 m and Royer, Hansen and Pashinski (1979) suggested that the stratified Ekman layer depth in the northern Gulf of Alaska is probably less than 35 m.

Table 2. - Correlation matrix.

	CURRENT			BOTTOM PRESSURE			WIND		BOTTOM PRESSURE DIFFERENCE	ATMOSPHERIC PRESSURE GRAD
	UP1	UP2	UP3	UP1	UP2	UP3	ALONG SHORE	CROSS SHELF	(ΔP)	
UP1	1.0	.67	.34	.47(4)	.69	.47(4)	.40(1)	.44(4)	.69(1)	.47(2)
UP2	--	1.0	.70(1)	*	.69	.79	.77(1)	.24(5)	.87	.76(2)
UP3	--	--	1.0	*	.38	.41	.57(1)	.24(6)	.50(1)	.55(1)
UP1	--	--	--	1.0	.78(1)	.66(1)	*	.25(5)	*	*
UP2	--	--	--	--	1.0	.93	.46(1)	.35(5)	.65	.54(1)
UP3	--	--	--	--	--	1.0	.54(1)	.38(6)	.50(1)	.58(2)
ALONG SHORE	--	--	--	--	--	--	1.0	*	-.65(-1)	.58(2)
CROSS SHELF	--	--	--	--	--	--	--	1.0	.32(6)	.29(2)
BOTTOM PRESSURE DIFF.	--	--	--	--	--	--	--	--	1.0	.60(2)

Note: rows lag columns and numbers in parentheses are multiples of 6 hr.

The linear relation between pressure difference and current at UP2 accounted for 76% of the current variance (85% in spring and 50% in summer). When alongshore winds increased, bottom pressure at UP3 decreased, however reponse at UP1 was not significantly correlated with alongshore wind. Further, the variance in the bottom pressure record from UP1 was only one-third of that estimated in the record at UP3. Thus, changes in the bottom pressure difference were primarily a result of forcing on the Gulf shelf with a large fraction, 42% (50% in spring and 25% in summer) accounted for by the relation with alongshore wind. To address the question why there was more energy in current and bottom pressure records from the Gulf shelf than from the Bering Sea at meteorological frequencies we use climatological data (Brower, *et al*, 1977) and principal storm track data from March through August 1980 (Mariner's Weather Log, 1981). We divided data from a 10° by 10° region (50° to 60°: 150° to 170°) into a Bering Sea area north of 55° and a Gulf of Alaska area south of that latitude. There were seven principal storm tracks located in the Gulf and three in the Bering Sea. During our observations in 1980, there were eleven principal and eight secondary storm tracks south of the Peninsula while over the Bering Sea there were only six principal and three secondary storm tracks. In general, we expect to find greater meteorologically induced activity over the Gulf shelf.

It appeared that cross-shelf wind also contributed to the pressure difference, with significant correlation to bottom pressure on both shelves. The strength of these relations only accounts for ~6% (12% in spring, not significant in summer) and 14% (28% in spring, not significant in summer) of the variance at UP1 and UP3 respectively. Hayes (1979) noted the importance of cross-shelf wind to pressure gradient and estimated correlation coefficients of similar magnitude over the northeast Gulf of Alaska shelf. Chao and Pietrafesa (1980) noted that a larger contribution from cross-shelf wind forcing usually results in a phase lag of sea level fluctuation response, and the results in TABLE 2 are consistent with their results. In general, our conceptual model of interaction between wind, bottom pressure and current in Unimak Pass accounts for much of the observed current fluctuations.

In order to examine relations between pressure difference and both Unimak Pass current and geostrophic wind as a function of frequency, we present coherence squared estimates in Figures 6 and 7. Current in the pass was coherent at all frequencies with the pressure difference series during both spring and summer with the largest coherence squared (~0.70 to 0.96) at periods of about 3 to 10 days. During both record segments coherence decreased at the longest period resolved (~23 days). In order to present coherence results as a single, phase independent measure, we use the following technique. At each frequency where coherence squared was significant at the 95% level, the product of the dependent variable (*i.e.* current) variance times the coherence squared was determined. Summing this product over all frequencies and dividing by the total record variance, we determined that 89% and 66% of the current fluctuations were accounted for by fluctuations in the pressure difference series during spring and summer, respectively.

Coherence squared estimates between the pressure difference and geostrophic wind components (Figure 7) were greatest during spring: 70% and 26% of the fluctuations in bottom pressure difference were accounted for by relations with alongshore and cross-shelf winds, respectively. During summer, the percent of variance explained was only 9% and 7% respectively. If the variance at periods longer than 10 days was neglected (the series were not coherent at these periods), then the values were 43% and 33%. It appears that at periods longer than ~10 days, the bottom pressure field was responding to

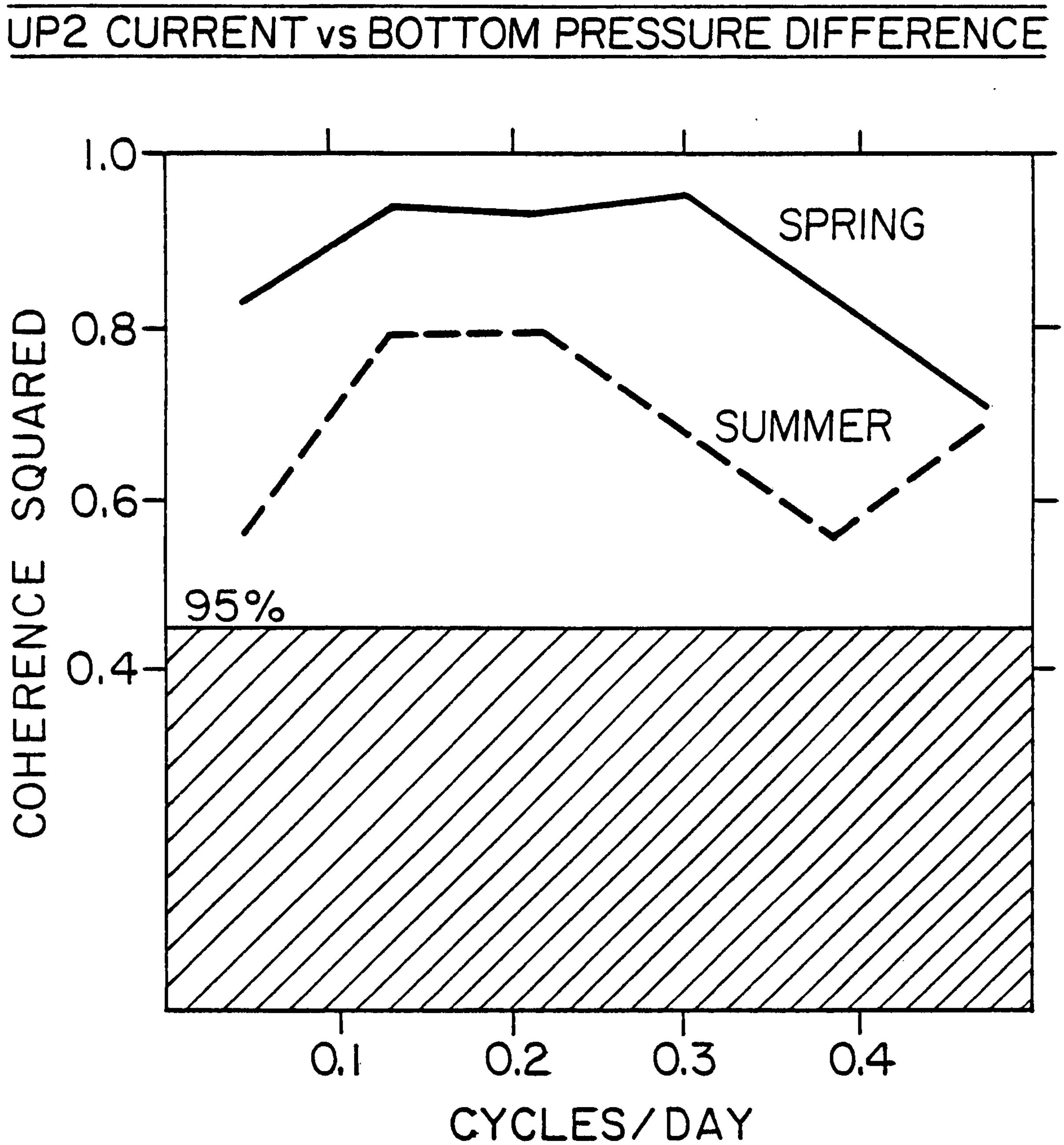

Figure 6. - Coherence between current in Unimak Pass (UP2) and bottom pressure difference along the pass for spring (solid line) and summer (dashed line) record segments.

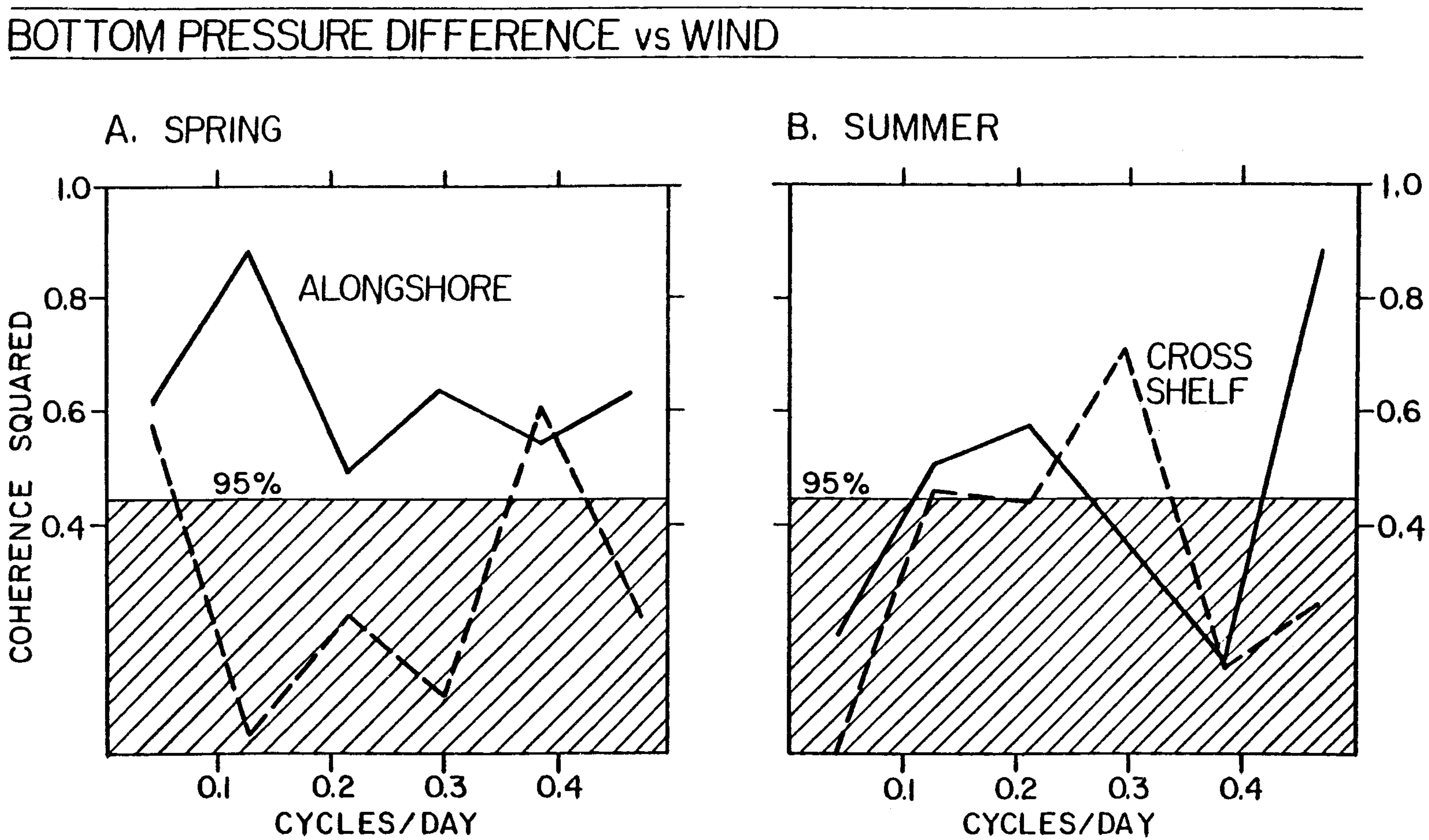

Figure 7. - Coherence between bottom pressure difference and geostrophic wind components during (a) spring and (b) summer record segments. The coherence with alongshore wind component is shown as a solid line and with the cross-shelf component as a dashed line.

forcing other than wind induced pressure gradients. It is most likely that changes of density were the cause; Reed and Schumacher (1981) noted that insolation is important to monthly mean sea level anomalies as early as June at Dutch Harbor.

The current time-series indicated that flow was generally from the Gulf of Alaska to the Bering Sea shelf and both mean and fluctuating currents were significantly greater during spring. Relations between the various series suggest that large scale atmospheric pressure fields, hence geostrophic winds, were responsible for the 3 to 10 day fluctuations. The mode of interaction was mainly peturbation in sea level along the Gulf of Alaska coast. The longer period wind stress was alongshore (northeastward) which would generate a barotropic component of current alongshore (towards the northeast), rather than the observed negative alongshore or westward mean flow through the Pass. So, we now examine hydrographic data to describe property distributions and to elucidate the role of mass distribution in generating long-term mean flow through Unimak Pass.

4.1.4 Property Distributions

Vertical sections of temperature, salinity and sigma-t for 4 to 5 September 1980 are shown in Figures 8A, B and C, respectively. Across the bottom of each panel the magnitude of the surface minus the bottom value of each parameter is also shown. Over the Gulf of Alaska shelf (stations 17 to 20) thermal stratification exceeded 4.0°C and the upper 50 m were considerably warmer than over the Bering Sea shelf (stations 14 to 10). Although tides and thus tidal mixing are more energetic within Unimak Pass proper (station 15), thermal stratification in the pass (~2.5C) was greater than thermal stratification (~0.9 to 1.5°C) observed in Bering shelf waters. A similar distribution

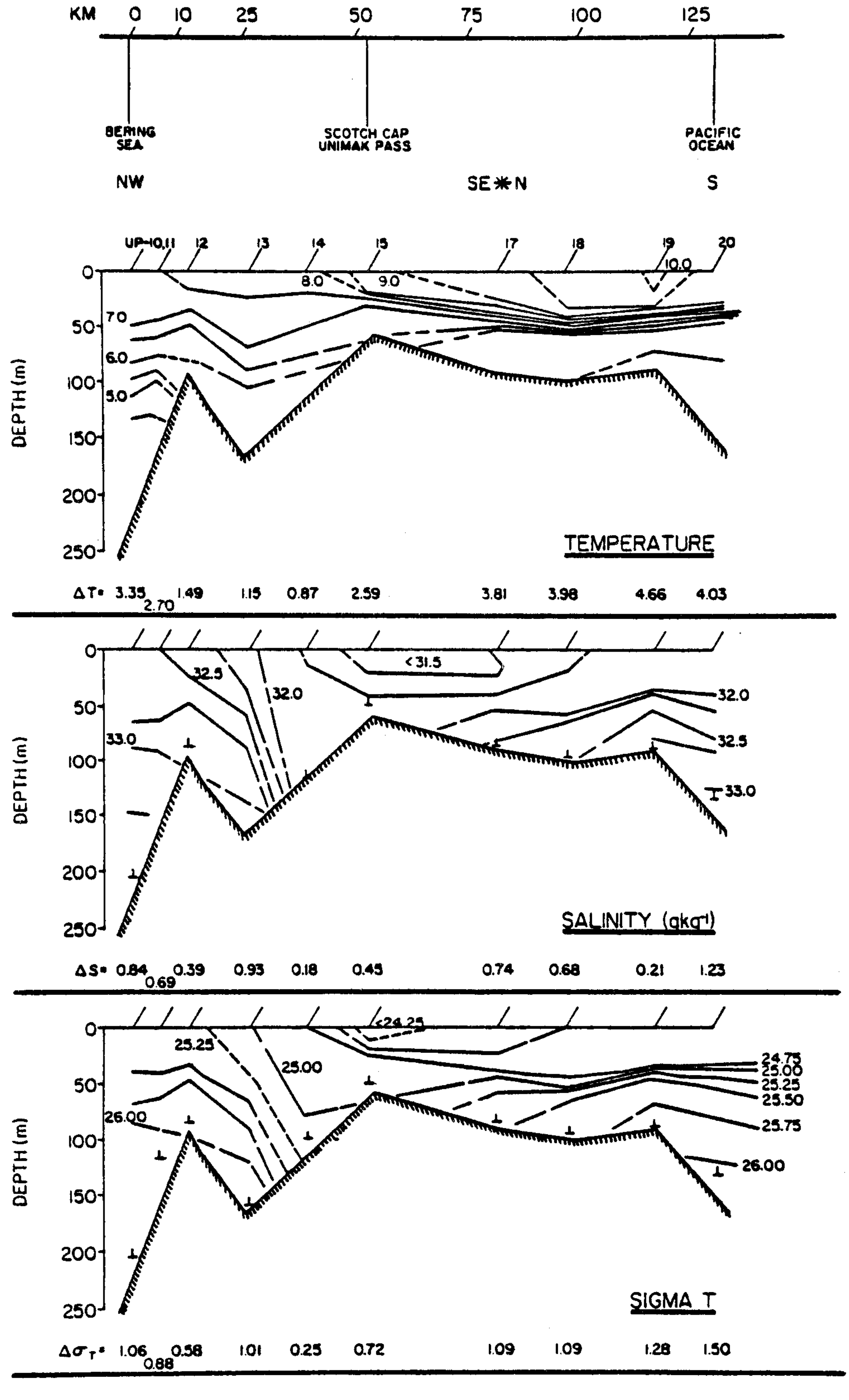

Figure 8. - Hydrographic data from September 1980 presented as temperature (°C), salinity, and sigma-t sections. The Δ values are the magnitude of surface minus bottom 1 m averaged values. See Figure 1 for station locations.

existed in salt content; ΔS values were greatest over the Gulf shelf, persisted within the pass and were least west of the pass proper. We note a region of low salinity ($\leq$31.75 gm/kg) existed within ~25 km of Unimak Island. The impact of temperature and salinity upon density is shown in the bottom panel of Figure 8. As expected, the distribution of density bears a marked resemblance to salinity. When water temperatures are less than 10°C, the equation of state for seawater dictates that variations of salinity contribute more than those of temperature to changes in density (Gebhart and Mollendorf, 1977).

A second hydrographic section through Unimak Pass was occupied on 17 February 1981 and we present the vertical section of salinity with the ΔT and $\Delta\sigma_t$ values across the bottom (Figure 9) for comparison to conditions observed in September 1980. Surface temperatures (not shown) were ~3.5 to 4.0°C and increased less than 1.0°C with depth so there was little structure in thermal field. Isohalines again indicated regions of low salinity ($\leq$31.75 gm/kg), however, the only substantial stratification ($\Delta\sigma_t \geq 0.5$) existed over the Bering Sea shelf. As was observed in September 1980, the strongest vertical and horizontal salinity gradients were found over the Bering Sea shelf. A five-station hydrographic section normal to Unimak Island was occupied on 13 May and again 2 June 1981. Both sections showed low salinity ($\leq$31.75 gm/kg) water within ~20 km of Unimak Island (cf., Figure 10) and little thermal structure.

The most extensive spatial coverage was attained on a cruise conducted between 2 and 3 September 1981. Hydrographic data are presented as the areal extent of waters with salinity less than 31.75 gm/kg in the upper 50 m (or to the bottom, Figure 11A) and as dynamic topography (0/50 db) in Figure 11B. West of the pass proper, the bulk of less saline water was in a band within ~10 km of the coast, while south of Unimak Island the band extended ~20 km

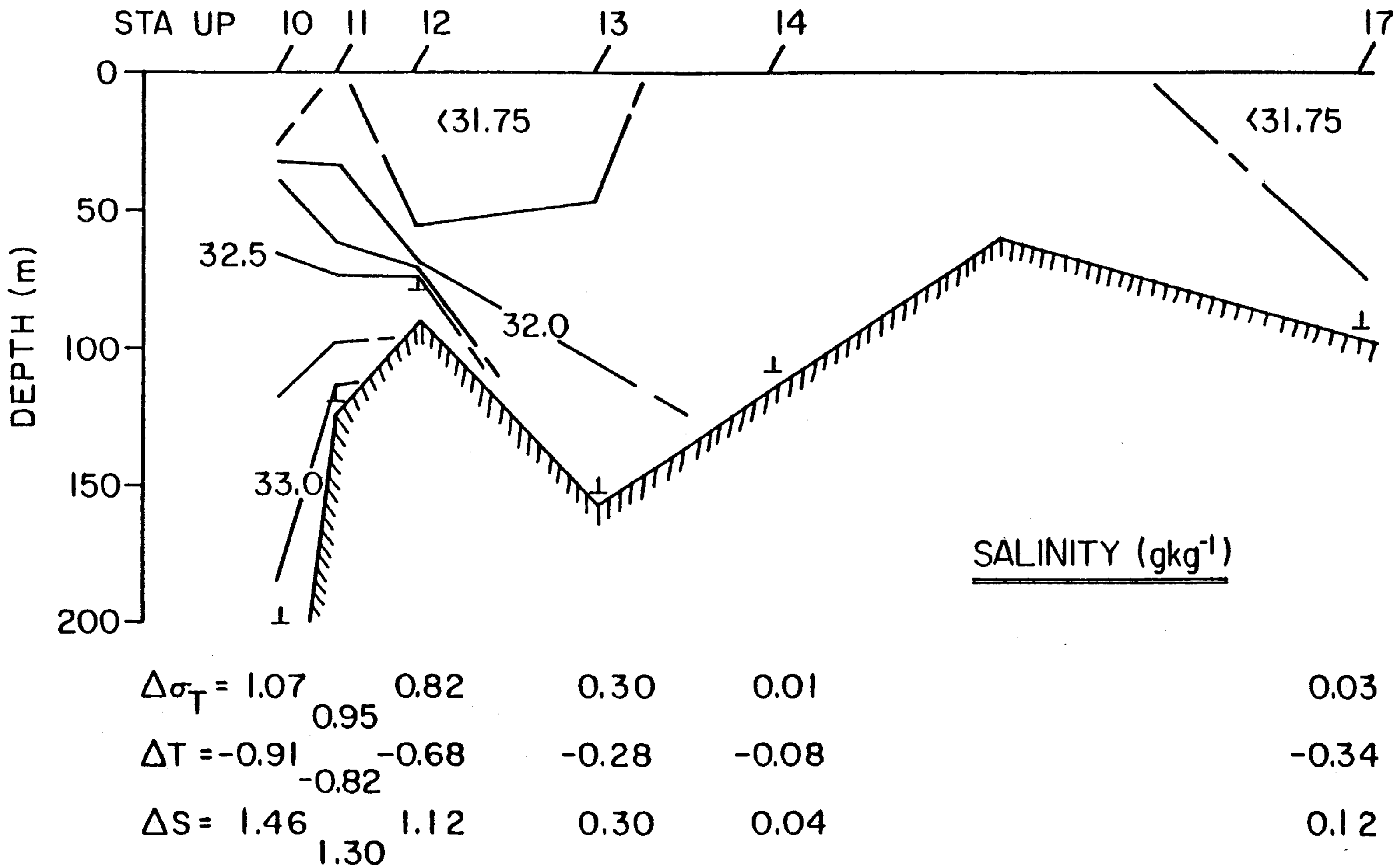

Figure 9. - Hydrographic data collected during February 1981 along the same section as in Figure 6. The Δ values are the magnitude of surface minus bottom 1 m averaged values.

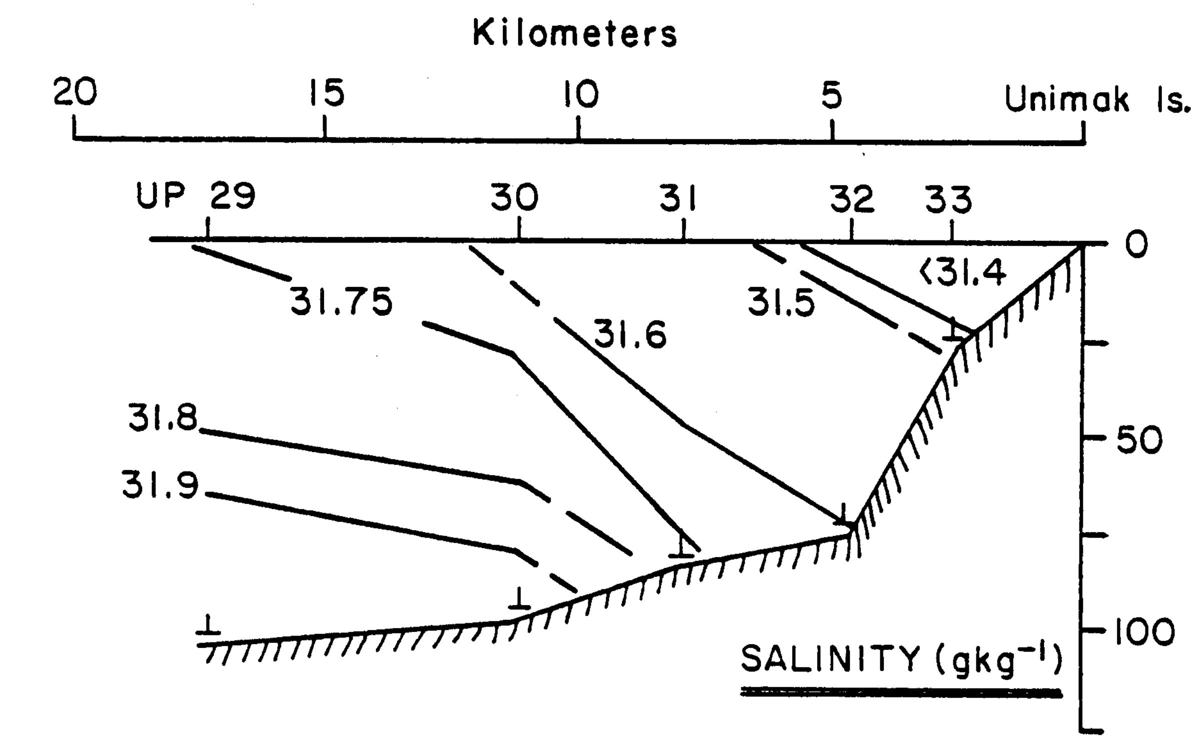

$\Delta\sigma_T$ =	0.23	0.35	0.18	0.36	0.09
ΔT =	0.80	0.70	0.30	0.91	0.33
ΔS =	0.21	0.34	0.21	0.33	0.14

Figure 10. - Hydrographic data for May 1981 from stations normal to Unimak Island. The Δ values are the magnitude of surface minus bottom 1 m averaged values.

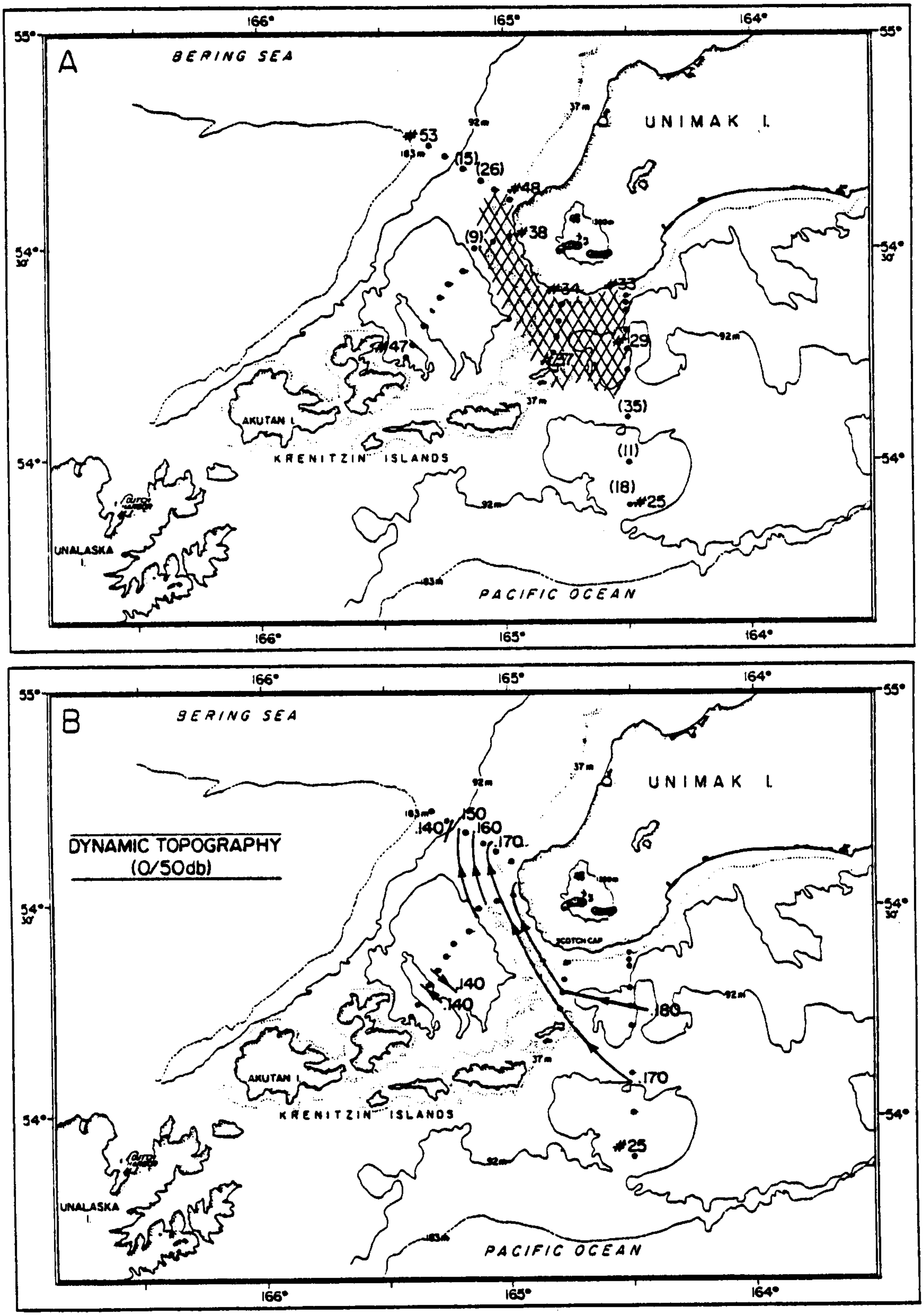

Figure 11. - Hydrographic data for September 1981 presented as (a) areal extent of waters with salinity ≥31.75 g/kg in the upper 50 m (or bottom) where the numbers in parentheses are depths of the low-salinity band for >50 m, and (b) dynamic topography (0/50 db) with a 0.01 dyn m contour interval. CTD station numbers are indicated by the number sign (#).

offshore and less saline waters existed in a thin layer at least 60 km offshore. The dynamic topography (0/50 db) reflects the narrowing trend of the low salinity band, with relief increasing from 0.008 dyn.m. between stations 32 and 29 south of Unimak Island to 0.025 dyn.m. between stations 48 and 51 northwest of the island. The steep relief between stations 51 and 52 resulted from the presence of saline (>32.50 gm/kg) water over the Bering Sea shelf. These waters also resulted in lower relief west of station 40. The suggested curvature of geopotential contours indicates that relative vorticity generated either by changes in depth or a horizontal velocity gradient in the pass proper may be important to flow dynamics west of the pass.

4.1.5 Baroclinic Geostrophic Currents

A persistent feature of the mass distribution in the five data sets was the presence of low salinity water along the coast of Unimak Island. Other hydrographic surveys (Kinder et al. 1978: Wright, 1980) have also shown less saline waters exist off Unimak Island and south of the Alaska Peninsula. We estimate the impact of the observed mass distribution on the velocity field by assuming a geostrophic balance. While this method neglects such factors as wind stress, bottom friction and barotropic pressure gradients, over the Bering Sea shelf (Kinder and Schumacher, 1981a) and along the Gulf of Alaska coast (Royer, Hansen and Pashinski, 1979: Schumacher and Reed, 1980) good agreement was shown between baroclinic geostrophic flow and both Eulerian and Lagrangian current observations.

In the TABLE 3, we present baroclinic currents of the surface relative to 50 db for each set of station pairs where the dynamic relief was ≥0.01 dyn.m.:

Table 3. - Dynamic relief and baroclinic speed

Observation Date	Station Pair	0/50 db Dynamic Relief (dyn.m.)	Speed (cm/s)	Direction (°T)
4 to 5 Sept. 1980	12/13	0.014	9	NE
	13/14	0.015	10	NNE
	14/15	0.011	7	NE
	18/19	0.012	5	W
17 Feb. 1981	11/12	0.011	13	NE
13 May 1981	32/29	0.011	12	W
2 June 1981	32/29	0.010	7	W
2 to 3 Sept. 1981	36/37	0.010	17	W
	38/39	0.012	20	N
	39/40	0.013	22	N
	49/50	0.012	19	NE
	50/51	0.014	33	NE
	51/52	0.020	30	NE
	27/26	0.010	7	W

The inferred flow from the first three station pairs in September 1980 and the first four pairs in September 1981 together with set 11/12 suggests moderate flow (7 to 22 cm/s) through Unimak Pass. This is consistent with our current observations and compares favorably with dynamic topographies presented by Coachman and Charnell (1977) from March 1976 CTD data collected north and west of the pass. Relief across the remaining station pairs suggests a weaker westward flowing current (5 to 12 cm/s) along the Gulf side of the Alaska Peninsula and a stronger current (19 to 33 cm/s) northwest of the pass.

Since 1975, sixty-one CTD stations were occupied within about 50 km of Unimak Pass proper. Separating these data into two sets, Gulf side (N=29) and Bering Sea side (N=32) of the pass we can strengthen our hypothesis that water east of the pass is generally less dense (due to lower salinity) than water west of the pass. We note that only data sets with casts on both sides during a given cruise were used to avoid aliasing the results. East of the pass, the mean dynamic height (0/50 db) and standard deviation was 0.162±0.016 dyn.m. and 0.136±0.016 dyn. m west of the pass. Thus, including CTD data from all seasons, we find that water along the Gulf side of Unimak Island was generally about 3 dyn.cm greater in height (over 50 db) than waters west of Unimak Pass.

4.1.6 Discussion

The results presented thus far have defined the behavior of current in Unimak Pass and the forcing for such flow: water is generally transported from the Gulf of Alaska onto the Bering Sea shelf. While subtidal flow with periods of 3 to 10 days was shown to be mainly driven by a wind-induced pressure difference along the pass, longer period (on the order of months) flow appeared to be driven by a coastal current existing along the Alaska Peninsula. Two important questions evolve from our results: what is the source of the coastal current and what is the impact of transport through Unimak Pass?

A recent study (Schumacher and Reed, 1980) has described and defined the Kenai Current, a strong coastal current which flows westward along the Gulf of Alaska coast from about 145°W to the southwest end of Shelikof Strait (~156°N). Royer (1981) has indicated that this feature is a component of the more extensive Alaska Coastal Current which is the consequence of the accumulation of runoff beginning along the British Columbia coast. He estimates transport in the northeast Gulf of Alaska to be $0.12\pm0.05 \times 10^6$ m^3/s and Reed, Schumacher and Wright (1981) show that the dynamic relief (0/90 db) is typically ~4 dyn. cm. in this portion of the Alaskan Coastal Current. To the west, along the Kenai Peninsula, there is an increase in dynamic relief (4 to 20 dyn. cm) and transport (0.10 to $1.2 \times 10^6 m^3/s$) both varying with season. The behavior of the Kenai Current west of Shelikof Strait is not well known, however, Wright (1980) indicates relatively low salinity water exists along the Alaska Peninsula as far west as Unimak Pass. Further, it is unlikely that the freshwater signal near Unimak Pass was of local origin since rainfall (Brower, et al. 1977) undergoes a four-fold reduction (323 to 84 cm) from ~158°W (Chignik) westward to 162.5°W (Cold Bay) and there are no gaged rivers. Current records from ~156°W and 158°W (Muench and Schumacher, 1980) indicate a substantial mean flow (~15 cm/s) westward along the coast. These results, together with the hydrographic data presented above indicate that some fraction of the Kenai Current continues along the peninsula and flows through Unimak Pass.

Using CTD data collected south of Unimak Island between stations 33 and 29 in May, June and September 1981, we estimate that baroclinic transport (computed to the greatest common depth) was ~6, 5 and 7×10^4 m^3/s respectively with maximum surface speeds of 12, 8 and 5 cm/s and dynamic relief (0/60 db) of ~2 dyn.cm. For all estimates, the largest fraction of the transport (>40%) occurred between the two most seaward stations. Thus total alongshore transport may be substantially greater; during September 1981 transport between stations 33 and 26 (see Figure 9A) was $\sim 24 \times 10^4 m^3/s$. Transport too far offshore to flow through the pass was also indicated in August 1980 data (see set 18/19 in TABLE 4). CTD data collected on a line normal to the Peninsula about 150 km east of Unimak Pass (at ~159°W) indicated alongshore transport of about

$\sim 24 \times 10^4 m^3/s$ in conjunction with a band of low salinity water of similar cross shelf extent to that observed south of Unimak Island. Transport estimates between stations 38/42 and 48/52 (see figure 9A) were about 12 and $16 \times 10^4 m^3/s$ respectively. The hydrographic data suggest a baroclinic current south of the Peninsula with a large fraction flowing westward through Unimak Pass and continuing along the northwest coast of Unimak Island. Caution is necessary in estimating transport through Unimak Pass from a signle current record. Assuming that the measured mean flow was representative over most of the cross-section (there were no reversals in baroclinic speed and vertical shear was moderate), we estimate ~ 6 to $20 \times 10^4 m^3/s$ were transported through Unimak Pass which is consistent with the baroclinic estimates.

The dearth of CTD data precludes establishment of a seasonal signal near Unimak Pass, however, off the Kenai Peninsula baroclinic transport varied by an order of magnitude with a maximum observed in October (Schumacher and Reed, 1980). Using an annual curve fitting technique on six years of data, Royer, (1981) suggested a maximum occurred in December. If continuity exists along the current, then maximum baroclinic transport through Unimak Pass should occur during sometime during the first three months of the year. This is consistent with the observed current in Unimak Pass and the increase in sea level anomaly observed during December and January at Dutch Harbor (Reed and Schumacher, 1981). While baroclinic spin-up may account for increased speeds for one to two months, wind induced coastal convergence was of equal magnitude along the Kenai Peninsula; during January through March 1978, vector mean speed was ~ 25 cm/s at a depth of 75 m in Shelikof Strait. Although there is uncertainty regarding phase and amplitude due to limited data, the nature of forcing suggests that changes in mean flow through Unimak Pass appear related to seasonal behavior of the Kenai Current, and not to local forcing.

We now consider the impact that transport through Unimak Pass has on water mass properties and on the water budget of the Bering Sea shelf. The CTD data presented above indicate a region of enhanced horizontal salinity gradient about 50 to 75 km west of Unimak Pass proper (figure 6, vicinity of station 13; figure 9, vicinity of stations 40/41 and 51/52). This feature can be compared to the 'middle front' which exists over the southeastern Bering Sea shelf (Coachman and Charnell, 1979: Coachman, et al, 1980: Kinder and Schumacher, 1981b) and has a profound influence on that region's productivity and nutrient fluxes (Iverson, et al., 1980: Coachman and Walsh, 1981). In these papers, the middle front, as determined from CTD data collected about 100 km northwest of Unimak Island, was characterized in terms of a vertical salinity gradient, $\Delta S/\Delta z$, and the horizontal gradient of the mean salinity, $\Delta\bar{S}/\Delta x$. Hydrographic data collected during 1980 and 1981 west of Unimak Pass indicated the following gradients existed: $\Delta\bar{S}/\Delta Z \sim 9 \times 10^{-5} gkg^{-1} cm^{-1}$, and $\Delta S/\Delta x \sim 45 \times 10^{-3} gkg^{-1} km^{-1}$ with a slight enhancement in the bottom 50 m. Thus, the vertical gradient was ~ fifty times stronger while the horizontal gradient of mean salinity was about five hundred times greater than that observed over the shelf to the northwest. The data indicate that the two fronts may be different dynamically and it is not known if they are contiguous, however, transport of less saline water from south of the Alaska Peninsula results in a strong salinity front west of Unimak Pass proper. Hattori and Goering (1981) note the role played by water flowing through Unimak Pass on the fertility of the region. Although these authors identify the water as being "Alaskan Stream," their temperature and salinity data suggest it was water of the coastal current. Upwelling along the Gulf side of Unimak Island, induced during summer by the mean alongshore (northeastward) wind-stress, may have provided the relatively high concentrations of nitrate and ammonium which they observed. Further, the less saline waters may contribute substantially to the baroclinic coastal flow observed along the Bering Sea side of the Alaska Peninula (Kinder and Schumacher, 1981b).

Recently, annual mean water transport through Bering Strait (from the Bering Sea into the Arctic Ocean) was reevaluated to be $0.8 \pm 0.2 \times 10^6 m^3/S$ (Coachman and Aagaard, 1981). The apparent source of most of this transport was flow along the Siberian coast (Coachman, Aagaard and Tripp, 1975; Kinder and Coachman, 1978). We note that our estimates of transport through Unimak Pass are five to ten times greater than gauged freshwater addition along the Alaska coast of the Bering Sea and may account for up to one-fourth the mean annual transport northward through Bering Strait.

4.2 The North Aleutian Shelf Transport Processes Experiment

In order to characterize currents and hydrography over the North Aleutian shelf, ten moorings (figure 12) were deployed between August 1980 and May 1981 and a seventy-two station CTD grid was designed (figure 13). The ensuing observations permit a description of currents and inferences to be made regarding the 50-m front.

4.2.1. Long-period Time-Dependence of Hydrographic Features

In this section, we present CTD data by cruise, where we selected the most synoptic period (about six days) set of casts. These data are presented as area distributions and both spatial and between-cruise changes are discussed.

Temperature: In August 1980, surface temperatures (figure 14A) varied along the peninsula from ~11.5°C in inner Bristol Bay to <8.0°C north of Unimak Island. Across the shelf, the strongest difference (~2.0°C) was in the vicinity

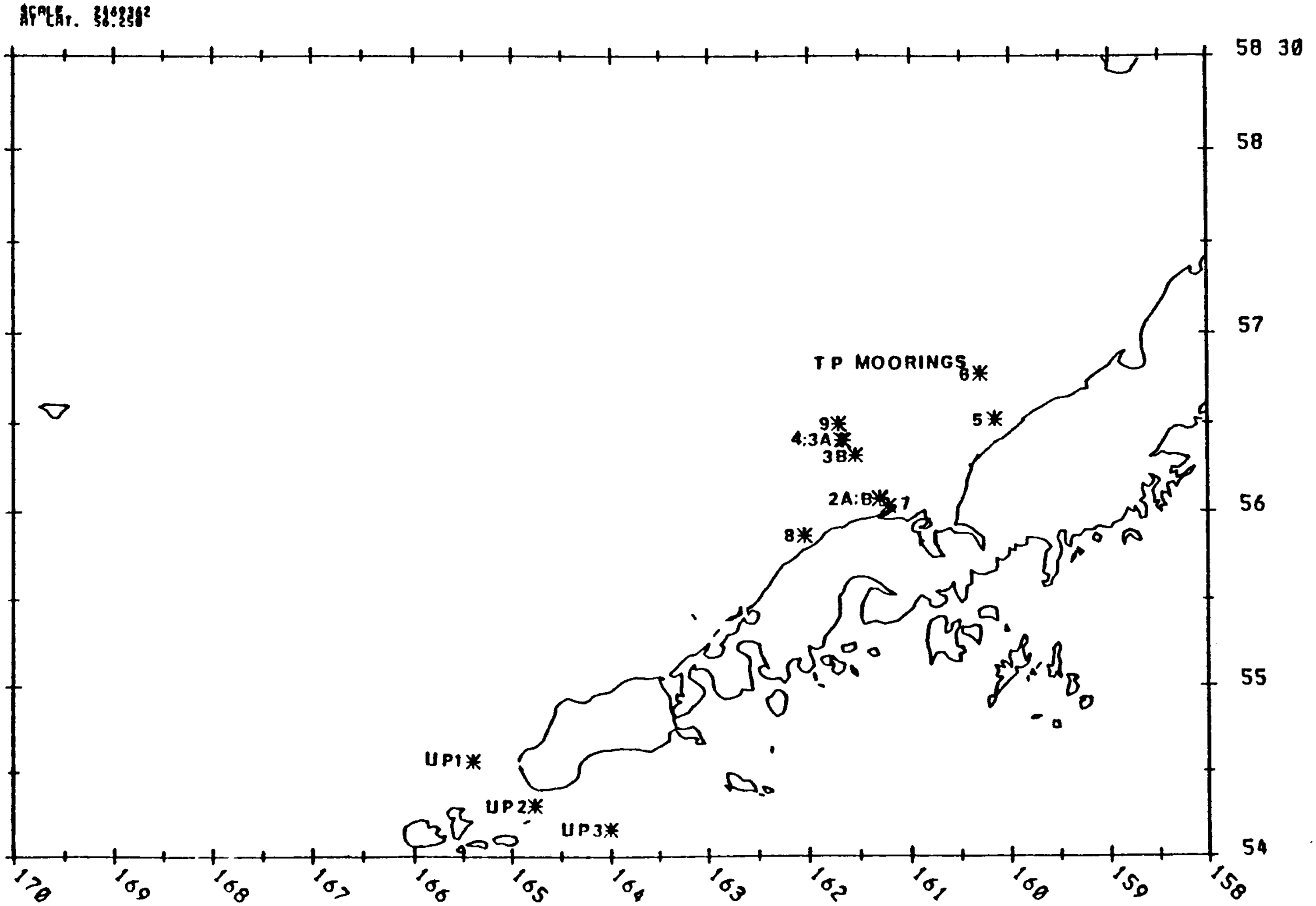

Figure 12. - Location of current meter moorings.

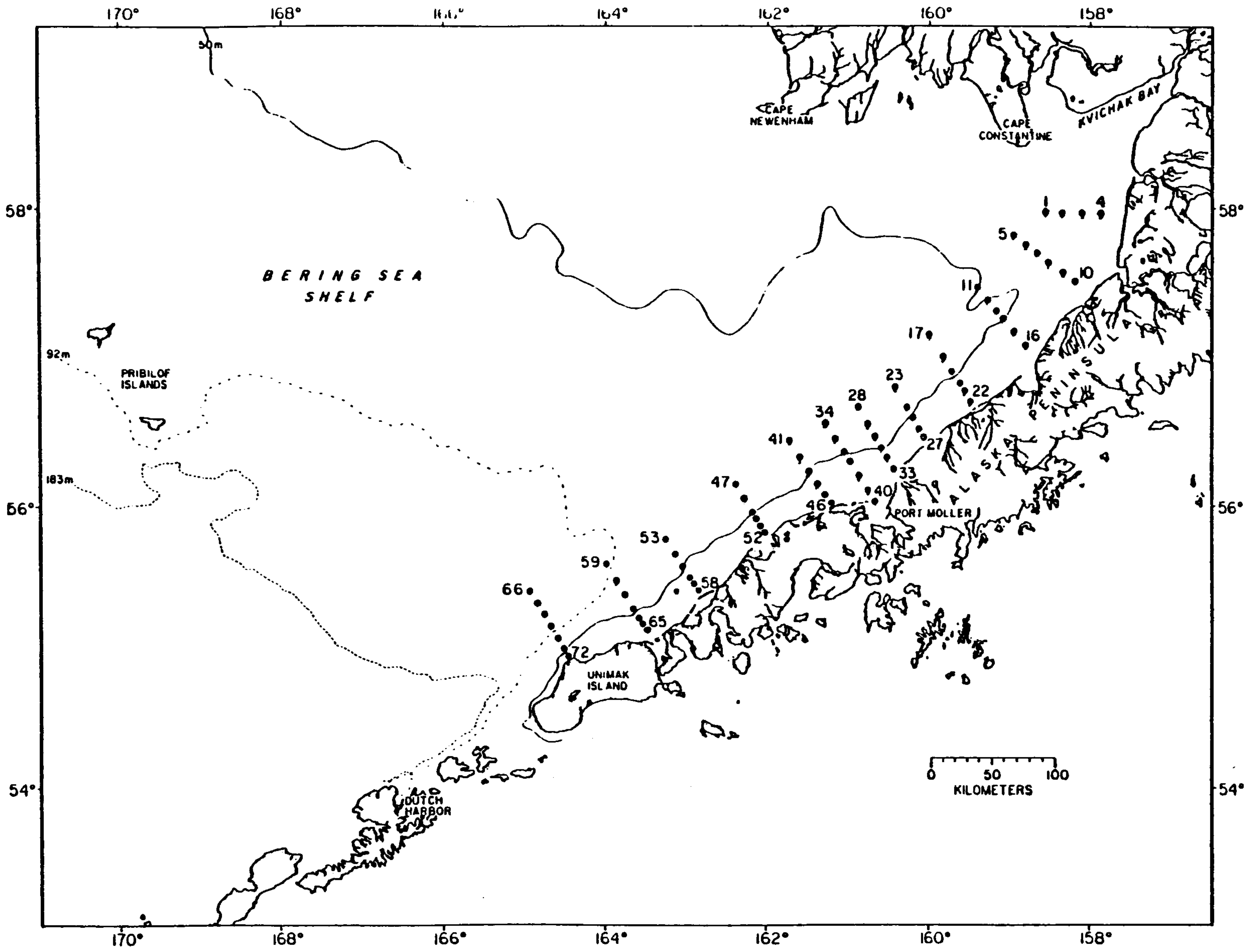

Figure 13. - Location of CTD stations (NA 1 to 72) for the North Aleutian Shelf study.

SURFACE TEMPERATURE (°C)

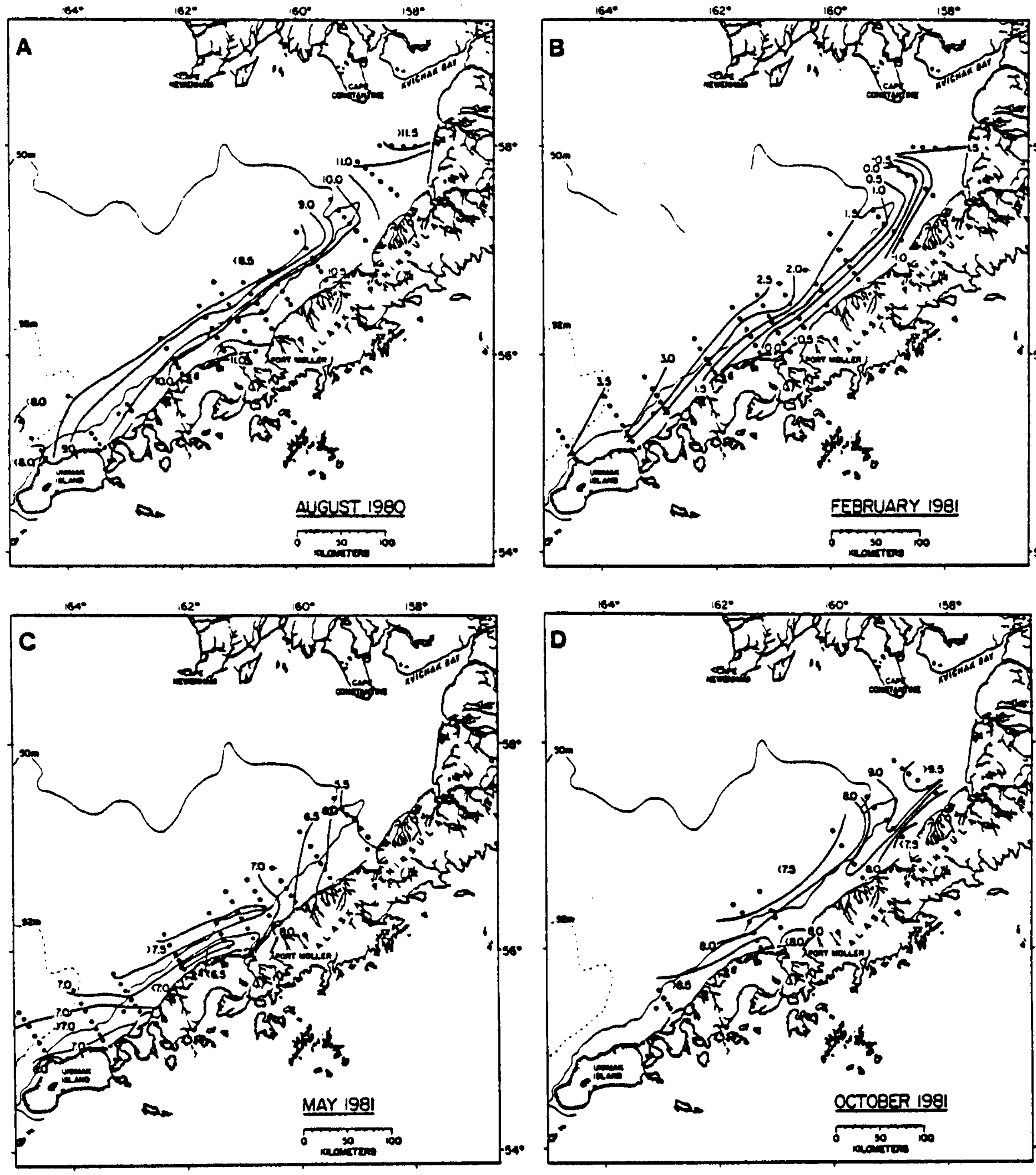

Figure 14. - Surface temperature (°C) contours.

of the 50-m isobath. This difference decreased and became perpendicular to the peninsula off Port Heiden as it followed the 50-m isobath toward the northwest. West of Port Moller, the cross-shelf temperature difference decreased to <1.0°C north of Unimak Island.

By February 1981, surface temperatures (figure 14B) were close to the freezing point in inner Bristol Bay and the 0°C contour extended westward to Port Heiden. Temperatures <0.5°C were also observed in Port Moller. Isotherms and the cross-shelf temperature difference (~2.5°C) followed a pattern similar to that observed in August, paralleling the trend of the 50-m isobath and decreasing west of Port Moller. Off Unimak Island, maximum surface temperatures (>3.5°C) were observed over the corner of the outer shelf domain and the cross-shelf temperature difference was minimal (<1.0°C) again.

In May, surface temperatures (figure 14C) increased from ~5.5°C off Port Heiden to ~8°C near Port Moller. West of Port Moller, surface temperatures were rather constant (with an average value of 7.0°C) and displayed a tendency to be aligned with the 50-m isobath, although the cross-shelf gradient was weak and had a banded structure. This distribution suggested the establishment of nominal middle shelf characteristics, i.e., two-layered as a result of solar insulation.

Surface temperatures (figure 14D) were generally warmer by October. However, since waters over the middle shelf domain were 1 to 2°C cooler than those inshore, the peak in thermal stratification had apparently passed and cooling was operative. Surface temperatures in the coastal domain were greatest in regions where stratification from freshwater addition was observed. Although surface cooling had affected contours, there was a tendency for isotherms to parallel the 50-m isobath as noted before.

Bottom (nominally 5m above the bottom) temperatures during August 1980 (figure 15A) varied from >11.5°C in inner Bristol Bay to <6.0°C off Port Moller with a minimum (~3.7°C at NA59) in the corner of the outer shelf domain north of Unimak Island. Shoreward of the 50-m isobath and between Port Moller and Port Heiden, bottom temperatures were ~10°C and they decreased to <8°C west of Port Moller. A strong (>3°C) difference existed from Port Heiden westward along the peninsula with a divergence of this trend off Port Moller. In general, the region of highest bottom temperature difference paralleled the 50-m isobath. Comparison with surface temperatures indicated that the coastal domain was well mixed thermally and both the middle shelf and outer shelf domains were stratified.

Near freezing temperatures (<1.5°C) were observed on the bottom in inner Bristol Bay in February 1981 (figure 15B), and temperatures <0°C were present westward to Port Heiden and in Port Moller. An ~2.5°C difference was located normal to the peninsula off Port Heiden. A similar difference paralleled the 50-m isobath to the vicinity of Port Moller. West of this area bottom temperatures increased to >4.0°C off Unimak Island. In general, there was negliable thermal stratification except over the outer shelf domain where bottom temperatures were ~0.5°C greater than surface values.

In May, bottom temperatures (figure 15C) varied from <4°C seaward of the 50-m isobath to >7°C in Port Moller and isotherms paralleled the entire peninsula. Between Port Heiden and Izembeck Lagoon, and within ~20km of the coast, thermal stratification was generally slight (<1°C), but seaward of the 50-m isobath thermal stratification was generally >3°C along the entire peninsula.

Bottom temperatures during October (figure 15D) had warmed from May by at least 1°C over the middle shelf and values >9.5°C were present in inner Bristol

BOTTOM TEMPERATURE (°C)

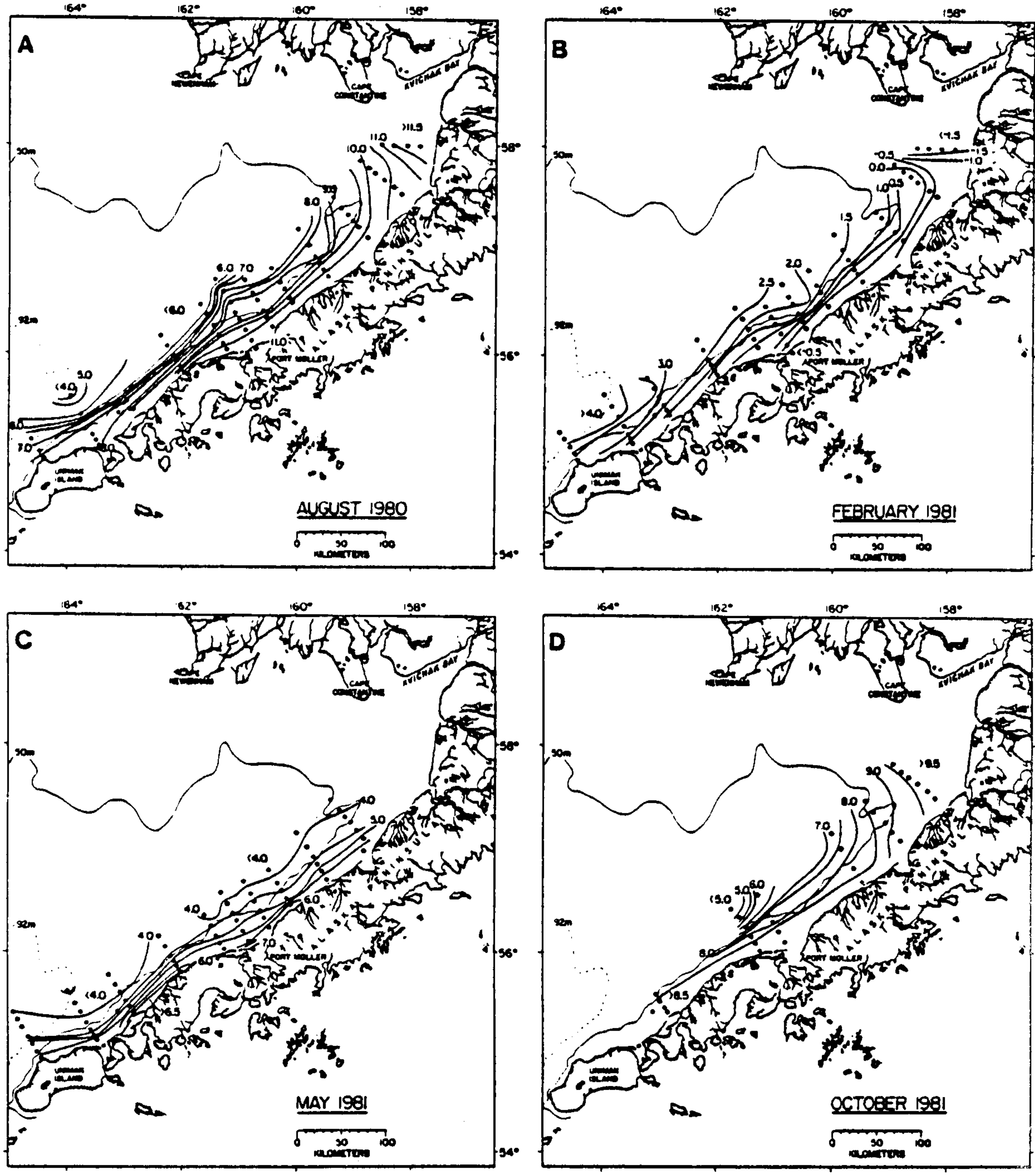

Figure 15. - Bottom temperature (°C) contours.

Bay. Isotherms again paralleled bathymetry and indicated a cross-shelf gradient of ~3.5°C. Comparison with surface temperatures indicated isothermal water in Bristol Bay extending westward to near Port Heiden. Coastal waters west of Port Heiden indicated cooling, with surface temperatures as much as 2°C cooler than bottom waters. Middle shelf waters were stratified with surface to bottom temperature differences $\geq$2°C.

Salinity: In August, surface salinities (figure 16A) ranged from <24.5 g kg^{-1} in inner Bristol Bay to >32 g kg^{-1} over the outer shelf domain north of Unimak Island. A strong (≥5 g kg^{-1}) difference existed normal to the peninsula (between the 50 and 25-m isobaths) in inner Bristol Bay. In the coastal domain between Port Heiden and Unimak Island, salinities increased by about 1 g kg^{-1}. Salinities over the middle shelf were $\geq$31.5 g kg^{-1} and relatively constant.

By February 1981, the impact of Kvichak River runoff had diminished in inner Bristol Bay and surface salinities (figure 16B) were ~31 g kg^{-1}. There was a remanant of the difference normal to the peninsula, but its magnitude was only ~0.5 g kg^{-1}. Salinities over the middle shelf were >32 g kg^{-1} while values in Port Moller were <30.5 g kg^{-1}. This cross-shelf difference diminished to less than 0.5 g kg^{-1} off Unimak Island. The region of coastal water west of Port Moller with salinity <31.5 g kg^{-1} was substantially greater than in August.

In May, surface salinities (figure 16C) were more uniform throughout the study area; values were <31 g kg^{-1} in Port Heiden and Port Moller with values >31.75 g kg^{-1} over the middle shelf domain between these ports. The cross--shelf difference varied from ~1 g kg^{-1} off Port Moller to <0.5 g kg^{-1} north of Unimak Island where an intrusion of more saline water (>31.8 g kg^{-1}) was observed over the outer shelf domain.

SURFACE SALINITY (g/kg)

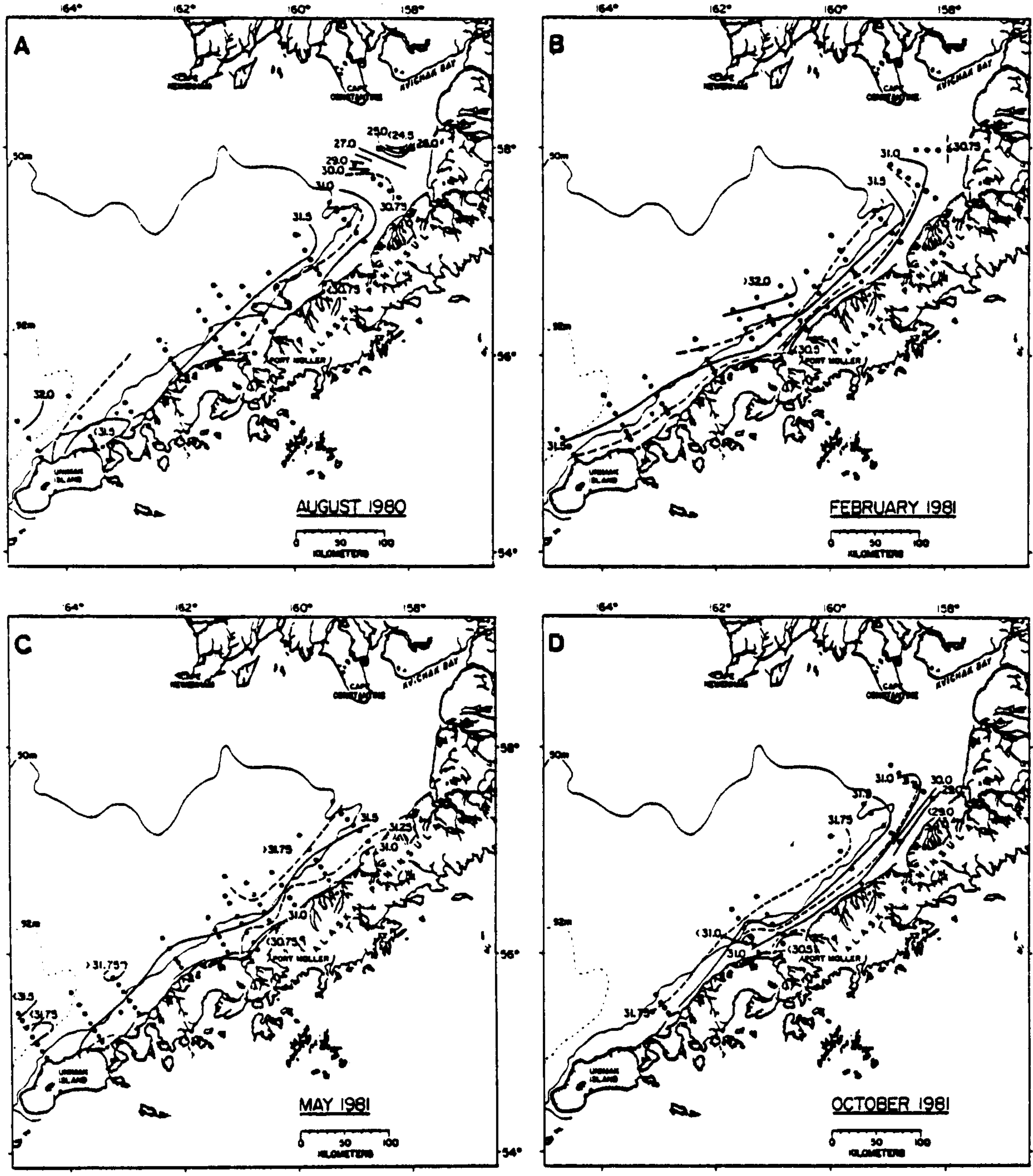

Figure 16. - Surface salinity (g/kg) contours.

By October, surface salinities (figure 16D) showed that the cross-shelf difference between Ports Heiden and Moller had increased to >2 g kg^{-1} and 1.25 g kg^{-1} respectively off the two ports. These data suggest substantial addition of freshwater along the peninsula as far west as Port Moller; however, farther west, surface salinities were greater than in May.

In August, bottom salinities (figure 17A) along the peninsula varied from <29 g kg^{-1} in inner Bristol Bay to >32.5 g kg^{-1} over the outer shelf north of Unimak Island. An alongshore gradient was concentrated between inner Bristol Bay and Port Heiden where it was normal to the peninsula. The cross-shelf difference was generally weak (<0.5 g kg^{-1}). Comparison with surface values showed the greatest stratification in inner Bristol Bay with values of ~5 g kg^{-1}. Over most of the coastal and middle shelf domains stratification was weak (<0.2 g kg^{-1}) but over the outer shelf region moderate (0.5 to 1.0 g kg^{-1}) stratification was observed.

By February, bottom salinities (figure 17B) indicated that the along-shelf gradient had diminshed with values ranging from <30.75 g kg^{-1} in inner Bristol Bay to >32. g kg^{-1} off Unimak Island. However, the cross-shelf difference was stronger (~1.5 g kg^{-1}) and more closely alined with the bathymetric trend. Although waters over the outer shelf were less saline than observed on any other cruise, they were more saline in the middle shelf off Port Moller. As was observed in surface salinity, the area of encompassed by the 31.5 g kg^{-1} isohaline was extensive (particularly west of Port Moller). Throughout most of the coastal and middle shelf domains, stratification was weak (~0.25 g kg^{-1}), whereas moderate values obtained over the outer shelf domain.

In May, bottom salinities (figure 17C) showed that coastal and outer shelf domain waters were generally more saline than in February, while middle shelf waters were less saline. Given the station coverage, the alongshore

BOTTOM SALINITY (g/kg)

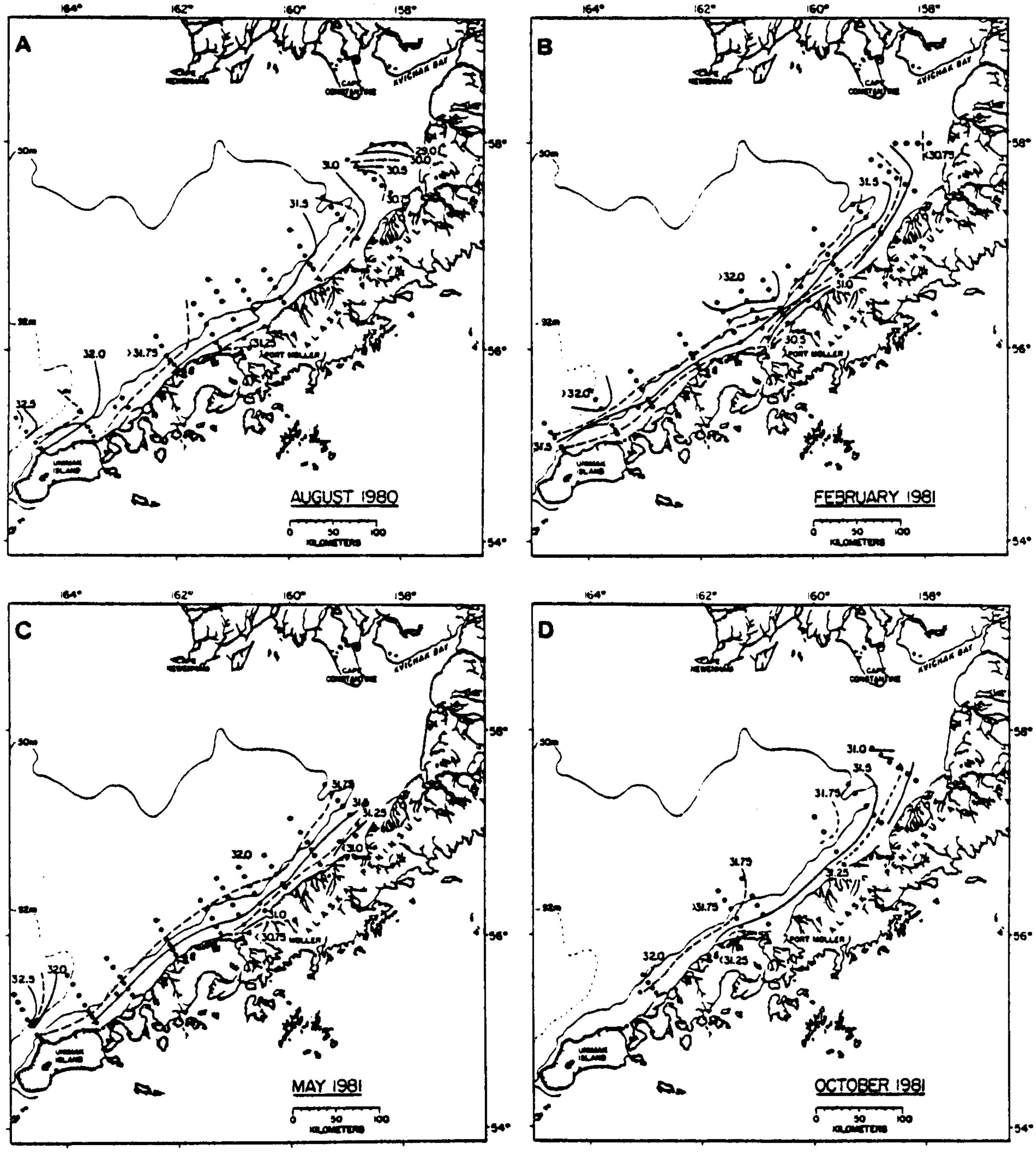

Figure 17. - Bottom salinity (g/kg) contours.

gradient did not exist and cross-shelf differences were weaker than in February, but still followed the bathymetric trend. Shoreward of the 50-m isobath, stratification was generally <0.25 g kg^{-1}, with slightly greater values over the middle shelf. As was noted for the previous data sets, stratification was moderate over the outer shelf domain.

Bottom salinities in October (figure 17D) indicated a slightly stronger alongshore gradient, ranging from <31 g kg^{-1} in Bristol Bay to >32 g kg^{-1} off Izembeck Lagoon, however, the cross-shelf difference was weaker than in May. The strong cross-shelf difference of surface salinity along the coast between Ports Heiden and Moller was not as strong across the bottom. This resulted in a band of stratification (~0.5 g kg^{-1}) along the coast east of Port Heiden which graded off to <0.1 g kg^{-1} over the middle shelf east of Port Moller. West of here, stratification was 0.25 to 0.7 g kg^{-1} except for the stations less than 50 m deep off Izembeck Lagoon.

We present surface to bottom mean salinity, $\bar{s}$, (Figure 18A to D) to further elucidate the impact of the various sources of fresh or less saline water. The lowest $\bar{S}$ (<27.75 g kg^{-1}) was observed in August and reflected the direct influence of the Kvichak River. Comparison with $\bar{s}$ from the three other cruises suggested that Kvichak River water had a controlling influence on salinity as far west as station line NA5 to 10, or ~100 km east of Port Heiden. By February, the mean salinity had increased by ~3 g kg^{-1} in this region while the values from October were similar to those in August.

Values of $\bar{s}$ from the middle shelf domain showed much less variability, minimum values were observed in August (>31.5 g kg^{-1}) with maximums in February (up to 32.1 g kg^{-1}) while values in May and October were intermediate (~31.75 g kg^{-1}). Mean salinity over the outer shelf domain north of Unimak Island showed similar magnitude of variability, but phasing was different; maximums occurred in August and minimums in February.

MEAN SALINITY (g/kg)

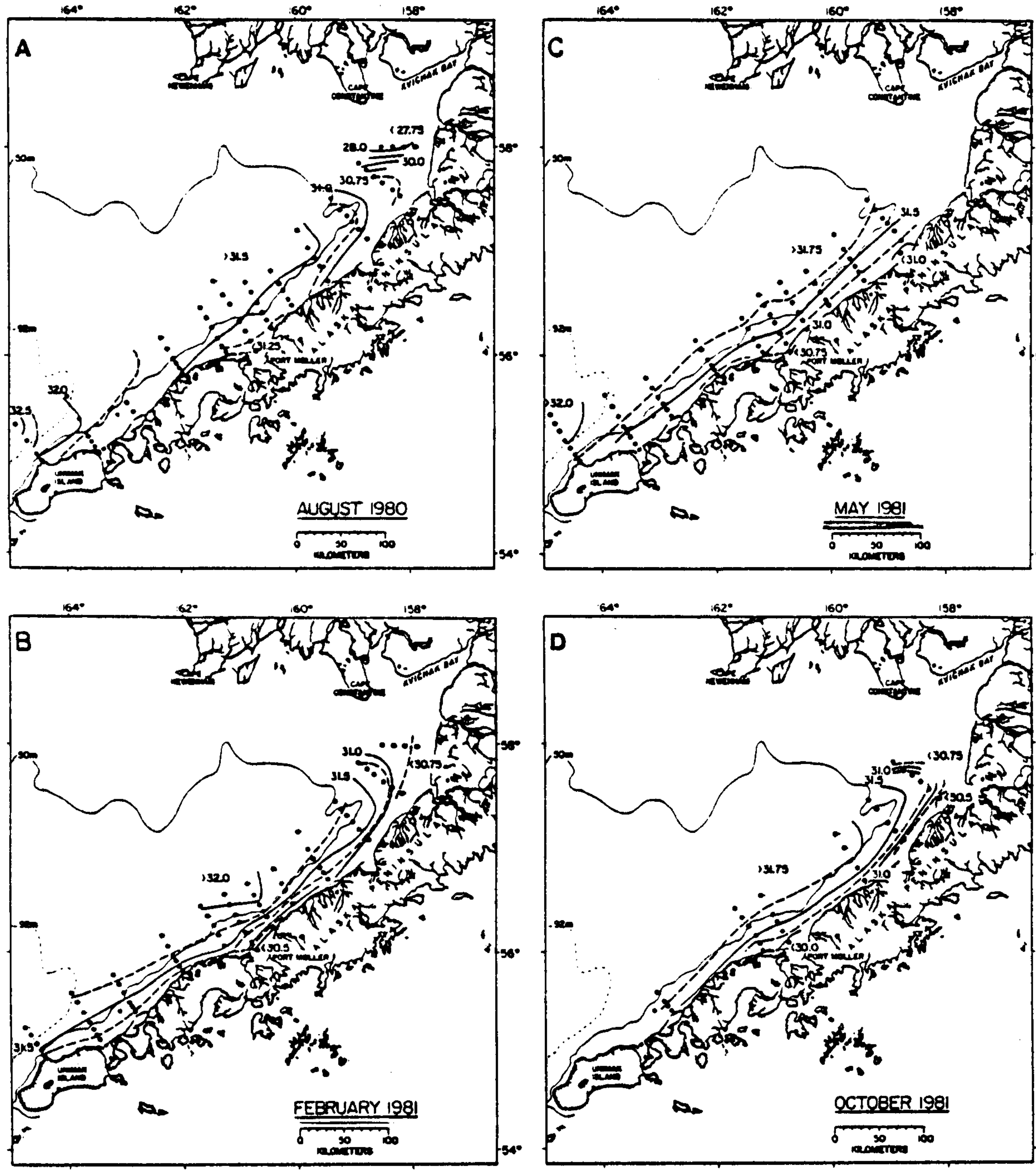

Figure 18. - Mean salinity (g/kg) contours.

In the coastal domain between Port Moller and Unimak Island, the range of $\bar{s}$ was again moderate ($\sim$0.5 g kg^{-1}), however there was a substantial change in the area encompassed by the 31.5 g kg^{-1} mean isohaline. This area was most saline in August and only slightly less so in October, with the lowest values observed in February and these increased slightly by May. The Kenai Current has a baroclinic maxima in October followed by a barotropic maxima between January and April (Schumacher and Reed, 1980) and some manifestation of these maxima were observed in Unimak Pass and persisted into May (Schumacher, Pearson and Overland, 1982). We suggest that less saline water from the Kenai Current was the cause for the observed reduction of mean salinity west of Port Moller (Particularly in February). Within Port Moller, the lowest mean salinity also occurred in February, and ice was observed to be a local feature (but offshore surface temperatures were >2.0°C). We suggest that ice is formed within the Port Moller complex and it melts when advected seaward; however, such local formation would not affect mean salinity over the vast region west of Port Moller. Ice formation along the shore of Kuskokwin Bay and the north coast of Bristol Bay may be advected (by wind) to this region of the coastal domain and provide a freshwater flux, but this process would generally occur between late February through March (see, figure 2).

Finally, we note that in the vicinity of Port Heiden, and to a lesser extent west of Port Moller, the mean salinity in a band along the coast was lowest in October. This region is more than 200 km from the Kvichak River, west of the region where river runoff is clearly identifiable in the data. Although there are no gaged rivers on the peninsula, there is substantial rainfall. An estimate of drainage area between Ports Moller and Heiden is about the same as that for the Kvichak River. Thus, the maximum freshwater flux should occur in October and be of similar magnitude to the Kvichak River. We suggest that it was this source that resulted in lower salinities in the coastal domain west of the Kvichak River influence and extending westward to the vicinity of Port Moller.

<u>Stratification</u>: Bottom-surface sigma-t values ($\Delta\sigma_t$) are a measure of stratification which combines the effects of both salinity and temperature. In general, coastal domain waters are well mixed, except in the presence of freshwater addition; middle shelf waters are two-layered during periods of positive bouyancy (insolation and ice melt) input and well mixed otherwise, and outer shelf domain waters are usually layered (Kinder and Schumacher, 1981a).

Area plots of $\Delta\sigma_t$ are shown in Figure 19 A to D. The strongest $\Delta\sigma_t$ (> 3.5) was observed in August in inner Bristol Bay and was primarily caused by salinity stratification resulting from Kvichak River discharge. Just south of this area, coastal domain waters westward to Port Heiden were mixed ($\Delta\sigma_t < 0.1$). In the vicinity of Port Moller, a complex distribution of $\Delta\sigma_t$ existed, with values ranging from 0 nearshore, to >0.25 over the adjacent portion of the middle shelf. As will be shown later (Section 4.2.6), this distribution was a result of storm mixing and cross-shelf advection. Between Port Moller and Izembeck Lagoon, $\Delta\sigma_t$ was generally <0.25, while near the 50-m isobath values were >0.5 and over the outer shelf domain they exceeded 0.75.

By February, most of the water column from inner Bristol Bay to west of Port Moller was mixed. Exceptions occurred near Ports Heiden and Moller, where $\Delta\sigma_t \sim 0.25$ and again was related mainly to salinity stratification. A likely source of less saline surface water was melting of local or regional ice. West of Port Moller, the coastal and middle shelf domains were mixed, while over the outer shelf moderate (up to 0.4) stratification existed.

Δ SIGMA-T

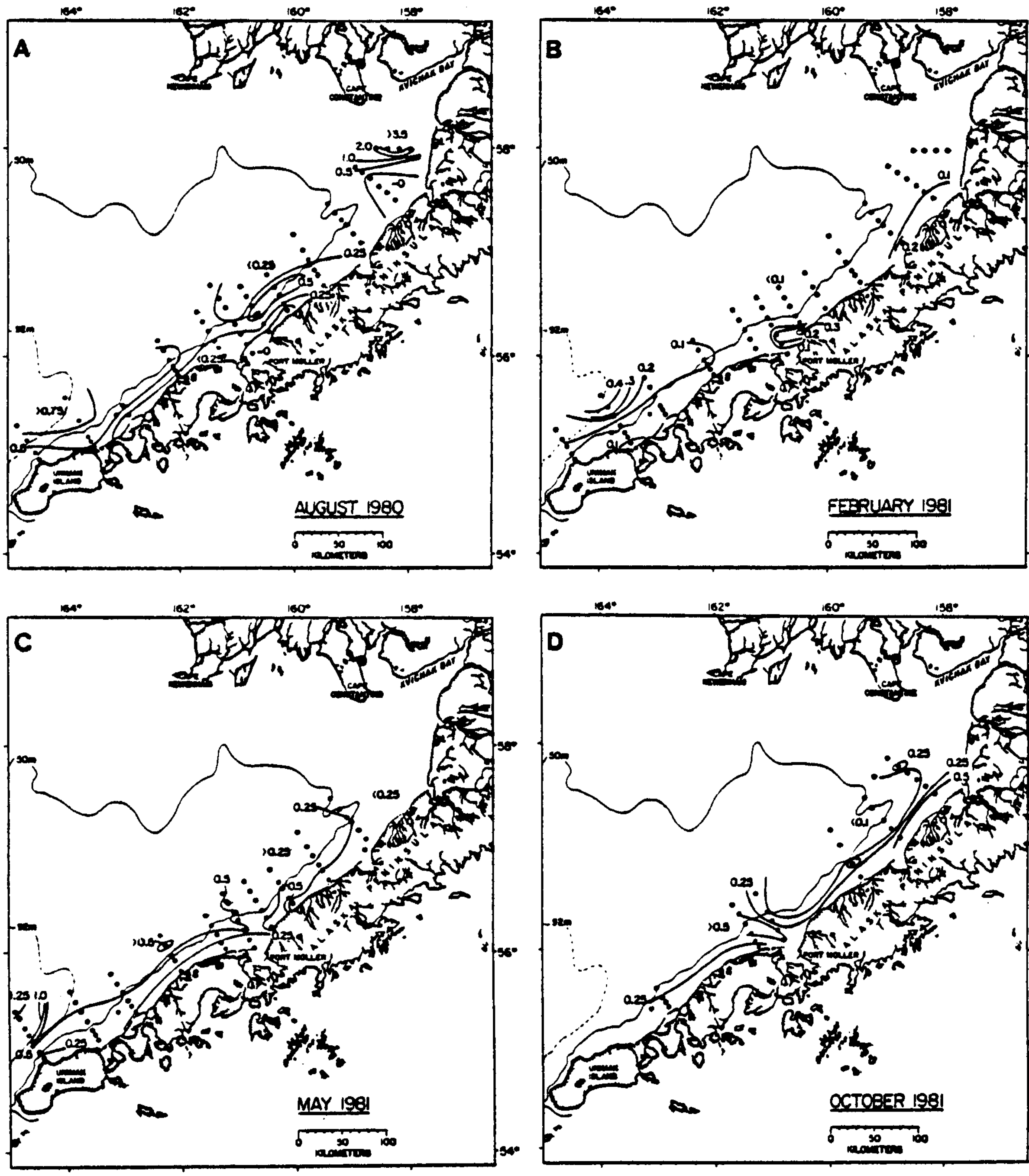

Figure 19. - Bottom minus surface sigma-t contours.

The effect of increasing insolation was evident in May; waters over the middle shelf were moderately stratified ($\Delta\sigma_t > 0.25$), although temperatures had increased from February by ~ 7°C, temprature differences and $\Delta\sigma_t$ were weak in the coastal domain. (an exception was near Port Moller where a lens of fresher water had not yet been mixed with more saline bottom water). Over the outer shelf, strong stratification existed as a result of low salinity surface water well offshore. The presence of a low salinity band in the vicinity of the middle front is a common feature and has been attributed to the southwest extent of the regional ice field (Kinder and Schumacher, 1981b).

Surface heat loss was evident by October, and coupled with weak haline stratification resulted in a mixed water column over most of the middle shelf domain. Along the coast east of Port Heiden and just west of Port Moller, $\Delta\sigma_t$'s exceeded 0.5 due to the presence of less saline surface waters. As noted above, this was likely due to freshwater addition not associated with the Kvichak River, but with local freshwater addition.

Dynamic Topography: The combined effect of temperature and salinity on the horizontal pressure field and hence the computed geostrophic flow is shown in Figure 20A to D and 21A to D. While caution is necessary in inferring currents in this manner, particularly to shallow reference levels, good agreement historically between Eulerian and Lagragian measurement and geostrophic flow exists exists over this shelf (Schumacher and Kinder, 1983: see Appendix B). Both the 0/25 and 0/50 dbar dynamic topography showed that relief of $\geq$1.0 dyn cm was a persistant feature of the baroclinic pressure field across the shelf. Contours typically aligned with the bathymetry and

DYNAMIC TOPOGRAPHY (0/25 db)

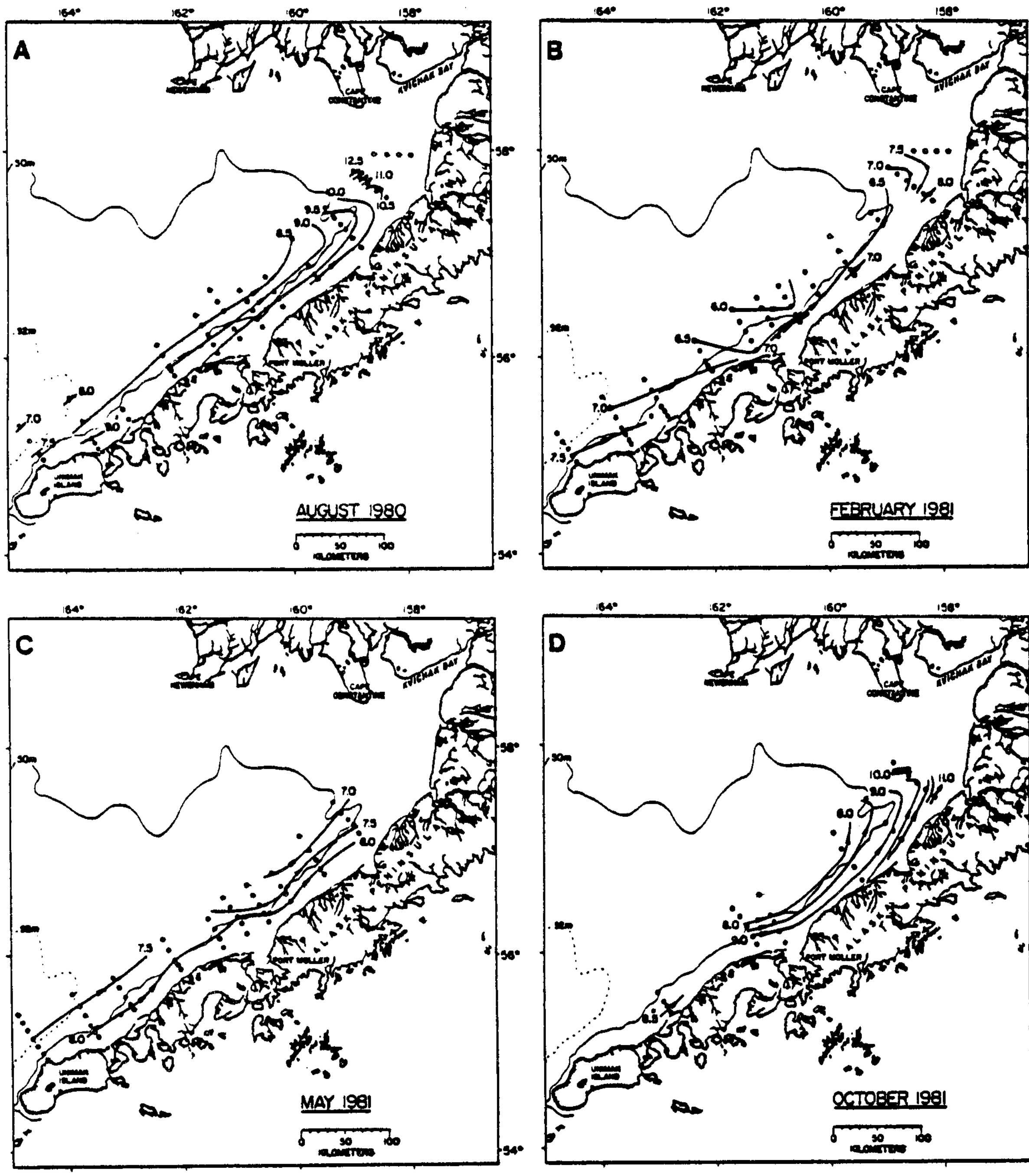

Figure 20. - Dynamic topography, 0/25 db.

DYNAMIC TOPOGRAPHY (0/50db)

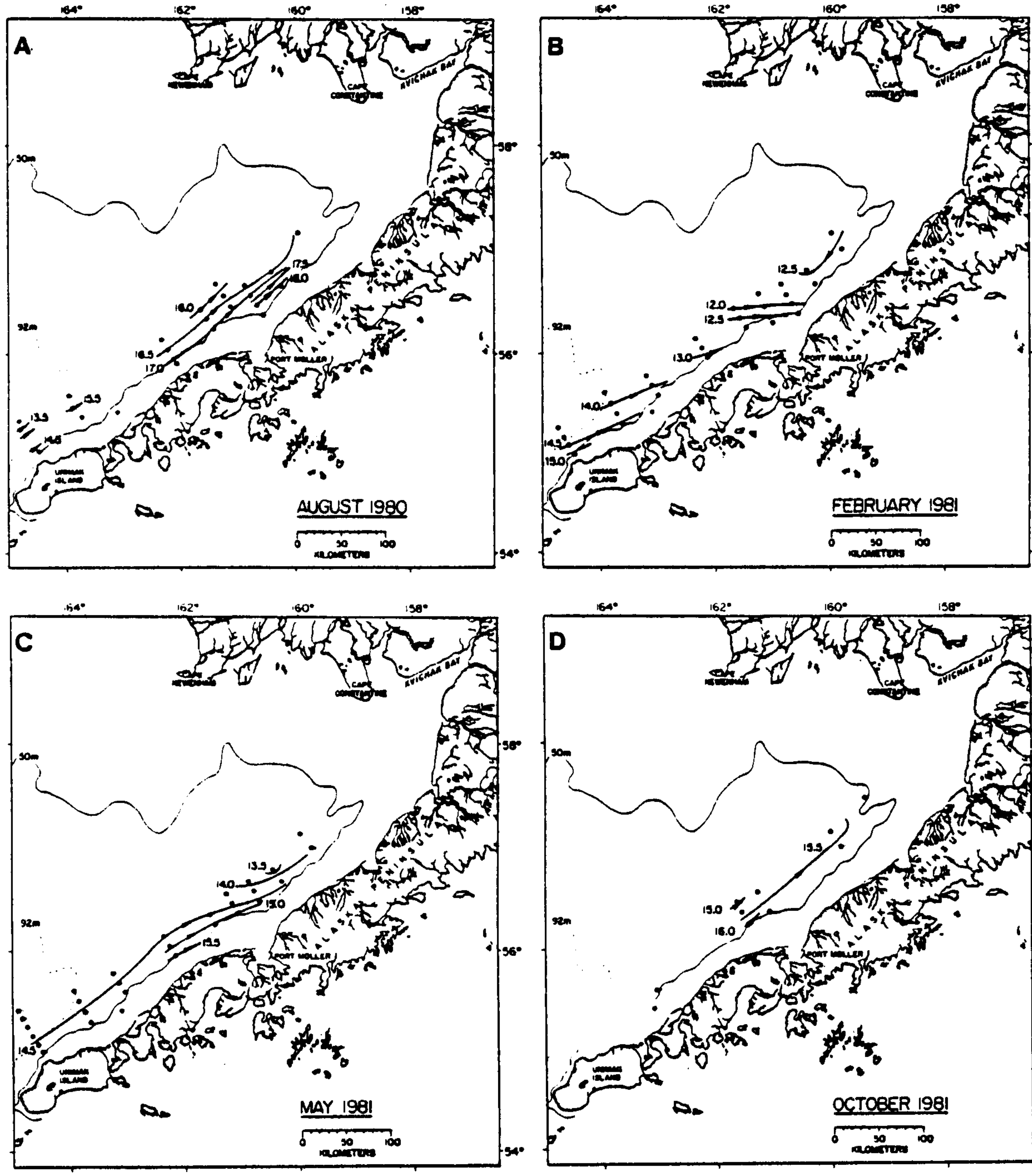

Figure 21. - Dynamic topography, 0/50 db.

the 0/25 dbar contours paralleled the offshore trend of the 50-m isobath north of Port Heiden. The impact of freshwater addition from the Kvichak River (figure 20A) and along the penisula westward to Port Heiden (figure 20D) was evident in the increased relief. Maximum surface speeds relative to 25 dbar were $\sim$7 cm s^{-1} off Port Moller in August and $\sim$11 cm s^{-1} in inner Bristol Bay during October. Maximum values (0/50 dbar) also occurred off Port Moller in August. In general, regardless of time of year, the cross-shelf density distribution was such that baroclinic geostrophic surface currents of 2 to 7 cm s^{-1} existed with inferred flow into Bristol Bay parallel to isobaths.

4.2.2 Short-Period Time-Dependence of Hydrographic Features

In the previous Section we showed that some processes (e.g. runoff, ice, change in insolation, etc.) result in changes of hydrographic characteristics on time scales from $\sim$ a month to seasonal. We present hydrographic, suspended particulate matter (SPM) wind and current data collected along the Alaska Peninsula (figure 22) during a 14-day period in August 1980. These data show that a storm significantly altered mean hydrographic conditions, vertically mixing middle shelf domain waters. Further, Ekman fluxes (coastal divergence and convergence) with time-scales of 2 to 5 days appeared to play an important role in reestablishment of stratification and together with enhanced tidal mixing (using the mean of the speed cubed as a measure of mixing energy) resulted in a return to nominal coastal and middle shelf domain conditions within 14 days.

Hydrography and Light Attenuation The line of CTD stations normal to the peninsula (figure 22) was occupied on 19, 24 and 31 August 1980. The time to complete a line was about six hours. About one day prior to running the first section, the remnants of typhoon Marge passed eastward through the study area. This storm resulted in winds up to 30 ms^{-1} and 6 to 8 m waves. The turbulence associated with this storm mixed the water column at least 50 km seaward of the coast i.e., into the middle shelf domain (figure 23). Suspended particulate matter was also well mixed within 10 km of the shore and seaward of station 45 isopleths exhibited weak monotonically increasing vertical gradients.

During the second occupation of this section (figure 24), the entire shelf region was themally stratified, with surface minus bottom temperature difference (ΔT) from 0.6 to 2.7°C. Colder bottom waters intruded onshore, with a displacement of the 8.5°C-isotherm of about 10 km. A similar change from mixed to stratified structure was observed in isohalines with the strongest difference (ΔS=0.13 g kg^{-1}) over the normally mixed coastal domain. Again, the data suggested an onshore flux, e.g. at station 42 bottom salinity increased by 0.05 g kg^{-1}, while upper layer salinities decreased. Light attenuation values indicated a 50% reduction in nearshore concentration of SPM, while over the middle shelf domain a subsurface minimum layer was established.

Hydrographic conditions observed on 31 August (figure 25) showed a return to more typical stratification; middle shelf waters were stratified with $\Delta\sigma_t \geq 0.43$ and coastal domain waters were vertically well mixed. We note that stratification was now stronger than that observed on May 31 (inset, figure 22) by about a factor of three. SPM profiles also indicated mixed conditions in the coastal domain and a minimum layer was clearly established near or below the pycnocline.

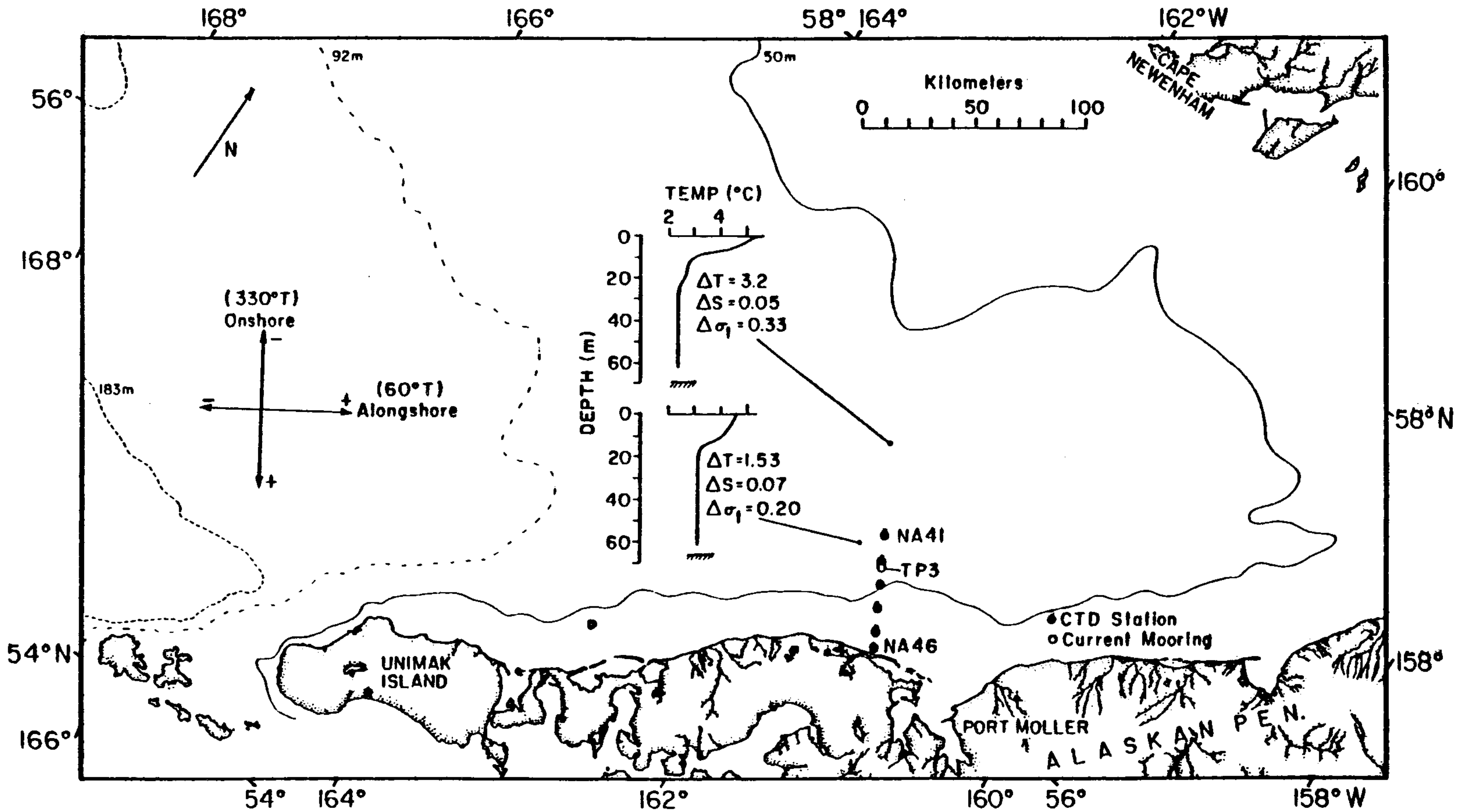

Figure 22. - North Aleutian Shelf study area, showing location of hydrographic data section (NA41 to NA 46) and mooring TP3A. Also shown are CTD data from 31 May 1980 and axes used for current and wind data.

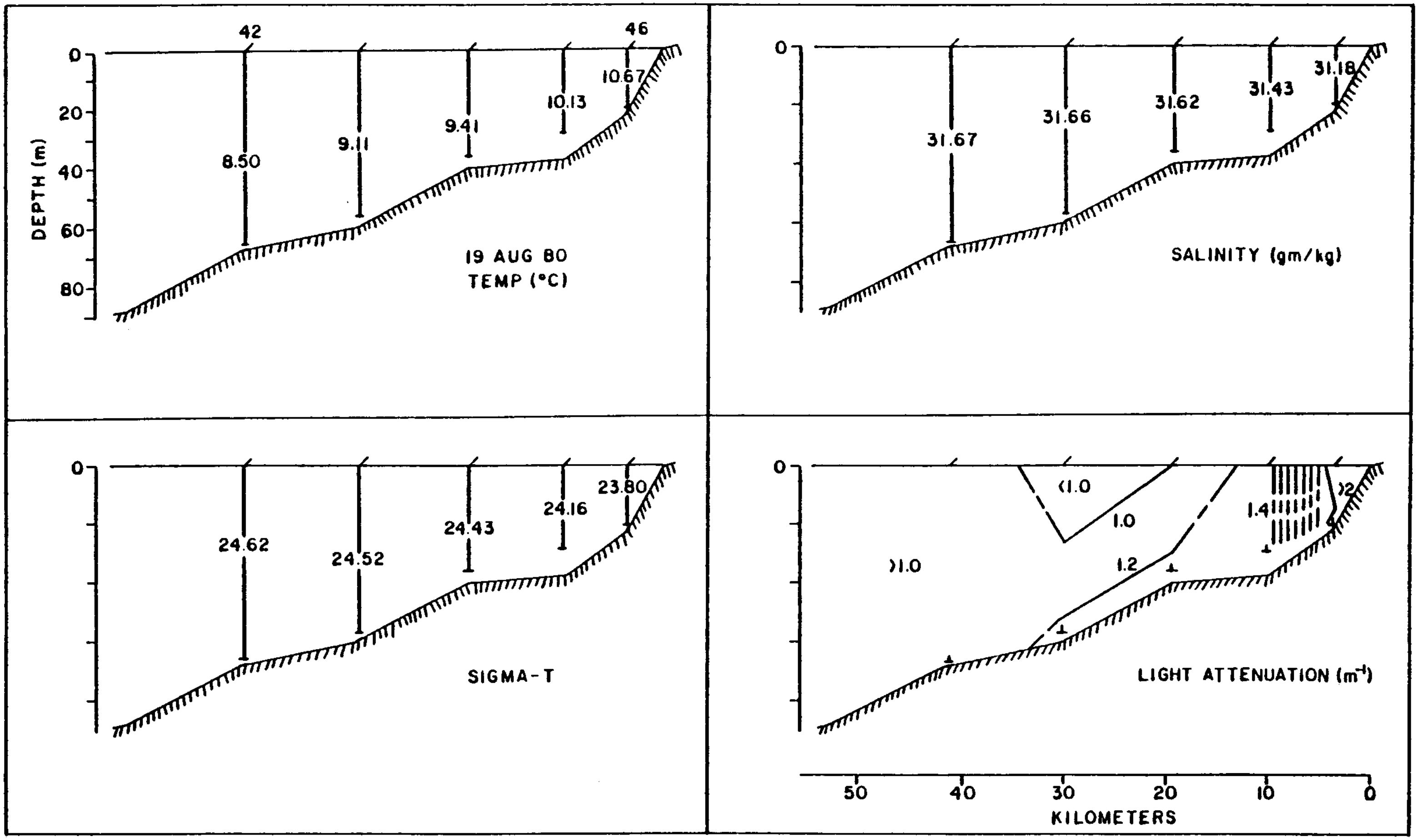

Figure 23. - Hydrographic and light attenuation sections from 19 August 1980. Note the location of the 8.5 °C isotherm.

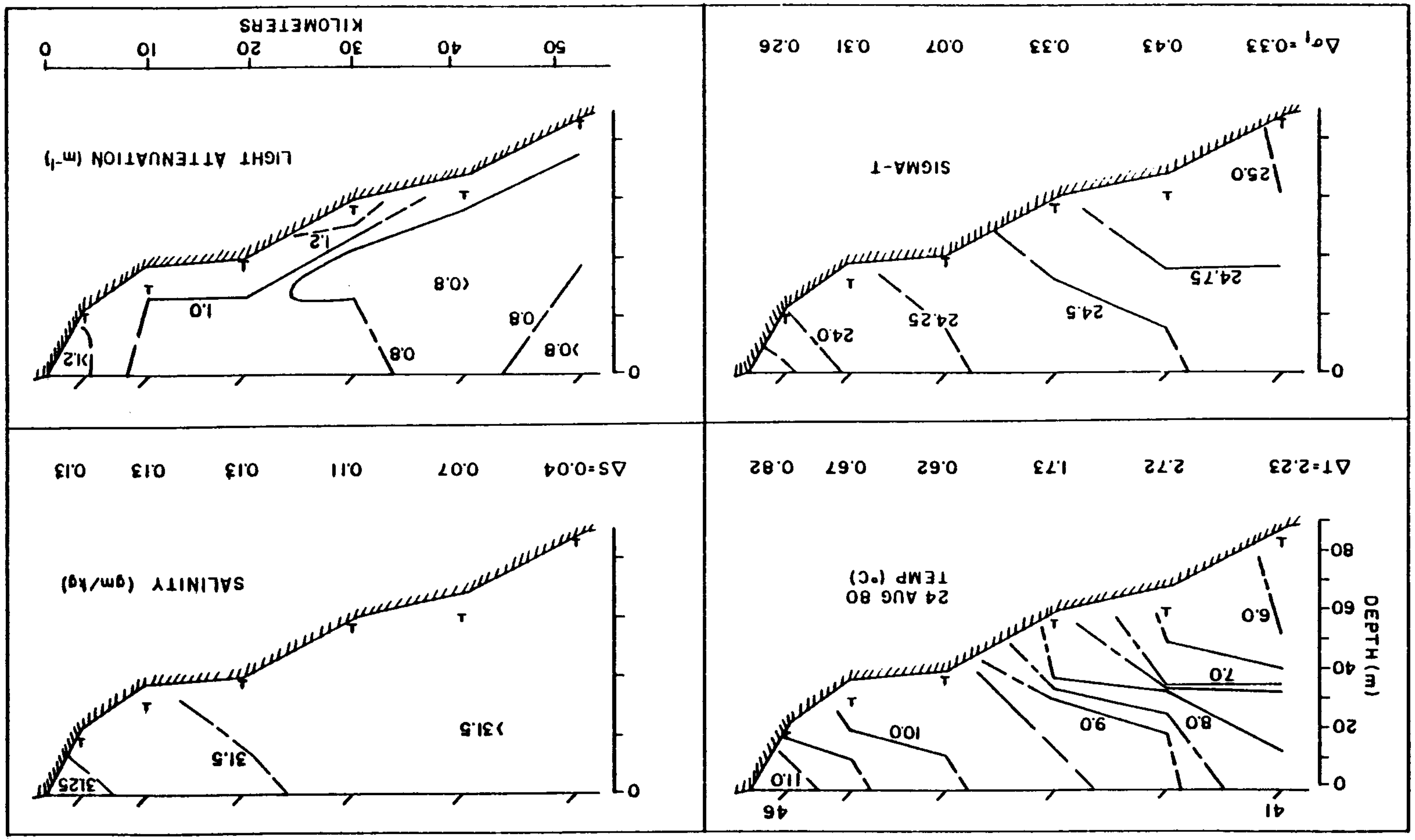

Figure 24. - Hydrographic and light attenuation setions from 24 August 1980. Contour intervals are 0.5 °C, 0.25 g/kg, 0.25 sigma-t units, and 0.2 m^{-1} for light attenuation. Magnitude of upper minus lowest 1 m average parameter is presented under a given station as a Δ. Note, lowest 1 m average salinity at station 42 was 31.71 g/kg.

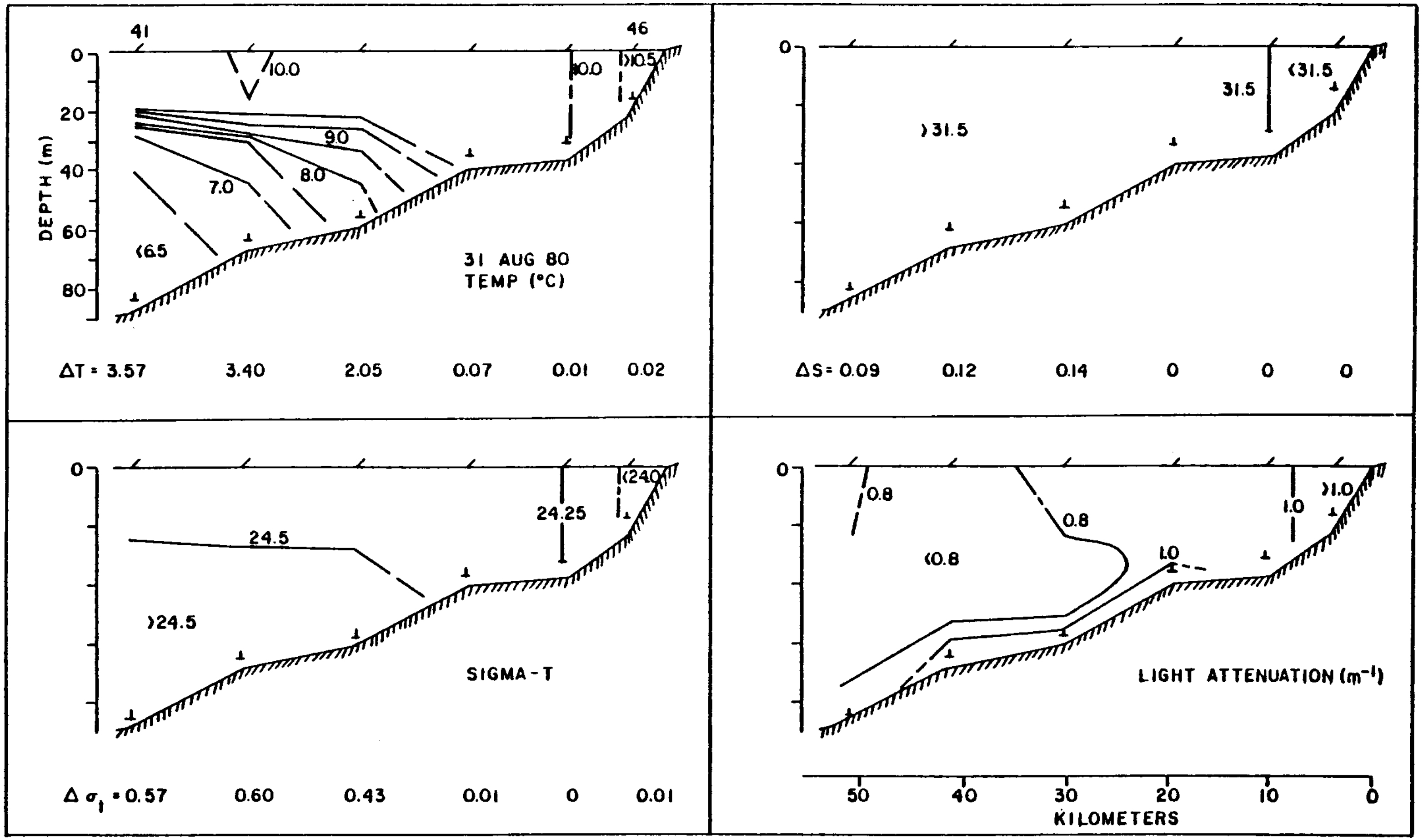

Figure 25. - Hydrographic and light attenuation sections from 31 August 1980.

Winds and Currents Alongshore (v positive 60°T, see figure 22) winds measured from the NOAA ship Surveyor are shown in Figure 26. The passage of the storm resulted in maximum alongshore wind speeds of about 25 ms^{-1}. About 3.5 days after the storm's peak speeds, a period of relatively steady alongshore winds existed for about 3 days with a mean speed of 5.5 ms^{-1}. We note that with the exception of the storm winds and those on 24 August, onshore wind speeds (not shown) were only about 1 ms^{-1}.

Currents at 5 and 39 m below the surface at TP3A are shown in the next two panels of figure 26, where the alongshore axis is the same as for the wind and the onshore axis is u positive 150°T. Near-surface currents reversed from onshore to offshore concomittant with the wind reversal and this initial offshore pulse lasted for about 3 days. While near surface currents were offshore those at 39 m were onshore for the same time period. The visual correlation between wind and near-surface current did not extend to currents at 39 m depth. The alongshore current appeared to be similar at the two depths.

In the bottom panel of Figure 26, we present 25-average s^{-3} values. The flux of turbulent energy generated at the seafloor, E_t, was estimated by assuming that the mean rate of work of tidal currents against bottom stress ($\tau = \rho_0 C_0 u\, u$) is $\bar{\tau} \cdot \bar{u}$ where u is the mean flow velocity near the bottom (Fearnhead, 1975). Here we have used hourly values of current speed from the 39 m depth current record, and have not included either a drag coefficient or density (including these parameters yields dimensions of tidal power, but s^{-3} gives a relative measure of this quantity). By the third occupation of the CTD section, tidal mixing power had increased by about a factor of three.

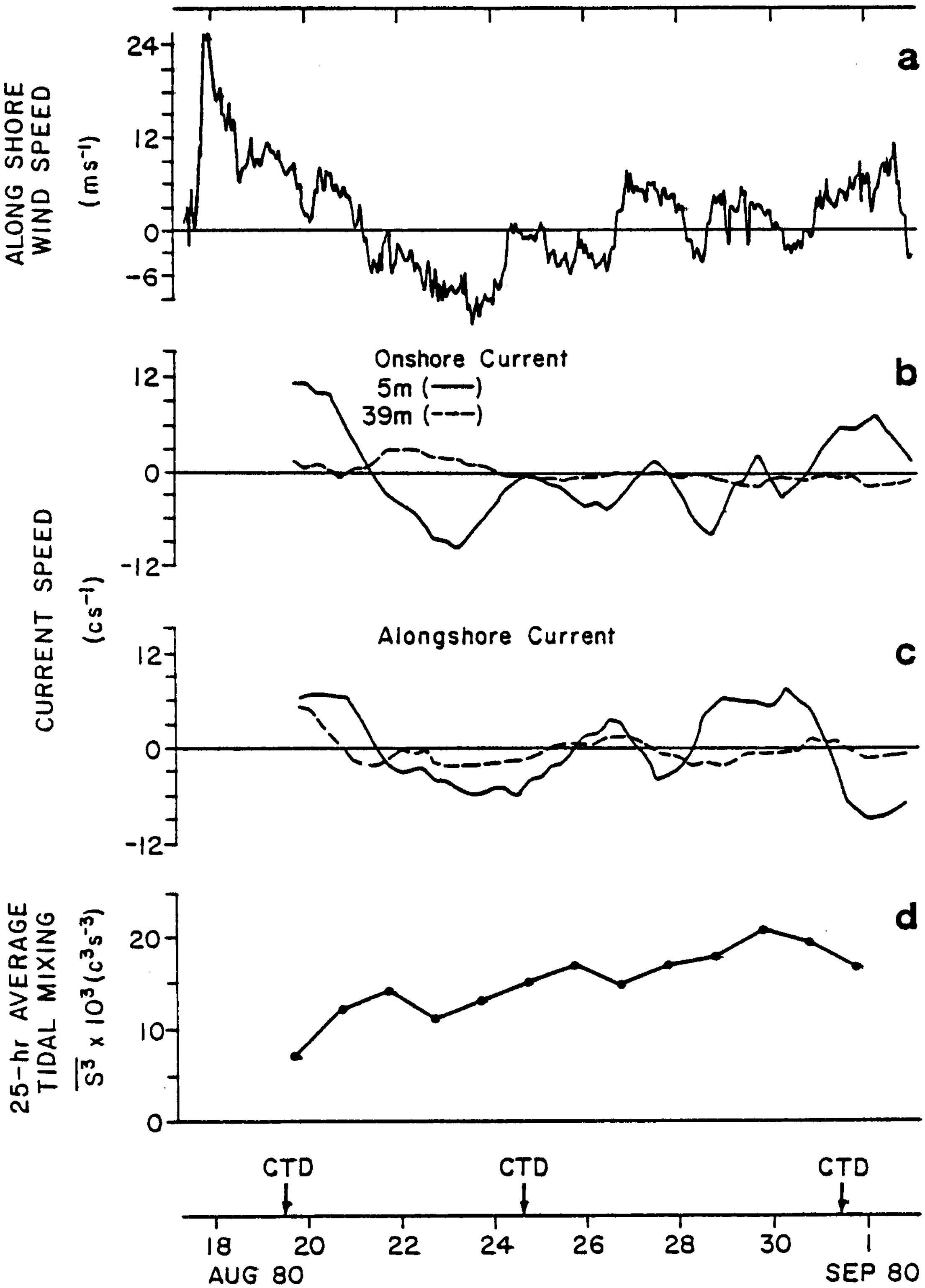

Figure 26. - Alongshore wind speed, onshore and alongshore current at 5 and 39 m, and 25-hr average tidal mixing from the 39-m depth current record.

Discussion The destruction and subsequent reestablisment of typical summer middle shelf and coastal domain hydrographic characteristics was related to winds and tides. The initial vertical mixing of the water column resulted from a combination of wind-wave and current shear turbulence which destroyed vertical structure to at least 50 km, or twice the usual distance, from the shore. Longshore winds then reversed and generated an offshore Ekman flux in the near surface waters and a continuity preserving onshore flux at depth. The offshore flux transported warmer less saline surface water offsore, while the onshore flux at depth provided colder more saline waters; the net result was stratification across the entire study area. As tidal mixing power increased, coastal domain waters became vertically mixed and middle shelf domain waters returned to a two-layered configuration.

Near-surface current spectra (not shown) indicated that of the total fluctuating horizontal kinetic energy ($KE = \frac{1}{2}[u'^2+v'^2]$) per unit mass, subtital energy was 31.6 $cm^2\ s^{-2}$ or about 6%. This is consistent with previous studies (Kinder and Schumacher, 1981b). We note that 50% of the subtidal KE was contained in the 2 to 5 day period bands. The wind spectrum contained little energy (1.3 $m^2\ s^{-2}$ or about 10% of the total KE'_w) at tidal or higher frequencies, however, 25% of the KE_w' was contained in 2 to 5 day periods with the remainder at periods ≥7 days.

The visual correlation between longshore winds and onshore currents, suggesting Ekman dynamics, was substantiated by a linear correlation coefficient between the two low-pass filtered time-series of r=0.83 at 0 lag. In frequency, the maximum coherence between hourly wind and current components was at a period of 2.9 days with a coherence squared of 0.995 or about 99% of the variance. A second maximum occurred at 4.8 days with a coherence squared of 0.91 (for both estimates the 95% level of significance was 0.78). Onshore currents and alongshelf winds were correlated to a lesser extent at lower depths, with correlations decreasing (0.57, 0.53, and 0.42) and lags increasing (0, 6 and 60 hours) at 10, 15 and 29 m respectively. The current record from 39m depth had a negative correlation ($r = -0.68$ at 48 hours) with alongshore winds. These results suggest that longshore winds generated off/onshore Ekman fluxes in an upper layer with, at times (e.g. 21 to 24 August), a compensating flow lower in the water column. During this particular event, coastal divergence would result in a barotropic pressure gradient toward shore. If this were geostrophically balanced, then an alongshore current (in this reference frame a negative value) would be generated. The observations indicated such flow during both 21 to 24 August and 30 August to 1 September wind events. An empirical estimate of 5m onshore current response to alongshore wind was 10^{-2} to 1, or a 10 ms^{-1} wind generated a 10 cm s^{-1} current.

4.2.3. Current and Wind Observations

In this Section we describe current characteristics from records collected at nine locations along the Alaska Peninsula and wind characteristics from observations near Port Moller (figure 12). Mooring information and editing procedures are given in Appendix A. In the following analysis, we have used the 35-h filtered data unless otherwise noted.

Mean and Low-Frequency Flow:

We present the current data as roses (where the direction was partitioned into twelve 30° sectors) and vector means with one standard deviation (along and orthogonal to the principal axis, or axis with the greatest variance) in Figures 27 and 28 for the first deployment period (August 1980-January 1981)

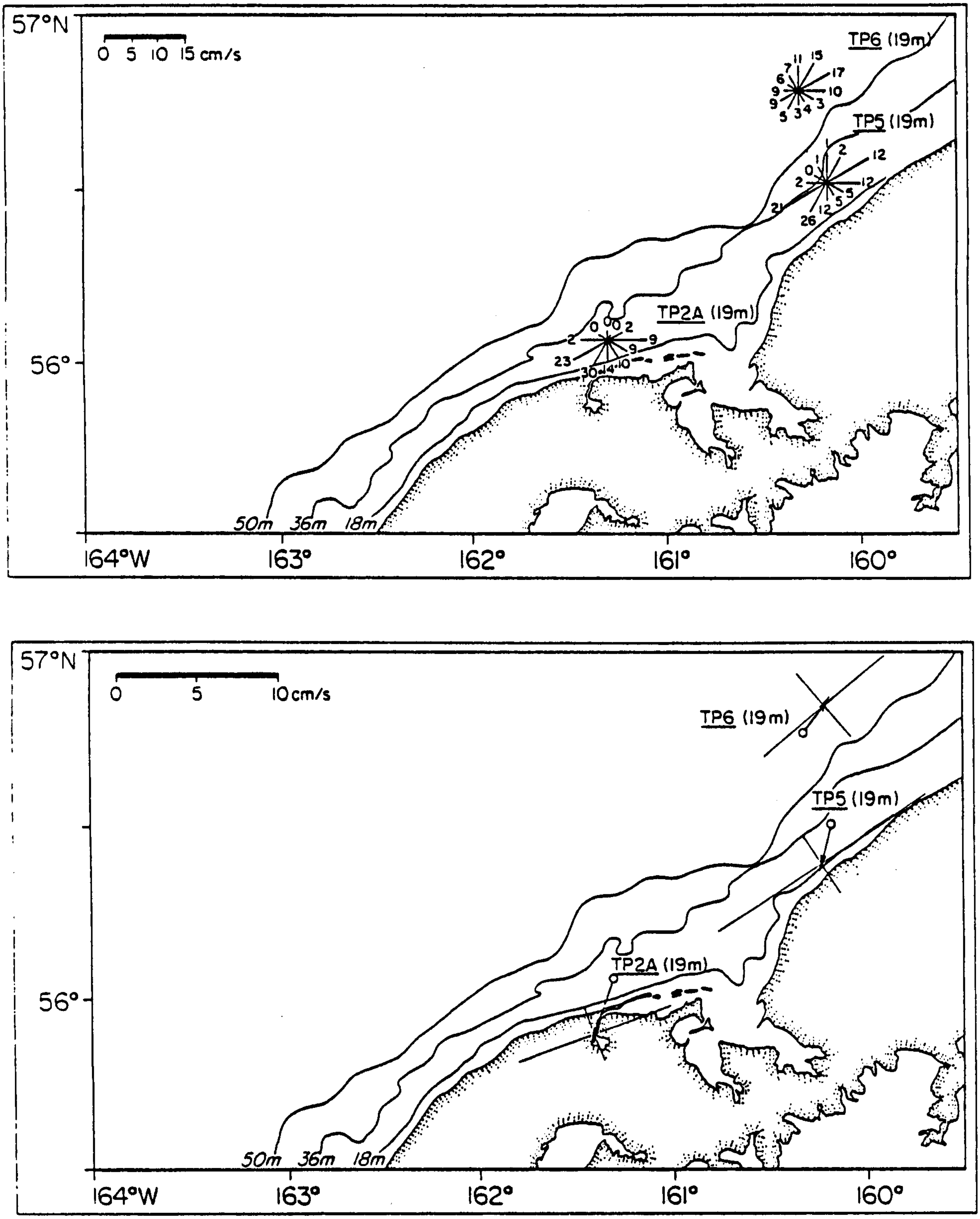

Figure 27. - Current roses and means for near-surface records between August 1980 and January 1981. The cross at the end of the current vector is the standard deviation along and across the principal axis. (Instrument depths are given in parentheses.)

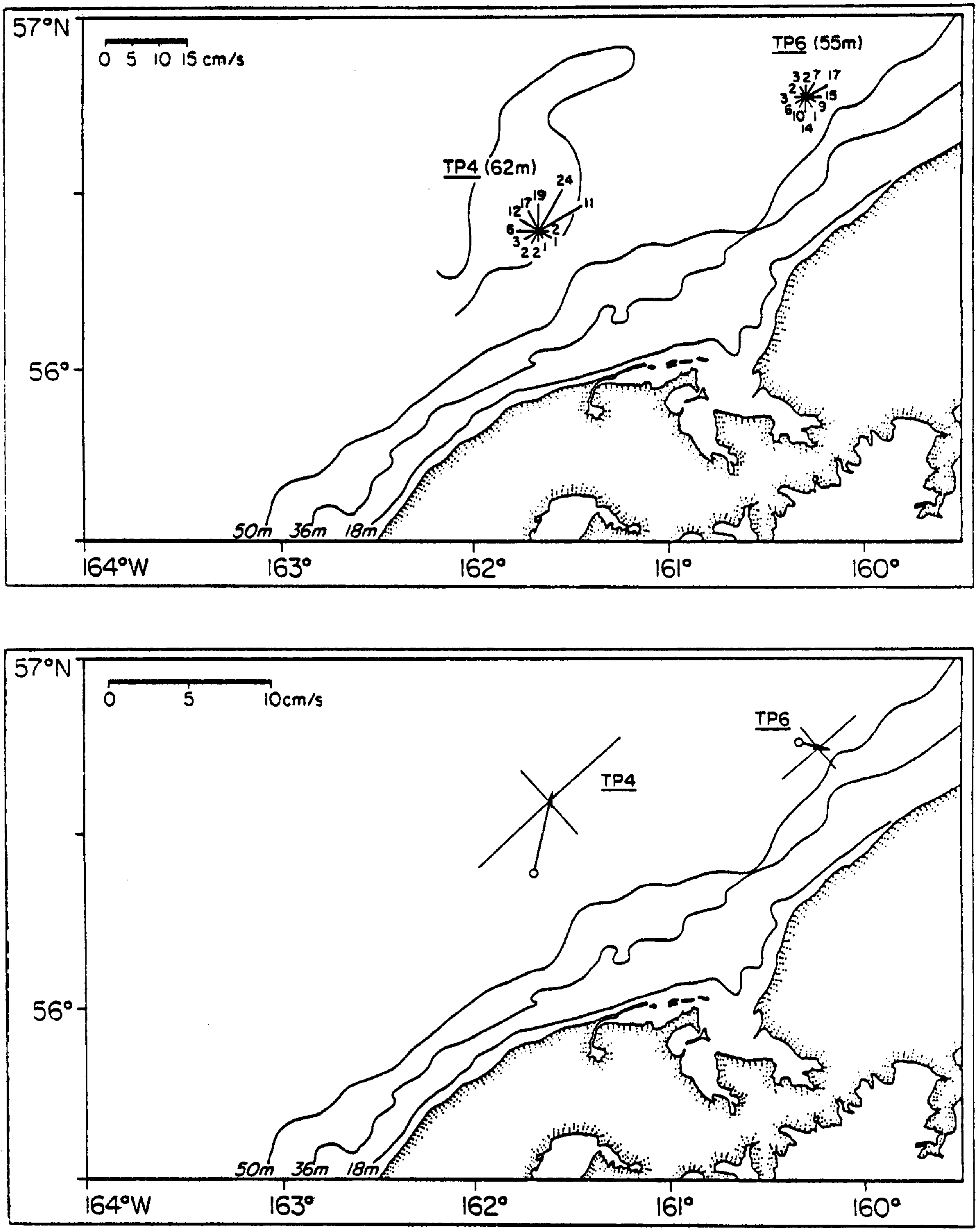

Figure 28. - Current roses and means for near-bottom records between August 1980 and January 1981.

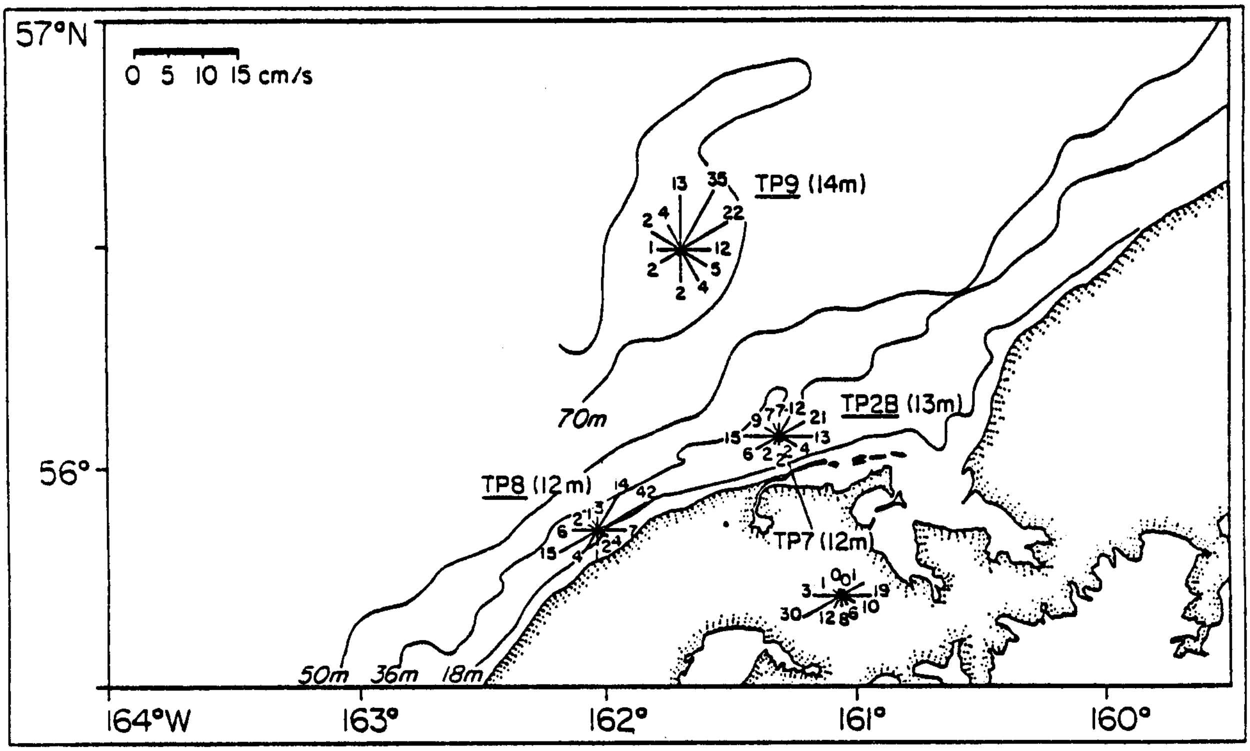

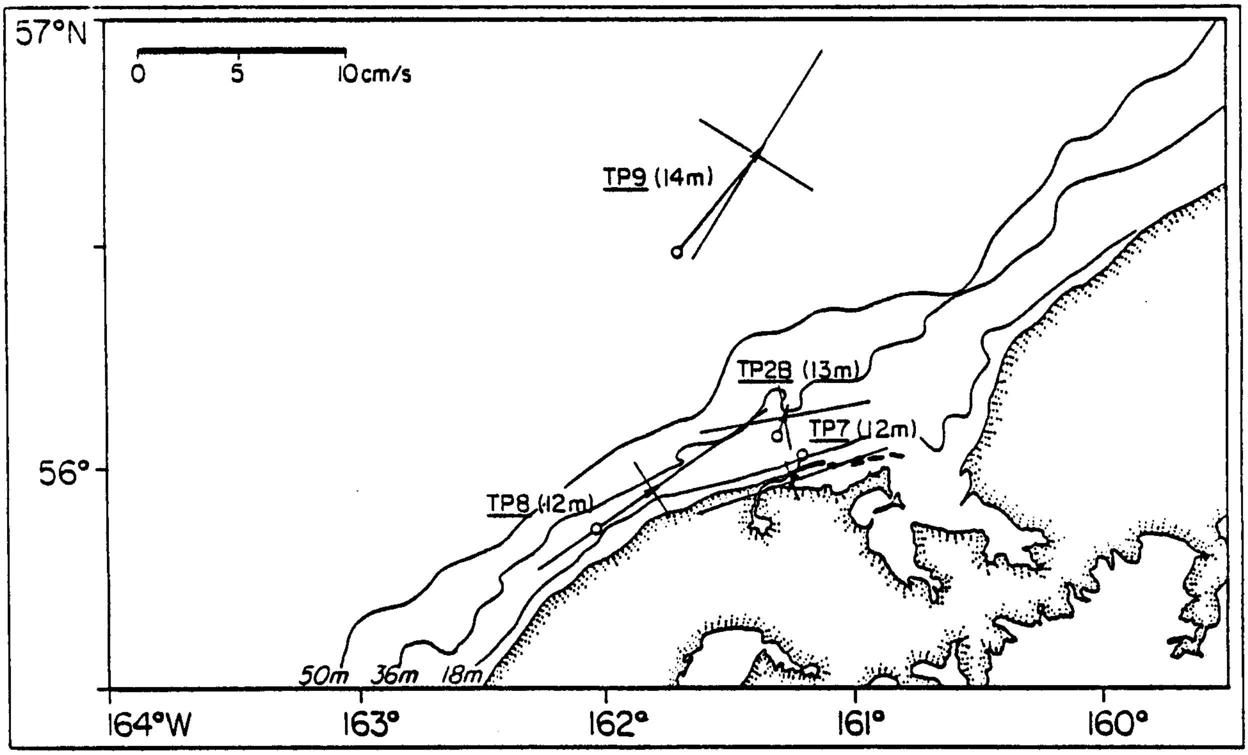

Figure 29. - Current roses and means for near-surface records between January 1981 and May 1981.

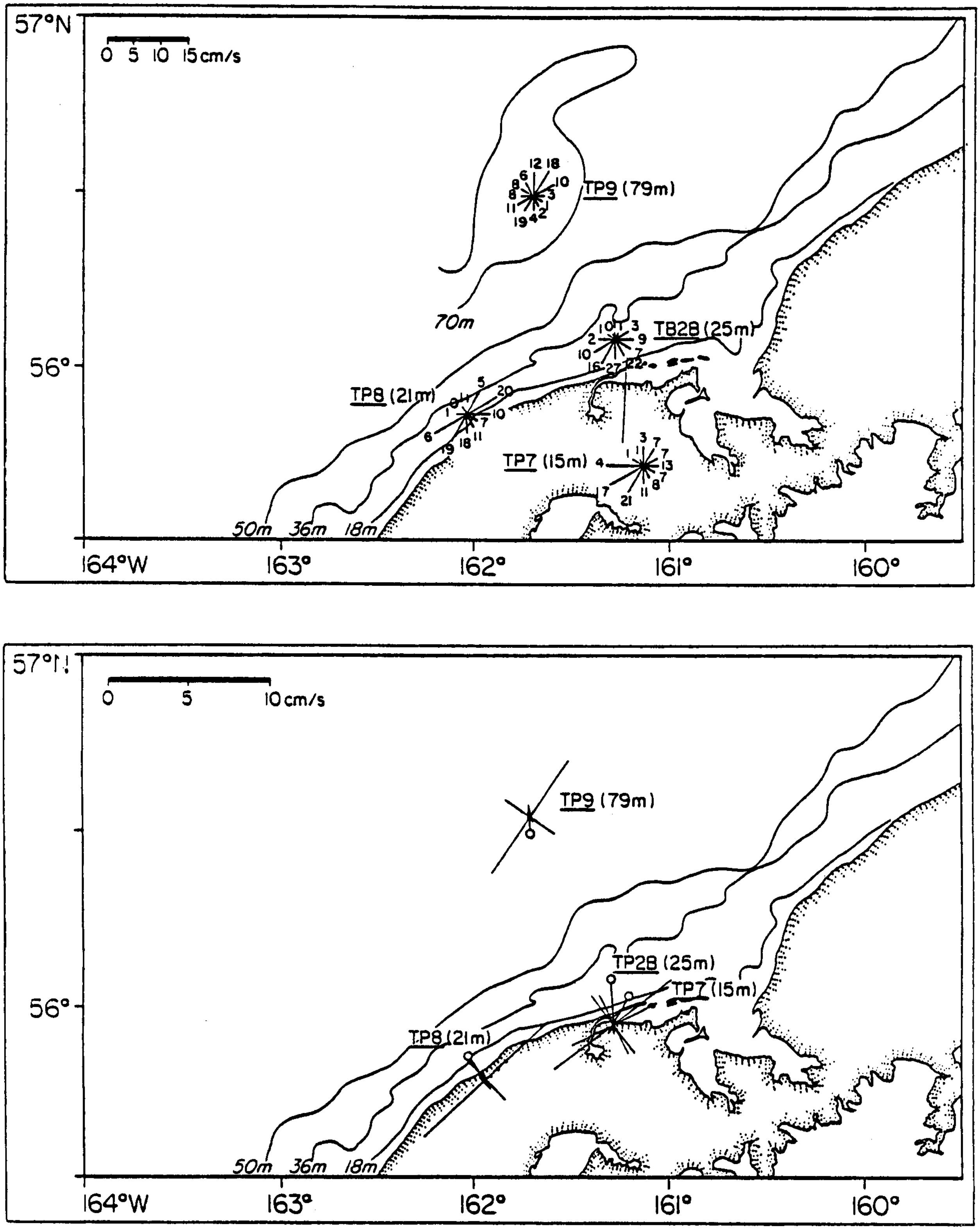

Figure 30. - Current roses and means for near-bottom records between January and May 1981.

and in Figures 29 and 30 for the second observation period (January-May 1981). A feature common to all records was that the majority of observations and the principal axes tended to be along the local bathymetry. Vector mean flow, however, was not consistently along bathmetry except seaward of the 50-m isobath. Shoreward of the 50-m isobath and in the vicinity of Port Moller (i.e. TP2A/B, TP7 and TP5), mean flow had a cross-isobath component.

To establish the statistical significance of the vector mean speeds, we employed a method similar to Allen and Kundu (1978). An independent time scale, τ, was defined as the area under the autocorrelation function for a particular record. This time scale was then used to provide a root mean square error estimate, E, given by

$$E = \pm 2\sigma/(t/\tau)^{\frac{1}{2}}$$

where t is the record length and σ the standard deviation along a given axis. The results of this technique, together with other record characteristics are given in TABLE 4. Note that all vectors are resolved into alongshore (positive toward 60°T) and cross-shelf (positive toward 150°T) axes, and that this definition of alongshore is consistent with the orientation of the peninsula, bathmetry, and generally within about 10° of the individual records principal axis.

The strongest alongshore mean current was observed either seaward of the 50-m isobath (TP4, 6, and 9) or west of Port Moller (TP8), with mean speeds along this component of ~1 to 6 cm s^{-1} where the larger values occurred in the near-surface (12 to 19m below the surface) records. Statistically significant, but weaker (<1 to 3 cm s^{-1}) mean negative alongshore flow existed near-shore in the vicinity of Port Moller (TP2A, B, and 7).

Table 4. - Current characteristics from TP moorings.

Mooring (depth,m)	Instur. Depth (m)	Vector Speed ($cm\ s^{-1}$)	Mean Dir (°T)	Principal Axis & % of Variance	Component Means RMS Alongshore ($cm\ s^{-1}$)	Component Means RMS Cross-shelf ($cm\ s^{-1}$)	KE of Components Alongshore ($cm^2\ s^{-2}$)	KE of Components Cross-shelf ($cm^2\ s^{-2}$)
				AUG 80/JAN 81				
TP2A	19N	3.7	200	70,89	-2.8±1.4	2.4±0.6	12.6	1.9
(32)	20	3.0	211	68,69	-2.6±1.4	1.4±0.8	13.5	5.7
TP5	19N	2.6	194	57,93	-1.8±1.8	1.9±0.5	30.6	2.3
(31)	20	3.7	180	52,83	-1.8±1.9	3.2±0.7	26.0	6.6
TP6	19N	2.1	038	50,78	2.0±1.0	-0.8±0.4	12.0	3.8
(69)	20	1.6	058	45,68	1.6±1.0	-0.1±0.4	10.8	5.7
	55	1.2	108	50,76	0.8±0.7	0.9±0.2	4.5	1.6
TP4	62N	4.4	013	48,84	3.0±1.5	-3.2±0.7	18.0	4.3
TP2B	13N	1.0	021	80,87	0.8±1.4	-0.6±0.8	8.9	2.4
(35)	25	2.8	176	63,68	-1.2±0.9	2.5±0.5	4.4	1.7
TP7	12N	1.4	203	71,96	-1.1±1.4	0.8±0.5	12.2	1.8
(25)	15	2.1	210	53,81	-1.8±1.5	1.0±0.6	9.8	2.6
TP8	12N	3.3	055	55,95	3.2±2.4	-0.3±0.4	22.3	1.4
(31)	21	1.8	145	46,90	0.2±1.9	1.8±0.7	13.8	2.5
TP9	14N	6.1	040	32,77	5.7±1.5	-2.1±1.9	13.4	8.4
(89)	79	1.0	357	34,83	0.5±1.3	-0.9±0.8	8.5	3.5

Where: All statistics are from 35h data, N represents accoustic current meter and alongshore and cross-shelf are positive 60° and 150° respectively.

Cross-shelf mean speeds were generally weaker and exhibited the tendency to be offshore in the upper water column and onshore closer to the bottom. This pattern was evident in the records from TP2B, where the cross-shelf component reversed sign over a 12 m vertical separation.

The characteristics of stronger alongshore mean flow was mirrored in the low frequency kinetic energy; the alongshore component was always greater than the cross-shelf componenent, generally by a factor of four. The relation between TP current record characteristics and those collected over the remainder of the southeastern Bering Sea shelf is discussed in Appendix B.

Vertical Structure:

In order to provide information illustrating vertical structure of currents over the middle shelf domain, moorings with surface flotation were deployed in August 1980 (TP3A) and in May 1981 (TP3B). The results are presented in Figures 31 and 32 as 35-hr stick plots and in Figure 33 as 2.9 hr mean speed, component speed and net current over the observation periods. During TP3A, stratification varied greatly, with the difference in sigma-t between lower and upper current meters ranging from 0 to 0.65, with an average of ~0.5); during TP3B, this index of stratification only varied from 0.25 to 0.44 with an average of ~0.3. The geostrophic wind during the two observation periods was significantly different: during TP3A winds were towards the south for the first four days and then were weakly northward, while during TP3B, winds were strongly northward throughout most of the current record. Despite these differences in stratification and wind forcing, the shear in mean speed was similar, being 2.8 and 1.9×10^{-3} s^{-1} during TP3A and B respectively. Further, the shear in alongshore speed was nearly identical below 20m, with

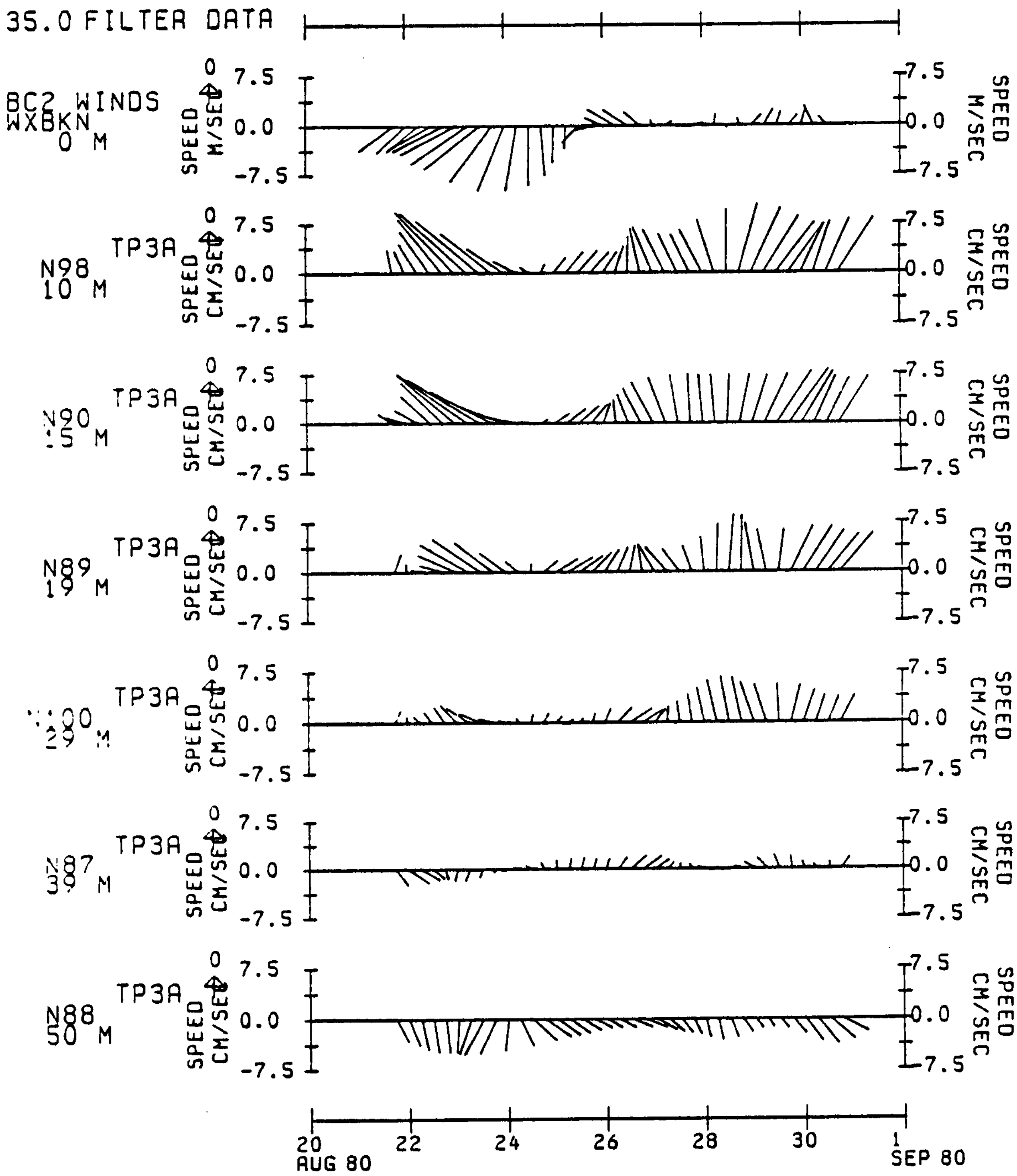

Figure 31. - Current records from TP3A presented as 6-hourly vectors.

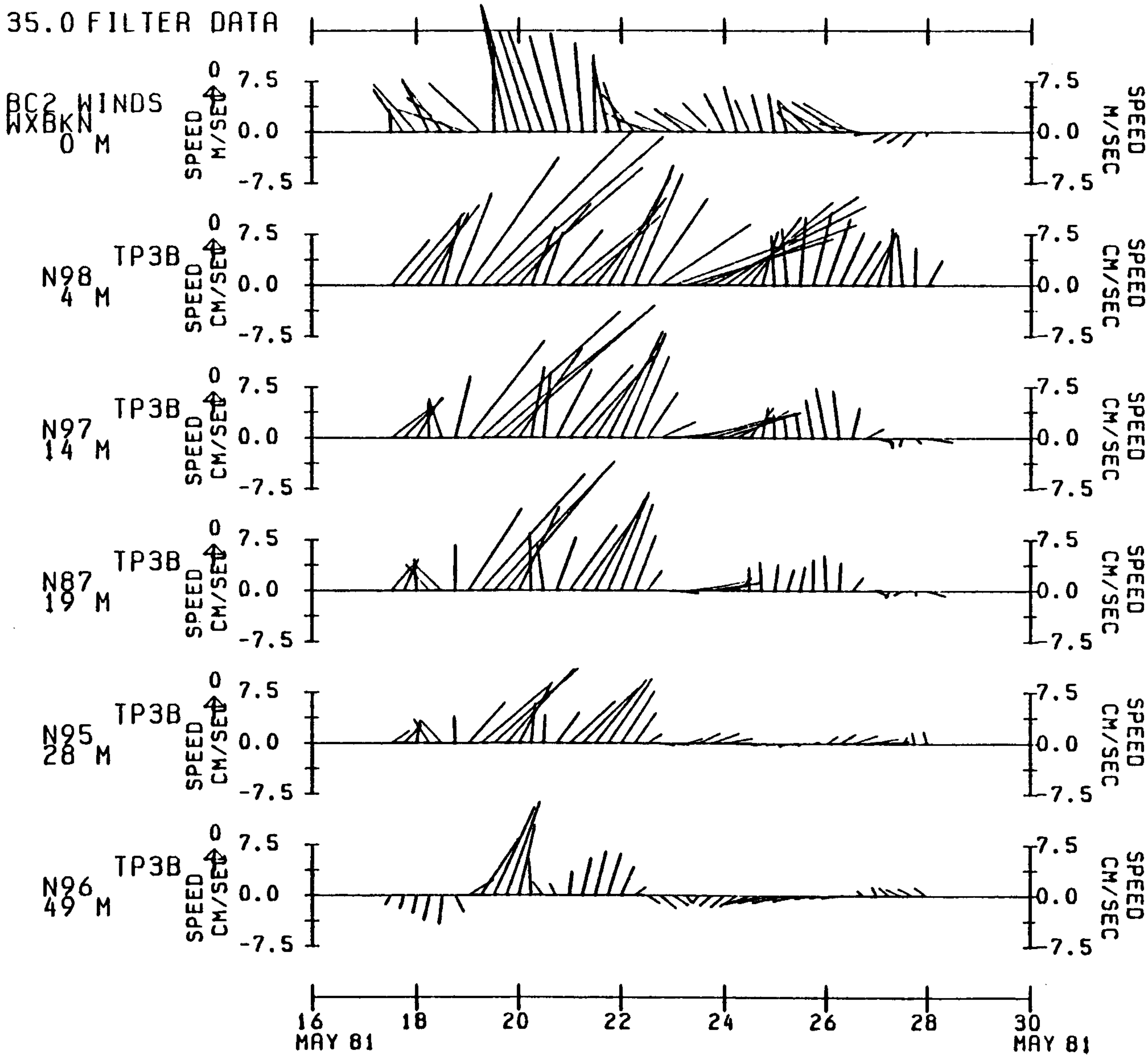

Figure 32. - Current records from TP3B presented as 6-hourly vectors.

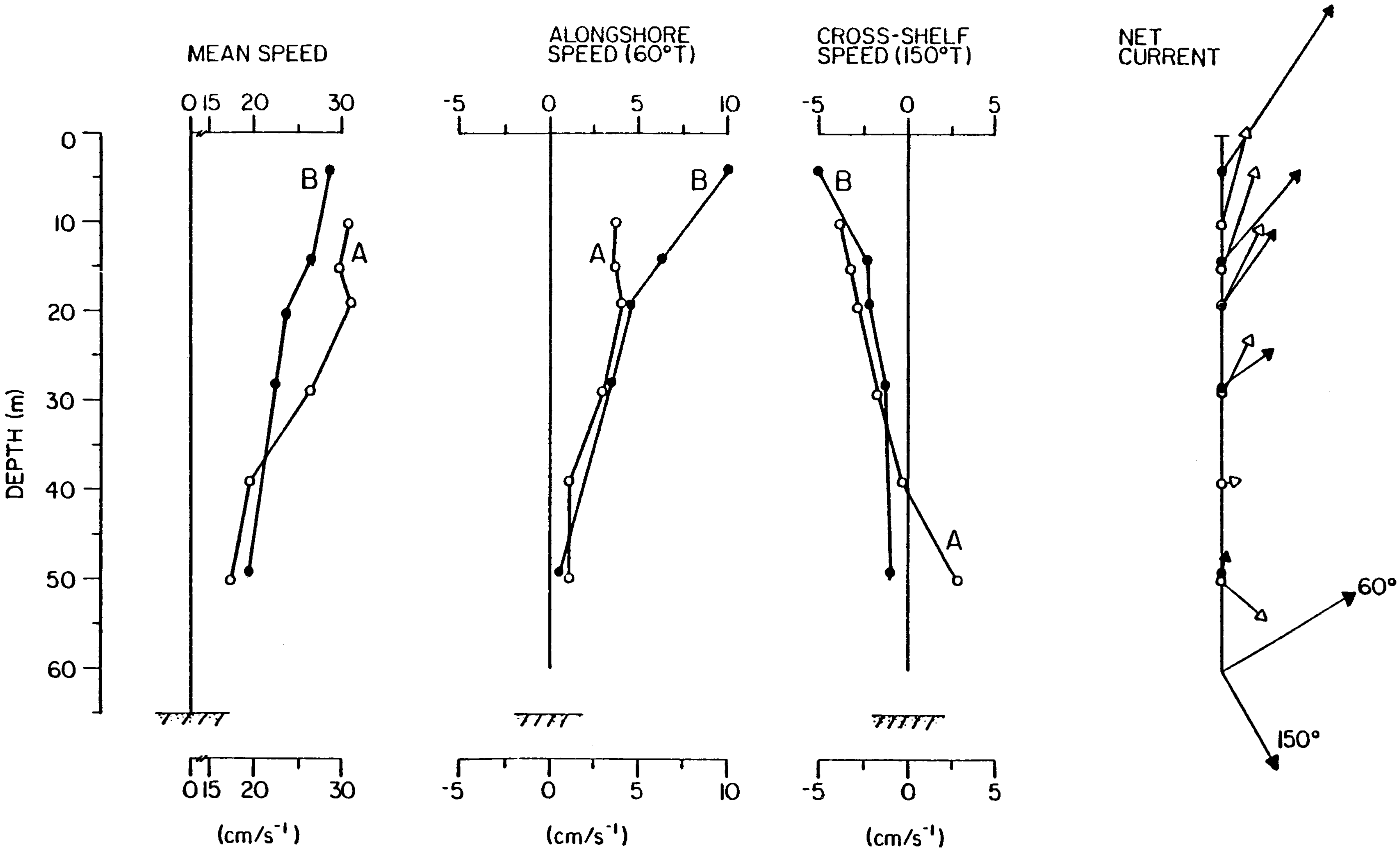

Figure 33. - Profiles of mean, alongshore, and cross-shelf speed and net current from TP3A and B.

the marked difference above this depth likely attributable to stronger and more consistent wind stress during TP3B. The cross-shelf speed profiles were also similar over most of the water column; however, during TP3A the profile indicated onshore flow in the bottom layer.

It is apparent that most of the shear resulted from wind stress (particularly during TP3B) and estimates of baroclinic shear would account for a 1 to 3 cm s^{-1} decrease of alongshore speed between the surface and 25db. There is also a contribution to the shear from tidal currents, although the majority of this contribution would occur in the bottom boundary layer (about 3 to 15 m thick). Hourly alongshore speeds at four levels are shown in Figure 34. During this period winds were light (3 to 4m s^{-1}), so that using a current response of 3% of the wind speed, the wind-induced shear in the upper mixed layer (about 25 m in depth) would be approximately 10cm s^{-1}. Combining this estimate with reasonable values for baroclinic shear would account for most of the shear indicated between 10 and 29 m depth records, but not the shear of 20 to 25cm s^{-1} shown to exist during floods and ebbs between the 29 and 50 m records. Although some fraction, perhaps up to 50%, may be accounted for by tides, and the observation that the lower water column leads (by about 15°) the surface is consistent with the tidal wave propagation, some of the observed shear is not accounted for by any of these mechanisms.

Wind: A comparison between alongshore and cross-shelf components of surface winds (herein called BC2 winds) and those measured on Lagoon Point (near Port Moller) is shown in Figure 35. The alongshore components are markedly similar, with BC2 winds indicating somewhat greater speeds (record mean, 2.5 ms^{-1} vs - 0.3 ms^{-1} for TPIA). The cross-shelf winds are also similar, but TPIA winds were generally greater than those computed for BC2 (record mean 1.1 ms^{-1} vs ~0 at BC2). Although there were differences in component speeds, the alongshore

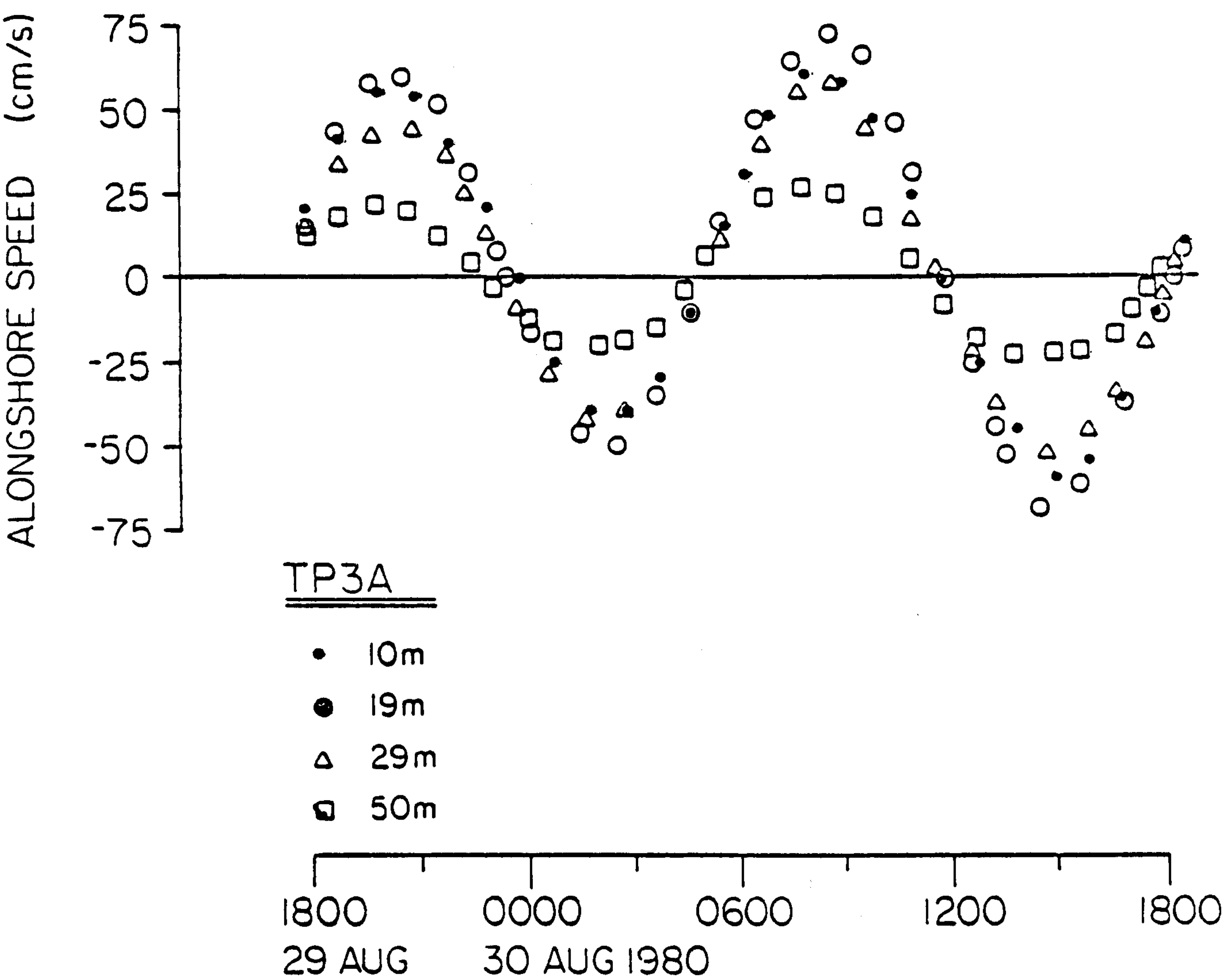

Figure 34. - Current speed at four depths from 2.9-hr data.

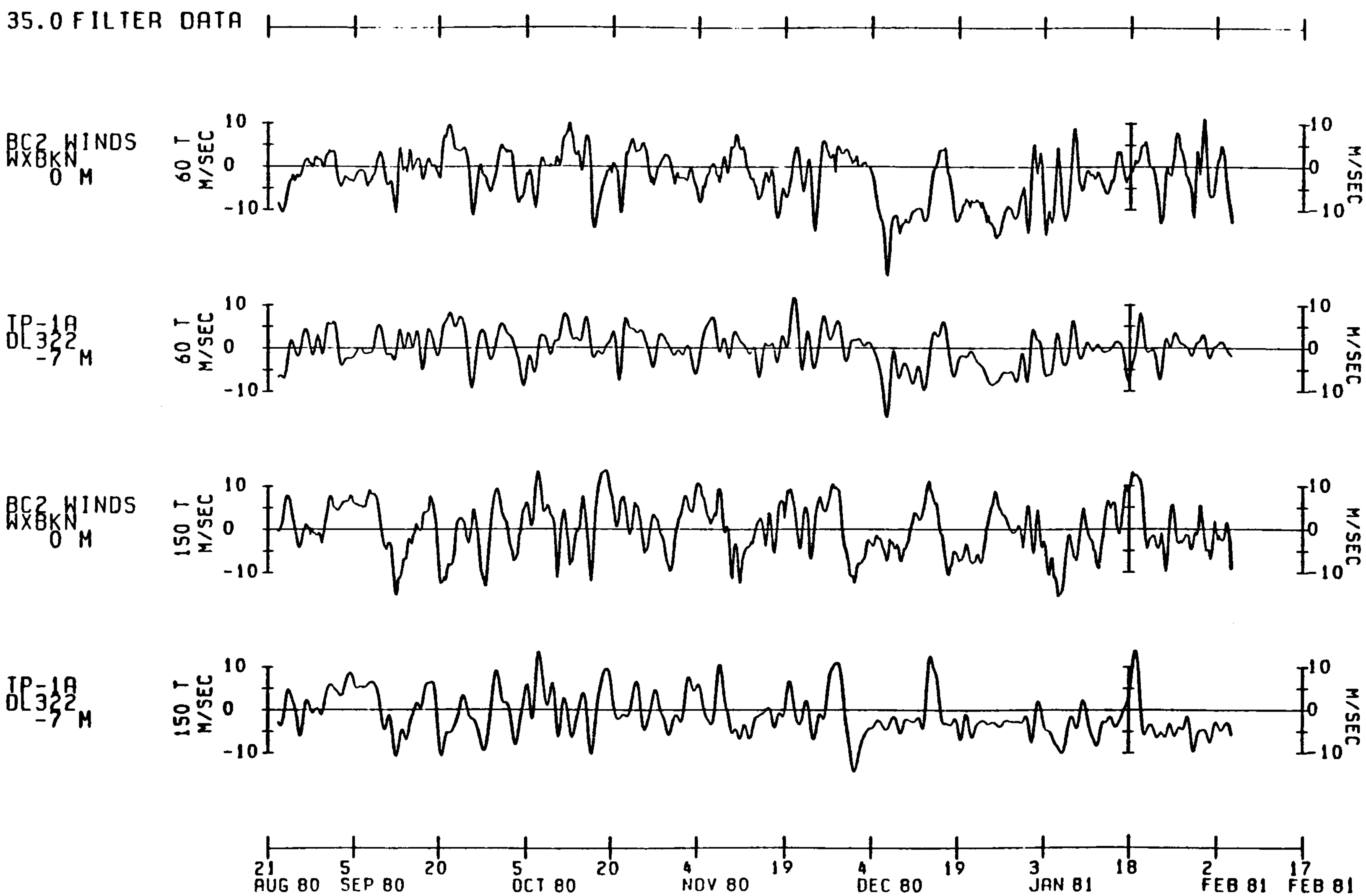

Figure 35. - Comparison of alongshore and cross-shelf components from surface (BC2) and observed (TP1A) wind.

series were highly coherent ($K^2 \geq 0.6$) at all frequencies (figure 36A). There was, however, significantly less coherence squared at periods between 2.5 and 3.3 days in the cross-shelf series (figure 36B). While some of these differences may be attributed to the method of computing geostrophic winds from surface atmospheric pressure (see Section 3.3), the wind roses generated by the two time series (figure 37) indicated that there was about at 20% difference in the percentage of wind observations in the secotrs between 270° to 330°, and 90° to 150°. Considering the local orography, some portion of the difference was likely due to pressure gradient winds along the orographic axis. In general, this affect may be present wherever there are gaps in the mountain range along the Alaska Peninsula, particularly in the vicinity of Cold Bay where the gap is both wide (about 20 km) and nearly flat.

4.2.4 Salinity Time-Series

Moored current meter records provided some further insight regarding temporal changes in salinity (as computed from temperature, conductivity and pressure). In figure 38, 15-day averages of salinity are shown, where the individual points were determind by finding the differences between successive 15-day averages and replacing this value at the mid-point of a given averaging interval. The relative change in mean salinity was greatest ($\sim$2g kg^{-1}) at TP2, but the other series showed a similar trend of decreasing salinity over a period of about one month and this change was in October. Because the advective transport is both sluggish and alongshore toward the east, Kvichak River discharge was not a likely source of the less saline water. Instead, the less saline water likely was a result of addition from numerous ungaged streams and ground-water injection. This addition could result in the bands of relatively stratified water shown in Figure 16D.

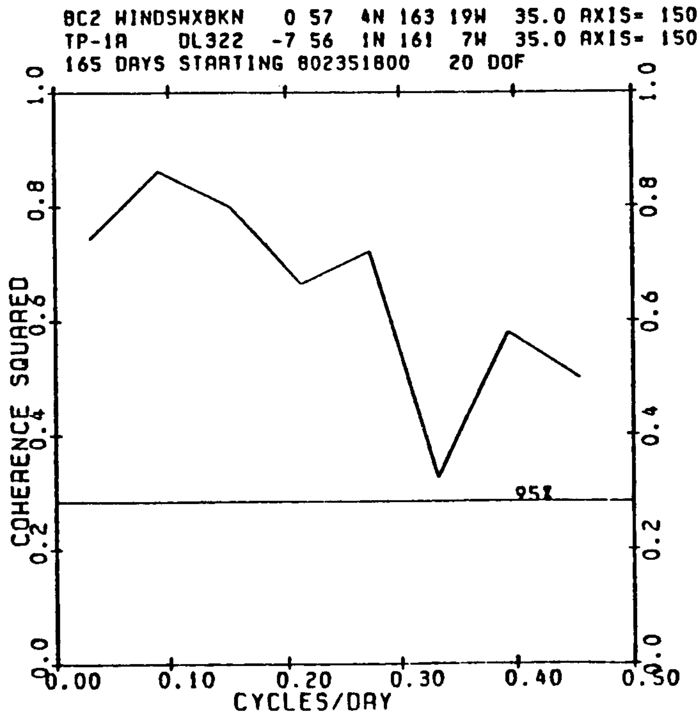

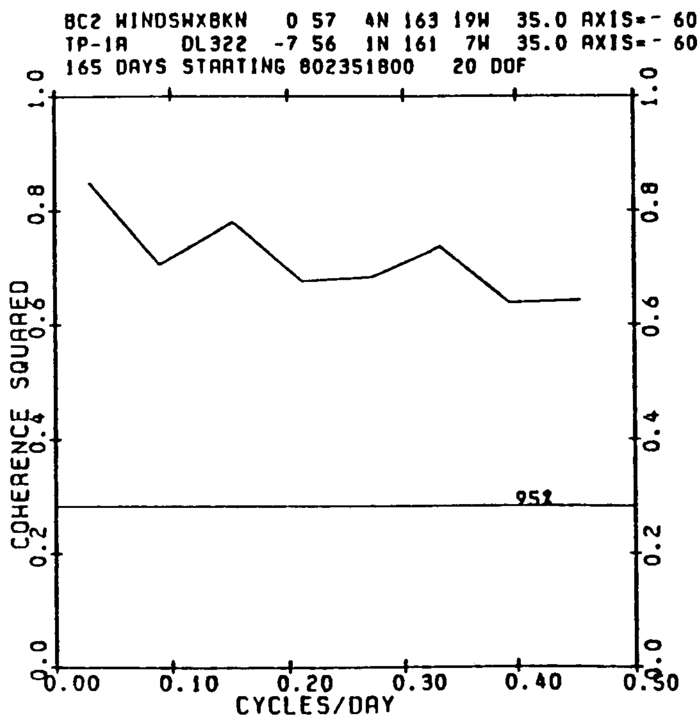

Figure 36. - Coherence squared estimates between surface and observed wind components.

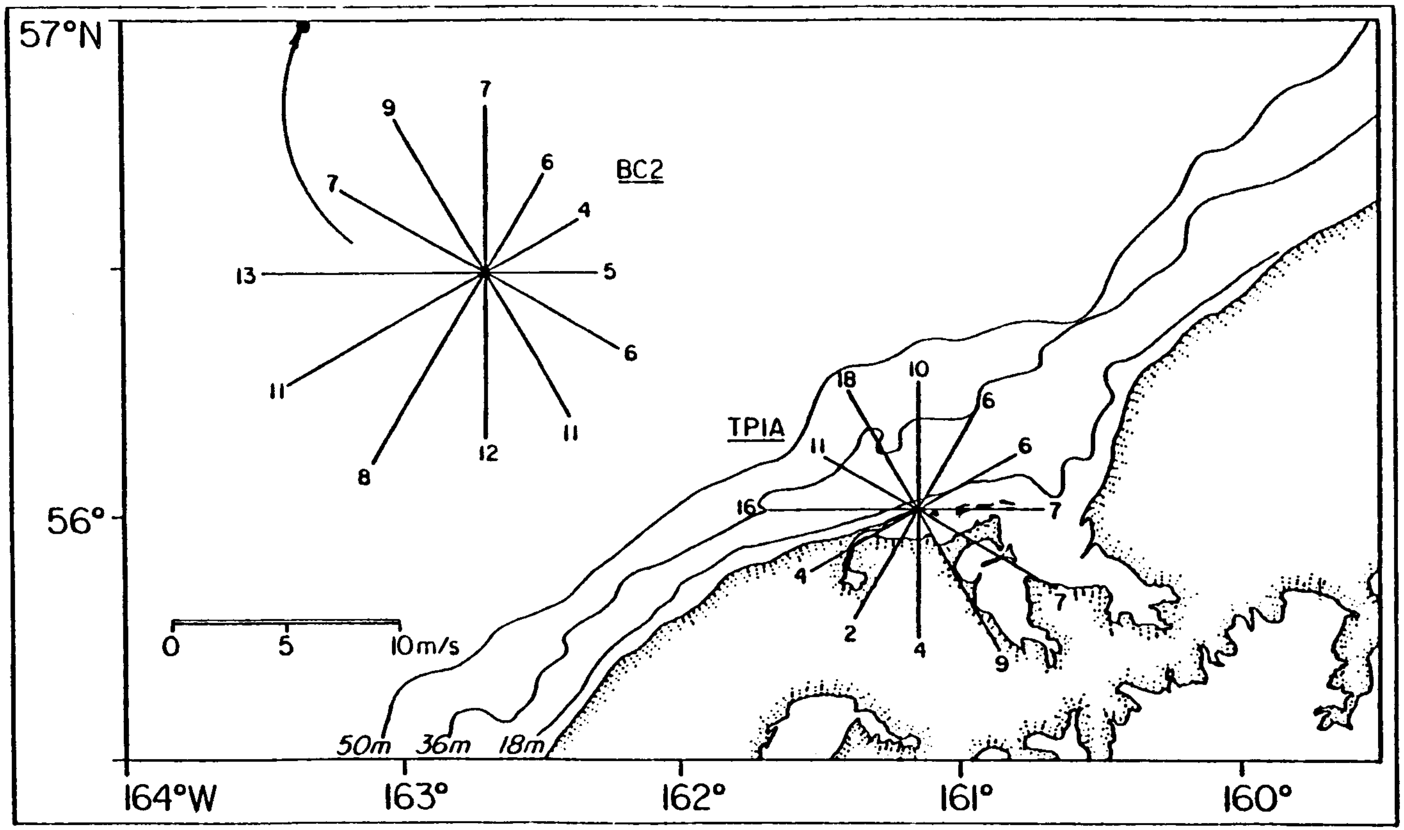

Figure 37. - Wind roses for BC2 and TP1A.

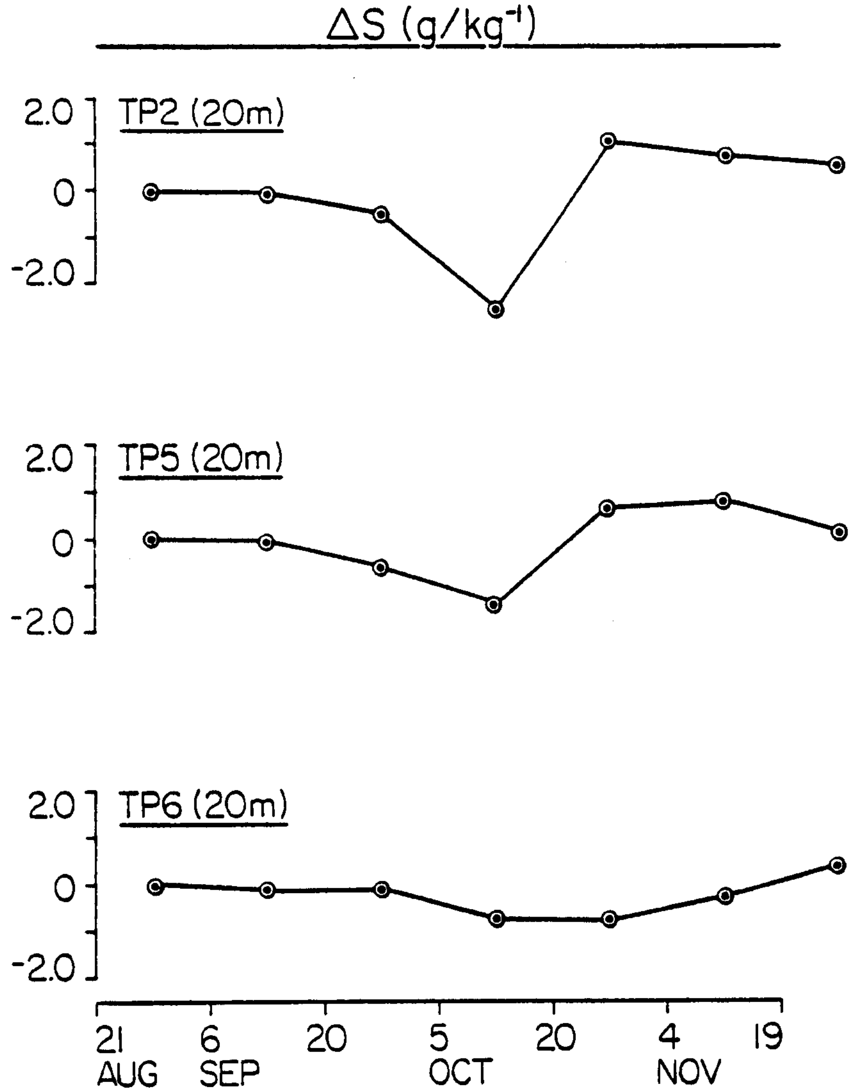

Figure 38. - Salinity time-series (15-day averages) from TP moorings.

5. SUMMARY AND CONCLUSIONS

The behavior of currents and bottom pressure observed between March an August 1980 has been described for Unimak Pass, Alaska. These data have been interpreted together with atmospheric pressure gradient, geostrophic wind, and CTD data. The following conclusions were reached:

(1) mean flow was from the Gulf of Alaska shelf westward through Unimak Pass, and reversals occurred in 18% of spring and 31% of summer 35-hr filtered current observations, with mean flow during spring three times greater than in summer.

(2) currents at periods between 3 and 10 days in Unimak Pass were highly coherent with the bottom pressure difference along the strait, which provided the dominant forcing for fluctuations. At these periods most of the bottom pressure difference was related to alongshore winds which induced sea level changes along the Gulf of Alaska coast.

(3) Longer period (on the order of months) flow and variablity was accounted for by the presence of a southwestward flowing coastal current. This feature appeared to be a westward extension of the Kenai Current.

(4) Flow of fresher coastal water through Unimak Pass resulted in formation of a front in the vicinity of Unimak Pass. This flow also may influence baroclinic flow along the northern side of Alaskan Peninsula and provide some fraction of the northward transport through Bering Strait.

A characterization of hydrographic feastures and current behavior between August 1980 and June 1981 has also been described for the north Aleutian shelf study area. These data were interpreted together with wind and river discharge data. The following conclusion were drawn:

1) In general, waters over the continental shelf adjacent to the Alaska Peninsula adhere to the previously defined hydrographic domains (Kinder and Schumacher,

1981a): outer shelf domain (the small portion of the study area north of Unimak Island with depths $\geq$ 80m) waters were always stratified with upper and lower mixed layers separated by a column of weak stratification. Both temperature and salinity showed small seasonal ranges; middle shelf (depths greater than 50m and less than ~80m) were typically two-layered during summer and well mixed from about October through March. An exception occurs when ice, primarily formed to the northeast, is transported over this domain and melts. Temperature and salinity ranged between ~10°C and ~1.0g kg^{-1} respectively. The coastal domain (less than 50m) was generally mixed, however, the addition of freshwater as a "line source" (particularly between Ports Moller and Heiden) and from the Kvichak River, resulted in stratification (up to 3 sigma-t units) even though the water is shallow and tidal mixing energy strong. There was also a suggestion that melting ice could impact the local bouyancy/tidal mixing balance. Both temperature and salinity varied greatly, with ~14°C and 8g kg^{-1} changes respectively (where most of the salinity range was a result of Kvichak River addition).

2) Hydrographic data from February 1981 showed the impact of less saline Kenai current water upon coastal water along the Peninsula. This was most apparent in a reduction of mean salinity between Port Moller and Unimak Island between August 1980 and February 1981. This lends support to a previous hypothesis that the Kenai Current was linked with flow around the perimeter of the southeastern Bering Sea shelf and continued northward toward Bering Strait (Schumacher, et.al., 1982).

3) Storms radically alter mean hydrographic domain characteristics. The enhanced turbulence can mix middle shelf water and increase SPM concentratons. These two factors could dominate vertical transport of oil, resulting in greater concentrations on the bottom in a shorter time than detrital rain.

4) Current records supported previous results (Kinder and Schumacher, 1981b: Schumacher and Kinder, 1983: see Appendix B) which infer a moderate (2 to 6 cm s^{-1}) Eulerian mean flow from the vicinity of Unimak Island, counter-clockwise around Bristol Bay, and thence northwest past Nunivak Island. A mechanism for long-term (order months) flow is the persistent cross-shelf density distribution, which resulted in baroclinic speeds of 1 to 5 cm s^{-1}, typically concentrated in a 10 to 20 km wide band in the vicinity of the 50-m isobath. Scaling of Eulerian tidal residual flow suggested a weak contribution, <1.0 cm s^{-1}, except were the tidal current was orthogonal to the 50-m isobath off Port Heiden (Schumacher and Kinder, 1983, see Appendix B).

5) Although wind energy was evident in alongshore current pulses, mean winds during the current observations were weak and toward the west, in opposition to the observed mean flow. Cross-shelf current pulses were also evident, and the observed tendency was for offshore flow in the upper water column.

6) Comparison between surface and measured winds indicated these series were highly coherent, particularly in the alongshore component. At short periods (>2.5 to 3.3 days), coherence was weak in the cross-shelf component and the observations showed that measured winds tended to be along the local orographic trend. Such down pressure gradient winds have been noted before (Schumacher and Pearson, 1981), and are likely to be more significant at Cold Bay and in Unimak Pass.

7) Substantial vertical shear in currents was observed during two mooring periods. The combination of wind induced shear and geostrophic baroclinic shear accounted for about one-half the observed values. The magnitude attributable to tides requires theoretical examination.

6. REFERENCES CITED

Allen, J. S. and P.K. Kundu, On the momemtum, vorticity and mass balance on the Oregon shelf, J. Phys. Oceanogr., 8, 13-27, 1978.

Bakun, A., Coastal upwelling indices, west coast of North America, 1946-71. Dept. of Commerce, Tech. Rep. NMFS SSRF-671, NOAA, Monterey, Calif., 1973.

Bowden, K.F., The flow of waters through the Straits of Dover related to wind and differences in sea level, Phil. Trans. R. Soc. London, Ser. A., 248, 517-551, 1956.

Brower, W.A., H.F. Diaz, A.S. Prechtel, H.W. Searby, and J.L. Wise, Climatic Atlas of the Outer Continental Shelf Waters and Coastal Regions of Alaska, vol. 1, Gulf of Alaska, Final Rep. RU-347, U.S. Dept. of Commerce/NOAA/ Alaska Outer Continental Shelf Environmental Assessment Program, Fairbanks, Alaska, 1977.

Chao, S.-Y., and L.J. Pietrafesa, The subtidal response of sea level to atmospheric forcing in the Carolina Capes, J. Phys. Oceanogr., 10, 1246-1255, 1980.

Charnell, R.L., and G.A. Krancus, A processing system for Aanderaa current meter data, Tech. Memo. ERL PMEL-6, NOAA, Boulder, Colo., 1976.

Coachmen, L.K., and K. Aagaard, Reevaluation of water transports in the vicinity of Bering Strait, in The Eastern Bering Sea Shelf: Oceanography and Resources, vol. 1, edited by D.W. Hood and J.A. Calder, pp. 95-110, U.S. Dept. of Commerce/NOAA/OMPA, Washington, D.C., 1981.

Coachmen, L.K., and R.L. Charnell, Finestructure in outer Bristol Bay, Alaska, Deep Sea Res., 24, 809-839, 1977.

Coachmen, L.K., and R.L. Charnell, On lateral water mass interaction: A case study, Bristol Bay, Alaska, J. Phys. Oceanogr., 9, 278-297, 1979.

Coachman, L.K., and J.J. Walsh, A diffusion model of cross-shelf exchange of nutrients in the southeastern Bering Sea, Deep Sea Res., 28, 819-846, 1981.

Coachmen, L.K., K. Aagaard, and R.B. Tripp, Bering Strait, the Regional Oceanography, University of Washington Press, Seattle, 1975.

Coachmen, L.K., T.H. Kinder, J.D. Schumacher, and R.B. Tripp, Frontal systems of the southeastern Bering Sea shelf, in Stratified Flows, edited by T. Carstens and T. McClimans, pp. 917-933, TAPIR, Norway, 1980.

Defant, A., Physical Oceanography, vol. 1, Pergamon, New York, 1961.

Favorite, F., and D.M. Fisk, Drift bottle experiments in the North Pacific Ocean and Bering Sea--1957-60, 1962, 1966, and 1970, Data Rep. 67, NOAA, NMFS, Seattle, Wash., 1971.

Favorite, F., A.J. Dodimead, and K. Nasu, Oceanography of the subarctic Pacific region, 1960-1971, Bull. 33, Int. N. Pacific Fish. Comm., Vancouver, Canada, 1976.

Fearnhead, P.G., On the formation of fronts by tidal mixing around British Isles, Deep Sea Res., 22, 311-322, 1975.

Garrett, C., and B. Petrie, Dynamical aspects of Flow through the Strait of Belle Isle, J. Phys. Oceanogr., 11, 376-393, 1981.

Garrett, C., and B. Toulany, Variability of flow through the Strait of Belle Isle, J. Mar. Res., 39, 163-189, 1981.

Gebhart, B., and J.C. Mollendorf, A new density relation for pure and saline water, Deep Sea Res., 24, 831-848, 1977.

Hattori, A., and J.J. Goering, Nutrient distributions and dynamics in the eastern Bering Sea, in The Eastern Bering Sea Shelf: Oceanography and Resources, vol. II, edited by D.W. Hood and J.A. Calder, pp. 975-992, U.S. Dept of Commerce/ NOAA/OMPA, Washington, D.C., 1981.

Hayes, S.P., Variability of current and bottom pressure across the continental shelf in the northeast Gulf of Alaska, J. Phys. Oceanogr., 9, 88-103, 1979.

Hughes, F.W., L.K. Coachman, and K. Aagaard, Circulation, transport and water exchange in the western Bering Sea, in Oceanography of the Bering Sea, edited by D.W. Hood and E.J. Kelley, pp. 59-98, Institute of Marine Science, University of Alaska, Fairbanks, Alaska, 1974.

Iverson, R.L., L.K. Coachman, R.T. Cooney, T.S. English, J.J. Goering, G.L. Hunt, Jr., M.C. Macauley, C.P. McRoy, W.S. Reeburgh, and T.H. Whitledge, Ecological significance of fronts in the southeastern Bering Sea, in Coastal Ecological, edited by R.J. Livingston, pp. 437-468, Plenum, New York, 1979.

Kinder, T.J., and L.K. Coachman, The front overlaying the continental slope in the eastern Bering Sea, J. Geophys. Res., 83, 4551-4559, 1978.

Kinder, T.J., and J.D. Schumacher, Circulation over the continental shelf of the southeastern Bering Sea, in The Eastern Bering Sea Shelf: Oceanography and Resources, vol. 1, edited by D.W. Hood and J.A. Calder, pp. 53-78, U.S. Department of Commerce/NOAA/OMPA, Washington, D.C., 1981a.

Kinder, T.J., and J.D. Schumacher, Hydrography over the continental shelf of the southeastern Bering Sea, in The Eastern Bering Sea Shelf: Oceanograph and Resources, vol. I, edited by D.W. Hood and J.D. Calder, pp. 31-52, U.S. Department of Commerce/NOAA/OMPA, Washington, D.C., 1981b.

Kinder, T.H., J.D. Schumacher, R.B. Tripp, and J.C. Haslett, The evolution of the hydrographic structure over the continental shelf near Bristol Bay, Alaska, during summer 1976, Tech. Rep. Ref: M78-16, Univ. of Washington, Seattle, 1978.

Lagerloef, G. R.D. Muench, and J.D. Schumacher, Low frequency variations in currents near the shelf break: Northeast Gulf of Alaska, J. Phys. Oceaonogr., 11, 627-638, 1981.

Livingstone, D., and T.C. Royer, Observed surface winds at Middleton Island, Gulf of Alaska and their influence on the ocean circulation, J. Phys. Oceanogr., 10, 753-764, 1980.

Muench, R.D., and J.D. Schumacher, Physical oceanographic and meteorological conditions on the northwest Gulf of Alaska, NOAA, Tech. Memo. ERL-PMEL-22, Boulder, Colo., 1980.

Overland, J.E., Marine climatology of the Bering Sea, in The Eastern Bering Sea Sea Shelf: Oceanography and Resources, vol. I, edited by D.W. Hood and J.D. Calder, pp. 15-22, U.S. Dept. of Commerce/NOAA/OMPA, Washington, D.C., 1981b.

Overland, J.E., and C.H. Pease, Cycline climatology of the Bering Sea and its relation to sea ice extent, Mo. Wea. Rev., 108, 2015-2023, 1980.

Pearson, C.A., H. Mofjeld, and R.B. Tripp, Tides of the eastern Bering Sea shelf, in The Eastern Bering Sea Shelf: Oceanography and Resources, vol. 1, edited by D.W. Hood and J.A. Calder, pp. 53-85, U.S. Dept of Commerce/NOAA/OMPA, Washington, D.C., 1981b.

Pearson, C.A., J.D. Schumacher, and R.D. Muench, Effects of wave induced mooring noise on tidal and low frequency current observations, Deep Sea Res., 28A(10), 1223-1229, 1981.

Pease, C.H., S.A. Schoenberg, and J.E. Overland, A climatology of the Bering Sea and its relation to sea ice extent, NOAA Tech. Report, ERL 419-PMEL 36, 29 pp., 1982.

Quadfasel, D., and F. Schott, Comparison of different methods of current measurements, Deut. Hydrogr. Zeit., 32, 27-28, 1979.

Reed, R.K., Nontidal flow in the Aleutian Island passes, Deep Sea Res., 18, 379-380, 1971.

Reed, R.K., and J.D. Schumacher, Sea level variations in relation to coastal flow around the Gulf of Alaska, J. Geophys. Res., 86, 6543-6546, 1981.

Reed, R.K., J.D. Schumacher, and C. Wright, On coastal flow in the northeast Gulf of Alaska near Yakutat, Atmos. Ocean., 19, 47-53, 1981.

Royer, T.C., Baroclinic transport in the Gulf of Alaska, II, A fresh water driven coastal current, J. Mar. Res., 39, 251-266, 1981.

Royer, T.C., D.V. Hansen, and D.J. Pashinski, Coastal flow in the northern Gulf of Alaska as observed by dynamic topography and satellite-tracked drogued drift buoys, J. Phys. Oceanogr., 9, 785-801, 1979.

Schumacher, J.D., T.H. Kinder, D.J. Pashinski, and R.L. Charnell, A structural front over the continental shelf of the eastern Bering Sea, J. Phys. Oceanogr., 9(1), 79-87, 1979.

Schumacher, J.D., and R.K. Reed, Coastal flow in the northwest Gulf of Alaska: The Kenai Current, J. Geophys. Res., 85, 6680-6688, 1980.

Schumacher, J.D., and C.A. Pearson, Bristol Bay Oceanographic processes, 5th Annual Report, RU549, U.S. Dept. of Commerce/NOAA/Alaska Outer Continental Shelf Environmental Assessment Program, Fairbanks, Alaska, 1980.

Schumacher, J.D., and C.A. Pearson, 6th Annual Report, RU549, U.S. Dept. of Commerce/NOAA/Alaska Outer Continental Shelf Environmental Assessment Program, Fairbanks, Alaska, 1980.

Schumacher, J.D., and T.H. Kinder, Dynamical characteristics of three low frequency current regimes over the Bering Sea shelf, submitted to J. Phys. Oceanogr., 1982.

Schumacher, J.D., C.A. Pearson, and J.E. Overland, On exchange of water between the Gulf of Alaska and the Bering Sea through Unimak Pass, J. Phys. Oceanogr., 87, 5785-5795, 1982.

Seifert, R., and D. Kane, Effects of seasonability and variability of streamflow on nearshore coastal areas, Final Rep. RU-111, (edited by R.F. Carlson), U.S. Dept. of Commerce/NOAA/Alaska Outer Continental Shelf Environmental Assessment Program, Fairbanks, Alaska, 1977.

Takenouti, A.Y., and K. Ohtani, Currents and water masses in the Bering Sea: A review of Japanese work, in Oceanography of the Bering Sea, edited by D.W. Hood and E. Kelley, pp. 39-75, Occ Pub. 2, Institute of Marine Science, University of Alaska, Fairbanks, 1974.

Thompson, W.F., and R.V. VanCleve, Life history of the Pacific Halibut: (2) Distribution and early life history, Rep. Inter. Fish Comm., 9, 1936.

Webster, B.D., Ice edge probabilities for the Eastern Bering Sea, Tech. Memo., NWS, AR-26, NOAA, Anchorage, Alaska, 1979.

Winant, C.D., Coastal circulation and wind-induced currents, Ann. Rev. Fluid Mech., 12, 271-302, 1980.

Wright, C., Observations in the Alaskan Stream during 1980, Tech. Memo. ERL PMEL-23, NOAA, Seattle, Wash., 1981.

APPENDIX A

FINAL DATA INVENTORY

James D. Schumacher and Thomas H. Kinder

Final Report, RU 549,
Transport Processes in the North Aleutian Shelf

James D. Schumacher
and
Thomas H. Kinder

Appendix A: Final Data Inventory

Data acquisition for RU 549 (North Aleutian Shelf Transport Processes, NAST) began in March 1980 with the deployment of three moorings in the vicinity of Unimak Pass. This work was conducted under the direction of R. B. Tripp, University of Washington, from the RV *Thompson.* The remaining field work for the NAST experiment was accomplished during three cruises in 1980-81. These cruises are listed on the Boulder computer system (R_2D_2) by the following cruise identifiers: RP4SU80AL4, Aug.-Sept. 1980, ship *Surveyor*, Chief Scientist: Curl; RP4SU81, Jan.-Feb. 1981, ship *Surveyor*, Chief Scientist: Schumacher; and RP4DI81A2, May-June 1981, ship *Discoverer*, Chief Scientist: Pearson. Operations during these cruises included 514 CTD casts, and deployment and recovery of 15 moorings and one shore-based meteorological station maintained throughout the current observation period.

Since the completion of field operations for RU 549, two supplemental cruises were conducted in North Aleutian Shelf waters: RP4DI81AL6, Aug.-Sept. 1981, ship *Discoverer*, Chief Scientist: Reed; RP4OC81AL3, Sept.-Oct. 1981, ship *Oceanographer*, Chief Scientist: Schumacher. A total of 61 CTD casts were conducted during these cruises. The data have been processed and loaded on R_2D_2.

I. <u>Hydrographic Data</u>: Temperature and salinity data were collected during the NAST cruises using Plessey Model 9040 CTD Systems:

NAST 1, Aug 15-Sept 5 1980, 199 casts

NAST 2, Jan 30-Feb 17 1981, 153 casts

NAST 3, May 13-May 30 1981, 189 casts

The sampling interval was five times per second for simultaneous measurements of conductivity, temperature and depth. Data were recorded during the down cast using a lowering rate of 30 meters per minute. Nansen bottle samples were taken at approximately half of the stations to provide temperature and salinity calibration. The calibration corrections used for each cruise are:

NAST 1, temp: -0.01°C	NAST 2, temp: -0.01°C	NAST 3, temp: +0.03°C
Salin: -0.04‰	salin: -0.05‰	salin: +0.09‰

Data from monotonically increasing depth were despiked to eliminate excessive values and were averaged over one-meter intervals to produce temperature and salinity values from which density and geopotential anomaly were computed.

All of the CTD data have been processed and are available for use on R_2D_2.

II. Time Series Observations: Time series observations were made using the following equipment:

B -	Neil Brown acoustic current meters
RCM -	Aanderaa RCM-4 current meters
RCM/T -	Aanderaa current meters with transmissometer
TG -	Aanderaa TG2 and TG3A bottom pressure gauges
ST -	Sediment Traps
TC -	Applied Microsystem temperature-conductivity sensors
DL -	Digital data loggers
MET -	Meteorological sensors (wind speed, direction, gust, and atmospheric temperature)

Taut wire moorings were used with an anchor and acoustic release at the bottom and a 450 kg buoyancy subsurface float about 2 meters above the upper current meter. Pressure gauges were located in a cage which was welded to the anchor. Wind sensors were located on a tower about 7 m above the ground. A compilation of observation period, position and instruments on a particular platform is given in Table A-1.

Current and pressure data were evaluated for quality, including time base accuracy and the presence of zero speeds. Tidal constituents were determined from edited sample interval time series. This is the final stage of our quality control procedures, i.e., the amplitude and phase of the dominant constituents are checked for relative and absolute consistency. The one-hour-interval time series available for use on R_2D_2 are produced from the edited data using a Lonczos filter. These series, called 2.9-hr data, are filtered such that over 90% of the amplitude is passed at periods greater than 5 hr, 50% at 2.86 hr, and less than 0.5% at 2 hr.

Table A-2 is a list by master reference numbers of time series observations that are available on R_2D_2.

Table A-1. - Time-series observations.

Mooring	Deployed	Recovered	Lat	Long	Depth	Instruments
UP-1	22 Mar 1980	17 Aug 1980	54°33.7'N	165°23.9'W	84m	2 RCM,TG
UP-2	22 Mar 1980	16 Aug 1980	54°18.1'N	164°45.9'W	80m	2 RCM,TG
UP-3	21 Mar 1980	16 Aug 1980	54°09.6'N	164°00.4'W	69.5m	2 RCM,TG
TP-1A	19 Aug 1980	6 Feb 1981	56°00.7'N	161°06.8'W	-7m	MET, DL
TP-2A	19 Aug 1980	30 Jan 1981	56°07.1'N	161°17.6'W	32m	RCM/T,N,TG
TP-3A	18 Aug 1980	2 Sep 1980	56°24.1'N	161°39.6'W	65.4m	MET, 7N
TP-4A	19 Aug 1980	31 Jan 1981	56°31.2'N	160°09.3'W	68.5m	RCM/T,N,TG
TP-5A	22 Aug 1980	29 Jan 1981	56°31.2'N	160°18.1'W	31m	RCM/T,N,TG
TP-6A	22 Aug 1980	30 Jan 1981	56°46.5'N	160°18.1'W	59m	RCM,RCM/T, N,TG
TP-1B	7 Feb 1981	29 May 1981	56°00.7'N	161°06.8'W	-7	MET,DL
BBL	14 May 1981	30 May 1981	56°18.8'N	161°33.2'W	64m	3 RCM
TC	14 May 1981	31 May 1981	56°25.8'N	161°42.8'W	74m	12TC,DL
TP-2B	30 Jan 1981	29 May 1981	56°04.6'N	161°18.2'W	35m	N,RCM/T, TG,ST
TB-3B	14 May 1981	30 May 1981	56°19.1'W	161°32.5'W	65m	N,RCM/T TG,ST
TP-7	31 Jan 1981	29 May 1981	56°02.0'N	161°13.1'W	25m	N,RCM/T, TG,ST
TP-8	2 Feb 1981	30 May 1981	55°51.8N	162°02.4'W	31m	N,RCM/T, TG,ST
TP-9	1 Feb 1981	30 May 1981	56°29.7'N	161°42.3'W	89m	N,RCM/T, TG,ST

Table A-2. - Time series available on R2D2.

MRef	Mooring	Meter	Depth	Start	End	Comments
42	UP-1	1811	64	800821400	802292100	
43	UP-2	1827	59	800821000	802291700	
44	UP-3	1815	47	800820400	802291300	
46	TP3A	N99	5	802320500	802461200	
47	"	N98	10	802320500	802461200	
48	"	N90	15	802320500	802461200	
49	"	N89	19	802320500	802461200	
50	"	N100	29	802320500	802461200	
51	"	N87	39	802320500	802461200	
52	"	N88	50	802320500	802461200	
75	UP-3	TG121	67	800820400	802291300	
76	UP-2	TG87	79	800821000	802291700	
78	TP-6	3293	20	802340800	810291800	
79	TP-5	2505	20	802341100	810291600	Transmissometer failed
80	TP-2A	2502	20	802321200	810291400	Pressure channel = light attenuation
81	TP-6	2500	55	802340800	810291900	Pressure channel = light attenuation
82	TP-2A	N95	19	802321100	810301400	
83	TP-4	N96	62	802320700	810311800	
84	TP-5	N94	19	802341100	810291700	
85	TP-6	N97	19	802340800	810291900	
88	TP-4	2501	63	802320800	803150500	Pressure channel = light attenuation
89	TP-4	TG209	66	802320700	810211000	
90	TP-6	TG120	57	802340800	810292000	

Table A-2 (continued).

MRef	Mooring	Meter	Depth	Start	End	Comments
97	TP-1A	DG322	-7	802330200	810372200	
98	UP-1	TG85	83	800821400	802292100	
99	TP-2B	N88	13	810310500	811491400	
100	TP-7A	N89	12	810310800	811491200	
101	TP-9A	N99	14	810320800	811501300	
102	TP-8A	N100	12	810340500	811471000	
106	TP-3B	N98	4	811350000	811501700	
107	TP-3B	N97	14	811350000	811501600	
108	TP-3B	N87	19	811350000	811501700	
109	TP-3B	N95	28	811350000	811501700	
110	TP-3B	N96	49	811350000	811501700	
111	TP-2B	2505	25	810310400	811291500	
112	TP-7	2500	15	810310700	811240900	
114	TP-2A	TG205	30	802321100	810190600	
115	TP-2B	2505	25	810310400	8112910500	
116	TP-9	2502	79	810320800	811410400	
117	TP-8	2501	21	810340500	811491900	
118	TP-7	TG121	24	810310700	811491400	
119	TP-8	TG87	30	810340500	811481200	
120	TP-2B	TG85	34	810310400	811491500	
121	TP-9	TG106	88	810320700	811501400	

All hydrographic and Time series data will be submitted to NODC by September 1982.

Note: In order to insure data acquisition, two current meters were located within 1 m of each other on UP-1, UP-2, and UP-3. When data from the two meters agreed (UP-1 and UP-3), only one data set was sent to Boulder. Redundant current meters proved to be useful in the case of UP-2 since one meter failed.

APPENDIX B

DYNAMICAL CHARACTERISTICS OF THREE LOW-FREQUENCY CURRENT REGIMES OVER THE BERING SEA SHELF

James D. Schumacher and Thomas H. Kinder

Final Report RU 549
Transport Processes in the North Aleutian Shelf

Appendix B: Dynamical Characteristics of Three Low Frequency Current Regimes over the Bering Sea Shelf

James D. Schumacher

and

Thomas H. Kinder

ABSTRACT

Using extensive direct current measurements made during the period 1975-1981, we describe the general circulation over the southeastern Bering Sea and its differentiation by regimes related to depth and forcing mechanisms. Three regimes are present, delineated by water depth (z): the coastal ($z \leq 50$ m), the middle shelf ($50 \leq z \leq 100$), and the outer shelf ($z \geq 100$ m), and these are nearly coincident with previously described hydrographic domains. Statistically significant mean flow (~1 to 10 cm s^{-1}) exists over the outer shelf, generally flowing towards the northwest but with a cross-isobath component. Flow of similar magnitude (1 to 6 cm s^{-1}) occurs in the coastal regime, paralleling the 50-m isobath in a counterclockwise sense around the shelf. Mean flow in the middle shelf is insignificant. Kinetic energy at frequencies >0.5 cpd is greater over the outer shelf than in the other two regimes, suggesting that oceanic forcing is important there but does not affect the remainder of the shelf. Kinetic energy in the band from 0.5 to 0.1 cpd follows a similar pattern, reflecting the greater number of storms over the outer shelf.

Mean flow paralleling the 100- and 50-m isobaths appears to be related to a combination of baroclinic pressure gradients (associated with frontal systems which separate the regimes) and interactions of tidal currents with bottom slopes located beneath the fronts. Although winds are energetic, their highly variable behavior suggests they are not a primary driving force for mean flow.

1. Introduction

Beginning in 1975, closely spaced hydrographic stations and long-term, direct-current measurements were obtained over the southeastern Bering Sea continental shelf for the first time. We use these measurements, which were gathered by us and by others (see Acknowledgements), to delineate three low-frequency current regimes. These current regimes are nearly coincident with three hydrographic domains that are separated by relatively narrow transition zones or fronts. While some aspects of similar current regimes have been reported on other shelves, the great width (~500 km) of the Bering Sea shelf apparently permits a clearer separation of processes that are more compressed on narrower shelves.

Shelf dynamics typically are taken to extend from within about 10 km of the shore (the coastal boundary layer) to the vicinity of the shelf break (Csanady, 1976; Fischer, 1980). The seaward edge of the shelf regime is often taken coincident with a shelfbreak front, which, in turn, may be a manifestation of upwelling (e.g., Mooers, Collins and Smith, 1976), or be closely associated with a strong offshelf boundary current (e.g., Mooers, Garvine, and Martin, 1979), or be independent of both upwelling and strong currents (e.g., Beardsley and Flagg, 1976; Flagg and Beardsley, 1978). Between the coastal boundary layer and the shelfbreak front, the hydrographic and current structures are often taken as uniform except for salinity in the presence of river runoff. Even when nonuniformities have been stressed, these differences have been smooth and usually do not allow a definition of separate zones or regimes. The concept of distinct dynamical regimes, which is clearly illustrated on the Bering shelf, may be useful in refining models and designing experiments on shelves where important dynamical differences are more subtle than in the Bering, but still present.

Following the preliminary results of Kinder and Schumacher (1981a), we *a priori* associate regimes with water depth (z): outer shelf ($z \geq 100$m), middle shelf ($100 > z > 50$ m) and inner shelf ($z \leq 50$m). Flow in the regimes is delineated by characteristics of the vector mean- and low-frequency (≤ 0.5 cpd) currents. The horizontal kinetic energy is examined using rotary spectral estimates in frequency (f) bands corresponding to tidal energy (KE_T), energy at frequencies related to meteorological forcing (KE_M: $0.5 \leq f \leq 0.1$ cpd), kinetic energy of low-frequency events (KE_L: $f \leq 0.5$ cpd), and the total fluctuating kinetic energy (KE'). Although the tides (KE_T) account for an average (using data from all three regimes) of 90% of the fluctuating kinetic energy and low-frequency fluctuations for only 6%, the low-frequency motions are not only of dynamical interest, but also have an influence on plankton and sediment distributions distinct from tidal currents. The observed flow characteristics are discussed in the context of 'first order' dynamics, which appear responsible for the observed sub-tidal flow features, and include baroclinic pressure gradients, tidal residual flow, response to wind, and effects due to oceanic (off-shelf) circulation.

2. Oceanographic Setting

The southeastern Bering shelf is bordered by the Alaska Peninsula, the Alaska mainland, and by a line running southwest from Nunivak Island to the Pribilof Islands, and thence following the shelfbreak southeastward to Unimak Pass (Fig. B-1). The shelf break occurs near the 200-m isobath, and this extremely broad (~500-km) shelf is unusually flat and featureless. Shelf waters receive an annual excess of precipitation over evaporation, and considerable freshwater runoff (notably from the Kuskokwim and Kvichak rivers) so that surface salinities decrease from 33 g/kg at the shelfbreak to less

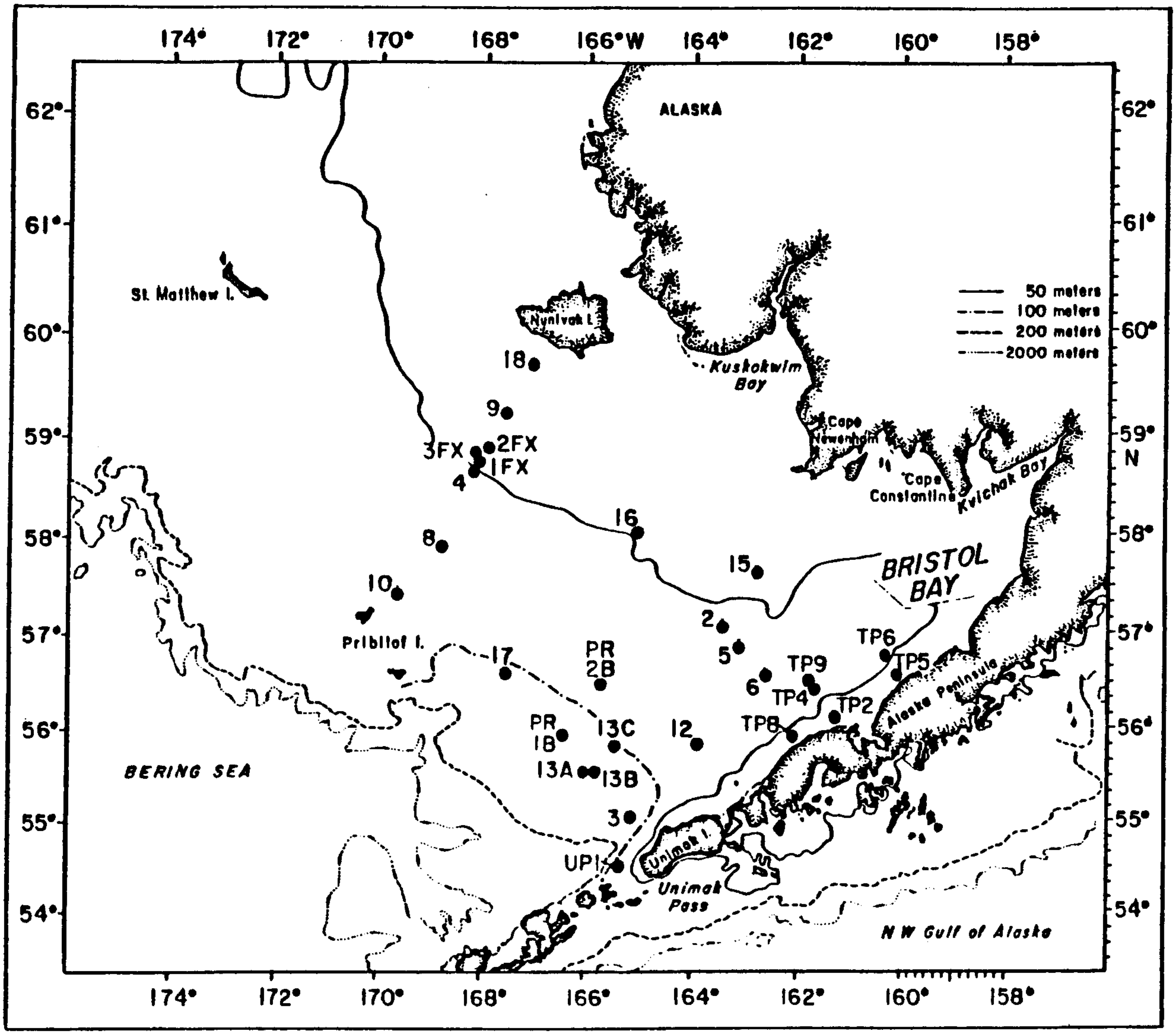

Figure B-1. - Geographic setting of the southeast Bering Sea with locations of current meter moorings. Most moorings had two current meters, one 10 m above the bottom and one 20 m below the surface. Unless otherwise noted, e.g., the three FX moorings southwest of Nunivak Island, all moorings have a BC prefix.

than 31 g/kg nearshore. Ice cover is seasonal, varying from none in summer to greater than 80% coverage of 0.5- to 1.0-m thick ice during late winter in some years (Neibauer, 1980; Pease, 1980). Weather also varies with the season and is dominated by the progression of storms through the Bering (Overland, 1981; Overland and Pease, 1981). Winds during winter are generally stronger than during summer, winter storms (generally four to five per month) are more severe, and the mean winter wind is from the north. During summer, storms are weaker and less frequent, and the mean wind direction is from the south (Overland, 1980).

The shelf and oceanic domains are separated by a shelfbreak front (Kinder and Coachman, 1978), which is about 50 km wide (Fig. B-2). There is a weak westward-flowing boundary current parallel to the slope (the Bering Slope Current; Kinder, Coachman, and Galt, 1975), and eddies probably occur frequently seaward of the shelfbreak (Kinder, Schumacher, and Hansen, 1980). Farther inshore is a front, approximately parallel to the 80/100-m isobaths, which separates the three-layered stratification of the outer shelf domain from the two-layered stratification of the middle shelf domain (Coachman and Charnell, 1979). Inshore of this front, a third front parallels the 50-m isobath and separates the middle shelf from the unstratified waters of the coastal domain (Schumacher et al., 1979). Kinder and Schumacher (1981a) summarized the hydrographic structure across the shelf and Coachman et al. (1980) discussed the system of fronts. The frontal system is most clearly defined during summer, but it can be distinguished throughout the year using appropriate parameters.

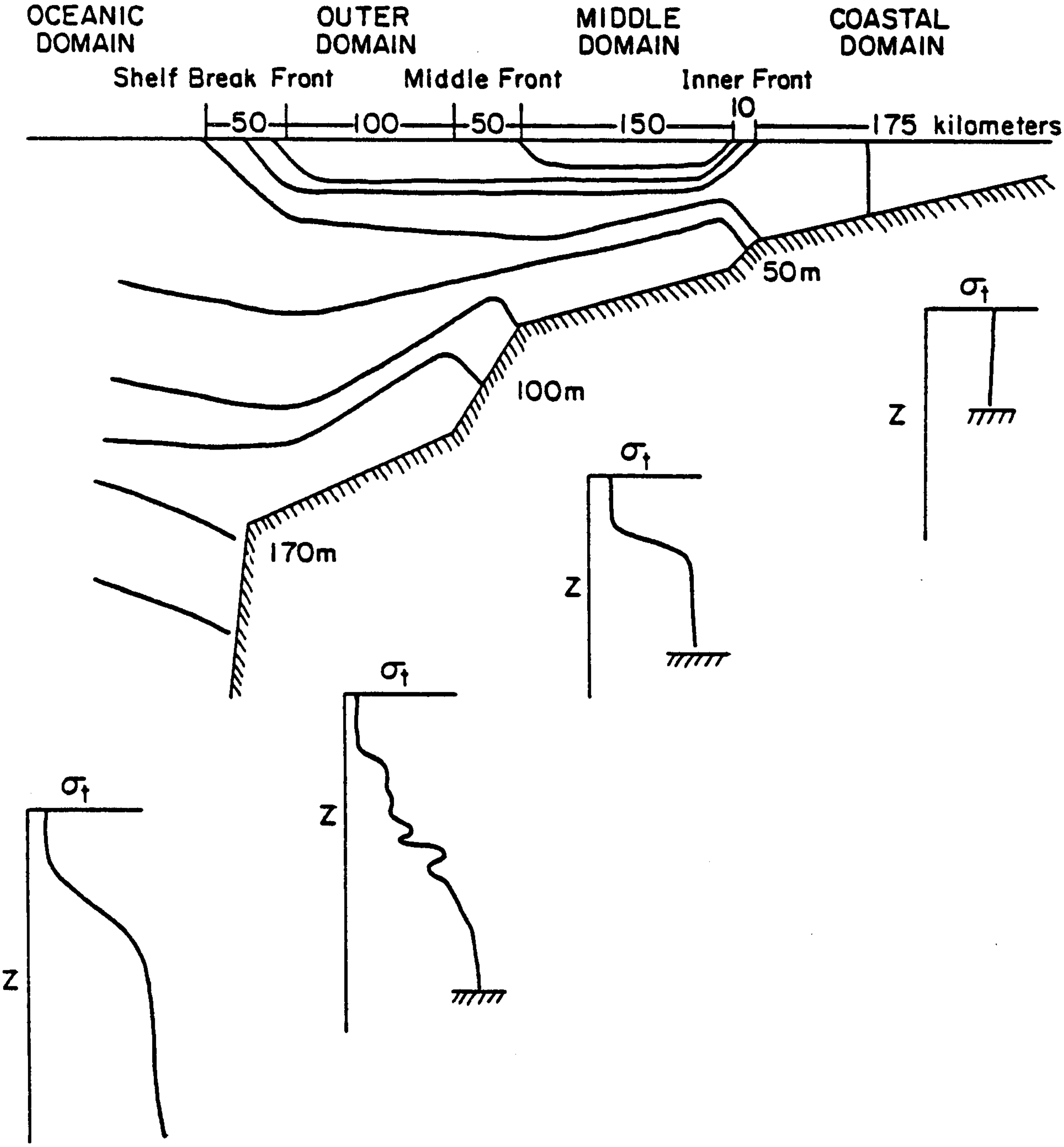

Figure B-2. - A schematic of the cross-shelf density structure illustrating the system of hydrographic domains separated by fronts. Vertical profiles are shown beneath each domain. This picture is representative of periods when there is positive buoyancy input at the surface, i.e., during summer or near melting ice.

3. Methods

Most of the measurements were made using RCM-4 Aanderaa recording current meters on taut-wire moorings. Typical instrument placement was 20 m below the surface and 10 m above the bottom. The subsurface flotation was usually at 18-m depth, and exerted about 1000 lb (1 lb = 4.45N) buoyancy. Sampling intervals varied between 10 and 60 minutes. We estimate that directions were accurate to $\pm 5^\circ$ and speeds to ± 1 cm/sec, exclusive of rotor pumping or mooring motion.

It is known that mechanical current meters such as the RCM-4 may give erroneous speeds because of effects from either mooring motion or high-frequency water motion (see Quadfasel and Schott, 1979, for several references.) Pearson, Schumacher, and Muench (1981) examined the performance of moorings like ours on the Alaskan shelves, and they found that speed differences at tidal frequencies were $\leq 10\%$ when data from windy seasons were compared with data from calm seasons. Extrapolating their results to lower frequencies, we believe that the effects of mooring motion and rotor pumping were minor and that errors were probably limited to a few percent increase of the speeds of the low-frequency current (which these flows were often strongest during windy periods).

At some locations along the Alaska Penninsula, Neil Brown accoustical current (ACM) meters were used to avoid biological fouling problems that had been encountered with RCM-4 current meters. We used ten-minute averages of the original one-minute sample intervals. Accuracy is similar to that of the Aanderaa meters, but rotor pumping does not occur.

Fifty-seven current meter time series records acquired during 1975-1981 were used in this study (Table B-1). Usable record lengths varied from 36 to 246 days, the average record length was about 100 days, and the total current-record years was about 20. A 35-hour low-pass filter was used to separate

Table B-1. - Summary of current data. The letters indicate consecutive observation periods.

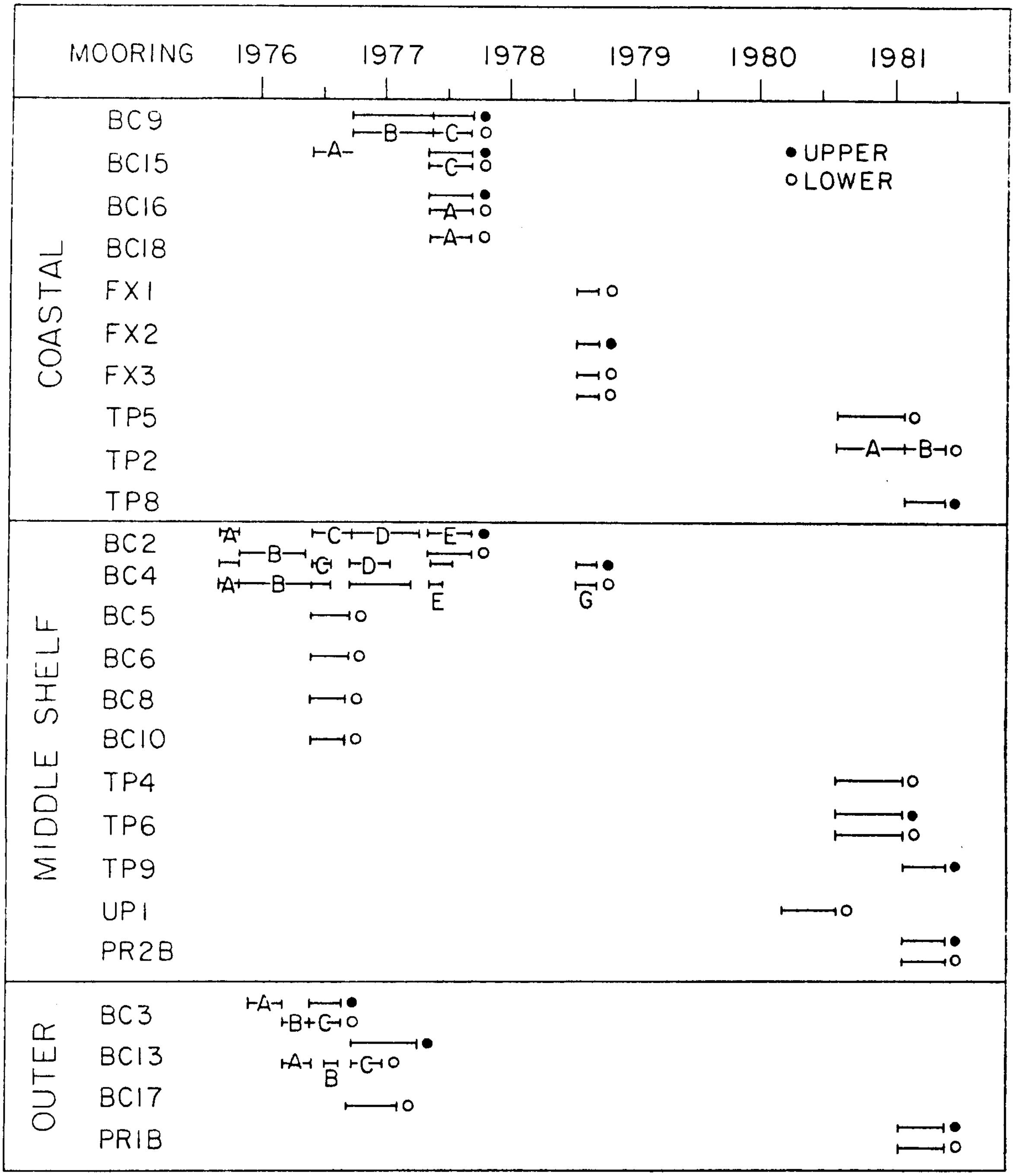

sub-tidal frequencies; the data processing is described in detail in Charnell and Krancus (1976).

4. Mean Flow

The vector mean velocity for each of the 35-hr filtered current records is given in Table B-2. We employed a method similar to Allen and Kundu (1978) to define an independent time scale (τ), estimated as the area under the autocorrelation function for a particular record. The time scale τ was then used to provide a root-mean-square error estimate E, given by

$$E = \pm \sigma/(T/\tau)^{\frac{1}{2}}$$

where T is the record length and σ the standard deviation along the vector mean axis. As a level of confidence in the vector mean flow, we used twice the root-mean-square error estimate which is analogous to a 95% level of significance.

The current regimes were apparent in the distribution of mean velocity (Table B-2, Fig. B-3). Vector mean speeds were highest in the outer shelf regime at 3 cm s^{-1} (>4 cm s^{-1} if BC3C at 20 m is included), and all but one (10/11) record mean was significant. In the middle shelf regime the vector mean speed was < 1 cm s^{-1}. Away from the inner front (BC2, BC5, BC6, BC8, BC10, and PR2B) fewer than half (5/12) of the record means were significant. Close to the front (BC4, TP4, TP6, and TP9), most (13/16) of the record means were significant. In the coastal regime the vector mean speed was ~ 2 cm s^{-1}, and most (15/18) of the record means were significant.

The outer shelf regime had the strongest mean, followed by the coastal and the middle shelf regimes. Mean flow was significant in the outer shelf and coastal regimes, but in the middle shelf regime it was significant only near the front. The distinctions between regimes would probably be heightened if attempts to obtain current meter records near the shelf break had not been

Table B-2. - Characteristics of observed currents.

Mooring:Depth Series (meter depth)	Mean Velocity ± 2 RMS Error (cm s^{-1} : °T)	Kinetic Energy (cm^2s^{-2}) Distribution				
		$\overline{KE}$	KE'	KE_T	KE_L	KE_M
		COASTAL				
BC9:41m						
B(23)	4.6±1.8 : 305	11	424	349	54	41
B(33)	3.0±1.4 : 311	5	189	154	25	19
C(23)	1.0±1.1 : 313	*	341	335	6	4
C(33)	1.0±0.7 : 278	*	234	223	6	5
BC15:49m						
A(20)	2.4±0.6 : 270	3	482	477	5	3
C(20)	2.3±0.6 : 271	3	489	479	6	4
C(34)	1.0±0.6 : 302	*	307	300	4	3
BC16:48m						
(20)	0.9±1.0 : 307	*	410	397	5	5
(37)	0.3±0.4 : 009	*	255	237	3	2
BC18:31m						
(20)	1.1±0.4 : 010	*	341	337	15	8
FX1:48m						
(38)	1.8±0.8 : 292	2	240	228	6	4
FX2:43m						
(20)	2.1±1.2 : 307	2	526	510	9	6
FX3:46m						
(14)	2.3±1.4 : 316	3	547	526	12	9
(36)	1.8±1.2 : 293	2	246	237	8	5
TP5:31m						
(20)N	2.5±1.2 : 194	3	756	684	35	25
TP2:32m						
A(20)N	3.0±1.3 : 211	4	627	576	19	14
B(20)N	1.0±0.7 : 021	*	647	628	10	5
TP8:31m						
(12)N	3.3±1.8 : 055	5	739	706	22	10

Table B-2 (continued).

Mooring:Depth Series (meter depth)	Mean Velocity ± 2 RMS Error (cm s^{-1} : °T)	$\overline{KE}$	KE′	KE_T	KE_L	KE_M
				Kinetic Energy (cm^2s^{-2}) Distribution		
		MIDDLE SHELF				
BC2:66m						
A(20)	0.3±1.6 : 272	*	188	158	17	13
B(55)	1.2±0.8 : 089	*	199	184	10	7
C(20)	0.8±0.6 : 320	*	174	161	4	3
D(21)	0.8±1.0 : 077	*	284	253	19	13
E(20)	0.6±0.6 : 217	*	219	183	3	2
E(55)	0.2±0.4 : 261	*	162	148	2	1
BC4:56m						
A(30)	2.5±2.2 : 272	3	432	390	34	27
A(47)	0.6±2.0 : 298	*	267	228	24	20
B(30)	1.9±0.7 : 286	2	337	298	20	15
C(25)	2.5±1.2 : 314	3	426	413	4	3
C(52)	1.1±0.9 : 295	*	221	215	3	3
D(20)	3.6±1.6 : 304	7	521	391	33	25
D(48)	2.9±1.4 : 305	4	187	148	24	18
E(20)	1.3±1.4 : 301	*	428	417	7	4
E(48)	0.8±1.0 : 284	*	194	190	3	2
G(18)	3.8±1.2 : 295	7	452	431	11	4
G(46)	2.1±1.2 : 302	2	158	150	6	1
BC5:70m						
(50)	0.1±0.6 : 023	*	199	193	3	1
BC6:76m						
(50)	1.0±0.4 : 041	*	224	221	3	2
TP4:69m						
(63)	4.5±1.4 : 013	10	362	330	22	12
TP6:59m						
(20)	1.6±0.8 : 058	1	643	606	16	12
(54)	1.2±0.4 : 108	*	324	311	6	4
BC8:73m						
(54)	0.3±0.7 : 325	*	275	272	2	1
BC10:66m						
(49)	1.0±1.3 : 171	2	232	227	3	1
TP9:89m						
N(14)	6.1±2.4 : 040	17	455	423	21	12
UP1:84m						
(64)	5.8±4.4 : 311	17	786	710	50	12
PR2B:89m						
(30)	1.3±0.9 : 096	*	214	199	7	4
(60)	0.7±0.9 : 128	*	185	168	6	4

Table B-2 (continued).

Mooring:Depth Series (meter depth)	Mean Velocity ± 2 RMS Error ($cm\ s^{-1}$: °T)	Kinetic Energy (cm^2s^{-2}) Distribution $\overline{KE}$	KE'	KE_T	KE_L	KE_M
		OUTER SHELF				
BC3:115m						
A(20)	4.1±3.8 : 015	8	544	384	112	46
B(105)	1.1±1.0 : 335	*	217	192	13	8
C(20)	16.7±6.2 : 011	140	512	352	146	62
C(100)	6.3±1.8 : 358	20	257	212	28	19
BC13: 120m						
A(100)	1.8±1.4 : 343	2	109	97	8	4
B(100)	1.9±1.6 : 329	2	187	171	4	2
C(96)	4.4±2.0 : 317	14	151	120	15	8
C(22)	5.3±2.8 : 333	10	304	205	75	37
BC17:104m						
(96)	3.2±1.6 : 292	5	196	171	17	9
PR1B:124m						
(33)	1.6±2.5 : 300	1	179	131	34	12
(93)	2.4±1.4 : 320	3	172	151	11	5

Where: the RMS error is defined in the text;the letter assigned to a given mooring was a sequential identification; an * indicates that the kinetic energy of the vector mean ($\overline{KE} = \frac{1}{2}\,\overline{u}^2$) was <1.0 cm^2s^{-2}; the remaining KE estimates are derived from ½ (sum of the rotary variance) in the respective frequency bands. An N after the meter depth represents an acoustic current meter.

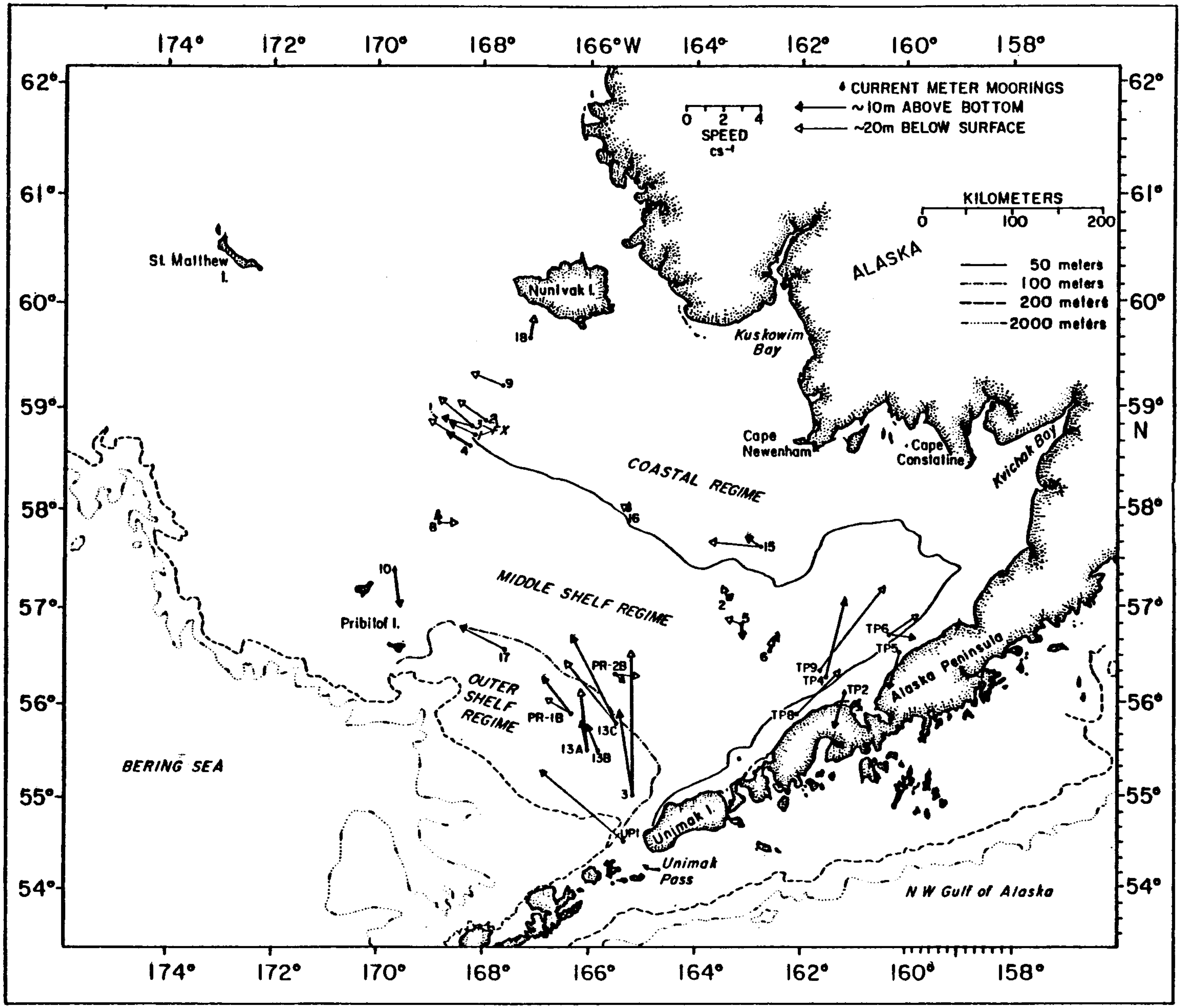

Figure B-3. - Mean flow based on all records at each mooring site. Table B-1 shows record lengths.

hampered by the intensive bottom trawl fishery in that area. The absence of current meter data can be partly remedied by considering at Lagrangian measurements. Data from shallow drogued (~17m) drifters, deployed over the outer shelf and middle domains and tracked by satellite, confirm current regime characteristics inferred from moored data. Six drifters, deployed in summer 1977 over the outer shelf and slope, indicated vector mean speeds over the outer shelf of 4 to 10 cm s^{-1} directed towards the northwest (Coachman and Charnell, 1979; Kinder, Schumacher, and Hansen, 1980). Two of these instruments drifted into middle shelf waters near the Pribilof Islands, and during this time their vector mean speeds were ~1.0 cm s^{-1}.Three drifters launched in June 1976 (in the middle shelf domain between BC2 and BC6) indicated vector mean speeds <1 cm s^{-1} towards the northeast over a 100-day period (Kinder and Schumacher, 1981b).

Vector mean flow over the outer shelf and coastal regimes generally had larger along-isobath than cross-isobath components. For most of the outer shelf regime, isobaths are aligned such that 315°T and 045°T can be taken as along-shelf and cross-shelf axes. Resolving all outer shelf vector mean currents along these axes yields mean along-shelf currents of 4.1 and 2.6 cm s^{-1} at the upper and lower observation levels with cross-shelf components of 3.1 and 0.9 cm s^{-1} at the same levels. For the coastal regime, we used the orientation of the 50-m isobath to define the along- and across-isobath currents. Along the Alaska Peninsula 060°T is the along-shelf direction, 270°T applies in the vicinity of BC15, and 315°T is used between Cape Newenham and Nunivak Island. The cross-isobath component is directed toward the middle shelf regime. Resolving significant vector mean currents from coastal and nearby middle shelf moorings along these axes yielded along-isobath currents of 2.8 and 1.6 cm s^{-1} at upper and lower levels and cross-isobath components of 0.5 and 0.1 cm s^{-1}, respectively.

5. Low-Frequency Currents

To illustrate the time-dependent nature of the low-frequency currents, progressive vector diagrams (PVD's) characteristic of the behavior in each of the regimes are shown in Fig. B-4. Each PVD was constructed from 100 days of current observations collected during winter and summer in each of the three current regimes. (Note that the length scales are different for each record). The outer shelf records had excursions of ~500 km in 100 days, maximum 5-day velocities of 20 to 30 cm s^{-1}, numerous low-frequency events of variable speed and direction, and periods of very weak flow. The examples of middle shelf regime flow show net 100-day excursions of 150km (for BC-2D during winter) but only 4 km at BC-5, with maximum 5-day velocities of 4 to 8 cm s^{-1}. We note that about one-half of the net excursion at BC-2D occurred during one 10-day period of eastward flow. No persistent mean-flow or low-frequency fluctuations appear in either record. The PVD's from the coastal regime indicate currents with the most persistent directions, although 5-day excursions included some reversals and periods of no net flow. Maximum excursions of 25 and 85 km with speeds of 6 and 20 cm s^{-1} were observed for BC 15 and 9, respectively. Thus, subtidal currents in the outer shelf and coastal waters were a resultant of low-frequency pulses superimposed on a significant mean flow component. Pulses in the coastal regime tended to be along the mean flow axis and of short duration (≤10 days), whereas in the outer shelf regime pulses had components both along and orthogonal to the vector mean (i.e., the isobaths) and were persistent over longer periods. In the middle shelf regime a super-position of pulses of variable direction led to very weak (~1 cm s^{-1}), statistically insignificant, vector mean flows.

A further dynamical characterization of the flow field within the three regimes is made by determining the frequency distribution of horizontal

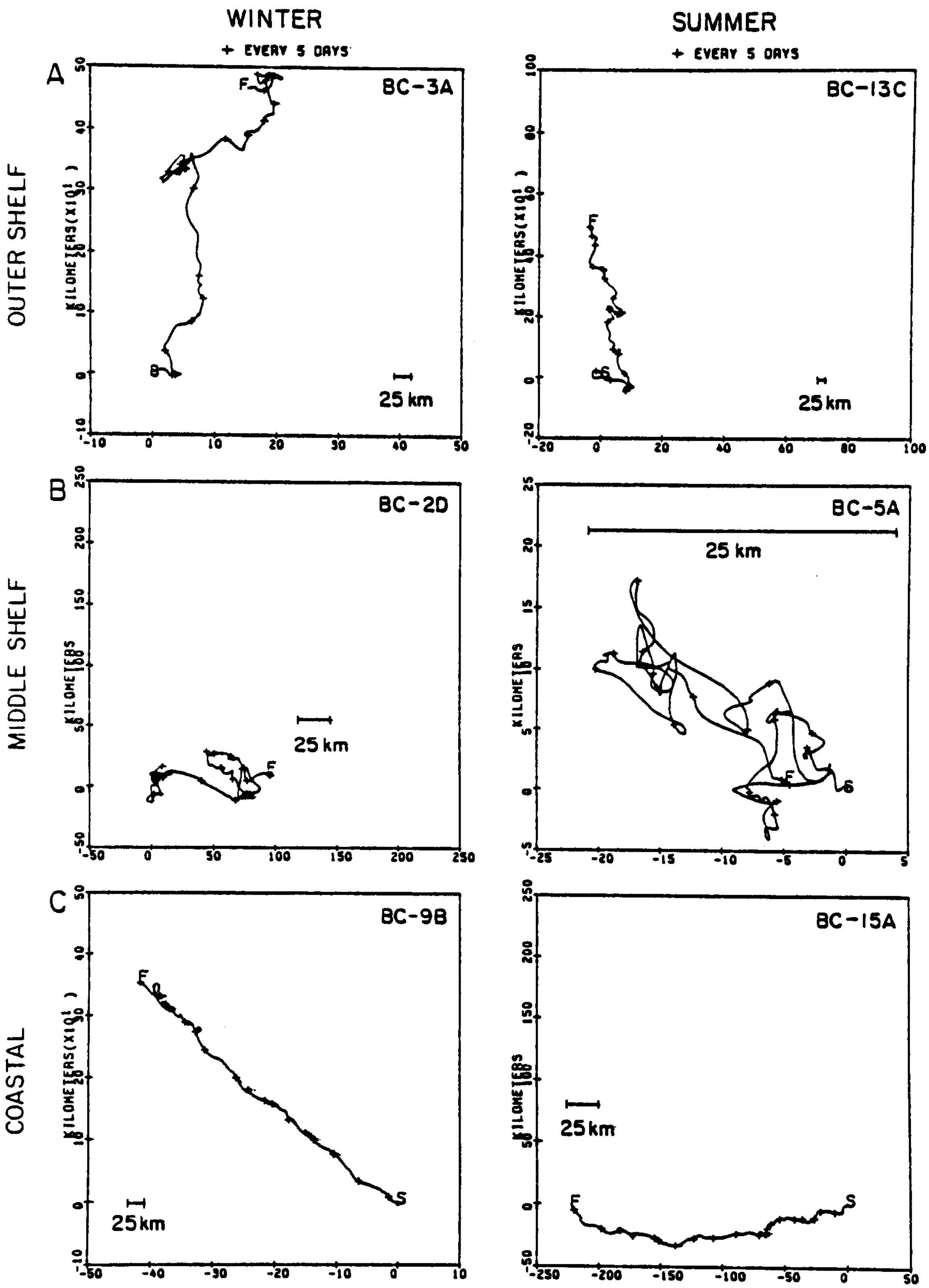

Figure B-4. - Progressive vector diagrams for winter and summer conditions in the outer, middle, and coastal regimes. A 25-km scale parallel to the east-west axis is shown on each PVD since scales are different. (S signifies the start and F the finish of each plot.)

kinetic energy per unit mass (KE; Table B-1). Rotary spectra were calculated from the 2.9 and 35-hr, low-pass-filtered current records. Spectra of the first series were used to determine kinetic energy in semidiurnal and diurnal tidal frequency bands (KE_T) and, by summing over all bands, the total fluctuating kinetic energy (KE'). Spectra of the second current series provided estimates of low-frequency (f<0.5 cpd) kinetic energy (KE_L). We assigned that subset of low-frequency energy between 0.5 and 0.1 cpd to kinetic energy related to meteorological forcing (KE_M). This band encompasses important meteorological forcing in the Bering Sea (see Section 6, below), although other mechanisms also can function at these frequencies.

We present KE_L, KE_M and [KE_L-KE_M] versus water depth for each current record (Fig. B-5). The highest energy levels were observed over the outer shelf, with moderately high levels in the coastal regime. All records except UP1 from the coastal or middle shelf regimes with KE_L>20cm^{2}s^{-2} had a substantial portion of their observation period during winter. A similar trend of energy versus depth of water was found at meteorological frequencies; KE_M levels were generally higher in the outer shelf regime, low in the middle shelf regime, and some records (from winter) in the coastal regime showed moderately high levels. The difference between KE_L and KE_M (Fig. B-5c) indicates that records with non-meterorological, low-frequency energy >10 cm^{2}s^{-2} were either from the outer shelf regime or from moorings located near the coast.

Mean kinetic energy over all records in each regime confirmed that the outer shelf regime is more energetic at subtidal frequencies (Table B-3).

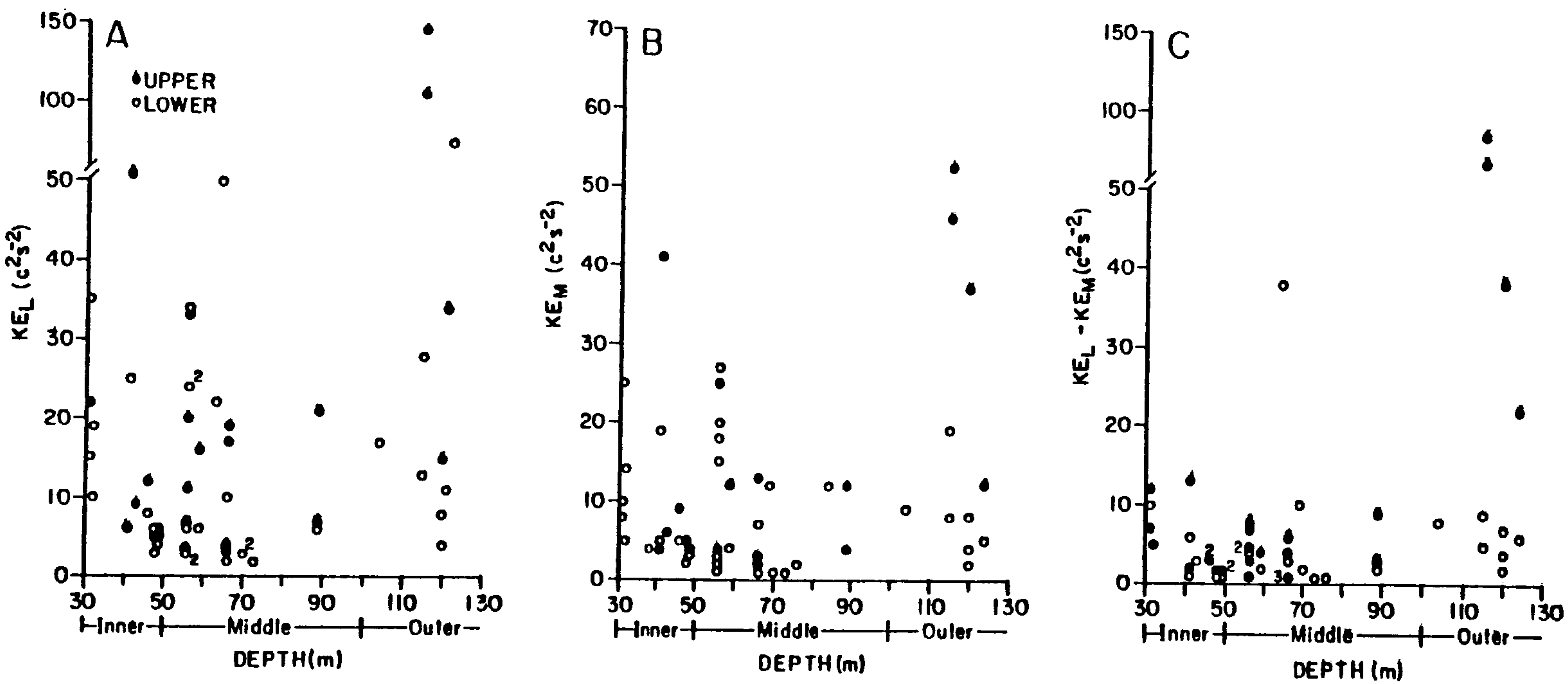

Figure B-5. - Estimates from all records of (A) KE_L (total low frequency energy), (B) KE_M (kinetic energy between 0.5 and 1.0 cpd), and (C) KE_L-KE_M versus mooring depth. Note that the record which indicates energy greater than 20 cm^2 s^{-2} in the middle regime is from UP1, in Unimak Pass. (For A and C the vertical scale changes units after 50 cm^2 s^{-2}: the small numbers represent repeated values.)

Table B-3. - Mean values of kinetic energy.

Regime	Number of Records	KE_T±St.D.	KE_L±St.D.	KE_M±St.D.	KE_L/KE' (% ± St.D.)	KE_M/KE_L (% ± St.D.)
Outer	11	199±91	41±48	19±20	13±8	50±9
Middle	28	289±145	12±10	8±8	4±3	64±17
Coastal	18	410±170	14±13	10±10	4±4	69±13

All units are $cm^2 s^{-2}$. The ratios were calculated by determining each record's ratio and then forming a mean value; all values were rounded to the nearest integer.

We tested the hypothesis that the difference between any pair of the mean percent of KE_L was not equal to zero at the 95% level of confidence using a two-sample "t-test" (Freund, 1971). The results indicate that a statistically significant difference existed between outer shelf and either middle shelf or coastal regime values of percent of KE_L, but that estimates from the latter two regimes were not significantly different.

Examination of KE_L values supports the concept of a distinction only between outer shelf and both of the two shoreward regimes. The lack of a significant difference between energy levels in the middle shelf and coastal regimes suggests that the dominant forcing mechanism for low frequency flow in these regimes is similar. In both regimes, KE_M accounted for approximately two-thirds of KE_L, compared to ~ one-half in the outer shelf regime. (The difference between the mean percent of KE_M over the outer shelf and that applicable to either middle shelf or coastal regime records is statistically non-zero.)

Bristol Bay weather is dominated by storms that migrate through the area; thus winds tend to rotate around the compass (Overland, 1981; Overland and Pease, 1981). Such rotation is reflected in current response as loops with 2- to 5-day time scales in the PVDs or as rotating vectors (Fig. B-6). The exact nature of the current response varies with the translation velocity and intensity of the storm and with pre-storm characteristics of the current and mass field. As an example, we present in Fig. B-6 the current response to a typical March cyclone during a period when there are records from all three regimes. The track of the low-pressure center (Mariner's Weather Log, 1977) indicated that it was located at ~ 52°N, 170°W on 24 March 0000 GMT, and that by 1200 it had crossed the Aleutian chain and was located north of Unimak Island (55.5°N, 164°W). On the following day (0000 GMT, 25 March), the center had crossed the Alaska Peninsula and was located at ~58°N, 155°W. This storm passed close to BC-13 and BC-2 and continued approximately 100 km south of BC-9. The strong winds associated with this storm blew first toward the northwest and then veered to southeastward as the storm passed a given location. North of the center, winds were initially more westward, then shifted to eastward. The change in current direction reflected rotating wind vectors and the storms influence was apparent for about 3 days. We thus interpret many of the 2- to 10-day loops in the PVDs (like those in Fig. B-4) to be storm responses.

6. Seasonal Variations of Meteorological and Oceanographic Characteristics

Before examination of seasonal characteristics in the current records, we establish general climatological conditions and the associated wind conditions in the study area. Overland and Pease (1981) have produced maps of storm counts

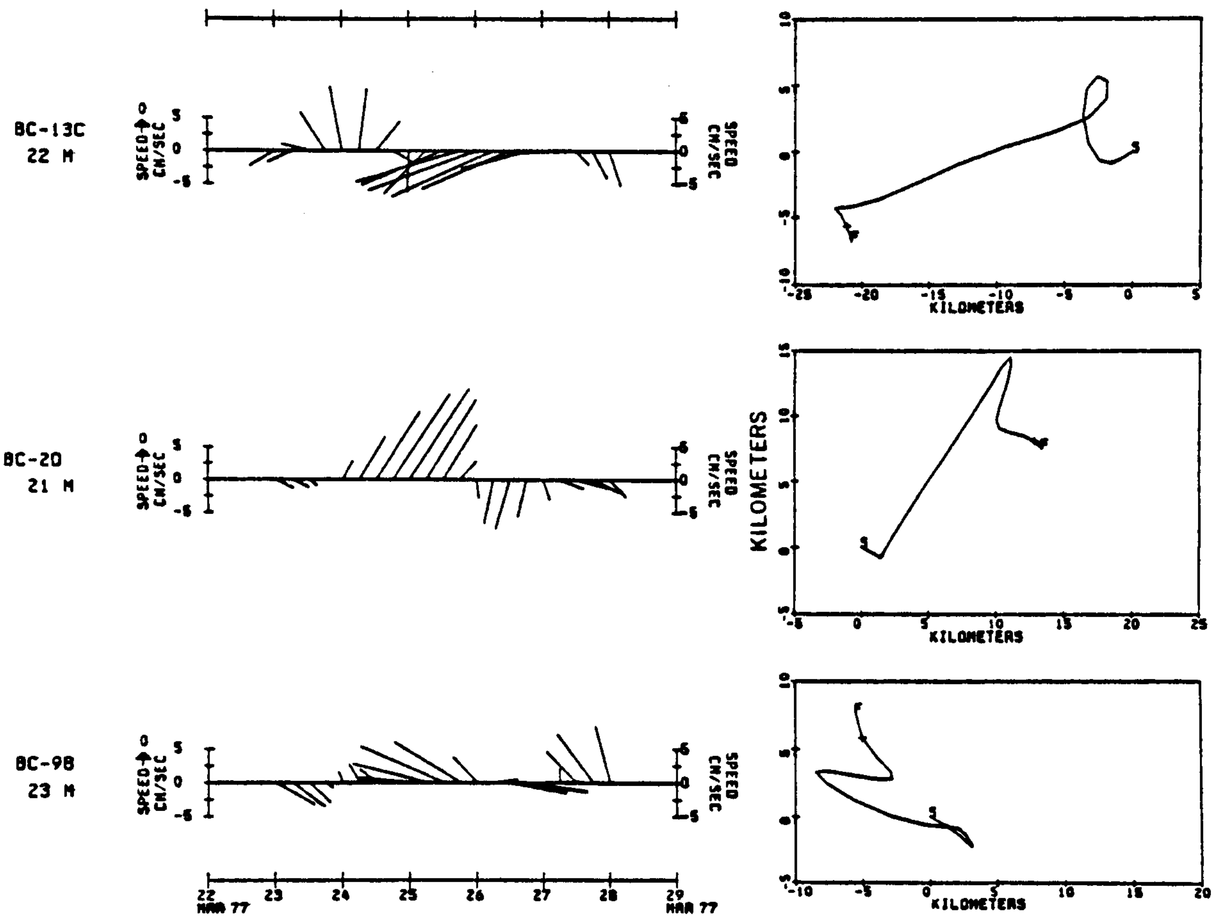

Figure B-6. - An example of current response depicted as 6-hr vectors and PVDs to a storm which transversed the outer, middle, and coastal regimes.

from October through March by 2°- latitude by 4°-longitude squares for 23 years of observations (see their Figure 2). The most marked feature of these maps relevant to the study area is that there are significantly more storms over the outer shelf and adjacent basin than over the middle shelf. For example, during the 23 Novembers there were more than 60 storms over the former outer shelf less than 30 over most of the middle shelf. There is also a tendency for more storms along the Alaska Peninsula (40) than over the middle shelf (30). Using a climatic atlas (Brower et al., 1977), we can extend the results of Overland and Pease to include April through September. Scalar mean winds over the outer shelf regime are greater than those over the middle shelf and coastal regimes for April, May, and September (by 28, 25, and 12 percent), respectively. During June, July and August there is little difference throughout the study area.

Geostrophic winds were computed by Fleet Numerical Weather Central (Bakun, 1973) from a 3°- latitude by 3°- longitude model grid and interpolated to a surface position near mooring BC-2 for the 6-yr. period September 1975 to September 1980. The resulting speeds are plotted in Fig. B-7 where the values are the average of the six monthly means for both speed and variance of speed. Using the six- year mean wind speed ($7.4 \pm 1.7\ ms^{-1}$) and mean variance ($14.1 \pm 4.2\ m^2 s^{-2}$) as guidelines, 'summer' is defined as June through August and 'winter' as October through March, with the remainder being transitional. With these definitions of summer and winter, we present current characteristics from representative current record segments from each of the regimes (Table B-4).

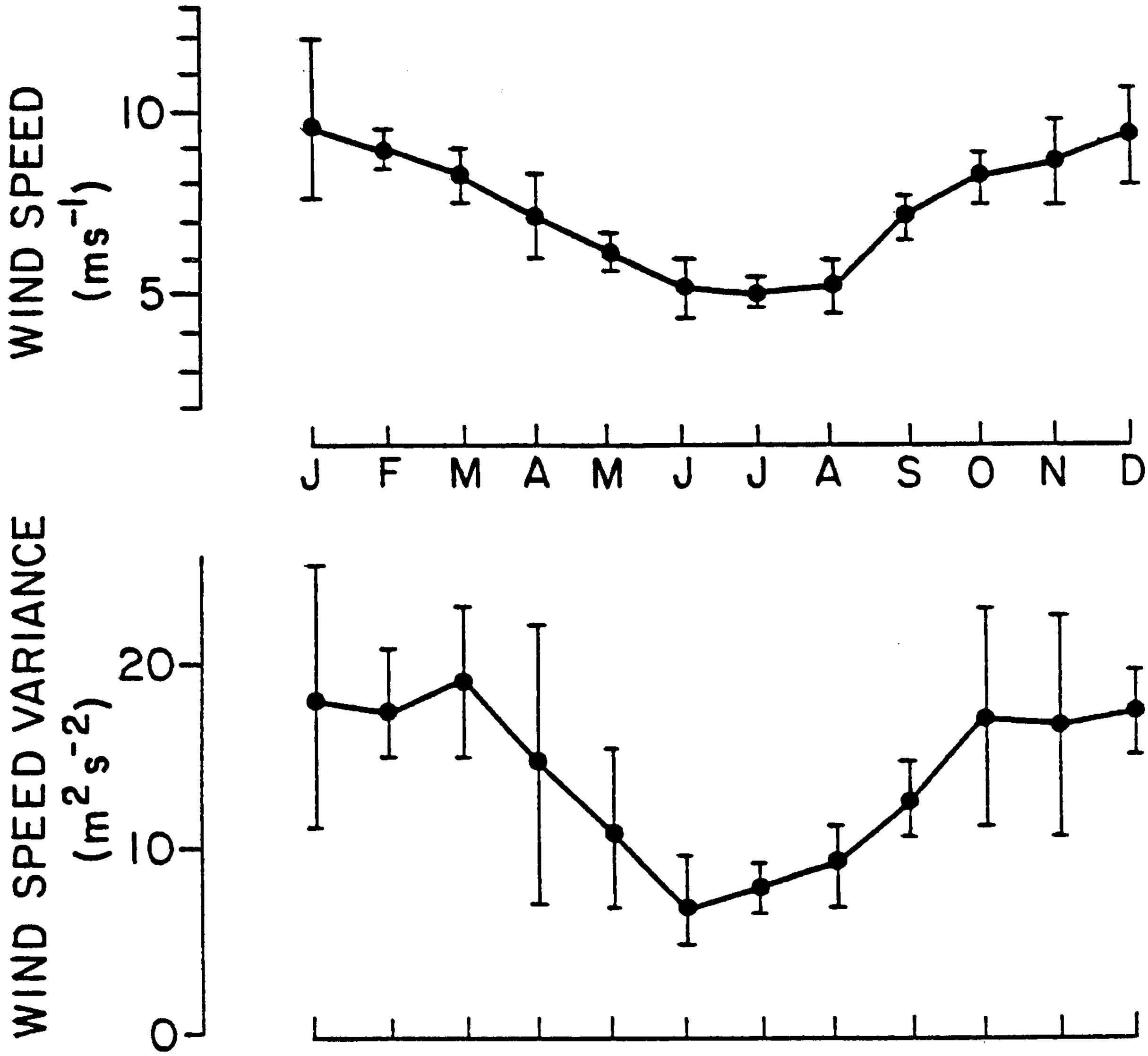

Figure B-7. - Mean and variance of wind speed from monthly averages of surface geostrophic wind between September 1975 and September 1980. The error bars represent the standard deviation for each value.

Table B-4. - Seasonal characteristics of currents.

Mooring (instru.)	Segment Length (days)	Vector Mean (cm s^{-1}: °T)	KE_L (cm^2s^{-2})	KE_M	Mooring	Vector Mean (cm s^{-1}: °T)	KE_L (cm^2s^{-2})	KE_M
		WINTER				SUMMER		
			COASTAL					
BC9B(23)	92	6.2:310	60	45	BC9C(23)	1.0:303	6	4
(33)	92	4.0:317	24	20	(33)	1.0:275	6	4
TP5 (20)	38	4.0:178	37	21	TP5(20)	2.3:171	14	11
			MIDDLE SHELF					
BC2B(50)	92	1.8:081	12	9	BC2E(50)	0.2:232	2	1
D(21)	92	1.1:085	19	12	BC2E(20)	0.4:197	2	1
BC4D(20)	54	3.1:315	33	24	BG4G(18)	2.1:296	11	5
D(48)	40	2.6:314	11	6	E(49)	0.9:284	3	2
B(30)	50	3.9:335	23	16	C(25)	2.5:346	4	3
PR2B(30)	45	2.1:107	14	7	PR2B(30)	0.7:025	4	2
(60)	45	1.1:148	12	5	(60)	0.4:034	3	2
			OUTER SHELF					
BC3A (20)	92	5.6:018	123	47	BC3C (20)	15.6:008	123	48
BC13C(96)	36	3.0:318	14	4	BC13B(100)	1.9:329	5	1
PR1B (33)	60	1.7:353	34	12	PR1B (33)	3.9:262	18	5
(93)	60	1.4:346	12	5	(93)	2.9:316	7	4

Within the coastal regime, winter currents were more energetic in kinetic energy of the vector mean flow, KE_L and KE_M; energies increased above the summer values by about 2 to 38 times, 3 to 10, and 2 to 11 times in the respective bands. The magnitude of vector mean speeds also showed substantial increases, but direction varied by less than 45°. The middle shelf regime also exhibited a substantial increase in kinetic energy from summer to winter with changes in KE_L and KE_M ranging from about 3 to 10 times and 2 to 12 times, respectively; the seasonal change in vector mean speed at BC4 was similar to that observed in coastal records. There were, however, substantial changes in direction at both BC2 and PR2B. Over the outer shelf the seasonal change in kinetic energy was less than observed in the other two regimes, and furthermore, outer shelf vector mean speeds were greater in summer. (We note that for these records, the average KE_T in a given regime varied between seasons by less than 18% with the largest seasonal changes occurring in the coastal and middle shelf regimes. Here, KE_T was generally less in winter than in summer. Because this reduction was accompanied by changes in phase, it has been suggested (Pearson, Mofjeld, and Tripp, 1981) that ice cover alters the propagation characteristics of the tidal waves on the shelf.) These comparisons are consistent with the proposition that meteorological forcing of low-frequency currents is important in all three regimes, but dominant only in the coastal and middle shelf regimes. In the outer shelf regime, the lack of seasonal correlation between current and wind strengths, and the large values of K_L-K_M strongly suggest a non-meterological cause.

7. Causes of the Mean Circulation

The mean circulation of the southeastern Bering Sea shelf is now well defined (Fig. B-3). There is a low-speed current (1-5 cm s^{-1}) in the coastal regime, perhaps more concentrated in the vicinity of the 50-m isobath and inner front, which flows northeast along the Alaska Peninsula, around Bristol Bay, and then northwest past Nunivak Island. Water to maintain this circulation is from the southeast corner of the basin and from the Alaskan shelf south of the peninsula via Unimak Pass (Schumacher, Pearson, and Overland, 1982), reinforced by freshwater that accumulates inshore of the inner front.

There is no significant mean circulation within the middle shelf regime.

In the outer shelf regime there is a low-speed northwesterly drift (1-10 cm s^{-1}) toward the Pribilof Islands, which is perhaps more concentrated near the 100-m isobath and middle front. Water to maintain this circulation flows also from the southeastern corner of the basin with a possible contribution from Unimak Pass.

The tendency for mean flows in both outer and coastal regimes to parallel isobaths suggests that they are at least in part driven by cross-shelf variations in the mass field. Although inferring currents from dynamic calculations in shelf seas is tenuous, on the southeastern Bering Sea shelf approximate agreement with direct measurements is observed. Dynamic topographies for the outer shelf regime (Kinder, 1977; Kinder et al., 1978; Coachman and Charnell, 1979) indicate a northwestward baroclinic flow of ~ 5 cm s^{-1}, in agreement with the measured mean flows. Baroclinic geostrophic currents and measured mean flow along the 50-m isobath from Cape Newenham to Nunivak Island also agree (Schumacher et al., 1979). Further, the freshwater flux into the coastal domain has a long residence time so that during winter when the $\sim$10-km-wide inner front often vanishes, horizontal pressure gradients still exist between the coastal and middle shelf domains (Kinder and Schumacher, 1981b). We used hydrographic data collected through the ice in February 1978 to compute geostrophic speeds of 3 to 4 cm s^{-1} toward the northwest in the vicinity of BC-4. Dynamic topographies previously computed over the middle regime suggested either very weak flow towards the southeast (Kinder, 1977; Kinder et al., 1978) or spatially complex and weak flow (Reed, 1978). In Fig. B-8 we present a composite of dynamic relief, based on data collected on six cruises during summer in 1975, 1976, 1980, and 1981. Dynamic height contours are shown only for synoptic data (over the outer shelf), and the differences in dynamic heights across a particular section are presented for sections not occupied on the same cruise. In general, calculated geostrophic flow in the outer and coastal regimes approximates the observed vector mean currents, and the weak and variable dynamic height differences of the middle shelf agree with the negligible mean currents directly observed in this regime.

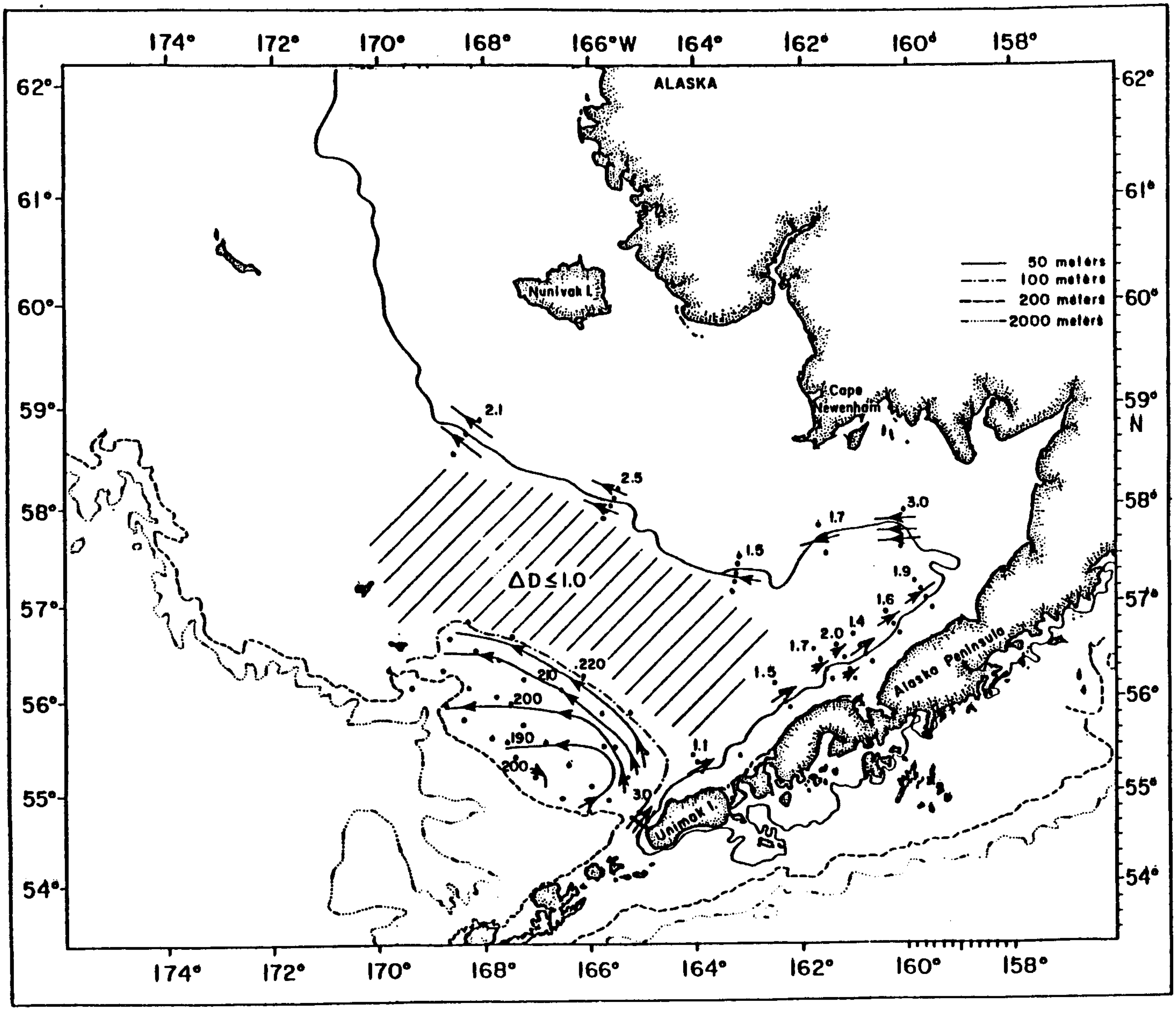

Figure B-8. - A compilation of hydrographic data from six cruises during summer conditions presented as dynamic relief contours (0/80 dbar) for the outer shelf and dynamic height (0/40 dbar) difference along sections normal to the inner front. The dots represent CTD station locations and the contour interval is 1 dyn cm. The shaded portion of the middle shelf regime shows that $\Delta D \leq 1$ dyn cm (0/40 dbar) throughout this area for the six cruises.

There are other mechanisms that might contribute to driving mean flow, including various interactions of tidal currents with the topography. The largest tidal amplitudes are found along the Alaska Peninsula where the nearly rectilinear M_2 tide has an amplitude of $\sim$35 cm s^{-1} (Pearson, Mofjeld, and Tripp, 1981). The M_2 constituent contributes 53, 67 and 75 percent of KE_T in the inner, middle, and outer shelf regimes, respectively, and thus is a possible source for generating residual flow.

Residual current can be generated by the interaction of oscillating velocity with either sea surface height or mean depth. Longuet-Higgins (1969) described in theoretically terms the former mechanism. This mode of interaction generates a Stokes drift whose velocity is scaled by $\overline{\eta u}/h$, where η is the perturbation about mean sea level (h) and u is the tidal velocity. Throughout most of the study area $\bar{\eta} \leq 0.5$m, $\bar{h} \geq 55$m and $\bar{u} \sim 20$ cm s^{-1} so that the depth-averaged Stokes velocity is less than 1.0 cm s^{-1}, but along the Alaska Penninsula and in inner Bristol Bay where tidal heights and speeds are maximum, Stokes velocities could be as large as 5 cm s^{-1}. Thus, this mode of interaction between tides and topography may be important in the shallow coastal regime, but not over the entire shelf.

The interaction of oscillating tidal currents with mean depth and changes in depth was examined by Robinson (1981), and Loder (1980) presented convincing evidence that this mechanism results in significant mean flow around Georges Bank. This mechanism requires changes in mean depth normal to the tidal flow. Over the study region, strong tidal currents flow normal to the isobaths only in the coastal regime away from the Alaska Peninsula (Pearson, Mofjeld, and Tripp, 1981, Figure 8-13). Over most of the shelf (away from the Peninsula) the bottom slope is extremely small (less than 10^{-4}) except in the vicinity of the middle and inner fronts where the slope is about 0.5×10^{-3}. Even where mean velocity is statistically significant, it is small so that following Loder (1980) we assumed weak nonlinearity so that the depth-averaged Eulerian velocity is approximated by his equation (29):

$$\bar{V} \sim - \frac{H_d U_d^2 f \, dH/dx}{2\omega^2 H^2} \; \frac{3H_d}{H} - 2$$

where H_d is the depth on the deep side of the bathymetric feature, U_d is the cross-isobath tidal velocity at frequency ω, H is the depth at the location of interest and f is the local Coriolis parameter. Using observed values, we estimate along-isobath speeds of about 2 to 4 cm s^{-1} in the vicinity of the inner and middle fronts. Robinson (1980) also provided equations for magnitude estimates which have the form $v \sim 0.11 \Delta h/h$ and $v \sim 0.225 \Delta h/h$ for the middle and inner front regions. The maximum change in depth is $\sim$10% and 5% for the two regions and therefore this approach for scaling residual tidal speeds gives magnitudes of about 1 cm s^{-1}. These estimates of along-isobath velocities generated by tidal interaction with bathymetry are consistent with our observations of vector mean flow, so that such interactions may be important in the two regions noted above.

8. Causes of Low-Frequency Fluctuations.

That portion of the KE' associated with periods greater than 10 days (i.e., KE_L-KE_M) was most evident in current records from the outer shelf (cf. Figures 4A and 5C). Csanady (1978) and Beardsley and Winant (1979) suggest that interaction between oceanic circulation seaward of the shelf and shelf bathymetry can produce mean and low frequency shelf currents. Lagerloef, Muench, and Schumacher (1981) show that in the Gulf of Alaska a current component existed at periods greater than 10 days and was stronger than the seasonal signal. Smith and Petrie (1982) suggest that over the Scotian shelf topographic Rossby waves resulted in enhanced kinetic energy at oceanic forcing periods (10 to 90 days) and alongshelf current pulses. Flow over the basin adjacent to the present study area includes mesoscale features that can persist for months (Kinder, Schumacher, and Hansen, 1980). The interaction of such features and possibly Rossby waves (Kinder, Coachman, and Galt, 1975) with shoaling shelf bathymetry could result in the observed kinetic energy at time scales between those of storm and seasonal forcing.

The observed spatial and seasonal wind behavior was manifested in current kinetic energy: winter being more energetic and energy levels being greater over the outer shelf. The spatial change in fluctuating wind energy may drive the convergence between the outer and the middle shelf regimes that is implied from the lack of mean flow in the latter regime. Coachman (1982) reported a convergence of ~ 3 cm s^{-1} from one month's records collected at the same locations as PR 1B and PR 2B and suggests that this may be due either to atmospherically forced 'sloshing' of water on the outer shelf or to fluctuations in the oceanic forcing. Because the climate is dominated by storms, vector mean winds tend to be weak. Direct observations of wind on St. Paul Island indicate that the strongest monthly mean was only ~ 3.4 ms^{-1} toward the southwest (Brower _et_ _al_., 1977). Thus, winds likely contribute little to mean current generation in any of the regimes. Further, since most of the outer and middle shelf waters are farther than a Rossby radius from the coast, they respond by following the rotating winds.

9. Summary

Using rotary spectral and standard statistical techniques, we analyzed an accumulation of ~20 years of current records from twenty-five locations on the vast southeastern Bering Sea shelf. The results permit a general characterization of mean and low-frequency current and kinetic energy regimes that exist in these three zones differentiated by depth and hydrography--coastal, middle shelf, and outer shelf.

Coastal: This regime is bounded by the coastal boundary layer and by the 50-m isobath or inner front. Vector mean flow parallel to the 50-m isobath is statistically significant . Speeds paralleling this feature are generally between 1 and 6 cm s^{-1}, with the higher values during winter. The coastal current was observed from the vicinity of Unimak Pass, along the Alaska Peninsula to the vicinity of Nunivak Island. Although kinetic energy in this regime is dominated by tides (~96%), significant energy at meteorological frequencies can be clearly distinguished as current pulses. Because vector mean winds are weak, we believe wind-driven circulation contributes little to the observed mean flow; instead, a combination of baroclinic geostrophic current and current generated as a result of interaction between tides and shoaling bathymetry are the primary forcing mechanisms.

Middle Shelf: This regime is bounded by the 50-m and 100-m isobaths, and hence by the inner and middle fronts. Vector mean flow within this regime is not significant except near its boundaries, where it parallels isobaths. As is the case with the coastal regime, kinetic energy in this regime is mostly at tidal frequencies. Kinetic energy at meteorological frequencies is only slightly less than in the coastal regime, but the lack of coastal boundaries precludes large changes in sea level and resultant rectification of current pulses,so that currents respond to the wind as rotating vectors.

Outer shelf: This regime lies between the 100-m isobath and the shelf break or the middle and shelf break fronts. Vector mean flow us statistically significant, with along- (toward the northwest) and across- (toward the northeast) isobath speeds generally between 1 to 10 cm s^{-1} and <1 to 5 cm s^{-1}, respectively. In this regime, KE_T accounts for about 60% of the fluctuating kinetic energy, and both KE_M and energy at oceanic forcing frequencies are greater here than in the other regimes. Estimates of both baroclinic geostrophic speeds and those generated by tidal interaction with shoaling bathymetry (under the middle front) are similar in magnitude and direction to the observed flow along isobaths. The cross-shelf flow may be a response to wind forcing at higher frequencies. The kinetic energy at oceanic forcing frequencies, however, is of equal magnitude to that in the meteorological forcing frequency (cf., Table B-3).

Although this analysis provides a picture of the general circulation over the southeastern Bering Sea and its differentiation by regimes related to depth and forcing mechanisms, many questions still remain regarding the dynamics responsible for observed features. In particular, why is the low-frequency energy, which is abundant over the outer shelf, not propagated into the middle shelf? Further, no measurements are available to relate pressure and current fields in the Bering Slope current, whose flow field has been interpreted as planetary waves interacting with the slope (Kinder, Coachman, and Galt, 1975), with those over the outer shelf.

ACKNOWLEDGMENTS

We acknowledge the aid of a large number of persons, not only in the preparation of this paper but in carrying out the field work and data processing which have led to its existence. Most of the current meter data were obtained during a project on which we were co-investigators with L. K. Coachman and the late R. L. Charnell. In particular, we thank Dr. Coachman for both useful discussions and current meter data from the PROBES moorings.

This study was supported in part by the Bureau of Land Management through interagency agreement with the National Oceanic and Atmospheric Administration, under which a multiyear program responding to needs of petroleum development of the Alaskan continental shelf has been managed by the Outer Continental Shelf Environmental Assessment Program (OCSEAP) Office, Juneau, Alaska.

REFERENCES CITED

Allen, J.S. and P.K. Kundu, 1978. On the momentum, vorticity and mass balance on the Oregon Shelf. J. Phys. Oceanogr., 8: 13-27.

Bakun, A., 1973. Coastal upwelling indices, west coast of North America, 1946-71. U.S. Dept. of Commerce, Tech Report NMFS S5RF-671. NOAA Seattle, WA.

Beardsley, R.C. and C.N. Flagg. 1976. The water structure, mean currents, and shelf-water/slope-water front on the New England continental shelf. Mem. Soc. Roy. Sci. Liége. Ser 6. 10:209-225.

Beardsley, R.C. and C.D. Winant, 1979. Mean circulation in the mid-Atlantic bight. J. Phys. Oceanogr., 9: 612-619.

Brower, W.A., H.F. Diaz, A.S. Prechtel, H.W. Searby and J.L. Wise. 1977. Climatic Atlas of the Outer Continental Shelf Waters and Coastal Regions of Alaska, Vol 1, U.S. Dept. of Commerce/NOAA, Arctic Envir. Info. and Data Center Anchorage, AK: 443 pp.

Charnell, R.L. and G.A. Krancus. 1976. A processing system for Aanderaa Current Meter Data. NOAA Tech. Memo. ERL PMEL-6, 50 pp.

Coachman, L.K. and R.L. Charnell. 1979. On lateral water mass interaction - a case study, Bristol Bay, Alaska. J. Phys. Oceanogr. 9(2):278-297.

Coachman, L.K., T.H. Kinder, J.D. Schumacher, and R.B. Tripp. 1980. Frontal systems of the southeastern Bering Sea Shelf. In: Stratified Flows, 2nd Int. Assoc. Hydraulic Res. Symposium, Trondheim, June 1980, T. Carstens and T. McClimans, Eds., TAPIR Publishers, Norway: pp. 917-933.

Coachman, L. K., 1982. Flow convergence over a broad, flat continental shelf. In press, Continental Shelf Res., Vol 1.

Csanady, G.T. 1976. Mean Circulation in Shallow Seas. J. Geophys. Res. 81(30):5389-5399.

Csanady, G.T., 1978. The arrested topographic wave. J. Phys. Oceanogr., 5: 231-244.

Fischer, H.B. 1980. Mixing Processes on the Atlantic Continental Shelf, Cape Cod to Cape Hatteras. Limnol. Oceanogr. 25(1):114-125.

Flagg, C.N. and R.C. Beardsley. 1978. On the stability of the shelf water/slope water front south of New England. J. Geophys. Res. 83(C9):4623-4631.

Freund, J.R., 1971. Mathematical Statistics, Prentice-Hall, Inc. Englewood Cliffs, NJ: 463 pp.

Kinder, T.H., 1977. The hydrographic structure over the continental shelf near Bristol Bay, Alaska, June 1976. Univ. Wash, Dept. Oceanogr. Technical Report (Ref. M77-3): 61 pp.

Kinder, T.H. and L.K. Coachman. 1978. The front overlaying the Continental slope in the eastern Bering Sea. J. Geophys. Res. 83(C9):4551-4559.

Kinder, T.H. and J.D. Schumacher. 1981a. Circulation over the continental shelf of the southeastern Bering Sea. In: The Eastern Bering Sea Shelf, Oceanography and Resources, Vol I, D.W. Hood and J. A. Calder, editors, U.S. Dept. Commerce/NOAA/OMPA: 31-52.

Kinder, T.H. and J.D. Schumacher. 1981b. Hydrographic structure over the continental shelf of the southeastern Bering Sea. In: The Eastern Bering Sea Shelf, Oceanography and Resources. Vol. I, D. W. Hood and J. A. Calder, editors, U.S. Dept. Commerce/NOAA/OMPA: 31-52.

Kinder, T.H., L.K. Coachman and J.A. Galt. 1975. The Bering Slope current system. J. Phys. Oceanogr. 5(2):231-244.

Kinder, T.H., J.D. Schumacher, and D.V. Hansen. 1980. Observation of a baroclinic eddy: An example of mesoscale variability in the Bering Sea. J. Phys. Oceanogr. 10(8):1228-1245.

Kinder, T.H., J.D. Schumacher, R.B. Tripp and J.C. Haslett. 1978. The evolution of the hydrographic structure over the continental shelf near Bristol Bay, Alaska, during summer 1976. Univ. Wash., Dept. Oceanogr. Technical Report (Ref: M78-16): 72 pp.

Lagerloef, S.E., R.D. Muench and J.D. Schumacher, 1981. Very low frequency variations in currents near the northeast Gulf of Alaska shelf break. J. Phys. Oceanogr., 11(5):627-638.

Loder, J.W. 1980. Topographic rectification of tidal currents on the sides of Georges Bank. J. Phys. Oceanogr., 10:1399-1415.

Lonquet-Higgins, M.S. 1969. On the transport of mass by time-varying ocean currents. Deep-Sea Res., 16, 431-447.

Mooers, C.N.K., C.A. Collins, and R.L. Smith. 1976. The dynamic structure of the frontal zone in the coastal upwelling region off Oregon. J. Phys. Oceanogr. 6(1):3-21.

Mooers, C.N.K., R.W. Garvine, and W.W. Martin. 1979. Summertime synoptic variability of the Middle Atlantic shelf water/slope water front. J. Geophys. Res. 84(C8):4837-4854.

Niebauer, J.H. 1980. Sea ice and temperature variability in the eastern Bering Sea and its relation to atmospheric fluctuations. J. Geophys. Res. 85(C12):7507-7515.

Overland, J.E. 1981. Marine climatology of the Bering Sea. In The Eastern Bering Sea Shelf, Oceanography and Resources. Vol I, D.W. Hood and J. A. Calder, editors, U.S. Dept. Commerce/NOAA/OMPA: 15-22.

Overland, J.E. and C.H. Pease, 1981. Cyclone climatology of the Bering Sea and its relation to sea ice extent. Monthly Weather Review, 110(1):5-13.

Pearson, C.A., H. Mofjeld, and R.B. Tripp. 1981. Tides of the eastern Bering Sea shelf. In: The Eastern Bering Sea Shelf, Oceanography and Resources, Vol. 1, D.W. Hood and J.A. Calder, eds. U.S. Dept. Commerce/NOAA/OMPA:53-85.

Pearson, C.A., J.D. Schumacher, and R.D. Muench. 1981. Effects of wave-induced mooring noise on tidal and low-frequency current observations. Deep-Sea Res., 28A(10):1223-1229.

Pease, C.H., 1980. Eastern Bering Sea ice processes. Monthly Weather Review, 108: 2015-2023.

Quadfasel, D. and F. Schott. 1979. Comparison of different methods of current measurement. Dt. hydrogr. Z. 32(1):27-38.

Reed, R.K., 1978. The heat budget of a region in the eastern Bering Sea, summer 1976. J. Geophys Res., 83: 3636-3645.

Robinson, I.S. 1981. Tidal vorticity and residual circulation. Deep-Sea Res., 28A:195-212.

Schumacher, J.D., T.H. Kinder, D.J. Pashinski, and R.L. Charnell. 1979. A structural front over the continental shelf of the eastern Bering Sea. J. Phys. Oceanogr. 9(1):79-87.

Schumacher, J.D., C.A. Pearson and J.E. Overland, 1982. On exchange of water between the Gulf of Alaska and the Bering Sea through Unimak Pass. J. Geophys. Res., 87(C8): 5785-5795.

Semtner, A.J. and Y. Mintz, 1977. Numerical simulation of the Gulf Stream and mid-ocean eddies. J. Phys. Oceanogr., 7: 208-230.

Smith, P.C. and B.D. Petrie, 1982. Low-frequency circulation at the edge of the Scotian shelf. J. Phys. Oceanogr. 12:28-46.

PERFORMANCE AND COMPATIBILITY ANALYSIS OF OIL WEATHERING AND TRANSPORT-RELATED MODELS FOR USE IN THE ENVIRONMENTAL ASSESSMENT PROCESS

by

M. D. Coon and G. S. Knoke

BDM International, Inc.
16300 Christensen Road, Suite 315
Seattle, Washington 98188

Final Report
Outer Continental Shelf Environmental Assessment Program
Research Unit 706

August 1990

ACKNOWLEDGMENTS

This study was funded by the Minerals Management Service, U.S. Department of the Interior, through an Interagency Agreement with the National Oceanic and Atmospheric Administration, U.S. Department of Commerce as part of the Alaska Outer Continental Shelf Environmental Assessment Program. This document has been prepared in accordance with Contract No. 50ABNC-8-00119.

The authors hereby acknowledge the contributions of D. L. Bair, Dr. S. Martin, Dr. M. McPhee, and Dr. R. S. Pritchard during the project and the preparation of this report.

ABSTRACT

OCSEAP has developed and verified, through both field and laboratory work, a suite of models to study the transport, effects, and fate of oil spills for use in the Alaskan OCS. Each model addresses a particular aspect of an oil spill and is currently designed to be executed independently. The objectives of this study are to analyze four specific oil spill models and to recommend modifications allowing their sequential or integrated use in defining the fate of an oil spill. The four models are the Coastal Zone Oil Spill (COZOIL) Model, the Circulation and Oil Spill Trajectory Model (also referred to as the Coastal Sea Model System or the Circulation/Trajectory Model), the Oil Weathering Model, and the Oil/Suspended Particulate Matter (Oil/SPM) Model . While each of these models addresses certain aspects of an oil spill, they individually fall short of the ultimate goal -- to predict the fate of an oil spill. This project consisted of a comprehensive review of the model characteristics and physical assumptions incorporated into existing models and a study of how they can be effectively combined to support environmental assessment using microcomputers. Eight oil spill scenarios were considered. A study of the applicability of the models to each of these scenarios suggested methods for coupling the models and led to an organized approach for model synthesis.

Redundant model features and missing model features were identified. Various methods for combining the computer codes were compared. These were limited to three sets of the following tasks:

Task 1 - Development of Input/Output Software

Task 2 - Combined Oil Spill Model Development

Task 3 - Addition of Missing Features

Task 4 - Acquisition of Databases

A low cost task set is to develop the I/O software with simple architecture, combine the existing oil spill models in the simplest manner, and prepare a database, without addressing the missing features. An intermediate task set is to develop menu-driven I/O software, combine the four oil spill models around the Circulation/Trajectory model, and prepare a database, again without addressing the missing features. The top of the line task set is to develop menu-driven I/O software, develop a new integrated oil spill model, add code to address the missing features, and to prepare a database. It is recognized, however, that the final selection will depend strongly upon the desired applications of the combined code and the funds available.

TABLE OF CONTENTS

TABLE OF CONTENTS (continued)

LIST OF FIGURES

LIST OF TABLES

SECTION I
INTRODUCTION

A. OBJECTIVE

The overall goal of Alaskan Outer Continental Shelf (OCS) pollutant transport studies is to describe the trajectory of an oil spill as well as the amount and persistence of the spilled oil on the sea surface, in the water column, and on the sea bed along the spill trajectories and at landfalls. The objectives of this study are to determine the feasibility of meeting this goal by analyzing four oil spill models and to recommend modifications allowing their sequential or integrated use in defining the fate of an oil spill. The four models are the Coastal Zone Oil Spill (COZOIL) Model, the Circulation and Oil Spill Trajectory Model (also referred to as the Coastal Sea Model System or the Circulation/Trajectory Model), the Oil Weathering Model, and the Oil/Suspended Particulate Matter (Oil/SPM) Model. While each of these models addresses certain aspects of an oil spill (surf interaction, transport in the open ocean, weathering, and interaction with suspended particulate matter), they individually fall short of the ultimate goal -- to predict the fate of an oil spill. This project provides an intermediate step in the process of synthesizing the four models and developing a combined oil fate model.

B. BACKGROUND

For more than a decade the Outer Continental Shelf Environmental Assessment Program (OCSEAP) has performed and sponsored studies to develop knowledge and understanding of transport, effects, and fate of oil spills in the marine environment, including Arctic conditions. The first of these studies, entitled "The Transport and Behavior of Oil Spilled In and Under Sea Ice," began in 1978 with Dr. Max D. Coon and Dr. Robert S. Pritchard as Principal Investigators. This study, documented in Coon and Pritchard (1979), involved the calculation of trajectories of oil spilled on the ice in Prudhoe Bay using buoy data and a computer model.

Computer models for simulating the transport and fate of spilled oil in the marine environment are important tools in environmental assessment. OCSEAP/MMS-sponsored studies have developed and verified, through both field and laboratory work, a suite of models for use in the Alaskan OCS. All of the models were designed and developed individually over a period of years using a variety of scientific approaches, methodologies, and levels of detail. Each model addresses a particular aspect of an oil spill and is currently designed to be executed independently. The ideal case, however, would be to use them in an interactive manner, sequentially or in combination, to simulate the anticipated spill scenario.

The scope of the combined oil spill fate model is illustrated in Figure 1, Oil Spill Fate, which shows a three-dimensional perspective of an offshore and a nearshore oil spill. On the open ocean, an oil spill disperses by a combination of processes: evaporating into the atmosphere, sinking to the ocean floor, and moving to another location. Sea ice, an important feature of the Alaskan OCS, is shown in the vicinity of this spill. The second spill shown in Figure 1 depicts an oil spill near shore, where some of the oil reaches land. Predicting the fate of an oil spill is an important yet difficult task.

C. APPROACH

The BDM technical approach to this project consisted of a comprehensive review of the model characteristics and physical assumptions incorporated into existing models and a study of how they can be effectively combined to support environmental assessment using microcomputers. Eight basic oil spill scenarios were considered. These scenarios are combinations of nearshore/offshore, ice/no ice, and surface/subsurface spills. A study of the applicability of the models to each of these scenarios suggested methods for coupling the models and led to an organized approach for model synthesis.

The computational features that BDM characterized included the source code (e.g., lines of code, programming language); compilation and execution requirements (host hardware and operating system); required inputs and outputs; identification of numerical algorithms; and model documentation. The scientific attributes that BDM studied include physical and chemical assumptions; inputs and outputs; numerical methods of solution; constraints on inputs and outputs; resolution; and boundary conditions.

D. OVERVIEW

For ease of understanding, the report has been organized into six sections. Section I provides an introduction and background to the project, Section II describes the characteristics of each model, Section III compares the models, Section IV discusses model integration, Section V describes recommendations for modifying and linking the models, and Section VI provides conclusions, followed by complete bibliographic references for the works cited in this report.

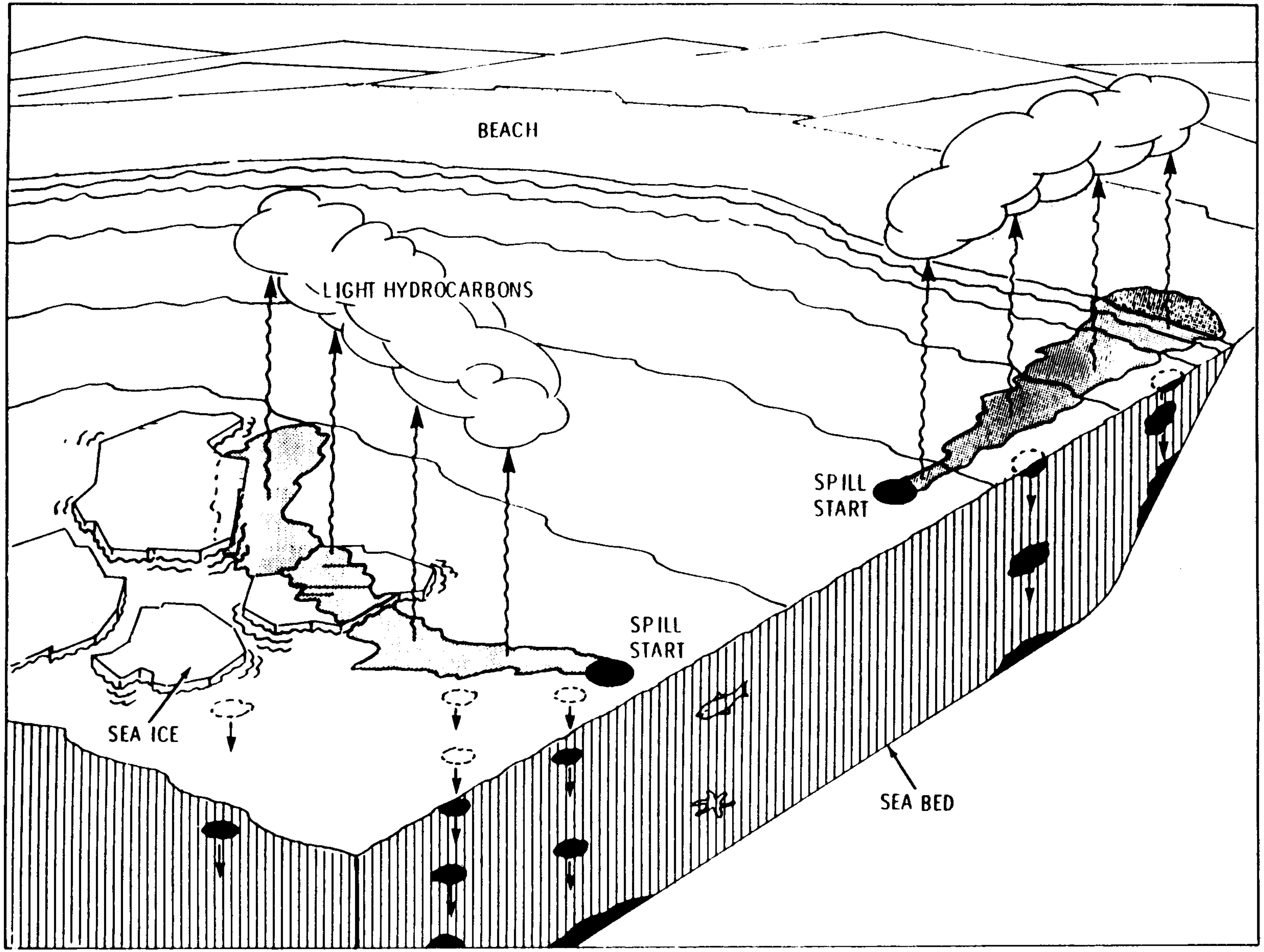

Figure 1. Oil Spill Fate

In Section II, each model is first described in terms of what it does, how it does it, what inputs are required from the user, and what outputs are produced. The physical and chemical attributes of the model are described, including assumptions and limitations of the model, and the physical laws and principles that apply. Next the computational features of the model are described, including the mathematical aspects, the numerical methods used, size of time steps and grid spacing. Section III, Comparison of Models, presents and interprets tables that concisely summarize the important features of each model and compare the most important characteristics of each model. Section IV considers the oil spill scenarios, redundant and missing model features, and viable structures for combining the models. Section V provides a basis for selecting a structure for the combined oil fate model, while Section VI summarizes our conclusions for the program.

SECTION II
CHARACTERIZATION OF MODELS

A. COASTAL ZONE OIL SPILL MODEL

1. Model Description

The COZOIL Model, developed by Coastal Science and Engineering, Inc., was designed to predict the time-varying distribution of oil introduced into a domain separated into three partitions: the nearshore, the surf zone, and the coast. The coast can include gravel and sand beaches, rocks, tidal flats, lagoons, and permafrost bogs. This model was intended to run in close coordination with outputs from an open ocean trajectory model; it is however capable of operating independently as well. A typical simulation run consists of initializing the model domain with a specific grid system, shore type, topography, and physical characteristics and then introduces oil into the system either on the surface (as if a slick were approaching the shoreline) or subsurface (as if a pipeline had failed). The amount of oil in each of the three partitions is then calculated and followed by time stepping through changing environmental conditions, nearshore wave and current conditions, and surface and subsurface oil weathering conditions. The model was written in FORTRAN and is capable of running on a microcomputer. An earlier version (the Smear Model) was documented by Kana et al. (1986); the Coastal Zone Oil Spill Model was documented by Reed (1987).

The COZOIL Model tracks multiple, discrete batches of oil (spillets) in the three partitions. A spillet is a portion of an oil spill having uniform thickness and weathered state. The COZOIL Model is a deterministic model of a shoreline approximately 30 x 300 km using a grid size of about 10 x 10 km, and time steps of 3-6 hours for up to 90 days.

The input parameters define the study area location and physical properties (bathymetry, topography, sediment size, beach slope, and shoreline type), environmental data (wind fields, current fields, air temperature, water temperature, ice cover and movement, water surface elevation, and SPM in the water column), and the oil spill (oil type, mass, diameter, and location).

The output parameters define the spatial distribution of oil droplets and oiled particles. For each coastal segment, the oil mass, thickness, weathered state, and location (surface or buried) are provided. The surface spillets are defined in terms of location, mass, weathered state, thickness, and areal extent. The mass of oiled SPM and oil droplets in the seabed is determined as well as the concentration of oiled SPM, SPM, and oil droplets in the water column.

2. Physical and Chemical Attributes

a. Hydrodynamics

Wind is constant over the study area. The user can either prescribe a deterministic wind for each spillet, or run the model in a stochastic mode in which wind speed, direction, and air temperature for each spillet are drawn from a statistical distribution.

Waves at the offshore boundary of the model domain are either specified or computed from the wind at the option of the user. As the bottom shoals, the waves are transformed by refraction and diffraction. In the surf zone, the waves steepen and break, thus undergoing further modification. Refraction, diffraction, wave height, and phase transformations are calculated according to a published linear wave propagation model (RCPWAVE from the Corps of Engineers Coastal Engineering Research Center (CERC)). Wave runup (the vertical height above still water level to which incident waves will run up a beach) and wave setup (the vertical average wave height above still water arising from wave radiation stress) are calculated from empirical formulas derived from CERC data.

For the offshore region, currents are the sum of a simple sinusoidal alongshore tidal current and a time-dependent, depth-averaged current that depends on the wind. In the surf zone, the wind-driven current is supplanted by an alongshore wave radiation stress current. The latter is taken from a empirical CERC formula. Since the wind-driven current is not applied in the surf zone, onshore wind-driven transport is balanced by an offshore volumetric flux. This can transport oil entrained in the water column away from the surf zone.

b. Oil Spill Models

Thin (sheen) slicks are ignored. Spreading is radial, representing a balance among gravitational, viscous, and inertial forces, except in the surf zone, where wind stress in the onshore direction can counteract the tendency to spread, thus elongating the slick. Wave action is not directly incorporated into the transport models. Mass transfer rates for up to 15 constituents of the oil in a spillet are calculated using standard vapor transfer equations.

The user is given a choice of two algorithms for entrainment (dispersion) of oil into the water column. In both the mass transfer rate varies as the square of the wind speed. In one, it is also proportional to the inverse time exponential, while in the other it varies directly as the mass and inversely as a term involving interfacial tension, dynamic viscosity, and slick thickness. There is no reason given for presenting both algorithms. Entrainment is the same in the offshore and surf zones.

The slick is advected with a velocity that represents the sum of 3% of the wind speed, the tidal and wind-driven currents, and the wave radiation stress current. Oil that is entrained at the surface is distributed randomly vertically under the slick, then advected by the interpolated horizontal current, and diffused randomly as well. The model downplays the importance of entrained transport, and it is not clear from the description how depth-dependent concentrations are accounted for in the overall oil mass balance. Advection in the surf zone is dominated by the wave radiation velocity, which is ignored elsewhere. It is worth noting that alongshore currents from wind transport setup/setdown (downwelling/upwelling) are not considered, nor are changes in beach water level from such effects taken into account.

An oil slick in contact with the shoreline will deposit oil according to the ratio of the spillet radius (in the onshore/offshore direction) to the exposed beach face, if an empirical holding thickness has not been exceeded. This criterion holds for the foreshore, between the near low water level and the beach berm, and backshore, from the berm to the cliff, vegetation, or dune line. Oil deposited on a beach section from different times or different spillets adds its characteristics to the oil already present in a weighted average sense.

Oil from a surface deposit can penetrate into underlying sediments following Darcy's Law, a common approach to calculating groundwater movement. Oil which has penetrated into sediments above the water table can be removed by beach erosion, for which an empirical equation is written. Oil in the beach groundwater system is removed each tidal cycle according to a simple mass flux equation involving the specific yield and porosity of the sediment. This oil is partitioned into water-accommodated and adsorbed phases.

Waves breaking on a contaminated beach tend both to enhance penetration into the groundwater and to resuspend oil particles, washing them back into the surf zone. An empirical mass removal rate equation describes this process, with partitioning between groundwater and surf zone return determined by constant coefficients. Oil on a beach inundated by a rising tide is refloated and mixed with an existing spillet, if one is present.

Oil which has been emulsified into an oil/water mousse and deposited on a beach face may be released from the mousse according to a simple first-order process. The suggested time constant results in an emulsion half life of 12 hours on land.

3. Computational Features

None of the documentation accompanying the COZOIL Model discusses the numerical methods employed in the model. Behavior offshore, outside the surf zone, is modeled using concepts developed by previous investigators who are identified in the references. A modified version of RCPWAVE, developed by the U. S. Army Corps of Engineers, is used to model wave behavior. Inside the surf zone some of the concepts used are said to be lacking "strong empirical evidence for values of the necessary parameters."

B. CIRCULATION AND OIL SPILL TRAJECTORY MODEL

1. Model Description

The Circulation and Oil Spill Trajectory Model, developed by Applied Science Associates, is designed to calculate the hydrodynamics, wind, ice, and oil spill trajectories and fates for Alaskan coastal waters. The Circulation Model generates, or takes from its program libraries, wind, sea ice, and surface wave forces. From that information, the Oil Spill Trajectory Model calculates the oil spill trajectory and predicts its fate, including drifting, spreading, evaporation, dispersion, emulsification, and subsurface transport. Spills of any hydrocarbon release, from crude oil to refined products, can be simulated. Documentation is provided in Spaulding et al. (1988).

The Circulation Model is a three-dimensional spectral hydrodynamics model based on the solution, in spherical coordinates, of the conservation equations for water mass, density, and momentum using the Boussinesq and hydrostatic assumptions. The model generates surface velocity vectors for tidal currents and residual currents at each grid point in the modeled domain for each season. Fleet Numerical Oceanographic Center (FNOC) data sets and other historical data are used to assemble a wind field coincident with the simulation period. Oil spill trajectories are then simulated from the hydrodynamic model results by superposition of wind-induced, tidal, and residual current drift. Wave-generated transport is not directly modeled; spill trajectory and emulsification include only wind-induced factors. Model components were implemented in FORTRAN and developed on a minicomputer.

The hydrodynamics model was used by Spaulding et al. (1987) to predict wind-forced circulation in the Bering and Chukchi Seas. Two model resolutions were used: a coarse grid model (0.25 degrees latitude by 0.6 degrees longitude) and a fine model which had double this resolution. Isaji and Spaulding (1978) applied this model to the calculation of the M_2 and K_1 tidal elevations and currents in the northwestern Gulf of

Alaska. The M_2 and K_1 constituents are generally representative of the semidiurnal and diurnal tides, respectively. Schwiderski's global tidal models (1979, 1981) provided the input boundary conditions. A grid resolution of 0.2 degrees latitude and 0.35 degrees longitude (about 20 x 20 km) produced good results.

The user must set up a grid for the study area, and either provide data on wind, ice, and type of oil spilled, or use data from the program libraries. Final model output is the trajectory, material balance data, and cell-by-cell location of the spilled oil.

2. Physical and Chemical Attributes

a. Hydrodynamics

Forces applied to the ice and upper ocean by the wind provide the primary source of energy for moving oil near the surface. The Circulation Model uses the marine surface winds at 19.5 m above sea level from the U. S. Navy Fleet Numerical Oceanographic Center (FNOC) to estimate this driving force for Alaskan waters. Orographic effects are added based on the literature and nearshore buoy and land station wind records. The FNOC model predicts the global winds on a 2.5 degree grid at 6 hour intervals. Historical wind fields are available from 1976 until the present from this model. Waves play a role only indirectly through parameterization of Stokes drift in the wind drift rule (3%) and in the entrainment process.

Currents are calculated with a three-dimensional numerical model that solves conservation equations for momentum, salt, and heat (energy) using an equation of state that depends on salinity. The fully three-dimensional model is used only in a diagnostic mode to solve once and for all for the baroclinic currents implied by the archived hydrographic data. Tides, wind-driven barotropic, and sea-surface elevation currents are solved for using the depth-averaged (two horizontal dimensions) version of the model. This was used to model currents in the Bering Sea (Spaulding et al., 1987).

b. Ice Mechanics

For areas where internal ice stress and boundary effects are not important, a free-drift model for ice mechanics is used. The model is not described in the documentation, nor is there a description of the method used to couple the free-drift and hydrodynamics models. It appears that this model is not actually coupled but instead is an independent model that is not used in oil spill trajectory simulations. The model is steady-state and accounts for Coriolis and tilt accelerations, applied air stress, water stress, and bottom drag effects. The water drag is estimated from a two layer model: a quadratic drag law is used for the top two meters, and the bottom log-layer allows an increase in eddy viscosity.

For areas where free-drift is not appropriate, a viscous constitutive law is used. Ice velocity is described by the momentum equation that includes inertial, Coriolis, and tilt accelerations, applied air stress, water stress, and ice stress divergence. Ice compactness and thickness satisfy the conservation laws for a two-component model. Climatological ice growth rates are included.

The water stress is described as following a quadratic drag law. This drag law and the drag coefficient were developed to relate water drag to the ice velocity relative to current beneath the mixed layer. This approach, if actually used, would ignore the mixed layer structure potentially available from the hydrodynamic model. Turning angle is not included in the description.

The full ice model requires that either ice velocity or traction (the shear force component from the internal stress) be specified around the boundary. The report does not describe this boundary condition.

c. Oil Spill Models

Oil spill drift, spreading, evaporation, dispersion (entrainment), emulsification (mousse formation), and subsurface transport are included in the oil spill trajectory and fate model. A spill is represented as a set of oil spillets, each of which is assumed circular. The rate of release of spillets describes the oil spill release rate. This feature allows a continuous spill to be approximated and can describe a variety of large-scale forms, rather than just circular ones. Arbitrary shapes to the oil slick and patchiness are modeled by combining individual spillets. The Trajectory Model is limited to tracking 25 spillets simultaneously. Oil spill trajectories are calculated by accumulating (or integrating) motions, which include effects of tidal currents, density-induced net transport, and a wind-driven velocity.

In the absence of ice, the wind-driven velocity of the oil is assumed to be the sum of a barotropic current caused by sea surface gradients generated by the wind and an Ekman transport due to the direct action of the wind stress acting on the sea surface. Ekman transport is modeled as 3% of the wind velocity turned through a deflection angle. The deflection angle ranges from 25 degrees at low wind speeds to zero at winds of 20 m/s or more.

In the presence of ice, the wind-driven velocity of the oil is the sum of ice velocity and oil velocity relative to the ice. When the relative speed is below a threshold value, the oil is trapped and moves with the ice. In free-drift, wind-driven surface currents are neglected, and the ice velocity is assumed to be 3.3% of the wind velocity deflected 35 degrees to the right. The text suggests that in full ice coverage, the ice is assumed immobile. In partial ice coverage, when ice stress is important (typically north of St. Lawrence Island), the fully coupled ice-hydrodynamics model is used to describe the ice motion. Although the fully coupled ice-hydrodynamic model can be used, the report leaves some question as to whether or not it has actually been used.

Tidal currents are comprised of a tidal residual, and semi-diurnal (M_2) and diurnal (K_1) components. The vertically averaged hydrodynamics model is used to predict one cycle of tidal motions. The residual is estimated by integrating these motions over a tidal cycle.

Density-induced or residual current is estimated using the three-dimensional model in a diagnostic mode, i.e., with the density field determined from the NOAA/NODC climatological salinity and temperature data set. The steady-state current balancing the density field is determined for winter and for summer.

Wind-driven barotropic currents are the sum of Ekman transport due to the direct action of wind stress on the sea surface (modeled by the 3% rule) and the vertically averaged wind-driven current. Note the same two dimensional model is used for both the tidal and barotropic calculations. Representative wind fields, predominant wind patterns in the Beaufort Sea and Gulf of Alaska, and storm events in the Bering and Chukchi Seas are all used to develop oil trajectories.

When ice concentration is less than 30%, an open water spreading model is used where the gravity and viscous forces are in balance (after initial inertial forces diminish, and before surface tension becomes dominant). The rate of increase of oil surface area is proportional to area to the power 1/3 times the ratio of volume to area to the power 4/3.

Under ice, oil is trapped by under-ice roughness. Trapped volume per unit area is linear with ice thickness. The diameter of a spillet is determined by assuming it circular, and with thickness given by the trapped volume per unit area. According to the documentation, the SAIC model is used.

According to the documentation, the SAIC evaporation model for open water is used (Payne et al., 1984a). Oil is characterized by fractionation cuts determined by true-boiling-point distillation (TBP). Identical first order kinematics is used, with mass-transfer coefficients dependent on wind speed and Schmidt number.

The Trajectory Model accounts for oil under fast or pack ice, where loss by evaporation is prohibited. If the ice subsequently retreats, the oil begins to weather. In ice concentrations above 30%, the open water evaporation rate is linearly reduced, and above 90% it ceases.

According to the documentation, the mousse formation algorithm of Mackay et al. (1980) is used; according to the computer code, the SAIC model is used.

Although the documentation claims to use the same emulsification model as does SAIC, it is not obvious from the models presented and described. The documentation describes the rate of increase of fraction of water in oil to be proportional to wind speed (plus one) squared times a linear function of the amount of water in oil. The linear function contains an empirical constant. The report also presents equations for estimating viscosity corrections due to emulsification, evaporation, and temperature. It is not apparent where the viscosity is used.

The fraction of a surface slick that can be dispersed into the water column by breaking waves is proportional to wind speed to power two, and decays exponentially with a two day time constant. Alternately, the SAIC formulation (Mackay et al., 1980) may be used. It is also proportional to wind speed squared, and produces similar dispersion rates. Dispersion is prohibited under ice or in broken ice if compactness exceeds 30%. This feature appears to differ substantially from the SAIC model, where dispersion is enhanced in the presence of ice.

3. Computational Features

a. Circulation Model

In the Circulation Model, vertical variations of ocean current, temperature, and salinity are approximated by a set of basis functions with equations governing the coefficients determined using the Galerkin method of weighted residuals. Prior to introducing the basis functions, the vertical coordinate z is transformed linearly into a sigma-coordinate ranging in value from -1 at the ocean bottom to +1 at the sea surface.

Transformation of momentum and salt balances, and conservation of mass and heat into the sigma-coordinate system provides a set of governing equations. For horizontal velocity components, two equations are derived from a horizontal momentum balance. For heat and salt balances, one equation each is derived from a horizontal flux balance. There is one equation relating sea surface elevation and the depth-averaged values of horizontal velocity, which has the appearance of mass conservation. There is also one equation defining a new dependent variable, analogous to the vertical velocity component, as a function of the sea surface height and horizontal velocity, integrated from the bottom to each level.

The two horizontal velocity components, temperature, and salinity are expanded in a series of Legendre functions that vary in depth with the sigma-coordinate

$$u(x,y,\sigma,t) = u_1(x,y,t)P_2(\sigma) + \ldots$$

where σ suggests the sigma coordinate. The first Legendre function P_1 is a constant so that the first coefficient represents the vertically averaged value.

The Galerkin method of weighted residuals is introduced to derive equations governing each of the coefficients. Each coefficient may vary with horizontal position (x,y) and time (t). Each of the four basic transformed governing equations (u, v, temperature, and salinity) is multiplied in turn by each of the Legendre functions and integrated over the vertical domain ($-1 < \sigma < 1$). Errors in the equation governing the coefficients are orthogonal to the Legendre basis.

After the sigma transformation and Legendre approximation, the Circulation Model consists of a system of coupled nonlinear partial differential equations approximating the conservation laws and describing changes in the coefficient of the Legendre polynomials. Integration of these equations requires that we discretize the horizontal domain and time. A split mode difference scheme is introduced, with the free-surface elevation treated separately from the three-dimensional flow variables.

A staggered spatial grid is introduced in the x-y plane. A rectangular mesh is formed with Δx and Δy as horizontal grid increments. Sea surface elevation, temperature, salinity, and vertical velocity are specified in the center of each cell. The u velocity component is specified on the cell face normal to the x direction, and the v velocity component is specified on the cell face normal to the y direction. This is the standard Arakawa C-grid.

Text and plots in the documentation suggest, and the coding confirms, that a geographic grid is available. In addition, nesting of finer grids has been performed, and triangular cells have been used in specific applications. The model description does not include these features.

Spatial grid resolution is roughly 15-25 km for simulation grids over several regional domains: the Gulf of Alaska; and the Bering, Chukchi, and Beaufort Seas. Fine scale grids of about 1 km were also used in embedded simulations.

Temporal variations in the height or elevation of the free surface depend only on the vertical average of the horizontal current components, which are represented by the coefficients of the first Legendre polynomial. An explicit finite difference approximation is introduced for this mode, and it must satisfy the Courant-Fredrichs-Levy (CFL) condition, which limits the time step to the time required for a shallow water wave to propagate across a cell, given by:

$$\Delta t < \Delta x / \mathrm{sqrt}(gh).$$

The text suggests that external mode equations (higher order Legendre modes) are solved by an implicit finite difference method, with time derivatives and vertical diffusive terms approximated by centered time differences. However, the computer program included in the documentation states that a fully explicit momentum balance equation is used.

b. Oil Spill Trajectory Model

No mention is made of the time steps used in the hydrodynamic calculations. The following values were listed as time steps for the Trajectory Model, although it is possible that smaller time steps were required to avoid instabilities in simulations of the barotropic mode. The FNOC wind field was input on a 2.5 degrees lat/long grid every six hours. The spatial grid used with the hydrodynamic model was geographically rectangular, with increments of 0.2 degree latitude and 0.313 degree longitude. Tidal currents (vertically averaged and therefore two dimensional) had time steps of one hour. Simulations of density-driven baroclinic flow were performed using three-dimensional simulations for each season. Wind-driven barotropic flow (vertically averaged and therefore two dimensional) had time steps of six hours. These simulations used either the free-drift or the full ice model. Hourly and six-hourly values could then be obtained by interpolation.

The documentation states that computer programs for evaporation, entrainment (dispersion), spreading, and mousse formation (emulsification) are the SAIC routines.

C. OIL WEATHERING MODEL

1. Model Description

The Weathering Model, developed by Science Applications International Corporation (SAIC), utilizes a pseudocomponent characterization of crude oil to derive the time-dependent mass balance and composition of oil remaining in a slick (a single spillet). The model considers weathering by evaporation, dispersion (entrainment), mousse formation (emulsification), and spreading. The code was written in FORTRAN and includes all necessary I/O routines, error routines, and integration routines, and is capable of running on a microcomputer. The model was documented in a project final report by Payne et al. (1984a). The model is interactive and requests environmental data such as wind speed and scenario definitions by prompting the user with questions and suggested input. Specific crude oils and their physical parameters are contained in an internal library. The user may choose physical parameters of the oil either from this data base or input them separately.

Output from the model consists of mass remaining in the slick, mass dispersed, mass evaporated, fraction of mass remaining in the slick, area of the slick, thickness of the slick, viscosity, specific gravity, total volume of the slick, and dispersion and evaporation rates. These quantities are provided for each time step.

Oil weathering in the presence of sea ice presents a variation on the problem of oil weathering. The Weathering Model has been modified to accommodate four scenarios: oil in pools on surface of ice, oil spreading under the ice, oil trapped in a broken ice field, and open ocean (no sea ice). Oil weathering in the presence of sea ice has been documented in a report by Payne et al. (1984b). The user's manual for this model is given in Kirstein and Redding (1987).

2. Physical and Chemical Attributes

An oil spill can weather in open water by four processes: evaporation, dispersion, mousse formation, and spreading. For an open ocean spill which takes place at time zero, these processes should be nearly complete at the end of 100 hours.

The evaporation portion is probably the best defined part of the computer model. The evaporation of oils has a solid theoretical base, both in terms of the dependence of evaporation on wind speed and temperature, and on the boiling points of the various oil fractions. The authors present this material well, and it is the strongest part of the model.

The major over-simplifying assumption is that the oil is always well mixed, or that the evaporative loss is independent of slick thickness. When the slick is thick and there is sunlight, this is not true, but, given the approximations and deficiencies in the descriptions of the other processes, this is hardly an important defect. Also the scale of the spill is not taken into account in the program; large and small spills are treated the same.

When the program runs, it presents the user with a series of menus or screens. The user then steps through the questions asked on each screen to run the program. In the first step of running the model, the operator needs to load the distillation characteristics of the spilled oil. For contingency planning, this information is either available as a library function within the program, or can be loaded by the operator. The first screen allows the operator to specify the kind of crude oil which is spilled.

The next screen specifies the weathering process. The operator gives the size of the spill in barrels, what is apparently the air temperature (for some reason the water temperature is left unspecified), and the wind speed. The operator is then asked to choose whether he wishes the process to occur with spreading, dispersion, and mousse formation. Then the model runs. The output from this process is presented in the form of tables, which show the amount of oil in each distillation cut, as well as the change in the amount of spill remaining.

The dispersion into the water column model is described by two empirical equations. The first equation yields a function 'F', which is defined as "the fraction of sea surface subject to dispersions per second." F is not coupled to the second equation, which gives the fraction of oil for each cut which is dispersed into the water column as droplets. The amount dispersed into the water column is a function of wind speed, component viscosity, surface tension, and slick thickness. Since dispersion really depends on wave breaking and the total length or circumference of the oil slick exposed to the wave field, this dispersion model is suspect.

The mousse formation model is also drawn from Mackay et al. (1980), and again the reader is presented with little or no discussion as to how the model works. Mousse formation is described by an empirical equation, probably based on a few laboratory experiments, which appears to give the formation rate of mousse. Again, the original report would need to be checked to verify how this model works, but unlike the evaporation model, it appears to have an empirical rather than a theoretical basis.

This model uses an empirical spreading model developed by Mackay, which is not based on the classical oil spreading theory model. The reason for use of the empirical model is that the authors feel it applies better to rough seas than the theoretical spreading models. This model apparently has as its input the viscosity derived from the evaporation model. Also examination of the spreading code shows that the slick starts its spreading at a thickness of 2 cm. Judging by the news reports of the Exxon Valdez spill, it appears that wind herding and wave herding can maintain a slick at a greater thickness, so that this thickness stipulation may be a problem. The authors of the code realize that the spreading model needs improvement, and claim to have designed the code so that a newer version can be inserted.

Sea ice enters the Weathering Model in two ways: the oil can weather on top of the ice, or in a broken ice field. If it is in a broken ice field, then the rate of mousse formation is increased, the rate of dispersion into the water column is increased, and the spreading rate is apparently reduced. If the oil is allowed to weather in pools on top of the ice, the user specifies the pool depth, temperature, wind speed, and so forth. The only difference between this model and the open ocean model is that there is no spreading, dissolution, or mousse formation. The oil pool model then, is simply a model for the evaporation of a contained patch of oil.

More importantly, this part is the entire model for the direct interaction of oil and sea ice. There is no mechanism for getting the oil to the top of the ice. Nowhere in any of the material is there reference to brine channels, oil entrapment under the ice by freezing into under-ice pools, nor any seasonal dependence to the release of oil frozen into the ice.

The broken ice field is characterized by a single number, the ice concentration, which is the area fraction covered by ice, such as 0.7. The model makes no provision for the size or roughness of the broken ice. The broken ice cover affects the oil in three ways. First, the mousse formation rate is accelerated by changing a constant from its open water value of 1 to a broken ice default of 10 (page 26). There is no documentation cited for this, however. Second, the dispersion rate into the water column is accelerated by changing the value of a constant from its open water default of 1 to a broken ice default of 10 (page 30). The authors say this change is based on "limited data", again with no documentation cited. And third, the spreading rate across the surface is reduced. Their spreading model is a non-mechanistic model based on Mackay et al. (1980). The computer code states that "The functional dependence of spreading with fraction of ice cover is not known. For now, a linear dependence is assumed". The authors assume that the spreading rate is reduced linearly with ice concentration, so that the spreading rate in a 50% ice concentration is one-half the spreading rate in open water. The authors also recommend (page 24) that the present model be replaced by a "more realistic and mechanistic one."

3. Computational Features

The Weathering Model describes behavior at one location as a function of time. There are no spatial variations, horizontal or vertical, through the water column. A fourth order Runge-Kutta time integration is performed. The time integration for each configuration (oil in surface pools, oil in broken ice, oil on open water) is performed within a single integration subroutine, so intermediate solutions are not available.

The time step for temporal integration is set to allow a five percent change in the most rapidly varying pseudo-component, but may not exceed 0.5 hours nor be less than 0.05 hours. Components that weather too fast are assumed to be gone within a time step and removed from the simulation.

D. OIL/SPM MODEL

1. Model Description

The Oil/SPM Model, also developed by SAIC, was designed to provide predictions of oil droplet and SPM interactions in the range of parameters encountered in the environment. The models, documented in Payne et al. (1987), are one-dimensional and provide a vertical oil concentration profile as well as the mass of oil associated with free oil drops in the water column, mass of oil drops attached to SPM, and the mass of oil drops attached to the bottom, all as a function of time. The model is written in BASIC, is interactive, and provides typical values when requesting user-required inputs. The model was developed on an IBM-compatible microcomputer.

The studies reported by Payne et al. (1987) indicate that complete modeling of these interactions is extremely complex in a full three-dimensional model. A model with that detail would encompass dispersion of oil droplets, the kinetics of interaction of a distributed size range of oil droplets with a distributed size range of SPM, the agglomeration rate of oiled SPM, selective partitioning behavior due to varying chemical composition, and resuspension and transport of bottom sediments. Selective partitioning occurs among the discrete phases of dispersed oil droplets, dissolved oil droplets, free SPM, oiled-SPM agglomerates, and oiled-SPM sediments.

As a result, a much-simplified, one-dimensional computer model was prepared to predict the rate of agglomeration of free oil droplets with the SPM. The agglomeration rate is closely analogous to a chemical reaction rate in that it is proportional to the concentrations of oil droplets and SPM and considers collision cross-sections, with only a fraction of collisions actually resulting in an agglomeration. The agglomeration rate depends upon the turbulent energy dissipation rate, the water viscosity, the SPM concentration, and a lumped rate parameter derived from laboratory experiments. The turbulent energy dissipation rate will vary with depth, sea state, and weather conditions, especially wind speed. The lumped rate parameter depends upon characteristics of the oil and SPM, most of which have not been determined in sufficient detail at this time for the full model. In addition, the output from the Oil/SPM Model depends upon the rate of dispersion (entrainment) of discrete oil droplets from the oil slick (the oil source term), which needs to be supplied by other models.

2. Physical and Chemical Attributes

a. OILSPMXS Code

This code describes the dispersion of oil droplets into the water column. From other work by the authors, the dispersion of oil and sediment into the water column depends on ocean currents and ocean waves; namely the breaking of oil-covered waves disperses oil into the water column, and the non-linear interaction of waves and currents generates a suspended sediment. Instead of using this information, however, the initial screen prompt asks for either operator values or default values for the turbulent diffusivity, rise velocity, initial oil flux, and water depth. The code then gives the amount of oil suspended in the water column.

b. SPMONLY Code

This code gives the amount of sediment suspended in the water column. The criticisms are the same as above. The physical process depends on the non-linear interaction of an ocean current with surface waves, and the fact that the ocean floor is covered with a fine grain sediment. The first screen in this model allows the operator to either specify or accept as default constants the turbulent diffusivity, the terminal velocity, and the sediment flux rate from the bottom. The program then solves the diffusion equation for a sediment profile at various time intervals.

c. OILSPM3 Code

This code describes the interaction of the oil droplets with the suspended sediment profile. The model follows a diffusion equation similar to OILSPMXS and SPMONLY. Again this is a 1-D model, where the various parameters described in the two previous codes are specified on the screen. The code uses a steady-state SPM profile to start the calculation; the oil in the water column starts at zero. This code gives, as a function of time, the amount of oil lost to the bottom, the amount suspended in the water column, and the amount bound to suspended sediment in the interior. Again, environmental inputs are ignored, and the program uses default fluxes of sediments and oil droplet entrainment.

3. Computational Features

The models are dependent on time and vertical position. There is no horizontal variation. Concentrations of oil droplets, SPM, and oil-SPM agglomerate each satisfy a linear partial differential equation where the partial time derivative plus advection balances diffusion and a source term. The three equations are coupled through the source terms. The user inputs the particle velocities at which components are advected.

Separate equations for concentration of oil droplets and for concentration of SPM are presented. Each of these is solved analytically using a Laplace transform. The inverse transforms are expanded analytically, with the roots of the transcendental equations determined numerically. The oil droplet concentration profile is coded in program OILSPMXS. The SPM concentration profile is coded in program SPMONLY.

In the program OILSPM3, the coupled equations are solved numerically using a Crank-Nicholson scheme. This implicit numerical integration scheme is unconditionally stable. Time steps are therefore restricted only to capture physical changes in the solution.

Time steps are input as a fraction of a dimensionless time, with 1/20 recommended. Dimensionless time is water depth (cm) squared divided by turbulent diffusivity (recommended 100 cm*cm/s) divided by pi squared. This time step assumes that advection is slower than diffusion. Smaller time steps can be used if the user desires to print solutions more frequently.

The documentation suggests that SPM be distributed throughout the water column initially. The initial conditions could therefore be determined from steady-state conditions obtained from program SPMONLY, a capability also included in OILSPM3. Oil is then spilled into water that has sediment.

The computer programs are coded in BASIC; the other three oil spill computer models are FORTRAN 77 programs. Converting the BASIC codes to FORTRAN is an option. Also, there are compilers available for BASIC and FORTRAN which allows FORTRAN codes to call subroutines written in BASIC.

SECTION III
COMPARISON OF MODELS

The oil spill models were loaded onto, compiled with, and linked on a MicroVAX and an IBM PC/AT to characterize and compare the models. Informational matrices were prepared to summarize the important features of each model. The matrix for operating on the MicroVAX, Table 1, (1) lists the operating system, compiler, and external libraries required when running these models on a MicroVAX, (2) details the language used and the file sizes for the source code, the compiled code, and the executable code, and (3) provides the total memory required to run each model. Table 2 lists similar information for operating on the IBM PC/AT. The two parts shown for the Circulation/Trajectory Model are listed separately since they are compiled separately and run sequentially, passing the data in a static data file. The Oil/SPM Model was compiled on the IBM PC/AT using QuickBASIC. It is the smallest of the models; it was not compiled on the MicroVAX.

The data in Tables 1 and 2 require some explanation. In these tables, the size of source code is the total size of the FORTRAN or BASIC source code statements in ASCII. The MicroVAX files were created by modem transfer from an IBM PC/AT. The compiled size refers to the object files created by the respective FORTRAN or BASIC compilers. On the MicroVAX, they include the cross-reference information for the link map and source-level debugging. The size of the executable files are very different; they include space for the arrays on the IBM PC/AT but not on the MicroVAX. The memory required on the MicroVAX was the maximum memory used during execution; on the IBM PC/AT, the size of the executable file was used since there is no way to monitor it during execution on a non-multi-tasking system and it included all the necessary data storage.

This data indicates that all of these codes can easily be stored on readily-available hard drives for microcomputers (e.g., 20 MByte disk drives). With the exception of the Circulation Model, they all are small enough to execute on microcomputers with 1 MByte of RAM. The Circulation Model will probably require 4 MBytes of RAM, which is now readily available on Macintosh and MSDOS microcomputers.

The matrix shown in Table 3 was prepared to facilitate comparison of the models and aid in the evaluation of compatibility between the models. It combines the physical modeling, the numerical modeling, and the computer requirements into one table. In effect, the BDM team has distilled the data in the source codes, the user's manuals, the reports, and the data sets to provide the essence of the four computer models in this table.

In particular, the matrix summarizes the important elements of each model: input, output, time step values, grid resolution, applied force, boundary conditions, physio-

Table 1. VAX Comparison Matrix

	Coastal Zone Oil Spill	Circulation and Oil Spill Trajectory Model		Oil Weathering	Oil/Suspended Particulate Matter
		Circulation	Trajectory		
Language	FORTRAN	FORTRAN	FORTRAN	FORTRAN	BASIC
Source Size	380kB	78kB	151kB	107kB	35kB
Compiled Size	206kB	57kB	85kB	73kB	*
Executable Size	140kB	39kB	43kB	56kB	*
Memory Required	179kB	1713.5kB	147.5kB	58kB	*

Host Hardware: MicroVAX - 630QB
Operating System: VAX/Micro VMS v-4.7
Compiler Name: VAX FORTRAN v4.5

External Libraries: DEC STARLET.OLB
DEC FORRTL.EXE
DEC UVMTHRTL.EXE
DEC LIBRTL.EXE

* not compiled on VAX

Table 2. IBM Comparison Matrix

	Coastal Zone Oil Spill	Circulation and Oil Spill Trajectory Model		Oil Weathering	Oil/Suspended Particulate Matter
		Circulation	Trajectory		
Source Size	366kB	74kB	143kB	108kB	35kB
Compiled Size	303kB	122kB	98kB	108kB	43kB
Executable Size	403kB	1877kB	244kB	146kB	62kB
Memory Required	403kB	1877kB	244kB	146kB	119kB

Host Hardware: IBM PC-AT
Operating System: DOS 3.3
Compiler Name: Lahey FORTRAN F77L and
Microsoft QuickBASIC V4.00 with Overlay Linker V3.61

External Libraries: none

Table 3. Model Comparison Matrix

	Coastal Zone Oil Spill	Circulation and Oil Spill Trajectory Model: Circulation	Circulation and Oil Spill Trajectory Model: Trajectory	Oil Weathering	Oil/Suspended Particulate Matter
Input	coastal reach & wind data, type of oil	wind, tide, & ice data	point of spill, type of oil	oil characteristics, weathering scenario	oil and SPM data
Output	location & distribution of oil	velocity profiles	oil spill trajectory, mass balance	amt. of oil in each cut, amt. remaining	concentration gradients, material balance data
Time Step Values	3-6 hrs.	6 hrs.	1 hr.	3-30 min.	1 min.
Grid Resolution	1-10 km	wind 2.5 deg. lat/long; others 0.2 deg. lat., 0.313 deg. long.	10-40 km	spillet	1m
Applied Force	winds, currents, waves	winds	winds, currents, tides	none	none
Boundary Conditions	type of coast and dimensions	applied stress function of wind stress at surface, no salt flux through top or bottom	oil spill can be in open water, broken ice, or pack ice	oil can weather in open water, in pack ice, or on top of ice	no oil lost horizontally by dispersion or spreading
Physio-Chemical Assumptions	no ice present, oil represented as circular spillets	incompressible flow, vertical accelerations small	ice follows viscous model, ignores losses by evaporation and dispersion	one location, oil always well-mixed, no disperson from wave action	independent of wind, waves, 1-D model only, no ice present
Numerical Method of Solution	explicit time integration	basic conservation eqns. solved in explicit FD form by Galerkin method	3-D mass transport eqn. solved by particle-in-cell technique	4th order Runge-Kutte time integration	1-D PDE solved by Laplace transforms, Crank-Nicholson integration each time step
Runtime Memory	403kB	1877kB	244kB	146kB	119kB
I/O Storage	500 kB	30 MB	2 MB	10 kB	1 kB
Model Author	Applied Science Associates, Inc.	Applied Science Associates, Inc.	Applied Science Associates, Inc.	Science Applications Int'l. Corp.	Science Applications Int'l. Corp.
Date Completed	1988	1988	1988	1987	1987

chemical assumptions, numerical methods employed, runtime memory, I/O storage, model author, and date completed. The information regarding the Circulation/Trajectory Model is again divided into two columns.

BDM has interpreted the data in Table 3 as follows. The inputs for all models are similar: climatological data, bathymetric data, and oil characterization data. Data arrays, such as winds, can easily be interpolated between the grids of each model. To assemble sufficient data to run all of these models together will, however, be a significant effort. Sea ice is included only in the Trajectory Model and Weathering Model, not in the others. Therefore, further modelling and code development effort will be necessary to model oil in sea ice near shore and oil/SPM interactions under sea ice. The output data formats are highly varied. To allow the models to work together, their output routines will have to be modified to provide the necessary input data for other models. Graphical displays of output data will also be very useful in visualizing the results of the combined models. The time step sizes are compatible except for the Oil/SPM Model, which has a much shorter time step. The Weathering Model will start with short (3 minute) time steps with fresh oil but will quickly lengthen its step size to its maximum. To integrate the Oil/SPM Model, it may have to run hundreds of time steps for each time step for the other models. The Oil/SPM Model grid resolution is much smaller than the others but refers to the vertical direction. If it were to be converted to a two-dimensional model, its horizontal grid will be similar to the others. The applied forces are similar: winds, currents, tides, and waves. The redundant and missing physio-chemical assumptions are discussed in more detail later in this report. The numerical methods of solutions shown are highly varied. It would be a significant effort to convert them all to a common time-integration method. It would be less effort to leave these time-integration routines intact and run each model independently for a global time step, such as 6 hours. The Circulation Model is by far the largest, with the largest I/O and runtime memory requirements; it will require the largest available microcomputers to operate.

SECTION IV
MODEL INTEGRATION

The objectives were to analyze the four models and recommend necessary modifications to allow their sequential or integrated use in a combined oil fate model.

BDM has evaluated various combinations of the four oil spill model. Comparisons of code organization and potential changes to the individual models (to improve the functionality and usefulness of the combined model) were evaluated in terms of the ability of the combined model to perform its primary function of predicting the fates of oil spills.

BDM has considered combining models by matching the time steps, grid sizes, and data sets, by recommending ways of eliminating redundancies between the models being coupled, and by identifying missing features. The process of combining the models also considered the various subsets of the four models which are required to simulate the various scenarios.

A. OIL SPILL SCENARIOS

The BDM approach to the development of a combined oil spill model has considered:

(1) A wide range of Alaskan OCS oil spill scenarios

(2) The applicability of the models to each scenario

(3) Methods for coupling the models

(4) The structure of the synthesized model.

The combinations of three choices (nearshore/offshore, ice/no ice, and surface/subsurface oil spills) lead to eight possible oil spill scenarios which provide a full range of situations against which combined models can be tested for applicability, as illustrated in Figure 2. Ideally, various combinations of the four models should be able to accommodate any of the scenarios. Figure 3 compares the four models to the scenarios. The top portion of Figure 3 shows the capabilities of each model mapped against the scenarios. The bottom figure indicates which models can be used in each scenario. There are many open squares -- the whole issue of nearshore sea ice is not addressed by any of the models. All other situations are at least addressed, if not always satisfactorily (see Section II). For nearshore, COZOIL contains features to model oil weathering and Oil/SPM interaction, albeit in a less sophisticated manner than the Weathering and Oil/SPM Models. The Weathering and Oil/SPM Models could be adapted to the nearshore environment if needed. It is appropriate that subsurface weathering be open squares on

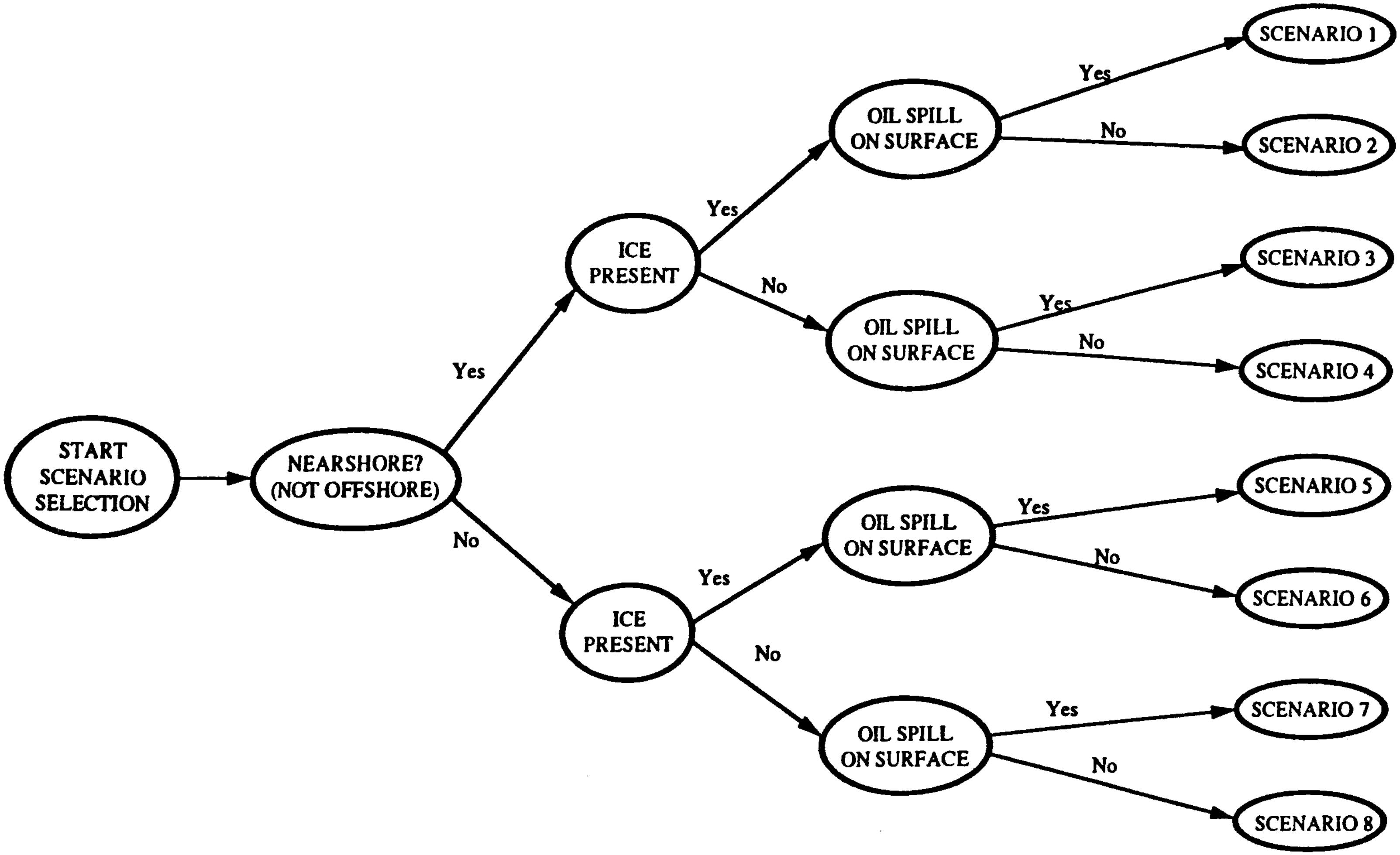

Figure 2. Basic Oil Spill Scenarios

MODEL	NEARSHORE	OFFSHORE	ICE	NO ICE	SURFACE	SUBSURFACE
COZOIL	●			●	●	●
CIRCULATION/ TRAJECTORY		●	●	●	●	●
WEATHERING		●	●	●	●	
OIL/SPM		●		●	●	●

(a) Capabilities of Each Model

<table>
<tr><th>SCENARIO</th><th></th><th></th><th></th><th>COZOIL</th><th>CIRCULATION/ TRAJECTORY</th><th>WEATHERING</th><th>OIL/SPM</th></tr>
<tr><td>1</td><td rowspan="4">NEARSHORE</td><td rowspan="2">ICE</td><td>SURFACE</td><td></td><td></td><td></td><td></td></tr>
<tr><td>2</td><td>SUBSURFACE</td><td></td><td></td><td></td><td></td></tr>
<tr><td>3</td><td rowspan="2">NO ICE</td><td>SURFACE</td><td>●</td><td></td><td></td><td></td></tr>
<tr><td>4</td><td>SUBSURFACE</td><td>●</td><td></td><td></td><td></td></tr>
<tr><td>5</td><td rowspan="4">OFFSHORE</td><td rowspan="2">ICE</td><td>SURFACE</td><td></td><td>●</td><td>●</td><td></td></tr>
<tr><td>6</td><td>SUBSURFACE</td><td></td><td>●</td><td></td><td></td></tr>
<tr><td>7</td><td rowspan="2">NO ICE</td><td>SURFACE</td><td></td><td>●</td><td>●</td><td>●</td></tr>
<tr><td>8</td><td>SUBSURFACE</td><td></td><td>●</td><td></td><td>●</td></tr>
</table>

(b) Applicability to Eight Oil Spill Scenarios

Figure 3. Applicability of the Four Models to the Scenarios

Figure 3, since it is not an important fate mechanism to model. The Oil/SPM Model is most suitable for waters outside the surf zone, but on the continental shelf because the Oil/SPM Model does not incorporate the surf zone or beach environments, and because Oil/SPM interaction is not an important fate mechanism in the deep ocean where SPM concentrations are low. Oil/SPM interactions with sea ice is however an important feature which is not included in these models. Examples are springtime spills near estuaries when heavy sea ice is present, spills near shore when fast ice is present, and spills in harbors and bays when pancake ice is present. In each case the spilled oil will simultaneously interact with the ice and the SPM.

B. CONSIDERATIONS FOR COMBINING THE MODELS

Whatever form the combined oil spill model takes, the complete model will have several components. Consider Figure 4, which shows the need for input/output and database components of the model. It also shows a need for a way to define a new spill. The new spill will account for where the oil went in the last time step of the model as well as for additional oil spilled and for oil cleaned up. An expanded version of Figure 4 is shown in Figure 5, where input includes scenario rules and a library of oil spill models. The output has interactive post-processing and spill analysis, and the database has climatological and oil properties data. Nevertheless, the elements are the same, including the need to define a new spill.

1. General Considerations

The strengths of the four oil spill models have been summarized in Table 4. The COZOIL and Circulation/Trajectory Models are similar in that they both use large, horizontal grids; in contrast, the Weathering Model is applied at a point, and the Oil/SPM Model equations are solved over a single vertical array representing the water column. Knowing this, it is conceivable that the COZOIL and Circulation/Trajectory Models could be run jointly by passing oil spill and hydrodynamic data across a common boundary. The hydrodynamics in the Circulation/Trajectory Model should be used to drive the nearshore hydrodynamics of the COZOIL Model in any case. The Weathering and Oil/SPM Models could conceivably be applied as needed at the locations of spillets.

The Circulation/Trajectory Model is a collection of models which in some sense demonstrates within its own system one of the major aims of this project. In the way it is used, it essentially amounts to running independent models for tidal currents, barotropic currents, baroclinic currents, ice and/or surface currents, then combining (in a

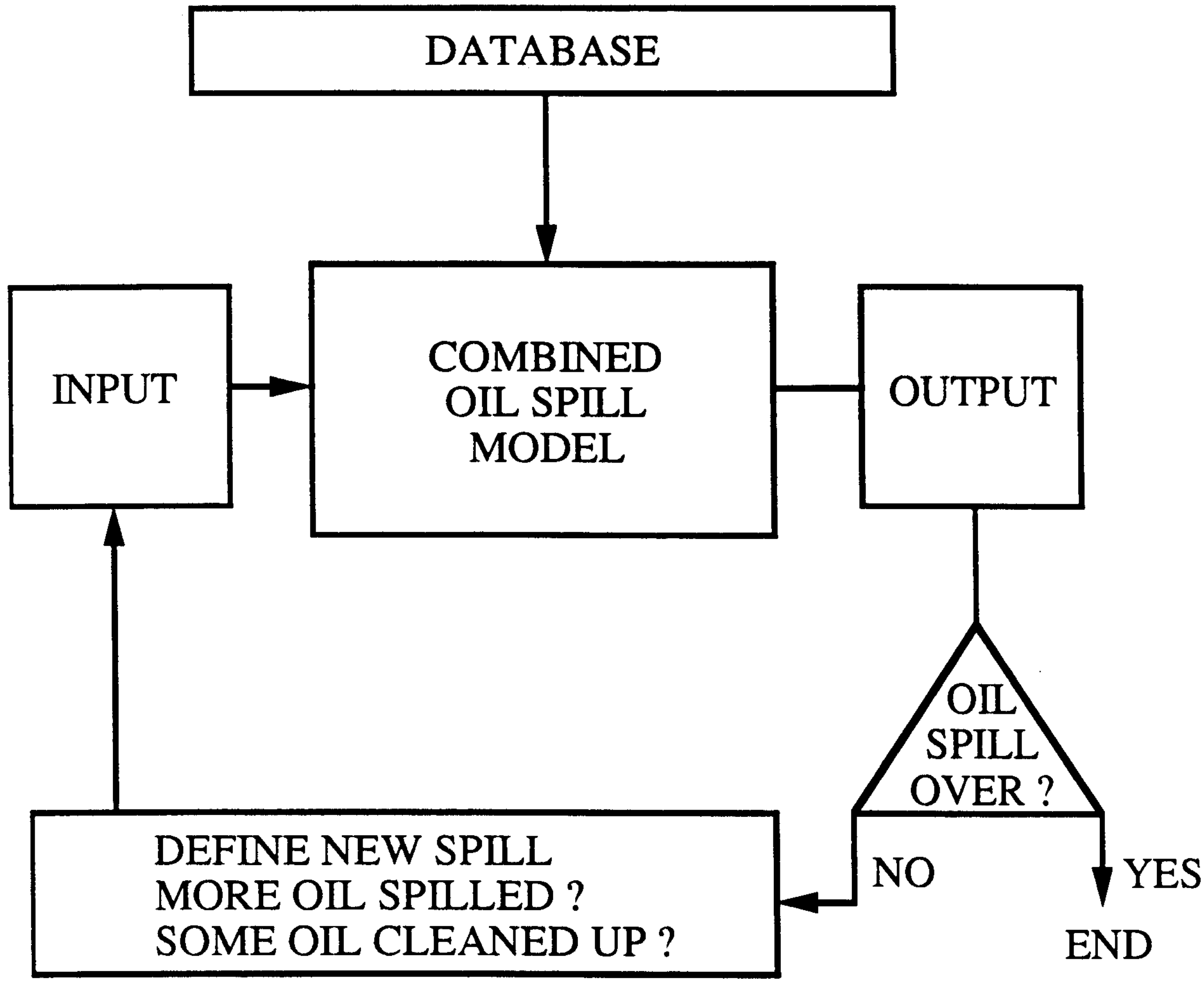

Figure 4. Top Level Flow Chart

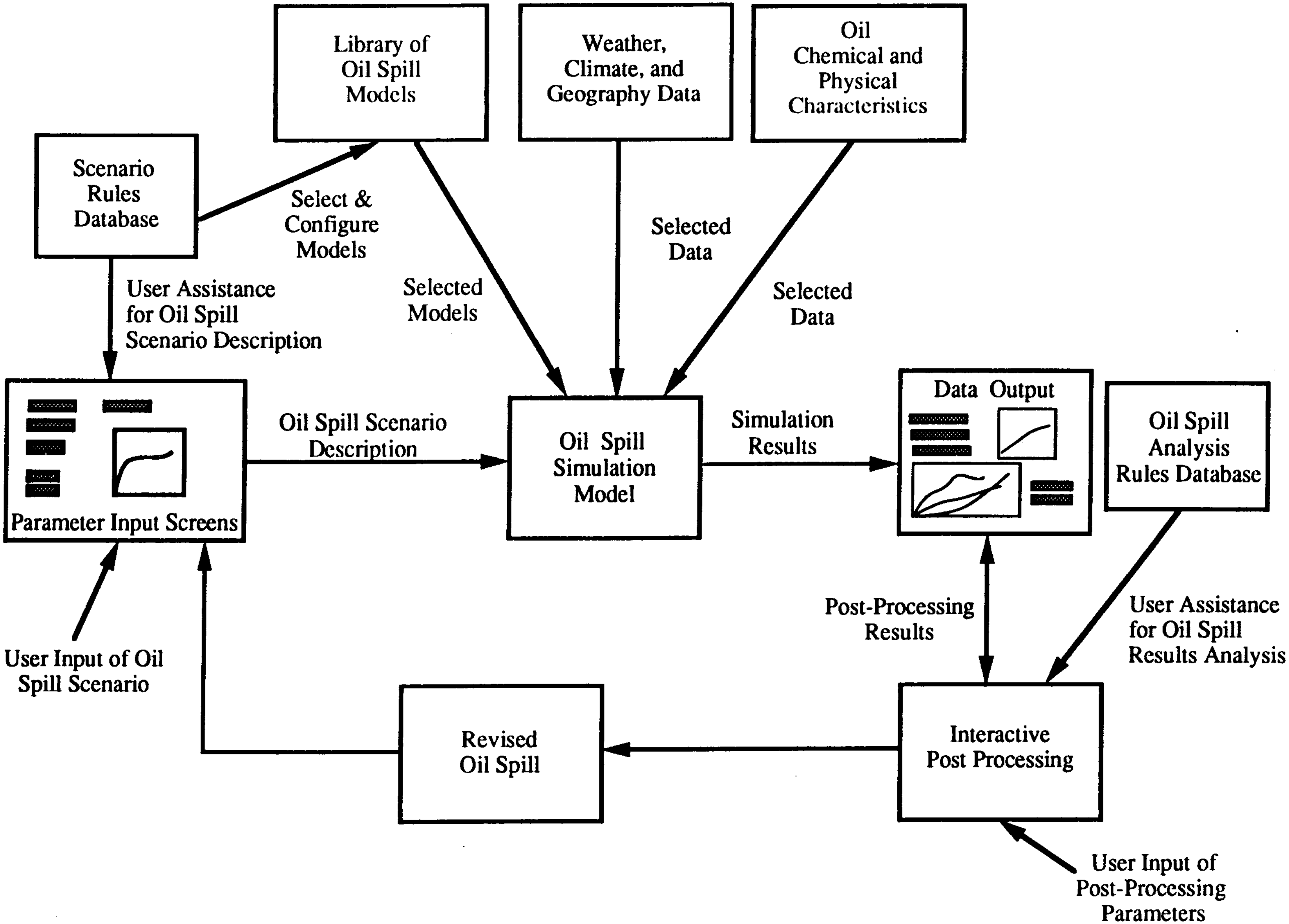

Figure 5. Combined Oil Spill Fate Model

Table 4. Summary of Model Features

- Coastal Zone Oil Spill Model
  - Predicts time-varying distribution of oil introduced into ice-free coastal domain separated into three partitions: nearshore, surf zone, and coast
  - Tracks spillets (multiple, discrete batches of oil) on and below surface
  - Deterministic model of shoreline: 30 x 300 km area, 10 x 10 km grid size, and 3-6 hour time steps for up to 90 days
  - Input parameters define study location and physical properties, environmental data, and oil spill properties and dimensions
  - Output parameters define spatial distribution of oil droplets and oiled particles

- Circulation and Oil Spill Trajectory Model
  - Calculates hydrodynamics, wind, ice, and oil spill trajectories and fates with two computer codes: Circulation and Trajectory
  - Circulation Model
    - 3-D spectral hydrodynamics model solves conservation equations for water mass, density, and momentum
    - Generates surface velocity vectors for tidal and residual currents
    - Incorporates FNOC data sets into concurrent wind fields
    - Does not include surf zone or coast features
  - Oil Spill Trajectory Model
    - Calculates trajectory of spilled oil and predicts its fate with sea ice effects
    - Superposes wind-induced, tidal, and residual current drift to get trajectories for multiple spillets
    - Performs oil weathering on spillets (evaporation, dispersion, emulsification, and spreading)

- Oil Weathering Model
  - Provides pseudocomponent characterization of crude oil to derive time-dependent mass balance and composition of oil in slick
  - Weathering by evaporation, dispersion, mousse formation, and spreading, but no surf zone or coast effects
  - Accommodates three ice scenarios: oil in pools on surface, spreading under ice, and trapped in broken ice field
  - Input parameters define environment and physics of crude oil
  - Output parameters define oil fates (mass in slick, dispersed, and evaporated), slick dimensions and properties, and dispersion and evaporation rates

- Oil/SPM Model
  - Predicts oil droplet and SPM interactions using 1-D vertical oil concentration profile to calculate rate of agglomeration of free oil droplets with SPM
  - Does not include sea ice, surf zone, or coast effects
  - Input parameters define rate of dispersion of discrete oil droplets from oil slick and environmental data
  - Output parameters define vertical oil concentration profile and mass of free oil drops in water column, mass of oil drops attached to SPM, and mass of oil drops attached to bottom

linear fashion) the resulting output to advect an oil spillet, which undergoes transformation according to another "oil fate" model similar to the COZOIL weathering model.

Ice dynamics, which are not present in the COZOIL Model, are treated either with a free drift model of Overland et al., 1984; or by a full ice model adapted from Kowalik. The Overland work describes a neutral boundary layer model that uses "second-order" closure to solve for the surface velocity in terms of stress, including bottom effects if the water is shallow. It is not clear how this is incorporated into the Circulation/Trajectory free-drift model, although it is doubtful that the model solves the equations over a 1001 point vertical grid as Overland did. In the full ice model, equations for ice compactness and ice thickness are carried for two categories of ice thickness, following Hibler's approach. A viscous constitutive relation between ice stress and strain is used instead of the viscous/plastic or elastic/plastic rheologies, which would probably allow more realistic shear in near shore regions.

It would be a major undertaking to use the Circulation/Trajectory Model in any way different from the demonstration scenarios presented in the manual. Presumably the wind and hydrographic data would be available for running the hydrographic models, although the North Slope demonstration run misses the westward intensification of the Beaufort Gyre offshore of the shelf break--which is certainly present in Mountain's dynamic topography, and should show up in the baroclinic model (Mountain, 1974). Thus to use it in the Beaufort or Chukchi might require a good deal more preparation of the driving data sets. The User's Guide was not very helpful in laying out the sequential steps required for actually setting up and running the model.

In most respects, the Circulation/Trajectory Model already has an interface to a separate oil-fate model. To simulate a set of spill scenarios including nearshore/beach effects, one option is to modify the oil-fate section of the Circulation/Trajectory Model rather than build an interface which would, for example, pass a file of spillet characteristics from the Circulation/Trajectory Model to COZOIL. In other words, someone with enough skill to set up and use the Circulation/Trajectory Model would probably find it easier to just incorporate the desired features of COZOIL into the Circulation/Trajectory code.

In contrast to the COZOIL report, the Circulation/Trajectory Model documentation includes a helpful set of parameter studies. In the central Bering, for example, we find that various assumptions regarding the wind-driven barotropic current (including no barotropic current at all) have little impact on the results. It is doubtful whether the barotropic current emphasis is worth while, since it is probably the baroclinic response to particular storm events that matters. In terms of the user interface and the interface with other models, someone setting out to do a meaningful study of oil spill impact in a particular region would face a formidable task in setting up this model. In addition to the unavoidable task of setting up grids, assembling meteorological and oceanographic data, and developing algorithms for output interpretation, one would find themselves questioning and perhaps adapting many of the underlying model algorithms as well.

2. Overlapping Parameters, Time Steps, and Grid Scales

BDM has addressed which models have overlapping parameters and, where input and output parameters do overlap, whether the time step, grid scale, and forcing of the models logically allows them to be used together. The input parameters on the grids (such as winds and temperatures) require an interpolation routine to use the same data source.

The COZOIL Model was developed with coupling to the Circulation/Trajectory Model in mind (note that ASA was involved in the development of both models). The COZOIL Model can accept hydrodynamic data from a two or three dimensional circulation model. Furthermore, if the Circulation/Trajectory Model is used, then oil conditions can serve as initial conditions for COZOIL when oil is transported nearshore.

The COZOIL Model is essentially a standalone system. The user sets up the grid, specifies coastal characteristics, prescribes the wind time series and a simplistic tidal current model, and either looks at the statistics of several spillets, or synthesizes an actual spill event out of a series of spillets. The boundary conditions and perhaps interior grid oceanographic conditions could be coupled with the corresponding output of, e.g., the Circulation/Trajectory Model. This would only apply in an ice-free scenario.

In the Weathering Model, a fourth order Runge-Kutta time integration is performed. The time integration for each configuration (oil in surface pools, oil in broken ice, oil on open water) is performed within the time integration subroutine, but intermediate solutions are not available. The time step for temporal integration is set to allow a five percent change in the most rapidly varying pseudo-component, but may not exceed 0.5 hours nor be less than 0.05 hours. Components that weather too fast are assumed to be gone within a time step and removed from the simulation.

The Weathering Model is probably the most comprehensive yet developed. It has been tested against laboratory and field spill data. It can probably be used in conjunction with a hydrodynamics 'point' model, but the Weather Model will have to be extended to describe the behavior of a field of values. This will require more than just applying it to a set of cells in a horizontal grid because the spreading process must describe the spread of oil from one cell to its neighbor.

Although the weathering code is rather linear in its structure, it appears to be a modified version of the open ocean code, and as such suffers in its structure. Too much work is performed within the time interaction subroutine, and many of the calculations are made in duplicate parts of the code. It would be far better to develop a new set of subroutines to do these calculations. Furthermore, the time integration must be extracted from the time integration subroutine, BRKG4, if the code is to be integrated into a more complete model.

3. Redundant Model Features

The bullets in Figure 6 indicate which models have which redundant features. The COZOIL Model is involved in all redundant features since it is a comprehensive model.

It appears that the weathering behavior is rather similar in the Circulation/Trajectory Model (ASA), COZOIL (ASA), and the Weathering Model (SAIC). Features of the SAIC Weathering Model have already been incorporated into the Circulation/Trajectory and COZOIL Models. It appears that the Circulation/Trajectory Model includes all features of the SAIC Weathering Model but, in addition, includes transport by ice and relative to ice. It therefore includes and supercedes the SAIC Weathering Model.

The COZOIL Model contains a simplified model for Oil/SPM interaction, similar to those features in the Oil/SPM Model. The Oil/SPM Model is not very interesting in the deep ocean; it is applicable on the continental shelf and nearshore. Thus, these models are redundant in the nearshore. The 1-D Oil/SPM Model is more detailed but would need to be implemented in a 2-D or 3-D version to be used nearshore.

There are numerous redundant features between the Circulation/Trajectory Model and the COZOIL Model, except that the former is mainly an open ocean model and the latter a nearshore model as they now stand. Having these two models interface about 30 km offshore avoids a redundancy.

4. Missing Model Features

BDM has determined that all four models could reasonably and economically be adapted for sequential or integrated use in the combined oil fate model with minor modifications. Missing features and suggested modifications are identified in Table 5 and described in detail in the following.

The glaring omission in COZOIL for much of Alaskan waters is sea ice. It seems that many of the processes so painstakingly detailed in both the environmental and "fates" sections of the model would be entirely inappropriate if sea ice were present, or even if the beach were frozen. Certainly these conditions are found along much of the

Model Feature	Coastal Zone Oil Spill	Circulation and Oil Spill Trajectory	Oil Weathering	Oil/Suspended Particulate Matter
Weathering				
Spreading	•	•	•	
Evaporation	•	•	•	
Dispersion	•	•	•	
Mousse formation	•	•	•	
SPM Interaction	•			•
Spillet Transport	•	•		
Hydrodynamics	•	•		

Figure 6. Redundant Model Features

Table 5. Missing Model Features

- COZOIL
  - No Sea Ice and Frozen Beaches for Nearshore
  - No Nearshore Transport Mechanisms
    - Wind Drift with Coast Effects
    - Storm Surge Setup and Setdown
    - Steady-State Currents to Start Model

- Circulation/Trajectory
  - Lacks Sophisticated Offshore Wind Drift with
    - Accurate Surface Currents
    - Wind Spreading Mechanisms
  - Lacks Detailed Offshore Subsurface Pollutant Transport

- Weathering
  - No Spatial Variations
  - Lacks Validated Model of Dispersion, Spreading, and Mousse Formation with Sea Ice

- Oil/SPM
  - No Horizontal Advection and Diffusion of Oil with Suspended Particulate Matter
  - No Oil/SPM Interactions Under Sea Ice
  - No Surface Flux of Oil into Water Column Based on Sea State
  - No Sediment Flux at Bottom Based on Sediment, Wind, Wave, and Current Conditions
  - No Oil Flux into Sediment Based on Sediment Conditions
  - No Oil Droplet Size Dispersed into Water Column
  - No Biological Uptake of Oil

Alaskan coast line for much of the year (10 months a year on the Beaufort Sea coast and 6 months a year on the Bering Sea coast).

In the area of upper ocean currents and near surface transport, the COZOIL Model seems fairly naive. An example is the wind-drift current model, which is basically a simple momentum balance in which average current is obtained by dividing the slab momentum by the water depth. Some of its simplicity is sacrificed by making it time dependent. Also, the model is "spun up" with the full inertial terms for each spillet. This is incorrect because the current does not start when the oil spills. It would be more realistic to use the simpler steady-state response. Even in the context of microcomputer computing power, the processes could be treated much more realistically.

We question the balance of the COZOIL Model in its overall approach. As stated above, the treatment of the transport mechanisms, even in the absence of ice, is pretty crude. COZOIL has a "3%" rule for wind drift despite the proximity of the coast, no provision for "storm surge" setup or setdown, and a very simplistic wind driven current regime. Is this commensurate with an exhaustive description of a particular section of beach, and the small scale details of deposition and weathering there? In other words, is it really important to know whether some small amount of oil leaches out of emulsified mousse along a particular section of beach, if the uncertainty in a spill's beachhead is several tens of kilometers? It would be well worth the effort to do some carefully planned "parameter studies" for gauging the relative importance of the various processes listed above.

The COZOIL Model is essentially concerned with oil/beach interaction, with the offshore transport part tacked on rather haphazardly. It may be necessary to track a slick close to the surf zone with a more sophisticated hydrodynamics model (something along the lines of the Circulation/Trajectory Model but with closer attention paid to coastal processes). When an oil beachhead is established, calculate the oil/beach deposition and weathering with COZOIL or a similar model. This could reduce the domain size (thus increasing grid resolution) and simplify calculations considerably. Perhaps a completely separate module could then be used for the scenario with sea ice and/or frozen beach.

In the Circulation/Trajectory Model, by far the most important factor is the wind drift, so this should be of top priority--unfortunately, this seems to be the least sophisticated aspect of the entire model. Recent test results reported by Reed, et al. (1990) show that the wind plays a major role in the spill on the surface by pushing a heavy patch of oil faster, leaving a streamer of thick oil behind, and spreading an oil sheen out to the sides. The subsurface pollutant transport part of the Circulation/Trajectory Model is also weak.

In the presence of ice, the wind-driven velocity of the oil is the sum of ice velocity and oil velocity relative to the ice. When the relative speed is below a threshold, the oil is trapped and moves with the ice. In free-drift, wind-driven surface currents are neglected, and the ice velocity is assumed as 3.3% of the wind velocity deflected 35 degrees to the right. The text suggests that in full ice coverage, when ice stress is important (typically north of St. Lawrence Is.), the fully coupled ice-hydrodynamics model is used to describe the ice motion. Although the fully coupled ice-hydrodynamic model can be used, the report leaves some question as to whether or not it has actually been used. It would be better to use the fully coupled ice-hydrodynamic model whenever ice was present.

The Weathering Model describes behavior at one location as a function of time. There are no spatial variations, horizontally or vertically, through the water column. In addition, sea ice enters the Weathering Model in a very casual way. In the mousse and dispersion model, a constant changes from 1 to 10; in the spreading model, the rate varies linearly with the open water fraction. The evaporation code is suitable for use in a more sophisticated oil/ice model, but the dispersion, mousse formation, and particularly the spreading model features should be carefully examined for use with sea ice before incorporation.

For sea ice models, more research and model development is needed on topics such as the under-ice dispersion of oil into the water column. We know qualitatively how oil disperses into the water column under open ocean conditions. Namely, the cause of droplet formation from oil slicks is due to wave breaking at the edges of the slicks, following which the oil droplets are thrown into the water column. What about oil under the ice? Are there similar mechanisms for dispersing oil under a sea ice cover? For example, in early OCSEAP laboratory experiments (Martin, 1977), it was observed qualitatively in laboratory studies that droplet formation occurred during pressure ridge formation. Can droplets form also from turbulent shear generated under an ice cover? To model the dispersion of an under-ice oil spill, questions such as these need to be investigated.

The Oil/SPM Model appears to couple sensibly with the other models. The problem is that it is concerned only with the rate of change in the vertical profile of suspended oil and solid particulate. Horizontal advection and diffusion are not considered. Perhaps the simplest way to couple the SPM effects would be to rewrite the subsurface transport model in the Circulation/Trajectory Model. This would not be a trivial task, but at present no simple realistic coupling appears possible. Problems in coupling the Oil/SPM code to other physics is comparable to coupling the SAIC Weathering Model to the Circulation/Trajectory Model, except that ASA has already done the latter.

There is no sea ice in the Oil/SPM Model, and, given that we do not even know how oil dispersion occurs under sea ice, it will be difficult to generate a realistic model of this process. From the qualitative OCSEAP experiments (Martin, 1977), we suspect that dispersion will take place through ridge formation or oil entrainment in a turbulent shear flow. There are also plenty of ice core observations showing a strong sediment signal at different depths, so that sediment is sometimes suspended under sea ice. The problem is important, but modelling it will be very difficult.

The one-dimensional Oil/SPM Model is useful because it allows an estimate of how long it will take for spilled oil to reach the bottom in an environmentally sensitive region. The problem with the model is that the surface fluxes of oil and sediment at the top and bottom of the water column depend only on default constants and are decoupled from any environmental model. This means for the naive user that oil would be entrained at the same rate on a day with zero winds and no surface waves as during a severe storm! Additionally, for application to the real world, this model should be coupled to a data base of nearshore sediment conditions. This serves two purposes. The user would have some idea first, whether the bottom material is capable of going into suspension, and second, whether it is a favorable material for taking up oil.

It is possible to use the oil weathering model's dispersion term as input to the Oil/SPM Model. The problem is that the ability of sediment to take up oil strongly depends on the oil droplet sizes being on the order of 1-10 microns. The Weathering Model does not consider droplet size but gives only an estimate of the amount of oil dispersed into the water column. To quote from Payne, et al., (September 15, 1987) the "existing open-ocean oil-weathering code contains an algorithm for dispersion of oil into the water column"(page 2-5), but that "there are no acceptable models which predict oil-droplet size from a dispersing slick." This difficulty with oil droplet size must be resolved before the Oil/SPM and Weathering Models can be coupled together. Also, the Oil/SPM Model still requires ocean wave and current data to describe the sediment flux from the bottom.

In summary, there is no point incorporating either of these models into a general oil spill model unless two improvements are made. First, the oil dispersion and sediment uptake terms must be tied into a wind, wave and current data base; second, the model must be tied to a sediment inventory data base.

The Oil/SPM Model is primarily applicable to shallow water, where winds and waves generate suspended sediment. The depths cited throughout the report include 2-10 m, so that this is a near coastal phenomena. The oil interacts with the SPM through two mechanisms:

(1) oil droplets collide with SPM, and

(2) dissolved species are absorbed by SPM.

The Oil/SPM Model considers only the first effect. As an example of the importance of this process, under high SPM concentrations, 10-15% of a spill in the Baltic was removed from the water column by sedimentation. Note also that there are different kinds of SPM's. For example, clay and glacial derived tills attract much more oil than minerals. The model also ignores biological effects, so that the uptake of oil droplets by phytoplankton and the incorporation of oil into fecal pellets, which then fall to the bottom, are neglected. There is speculation in the recent Exxon Valdez reports that this source of oil for the bottom sediments is greater than oil incorporation into SPM.

The critical parts of the model are as follows. Any predictive model must be able to predict the amount of SPM in the water column, which will depend on the wind, wave, and nearshore environment, then predict if the spilled oil will be broken into small droplets by waves, and finally predict if the droplets will be collected by the SPM. Therefore, the predictive equations for the oil and SPM depend strongly on the wind, wave, and ocean turbulence equations, as well as on the local sediment properties.

The Oil/SPM Model contains a suspended sediment, bottom boundary layer submodel, which takes into account the non-linear dynamics of surface wave and current interactions in bottom boundary layers. It is the long waves and low frequency currents which resuspend sediments; whereas it is the short choppy seas that generate oil droplets from slicks. For sea ice, the long waves and currents will continue to be important in ice-covered seas, and thus oil /SPM interactions will probably occur under ice.

C. VIABLE STRUCTURES OF THE COMBINED OIL FATE MODEL

Some considerations for combining the models were discussed in Section IV, Heading B, above. In the earlier discussion it was pointed out that the complete oil spill simulation model required components that were input/output software, database components, and a component which defined a new oil spill after some time step of having run the model. This new scenario section would account for the fate of the oil previously spilled as well as any new oil spilled or any oil cleaned up during the time period. In this section the discussion will concentrate only on the portion of the complete oil spill simulation model which represents the combination of the four oil spill models being reviewed in this report. After consideration of the physics, chemistry, numerics, and code structure of the four codes, it appears that there are three logical ways of combining the codes. Each of the three possible methods of combining the codes have some advantages and some limitations which will be discussed in detail below. The three possible approaches are:

(1) Sequential approach for combining the existing codes.

(2) Development of a code based on the Circulation/Trajectory Model.

(3) Develop a new code from the basic equations of each code.

Nearshore, the COZOIL Model is nearly complete, but the Weathering Model may improve the quality of the weathering effects and include sea ice. Offshore, the COZOIL Model is not appropriate. It thus appears that two unique subsets of the models are required: Weathering with COZOIL, and Circulation/Trajectory with Weathering and Oil/SPM. It will occur, however, that an oil spill will extend from one scenario to another as, for example, an offshore spill that drifts next to a land mass.

It would, however, be a fairly major undertaking to interface the COZOIL Model properly with the Circulation/Trajectory Model. It might be less effort to incorporate the desired features of COZOIL into the Circulation/Trajectory Model rather than build an interface between the two models.

No matter which method of combining the models is selected (including *status quo*), the issue of shelf life should be raised. To have a shelf life of five years, individual models need to be updated or replaced with codes reflecting new field data and test results. A viable structure for the combined oil fate model should readily allow the incorporation of these updates without impacting the overall function of the combined model. The list of missing model features in Table 5 is representative of potential technical developments (by test or modelling) which might render the existing codes obsolete if they were not incorporated.

1. <u>Sequential Approach for Combining the Existing Codes</u>

One candidate for combining the four models is to leave each model separate and operate them sequentially, and, after each time step (which might represent an hour or a day), redefine the oil spill in terms of the output from each model. The actual time steps used within each model might be quite different; however, they would be run until they had each provided output over the chosen time step. This approach will be discussed in this section.

At one time OCSEAP thought it desirable to have one comprehensive model to describe ice trajectories, oil trajectories, oil weathering, and fate. Another approach, however, is to isolate each model where possible and to perform the calculations sequentially. The sequential approach simplifies each calculation and allows the oil spill behavior and fate to be recalculated by different methods without recalculating the ice and ocean motion fields. There are situations in which this speed and flexibility is desirable.

Such an approach, however, may require more user interaction with the model than is desired.

A flow chart of the sequential approach is shown in Figure 7. As the flow in the figure shows, environmental and oil spill data must be entered to the models. First the code must determine whether the location of the spill is nearshore or offshore. Only if the spill is nearshore is the COZOIL Model used. In most ways, this model is complete since it has weathering, circulation, and fate combined in it. However, for offshore spills, the Weathering, Circulation/Trajectory, and Oil/SPM Models could be operated independently. At present there is a weathering module within the Circulation/Trajectory Model which one would suppress in favor of using the Weathering Model. The Oil/SPM Model is a one-dimensional model looking at vertical variations; it could be applied to vertical variations of oil transported using the Circulation/Trajectory Model from the previous time step. If the oil spill involved both nearshore and offshore regions, then all four models would be used and the new oil spill volume, location, and oil type would be combined for both nearshore and offshore to describe the new spill. The major advantages of this sequential operation are that each model can operate on its appropriate time and space scales and that the results are brought together only after the operation of each model. The primary disadvantage of the sequential approach is that by separating the physics into the component models, the optimal solution for the physics may not be obtained.

2. Develop a Code Based on the Circulation/Trajectory Model

Another approach is to fully integrate two or more of the models using common data sets, time steps, grid sizes, and sharing data between time steps for full coupling of the models. For example, (1) use the Weathering, Circulation/Trajectory, and Oil/SPM Models and incorporate features from the COZOIL Model for the nearshore area, or (2) add open ocean circulation to the COZOIL Model and improve the Oil/SPM and Weathering features with those codes. The models are used on a time step (to be determined) to define a new oil spill and the fate of the oil over this time step. The process continues until the quantity of oil remaining is insignificant.

If the four models are to be integrated with one model as the central link pin, then the Circulation/Trajectory Model is the clear candidate. Essentially, the Weathering Model has been previously incorporated into the circulation model. The COZOIL Model has most of the features of the other three models built in, with the additional feature of interaction with the beach. However, the COZOIL Model treats the oceanography in a considerably simpler manner than the Circulation/Trajectory Model. Therefore, if one is seeking a single code developed from the four, it would seem advisable to extend the oceanography in the Circulation/Trajectory Model to the nearshore and incorporate the oil

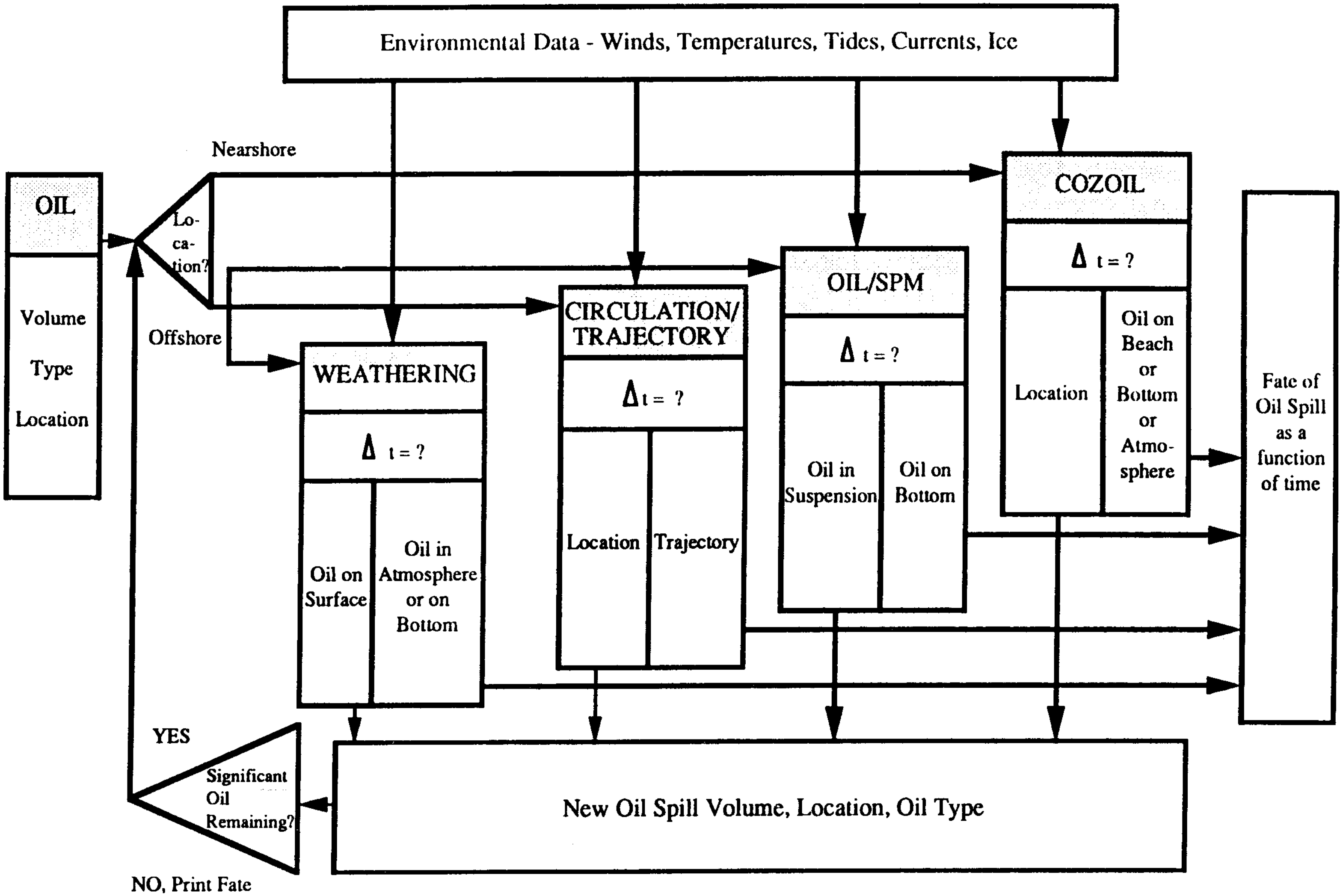

Figure 7. Sequential Approach

interaction with the beach from the COZOIL Model. Following this line then, the Circulation/Trajectory Model can provide the structure to integrate the Weathering and COZOIL Models. The Oil/SPM Model appears to couple sensibly with the Circulation/Trajectory Model. The difficulty is that the Oil/SPM Model is concerned only with the rate of change in the vertical profile of suspended oil and solid particulate. Horizontal advection and diffusion are not considered. Probably the simplest way to couple the Oil/SPM effects would be, however, to rewrite the subsurface transport module in the Circulation/Trajectory Model. This would not be a trivial task, but, at present, no simple realistic coupling appears possible. The problems of coupling the Oil/SPM code to the other physics is comparable to coupling the Weathering Model to the Circulation/Trajectory code, which has already been done.

This approach of using the Circulation/Trajectory Model as the cornerstone to the model integration retains most of the previous code development and provides for a unified model. However, it should be pointed out that the documentation for using the Circulation/Trajectory Model is lacking in many ways and, therefore, code documentation will be a significant effort. Also, amassing data for input to the Circulation/Trajectory code as it presently stands is a lengthy task requiring a knowledgeable operator.

3. Develop a New Code from the Model Physics

A third option for the development of a unified model from the four existing models would be to start with the physics and chemistry as described in the basic equations that underlie the models and develop a new unified code. Such an approach has many advantages. One advantage is code efficiency, since each physical process would only be considered once. A second is numerical optimization, in that all required numerical schemes could be considered simultaneously. Also, the unified code could be tailored to a specific given computer hardware and/or tailored to available, commercial software for handling the input/output as well as pre- and post-processing, etc. With proper architecture, the new code could have the features of being updated easily later. This approach has one major disadvantage in that it does not utilize the considerable effort which has already been expended in model development. It will therefore be the most costly of the three approaches discussed here. If, however, a single model is desired, it will lead to the optimum model when properly exercised, debugged, and documented.

SECTION V
COMBINED OIL FATE MODEL DEVELOPMENT

In general, the combined oil fate model will consist of input/output software, some combination of the existing four oil spill models, new oil spill model features to be developed, and the required database. The effort to develop these code segments has been divided into the four tasks described in Section A below. These tasks were then combined into various combinations to assess the development effort required to create the desired combined model.

A. COMPONENTS OF DEVELOPMENT EFFORT

The development of the combined code will involve the following four tasks:

Task 1 - Development of Input/Output Software

Task 2 - Combined Oil Spill Model Development

Task 3 - Addition of Missing Features

Task 4 - Acquisition of Databases

The required levels of effort for Tasks 1 and 2 depend upon priorities yet to be established. Consequently, several options are described for Tasks 1 and 2 in the following. Table 6 provides relative estimates for the levels of effort for each of these task options. Programmatic decisions regarding the exact scope of each task are required before more precise estimates can be made.

Task 1a - Development of Input/Output Software with Simple Architecture
Use a minimum, simple architecture which can be operated by a knowledgeable person experienced in oil spill modeling.

Task 1b - Development of Menu-Driven Input/Output Software
Develop menu-driven input/output software which will guide the generation of input data, perform data transfer between I/O routines and the oil spill models, and produce the desired output plots, all with a few key strokes.

Table 6. Development Effort by Task, by Skill Type, in Man-Months

DEVELOPMENT TASK		TASK TITLES	OCEANOGRAPHER, ATMOSPHERIC SCIENTIST, CHEMIST	NUMERICAL ANALYIST	SYSTEMS ANALYIST, SENIOR PROGRAMMER	PROGRAMMER	TOTAL
1	a	Development of Input/Output Software with Simple Architecture	—	—	2	4	6
	b	Development of Menu-Driven Input/Output Software	—	—	4	8	12
2	a	Combined Existing Oil Spill Models	—	—	4	8	12
	b	Combined Model Based on Circulation/Trajectory Model	4	3	3	8	18
	c	New Integrated Oil Spill Model	4	8	4	8	24
3		Addition of Missing Features	16	2	2	4	24
4*		Acquisition of Databases	—	—	—	—	—

* A Database is Needed, but It Does Not Effect the Model Development

Task 2a - Combine Existing Oil Spill Models

Combine the four existing oil spill models as they stand with an executive program that will allow each program to run by itself or in a linked mode, passing a minimum of data between models.

Task 2b - Combined Model Based on Circulation/Trajectory Model

Build a model around the Circulation/Trajectory Model by combining the vertical SPM model with the Circulation/Trajectory Model's transport through the water column, adding the Weathering Model components not all ready in the Circulation/Trajectory Model, and adding the surf zone and beach interaction features from the COZOIL Model.

Task 2c - New Integrated Oil Spill Model

Develop a new integrated oil spill model by starting with the physio-chemical equations from each existing model, coding a coupled, simultaneous solution technique, and optimizing the resulting code.

Task 3 - Addition of Missing Features

Improve the existing four oil spill models by adding the missing and inadequate features discussed in Section IV, Heading B, Subheading 4.

Task 4 - Acquisition of Databases.

Build the climatological, bathymetric, and oil characterization databases needed for the running the combined model.

B. ASSESSMENT OF DEVELOPMENT EFFORT

The development effort will depend strongly upon the selected levels of effort for each task. Table 7 delineates various sets of the task options, discusses the advantages and disadvantages of various sets, and provides the total level of effort based on the estimates in Table 6. No estimates for the levels of effort for building a database have been made. The estimates will be required but are separate from the model. Many task option sets were rejected outright since they would produce an unbalanced level of detail in various aspects of the code. Set 1 would combine the four models with no improvements and would not

Table 7. Description of Possible Combined Models

SET	TASKS FROM TABLE 6	COMMENTS	PERSON-MONTHS * OF DEVELOPMENT
1	1a, 2a	Adequate, Low Cost	18
2	1a, 2a, 3	Not User Friendly, Better Than Set 1	42
3	1a, 2b	Good Spill Model, Not User Friendly	24
4	1a, 2b, 3	Too Much on Spill Model, Not Enough on Input/Output	48
5	1a, 2c	Too Much on Spill Model, Not Enough on Input/Output	30
6	1a, 2c, 3	Too Much on Spill Model, Not Enough on Input/Output	54
7	1b, 2a	User Friendly but Too Much on Input/Output, Not Enough on Models	24
8	1b, 2a, 3	User Friendly but Too Much on Input/Output, Not Enough on Models	48
9	1b, 2b	User Friendly, Balanced Model, Moderate Cost	30
10	1b, 2b, 3	Improvement of Model 9	54
11	1b, 2c	Good Single Model	36
12	1b, 2c, 3	Best of Everything	60

* Does Not Include Database Acquisition

be very user-friendly. However, it would require the least effort. Other than Set 1, the next sets that seem reasonable are Sets 9-12. Set 9 is balanced between operating the system and oil spill model. Set 10 improves the model by including the missing features of Section IV, Heading B, Subheading 4. Sets 11 and 12 are like Sets 9 and 10 but with a simple model for the spill. In summary, Sets 1, 9, and 12 provide a broad range of reasonable choices for the further development of these oil spill models. A final selection among these three cannot be made without additional information, such as the eventual applications of the combined model and the development funds available.

SECTION VI
CONCLUSIONS

BDM has examined the four oil spill models provided by the government for this study. Eight basic oil spill scenarios were considered for the Alaskan OCS region. Redundant model features and missing model features have been identified. Various methods for combining the computer codes were compared. Three sets of the following tasks were selected:

Task 1 - Development of Input/Output Software

Task 2 - Combined Oil Spill Model Development

Task 3 - Addition of Missing Features

Task 4 - Acquisition of Databases

A low cost task set is to develop the I/O software with simple architecture, combine the existing oil spill models in the simplest manner, and prepare a database, without addressing the missing features. An intermediate task set is to develop menu-driven I/O software, combine the four oil spill models around the Circulation/Trajectory Model, and prepare a database, again without addressing the missing features. The top of the line task set is to develop menu-driven I/O software, develop a new integrated oil spill model, add code to address the missing features, and to prepare a database. It is recognized, however, that the final selection will depend strongly upon the desired applications of the combined code and the funds available.

The combined oil fate model should have a shelf life of five years if individual models are updated to reflect new field data and test results. Incorporating the most significant missing model features (e.g. adding sea ice to the COZOIL Model) will greatly strengthen the combined model. Also, more user-friendly input and output procedures would increase utilization and productivity of the models.

SECTION VII
REFERENCES

Coon, M. D. and R. S. Pritchard. 1979. "The Transport and Behavior of Oil Spilled in and Under Sea Ice." *Annual Report to Outer Continental Shelf Environmental Assessment Program on Research Unit 567.* National Oceanic and Atmospheric Administration. Boulder, CO.

Isaji, T. and M. Spaulding. 1987. "A Numerical Model of the M_2 and K_1 Tide in the Northwestern Gulf of Alaska." *Journal of Physical Oceanography.* 17:698-704.

Kana, T. W., E. R. Gundlach, M. Reed, S. Jonathan Siah, P.D. Boehm, A. Requejo, and M. Spaulding. 1986. "Development of a Coastal Oil Spill Smear Model, Phase I: Analysis of Available and Proposed Models." *OCS Study MMS 85-0098.* Prepared for Minerals Management Service, Anchorage, Alaska, March.

Kirstein, B. E. and R. T. Redding. 1987. "Ocean-Ice Oil-Weathering Computer Program Users Manual." *OCSEAP Contract no. 84-ABC-00121 (RU 664).* July.

Mackay, D., I. Buist, R. Mascarenhas and S. Paterson. 1980. *Oil Spill Processes and Models.* Research and Development Division, Environmental Emergency Branch, Environmental Impact Control Directorate, Environmental Protective Service, Environment Canada, Ottawa, Ontario, K1A 1C8.

Martin, S. 1977. "The Seasonal Variation of Oil Entrainment in First Year Sea Ice: A Comparison of NORCOR/OCS Observations." Dept. of Oceanography, Spec. Report #71, University of Washington, March.

Mountain, D. G. 1974. "Bering Sea Water in the North Alaskan Shelf." Ph.D. Dissertation, University of Washington, Seattle.

Payne, J. R., B. E. Kirstein, G. D. McNabb, Jr., J. L. Lambach, R. Redding, R. E. Jordan, W. Hom, C. deOliveira, G.S. Smith, D.M. Baxter, and R. Gaegel. 1984a. "Multivariate Analysis of Petroleum Weathering in the Marine Environment - Sub Arctic, Volume I - Technical Results." *OCSEAP Contract No. NA 80 RAC 00018 (RU 597), OCSEAP Final Reports Volumes 21 and 22,* January and February.

Payne, J. R., G. D. McNabb, Jr., B. E. Kirstein, R. Redding, J. L. Lambach, C. R. Phillips, L. E. Hachmeister, and S. Martin. 1984b. "Development of a Predictive Model for the Weathering of Oil in the Presence of Sea Ice." *Final Report on Outer Continental Shelf Environmental Assessment Program (OCSEAP), Contract No. 83-ABC- 00062 (RU 640).* November.

Payne, J. R., B. E. Kirstein, J. R. Clayton, Jr., C. Clary, R. Redding, D. McNabb, Jr., and G. Farmer. 1987. "Integration of Suspended Particulate Matter and Oil Transportation Study." *OCS Study MMS 87-0083*. Prepared for Minerals Management Service, Anchorage, Alaska, September.

Reed, M. 1987. "A Coastal Zone Oil Spill Model," Oseanografisk Senter, Trondheim, Norge, Oktober.

Reed, M., C. Turner, A. Odulo, T. Isaji, S. Sorstrom, J. Mathisen. 1990. "Field Evaluation of Satellite-Tracked Surface Drifting Buoys Simulating the Measurement of Oil Spilled in the Marine Environment." Final Report to USDOI MMS, Atlantic Regional Office, MMS Contract No. 14-35-0001-30485, in review.

Schwiderski, E. A. 1979. "Ocean Tides II; a Hydrodynamic Interpolation Model." *Journal of Marine Geology*. 3:219-255.

Schwiderski, E. A. 1981. "Global Ocean Tides: Part I - Global Ocean Tides: A Detailed Hydrodynamical Interpolation Model." *NSWC DL-TR- 3866*. "Part II - The Semidiurnal Principal Lunar Tides (M_2) Atlas of Tidal Charts and Maps." *NSWC TR-79-414*. "Part IV - The Diurnal Lunisolar Declination Tide (K_1) Atlas of Tidal Charts and Maps." *NSWC TR-81-142*. Naval Surface Weapons Center, Dahlgren, Virginia.

Spaulding, M., T. Isaji, D. Mendelsohn, and A. C. Turner. 1987. "Numerical Simulation of Wind-Driven Flow Through the Bering Strait." *Journal of Physical Oceanography*. 17:1799-1816.

Spaulding, M. L., K. Jayko, T. Isaji, and E. Anderson. 1988. "Coastal Sea Model System User's Manual." Applied Science Associates, Inc. Report No. ASA-85-04 to NOAA/OCSEAP (3 volumes).

U.S. DEPARTMENT OF COMMERCE
NATIONAL OCEANIC AND ATMOSPHERIC ADMINISTRATION
NATIONAL OCEAN SERVICE

Alaska Office
Federal Bldg., U.S. Courthouse, Room A13
222 W. Eighth Ave., #56
Anchorage, Alaska 99513-7543

UNIV OF ALASKA/INFO SERVICES
ARCTIC ENV INFO AND DATA CTR
707 A STREET
ANCHORAGE, AK 99501